UNIVERSITY OF COPENHAGEN

The particle physics discovery potential in the ultra-high-energy neutrino era

DOCTORAL THESIS

by

VÍCTOR BRANCO VALERA BACA

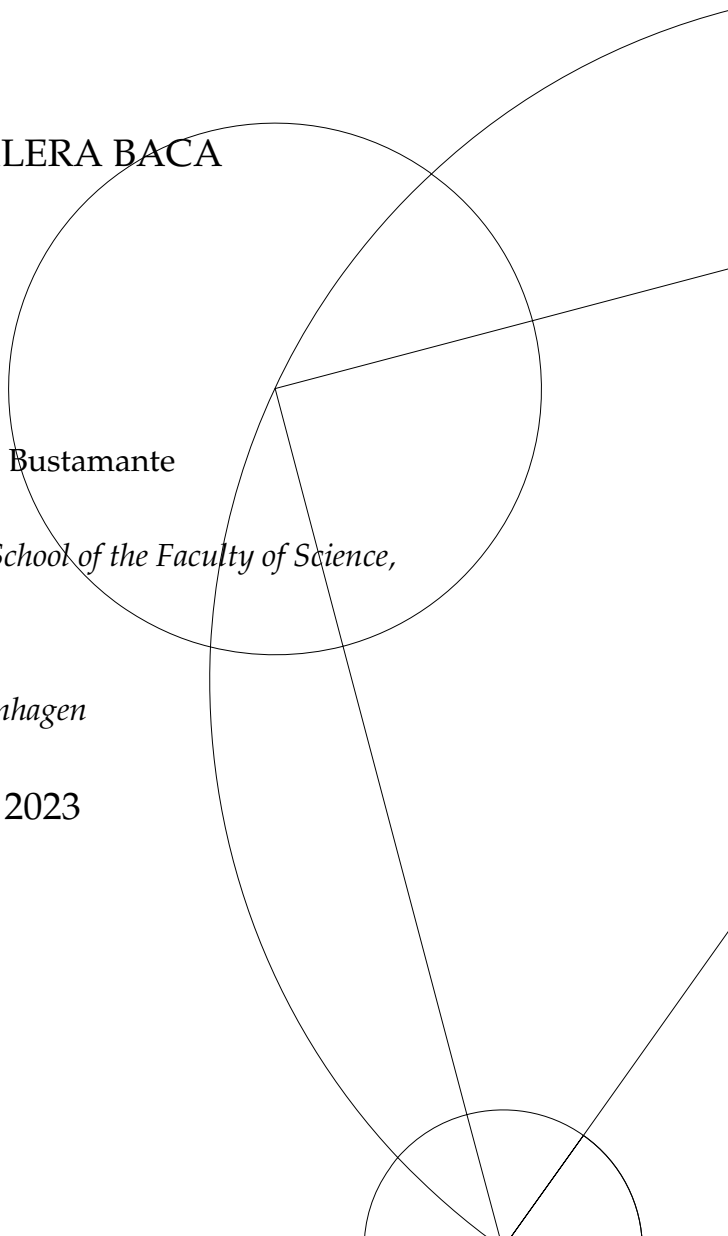

Supervised by Mauricio Bustamante

This thesis has been submitted to the PhD School of the Faculty of Science,

University of Copenhagen

September 30, 2023

A la mamá Mery, Fernan, y el abuelo loco.

Quienes a pesar de no poder ver este momento,

nunca dudaron de que lo lograría

ABSTRACT

Ultrahigh-energy (UHE) neutrinos, with energies in the EeV (10^{18} eV) range, are a promising new probe of astrophysical and particle physics phenomena. In a Universe where opacity and magnetic fields hinder the passage of high-energy cosmic rays and gamma rays, UHE neutrinos provide an unobstructed view of the most energetic and distant astrophysical phenomena. Nevertheless, UHE neutrinos remain undiscovered so far due to their very low expected flux. This thesis explores the transformative potential of UHE neutrinos in the fields of astrophysics and particle physics, motivated by the upcoming availability of UHE neutrino telescopes with sensitivities that hold the potential of finally discovering EeV neutrinos in the near future.

The research employs advanced simulations, detailed theoretical modelings, and statistical analyses to assess the prospects of discovering UHE neutrinos in the energy range of 10^{16} eV to 10^{19} eV. Comprehensive investigations consider factors such as experimental designs, energy and angular resolution, neutrino absorption inside the Earth, and background contamination to determine the discovery potential of future UHE neutrino telescopes.

The first part of this thesis presents a broad overview of neutrinos, from their proposal as the solution to the anomalies observed in the beta decay energy spectrum, to their role in the latest developments of multimessenger astronomy. The origin of UHE neutrinos from the interaction of ultra-high-energy cosmic rays with background radiation and the involved kinematics is discussed. Next, a brief review of the experimental landscape in the context of astrophysical neutrinos is presented. This shows the status of current and future neutrino telescopes with sensitivity in the UHE range, as well as their corresponding detection techniques. Finally, the research opportunities with UHE neutrinos explored in this thesis are discussed.

The second and third part of the thesis, present the results from the research projects concluded during the doctoral studies of the PhD candidate. The second part focuses on the potential of UHE neutrino telescopes to discover the diffuse flux of UHE neutrinos and to provide the first measurement of the neutrino-nucleon cross section at ultra-high energies. This part of the thesis

introduces a framework for computing the number of UHE neutrino events in radio-based UHE neutrino telescopes. This framework encompasses neutrino propagation within Earth, state-of-the-art predictions of the neutrino-nucleon cross section, radio signal generation in ice, and detector response. In combination with advanced numerical methods for performing statistical inference on complex parameter spaces, this framework underpins a series of investigations aimed at revealing the full potential of UHE neutrinos. The second part of the thesis shows that a detector like the radio component of IceCube-Gen2 can unveil benchmark models of the diffuse UHE neutrino within a decade of exposure. Furthermore, it is also possible to simultaneously infer the neutrino-nucleon cross section at the highest energies.

The third part of the thesis explores the physics opportunities that the discovery of EeV neutrino can bring. In particular, it studies the cases of identifying point sources of UHE neutrinos and the use of UHE neutrino telescopes for dark matter detection. The point source study uses multiplet-based searches to set constraints on the properties of populations of UHE neutrino sources and possibly unveil the origin of the most energetic particles in Nature, ultra-high-energy cosmic rays. The dark matter study reveals the feasibility of detecting signatures of heavy dark matter decay into neutrinos against a non-dark matter neutrino background.

In closing, the research presented in this thesis is relevant to the upcoming availability of UHE neutrino telescopes. The findings of this thesis reveal the exciting possibilities that UHE neutrinos offer for advancing our understanding of astrophysics and particle physics. UHE neutrinos can provide a unique window into the most energetic and distant astrophysical phenomena, such as the sources of ultra-high-energy cosmic rays and the early Universe. Additionally, UHE neutrinos can be used to contrast our understanding of the Standard Model and probe new theories of physics beyond the Standard Model. The discovery of UHE neutrinos would be a major breakthrough in astroparticle physics. It would open up a new era of discovery and allow us to explore the Universe from a new perspective.

ABSTRAKT

Ultra-høj-energi (UHE) neutrinoer, med energier omkring EeV (10^{18} eV), udgør en lovende ny måde at undersøge astrofysiske og partikelfysiske fænomener på. I et univers hvor opacitet og magnetfelter hindrer passage af høj-energi kosmiske stråler og gammastråler, giver UHE neutrinoer en uhindret udsigt til de mest energiske og fjerne astrofysiske begivenheder. Ikke desto mindre forbliver UHE neutrinoer hidtil uopdagede på grund af deres meget lave forventede flux. Denne PhD-afhandling udforsker det transformative potentiale af UHE neutrinoer inden for astrofysik og partikelfysik, motiveret af den forestående tilgængelighed af UHE neutrinoteleskoper med en sensitivitet, der har potentiale til endelig at opdage EeV neutrinoer i den nærmeste fremtid.

Forskningen anvender avancerede simuleringer, detaljerede teoretiske modelleringer og statistiske analyser for at vurdere udsigterne til at opdage UHE neutrinoer i energiområdet fra 10^{16} eV til 10^{19} eV. Omfattende undersøgelser tager hensyn til faktorer som eksperimentelt design, energi- og vinkelopløsning, neutrinoabsorption i Jorden og baggrundskontaminering for at bestemme opdagelsespotentialet for fremtidige UHE neutrinoteleskoper.

Den første del af denne afhandling præsenterer et bredt overblik over neutrinoer, fra deres forslag som løsningen på de anomalier der er observeret i energispektret for beta-henfald, til deres rolle i de seneste udviklinger inden for multimessenger-astronomi. Oprindelsen af UHE neutrinoer fra interaktionen mellem ultra-høj-energiske kosmiske stråler og baggrundsstråling samt de involverede kinematikker diskuteres. Derefter præsenteres en kort gennemgang af det eksperimentelle landskab inden for astrofysiske neutrinoer, der viser status for nuværende og kommende neutrinoteleskoper med sensitivitet i UHE-området samt tilhørende detektionsteknikker. Endelig diskuteres de forskningsmuligheder for UHE neutrinoer, der udforskes i denne afhandling.

Den anden og tredje del af afhandlingen præsenterer resultaterne fra de publikationer, der blev afsluttet under doktorandens ph.d.-studier.Anden del fokuserer på potentialet for UHE neutrinoteleskoper til at opdage den diffuse flux af UHE neutrinoer og give den første måling af neutrino-nukleon tværsnittet ved ultra-høje energier. Denne del af afhandlingen introducerer

rammebetingelser for beregning af antallet af UHE neutrinohændelser i radio-baserede UHE neutrinoteleskoper. Disse rammebetingelser omfatter neutrino-propagation inden i Jorden, state-of-the-art forudsigelser af neutrino-nukleon tværsnittet, generering af radiosignaler i is og detektor-respons. Dette kombineres med avancerede numeriske metoder til udførelse af statistiske inferenser i komplekse parameterområder. Denne opsætning udgør grundlaget for en række undersøgelser, der har til formål at afsløre UHE neutrinoernes fulde potentiale. Denne del af afhandlingen viser, at en detektor som radio-komponenten af IceCube-Gen2 kan afsløre benchmark-modeller for den diffuse UHE neutrino flux inden for et årti af eksponering. Desuden er det også muligt samtidigt at udlede neutrino-nukleon tværsnittet ved de højeste energier.

Den tredje del af afhandlingen udforsker de fysiske muligheder, som opdagelsen af EeV neutrinoer kan bringe. Især studerer den tilfældene af at identificere punktkilder til UHE neutrinoer og bruge UHE neutrinoteleskoper til observationer af mørkt stof. Studiet af punktkilder anvender multiplet-baserede søgninger for at fastlægge begrænsninger på egenskaberne hos populationer af UHE neutrino-kilder og muligvis afsløre oprindelsen af de mest energiske partikler i naturen, ultra-høj-energi kosmiske stråler. Undersøgelsen af mørkt stof afslører muligheden for at opdage signaturer af tungt mørkt stof, der henfalder til neutrinoer, mod en baggrund af ikke-mørkt stof neutrinoer.

Afslutningsvis er den forskning, der præsenteres i denne afhandling, relevant i lyset af den kommende tilgængelighed af UHE neutrinoteleskoper. Resultaterne af denne afhandling afslører de spændende muligheder, som UHE neutrinoer tilbyder for at fremme vores forståelse af astrofysik og partikelfysik. UHE neutrinoer kan give et unikt vindue til de mest energiske og fjerne astrofysiske begivenheder, såsom kilderne til ultra-højenergetiske kosmiske stråler og den tidlige univers. Derudover kan UHE neutrinoer bruges som kontrast til vores forståelse af Standardmodellen og undersøge nye teorier inden for partikelfysik ud over Standardmodellen. Opdagelsen af UHE neutrinoer ville være et gennembrud inden for astropartikelfysik og ville åbne en ny æra af opdagelse og tillade os at udforske universet fra et ny perspektiv.

THESIS OUTLINE

The thesis is divided into five parts:

- Part I: Introduction
- Part II: Measuring the UHE neutrino flux
- Part III: Exploiting the UHE neutrino flux
- Part IV: Summary and conclusions
- Part V: Appendices

Part I offers a broad introduction to the topic of multimessenger astronomy and ultra-high-energy neutrinos, as well as the main physical concepts and phenomena discussed along the thesis. Parts II and III of this thesis consist of the reprints of the following published journal articles

1. **Víctor B. Valera Baca**, Mauricio Bustamante, Christian Glaser, *The ultra-high-energy neutrino-nucleon cross section: measurement forecasts for an era of cosmic EeV-neutrino discovery*, JHEP06(2022)105, arXiv:2204.04237
2. **Víctor B. Valera Baca**, Mauricio Bustamante, Christian Glaser, *Near-future discovery of the diffuse flux of ultra-high-energy cosmic neutrinos*, Phys. Rev. D 107, 043019, arXiv:2210.03756
3. **Víctor B. Valera Baca**, Mauricio Bustamante, Olga Mena, *Joint measurement of the ultra-high-energy neutrino spectrum and cross section*, arXiv:2308.07709, sent for publication to Physical Review D.
4. Damiano F. G. Fiorillo, Mauricio Bustamante, **Víctor B. Valera Baca**, *Near-future discovery of point sources of ultra-high-energy neutrinos*, JCAP03(2023)026, arXiv:2205.15985
5. Damiano F. G. Fiorillo, **Víctor B. Valera Baca**, Mauricio Bustamante, Walter Winter, *Searches for dark matter decay with ultra-high-energy neutrinos endure backgrounds*, arXiv:2307.02538, accepted for publication in Physical Review D.

Each chapter of the thesis corresponding to a given publication includes a section called "Critical Outlook", which provides a brief overview of the project, its context, and a critical discussion of the findings of the corresponding publication. Part II consists of publications 1, 2, and 3, while Part III consists of publications 4 and 5. Publications 3 and 5 are available as pre-prints and are currently under in the journals that they have been submitted to.

Part IV summarizes the main findings and results of this research, discusses some of the limitations of the field, and suggests directions for future research. Finally, Part V contains the appendices of the publications that are not included in the main body of the thesis.

ACKNOWLEDGEMENTS

A PhD is a long run, not only a run impossible to complete alone, but one that is not worth running on your own. For the past three years I have grown in a personal, academic, and professional way; achieving goals that make me truly proud of myself. However, it would be far from the truth to claim that I owe this achievement only to myself. This Section is dedicated to all the people who have been part of this long run, and without whom, any goal achieved would have not been possible or would be nothing but an empty trophy.

Antes que nada, debo dedicar este logro a las personas responsables de cada logro en mi vida, grande o pequeño, mis padres; ustedes son mi más grande inspiranción. Gracias por todos los consejos y su apoyo constante. Incluso, y especialmente, cuando tomé la extraña y arriesgada decisión de estudiar Física, una carrera plagada de retos e incertidumbres. Ustedes nunca dudaron de mi, ni siquiera en los momentos cuando yo dudé de mi mismo. A mi hermana, Mayte, quien ha estado a mi lado desde que tengo memoria, y cuya fortaleza y resilencia admiro inmensamente. A mi sobrino Mateo, quien tuvo un rol importante en mi carrera, llorar incansablemente por las noches para evitar que me duerma y pueda terminar mi trabajo. Verte crecer, de la mano de mi hermana, es una gran inspiración. Así también, no puedo dejer de mencionar a la Fochi y su inacabable cariño, gracias por mantener la casa siempre llena de invitados y en constantes fiestas que me recuerdan que tan grande es mi familia. Gracias en general a toda mi familia, a mis incontables tíos y primos, a quienes debo muchos de los mejores recuerdos en mi vida.

I would like to express my sincere gratitude to my supervisor, Mauricio Bustamante, for being a mentor and an inspiration during these years of PhD. I am grateful for your dedication and commitment with my academic growth. Thank you for the long hours dedicated to scientific discussions, specially those in which we disagreed, since they were by far the most stimulating ones. I am confident you will agree. When I was applying for PhD positions, someone told me to apply to as many places as possible, because it only takes one person to make the mistake of giving

me an opportunity for me to show what I can do. Thanks for making that mistake and believing in me as a young scientist who could aim to earn a PhD.

Adesso devo cambiare ancora una volta linguaggio per ringraziare la persona che mi è stata accanto in questi tre anni. La mia amica, compagna e collega Ersilia. Grazie per essere un supporto costante e per avermi permesso di avere un pezzo di casa qui a Copenaghen. Non riesco a immaginare come sarebbe stato questo viaggio senza di te. Insieme ad Ersilia è arrivato nella mia vita un gruppo di persone meravigliose. È dura essere così lontano da casa, ma mi hanno aperto le porte della loro casa e della loro città e mi hanno accolto come uno di famiglia. Grazie Mimmo, Rosa, Giusy e Martina; e grazie a tutta la mia famiglia di Trani. Grazie anche a tutti gli amici che ho conosciuto in questa bellissima città, per tutte le birre e le feste, e tante altre ancora in arrivo.

Back to English. I am very grateful to the friends and colleagues I met during the PhD. From the very first person I met at the Niels Bohr Insitute (NBI): an overwhelmed Ian who barely found time to opened me the door while he was in between presentations in a Journal Club and a seminar. He only had time to said to me: "For now sit there, we'll go for beers when I am done". That is how you know the next three years will be amazing. During the next three years I met a wonderful group of people at NBI. Thanks to Enrico Peretti for being a good friend and mentor, he holds the ultimate Swiss Knife for moving in the jungle of the academic world and there is so much I learned from him. Thanks to Damiano Fiorillo for being the kind of scientific collaborator everyone should aspire to become, if you are not trying to be like him you are simply doing everything wrong. Thanks to Kays Haddad, Annia Suliga, Tania Pitik, and Yoann Genolini, with whom, together with Ersilia, I survived the first part of my PhD, marked by the lock-down an the limited social activities due to a global pandemic.

During the second part of my PhD things were coming back to normality, and this allowed me to meet new great people arriving at NBI and also travel abroad for either conferences or research visits, always finding great hosts. Let me express my thanks to Youyou Li, Marina De Amicis, Pedro Dedin, Marie Cornelius Hansen, Evelyn-Andreea Ester, Bernanda Telalovic, Kathrine Mørch Groth, Shashank Shalgar, Annika Rudolph, Markus Ahlers, Rasmus Hansen, Edoardo Vitagliano, Manuel Goimil García, and Aysu Arat; for making of NBI an alive environment where we can work together, support each other, and laugh non-stop. It is sad we never found the size of the

grain. I am also thankful to three particular individuals, Tania Kozynets, Antonio Capanema, Kevin Urquia, whom I previously had met somewhere else far from Copenhagen and to whom I did not expect to see again, but having them here is a reminder to me of how small the world i.

During the PhD I visited Valencia, thanks to hospitality of Olga Mena. Thank you Olga for being a great mentor and collaborator, and for always making science an exciting thing. In Valencia, I was welcome by a great environment, and I want to express my gratitude to Giacomo Landini, Nico Loayza, Federica Pompa, Rasmi Hajjar, Pablo Matínez Miravé, Catarina Cosme, Francesco Di Meglio, and Sergio Palomare Ruiz. I hope our paths can cross again in the future. I also want to give special thanks to Christian Glaser, with whom we had two years of successful scientific collaboration. I also want to thank Kumiko Kotera for her mentorship and support, and for being an inspiring scientist. Similarly, I am grateful to Walter Winter for a great scientific collaboration.

In the preamble of this journey I have been supported by the unconditional friendship of some of the best people I know in the world. Gracias a Luis Angel Gutierrez, Carlos Cirilo, y William Bernal por los momentos compartidos desde que teníamos 4 años!. Hoy estamos muy lejos, pero volver a verlos es como si el tiempo no hubiera pasadao jamás. Gracias también Eduardo Angulo, Beto Gutierrez, Junior Espinoza, y Gerald Carranza por los años heroicos de la secundaria ¿Quien diría que solo hace falta un sol para ir a una fiesta?. Ya en la universidad, tuve la fortuna de conocer grandes amigos y colegas, en particular al "mustar code": Coco Benel, Miguel Piñeiro, Fabio Menacho, Henry Rios, Jorge Romero, Fabrizzio Ferreyros, Daniel, Melvin, Joel, y Diego (quizá me está faltando un puntero). Ojalá pronto salga la parrilla. Una parte fundamental de mi desarrollo como científico fue el haber sido parte del Grupo Astronomia, donde conocí a grandes amigos y colegas. Muchas gracias a Erika Torre, Diego Alvarado, Ysaac Suaña, Karol, Katty Aybar, el Prof. Julio Tello, William Core, and Sergio Nuñez. Agradezo profundamente también a grandes amistades como Katherine Miranda y Macarena Tolmos. Finalmente, un agradecimiento muy especial a Luz Saavedra, la persona más motivadora en el mundo.

Finally, all the emotional and intellectual support would not make anything possible without a key ingredient. My deepest gratitude to the VILLUM FONDEN for supporting this thesis project under the project no. 29388.

CONTENTS

Todo aquel que piense que la vida siempre es cruel

Tiene que saber que no es así

Que tan solo hay momentos malos y todo pasa

Todo aquel que piense que esto nunca va a cambiar

Tiene que saber que no es así

Que al mal tiempo, buena cara, y todo cambia

La vida es un carnaval by Celia Cruz

My English is not very good looking.

by Celia Cruz

Part I

INTRODUCTION

1

MOTIVATION

The history of neutrino physics is a long and fascinating one. The first hints of the existence of neutrinos came in 1930 when Wolfgang Pauli proposed the existence of a new neutral massless particle to explain the energy and momentum balance in beta-decay observations. However, it was not until 1956 that neutrinos were first detected experimentally by Frederick Reines and Clyde Cowan [1]. They observed reactor electron antineutrinos ($\bar{\nu}_e$), through the inverse beta decay process. Since then, neutrinos have gone from particles that could not be detected, to be key for pushing forward our understanding of fundamental particle interactions. We have learned a great deal about neutrinos, including their properties, their interactions with matter, their potential to unveil hints of new physics, and their role in astrophysics and cosmology.

Neutrinos, or the *little neutral ones*, are fundamental particles in the Standard Model of particle physics. They are massless neutral fermions (spin 1/2) that come in three flavors: electron (e), muon (μ), and tau (τ) neutrinos. This picture would be challenged when the discovery of neutrino oscillations suggested that neutrinos have non-zero masses. Neutrino oscillation is the phenomenon that describes the transformation or oscillation of neutrinos from one flavor to another as they travel through space. This happens because the neutrino flavor eigenstates and the neutrino mass eigenstates are not the same. The formal description of neutrino oscillation involves the Pontecorvo-Maki-Nakagawa-Sakata (PMNS) matrix [2, 3], which is analogous to the quark flavor mixing matrix in the Standard Model of particle physics. The PMNS matrix describes the transformation between the flavor and mass eigenstates of neutrinos. Neutrino oscillation experiments have provided evidence for non-zero neutrino masses and mixing angles, confirming that neutrinos do not have definite flavors but exist as mixtures of the three flavor states as they propagate.

The discovery of neutrino oscillation was a extended and winding road. It involved multiple, different experiments, and it took time to realize that they were converging on the same phe-

nomenon. The first hints of neutrino oscillation came from the Homestake experiment, which was conducted between 1968 and 1998 [4]. This experiment detected a deficit of solar neutrinos compared to the theoretical expectations [5–7], which could be explained by neutrino oscillations. However, the results of the Homestake experiment were not conclusive, and at the time the possibility of an incomplete understanding of nuclear physics inside the Sun was also considered as a potential explanation of the neutrino deficit. More experimental evidence was needed to solve the puzzle. One of the most important experiments was the Kamiokande experiment, which was conducted between 1983 and 2001 [8]. This experiment also detected a deficit of solar neutrinos, and provided more precise measurements of the oscillation parameters. The Super-Kamiokande experiment, which has been operating since 1996, has confirmed the results of the Homestake and Kamiokande experiments [9], and has also made measurements of atmospheric neutrinos [10]. Another important experiment was carried out at the Sudbury Neutrino Observatory (SNO), and took place between 1999 and 2006. This experiment was designed to be sensitive to neutral current interactions of all neutrino flavors and charged current interactions for electron neutrinos. This particular design allowed SNO to directly compare the all-flavor neutrino flux to a single-flavor flux, hence measuring directly the electron neutrino deficit, and providing further confirmation of neutrino oscillations [11]. The KamLAND experiment, which has been operating since 2002, has measured the oscillation of reactor neutrinos, and has provided further constraints on the oscillation parameters [12].

The discovery of neutrino oscillations provided compelling evidence for claiming that neutrinos have non-zero masses, challenging the initial hypothesis that assumed they were massless. Each flavor eigenstate is a superposition of the three mass eigenstates. Since the mass eigenstates are not massless they do not travel at the speed of light. Instead, they travel at different speeds depending on the mass of each state, eventually leading to quantum decoherence, and this leads to the phenomenon of neutrino oscillation. While other particles in the Standard Model acquire mass through the Higgs mechanism, neutrinos appear to gain mass through a different mechanism due to the smallness of their mass and because in the Standard Model they are only left-handed particles, potentially hinting at new physics beyond the Standard Model. Although the nature of neutrino masses remains an unsolved puzzle, the discovery of neutrino oscillations has profound

implications for our understanding of neutrinos and their role in the Universe. It has also opened up new possibilities for neutrino astronomy, as it is now possible to use neutrinos to study the inner workings of distant objects, such as supernovae [13, 14] and active galactic nuclei [15, 16].

Parallel to the history of neutrino physics, during the 20th century it took place the development of the field of cosmic rays. In 1912, Victor Hess made the first definitive detection of cosmic rays, while conducting balloon experiments in the Austrian Alps [17]. Hess showed that cosmic rays are high-energy particles that originate from outside the atmosphere of the Earth. In the years since this discovery, much has been learned about cosmic rays. We now know that they are a diverse population of particles, including protons, nuclei of helium, and heavier nuclei. We also know that cosmic rays have a wide range of energies, from a few MeV to beyond 10^{20} eV [18].

Of particular interest for this thesis are ultra-high-energy cosmic rays (UHECRs), the highest-energy particles ever observed in Nature. They have energies that exceed 10^{18} eV. They were first observed in 1962 by the Fly's Eye experiment [19, 20], and their origin remains an open and important question, often referred to as the *Saint Graal* of particle astrophysics.

The sources of UHECRs can be classified as galactic and extragalactic sources [21–23]. Extragalactic sources produce UHECRs in distant galaxies, such as active galactic nuclei (AGNs) or gamma-ray bursts (GRBs). On the other hand, galactic sources produce UHECRs in our own galaxy, such as in supernova remnants (SNRs) or pulsar wind nebulae (PWNe). It is currently believed that a transition between a spectrum dominated by galactic sources to one dominated by extragalactic sources takes place at 10^{17} GeV. Extragalactic sources are related to the high-end of the UHECR spectrum as they can more easily explain the high energies of UHECRs. However, there are still some challenges with these models, such as the need to accelerate particles to very high energies and the need to transport them through the intergalactic medium without losing too much energy.

Some of the most recent observations of UHECRs have been made by the Pierre Auger Observatory in Argentina [24, 25]. The Pierre Auger Observatory is a large-scale air shower array that can detect UHECRs by measuring the particles produced when they interact with the atmosphere. The Pierre Auger Observatory has also observed a cutoff in the energy spectrum of UHECRs, which suggests that there is a limit to how high the energy of a cosmic ray can be [25, 26]. This

cutoff is known as the Greisen-Zatsepin-Kuzmin (GZK) cut-off and it arises from the interaction of UHECRs with the cosmic microwave background radiation [27, 28].

There are a few reasons why the origin of UHECRs is challenging to determine. As these particles travel through the Universe, they are deflected by magnetic fields, making it difficult to trace their paths back to their exact sources [29]. Additionally, their flux is low, which means that statistical analyses are typically limited by the paucity of detected UHECRs, especially at the highest energies. These reasons, coupled with the limited accuracy of current detection methods, contributes to the ongoing difficulty in pinpointing the precise origins of the most energetic particles observed in nature.

Cosmic rays may interact with background matter and radiation within their sources or or with cosmological photon fields as they propagate in the Universe. These interactions may be either through proton-proton collisions (pp or hadronic production) or proton-photon collisions ($p\gamma$ or photohadronic production). Therefore, it is expected that together with cosmic rays other messengers, such as high-energy gamma rays and high-energy neutrinos, are produced; we expand on this later. These additional particles carry valuable information about the origin of cosmic rays and their acceleration mechanism. Hence a combined effort, called multimessenger astronomy, is paramount for unveiling the nature of the most violent corners of our Universe. Additionally, in recent years, the field of observational gravitational waves has entered into the picture [30]. Some source candidates for UHECRs are also believed to emit gravitational waves [31–33].

In the context of multimessenger astronomy, neutrinos hold the potential to provide valuable insight about the origin of cosmic rays. Their zero electrical charge, together with their very low interaction rate with matter, allows neutrinos to travel in straight paths from their production point to the Earth without being deflected or absorbed. Hence, neutrinos are ideal messengers from the most energetic and distant objects in the Universe. This is in contrast to cosmic rays and gamma rays to which the Universe is opaque at high energies due energy losses and deflections caused by interactions with background light and Galactic and extragalactic magnetic fields.

The first detection of neutrinos from outside our Solar System was made in 1987, when the supernova SN 1987A in the Large Magellanic Cloud was observed to produce a burst of neutrinos [13, 14]. This was a major breakthrough in neutrino astronomy, and it showed that neutrinos

could be used to study supernovae. Since then, there have been a number of other detections of neutrinos from astrophysical sources. In 2013, IceCube reported the observation of two PeV neutrino events [34], making the first detection of high-energy astrophysical neutrinos. Later that year, IceCuve reported 28 high-energy neutrino events, between 30 and 1200 TeV [35], which were consistent with an origin outside the solar system. This was the first measurement of a high-energy astrophysical neutrino flux, and it opened up a new window on the Universe.

IceCube has made many important discoveries since its first detection of astrophysical neutrinos in 2013. In 2017, IceCube detected a high-energy neutrino that was likely produced by the blazar TXS 0506+056 [15]. This was the first time that a neutrino was linked to a blazar whose gamma-ray flare was detected by other instruments [36]. In 2021, IceCube released the latest report of the diffuse neutrino flux [37]. This measurement is based on data from the first decade of IceCube operations. In this report, the measured high-energy neutrino flux is consistent with a simple power law model. During the past decade, the continuously growing statistical evidence has supported the hypothesis that the high-energy diffuse neutrino flux has an extragalactic origin. However, the exact nature of the sources remains unknown.

Later, in 2022, the IceCube Neutrino Observatory announced the detection of the first steady point-like source of high-energy neutrinos, located in the direction of the nearby active galactic nucleus (AGN) NGC 1068 [16]. This is the first time that a steady-state astrophysical source of high-energy neutrinos has been identified, representing a pivotal advancement in neutrino astronomy. Most recently in 2023, IceCube identified the neutrino emission from the Galactic Plane [38]. Neutrino astronomy is a rapidly developing field, and there are many exciting possibilities for future research. With the construction of new neutrino telescopes, such as the IceCube-Gen2 [39], KM3NeT [40], P-ONE [41], among others.

Neutrino interactions with matter are difficult to study due to the low interaction rates, nevertheless the effort is well rewarded. Since they were first observed, neutrino–matter interactions have been studied in detail across a wide range of energy scales. The higher the interaction energy, the deeper we can probe the structure of matter. This simple rule has motivated the construction of large accelerators for the past decades [42–59]. With the dawn neutrino astronomy and the observation of an astrophysical neutrino flux with energies in the TeV–PeV energy range,

we enter a new regime for the exploration of neutrino–matter interactions. Various works have exploited high-energy neutrinos to measure the neutrino-nucleon cross section, test the validity of the Standard Model at a new energy regime, and probe new theories beyond the Standard Model [60–64].

Now is time to look forward to the next energy frontier, the ultra-high-energy (UHE) neutrino era. This refers to neutrinos with energies in the EeV (10^{18} GeV) range. The existence of an UHE neutrino flux is suggested from the observation of UHECRs and their likely interactions with low-energy photon backgrounds such as the cosmic microwave background (CMB) [27, 28, 65]. Therefore, the potential observation of an UHE neutrino flux would be in direct connection with the origin of UHECRs. Nonetheless, these neutrinos have remained undetected so far due to their extremely low predicted flux [66–69].

Fortunately, after decades of continuous developments, the next generation of neutrino telescopes is expected to reach sensitivities that have realistic chances of detecting the UHE neutrino flux [39, 41, 70–83]. Experimental designs, such as the radio component of IceCube-Gen2 [39], RNO-G [84], and GRAND [72], targe to detect make the first observation of an EeV neutrino event.

In preparation for the dawn of the UHE neutrino astronomy era, the works contained in this thesis provide the first detailed study of the discovery potential of UHE neutrino telescopes in the next two decades. This thesis include a detailed modeling of the physical processes involved in the discovery of UHE neutrinos from their production to their detection, including known systematic uncertainties. It also provides detailed statistical analysis frameworks that allow to quantify the discovery potential in terms of meaningful observables, such as the UHE neutrino-nucleon cross section, the number of discovered UHE neutrino point sources, and the exposure time needed for a decisive discovery, among others. Furthermore, theses results serve as a guide for the decision-making of the ongoing design efforts of multiple UHE neutrino telescopes. Only with a detailed theoretical modeling of the physical processes involved in the detection of UHE neutrinos, we can maximize the discovery potential, in hope to reach a new frontier for both particle physics and astrophysics.

2

FUNDAMENTALS OF MULTIMESSENGER ASTRONOMY

2.1 BRIEF HISTORICAL DEVELOPMENT TO MULTIMESSENGER ASTRONOMY

Multimessenger astronomy is a rapidly growing field that uses multiple messengers, such as photons, neutrinos, gravitational waves, and cosmic rays, to study astronomical objects and phenomena. This allows astronomers to get a more complete picture than they would be able to get from using just one type of messenger. For example, the observation of gravitational waves from a binary neutron star merger in 2017 was later followed by observations of the event in visible light, X-rays, and radio waves. This allowed scientists to study the event in unprecedented detail [85].

The term "multimessenger astronomy" has its roots in the early days of modern astronomy, when astronomers used different types of radiation to study the universe. In this case we refer to it as "multi-wavelength" astronomy. For example, in the 1930s, astronomers began to use radio waves to study the Milky Way [86]. In the 1960s, astronomers used X-rays to study the hot gas in galaxy clusters [87]. And in the 1980s, astronomers used gamma rays to study very energetic systems [88].

Multimessenger astronomy has the potential to revolutionize our understanding of the Universe. This can help us to understand the origins of the most energetic particles, their acceleration mechanisms, their sources, the environment of the sources, and how very energetic particle propagate in the Universe.

2.1.1 *Photons*

For centuries, astronomers have used only photons to observe the universe. The first instrument was our own eyes, which are only capable of detecting visible light. With the invention of lenses

and the telescope, astronomers were able to access optical radiation from more distant sources. In the early 20th century, the development of radio astronomy allowed astronomers to study the universe in the radio wave band [86]. Similarly, in the second half of the 20th century, the development of X-ray astronomy and gamma-ray astronomy opened up new windows on the universe in these high-energy bands [87, 88]. Electromagnetic radiation from different sectors of the electromagnetic spectrum is connected with physical processes at different energy scales. Therefore, studying photons in various frequency bands allows us to look at different processes, regions, and timescales of the same astrophysical event.

2.1.2 *Cosmic rays*

Cosmic rays are charged particles that are produced by a variety of astrophysical sources, such as supernovae and active galactic nuclei. Cosmic rays joined photons as messengers of Universe when in 1912, Victor Hess discovered that charged particles of an astrophysical origin were raining down on Earth from space [17]. These particles, now known as cosmic rays, are the highest-energy particles in the universe. Their origin remains an open question, as they undergo strong deflections due to Galactic and extragalactic magnetic fields when they propagate through space.

2.1.3 *Neutrinos*

Neutrinos are weakly interacting particles. High-energy astrophysical neutrinos are produced in environments with a high density of interacting particles, such as protons and photons, including supernovae and black hole mergers. They are difficult to detect, but they can provide information about the most energetic and violent events in the universe. In 1968, a team of physicists led by Raymond Davis Jr. detected neutrinos from the Sun [4]. This was the first time that neutrinos from a non-terrestrial source had been observed. The detection of solar neutrinos was a major breakthrough in astronomy, and it helped to confirm our understanding of the interior of the Sun. In 1987, the supernova SN 1987a was observed in the Large Magellanic Cloud [13, 14]. This was the first time that an identified astrophysical event beyond our solar system had been observed with

more than one kind of messenger. In addition to the optical light from the supernova, neutrinos and radio waves were also detected. The detection of neutrinos from SN 1987a marked a milestone in multimessenger astronomy, and it showed the potential of this new field to study the universe.

2.1.4 *Gravitational waves*

Gravitational waves are ripples in the fabric of spacetime that are produced by some of the most energetic events in the universe, such as the merger of black holes or neutron stars [89]. They are difficult to detect, but they can provide information about the geometry of spacetime and the nature of gravity. In 2015, the first gravitational waves were detected [30]. Gravitational waves carry unique information about astrophysical phenomena that is not accessible through electromagnetic radiation. For example, they can reveal the dynamics of massive objects like black holes and neutron stars during their mergers, shedding light on their masses, spins, and orbital parameters. Being the fastest messengers, the detection of gravitational waves from events like neutron star mergers or black hole mergers can trigger follow-up observations using other telescopes, such as optical, radio, gamma-ray, or even neutrino telescopes.

The field of multimessenger astronomy is still in its early stages, but it has the potential to revolutionize our understanding of the universe.

2.2 CHALLENGES OF MULTIMESSENGER ASTRONOMY

Each messenger has its own advantages and disadvantages. Cosmic rays are the most energetic messengers, but unfortunately they do not point back to their sources, making it very challenging to reveal their origin. They are subject to strong angular deviations due to the presence of Galactic ($B \sim \mu$ G) and extragalactic ($B \sim$ nG) magnetic fields, which can lead to angular deflections of up to tens of degrees [90]. Furthermore, the Universe is opaque to UHECRs [90]. Cosmic

rays continuously lose energy through scattering with background light, the cosmic microwave background (CMB), through either pair production,

$$p + \gamma_{\mathrm{CMB}} \rightarrow p + e^{+} + e^{-}, \tag{2.1}$$

or, at the highest energies, by photohadronic processes, mainly through Δ-resonance production,

$$p + \gamma \rightarrow \Delta^{+} \rightarrow \begin{cases} p + \pi^{0} \\ \\ n + \pi^{+} \end{cases} . \tag{2.2}$$

As a result, protons with energies above 4×10^{9} GeV do not survive more than ~ 100 Mpc [27, 28].

Fortunately, cosmic accelerators of UHECRs are largely unregulated astrophysical environment, inevitably leading to the production of secondary high-energy particles such as photons and neutrinos. Gamma rays with PeV energies may be produced from the decay of neutral pions from photohadronic interactions of UHECRs. Nevertheless, the Universe is also opaque to PeV gamma rays approximately beyond ~ 10 kpc [91]. An originally PeV gamma ray flux cascades down to a GeV–TeV flux via pair production and inverse Compton scattering, that is,

$$\gamma + \gamma_{\mathrm{CMB}} \rightarrow e^{+} + e^{-} \tag{2.3}$$

and

$$e^{\pm} + \gamma_{\mathrm{CMB}} \rightarrow e^{\pm} + \gamma, \tag{2.4}$$

respectively.

Along with gamma rays, neutrinos are also produced as secondaries via the decay of charged pions. The interaction of UHECRs with energies in the range of 100 TeV–100 PeV with low-energy background photons with energies in the MeV range, lead to the production of high-energy neutrinos (HE ν) in the TeV–PeV energy range. Similarly, UHECRs with higher energies in the EeV–ZeV range interacting with a colder photon background in the meV energy range, produces a flux of ultra-high-energy neutrinos (UHE ν) in the 1–100 EeV range.

Neutrinos are ideal astrophysical messengers for two main features: they are neutral and they only interact weakly. The first allows them to avoid deflections due to magnetic fields permeating the Universe. This means that, unlike cosmic rays, neutrinos point back directly to their source of production, allowing us to discover and study the sources of the most energetic particles in

nature. The second feature implies that neutrinos are not attenuated of absorbed by interactions with matter or radiation as it happens with UHECRs and gamma rays. Hence, neutrinos bring untainted information across cosmological scales. Furthermore, this also means that neutrinos may escape from the core of their sources without undergoing further interactions, allowing us to study regions of astrophysical environments that are not accessible otherwise. Nevertheless, the weak interactions of neutrinos also makes their detection particularly difficult, as compared to cosmic rays and gamma rays.

2.3 LATEST DEVELOPMENTS IN MULTIMESSENGER ASTRONOMY

In 2017 the observation of a neutron star merger, known as GW170817, was a monumental event in astrophysics, providing a wealth of scientific insights into the behavior of matter under extreme conditions and the production of heavy elements [85]. This observation was made possible through multimessenger astronomy, where multiple types of cosmic signals were detected and analyzed concurrently.

The signal detected from GW170817 on August 17, 2017, was generated by the inspiral and merger of two compact objects, later identified as neutron stars. Unlike previous gravitational wave events involving black hole mergers, GW170817 had a relatively well-constrained sky localization, thanks to the network formed by LIGO and Virgo. This localization was crucial for follow-up observations across the electromagnetic spectrum. Within two seconds of the gravitational wave detection, the NASA Fermi Gamma-ray Space Telescope detected a short-duration gamma-ray burst, known as GRB 170817A [92]. This nearly simultaneous detection provided strong evidence for a neutron star merger, as such events were theorized to produce both gravitational waves and gamma-ray bursts. The merger of two neutron stars is expected to produce a variety of electromagnetic radiation, including gamma rays, X-rays, optical light, and radio waves. In the case of GW170817, the electromagnetic counterpart was detected by a variety of telescopes, including the Fermi Gamma-ray Space Telescope, the Swift Gamma-ray Burst Explorer, the INTEGRAL space observatory, the Karl G. Jansky Very Large Array, among others [85].

The detection of the electromagnetic counterpart to GW170817 was a milestone achievement for multimessenger astronomy. It was the first time that a gravitational wave event had been seen to be accompanied by electromagnetic radiation, and it provided new insights into the physics of neutron stars. Among the key scientific discoveries of this multimessenger campaign we can highlight a better understanding of the origin of heavy elements [93], further constraints of the equation of state of neutron stars [94, 95], and new alternatives for the measurement of the Hubble constant [96].

Unfortunately, neutrinos, the main messengers in this thesis, were not observed in this event. One possible explanation for why we did not detect any neutrinos is that the event was observed from a large angle away from the direction of the jet, so the jet was not pointing towards Earth [97].

Nevertheless, this multimessenger campaign was a global success and a reward to years of constant effort and collaboration. Future upgrades on current experiments and the deployment of new instruments will bring us to an era where these kind of events will become common [98], which will make our understanding of high-energy astrophysics richer

3

PRODUCTION OF UHE NEUTRINOS

3.1 ASTROPHYSICAL SOURCES OF UHE PARTICLES

Neutrinos are neutral particles, therefore they can not be accelerated in an astrophysical environment through electromagnetic fields. Instead, we expect high-energy and ultra-high-energy neutrinos to be produced from the decay of intermediary particles, such as pions, produced from the interaction of UHECRs with background matter and radiation [99]. Although the sources of UHECRs are currently unknown, we can point to some conditions that a population of astrophysical sources must fulfill to be considered candidates for the origin of UHECRs [100].

- **Strong magnetic field:** A strong magnetic field is necessary for two reasons: first, to confine charged particles and prevent them from escaping and, second, because it is a key element in the most popular particle acceleration mechanisms, such as Fermi acceleration and magnetic reconnection, more details below. The magnetic field strength required depends on the energy of the particles expected to be produced.

- **Particle acceleration**: A mechanism able to accelerate charged particles to very-high energies. For example the shocks occurring in the collision of two galaxies, the explosion of a supernova, or the accretion of matter onto a black hole, see Sec. 3.2 for more details.

- **Reservoir of charged particles:** Since the acceleration mechanism may not be very efficient, the sources of UHECRs need a large number of charged particles to accelerate. The particle reservoir can be the interstellar medium, the gas in a galaxy, or the plasma in an active galactic nucleus.

- **Energy losses:** The energy gained by a particle through any acceleration mechanism should not be smaller than the energy losses that the particle undergo through radiation or interactions with background.

- **Total flux:** The flux of UHECRs produced by any candidate source population population should not be greater than the current measurements of the UHECRs flux. The total flux can be smaller, since the observed spectrum of UHECRs could be produced by multiple types of sources.

- **Secondary particles:** The flux of secondary particles produced from the interaction of UHECRs with the medium, such as photons or neutrinos, should not be larger than their corresponding observed fluxes and upper limits.

Candidate factories of UHECRs include:

- **Active galactic nuclei (AGN):** [101–103] Active galactic nuclei (AGN) are the central regions of galaxies powered by a supermassive black hole. The black hole is surrounded by an accretion disk, which is a rotating disk of gas and dust that is falling back onto the black hole. The friction and heat generated by the accretion disk causes the emission of electromagnetic radiation, including radio waves, visible light, and gamma rays. Protons and heavier nuclei may be accelerated at several regions of the AGN including the jets, the accretion disk, and the corona. They are thought to be the most likely sources of UHECRs.

- **Gamma-ray bursts (GRBs):** [104–106] Gamma-ray bursts (GRBs) are the most powerful explosions in the Universe. They are thought to be caused by the collapse of a massive star, or the merger of two neutron stars. GRBs consist of a burst of gamma rays that can last for a few seconds to a few minutes. GRBs are thought to be a potential source of UHECRs since particles can be accelerated to very high energies in a relativistic jet. The mechanism by which GRBs accelerate particles is not fully understood, but it is thought to involve shock acceleration (see Sec. 3.2). However, there are also some challenges to the GRB hypothesis as the sources of UHECRs.

- **Supernova remnants (SNRs):** [107] Supernova remnants (SNRs) are the expanding shells of gas and dust that are left behind by exploding stars. SNRs are much more common than

GRBs, and they are thought to be able to produce enough cosmic rays to account for the observed cosmic ray flux. However, there are also some challenges to the SNR hypothesis. For example, it is currently unknown if SNRs can efficiently accelerate particles to the highest energies observed in the UHECRs spectrum.

- **Clusters of galaxies:** [108–110] Clusters of galaxies are the largest gravitationally bound structures in the Universe. These massive cosmic conglomerates contain not only hundreds, or even thousands, of galaxies but also vast reservoirs of hot, ionized gas. The extreme environments within galaxy clusters, characterized by powerful shocks resulting from the gravitational dynamics and merging processes, offer the potential for efficient particle acceleration to ultra-high energies. These accelerated particles may gain their enormous energies through interactions with these shocks and magnetic fields.

3.1.1 *The Hillas criterion*

The Hillas criterion is a theoretical limit on the maximum energy that a particle can gain in an accelerator. It is named after the British astrophysicist Alan Hillas, who first proposed it in 1984 [18]. The underlying observation is that once a particle has escaped its source, it can not longer gain energy. The Hillas criterion states that the Larmor radius of the particle, which is the radius of the circular motion of the particle in the magnetic field, must not exceed the size of the accelerator. The Larmor radius is given by,

$$R_L = \frac{E}{qB}, \tag{3.1}$$

where E is the energy of the particle, q is the charge of the particle, and B is the strength of the magnetic field. We can rewrite this expression to express the maximum energy, $E_{\max}$, that a particle moving in an internal jet with a speed β, in units of the speed of light, can reach in an accelerator with a characteristic radius R and an efficiency of acceleration characterized by η,

$$E_{\max} = \eta^{-1} q \cdot B \cdot R\Gamma, \tag{3.2}$$

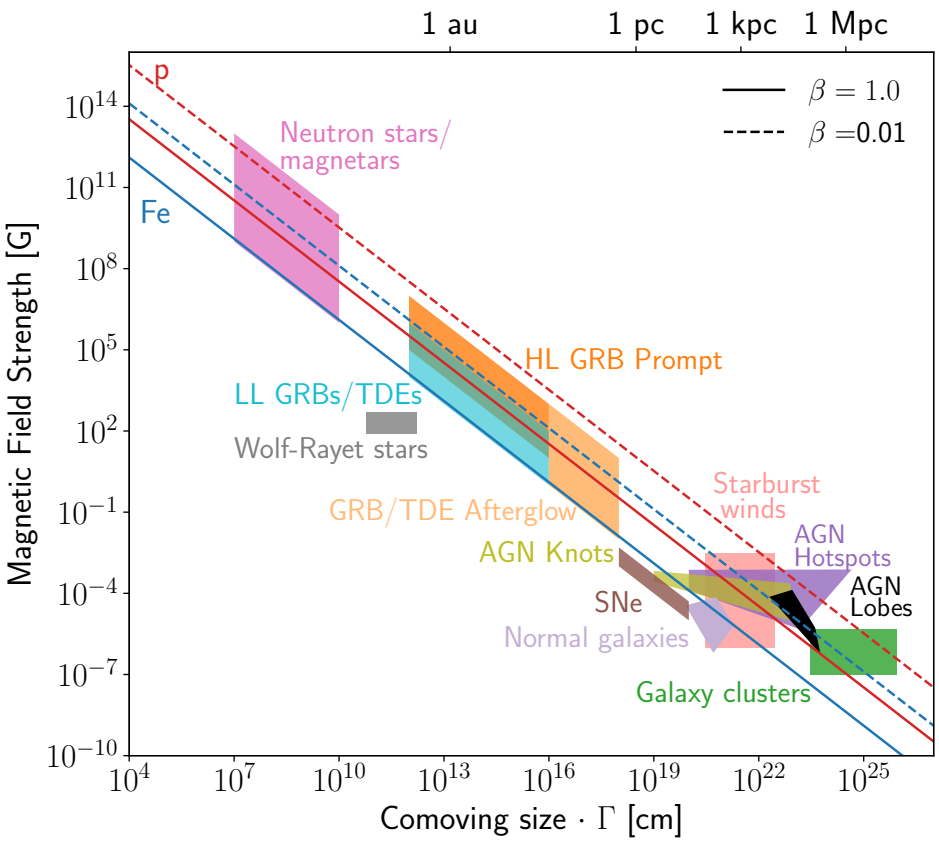

Figure 1: Hillas diagram. Source categories are depicted based on their characteristic size (R) and magnetic field strength (B) under the idealized Bohm limit scenario where $\eta = 1$. Magnetic field values are in the comoving frame of the source. The horizontal axis represents the distance from the central engine of the source and is equivalent to the comoving size of the source multiplied by the Lorentz factor (Γ) of the outflow. Solid and dashed lines indicate the $B \times R$ product thresholds beyond which confinement becomes feasible for protons (in red) and iron nuclei (in blue) with energies of 10^{20} eV, considering outflows with velocities $\beta = 1$ and $\beta = 0.01$, respectively. The magnetic field and size estimates for various source types are drawn from a variety of sources. Low-luminosity gamma-ray bursts (LL GRBs) and high-luminosity GRBs (HL GRBs) [111, 112], tidal disruption events [113–115], starburst galaxies and normal galaxies [116], values for AGN lobes, hotspots, and knots [117], galaxy clusters [100], supernovae [118–120], Wolf-Rayet stars [121], and neutron stars and magnetars [122–124]. This information was compiled for Ref. [125] by F. Oikonomou and K. Murase. Figure taken from Ref. [125]

where Γ is the Lorentz factor of the moving jet ($\Gamma \sim 10 - 50$ for AGN jets and $\Gamma \sim 10 - 1000$ for GRBs [125, 126]). The case $\eta = 1$ corresponds to the maximum achievable efficiency and is related to diffusion processes in the Bohm limit, the ideal scenario for energy diffusion in a plasma.

In Fig. 1, source classes falling to the left of the diagonal lines fail to meet the Hillas criterion for confinement. This plot illustrates that normal galaxies, supernovae, and stars generating massive magnetized winds, such as Wolf-Rayet stars, do not meet the confinement requirement. In contrast, the remaining source categories satisfy the confinement condition.

The Hillas criterion can be used to estimate the maximum energy of particles that can be accelerated in a particular astrophysical object. For example, if we know the size of a supernova remnant and the strength of the magnetic field in the remnant, we can use the Hillas criterion to estimate the maximum energy of protons that can be accelerated in the remnant. This information can then be used to narrow down the list of potential sources of UHECRs.

However, it is important to acknowledge certain limitations of the Hillas criterion. It does not account for energy losses experienced by the particles during acceleration. Additionally, the criterion assumes a uniform magnetic field as the accelerating medium and does not consider the effects of turbulence. These limitations underscore the need for a comprehensive understanding of the astrophysical environment in which particle acceleration occurs.

3.2 UHECR ACCELERATION MECHANISMS

3.2.1 *Fermi acceleration*

Fermi acceleration is a mechanism by which charged particles can be accelerated to very high energies in astrophysical environments. It was first proposed by Enrico Fermi in the late 1940s [127]. Fermi acceleration occurs in a region where there are strong magnetic fields and a moving plasma. The charged particles are repeatedly scattered by the magnetic field, and each time they are scattered, they gain a small amount of energy. Over time, the particles can gain enough energy to escape the source. The Fermi mechanism could operate in several astrophysical settings, including SNRs and AGN, and it provides a way to accelerate particles to extremely high energies.

In the Fermi mechanism a macroscopic environment, such as a moving magnetized plasma, transfers kinetic energy to charged particles. In astrophysical environments like supernova remnants or the jets of active galactic nuclei, shock waves are very common. Charged particles, which could be protons or heavier atomic nuclei, are present in these regions. When particles encounter the shock wave, they undergo scattering interactions with magnetic fields and turbulence in the surrounding medium. These scatterings cause the particles to gain energy. The key of Fermi mechanism is that the particles undergo multiple scatterings as they move back and forth across

the shock front. During each scattering, they gain energy, and over time, this process can lead to a significant increase in particle energy. This leads to a power-law energy spectrum for the accelerated particles, which is an observed feature of cosmic rays.

At each scattering or encounter with the shock wave, an individual particle will gain an energy proportional to its initial energy, that is, $E_i - E_f = \Delta E = \varepsilon E_i$, where E_i and E_f are the energies of the particle before and after a scattering respectively. As mentioned above, Fermi mechanism accelerates particles through multiple scatterings. After n scatterings the energy of a particle with initial energy E_0 will become $E_n = E_0(1+\varepsilon)^n$. Particles will not scatter indefinitely; after some time they will escape the acceleration region. If P_{esc} is the probability of escaping the shock-crossing or scattering region after one interaction, then, if the initial number of particles is N_0, after n scatterings the number of particles will be $N_n = N_0(1 - P_{\text{esc}})^n$. We can use the expression for the final energy and final number of particles after n crossings to eliminate n and we obtain

$$\frac{\log(N_n/N_0)}{\log(E_n/E_0)} = \frac{\log(1-P_{\text{esc}})}{\log(1+\varepsilon)}, \tag{3.3}$$

which gives

$$\frac{N_n}{N_0} = \left(\frac{E_n}{E_0}\right)^{\frac{\log(1-P_{\text{esc}})}{\log(1+\varepsilon)}}, \tag{3.4}$$

which if written in a differential form reads

$$N(E)dE \propto E^{\left(-1+\frac{\log(1-P_{\text{esc}})}{\log(1+\varepsilon)}\right)}. \tag{3.5}$$

The Fermi mechanism leads to the characteristic power-law spectrum observed for cosmic rays. Taking into account the characteristic time of one scattering and the characteristic time for a particle to escape the confinement, then one can find a maximum energy per particle that a certain environment can produce. The Fermi mechanism can accelerate particles to extremely high energies because it operates over long timescales, allowing particles to undergo many scatterings and accumulate energy.

There are two types of Fermi acceleration: first-order Fermi acceleration and second-order Fermi acceleration [90].

- First-order Fermi acceleration occurs in shocks, which are regions where the plasma is moving at different speeds. The charged particles are accelerated by the shock wave, which is a region of high-pressure and high-density plasma.

- Second-order Fermi acceleration occurs in the environment of moving magnetized gas clouds. The charged particles are accelerated by the magnetic field, which is distorted by the motion of the gas clouds.

The name in each case comes from the dependency of the energy gain factor, ε on the relative velocity of the plasma flow, $\beta = v/c$, where v is the velocity of the plasma in the lab frame and c the speed of light. While in the first-order Fermi acceleration one can show that $\varepsilon \propto \beta$, in the second-order Fermi acceleration mechanism one obtains $\varepsilon \propto \beta^2$. While in first-order acceleration v is interpreted as the velocity of the shocked gas relative to the unshocked gas, in the second-order acceleration v corresponds to the velocity of the magnetized cloud.

3.2.2 *Magnetic reconnection*

Magnetic reconnection is a mechanism that can potentially accelerate UHECRs, in astrophysical environments [128, 129]. Magnetic reconnection is a process where magnetic field lines in a plasma break and reconnect, releasing energy and accelerating charged particles in the process.

In regions of space with a high magnetic field, such as near compact objects like neutron stars or black holes, or in solar flares, magnetic reconnection can occur. When magnetic field lines become highly twisted and stressed, they can break and reconnect, releasing energy in the form of magnetic and kinetic energy. During magnetic reconnection events, charged particles, such as electrons and protons, can be accelerated. This occurs because the changing magnetic fields induce electric fields, which can accelerate charged particles. The key to potentially accelerating particles to ultra-high energies is the repetition of magnetic reconnection events. As particles are accelerated in one event, they gain energy and become more energetic. When they encounter another reconnection event, they can gain additional energy. This process can be repeated multiple times, gradually increasing the energy of the particle. For UHECRs to escape their source and become part of the cosmic ray population, they need to overcome magnetic confinement within the source environment. The combination of repeated magnetic reconnection events and the gradual acceleration of particles can provide the necessary energy for some particles to escape into interstellar space.

3.3 KINEMATICS OF UHE NEUTRINO PRODUCTION

When UHECRs interact with a low-energy photon background above a certain energy threshold (further details on this later), they produce a short-lived Δ^+ particle, which promptly decays and eventually produces high-energy and ultra-high-energy neutrinos. This interactions can take place inside the astrophysical sources, or as neutrinos propagate towards the Earth. The interaction and decay chain process is given by

$$p + \gamma \to \Delta^+ \to \begin{cases} p + \pi^0 \to p + \gamma + \gamma & \text{BR} = 2/3 \\ n + \pi^+ \begin{cases} n \to p + e^- + \bar{\nu}_e \\ \pi^+ \to \mu^+ + \nu_\nu \to e^+ + \bar{\nu}_\nu + \nu_e + \nu_\mu \end{cases} & \text{BR} = 1/3 \end{cases} . \tag{3.6}$$

Neutrinos produced in neutron decay have a much lower energy as compared with the neutrinos produced from the pion decay. This is because the masses of the proton and of the neutron are very similar, leaving only a small fraction of energy available for the neutrino production after de decay. On the other hand, the neutrinos produced from the decay of charged pions are the ones that can reach ultra-high-energies, and which are central in the development of this thesis.

To find the energy threshold for a proton to allow for the production of a Δ^+, we define as p_p the four-vector momentum of the incoming proton and as p_γ the four-vector momentum of the cold photon in the background. Then we have that

$$p_\Delta^2 = \left(p_p + p_\gamma\right)^2 \tag{3.7}$$

$$p_\Delta^2 = p_p^2 + p_\gamma^2 + 2p_p \cdot p_\gamma. \tag{3.8}$$

Since for massive particles we have that $p^2 = m^2$, then we can replace $p_p^2 = m_p^2$, $p_\gamma^2 = 0$ and $p_\Delta^2 = m_\Delta^2$ in Eq. (3.7), where m_p and m_Δ are the masses of the proton and the delta particle. Then, in Eq. (3.7), we have that $m_\Delta^2 = m_p^2 + 2p_p \cdot p_\gamma$. For the $p_p \cdot p_\gamma$ we can write,

$$p_p \cdot p_\gamma = E_p E_\gamma - \bar{p}_p \cdot \bar{p}_\gamma = E_p E_\gamma - |\bar{p}_p| \cdot |\bar{p}_\gamma| \cos\theta_{p\gamma}. \tag{3.9}$$

In the case of the photon, since it is massless we can write $|\bar{p}_\gamma| = E_\gamma$. For the high-energy proton, in the relativistic approximation, we have that $|\bar{p}_p| = \sqrt{E_p^2 - m_p^2} \approx E_p$. So Eq. (3.9) becomes

$$p_p \cdot p_\gamma = E_p E_\gamma (1 - \cos\theta_{p\gamma}). \tag{3.10}$$

Combining both results into Eq. (3.7) we obtain the energy condition for the delta resonance,

$$E_p E_\gamma = \frac{m_\Delta^2 - m_p^2}{2(1 - \cos\theta_{p\gamma})}. \tag{3.11}$$

Replacing $m_\Delta = 1.232$ GeV and $m_p = 0.938$ GeV in Eq. (3.11) and considering a head-on collision ($\cos\theta_{p\gamma} = -1$), we obtain that the energy threshold for protons propagating on a photon background with energy E_γ is

$$E_p \approx \frac{0.16\ \text{GeV}^2}{E_\gamma}. \tag{3.12}$$

The energy of the charged pions produced in Eq. (3.6) is on average one-fifth of the energy of the parent proton, that is $E_\pi = E_p/5$. Then, the energy of each neutrino from the pion decay is a quarter of the pion energy, $E_\nu = E_\pi/4$ [130, 131]. Therefore, on average neutrinos are produced with 5% of the initial proton energy.

3.3.1 *The GZK cut-off*

The development of cosmic-ray detectors has allowed us to reconstruct the spectrum of cosmic across multiple energy scales. This study revealed features in the spectrum that are identified as hints of a change in the dominant population of sources, or a transition between galactic to extragalactic sources. In particular, changes in the spectral index and the mass composition of cosmic rays. Of particular interest for this thesis is the so-called *ankle*, which corresponds to a suppression of the cosmic ray spectrum above 6×10^{19} eV. This suppression was first noted by the Hi-Res stereo Fly's Eye detector [20], and now confirmed with observations of the Pierre Auger Observatory [25] in the southern hemisphere, and the Telescope Array (TA) [132] detector in the northern hemisphere. One possibility for the origin of this suppression is the GZK cutoff [27, 28], which follows form the interaction of UHECRs with low energy background photons, such as those from the CMB. Alternatively, the suppression could be a sign of the maximum energy reached by cosmic accelerators. The discovery of a UHE neutrino spectrum could help us better understand the physics of UHECRs, their sources, and their propagation through the Universe.

In the particular case of propagation on the CMB, where the peak photon energy is $\langle E_\gamma \rangle = 0.66$ meV, Eq. (3.12) leads to minimum proton energy of $E_p \approx 2 \cdot 10^{11}$ GeV. A more detailed

calculation accounting for pair production and the width of the CMB spectrum leads to a threshold energy of $E_p \approx 5 \cdot 10^{10}$ GeV.

Taking into account the cross section of the $p\gamma$ process in Eq. (3.6), $\langle\sigma\rangle_{p\gamma}$, the number density of CMB photons, $n_\gamma = 413$ cm^{-3}, and the average energy loss protons, $\Delta E = 0.2E_p$, we can estimate the GZK horizon for protons around $L_{\mathrm{GZK}} = 50$ Mpc. That means that above a certain energy threshold, the Universe becomes opaque to UHECRs. Nevertheless, the observation of UHE neutrinos may reveal the existence of higher energy cosmic rays that do not reach the Earth. For example, observing a neutrino with energy $E_\nu = 10$ EeV implies a parent proton with energy $E_p = 200$ EeV. This could help us answer the question of whether the flux suppression measured of UHECRs at the highest energies is related to the GZK cutoff or if it is a manifestation of the maximum energy reachable in cosmic accelerators.

4

DETECTION OF UHE NEUTRINOS

Neutrinos are almost-ideal astrophysical messengers. Unlike cosmic rays, they point back to their sources. The Universe is not opaque to them, as it is for cosmic rays and gamma rays after a few tens of Mpc at ultra-high energies. They do not undergo severe energy degradation processes. Nevertheless, the one feature of neutrinos that allows them to travel the Universe without disruptions, also implies the major difficulty for studying astrophysical neutrinos. Neutrinos interact only weakly with matter. Therefore, detecting them is particularly challenging compared to detecting cosmic rays or gamma rays.

Kilometer-scale detectors are needed to reach realistic sensitivities for the detection of neutrinos from astrophysical origin. To motivate the construction of large-scale neutrino detectors, also called neutrino telescopes, we can invoke the Waxman–Bahcall upper bound [133]. The Waxman-Bahcall upper bound is a theoretical constraint on the flux of high-energy astrophysical neutrinos. It was proposed by Eli Waxman and John Bahcall in 1998 and is derived based on considerations of astrophysical sources of neutrinos and the observed cosmic ray flux, assuming that both share a common origin, as well as high-energy gamma rays. They claimed that the observed cosmic-ray flux provides a constraint on the total energy budget of astrophysical sources that can accelerate particles to ultra-high energies. If these astrophysical sources are capable of accelerating protons to ultra-high energies, they should also produce high-energy neutrinos through the interactions of protons with ambient matter or radiation. These neutrinos would be produced via processes like pion production and subsequent pion decay (see Sec. 3.3 for details). The neutrinos produced in these sources would contribute to a diffuse neutrino flux that should be observable on Earth. The Waxman–Bahcall upper bound for the neutrino flux from extragalactic sources, Φ_ν, is in the range of approximately $E_\nu^2 \Phi_\nu = 10^{-8}$ to 10^{-9} GeV cm^{-2} s^{-1} sr^{-1}.

Considering that the neutrino-nucleon cross section at high-energies can be approximately modeled as $\sim 10^{-35}$ cm$^2 (E_\nu/\text{GeV})^{0.36}$ [134], and that 1 km^3 of water contains about 6×10^{38} target

nucleons, the Waxman-Bahcall flux yields ~ 20 neutrino events per year per km^3 at 100 TeV. If on top of that we consider that at these energies a neutrino flux is subject to a significant attenuation while traversing the Earth, then the expected number of neutrino events is halved, leading to ~ 10 neutrino events per year per km^3 at 100 TeV.

4.1 NEUTRINO DETECTION IN THE TEV–PEV RANGE

In 2013, IceCube discovered high-energy astrophysical neutrinos, with energies in the TeV–PeV range [35]. IceCube is a cubic-kilometer in-ice Cherekov detector located at the South Pole. It was built over the experience gained from previous experimental efforts [135].

High-energy astrophysical neutrinos can be detected through the observation of Cherenkov radiation, a phenomenon that occurs when charged particles traverse a medium at speeds greater than the phase velocity of light in that medium [136]. This process is a cornerstone of neutrino detection in experiments like IceCube.

At high energies, the predominant interaction channel for neutrino-matter interactions is deep inelastic scattering (DIS). In DIS, neutrinos interact with one of the nucleon partons. The DIS can be neutral-current (NC) or charged-current (CC), depending on whether the mediator is a charged $W^{\pm}$ or a neutral Z boson. In the case of a NC DIS the nucleon-level process for an incoming neutrino of flavor α is $\nu_\alpha + N \to \nu_\alpha + X$, where N is the target nucleon, X is an hadronic shower, and $\alpha = e, \mu, \tau$. The outcome of this interaction is that the outgoing neutrino loses energy, that is, a neutrino flux after NC DIS is energy-damped. If the interaction is a CC DIS, the process is $\nu_\alpha + N \to l_\alpha + X$, where the outgoing l_α is a charged lepton of the corresponding flavor, that is $l_\alpha = e, \mu, \tau$.

The outgoing charged leptons travel through the detection medium and emit Cherenkov radiation at a characteristic angle (Cherenkov angle) with respect to the trajectory of the particle and within the optical wavelength range.

Optical sensors embedded within the detection medium capture the Cherenkov light emitted by these charged particles. The sensors are equipped with photomultiplier tubes (PMTs). By analyzing the timing and spatial distribution of the Cherenkov photons detected by multiple sensors, it is

possible to ascertain both the arrival time and the direction of the incident neutrino. Depending on the neutrino flavor and interaction type (NC or CC DIS), different event topologies may be reconstructed at IceCube, *tracks* and *cascades*.

Tracks are produced by muons from the CC interaction of a ν_μ. The ν_μ can interact both inside the detector volume, or in the detector surroundings. In both cases the outgoing muon will cross the detector, triggering multiple optical modules as it propagates, leaving a track-like signal, which allows for a good angular resolution. On the other hand, the energy resolution is generally poor as only the energy deposited while the muon was crossing the detector is recorded. Additionally, since neutrino events can initiate outside the detector, known as through-going tracks, the effective volume is bigger and the number of events in this channel is larger. This also means that the background contamination from atmospheric muons is larger. Different background rejection, energy cut, and veto techniques are applied to significantly reduce the background contamination. In the case of events initiated inside the detector, called starting tracks, the background contamination is significantly smaller [137, 138].

Cascades are produced from NC interactions of all neutrino flavors and CC interactions of ν_e and ν_τ inside the detector, or close to it. In the case of NC interaction, Cherenkov radiation is produced from the hadronic shower. For ν_e CC interaction, the outgoing charged lepton also contributes to the signal, in addition hadronic shower. At low energies, $E_\nu \lesssim$ PeV, the CC interaction of a ν_τ produces a hadronic shower as the NC interaction. At higher energies, the outgoing τ will decay after propagating $\sim$ 50 m per PeV, leading to a double-bang feature [139]. The first bang being the initial interaction vertex, and the second the τ–decay vertex. As most of the interaction energy is deposited in the detector, cascades usually present a better energy resolution, however the angular resolution is generally poorer. Additionally, the number of detected cascades is smaller than that of tracks, as interactions are restricted to happen in a smaller volume.

For the past decade, IceCube has advanced the study of astrophysical neutrinos. Among the most relevant scientific outputs by IceCube are the discovery of the astrophysical neutrino flux [34, 35], the identification of the first potential transient source of neutrinos, TXS 0506+056 [15, 36], the discovery of the first steady-state high-energy neutrino source, NGC 1068 [16], pioneering studies

on the flavor composition of astrophysical neutrinos [140, 141], probes of BSM signatures [142–146], among others.

The success of IceCube motivated the construction and expansion of new neutrino telescopes worldwide. Additional detectors will corroborate findings, improve statistics, and provide complementary observations. Some examples are the Gigaton Volume Detector (GVD) [147], a planned extension of the Baikal Neutrino Telescope in Siberia, Russia, the Cubic Kilometer Neutrino Telescope (KM3NeT) [40] in the Mediterranean sea, the Pacific Ocean Neutrino Experiment (P-ONE) [41], the Tropical Deep-sea Neutrino Telescope (TRIDENT), an 8 km^3 at South China Sea [148], the Huge Underwater high-energy Neutrino Telescope (HUNT) [149], which aims for a total volume of 30 km^3 and is planned to be deployed either in Lake Baikal or the South China Sea, and the next upgrade of IceCube, IceCube-Gen2 [39]. All these detectors are designed to complement the observations made by IceCube by exploring different regions of the sky and increasing the total effective volume. Figure 2 shows some of the neutrino telescopes currently operational, on the prototype phase, or planned for the future that are be sensitive to the TeV–PeV energy range. It also describes some of the detector characteristics, such as, flavor sensitivity, detection technique, target volume, and detector geometry. For the TeV–PeV range the use of optical Cherenkov emission from interactions in a detector embedded in a water volume is preferred.

4.2 NEUTRINO DETECTION AT THE EEV RANGE

4.2.1 *UHE neutrino detectors*

Above 10 PeV no neutrinos have been detected so far. Upper limits on their flux placed by IceCube [66], the Pierre Auger Observatory [67], ARA [68, 69] and ANITA [150] are shown in Fig. 3. Although the neutrino-nucleon cross section at ultra-high energies (PeV–EeV) is roughly fifteen times higher than at high energies (TeV–PeV), meaning that neutrinos are more likely to interact in the detector, the neutrino flux at ultra-high energies seems to be significantly smaller (see Fig. 3). This makes the detection of UHE neutrinos challenging.

Nevertheless, after the success of IceCube in the TeV–PeV range, there is an ongoing experimental campaign for advancing neutrino astronomy to the PeV–EeV energy range. Recent scientific and technological progress has envisioned novel techniques to target the detection of UHE neutrinos. Figure 2 shows the present status of ongoing and planned neutrino telescopes. Unlike neutrino detection at the TeV–PeV range, which only used optical Cherenkov light in water, for detecting UHE neutrinos other detection strategies are better suited. From the hadronic shower produced from the DIS interaction of UHE neutrinos, we can aim to directly observe the particle shower or the Askaryan radio emission form the developing particle shower (more details on this Sec. 4.2.2). Furthermore, besides water, other materials can be used as interaction medium for the detection of UHE neutrinos, such as the atmosphere, geographical formations (e.g., mountains or valleys), or even the lunar regolith. Since the works discussed in thesis are geared around the radio component of IceCube-Gen2, which is sensitive to the Askaryan emission from interactions in ice, we discuss in more detail the Askaryan effect below.

This diversification of detection strategies has motivated the design and construction of multiple UHE neutrino telescopes around the globe, therefore increasing our chances of discovering EeV neutrinos in the near future.

4.2.2 *Askaryan effect*

When an ultra-high-energy neutrino interacts with a dense dielectric medium, such as ice or salt, it produces secondary charged particles. These secondary charged particles move through the medium at relativistic speeds, exceeding the phase velocity of radio waves (typically in the MHz to GHz range) in that medium. The secondary shower of particles presents a charge anisotropy, with an excess of negative charges at the front and an excess of positive charges in the back of the propagating shower. This creates a dipole effect. As the shower develops, it creates effect of a varying dipole, leading to the emission of a cone of coherent radiation in the radio and microwave part of the spectrum [165]. The emitted Askaryan radiation is highly directional and is focused along the axis of the initial neutrino interaction. The direction of the radiation points back to the source of the ultra-high-energy neutrino. Radio antennas, such as dipole antennas or

				Flavor		Technique			Neutrino Target					Geometry				
Experiments	Phase & Online Date	Energy Range	Site	Tau	All Flavor	Optical / UV	Radio	Showers	H_2O	Atmosphere	Earth's limb	Topography	Lunar Regolith	Embedded	Planar Arrays	Valley	Mountains	Balloon	Satellite
IceCube	2010	TeV-EeV	South Pole		✓	✓			✓					✓					
KM3NeT	2021	TeV-PeV	Mediteranean		✓	✓			✓					✓					
Baikal-GVD	2021	TeV-PeV	Lake Baikal		✓	✓			✓					✓					
P-ONE	2020	TeV-PeV	Pacific Ocean		✓	✓			✓					✓					
IceCube-Gen2	2030+	TeV-EeV	South Pole		✓	✓	✓		✓					✓					
ARIANNA	2014	>30 PeV	Moore's Bay		✓		✓		✓					✓					
ARA	2011	>30 PeV	South Pole		✓		✓		✓					✓					
RNO-G	2021	>30 PeV	Greenland		✓		✓		✓					✓					
RET-N	2024	PeV-EeV	Antarctica		✓		✓		✓					✓					
ANITA	2008,2014,2016	EeV	Antarctica	✓	✓		✓		✓		✓							✓	
PUEO	2024	EeV	Antarctica	✓	✓		✓		✓		✓							✓	
GRAND	2020	EeV	China / Worldwide	✓			✓			✓	✓	✓			✓		✓		
BEACON	2018	EeV	CA, USA/ Worldwide	✓			✓				✓	✓					✓		
TAROGE-M	2018	EeV	Antarctica	✓			✓				✓	✓					✓		
SKA	2029	>100 EeV	Australia		✓		✓						✓		✓				
Trinity	2022	PeV-EeV	Utah, USA	✓		✓					✓						✓		
POEMMA		>20 PeV	Satellite	✓	✓	✓				✓	✓								✓
EUSO-SPB	2022	EeV	New Zealand	✓		✓					✓							✓	
Pierre Auger	2008	EeV	Argentina	✓	✓			✓		✓	✓	✓			✓				
AugerPrime	2022	EeV	Argentina	✓	✓		✓	✓		✓	✓	✓			✓				
Telescope Array	2008	EeV	Utah, USA	✓	✓			✓		✓					✓				
TAx4		EeV	Utah, USA	✓	✓			✓											
TAMBO	2025-2026	PeV-EeV	Peru	✓				✓				✓				✓			

Operational		Date full operations began
Prototype		Date protoype operations began or begin
Planning		Projected full operations

Figure 2: Overview of current and future neutrino telescopes [24, 39, 41, 72–75, 84, 151–163]. These experiments vary in their capability to distinguish tau neutrinos based on flavor, their chosen detection methods, and their geometric configurations. The experiments are categorized based on their current status, whether they are operational, in prototype operation or development, or planned for full-scale operations. This categorization is represented by the shaded regions. The color scheme matches that of Fig. 3. Figure taken from Ref. [164]

bowtie antennas, are strategically deployed in the detection medium (e.g., within the ice) or on its surface. These antennas are tuned to the radio frequency range associated with the Askaryan radiation [166].

A major advantage of radio-detection for UHE neutrinos, as compared to the usual optical Cherenkov detection in the PeV–TeV energy range, is that radio signals propagate ten times farther in a medium like ice compared to optical signals before undergoing significant attenuation. This allows to design a detector that covers a larger surface area by placing radio antennas more sparsely than what would be needed with optical modules [39]. Hence, achieving the larger effective areas needed to reach competitive sensitivities for the detection of the UHE neutrino flux.

The Askaryan effect has motivated the development of radio-based neutrino detectors, including the Radio Ice Cherenkov Experiment (RICE) [167], the Askaryan Radio Array (ARA) [68], the Antarctic Ross Ice-Shelf Antenna Neutrino Array (ARIANNA) [168], the Antarctic Impulsive

Transient Antenna (ANITA) [169], the Radio Neutrino Observatory in Greenland (RNO-G) [84], and in the future larger experiments like the radio component of IceCube-Gen2 [39] and the Giant Radio Array for Neutrino Detection (GRAND) [72]. These experiments aim to detect ultra-high-energy neutrinos from astrophysical sources and explore the most extreme cosmic phenomena. For a detailed discussion of ongoing experimental efforts in the ultra-high-energy regime, see Refs. [83, 164].

4.2.3 *Predictions of the UHE neutrino flux*

The predictions of the diffuse flux of UHE neutrinos are subject to multiple uncertainties. If UHE neutrinos are produced through the GZK mechanism from the interaction of UHECRs with their medium, then an accurate knowledge of the UHECR spectrum at the highest energy is needed to make a prediction of the expected UHE neutrino flux. Some of the parameters of the UHECR spectrum on which the UHE neutrino flux prediction depends include the maximum energy at which sources can accelerate cosmic rays, the spectral index of the UHECR spectrum at the highest energies, the source number density, and the UHECR mass composition. The uncertainty on the values of these parameters leads to a wide range of predictions for the spectral shape and overall normalization of the UHE neutrino spectrum [170–174]. The neutrino flux component obtained from the interaction of UHECRs with CMB photons is commonly called *cosmogenic* neutrinos.

In addition to cosmogenic neutrino, UHE neutrinos could also be produced from the interaction of UHE particles with background matter and radiation within their sources. This would be an additional component, commonly called *source* or *astrophysical* neutrinos. In the case of source neutrinos, the flux will depend on the type of astrophysical accelerator, its surrounding environment, and the neutrino production mechanism [175–180].

Figure 3 shows the allowed regions for the UHE neutrino flux according to different scenarios [177, 180–182] along with the current upper limits placed by different experiments [66–69]. Only in the most optimistic scenarios of the predictions for the UHE neutrino flux, the sensitivities of neutrino telescopes as IceCube or Auger could allow them a chance to make a detection.

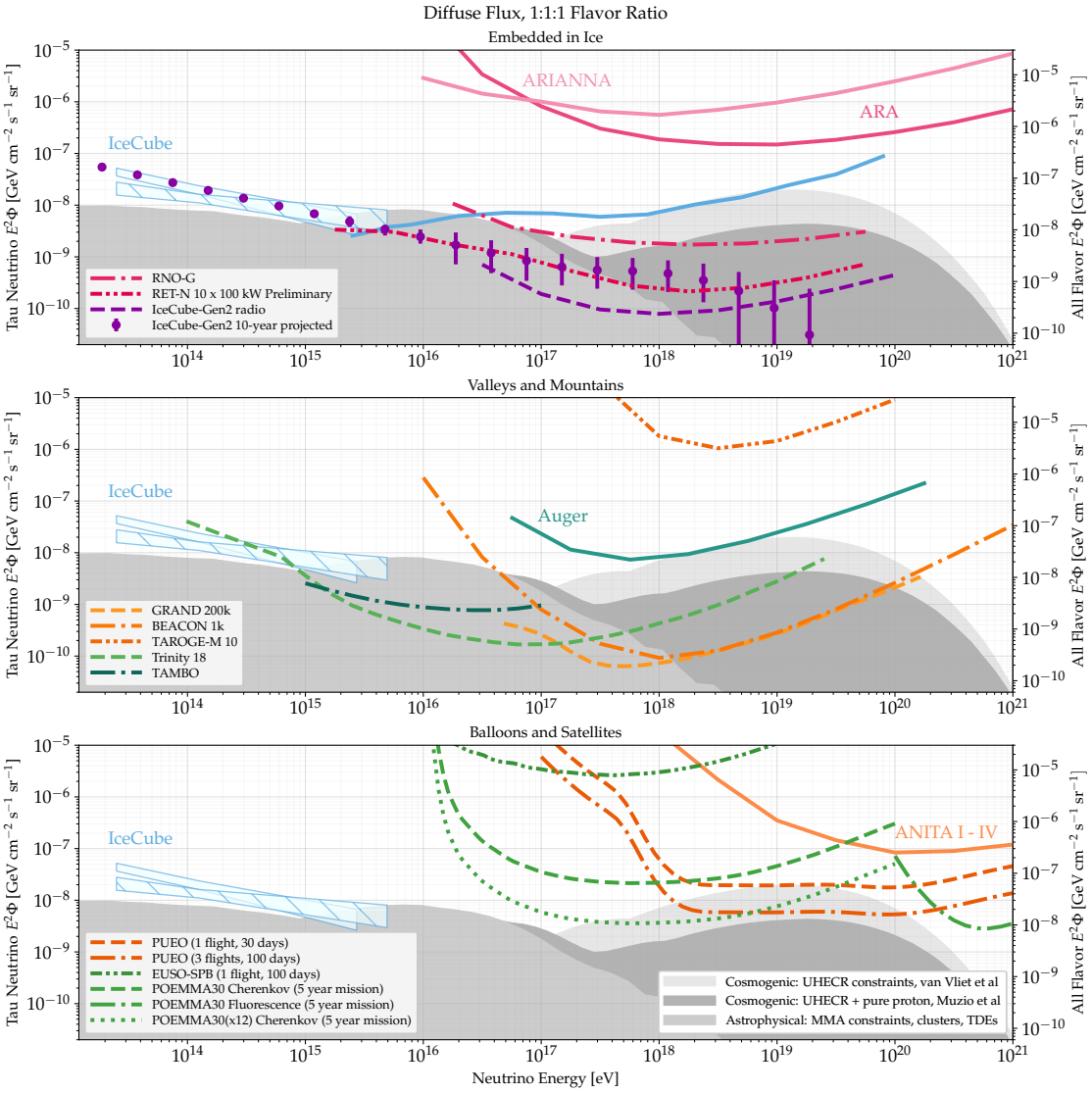

Figure 3: *Solid lines:* Current upper limits set on the diffuse flux of UHE neutrinos [66–69]. *Dashed and dashed-dotted lines:* Expected 90% confidence level sensitivity for a variety of upcoming UHE neutrino telescopes [72–75, 81, 84, 152, 153]. *Shaded areas:* Cosmogenic and astrophysical UHE neutrino models [177, 180–182]. *Top:* Experiments embedded in water and ice. *Middle:* Experiments sensitive to air showers. *Bottom:* Ballon-borne experiments and satellites. Figure taken from Ref. [164]

Nevertheless, the potential of UHE neutrinos for astrophysics and particle physics has motivated the design of a new generation of UHE neutrino telescopes with larger effective volumes and new detection techniques. Figure 3 shows the predicted sensitivities of future UHE neutrino telescopes. This shows that we might finally have realistic chances of detecting EeV neutrinos in the near future. In this thesis forecast the physics potential of UHE neutrinos, using a state-of-the-art, nuanced description of upcoming detection capabilities.

5

OPPORTUNITIES WITH UHE NEUTRINOS

In this thesis we focus on the potential of UHE neutrinos in advancing the field of astroparticle physics on multiple fronts.

First, in Part II, we study the perspective of discovering and measuring the UHE neutrino flux. Chapter 6 discusses the opportunities to measure the νN cross section at ultra-high energies, a measurement that would allow us to study neutrino-matter interactions at an energy regime that is inaccessible to the most powerful in-Earth particle accelerators. That means that UHE neutrinos hold the power to reveal the deep structure of nucleons. Furthermore, a precise measurement of the UHE νN cross section makes it possible to probe theories beyond the Standard Model that predict deviations of the cross section at these energies.

Chapter 7 focuses on the discovery of an UHE neutrino flux itself. Through a careful modeling of the response of the radio array of IceCube-Gen2, adopted as representative of upcoming UHE neutrino telescopes, we show that the UHE neutrino flux could be discovered within one decade of detector exposure. Moreover, we make a detailed study of how different factors may impact this claim; e.g., different backgrounds and detector characteristics. This study provides advise to the design of next-generation neutrino telescopes. The goal is to maximize the scientific output; in particular, the opportunities to discover the diffuse flux of EeV neutrinos.

Chapter 8 brings together the lessons learned in Chapters 6 and 7. After proving that the perspectives of discovering the UHE neutrino flux and using it to measure the νN cross section are encouraging, we will use this motivation to dive into a more ambitious goal: a joint reconstruction of the UHE neutrino flux and an energy-dependent trend of the νN cross section. To achieve that goal, this chapter implements many of the recommendations left at the end of the two previous chapters to maximize the information that can be extracted from UHE neutrino telescopes. We propose a flexible parametrization of the neutrino flux and compare its performance against simpler parametrizations commonly used in the TeV–PeV range. This chapter shows how a

poor parametrization of the neutrino flux may unknowingly lead to a biased result that yields an incorrect measured value of the cross section.

After the detailed discussion of the discoverability of the UHE neutrino flux, we move to Part III where the focus will be the physics opportunities in the UHE neutrino era. Chapter 9 focuses on the efforts for solving the enigma of the origin of UHECRs. The ultimate goal is to pinpoint the sources of the most energetic neutrinos and establish a connection between these sources and those of UHECRs. The work establishes constraints on candidate classes of UHE neutrino sources, both steady-state and transient. We use the detection of UHE neutrino multiplets as a smoking gun for point sources that stand out over a diffuse neutrino background.

Finally, Ch. 10 studies the perspective of using UHE neutrino telescopes as dark matter detectors. The goal is to seek signatures of the decay of heavy dark matter, with masses in the 10^8 to 10^{10} GeV, into UHE neutrinos. We show that signatures of the heavy dark matter decay in UHE neutrino telescopes endure significant non-dark matter backgrounds. We forecast competitive constraints on the mass and lifetime of heavy dark matter candidates.

To achieve the goals of the works presented in each chapter mentioned above, I developed a state-of-the-art framework to compute event rates in UHE radio neutrino telescopes, in particular in the radio component of IceCube-Gen2. This framework includes a detailed modeling of the neutrino propagation inside the Earth, the most updated predictions of the neutrino-nucleon cross section at ultra-high energies, the generation of radio signals from in-ice neutrino interactions and their propagation through the medium, and modeling of the detector angular and energy resolution. The framework for the calculation of UHE neutrino event rates is complemented with advanced statistical methods that allow for the exploration of large and complex parameter spaces efficiently. The optimization of these methods, together with the leverage of high-performance computing facilities, allowed for fast computations and made the studies described in this thesis feasible within reasonable time scales.

Somewhere in this section you should say that you develop a detailed, state-of-the-art framework to compute event rates in Gen2. Say briefly what this framework entails (neutrino propgation inside Earth, recent cross-section predictions, radio generation and propagation in ice, detector angular and energy resolution, etc.). Say that you use the same framework throughout all of your

work, adapted to the different goals of each chapter. Say that you complement that framework with advanced statistical methods to explore large parameters spaces efficiently.

In this way, this thesis covers a wide range of topics related to the upcoming era of the UHE neutrino flux. Covering from its perspective of discovery, its characterization, and its use to explore new physics avenues. This thesis aims to provide the first detailed and dedicated study of the physics potential of UHE neutrinos. The results shown in this thesis encourage the continuous study and development of more sophisticated numerical, mathematical, computational, and statistical methods what will, in the near future, serve to advance neutrino physics to the ultra-high energy regime.

Part II

MEASURING THE UHE NEUTRINO FLUX

6

INFERRING THE NEUTRINO-NUCLEON CROSS SECTION AT THE HIGHEST ENERGIES

Based on: **Víctor B. Valera Baca**, Mauricio Bustamante, Christian Glaser, *The ultra-high-energy neutrino-nucleon cross section: measurement forecasts for an era of cosmic EeV-neutrino discovery*, JHEP06(2022)105, arXiv:2204.04237

ABSTRACT Neutrino interactions with protons and neutrons probe their deep structure and may reveal new physics. The higher the neutrino energy, the sharper the probe. So far, the neutrino-nucleon (νN) cross section is known across neutrino energies from a few hundred MeV to a few PeV. Soon, ultra-high-energy (UHE) cosmic neutrinos, with energies above 100 PeV, could take us farther. So far, they have evaded discovery, but upcoming UHE neutrino telescopes endeavor to find them. We present the first detailed measurement forecasts of the UHE νN cross section, geared to IceCube-Gen2, one of the leading detectors under planning. We use state-of-the-art ingredients in every stage of our forecasts: in the UHE neutrino flux predictions, the neutrino propagation inside Earth, the emission of neutrino-induced radio signals in the detector, their propagation and detection, and the treatment of backgrounds. After 10 years, if at least a few tens of UHE neutrino-induced events are detected, IceCube-Gen2 could measure the νN cross section at center-of-mass energies of $\sqrt{s} \approx$ 10–100 TeV for the first time, with a precision comparable to that of its theory prediction.

6.1 INTRODUCTION

Neutrino interactions with matter are powerful probes of particle physics: they map the deep structure of nuclei and nucleons, and may unearth evidence of new physics. Broadly stated, the

higher the energy of the interacting neutrino, the sharper its probing power. Today, high-energy neutrino-matter interactions—in the form of the neutrino-nucleon (νN) cross section—are known experimentally up to PeV neutrino energies, the highest detected so far. Yet, a trove of further insight likely lies in the measurement of the νN cross section at higher energies. Presently, those energies are practically out of the reach of existing detectors, but this limitation will likely be overcome in the coming years.

Figure 4 shows the current landscape of measurements of the νN cross section. At neutrino energies from about 100 MeV to 350 GeV, the cross section is measured precisely using artificial neutrino beams from particle accelerators [42–59]. Soon, the planned accelerator-neutrino experiment FASERν [183] will reach TeV-scale energies, but not more. Beyond TeV neutrino energies, there is no existing or planned artificial neutrino beam. Thus, TeV–PeV cross-section measurements [60, 61, 63] used instead the high-energy cosmic neutrinos discovered by the IceCube neutrino telescope [34, 35, 184–188]. These are the most energetic neutrinos known so far, though not the most energetic neutrinos predicted. At even higher energies, of 100 PeV and above, the existence of *ultra-high-energy* (UHE) cosmic neutrinos was firmly predicted more than fifty years ago [27, 28]. They represent the only feasible way to extend νN cross section measurements to higher energies. Yet, because their predicted flux is low, they have so far evaded discovery [66, 67].

Fortunately, a host of new neutrino telescopes [39, 41, 70–83], designed to discover UHE neutrinos even if their flux is low in the next 10–20 years, may provide a way forward. For astrophysics, discovering UHE neutrinos would bring critical progress in understanding the long-standing origin of ultra-high-energy cosmic rays [83, 189]. For particle physics, discovering UHE neutrinos, in general, would allow access to tests of fundamental physics in a new energy regime and, in particular, would allow us to further cross-section measurements [82, 83, 190, 191].

However, detailed and realistic predictions for the capability of upcoming neutrino telescopes to measure the νN cross section, considering their design elements, are still lacking; see, however, Refs. [192] for important first estimates. To address this, and in order to capitalize on this upcoming opportunity, we present state-of-the-art forecasts for the measurement of the UHE νN cross section. We gear our forecasts to the promising case of radio-detection of UHE neutrinos in the planned IceCube-Gen2 neutrino telescope [39], one of the leading next-generation detectors under design.

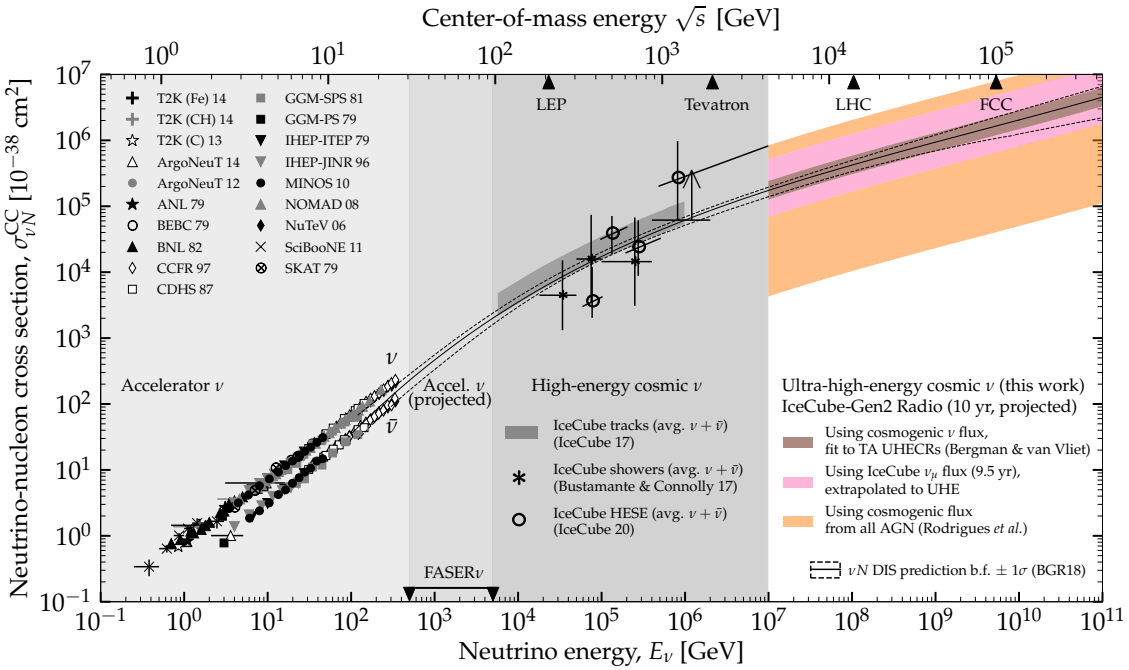

Figure 4: Neutrino-nucleon (νN) charged-current (CC) cross section, measurements and predictions. Sub-TeV measurements are from accelerator-neutrino experiments [42–59]. Few-TeV measurements will be covered by the upcoming FASERν accelerator-neutrino experiment [183]. TeV–PeV measurements use high-energy astrophysical neutrinos detected by the IceCube neutrino telescope [60, 61, 63]. We forecast cross-section measurements above 100 PeV—the ultra-high-energy (UHE) range—where no measurement exists presently. Our forecasts are for radio-detection of UHE neutrinos in the planned IceCube-Gen2 [39], and are based on sophisticated simulations of UHE neutrino propagation inside Earth (Section 6.5) and detector response (Section 6.6). In this plot, we showcase 10-year forecasts for three attractive flux scenarios that may afford the most precise cross-section measurements [37, 179] (models 2, 4, and 7 below). Table 2 shows results for many more flux models [37, 174–180, 188, 193] (Section 6.4). The precision of cross-section measurements that we report accounts for the significant uncertainty on the flux normalization (Section 6.7), and detector resolution (Section 6.6). For comparison, we show the state-of-the-art BGR18 calculation of the νN deep-inelastic-scattering cross section [194] (Section 6.3.1) on isoscalar matter, averaged between neutrinos and anti-neutrinos.

To make our forecasts realistic, we use state-of-the-art ingredients in every stage of the calculation (see Section 6.2). We model the propagation of UHE neutrinos inside the Earth and their radio-detection in detail. For the latter, we estimate the radio-detection response of the detector, via dedicated simulations of in-medium shower development and radio emission in IceCube-Gen2, and its energy and directional resolution. To capture the large uncertainty that exists in the prediction of UHE neutrinos, our cross-section forecasts factor in the uncertainty in the size of their flux and a wide variety of shapes of their energy spectrum from the literature [37, 174–180, 188, 193].

Figure 4 shows that, in optimistic flux scenarios, IceCube-Gen2 may be able to measure the UHE νN cross section to within 50% of its predicted value. This would be the first measurement

of neutrino interactions at center-of-mass energies of $\sqrt{s} \approx$ 10–100 TeV, comparable to those of particle collisions at the Large Hadron Collider and the Future Circular Collider. Measuring neutrino interactions at these energies has potentially transformative consequences. First, it will test Standard Model predictions of the νN cross section [194]. Second, it will probe non-linear effects in the distribution of quarks and gluons inside nucleons [195–198], the existence of color-glass condensates [199], and electroweak sphalerons [200]; see, *e.g.*, Refs. [200–203]. And, third, it will probe a large number of new-physics effects that could modify the cross section, including, *e.g.*, leptoquarks, extra dimensions, and new gauge bosons [192, 204–208].

The goal of our forecasts is double. On the one hand, they are intended to showcase the reach of IceCube-Gen2 to make particle-physics measurements in a new energy regime, in as realistic a way as it is presently possible. On the other hand, and more generally, our forecasts are intended to stimulate the development of the particle-physics research programs of upcoming high-energy neutrino telescopes. The calculation framework that we introduce as part of our analysis can be adapted to other neutrino telescopes, and other measurement goals. Because the design of telescopes that will run in 10–20 years is being decided upon presently, our forecasts are timely.

This chapter is organized as follows. Section 6.2 showcases the salient points and strengths of our analysis. Section 6.3 presents a brief introduction to neutrino-nucleon deep inelastic scattering and outlines the strategy that we use to measure the cross section. Section 6.4 introduces the various benchmark models of the cosmic UHE neutrino flux that we adopt. Section 6.5 describes the effect of neutrino propagation through Earth and how we compute it. Section 6.6 gives an overview of radio-detection of UHE neutrinos, introduces the response of IceCube-Gen2, and shows how we estimate event rates in it. Section 6.7 introduces the statistical analysis that we use to forecast cross-section measurements. Section 6.8 shows our resulting forecasts for the different benchmark flux models, and the effect on them of changing detector parameters. Section 6.9 points out potential future research directions. Section 6.10 summarizes and concludes.

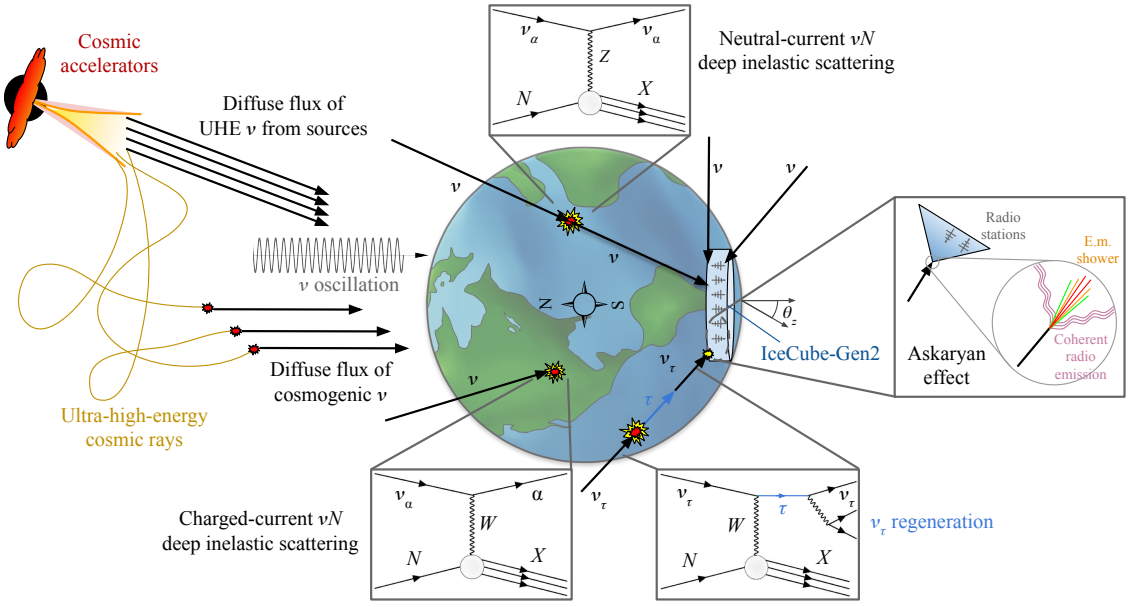

Figure 5: Overview of the calculation used to forecast ultra-high-energy (UHE) cross-section measurement capabilities. A diffuse, isotropic flux of UHE neutrinos, of energies in excess of 100 PeV, cosmogenic or from astrophysical sources, reaches the Earth. UHE neutrinos propagate through the Earth, across different directions, toward the envisioned IceCube-Gen2 neutrino telescope, located in the South Pole. Inside Earth, neutrinos interact with matter, mainly via neutrino-nucleon (νN) deep inelastic scattering. As a result, their flux is attenuated and shifted to lower energies. At IceCube-Gen2, neutrinos interact in the ice and induce particle showers that radiate coherent radio emission that may be detected by antennas buried in the ice. The sensitivity to the νN cross section stems from differences in the distribution of neutrino arrival directions, especially of neutrinos coming to the detector horizontally or near-horizontally. See the main text for details.

6.2 SYNOPSIS AND CONTEXT

Figure 5 illustrates the flow of calculations involved in producing our forecasts of the measurement of the UHE νN cross section. For a given prediction of the diffuse UHE neutrino flux, we propagate it through the Earth, where neutrinos interact with matter, and model its detection in the radio component of IceCube-Gen2. To make our forecasts realistic, timely, and representative of current unknowns, we use state-of-the-art ingredients at every stage of the calculation. In brief, these are:

UHE νN CROSS SECTION UHE neutrinos interact with matter while propagating through the Earth, and when detected. The sensitivity to the νN cross section stems from an interplay of both effects; see Section 6.3.3.2. In our forecasts, we use a state-of-the-art prediction of the UHE cross section [194], and deviations from it, to compute neutrino propagation and detection. See Section 6.3 for details.

DIFFUSE NEUTRINO FLUX We have not discovered a flux of UHE neutrinos yet, so we are forced to consider different possibilities. In our forecasts, we assume a wide variety of UHE neutrino flux predictions that span the breadth available in the literature, from pessimistic to optimistic [37, 174–180, 188, 193]. We model in detail the flavor content of neutrinos and anti-neutrinos in the flux, and keep track of it throughout. See Section 6.4 for details.

NEUTRINO PROPAGATION THROUGH EARTH When propagating UHE neutrinos through the Earth, we compute how neutrino interactions with matter modify the neutrino flux that reaches the detector. The modifications are energy-, direction-, and flavor-dependent, and are slightly different for neutrinos and anti-neutrinos. In our forecasts, we account for the dominant neutrino interaction—νN deep inelastic scattering—and for other interactions that are collectively non-negligible, via NUPROPEARTH [209, 210]. See Section 6.5 for details.

NEUTRINO DETECTION We gear our forecasts to the detection of UHE neutrinos in the radio component of IceCube-Gen2, optimized for neutrino detection above 10^7 GeV. In our forecasts, we model the detector geometry, simulate the development of particle showers in the ice, the emission and propagation of radio signals from them, the detector response, including the direction-dependent response of the different antenna types in the array, via NURADIOMC [211] and NURADIORECO [212], the calculation of the trigger condition, and the uncertainties in reconstructing the energy and direction of detected events. See Section 6.6 for details.

NON-NEUTRINO BACKGROUNDS In the radio-detection of UHE neutrinos, the main backgrounds that may mimic neutrinos are due to showers induced by atmospheric muons in the ice [213, 214] and to showers induced in the atmosphere, mainly by cosmic rays, that penetrate into the ice. In our forecasts, we model the detection of atmospheric muons and show its effect on our ability to measure the νN cross section. We comment on the tentative effect of showers induced by cosmic rays, whose importance in neutrino radio-detection is still unclear.

Below, we expand on each of the above elements.

Previous works studied the sensitivity of upcoming neutrino telescopes to the UHE νN cross section [205], or their capability to measure it [192, 215]. They incorporated some of the above elements, often partially or in less detail; none incorporated all of them, or in full detail. Our analysis is the first detailed, realistic forecast of the capability to measure the UHE νN cross section. It has the flexibility needed to explore how sensitive the measurements are to changes in detector features. It is geared at IceCube-Gen2, but serves as a template for other neutrino telescopes under planning [82–84, 193, 216].

6.3 NEUTRINO-NUCLEON DEEP INELASTIC SCATTERING

6.3.1 *The neutrino-nucleon DIS cross section*

At neutrino energies above 1 TeV, the neutrino-nucleon (νN) cross section is dominated by deep inelastic scattering (DIS) [217–220], where the interacting neutrino scatters off the partons—*i.e.*, quarks and gluons—that make up the nucleon. In the process, the nucleon, N, is broken up, and the final-state parton promptly hadronizes into hadrons, X. In charged-current (CC) DIS, mediated by a W boson, the final state contains in addition a charged lepton of the same flavor as the incoming neutrino, *i.e.*, $\nu_\alpha + N \to \alpha^- + X$ ($\alpha = e, \mu, \tau$). In neutral-current (NC) DIS, mediated by a Z boson, the final state contains instead a neutrino, *i.e.*, $\nu_\alpha + N \to \nu_\alpha + X$. Anti-neutrinos undergo the same DIS interactions, charge-conjugated.

In a νN DIS interaction, a fraction y—the inelasticity—of the initial neutrino energy, E_ν, is transferred to X; the remainder fraction $(1 - y)$ is transferred to the final-state lepton. The distribution of inelasticity values is important: it affects the passage of neutrinos through the Earth, where they interact with underground matter (see Section 6.5), and their detection at the neutrino telescopes, where they interact with the detector medium (see Section 6.6). At the energies that are relevant for us, the average inelasticity is about 0.25 [205, 221]. However, the distributions of values of y, given by the differential νN cross sections $d\sigma^{\rm CC}/dy$ and $d\sigma^{\rm NC}/dy$, are broad, peak at $y = 0$, and vary with neutrino energy; see Fig. 7. To produce our results below we use these energy-dependent inelasticity distributions.

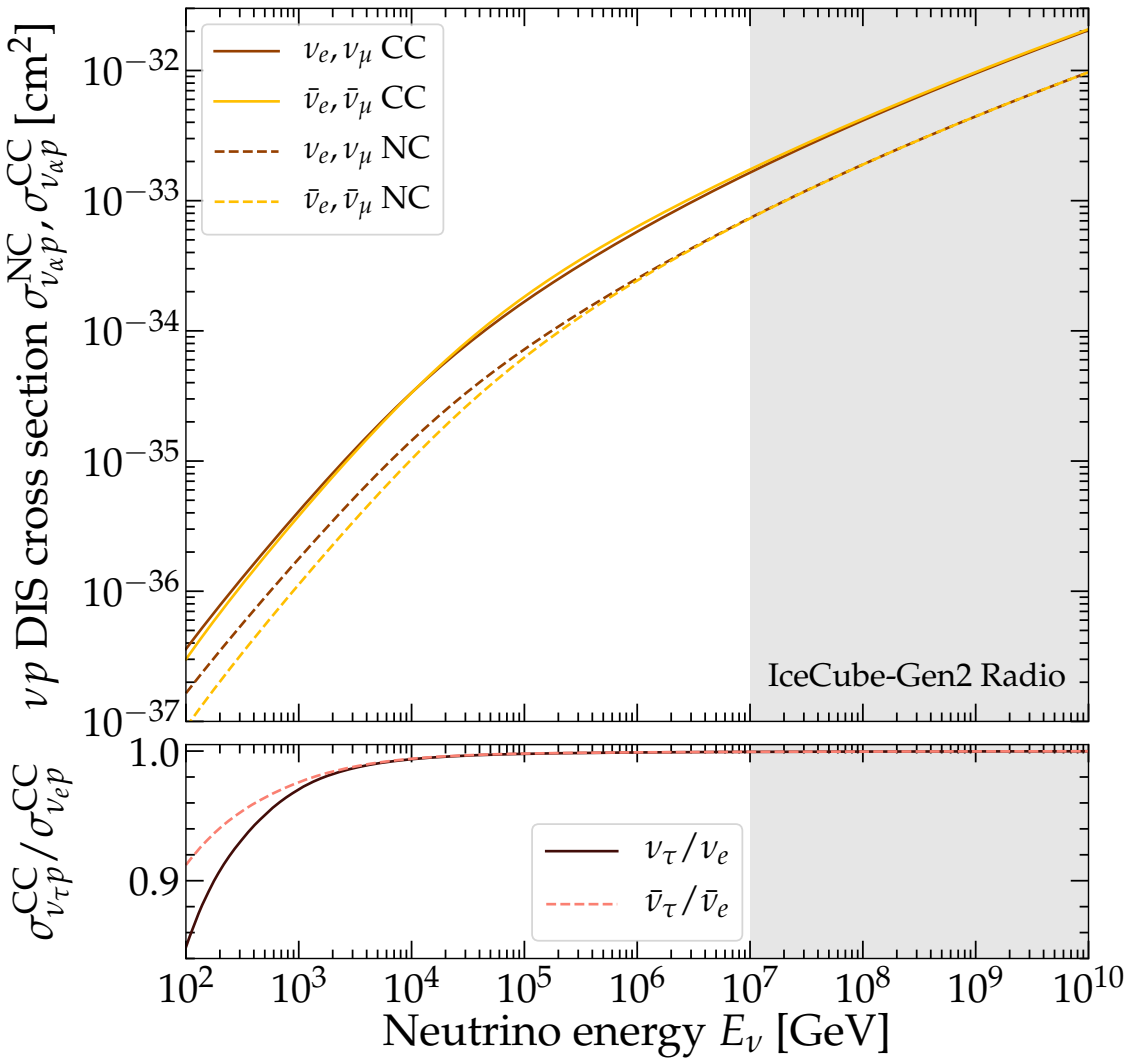

Figure 6: Neutrino-proton (νp) deep inelastic scattering (DIS) total cross section used in our analysis, during the propagation of neutrinos inside the Earth using NUPROPEARTH [209, 210] and in the computation of event rates at IceCube-Gen2. See Section 6.3.1 for details. This is the central value of the BGR18 calculation [194], extracted from the HEDIS [209] module of GENIE [222]. The shaded region is the approximate energy window where the radio array of IceCube-Gen2 will be sensitive. *Top:* Cross sections for ν_e and ν_μ; they are equal. *Bottom:* Ratio of the ν_τ to ν_e CC cross sections showing the low-energy suppression of the former.

The νN DIS cross sections are computed on the basis of the parton distribution functions (PDFs) inside the nucleon, *i.e.*, the probability densities of finding valence and sea quarks of different flavors, and gluons, inside the nucleon [217–220]. They depend on two kinematic variables: the four-momentum transferred to the interacting parton, Q^2, and the Bjorken scaling parameter x, the fraction of the nucleon moment carried by the interacting parton. PDFs are measured predominantly in charged lepton-nucleon scattering [223, 224]; because they describe the nucleon, and not the lepton that probes it, they apply also to neutrino-nucleon scattering.

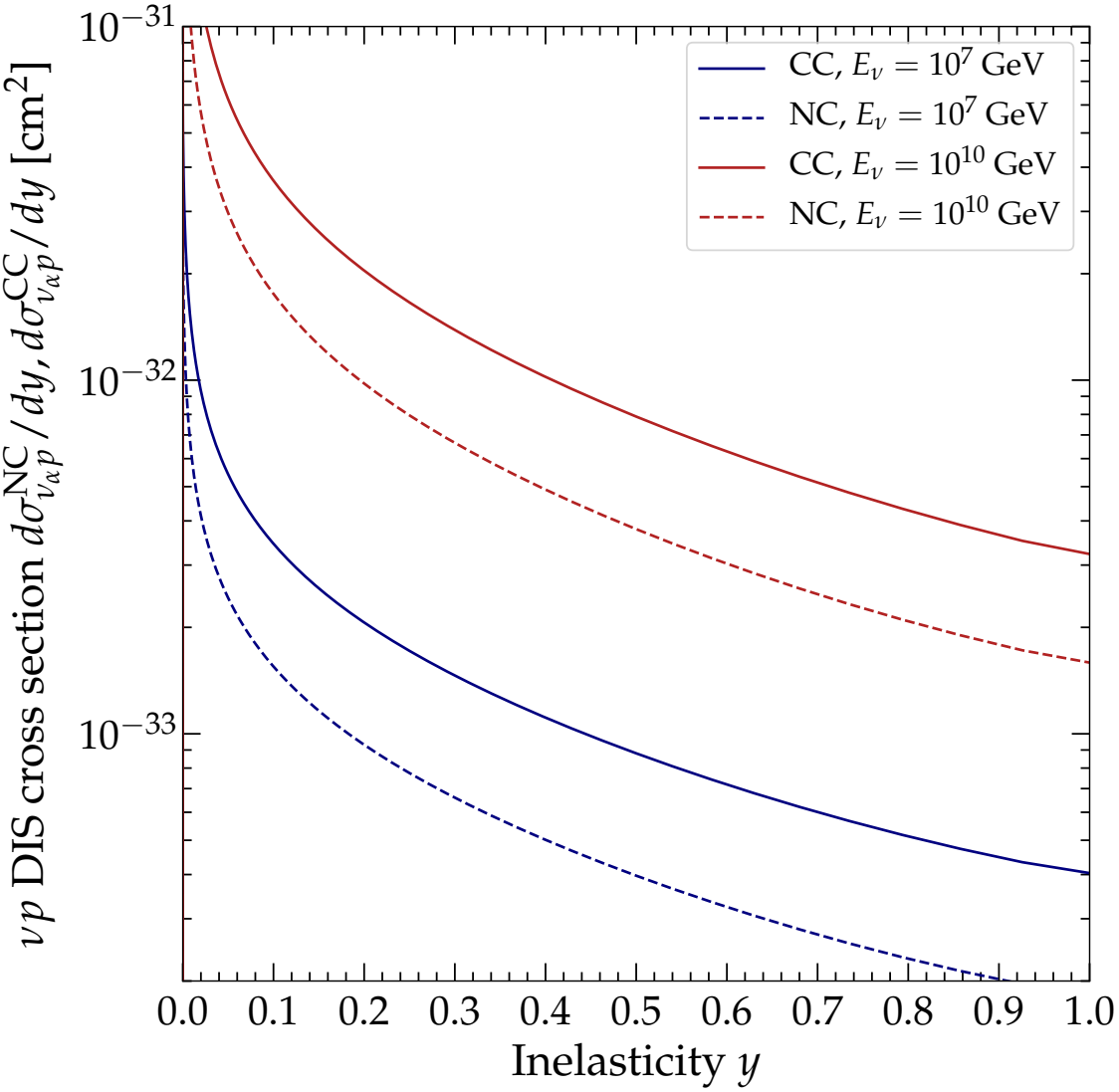

Figure 7: Inelasticity distributions in neutrino-proton (νp) DIS for the BGR18 cross section [194], for two illustrative neutrino energies. We use the inelasticity distributions to compute the expected shower rate at IceCube-Gen2 in Section 6.6.4. At the energies relevant to our analysis, the distributions are equal for ν_α and $\bar{\nu}_\alpha$ of all flavors.

To compute νN DIS cross sections at an energy E_ν, we need to evaluate PDFs at roughly $x \gtrsim m_W / E_\nu$, where m_W is the mass of the W boson. Presently, PDFs are known down to $x \sim 10^{-5}$. At TeV–PeV energies, this is sufficient to compute the cross section with low uncertainty. At EeV energies, relevant to our work, PDFs must be extrapolated to $x \sim 10^{-7}$; this extrapolation is the main source of uncertainty in the calculation of EeV cross sections. Broadly stated, different calculations of the high-energy νN DIS cross section [134, 194, 203, 205, 221, 225–229] differ in three aspects: the perturbative order to which the cross section is computed, the PDF set that they use, and the procedure they use to extrapolate PDFs to low values of x. Competing calculations are close at TeV–PeV, but diverge at EeV; see, *e.g.*, Fig. 3 in Ref. [61].

In our analysis, we adopt the state-of-the-art BGR18 νN DIS cross section calculation from Ref. [194], computed to next-to-next-to-leading order, as our baseline. It uses the recent NNPDF3.1SX PDFs [230], informed by D-meson data from LHCb [231–233], including the effect of nuclear corrections and heavy quarks, and treats consistently the behavior of the PDFs at small values of Bjorken-x. The reported uncertainty in the BGR18 cross section calculation ranges from $\lesssim 3\%$ at 100 PeV, to $\lesssim 10\%$ at 10 EeV; see Fig. 4. The uncertainty stems from uncertainties in the nuclear PDFs [209]. Later, in Section 6.8, we find that for the most optimistic UHE neutrino flux predictions, we might be able to measure the cross section to within comparable uncertainty; see Fig. 4. (The theory uncertainty in the cross section can be larger in the presence of nuclear corrections [194], which we ignore for Fig. 4, but comment on later.)

Figure 6, and also Fig. 4, shows the central value of the BGR18 CC νN DIS cross section (in the notation introduced later, in Section 6.7.1, this is $\sigma_{\rm std}$). The cross section grows with E_ν, and the softer-than-linear dependence on E_ν due to the W mass is apparent from a few TeV on. At EeV energies, the cross section grows roughly as $\propto E_\nu^{0.3}$ [221]. Within the energy window where IceCube-Gen2 will be sensitive, the cross sections are flavor-universal, yet, at low energies, 6 shows that the ν_τ CC cross section is kinematically suppressed due to the large mass of the tauon.

Figure 7 shows the corresponding inelasticity distributions, for NC and CC interactions. Later, in Section 6.6.4, we use them to compute the expected event rate at IceCube-Gen2. The distributions peak at $y = 0$, but they are broad, *i.e.*, there is a large spread in how the incoming neutrino energy in a νN DIS is split into the final-state particles. This, in turn, generates a large spread in the energies of the neutrino-initiated showers at the detector, and on their detectability.

To make our forecasts self-consistent, we use the same BGR18 cross sections to compute the propagation of neutrinos inside Earth and their detection. At the neutrino energies relevant to us, $E_\nu \gtrsim 10^7$ GeV, the CC cross section is roughly twice the NC cross section, and differences between the cross sections of ν_α and $\bar{\nu}_\alpha$ and between different flavors are small. Below 100 TeV, differences are larger, but those energies do not come into play in our analysis. We always use the CC and NC cross section of each flavor of ν_α and $\bar{\nu}_\alpha$ individually. Below, as part of our forecasts, we use the central value of the BGR18 cross section as a baseline ($\sigma_{\rm std}$), and also versions of it shifted up ($> \sigma_{\rm std}$) and down ($< \sigma_{\rm std}$) by constant factors.

6.3.2 *Other neutrino interactions*

At ultra-high energies, νN DIS is the dominant neutrino interaction. However, other sub-dominant interactions also affect the propagation of neutrinos inside the Earth. During propagation, we account for the following interactions, as implemented in NUPROPEARTH [209, 210]; we defer to Ref. [209] for details:

- νN **DIS on the partons of the nucleon:** The dominant interaction channel at ultra-high energies; see Section 6.3.1.

- **Neutrino DIS on the photon field of the nucleon:** The neutrino interacts with a lepton generated by the photon field of the nucleon. This is negligible except when the neutrino can produce an on-shell W boson that enhances the cross section resonantly, *i.e.*, when $\sqrt{2m_N E_\nu} \gtrsim m_W$, or $E_\nu \gtrsim 3$ TeV. It can account for a correction of up to 3% of the total DIS cross section [234–238].

- **Coherent neutrino-nucleus scattering:** The neutrino interacts coherently with the photon field of the target nucleus [239–241]. The cross section is $\propto Z^2$, where Z is the atomic number of the nucleus; thus, it matters mostly for heavy nuclei. This process is important only in scatterings with small transferred momentum, $Q \lesssim 1$ GeV, where it can contribute up to 10% of the total cross section.

- **Elastic and diffractive neutrino scattering on nucleons:** The neutrino interacts with the photon field of individual nucleons. This process is important in scattering with small $Q \sim$ GeV, where the elastic component of the form factors of the proton become relevant. When $E_\nu \gtrsim 3$ TeV, the process may create an on-shell W boson resonantly, contributing to the resonant cross section of the neutrino DIS on the photon field of the nucleon.

- **Neutrino scattering on atomic electrons:** Neutrino scattering on atomic electrons is negligible except for high-energy $\bar{\nu}_e$. When the center-of-mass energy is $\sqrt{2m_e E_\nu} \approx m_W$, *i.e.*, when $E_\nu \approx 6.3$ PeV, the $\bar{\nu}_e e$ scattering is resonance and produces an on-shell W; this is known as the Glashow resonance [242, 243]. Around the resonance energy, the $\bar{\nu}_e e$ cross section dominates;

it is roughly 200 larger than the νN DIS cross section. We adopt the Glashow-resonance cross section from Ref. [236], computed to next-to-leading order.

The sub-dominant interactions increase the attenuation of the UHE neutrino fluxes by up to 10%, when compared to νN DIS only, especially for neutrinos coming into the detector from around the horizon [209]. Below, when computing the propagation of neutrinos through the Earth and their resulting fluxes at the detector, we always account for all of the above interactions; see Section 6.5. In all of the interactions, because of the high energies, final-state neutrinos are nearly co-linear with initial-state neutrinos; any transverse momentum is negligible compared to the forward momentum, and we ignore it.

6.3.3 *High-energy νN DIS using cosmic neutrinos*

6.3.3.1 *Motivation*

Measuring the high-energy νN DIS cross section offers the possibility to probe fundamental physics on two fronts. First, the higher the energy of the neutrino, the smaller the value of x that it probes; see Section 6.3.1. This allows us to probe the structure of nucleons deeper, testing predictions of potentially non-linear behavior of the PDFs, such as from BFKL theory [195–198] and color-glass condensates [199], and to look for electroweak sphalerons [200]; see, *e.g.*, Refs. [200–203]. Second, the higher the neutrino energy, the higher the energy scale probed where new physics could affect the cross section. Possibilities include, *e.g.*, leptoquarks, extra dimensions, and new gauge bosons [192, 204–208].

Existing measurements of the νN DIS cross sections using accelerator neutrinos reach uo to 350 GeV [53]; see Fig. 4. Upcoming accelerator-neutrino experiments, like FASERν [183], should measure the cross section up to a few TeV. To measure it at higher energies, we must use neutrinos from natural sources: atmospheric neutrinos, from tens of TeV to roughly 100 TeV; high-energy cosmic neutrinos from 10 TeV to 10 PeV; and ultra-high-energy neutrinos, from 100 PeV on. Measurements using the former two exist [60, 61, 63]; we forecast measurements using the latter, where no measurement exists yet.

6.3.3.2 *Overview*

We base our forecasts of cross-section measurements on estimates of the expected number of detected neutrino-induced events in IceCube-Gen2. To understand where the sensitivity to the cross section comes from, we estimate the number of detected neutrinos of energy E_ν coming into the detector from zenith angle θ_z as

$$N_\nu(E_\nu, \theta_z) \propto \Phi_\nu(E_\nu)\sigma(E_\nu)e^{-L(\theta_z)/L_{\nu N}(E_\nu,\theta_z)} \,. \tag{6.1}$$

Here, Φ_ν is the diffuse, isotropic flux of UHE cosmic neutrinos that arrives at the surface of the Earth, σ is the νN cross section, L is distance from the surface of the Earth to the detector, $L_{\nu N} \equiv (\sigma n_N)^{-1}$ is the mean free path, and n_N is the average number density of nucleons encountered by the neutrino along its way inside Earth. The latter depends on θ_z and on the internal matter density of Earth. Equation (6.1) is merely a simplified expression for the purpose of providing insight, and is not used to produce our results. The full treatment of neutrino propagation and detection that we use to produce results is in Sections 6.5 and 6.6, respectively.

Equation (6.1) shows that the number of events depends on the νN cross section doubly. During propagation, the cross section acts via the exponential, attenuating the flux of neutrinos as they go through Earth (in the full calculation, there is also regeneration of lower-energy neutrinos, which we ignore momentarily). Higher neutrino energies—and, therefore, larger cross section—and longer distances traveled inside Earth lead to stronger attenuation. At detection, the cross section acts proportionally; the larger it is, the higher the chances of detecting a neutrino that arrives at the detector. The sensitivity of neutrino telescopes to the high-energy νN DIS cross section stems from the interplay of these two effects.

We extract the cross section by examining the angular distribution of detected events [60, 61, 63, 205, 244–247]. For events induced by neutrinos arriving from above the detector, *i.e.*, *downgoing events*, where L is small, the attenuation is negligible. In this case, the right-hand side of Eq. 6.1 becomes $\propto \Phi_\nu\sigma$ and, therefore, the sensitivity to the cross section is mild. This is due to the degeneracy between Φ_ν and σ: for a fixed event rate N_ν, a higher flux can be traded off for a lower cross section, and vice versa. For events induced by neutrinos arriving from well below the horizon, *i.e.*, *upgoing events*, where L is large, the attenuation is strong. In this case, the event

rate is low: the higher the neutrino energy—*i.e.*, the higher the cross section—the stronger the attenuation.

For events induced by neutrinos arriving horizontally and nearly horizontally into the detector, the two effects above balance out. Neutrinos from this direction travel tens to hundreds of kilometers underground, enough for the flux to be attenuated, but not eliminated. The higher the neutrino energy, the narrower the solid angle around the horizon from where neutrinos arrive to the detector. At ultra-high energies, neutrinos can only arrive at the detector from a few degrees around the horizon, where the distance traveled underground is not too long (see, *e.g.*, Fig. A2 in Ref. [61]); these are called *Earth-skimming neutrinos* [248].

Combining events from all directions breaks the degeneracy between Φ_ν and σ in downgoing events, and, via the attenuation of upgoing and near-horizontal events, grants us sensitivity to σ [205, 244–247]. Yet, to make use of this, the detector requires a good angular resolution around the horizon. This is necessary to infer the direction of the incoming neutrino precisely, and, therefore, the column density of matter that it traversed on its way to the detector. In IceCube, at TeV–PeV energies, the angular resolution varies from sub-degree for ν_μ-induced track events, to tens of degrees for shower events induced by all neutrino flavors. In our forecasts, geared at radio-detection of EeV-scale neutrinos in IceCube-Gen2, we adopt a baseline resolution of 2° to produce our main results, and also explore the effect of alternative choices; see Section 6.6 and Fig. 24 for details.

6.3.3.3 *Existing measurements: TeV–PeV*

Figure 4 shows the three existing measurements of the TeV–PeV νN DIS cross section, all based on IceCube data [60, 61, 63]. They used different analysis strategies and data sets; they agree with Standard Model (SM) predictions, though the measurement uncertainties are large. In addition to the TeV–PeV measurements, there are complementary studies to measure the cross section in IceCube from 100 GeV to a few TeV [249].

Reference [60] used roughly 10800 through-going neutrino-induced muon tracks, predominantly of atmospheric origin, to measure the cross section in a single neutrino energy bin spanning 6.30–980 TeV. In a through-going track event, a ν_μ interacts at an unknown position outside the detector and creates a high-energy muon that crosses part of it. This analysis let the normalization

of the CC and NC cross sections float, fit it to the data, and found the cross section to be $1.30^{+0.30}_{-0.26}$ times the SM prediction from Ref. [250]. The error is approximately equal parts statistical and systematic; the latter is mainly due to the difficulty in reconstructing the neutrino energy from the measured muon energy. Improvements on this measurement strategy are ongoing [64].

References [61, 63] used instead High Energy Starting Events (HESE), predominantly of cosmic origin, to measure the cross section from 20 TeV to a few PeV. Unlike a through-going track, in a HESE event the neutrino interacts inside the detector. The ensuing shower deposits a large fraction of its energy in the instrumented volume. As a result, the neutrino energy is reconstructed accurately, which facilitates measuring the cross section in multiple energy bins. However, because HESE events are relatively rare, these analyses are limited by low event rates. The CC interaction of ν_e or ν_τ, or the NC interaction of a neutrino of any flavor, induces a shower that is typically contained in the detector. The NC interaction of ν_μ induces in addition a muon track that starts inside the detector, but ranges out of it. Reference [61] used 58 HESE showers collected in 6 years to measure the cross section in bins in the range 18 TeV–2 PeV, with an accuracy of roughly half an order of magnitude in each bin. Reference [63] used 60 HESE showers and tracks collected in 7.5 years to measure the cross section in bins in the range 60 TeV–10 PeV with increased accuracy, thanks to reduced detector systematics. A related analysis [62] used contained events to make the first measurement of the multi-TeV inelasticity distribution.

6.3.3.4 *This work: forecasts at EeV*

To produce forecasts of UHE cross-section measurements in IceCube-Gen2, we adopt the BGR18 cross section as the baseline, and explore measurement prospects for a variety of diffuse UHE flux models. Our procedure is reminiscent of analyses that use HESE events [60, 61]. Section 6.7 describes it in detail. In our forecasts, variations in the cross section affect the neutrino propagation inside Earth and their detection. To account for the degeneracy between the flux and the cross section, we always forecast measuring both simultaneously. We adopt a Bayesian approach in our statistical analysis, and account for statistical fluctuations in the number of neutrino-induced events and non-neutrino backgrounds.

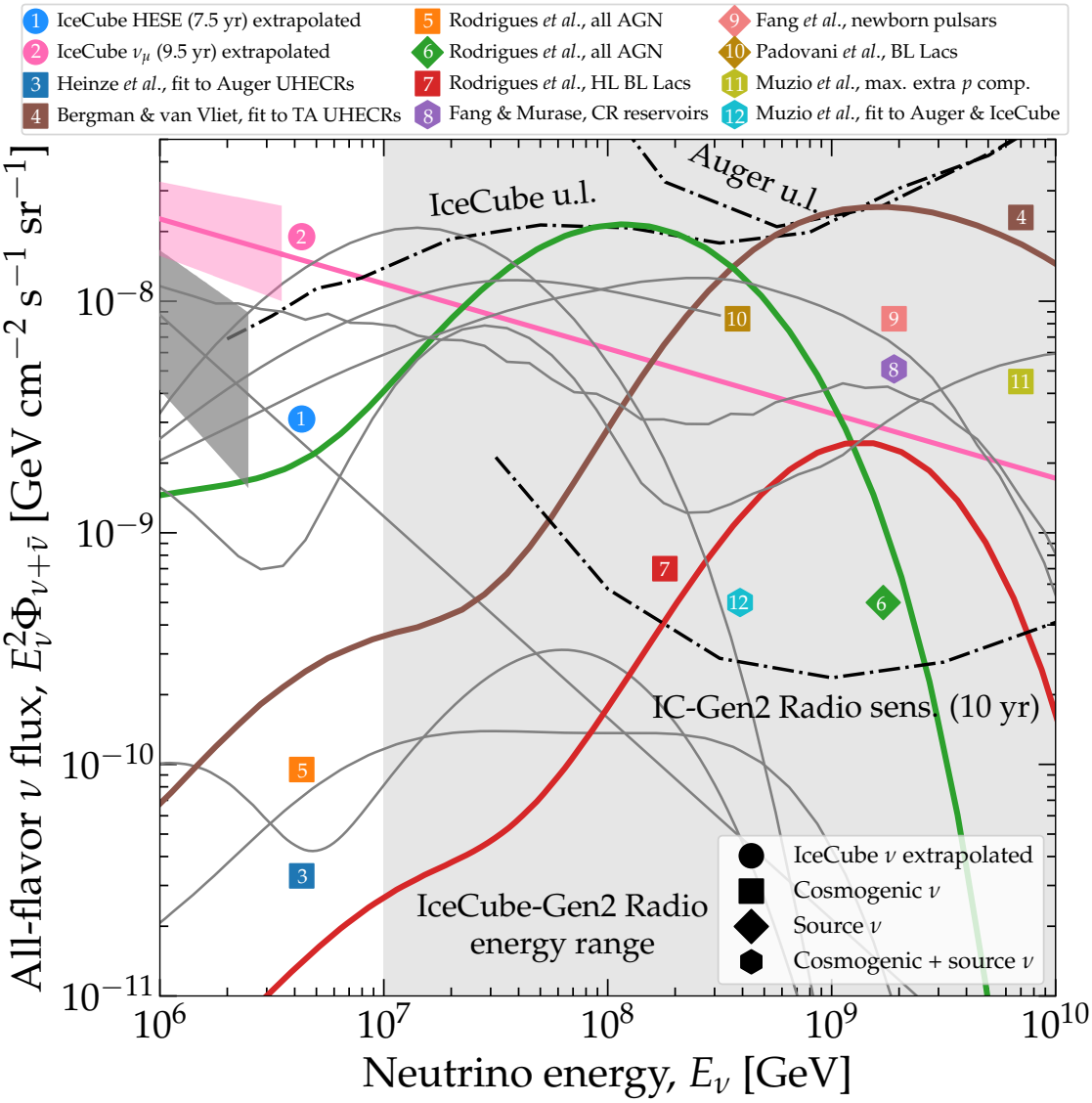

Figure 8: Benchmark UHE neutrino flux models used in our analysis [37, 174–180, 188, 193]. Highlighted models 2, 4, 6, and 7 receive special attention in the main text, but results for all models are shown in Tables 1 and 2, and in Appendix A.1. The upper limits on the UHE neutrino flux are from IceCube [66] and the Pierre Auger Observatory [67]. The projected sensitivity of the radio component of IceCube-Gen2 is from Ref. [77]. See Section 6.4 for an overview of the flux models.

6.4 ULTRA-HIGH-ENERGY NEUTRINOS

Ultra-high-energy neutrinos, with energies of 100 PeV and above, are expected to come from interactions of ultra-high-energy cosmic rays (UHECRs), of EeV-scale energies, on radiation or matter. UHECR interactions may occur inside the cosmic accelerators that are their sources or outside them, en route to Earth. In the former case, the resulting UHE neutrinos are dubbed *source neutrinos* (or *astrophysical neutrinos*); in the latter, they are dubbed *cosmogenic neutrinos*. Because of

unknowns in the properties of UHECRs and their sources, there is a large spread in the predicted neutrino flux normalization and the shape of the neutrino energy spectrum. In our analysis, we consider a wide breadth of benchmark flux models from the literature in order to represent this spread. Below, we introduce our benchmark flux models, and the choices that we make in building them.

6.4.1 *Overview*

Cosmic accelerators are expected to generate a population of non-thermal UHECRs with a power-law energy spectrum [251]. The interaction of UHECR protons on matter (pp) or radiation ($p\gamma$) often creates a short-lived $\Delta(1232)$ resonance that promptly decays into charged pions. Upon decaying, they create neutrinos, *i.e.*, $\pi^+ \to \mu^+ + \nu_\mu$, followed by $\mu^+ \to e^+ + \nu_e + \bar{\nu}_\mu$, and their charge-conjugated processes. Each final-state neutrino receives 5% of the energy of the parent proton, on average. En route to Earth, neutrino oscillations change the flavor composition of the flux, *i.e.*, the proportion of ν_e, ν_μ, and ν_τ in it; we account for this in Section 6.4.2.

For UHE neutrinos produced in pp interactions, the resulting neutrino energy spectrum follows the power-law energy spectrum of the parent protons, and may extend unbroken down to low energies [177]. The spectral index of the neutrino spectrum is inherited from the spectral index of the parent proton spectrum.

For UHE neutrinos produced in photohadronic, *i.e.*, $p\gamma$, interactions, the resulting neutrino energy spectrum is determined by the energy spectra of the interacting protons and photons. Because the proton spectrum is a power law and the photon spectrum is peaked or is a power law with a spectral break, the resulting neutrino spectrum is peaked. The neutrino spectrum peaks at an energy determined by the Δ resonance energy; the width of the neutrino peak is determined by the widths of the photon and proton spectra.

Cosmogenic neutrinos, or *GZK (Greisen-Zatsepin-Kuzmin) neutrinos*, were first predicted in the late 1960s [27, 28, 65]. They are expected to be made during the extragalactic propagation of UHECRs, in photohadronic interactions on the cosmic microwave background (CMB), for neutrinos of energies typically in the EeV-scale, and on the extragalactic background light (EBL), for neutrino of

energies typically in the tens of PeV. (Cosmogenic anti-neutrinos have an additional contribution from the beta-decay of neutrons produced in photohadronic interactions, typically around PeV energies, outside the region of interest for neutrino radio-detection in IceCube-Gen2.) Because the CMB photon spectrum is well-known, the uncertainty in the prediction of the cosmogenic neutrino flux comes mainly from uncertainties in the energy spectrum, mass composition, and maximum energies of UHECRs, as measured by the Pierre Auger Observatory [26, 252, 253] and the Telescope Array (TA) [132, 254], and in the abundance of the UHECR sources at different redshifts. See, *e.g.*, Refs. [83, 125] for an overview. Generally, a harder UHECR energy spectrum, lighter mass composition, higher maximum energy, and a source number density that peaks at intermediate redshifts lead to a higher cosmogenic neutrino flux; see, *e.g.*, Refs. [172–174, 255].

UHE source neutrinos are expected to be made in either pp interactions, $p\gamma$ interactions, or both, inside UHECR sources. When photohadronic interactions are dominant, the spectrum of UHE source neutrinos has a similar shape to that of cosmogenic neutrinos, except that it contains a single $p\gamma$ bump, since there is typically a single relevant target spectrum of photons inside the sources. (UHE source anti-neutrinos also have an additional contribution from the beta-decay of neutrons produced in photohadronic interactions, typically at energies too low to be relevant for our analysis.) In some models of UHE neutrino production in cosmic-ray reservoirs [177], the contribution of neutrinos from pp interactions extends to low energies, and the contribution of $p\gamma$ interactions is dominant at high energies.

In realistic models of high-energy neutrino production, including some of the ones that we consider in our analysis, different neutrino production channels become accessible at different energies. In $p\gamma$ interactions [256–258], neutrino production occurs dominantly via the $\Delta(1232)$ resonance at the lowest energies, with a sub-leading contribution from direct (t-channel) production, via heavier resonances at intermediate energies, and via multi-pion production at the highest energies. In pp interactions [130], the neutrino yield evolves with energy as a result of the evolving pion multiplicity. Moreover, the physical conditions in the production region affect the energy of charged particles—protons, muons, pions, and kaons—whose decay yields neutrinos. For instance, intense magnetic fields may induce important synchrotron energy losses [104, 133, 259, 260] that cap the high-energy neutrino yield, while re-acceleration of charged particles might counteract

these losses [261]. Further, the presence of nuclei heavier than protons, and the nuclear cascades initiated by their interactions with source environments, introduce additional nuance [262, 263].

6.4.2 *Flavor and ν vs. $\bar{\nu}$ composition in our analysis*

Because, at different energies, different neutrino production channels dominate (see Section 6.4.1) and the physical conditions at the sources affect charged particles differently, the flavor composition of the UHE cosmic neutrinos, *i.e.*, the proportion of $\nu_e + \bar{\nu}_e$, $\nu_\mu + \bar{\nu}_\mu$, and $\nu_\tau + \bar{\nu}_\tau$ in the total flux, and the ratio of ν_α to $\bar{\nu}_\alpha$, are expected to evolve with neutrino energy. This matters for the purpose of propagating neutrinos through the Earth, on their way to the detector, and of forecasting their detection rates. Section 6.5 shows that neutrinos of different flavor are affected differently by their passage through Earth. Differences between ν_α *vs.* $\bar{\nu}_\alpha$ are small, though we keep track of them. The exception where differences are significant is the case of ν_e *vs.* $\bar{\nu}_e$, since only $\bar{\nu}_e$ interact via the Glashow resonance [242]. Section 6.6 shows that neutrinos of different flavors have different interaction rates and deposit energy differently at IceCube-Gen2; there, differences between ν_α *vs.* $\bar{\nu}_\alpha$ are also small, though we keep track of them.

In Section 6.4.3, we introduce the benchmark UHE neutrino flux models that we later use to forecast νN cross-section measurements in IceCube-Gen2. In order to make our predictions as informed as possible, we model the flavor composition and ν_α *vs.* $\bar{\nu}_\alpha$ content of the benchmark fluxes as accurately as possible. In doing so, neutrino flavor transitions play a key role. Below, we explain how we compute them.

Because a neutrino of a particular flavor, ν_α ($\alpha = e, \mu, \tau$), is a superposition of neutrino mass eigenstates, ν_i ($i = 1, 2, 3$), it can change flavor as it propagates. The flavor and mass bases are connected by the Pontecorvo-Maki-Nakagawa-Sakata (PMNS) mixing matrix, $\mathbf{U}$, parametrized [264] via three mixing angles, θ_{12}, θ_{23}, θ_{13}, and one CP-violation phase, $\delta_{\rm CP}$, whose values are measured in neutrino oscillation experiments.

Formally, the probability $P_{\alpha\beta}$ of a flavor transition $\nu_\alpha \to \nu_\beta$ oscillates as a function of the distance traveled by the neutrino. However, for high-energy cosmic neutrinos, the oscillation length, which is $\propto 1/E_\nu$, is tiny compared to the typical traveled distance of Mpc–Gpc, so the probability oscillates

rapidly. In addition, neutrino telescopes have limited energy resolution [265]. As a consequence, in practice, oscillations average out, and we are sensitive only to the average probability [266],

$$P_{\beta\alpha} = \sum_{i=1,2,3} |U_{\beta i}|^2 |U_{\alpha i}|^2 \,. \tag{6.2}$$

Below, we compute the flux of each neutrino flavor at Earth for our benchmark flux models by evaluating $P_{\beta\alpha}$ using values of the mixing parameters forecast for the 2030s [267], anchored on present measurements [268, 269].

For this purpose, our benchmark flux models fall into three categories, depending on what information is available to us to build the model with. For each, we compute the flux of each neutrino species at Earth differently:

(a) *Flux models for which we have available the pre-oscillation flux of each neutrino species separately (models 3–7 below).* In this case, we compute the flux of ν_α at Earth, Φ_{ν_α}, from the pre-oscillation fluxes that we have available, $\Phi_{\nu_\beta,\mathrm{S}}$, as

$$\Phi_{\nu_\alpha}(E_\nu) = \sum_{\beta=e,\mu,\tau} P_{\beta\alpha} \Phi_{\nu_\beta,\mathrm{S}}(E_\nu) \tag{6.3}$$

and similarly for the flux $\Phi_{\bar{\nu}_\alpha}$ of $\bar{\nu}_\alpha$, but changing $\Phi_{\nu_\beta,\mathrm{S}} \to \Phi_{\bar{\nu}_\beta,\mathrm{S}}$. Because in all of our benchmark flux models neutrinos are produced by pion, kaon, and neutron decays, only ν_e, $\bar{\nu}_e$, ν_μ, and $\bar{\nu}_\mu$ exist pre-oscillation; however, after oscillations, all six species are populated in the flux at Earth.

(b) *Flux models for which we only have available the sum of the oscillated fluxes of all neutrino species at Earth (models 1, 8–11 below).* In this case, we consider the flavor composition to be energy-independent and split the flux of each flavor evenly between ν_α to $\bar{\nu}_\alpha$ at all energies. The latter assumption holds approximately, but can have large deviations at high energy, depending on model-dependent details of the neutrino production; see, *e.g.*, Ref. [257] and Fig. 9 below. To estimate the flavor composition, we assume that all neutrinos are made in pion decays, *i.e.*, $\pi^+ \to \mu^+ + \nu_\mu$, followed by $\mu^+ \to e^+ + \nu_e + \bar{\nu}_\mu$, and their charge-conjugated processes. Hence, pre-oscillation, the flavor composition is $\left(f^\pi_{e,\mathrm{S}}, f^\pi_{\mu,\mathrm{S}}, f^\pi_{\tau,\mathrm{S}}\right) \equiv \left(\frac{1}{3}, \frac{2}{3}, 0\right)$, where $f^\pi_{\beta,\mathrm{S}}$ is the ratio of $\nu_\beta + \bar{\nu}_\beta$ to the total. After oscillations, at Earth, the flavor ratios become

$$f^\pi_{\alpha,\oplus} = \sum_{\beta=e,\mu,\tau} P_{\beta\alpha} f^\pi_{\beta,\mathrm{S}} \,. \tag{6.4}$$

Thus, starting, from the all-species oscillated flux at Earth that we have available, $\Phi_{6\nu}$, we estimate the oscillated fluxes of ν_α and $\bar{\nu}_\alpha$ at Earth as

$$\Phi_{\nu_\alpha}(E_\nu) = \Phi_{\bar{\nu}_\alpha}(E_\nu) = \frac{1}{2} f^\pi_{\alpha,\oplus} \Phi_{6\nu}(E_\nu) \,, \tag{6.5}$$

where the factor of $1/2$ splits the flux of $\nu_\alpha + \bar{\nu}_\alpha$ evenly between them.

(c) *Flux models for which we only have available the $\nu_\mu + \bar{\nu}_\mu$ oscillated flux at Earth (model 2 below).* Like with fluxes in category (b), we consider the flavor composition to be energy-independent and split the flux of each flavor evenly between ν_α to $\bar{\nu}_\alpha$ at all energies. Starting from the flux of $\nu_\mu + \bar{\nu_\mu}$ at Earth that we have available, we estimate the oscillated fluxes of ν_α and $\bar{\nu}_\alpha$ at Earth as

$$\Phi_{\nu_\alpha}(E_\nu) = \Phi_{\bar{\nu}_\alpha}(E_\nu) = \frac{1}{2} \frac{f^\pi_{\alpha,\oplus}}{f^\pi_{\mu,\oplus}} \Phi_{\nu_\mu + \bar{\nu}_\mu}(E_\nu) \,, \tag{6.6}$$

where the factor of $1/2$ splits the flux of $\nu_\alpha + \bar{\nu}_\alpha$ evenly between them.

For benchmark flux model 12, the flux of each neutrino species at Earth is directly available [270]; we adopt them without modification.

In our analysis, we forecast measurements in IceCube-Gen2 in the 2030s. By then, the values of the mixing parameters are expected to be known more precisely than today [268, 269], thanks to the upcoming oscillation experiments DUNE [271], Hyper-Kamiokande [272], and JUNO [273]. Assuming that the true values of the mixing parameters are equal to their present-day best-fit values from the NuFit 5.0 global fit to oscillation data [268, 269], and that the neutrino mass ordering is normal, by 2030 we expect that [267] $\sin^2\theta_{12} = 0.304 \pm 0.00164$, $\sin^2\theta_{23} = 0.573^{+0.006288}_{-0.00659}$, $\sin^2\theta_{13} = 0.02219^{+0.00062}_{-0.00063}$, and $\delta_{\rm CP} = (197^{+11.22}_{-10.10})^\circ$. Thus, for neutrinos produced in pion decays, as in categories (b) and (c) above, the flavor ratios at Earth, computed with Eq. (6.4), are close to equipartition, *i.e.*,

$$f^\pi_{e,\oplus} = 0.298^{+0.001}_{-0.003} \,, \tag{6.7}$$

$$f^\pi_{\mu,\oplus} = 0.359^{+0.004}_{-0.006} \,, \tag{6.8}$$

$$f^\pi_{\tau,\oplus} = 0.342^{+0.009}_{-0.005} \,, \tag{6.9}$$

ignoring correlations between the mixing parameters. The uncertainties in $f^\pi_{\beta,\oplus}$ are tiny; accounting for correlations, they would be even smaller. Thus, we can safely neglect the uncertainty in

the future values of $f^{\pi}_{\beta,\oplus}$, and just use their best-fit above when computing Eqs. (6.5) and (6.6) henceforth. (If the mass ordering is inverted, the best-fit values of $f^{\pi}_{\beta,\oplus}$ change only slightly [267], so we do not explore that case separately.)

6.4.3 *Benchmark flux models*

Figure 8 shows the twelve UHE neutrino diffuse flux models [37, 174–180, 188, 193] that we use to benchmark the sensitivity of IceCube-Gen2. They include extrapolations of the flux of TeV–PeV neutrinos discovered by IceCube to ultra-high energies (●, models 1 and 2), cosmogenic neutrinos (■, models 3–5, 7), source neutrinos (◆, models 6, 9, 10), and joint predictions of cosmogenic plus source neutrinos (⬢, models 8, 11, 12).

Our selection of benchmark flux models is representative of the breadth of theoretical predictions available in the literature at the time of writing. The highest of our benchmark fluxes—models 4, 6, and 12—saturate the present upper limits on the UHE neutrino flux. The lowest—models 1, 3, and 5—lie below the 10-year differential sensitivity of IceCube-Gen2. The remaining flux models lie in-between these two extremes. Later, in Section 6.8, we find that measuring the UHE νN cross section should be possible for all but the lowest flux models.

Below we present an overview of the benchmark flux models. We defer to their original publications for details (see also Ref. [274]).

1. *IceCube HESE (7.5 yr) extrapolated [188]:* Using 102 High Energy Starting Events (HESE) collected over 7.5 yr, IceCube fit the all-species astrophysical neutrino flux using a power law, $\Phi_{6\nu}(E_\nu) = \Phi_{6\nu,0}(E_\nu/100\ \text{TeV})^{-\gamma_{6\nu}}$, with $\Phi_{6\nu,0} = 6.37^{+1.47}_{-1.62} \times 10^{-18}\ \text{GeV}^{-1}\ \text{cm}^{-2}\ \text{s}^{-1}\ \text{sr}^{-1}$ and $\gamma_{6\nu} = 2.87^{+0.20}_{-0.19}$, valid from 60 TeV to 10 PeV. To build our benchmark flux model 2, we extend this flux to 10^{10} GeV, unbroken, using the best-fit values of $\Phi_{6\nu,0}$ and γ. We assume that the flux of each neutrino species shares this common value of $\gamma_{6\nu}$ and estimate it using Eq. (6.5).

2. *IceCube ν_μ (9.5 yr) extrapolated [37]:* Using 6.5×10^5 through-going muon tracks collected over 9.5 yr, IceCube fit the $\nu_\mu + \bar{\nu}_\mu$ astrophysical neutrino flux using a power law, $\Phi_{\nu_\mu+\bar{\nu}_\mu}(E_\nu) = \Phi_{\nu_\mu+\bar{\nu}_\mu,0}(E_\nu/100\ \text{TeV})^{-\gamma_{\nu_\mu+\bar{\nu}_\mu}}$, with $\Phi_{\nu_\mu+\bar{\nu}_\mu,0} = 1.44^{+0.25}_{-0.26} \times 10^{-18}\ \text{GeV}^{-1}\ \text{cm}^{-2}\ \text{s}^{-1}\ \text{sr}^{-1}$ and

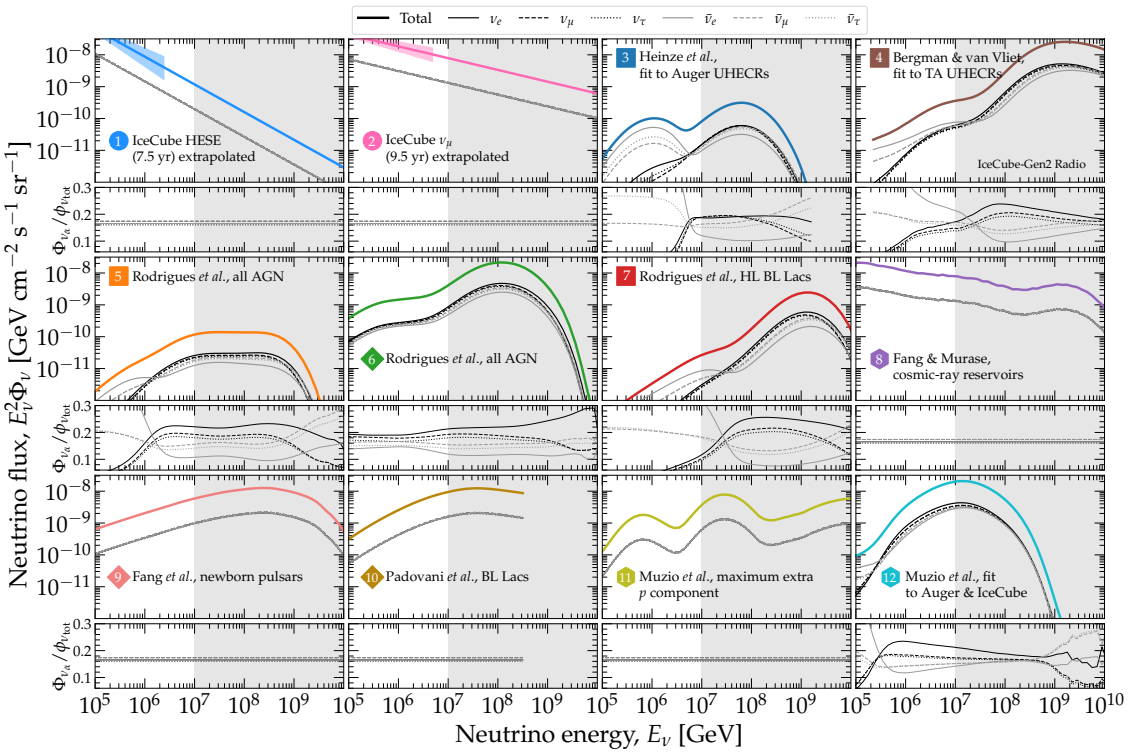

Figure 9: Flux of each neutrino species for each of the benchmark ultra-high-energy neutrino fluxes that we consider (see Fig. 8). Panels under the fluxes show the ratio $\Phi_{\nu_\alpha}/\Phi_{\nu_{\rm tot}}$ of the flux of ν_α to the total flux, *i.e.*, the sum of the fluxes of all species. For flux models 1, 2, and 7, the ratios are constant in neutrino energy and approximately equal to 1/6; the exact values are in Section 6.4.2. For all the other flux models, the ratios change with neutrino energy. See the main text for details. The shaded region indicates the approximate neutrino energy range to which the radio array of IceCube-Gen2 will be sensitive.

$\gamma_{\nu_\mu+\bar{\nu}_\mu} = 2.37 \pm 0.19$, valid from 15 TeV to 5 PeV. To build our benchmark flux model 3, we extend this flux to 10^{10} GeV, unbroken, using the best-fit values of $\Phi_{\nu_\mu+\bar{\nu}_\mu,0}$ and $\gamma_{\nu_\mu+\bar{\nu}_\mu}$. We assume that the flux of each neutrino species shares this common value of $\gamma_{\nu_\mu+\bar{\nu}_\mu}$, and estimate it using Eq.(6.6).

3. *Heinze et al., fit to Auger UHECRs (cosmogenic) [174]:* Cosmogenic neutrinos are generated by UHECRs emitted by a population of nondescript sources, distributed in redshift, and their flux is normalized by fitting the predicted UHECR energy spectrum and mass composition at Earth to recent data from the Pierre Auger Observatory [275, 276]. References [172, 173] predict similar fluxes, also from fits to Auger data. UHECR interactions on the CMB and EBL, including photodisintegration and photohadronic processes, are computed using PRINCE [277]. Because the best-fit value of the maximum UHECR rigidity is low, 2.5×10^9 GV, there are relatively few UHECRs at the highest energies, and so the neutrino yield is low. To build our benchmark model 3, we compute the pre-oscillation fluxes of ν_e, $\bar{\nu}_e$, ν_μ,

and $\bar{\nu}_\mu$ as functions of energy using PRINCE, and use Eq. (6.3) to transform them into the oscillated fluxes of all species at Earth.

4. *Bergman & van Vliet, fit to TA UHECRs (cosmogenic) [193]:* Cosmogenic neutrinos are generated in the same way as for the benchmark flux model 3, but instead fitting the UHECR energy spectrum and mass composition at Earth to recent data from TA [278, 279]. Reference [280] predicts a similar flux. Because the TA data is compatible with a lighter UHECR mass composition and a higher maximum rigidity, the neutrino flux inferred using TA data is larger than with Auger data (model 3). To build our benchmark model 4, the pre-oscillation fluxes of ν_e, $\bar{\nu}_e$, ν_μ, and $\bar{\nu}_\mu$ as functions of energy are computed using CRPROPA3 [281, 282], and use Eq. (6.3) to transform them into the oscillated fluxes of all species at Earth.

5. *Rodrigues et al., all AGN (cosmogenic) [179]:* Neutrinos are produced by the entire population of active galactic nuclei (AGN), which serve as UHECR accelerators. AGN are divided into three sub-populations: low-luminosity BL Lacs, high-luminosity BL Lacs, and flat-spectrum radio quasars (FSRQs). The number density of each sub-population evolves differently with redshift and luminosity [283, 284]. Before escaping, UHECRs interact in the AGN jets, via photodisintegration and photohadronic processes [262, 285]. Cosmogenic neutrinos are produced by the UHECRs that escape, and their flux is computed using PRINCE [277]. Source neutrinos are produced inside the jets, and their flux is computed using NEUCOSMA [257, 258, 286]. The predicted UHECR energy spectrum and mass composition at Earth agree with Auger data [275], while the UHE neutrino flux satisfies the IceCube upper limit [66]. Low-luminosity BL Lacs explain the UHECR flux, while FSRQs dominate neutrino production. To build our benchmark model 5, we adopt the maximum allowed cosmogenic neutrino flux from the entire population of AGN (Fig. 2 in Ref. [179]). We take the pre-oscillation fluxes of ν_e, $\bar{\nu}_e$, ν_μ, and $\bar{\nu}_\mu$ as functions of energy [287], and use Eq. (6.3) to transform them into the oscillated fluxes of all species at Earth.

6. *Rodrigues et al., all AGN (source) [179]:* We consider the flux of source neutrinos that is the counterpart to the cosmogenic flux of model 5. To build our benchmark model 6, we adopt the maximum allowed source neutrino flux from the entire population of AGN (Fig. 2 in

Ref. [179]). We take the pre-oscillation fluxes of ν_e, $\bar{\nu}_e$, ν_μ, and $\bar{\nu}_\mu$ as functions of energy [287], and use Eq. (6.3) to transform them into the oscillated fluxes of all species at Earth.

7. *Rodrigues et al., HL BL Lacs (cosmogenic) [179]:* UHECRs and neutrinos are produced only by high-luminosity (HL) BL Lacs. The predicted UHECRs agree with the Auger energy spectrum above the ankle, but are lighter than the Auger mass composition above a few EeV. We adopt the cosmogenic neutrino spectrum from HL BL Lacs (Fig. 5 in Ref. [179]) as benchmark because it peaks at energies higher than the benchmark models 5 and 6, and has a normalization in-between theirs. We take the pre-oscillation fluxes of ν_e, $\bar{\nu}_e$, ν_μ, and $\bar{\nu}_\mu$ as functions of energy [287], and use Eq. (6.3) to transform them into oscillated fluxes of all species at Earth.

8. *Fang & Murase, cosmic-ray reservoirs (cosmogenic + source) [177]:* Neutrinos are produced in a grand-unified multi-messenger model of high-energy emission where UHECRs are accelerated in the jets of supermassive black holes of radio-loud AGN embedded in galaxy clusters that act as cosmic-ray reservoirs. There, UHECRs remain confined for 1–10 Gyr and produce UHE neutrinos via $p\gamma$ and pp interactions. From 100 TeV to 100 PeV, neutrinos are primarily made inside the clusters, in UHECR interactions on the intra-cluster medium; above 10^9 GeV, neutrinos are primarily cosmogenic. The neutrino flux normalization results from fitting the predicted UHECR energy spectrum and mass composition to Auger data [288], and the predicted TeV–PeV neutrino flux to IceCube data [186, 289]. Reference [177] provided the all-species neutrino flux, $\Phi_{6\nu}$. To build our benchmark flux model 8, we use it to estimate the flux of each neutrino species using Eq. (6.5).

9. *Fang et al., newborn pulsars (source) [175]:* Fast-spinning newborn pulsars that harbor intense surface magnetic fields, of up to 10^{13} G, may efficiently accelerate charged particles in the pulsar wind during pulsar spin-down. Accelerated particles propagate through the expanding supernova ejecta that surrounds the pulsar; as they do, pp interactions on the ejecta produce neutrinos. Reference [175] computed the diffuse flux of neutrinos produced by the cosmological population of newborn pulsars, integrated over their neutrino-producing lifetimes, with a spread in magnetic field intensity and spin period, and distributed in redshift following the star formation rate (SFR). (We consider only the neutrino contribution from

the sources, not the contribution of cosmogenic neutrinos produced by UHECRs emitted by the pulsars, which is of the same order [175].) Reference [175] provided the all-species neutrino flux, $\Phi_{6\nu}$. To build our benchmark flux model 9, we use it to estimate the flux of each neutrino species using Eq. (6.5).

10. *Padovani et al., BL Lacs (source) [176]:* The neutrino flux is obtained within the framework of the simplified view of blazars [290]. Neutrinos are produced in photohadronic interactions inside the jets of BL Lacs, whose population is simulated using a spread of redshifts and source features like synchrotron peak energies and X-ray flux. The flux prediction was originally constructed to explain the TeV–PeV neutrino range; we adopt it because it spills into the UHE regime. A key parameter of the model is $Y_{\nu\gamma}$, the ratio of the neutrino intensity to the gamma-ray intensity. Following Ref. [291], to satisfy the IceCube upper limit on the UHE neutrino flux, we set $Y_{\nu\gamma} = 0.13$. Reference [176] provided the all-species neutrino flux, $\Phi_{6\nu}$. To build our benchmark flux model 10, we use it to estimate the flux of each neutrino species using Eq. (6.5).

11. *Muzio et al., maximum extra p component (cosmogenic + source) [178]:* Cosmogenic and source neutrinos are produced via photohadronic interactions within the UFA15 multi-messenger framework [292], where sources emit UHECRs whose energy spectrum and mass composition at Earth are fit to Auger data. Reference [178] added a sub-dominant UHECR pure-proton component that escapes the sources with energies above 10^9 GeV, motivated in part by the observation, in Auger, of a slowdown in the increase of average nuclear mass with energy [252], and that enhances the neutrino flux. We adopt the maximum allowed neutrino flux that results from the joint single-mass UFA15 plus pure-proton components, using SYBILL2.3C [293] for the hadronic interaction of UHECRs in the atmosphere (Fig. 9 in Ref. [178]). Reference [178] provided the all-species neutrino flux, $\Phi_{6\nu}$. To build our benchmark flux model 11, we use it to estimate the flux of each neutrino species using Eq. (6.5).

12. *Muzio et al., fit to Auger & IceCube (cosmogenic + source) [180]:* Cosmogenic and source neutrinos are produced via photohadronic interactions within the UFA15 multi-messenger framework (see above); in addition, source neutrinos are produced via pp interactions of UHECRs in the

source environment. Neutrinos from hadronic interactions dominate at low energies, below the Δ resonance energy. UHECR predictions are fit to Auger data. The total neutrino flux from Ref. [180] includes contributions from UHECR sources and non-UHECR sources; the total flux is fit to the IceCube TeV–PeV neutrino flux measurement [243, 294]. We adopt the best-fit total neutrino flux ("UHECR ν" plus "Non-UHECR ν from Fig. 1 in Ref. [180]). To build our benchmark model 12, we use the oscillated fluxes of each neutrino species at Earth as a function of energy, which are available directly from the calculation [270].

Figure 9 shows the breakdown into the flux of each neutrino species for the benchmark models; see Section 6.4.2. For models 1, 2, 8–11, the ratio of each species to the total flux is constant in energy. For models 3–7 and 12, for which non-trivial energy evolution of the flux of each species separately is available, common trends are evident. At low energies, typically below the energy range of the IceCube-Gen2 radio component, $\bar{\nu}_\alpha$ dominate due to the presence and oscillation of $\bar{\nu}_e$ produced in the beta-decay of neutrons and neutron-rich isotopes created in UHECR interactions, mainly during their extragalactic propagation. At higher energies, neutrinos are produced by pion decay; throughout the IceCube-Gen2 energy range, flavor equipartition holds approximately. Roughly within the range 10^7–10^9 GeV, there is a slight excess of neutrinos over anti-neutrinos, because more π^+ than π^- are produced. At the highest energies, multi-pion production dominates, and the excess flips. Later, in Fig. 14, we show how the flavor composition is affected by neutrino propagation through the Earth.

6.5 NEUTRINO PROPAGATION INSIDE EARTH

To compute the expected rate of neutrino-initiated showers at a neutrino telescope, first we compute the flux of neutrinos that reaches it, after propagating through the Earth across different directions.

6.5.1 *Computing neutrino propagation*

Above TeV energies, the dominant interaction that neutrinos undergo while propagating inside the Earth is νN DIS, NC and CC; see Section 6.3. NC scatterings pile up originally high-energy

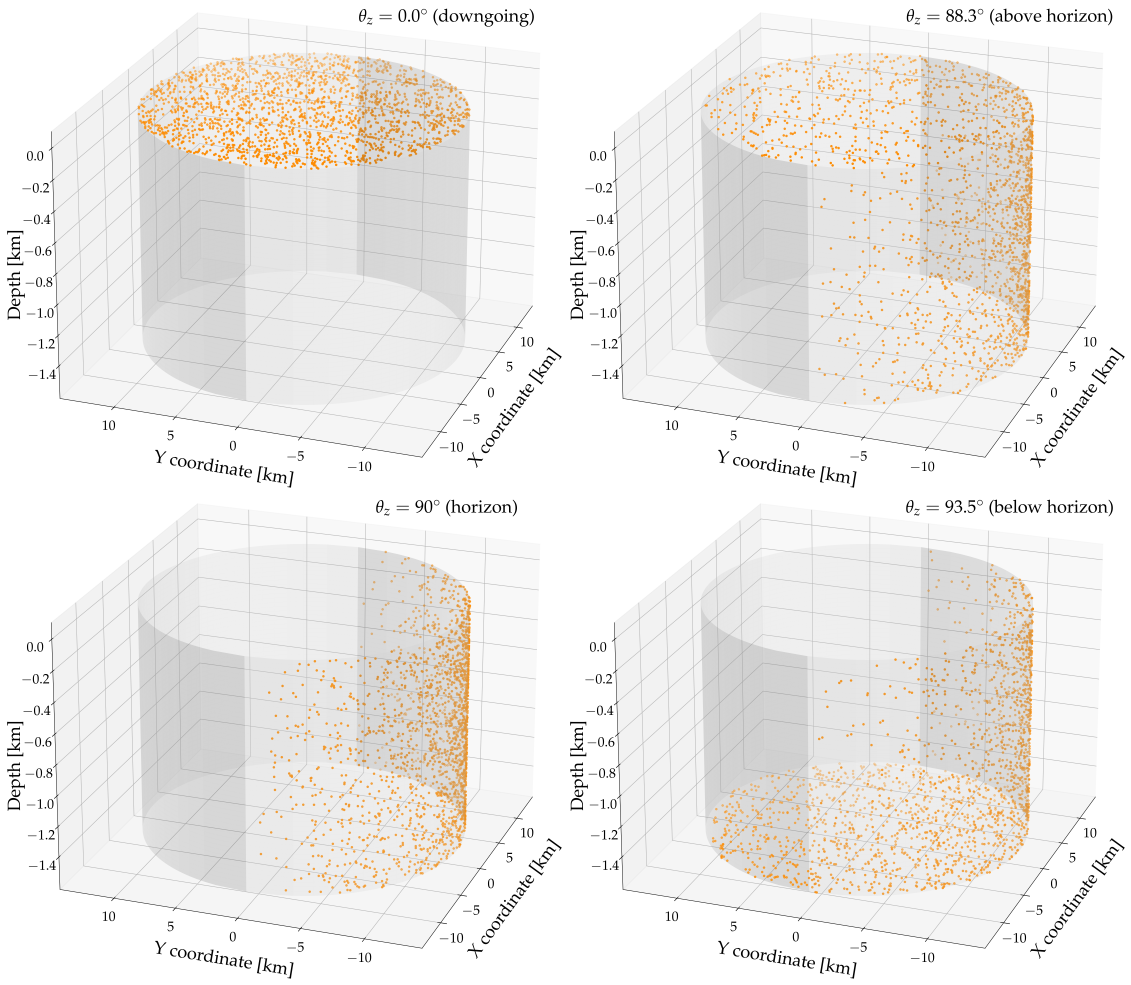

Figure 10: Distribution of neutrinos hitting or simulated IceCube-Gen2 detector volume, from four illustrative directions. See the main text for details. For this figure only, neutrinos are not attenuated while propagating inside the Earth.

neutrinos at low energies, while CC scatterings remove neutrinos from the flux altogether. The exception is the CC scattering of ν_τ, where the final-state tauon may propagate some distance before decaying into a ν_τ, albeit with an energy lower than that of the original ν_τ; this is known as "ν_τ regeneration". Because of it, the flux of ν_τ is less attenuated than that of other flavors. This becomes especially important above 10 PeV, where the final-state ν_τ are still high-energy.

We propagate UHE neutrinos towards the detector along different directions, parametrized as $\cos\theta_z$, where θ_z is the zenith angle measured from the location of the detector. For us, this is the South Pole ($\cos\theta_z = 1$), where IceCube-Gen2 will be located; see Fig. 5. We compute the energy spectra of each neutrino species that reach the detector from $-1 \leq \cos\theta_z \leq +1$.

Figure 10 shows examples of neutrinos hitting the surface of the simulated IceCube-Gen2 detector volume from different directions. We model the detector volume as a cylinder of radius

12.6 km and height 1.50 km, buried underground at a distance of 1.51 km from the surface of the Earth to the bottom of the cylinder. The top surface area of the cylinder is 500 km^2 [39]. Once a neutrino reaches the surface of the cylinder, we stop its propagation. Inside the cylinder, the propagation of the neutrino is computed separately, in the detection step of our calculation, where any further interaction that occurs within the detector volume initiates a particle shower that emits a radio signal that might be detected by underground antennas; see Section 6.6. Modeling the detector volume as a cylinder *vs.* as a point impacts by up to 10% the attenuation of neutrinos that reach it from directions around the horizon, *i.e.*, Earth-skimming neutrinos, for which the detector is of comparable size to the distance traveled inside the Earth. This is especially relevant because these neutrinos offer the greatest sensitivity to the νN cross section; see Section 6.3.3.

Depending on the direction of the neutrino, it will encounter a different matter column density. To account for this, for the internal matter density of Earth, we adopt the Preliminary Reference Earth Model [295], built from seismographic data, which models the density radially out from the center of a spherical Earth, as a series of concentric layers of increasing density towards the center. For our calculations, since IceCube-Gen2 will be embedded in the Antarctic ice, we add a layer of ice of thickness 3 km at the surface of the Earth. In addition, the composition of matter inside the Earth changes with radial distance: deeper layers contain heavier elements—iron, nickel—than shallower layers. Further, matter is, in general, not isoscalar, though this affects mainly neutrino energies below 1 TeV [209]. When propagating neutrinos inside the Earth, we account for the changes in density and composition as a function of position inside Earth.

As an illustration only, and not accounting for ν_τ regeneration, the exponential dampening in Eq. (6.1) describes the attenuation of the neutrino flux inside Earth. (We *do not* use those simplified expressions to produce our results, but more sophisticated methods; see Section 6.6.4.) The attenuation due to CC interactions is stronger the higher the neutrino energy and the longer the length of the path traveled by the neutrinos inside the Earth. The low-energy pile-up due to NC interactions has a similar dependence on energy and direction

As a result of the interactions inside the Earth, while the neutrino flux is isotropic at the surface of the Earth, it has become anisotropic by the time it reaches the detector. At EeV energies, no detectable flux reaches the detector from below; instead, the flux comes from above, where it

is only lightly attenuated by the detector overburden, and from around the horizon, where the attenuation is significant to modify the shape of the spectrum, but not enough to eliminate it.

We use the state-of-the-art neutrino propagation code NUPROPEARTH [209, 210] to compute the fluxes of ν_α and $\bar{\nu}_\alpha$, $\Phi^{\rm det}_{\nu_\alpha}(\cos\theta_z, E_\nu)$ and $\Phi^{\rm det}_{\bar{\nu}_\alpha}(\cos\theta_z, E_\nu)$. We propagate ν_e, $\bar{\nu}_e$, ν_μ, $\bar{\nu}_\mu$, ν_τ, and $\bar{\nu}_\tau$ separately, along different directions. In ν_τ regeneration, NUPROPEARTH accounts for the energy losses due to electromagnetic interactions during the propagation of intermediate tauons, via TAUSIC [296], and computes the distribution of decay products in tauon decays, via TAUOLA [297].

In NUPROPEARTH, for the νN DIS cross section, we use the central value of the BGR18 calculation [194] (see Section 6.3.1), as implemented in the HEDIS [209] module of the GENIE [222] neutrino event generator. HEDIS uses PYTHIA6 [298] to compute the hadronization of final-state particles [299]. We have modified NUPROPEARTH and HEDIS to be able to use versions of the BGR18 cross section that are scaled up and down by a constant factor, as part of our method of measuring the cross section; see Section 6.7. For the cross sections of the sub-dominant neutrino interactions (see Section 6.3.2), we use their implementations in HEDIS, unmodified.

Figure 11 shows energy histograms at the detector resulting from propagating a mono-energetic Earth-skimming neutrino beam inside the Earth. For ν_μ, the cascading down to lower energies due to multiple interactions inside the Earth is evident. For ν_τ, the effect of regeneration is evident as a pile-up at lower energies. Figure 11 shows that changes in the νN DIS cross section affect the propagation inside Earth significantly. For ν_μ, and also for ν_e, not shown, the main effect of a higher cross section is to attenuate the flux further. For ν_τ, a higher cross section shifts the peak of the pile-up to lower energies, due to a larger number of neutrino interactions.

6.5.2 *Computational speed-ups*

As part of our statistical analysis below (see Section 6.7.4), we need to propagate many different UHE spectra of ν_e, $\bar{\nu}_e$, ν_μ, $\bar{\nu}_\mu$, ν_τ, and $\bar{\nu}_\tau$ separately through the Earth, for different values of the νN DIS cross section, along different directions, and with high accuracy. This is a computationally taxing task.

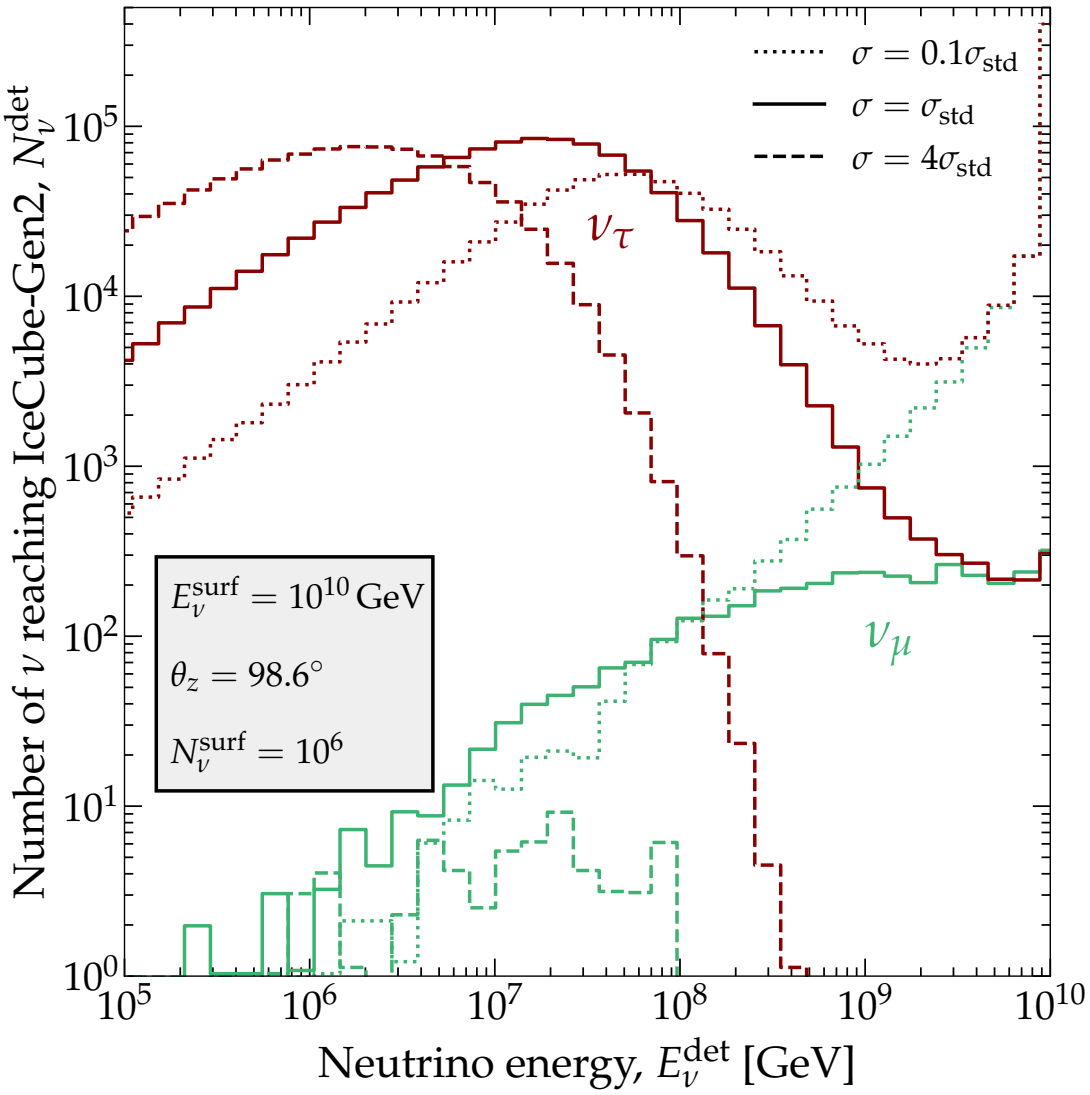

Figure 11: Sample histograms of the number of UHE ν_μ and ν_τ that reach the detector after propagating through the Earth. At the surface of the Earth, opposite to the detector, we inject a mono-energetic beam of $N_\nu^{\rm surf} = 10^6$ neutrinos, each with energy $E_\nu^{\rm surf} = 10^{10}$ GeV, pointed toward the detector along a zenith angle $\theta_z = 98.6^\circ$. We show cases of neutrinos propagated using the central value of the BGR18 νN DIS cross section ($\sigma_{\rm std}$) [194], and sample scaled-up and scaled-down versions of it. For our analysis, we pre-compute histograms for many more values of $E_\nu^{\rm surf}$, θ_z, and the cross section. Results for ν_e, not shown, are similar to ν_μ. See Section 6.5 for details.

We circumvent this limitation as follows. First, we inject a large number $N_{\nu_\alpha}^{\rm surf} = 10^6$ of ν_α at the surface of the Earth, each with initial energy $E_\nu^{\rm surf}$, and propagate it along different directions towards the detector, using NUPROPEARTH. Upon arriving at the detector, the neutrinos are no longer mono-energetic, but their final energies, $E_\nu^{\rm det}$, are spread out as a result of interactions inside Earth, *i.e.*, $N_{\nu_\alpha}^{\rm det} \equiv N_{\nu_\alpha}^{\rm det}(\cos\theta_z, E_\nu^{\rm surf}, E_\nu^{\rm det})$. Second, we compute the transmission coefficients as

$$T_{\nu_\alpha}(\cos\theta_z, E_\nu^{\rm surf}, E_\nu^{\rm det}) \equiv \frac{N_{\nu_\alpha}^{\rm det}(\cos\theta_z, E_\nu^{\rm surf}, E_\nu^{\rm det})}{N_{\nu_\alpha}^{\rm surf}}\,, \tag{6.10}$$

bin them in bins of $E_\nu^{\rm det}$ of width $\Delta E_\nu^{\rm det}$, *i.e.*,

$$\mathcal{T}_{\nu_\alpha}(\cos\theta_z, E_\nu^{\rm surf}, E_\nu^{\rm det}, \Delta E_\nu^{\rm det}) \equiv \sum_{x=E_\nu^{\rm det}}^{E_\nu^{\rm det}+\Delta E_\nu^{\rm det}} \frac{T_{\nu_\alpha}(\cos\theta_z, E_\nu^{\rm surf}, x)}{\Delta E_\nu^{\rm det}} \,, \tag{6.11}$$

and save $\mathcal{T}_{\nu_\alpha}$ as look-up tables. We do this separately for ν_α and $\bar{\nu}_\alpha$ of all flavors. Third, given any UHE neutrino spectrum at the surface of the Earth, Φ_{ν_α}, we use the pre-computed $\mathcal{T}_{\nu_\alpha}$ to estimate the average flux at the detector within an interval of final energy $[E_\nu, E_\nu + \Delta E_\nu]$ as

$$\Phi_{\nu_\alpha}^{\rm det}(\cos\theta_z, E_\nu, \Delta E_\nu) \simeq \Delta E_\nu \times \sum_{E_\nu^{\rm surf} > E_\nu} \Phi_{\nu_\alpha}(E_\nu^{\rm surf}) \mathcal{T}_{\nu_\alpha}(\cos\theta_z, E_\nu^{\rm surf}, E_\nu, \Delta E_\nu) \,, \tag{6.12}$$

and similarly for $\bar{\nu}_\alpha$. Finally, we approximate the true spectrum by its binned average, *i.e.*, $\Phi_{\nu_\alpha}^{\rm det}(\cos\theta_z, E_\nu) \approx \Phi_{\nu_\alpha}^{\rm det}(\cos\theta_z, E_\nu, \Delta E_\nu)$. We pre-compute the look-up coefficients $\mathcal{T}_{\nu_\alpha}$ in fine grids of $E_\nu^{\rm surf}$ and $E_\nu^{\rm det}$. We repeat the above procedure to generate look-up tables for different values of the νN cross section, since we need them for our statistical procedure; see Section 6.7.4.

Figure 12 shows sample transmission coefficients T_{ν_μ} and T_{ν_τ}, for directions at and around the horizon. For ν_μ, and also for ν_e, not shown, because the νN cross section grows with energy, the cascading down to lower energies becomes more important the higher the injected energy $E_\nu^{\rm surf}$. It is most significant when neutrinos arrive from below the horizon, due to the larger matter column density that they traverse. For ν_τ, in addition, the presence of regeneration is evident for $E_\nu^{\rm surf} \gtrsim 10$ PeV, for neutrinos coming from the horizon and below it. At the detector, regenerated ν_τ are concentrated in a band centered around $E_\nu^{\rm det} \approx 10$ PeV.

When producing our results, we use Eq. (6.12) to compute neutrino spectra. By doing this, we circumvent the computationally intensive need to propagate every time each benchmark neutrino flux from scratch, for each value of the νN cross section.

6.5.3 *UHE neutrino flux at the detector*

Figure 13 illustrates the effect of the propagation through Earth on the benchmark flux model 4, for an example arrival direction. We choose a direction from below the horizon because the column density traversed along it is large enough that changes in the νN cross section imprint sizeable changes in the flux that reaches the detector. For ν_μ, and also for ν_e, not shown, even the central value of the BGR18 νN cross section ($\sigma_{\rm std}$) is large enough to suppress the flux at the

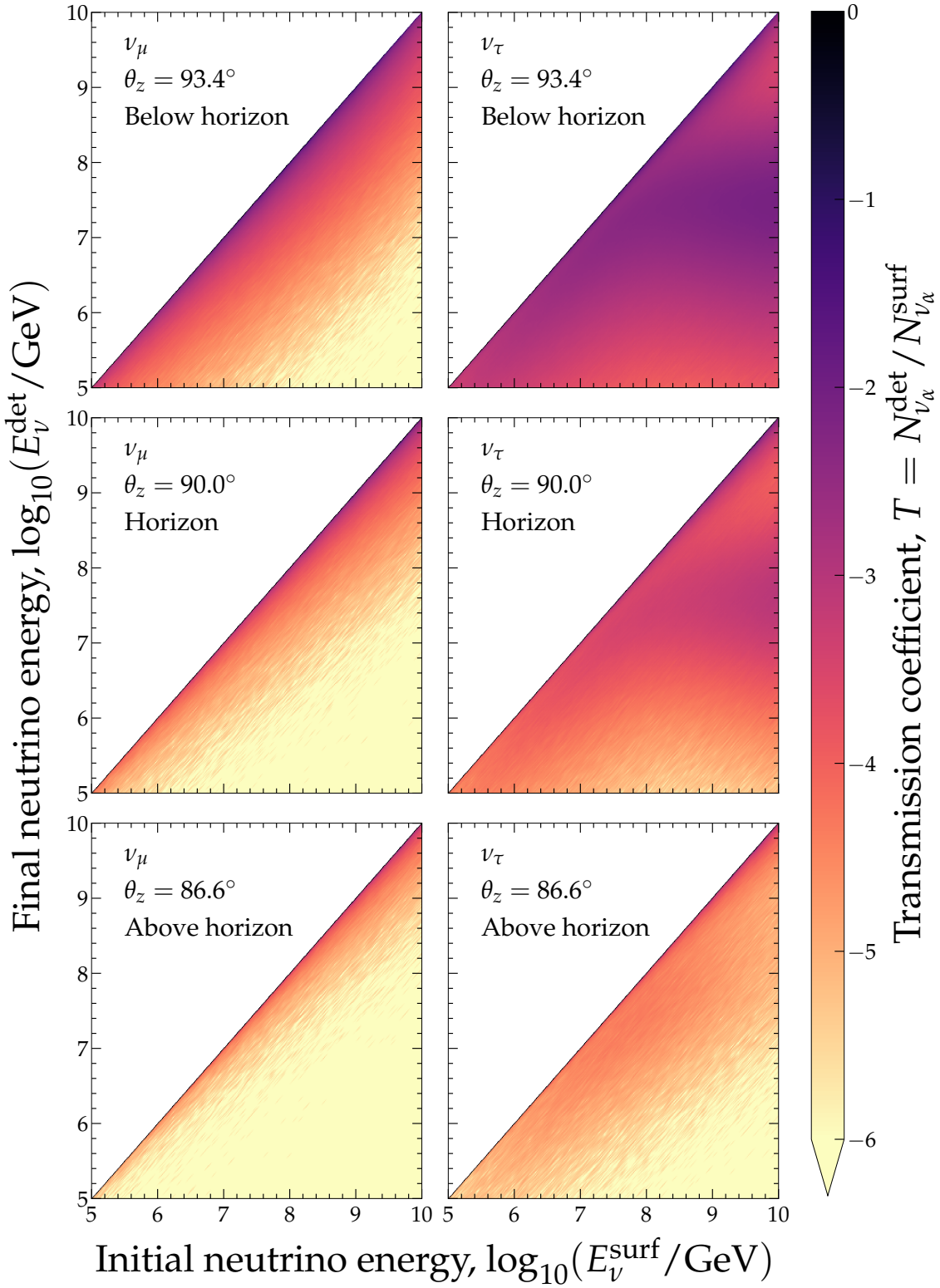

Figure 12: Examples of the transmission coefficient $T \equiv N_{\nu_\alpha}^{\rm det}(\cos\theta_z, E_\nu^{\rm surf}, E_\nu^{\rm det})/N_{\nu_\alpha}^{\rm surf}$ of ultra-high-energy ν_μ and ν_τ, from the surface of the Earth, across it, and up to the location of IceCube-Gen2, for illustrative directions $\cos\theta_z$. At every value of the initial neutrino energy $E_\nu^{\rm surf}$, a number $N_{\nu_\alpha}^{\rm surf} = 10^6$ of mono-energetic neutrinos, each with energy $E_\nu^{\rm surf}$, is injected at the surface of the Earth and, after propagating inside it, arrive at the detector with a spread of final energies $E_\nu^{\rm det}$. For this plot, we use the central value of the BGR18 νN cross section ($\sigma_{\rm std}$, in the notation of Section 6.7.1). See the main text for details.

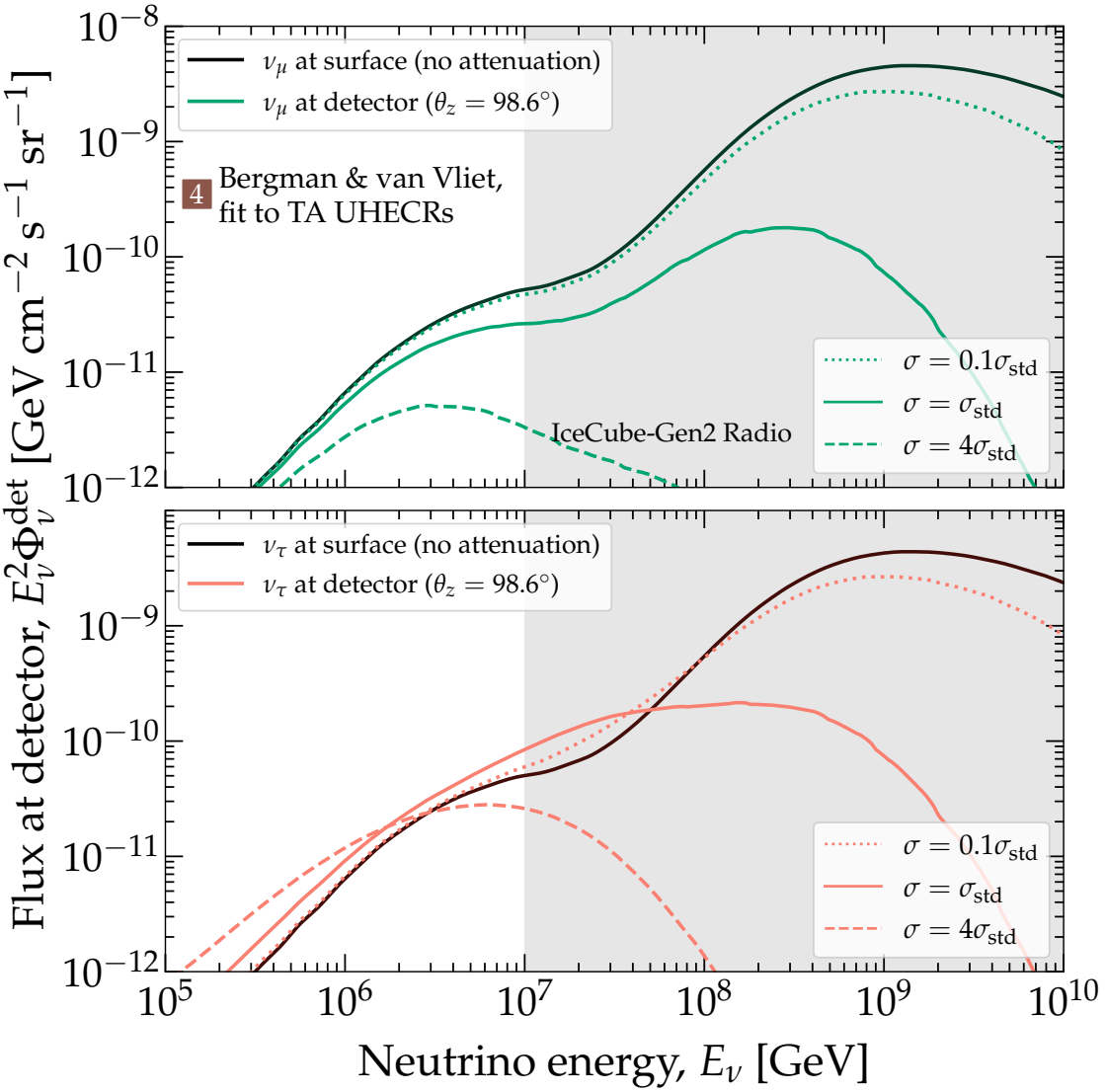

Figure 13: Benchmark UHE ν_μ and ν_τ flux model 4 [193] (see Section 6.4) at the surface of the Earth and at IceCube-Gen2, after propagating through the Earth along an illustrative direction, $\theta_z = 98.6°$. The flux of ν_e, not shown, is similar to that of ν_μ. The effect of in-Earth propagation on the fluxes of $\bar{\nu}_\alpha$ ($\alpha = e, \mu, \tau$), not shown, is similar to the effect ν_α. Fluxes at the detector are computed using NUPROPEARTH [209, 210]. We show fluxes propagated using the central value of the BGR18 νN DIS cross section ($\sigma_{\rm std}$) [194], and scaled-up and scaled-down versions of it. See Section 6.5 for details.

detector by more that one order of magnitude relative to the flux at the surface of the Earth, at the highest energies. Larger cross sections vanish the flux altogether. For ν_τ, the suppression is mitigated, though not counterbalanced, by the pile-up of low-energy, regenerated ν_τ. For downgoing neutrinos ($\theta_z \lesssim 80°$), not shown, the fluxes are unaffected even by large cross sections, due to the small column densities. Conversely, for upgoing neutrinos ($\theta_z \gtrsim 100°$), not shown, the fluxes vanish even if the cross section is small, due to the large column densities.

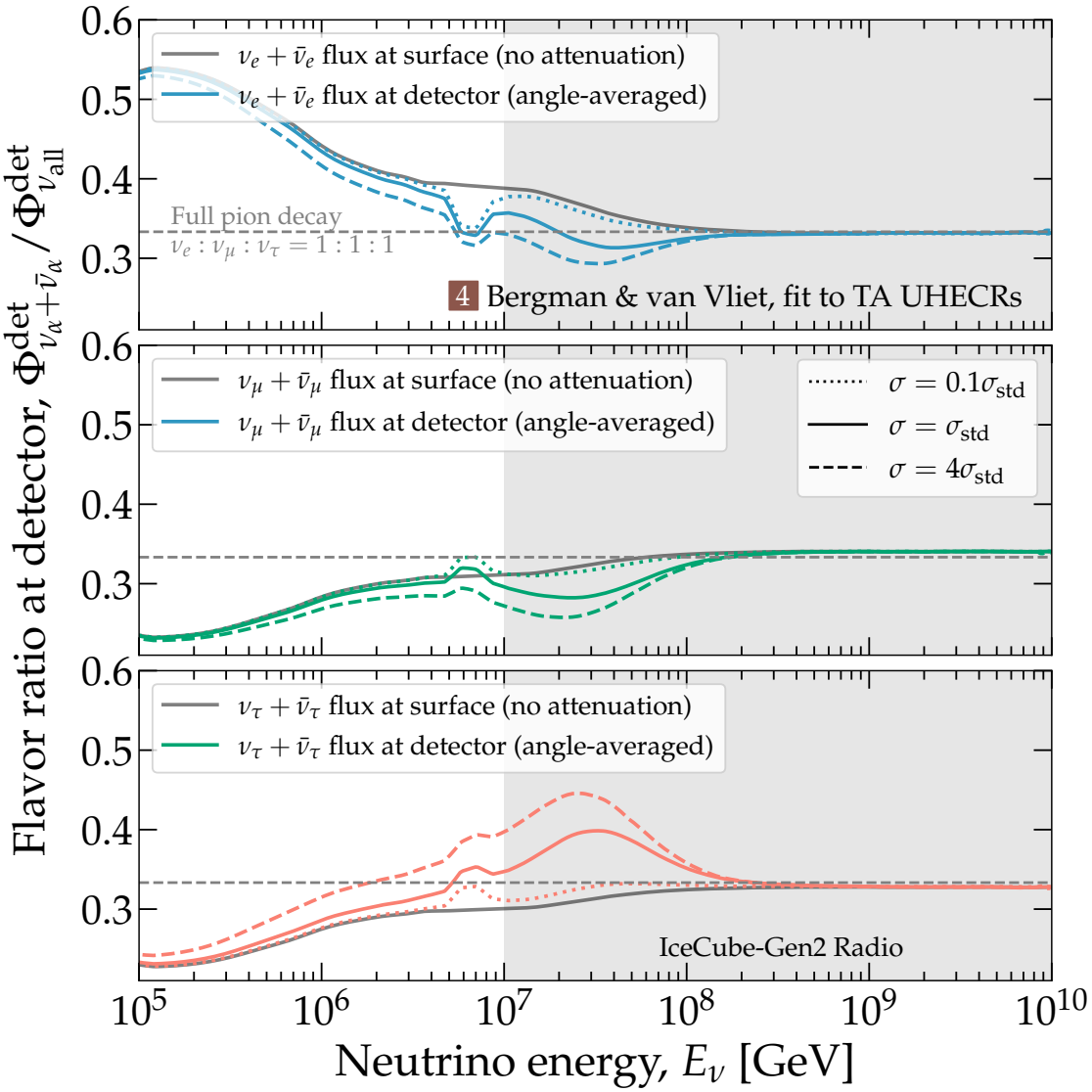

Figure 14: Flavor ratios of neutrinos, *i.e.*, ratios of the $\nu_\alpha + \bar{\nu}_\alpha$ flux compared to the all-flavor flux, at the surface of the Earth and at IceCube-Gen2, for the benchmark UHE flux model 4 [193] (see Section 6.4). In this plot, the flavor ratios at IceCube-Gen2 are the average for Earth-skimming neutrinos with $\theta_z \in [85°, 95°]$. Like in Fig. 13, we show flavor ratios of fluxes propagated using the central value of the BGR18 νN DIS cross section ($\sigma_{\rm std}$) [194], and scaled-up and scaled-down versions of it. For comparison, we show the nominal expectation of flavor equipartition at the surface of the Earth from neutrino production via the full pion decay chain.

Figure 14 shows how the flavor ratios, *i.e.*, the proportion of $\nu_\alpha + \bar{\nu}_\alpha$ to the all-flavor flux, are affected by the propagation through Earth, also for benchmark flux model 4. Above 10^8 GeV, neutrinos of all flavors are attenuated equally, and so their flavor ratios at the detector are equal; at these energies, they also match the flavor ratios at the surface of the Earth; see Fig. 9. The effects of the propagation become apparent at lower energies. There, the neutrinos of all flavors regenerated from NC interactions plus the ν_τ regenerated from CC interactions pile up. As a result of the latter, the tau-flavor ratio dominates over the electron- and muon-flavor ratios. The dip in

the electron-flavor ratio around 6.3 PeV is due to the Glashow resonance experienced only by $\bar{\nu}_e$. There are corresponding bumps at the same energy in the muon- and tau-flavor ratios. The above features become more prominent the higher the νN DIS cross section. While these features are an implicit part of our analysis, we do not make use of flavor identification, since the capabilities of IceCube-Gen2 in this direction are still under study [213, 214, 300]. Section 6.9 comments on this possibility for future work.

6.6 RADIO-DETECTING UHE NEUTRINOS

We gear our forecasts to the case of UHE neutrino radio-detection in the planned radio array of IceCube-Gen2 [39]. Once neutrinos have propagated through the Earth and reached the detector, they might interact inside the detector volume via NC and CC νN DIS. See Section 6.3 for details on the νN DIS process. In most of these interactions, a substantial fraction of the neutrino energy is transferred into a high-energy particle shower. As the shower develops, it produces coherent radio emission that might be detected by antennas of the array.

6.6.1 *Neutrino-induced radio emission in ice*

In the NC or CC DIS interaction of a neutrino or anti-neutrino of energy E_ν of any flavor, the final-state hadrons initiate a hadronic shower, rich in pions and muons [301]. The energy of the hadronic shower is $E_{\rm sh} = (1-y)E_\nu$, where y is the inelasticity; see Section 6.3. In the CC DIS interaction of a ν_e or $\bar{\nu}_e$, the final-state electron or positron initiates an additional electromagnetic shower, rich in photons, electrons, and positrons, co-located with the hadronic shower. The energy of the electromagnetic shower is $E_{\rm sh} = yE_\nu$.

At neutrino energies below roughly 10^9 GeV, the hadronic and electromagnetic showers develop in phase and appear as a single shower with energy $E_{\rm sh} = E_\nu$; see, *e.g.*, Ref. [211, 300]). At higher energies, the electromagnetic shower is subject to the Landau–Pomeranchuk–Migdal (LPM) effect [302, 303], which reduces the cross section of the high-energy electrons and positrons. The precise role of the LPM effect in the radio-detection of neutrinos is under study [300], but seems to

be significant: if present, it delays the first interactions of electrons and positrons in the shower or leads to multiple spatially displaced sub-showers. As a result, the hadronic and electromagnetic showers may develop differently, and the shower energy might not match the neutrino energy anymore. The simulations of ν_e-induced CC showers that we perform to describe the detector response, described in Section 6.6.2, include the LPM effect. Nevertheless, when computing ν_e-induced CC event rates, as described in Section 6.6.4, we maintain the relation $E_{\rm sh} = E_\nu$ across all energies, since further work is needed to find an equivalent form of it that accounts for the changing dominance of the LPM effect with energy.

Separately, in the CC DIS interactions of ν_μ and ν_τ, we also ignore the contribution of secondary interactions of final-state muons and tauons to the event rates, because they are challenging to simulate. Since their inclusion would increase the event rates by up to 25% [213, 214], depending on energy and spectral shape, ignoring them makes our forecasts conservative. Future revised estimates might isolate the contribution of the LPM effect and include secondary leptons, via changes to the relation between shower and neutrino energies, Eq. (6.14), and to the simulated detector effective volume; see below.

IceCube-Gen2 will be built in the Antarctic ice; see below for details. Because ice is dielectric, as a neutrino-induced shower develops inside it, it builds up a time-varying negative charge excess in the shower front which produces coherent radio emission. This *Askaryan radiation* [165] is strongest when the shower is observed along a cone with half-angle of $\arccos(1/n) \approx 56^\circ$, centered on the shower axis, where $n = 1.78$ is the index of refraction of deep ice. Along this "Cherenkov angle", the radiation emitted by the shower interferes constructively. The radio signal is a broadband, bipolar pulse a few nanoseconds long, predominantly in the frequency range 100 MHz–1 GHz. While the shower track itself is only a few tens of meters long, the radio emission can propagate over kilometers. However, the emission strength decreases quickly if the shower is observed from angles smaller or larger than the Cherenkov angle, even from only a couple of degrees away from it. Reference [166] first pointed out that Askaryan radiation can be used to detect neutrinos. Reference [304] contains an in-depth description of radio emission from high-energy particles.

Accelerator measurements have demonstrated the existence of in-ice Askaryan emission, and found agreement with theoretical predictions [169, 305, 306]. Additional evidence comes from the

observation of radio emission from extensive air showers—*i.e.*, particle showers in the atmosphere—to which Askaryan radiation contributes in a sub-dominant capacity [304, 307–309].

6.6.2 *The radio component of IceCube-Gen2*

The main advantage of radio-detection of UHE neutrinos is the large attenuation length of radio signals in polar ice, of roughly 1 km [310], versus the attenuation and scattering lengths of optical Cherenkov light, of roughly 100 m. This allows for a cost-efficient instrumentation of huge detector volumes with a sparse array of compact radio-detection stations. Each station contains several antennas buried in the ice at depths of up to 200 m and acts as an autonomous unit. To maximize the overall sensitivity of the array, the detector stations are separated by more than 1 km, so that coincidences between stations are rare. Each detector stations measures enough information to determine the shower energy and neutrino arrival direction; see, *e.g.*, Refs. [300, 311–315].

The envisioned design of IceCube-Gen2 [39] capitalizes on this opportunity by including an array of radio antennas covering a total surface area of 500 km^2 [77]. The radio array will be of critical importance in the quest for the discovery of UHE neutrinos. Its design combines the advantages found in the pathfinder experiments ARA [316], ARIANNA [69], and RNO-G [71] into a hybrid array. The IceCube-Gen2 array consists of two types of radio detector stations that measure and reconstruct neutrino properties with complementary accuracy, intended to maximize the discovery potential by mitigating risks and adding multiple handles for the rejection of rare backgrounds [77]. The design blends the hybrid stations explored by RNO-G [71]—narrow bicone and quad-slot antennas on three strings up to a depth of 200 m plus high-gain log-periodic-dipole-array (LPDA) antennas close to the surface—with shallow-only stations explored by ARIANNA—LPDA antennas close to the surface with one additional dipole antenna at a depth of 15 m to aid event reconstruction [317].

A key ingredient in our estimates of the neutrino-induced event rates below is the detector response of the IceCube-Gen2 radio component. We compute it via numerical simulations using the same open-source tools that are used by the IceCube-Gen2 Collaboration, NuRadioMC [211] and NuRadioReco [212]. Below we describe how we simulate the response of one radio station.

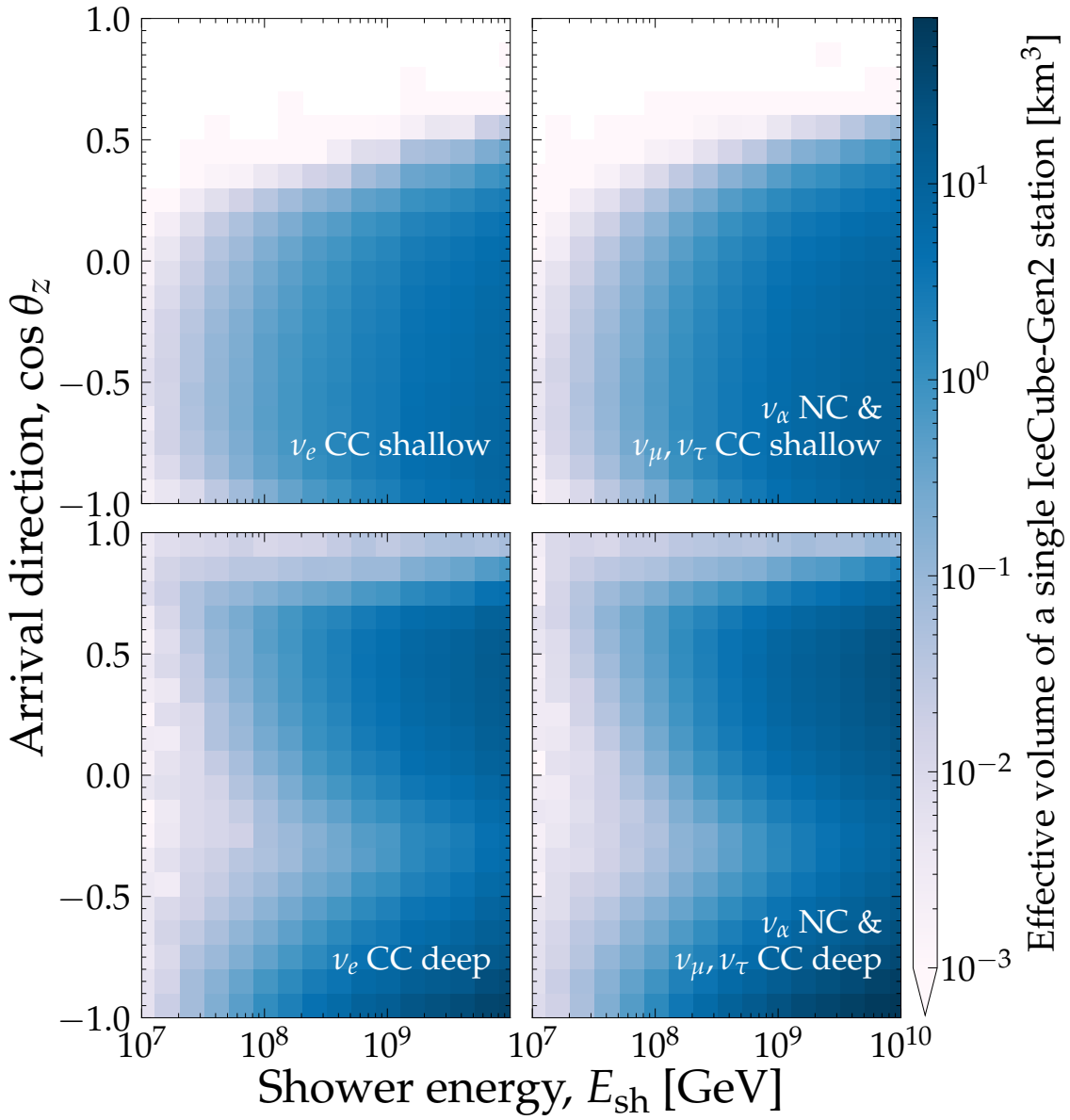

Figure 15: Effective volume of a single detector component of the IceCube-Gen2 radio array, simulated using NuRadioMC [211]. The effective volume does not include the effects of neutrino propagation inside the Earth; its directional dependence is due only to the station geometry and to the radio propagation in the Antarctic ice. The directional dependence resulting from neutrino propagation through the Earth is computed separately on the neutrino flux; see Section 6.5. *Top row:* Volume for a single shallow detector component. *Bottom row:* Volume for a single deep detector component. *Left column:* Volume for ν_e CC interactions. *Right column:* Volume for NC interactions of all flavors and CC interactions of ν_μ and ν_τ. See Fig. 16 for the effective volume of the full array and the main text for details.

After, we scale up its response, expressed in terms of the effective volume, to the size of the full radio array.

NuRadioMC simulates the neutrino interaction in the ice, the generation of the radio emission and its propagation to the antennas, and performs a full detector and trigger simulation. We simulate showers of varying energy, E_{sh}, that enter the detector from different directions, $\cos\theta_z$.

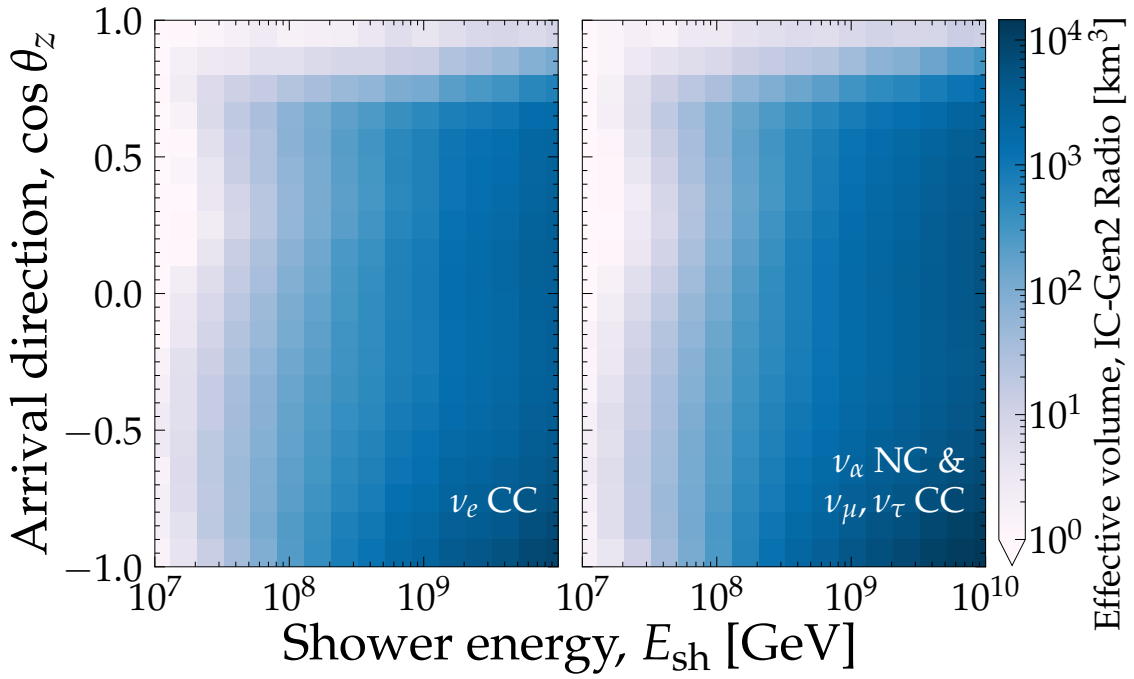

Figure 16: Effective volume of the baseline design of the full IceCube-Gen2 radio array. This is the sum of the effective volumes of 144 hybrid (shallow + deep) stations plus 169 shallow-only stations. *Left:* Volume for ν_e CC interactions, $V^{\rm CC}_{{\rm eff},\nu_e}$. *Right:* Volume for NC interactions of all flavors and CC interactions of ν_μ and ν_τ, $V^{\rm NC}_{{\rm eff},\nu_\alpha}$. See Fig. 15 for the effective volumes of single stations and the main text for details.

To compute the Askaryan emission, we adopt the ARZ prescription [318], combined with a representative shower library of charge-excess profiles [211], which provides realistic modelling of the LPM effect for ν_e CC interactions. The deep antennas of the station are triggered by a four-channel phased array [71, 319] and the shallow antennas by a high/low-threshold trigger with a time-coincidence trigger requiring coincident detection of two out of the four LPDA antennas, using an optimized trigger bandwidth [320]. We use the exact same simulation settings as in Ref. [77].

We report the detector response via its effective volume, *i.e.*, the simulation volume multiplied by the ratio of the number of detected showers to the number of simulated showers; see, *e.g.*, Ref. [321]. We do this separately for the shallow and deep detector components of the simulated station, and separately for the NC interactions of all neutrino flavors and CC interactions of ν_μ and ν_τ, and for the CC interactions of ν_e. Results for ν_α and $\bar{\nu}_\alpha$ are the same, since their UHE νN DIS cross sections and inelasticity distributions are nearly equal; see Section 6.3 and Refs. [194, 205, 250]. The resulting effective volumes are functions of $E_{\rm sh}$ and $\cos\theta_z$.

There are two notable differences in the effective volumes that we have generated compared to previously reported results. First, we do not fold in the effects of in-Earth propagation into the effective volumes. Those effects are instead imprinted on the neutrino flux that arrives at the detector; see Section 6.5. As a result, the directional dependence of the effective volumes is due solely to the geometry of the detector components and the propagation of radio signals in the Antarctic ice. This facilitates exploring the effect of using different values of the cross section during neutrino in-Earth propagation and detection. Second, the effective volumes that we use are functions of shower energy, not of neutrino energy. In our calculation of shower rates below, this choice allows us to account for all possible combinations of E_ν and y that produce a shower of a given energy $E_{\rm sh}$ (see Section 6.3.1), and to assess the detectability of that shower.

Figure 15 shows the resulting effective volumes for single stations and their dependence on shower energy and direction. The effective volumes are higher for higher shower energy, since the radio signal intensifies with energy. The directional dependence of the effective volumes is more nuanced. Broadly stated, shallow antennas have a higher effective volume around the horizon ($\cos\theta_z \approx 0$) and deep antennas have a higher effective volume for downgoing directions ($\cos\theta_z \gtrsim 0$). This is because deeper antennas are less affected by shadowing due to the changing index of refraction in the 200 m of overhead ice that leads to a downward bending of signal trajectories; see, *e.g.*, Ref. [211]. Since the capability to measure the UHE νN cross section is contingent on the observation of near-horizontal events (see Section 6.3.3), shallow antennas are key. Later, in Fig. 22, we quantify their importance. (In Fig. 15, the effective volume for the deep detector component dips at $\cos\theta_z \approx -0.3$ because the beams of the phased-array trigger system have not been optimized for upgoing neutrinos, as they will anyway be attenuated by propagating through the Earth; see Section 6.5 and Fig. 17.)

Figure 16 shows the effective volume of the full IceCube-Gen2 radio array. We adopt the baseline array design from Ref. [77]: 144 hybrid stations, containing shallow and deep detector components, plus 169 shallow-only stations. Because few showers are expected to be detected simultaneously by multiple radio stations [77], it is straightforward to scale the single-station effective volumes up to the size of the full array: it is equal to the single-station volume of shallow antennas times the number of stations that contain shallow antennas (313) plus the single-station volume of deep

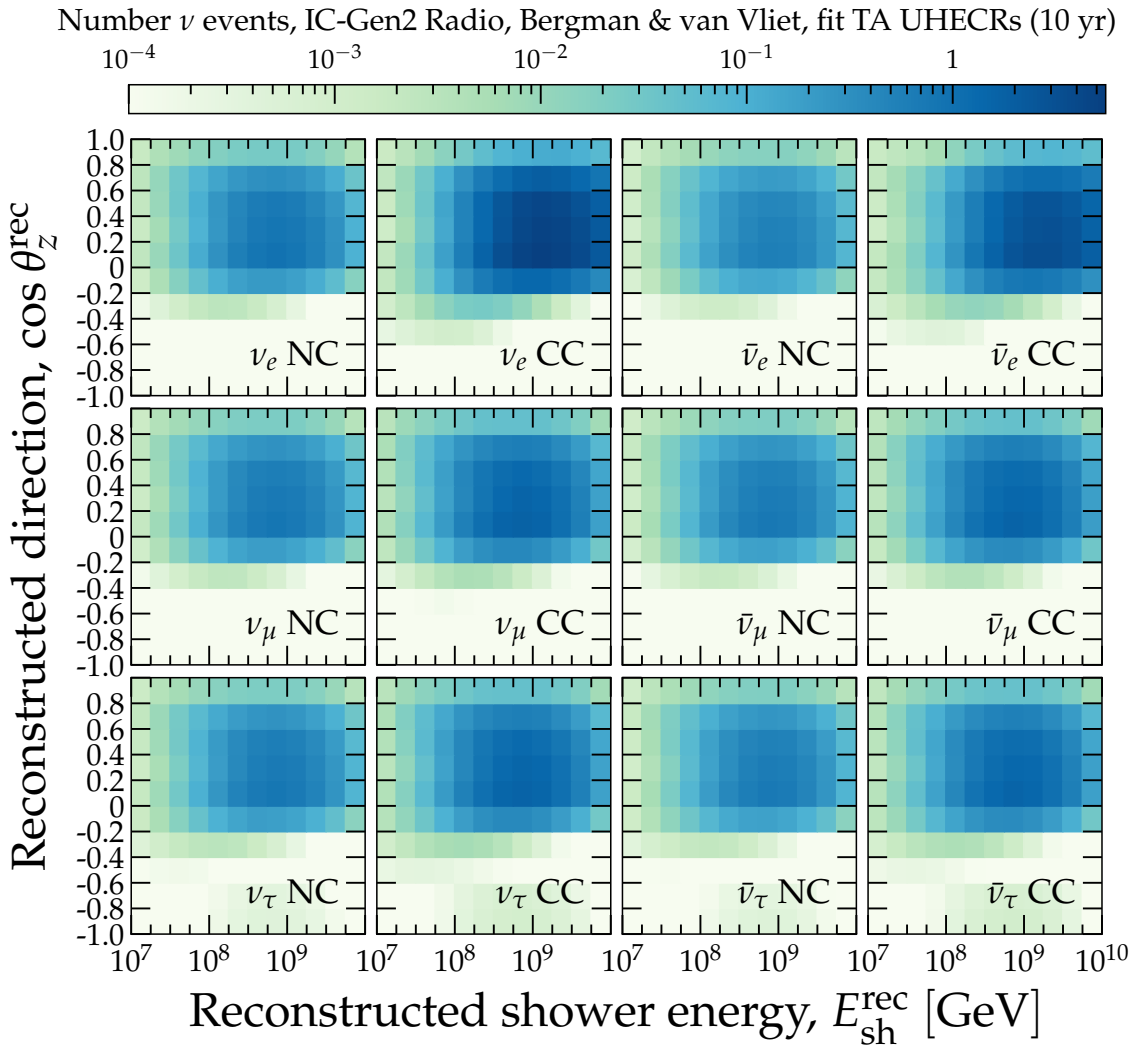

Figure 17: Mean expected number of neutrino-induced events detected in the IceCube-Gen2 radio array, for the benchmark UHE neutrino flux model 4 [193] (see Section 6.4), separately for NC and CC νN DIS, and for each neutrino species. For this plot, for Table 1 and Fig. 18, and in our main results, we use the baseline choices for the energy and angular resolution, $\sigma_\epsilon = 0.1$ and $\sigma_{\theta_z} = 2^\circ$, respectively. See Section 6.6 for details.

antennas times the number of stations that contain deep antennas (144). Below, when forecasting event rates, we use the full-array effective volumes from Fig. 16, computed separately for the NC interaction of all neutrino flavors or the CC interaction of ν_μ and ν_τ, $V^{\rm NC}_{{\rm eff},\nu_\alpha}$, and for the CC interaction of ν_e, $V^{\rm CC}_{{\rm eff},\nu_e}$. At the time of writing, the number of shallow and deep stations in the IceCube-Gen2 array is under consideration; our results might provide guidance to optimize it for cross-section measurements.

6.6.3 *Reconstruction of energy and direction*

The reconstruction of the shower direction and energy requires the measurement of the signal arrival direction, polarization, viewing angle, *i.e.*, the angle under which the shower is observed, and the distance to the neutrino interaction vertex, as well as accurate modelling of the ice properties to correct for the bending of the signal trajectories due to the changing index of refraction [311].

The signal arrival direction can be determined to sub-degree precision via the signal arrival times to the different antennas of a detector station [314, 322, 323]. The index-of-refraction profile is known well enough to achieve sub-degree precision on the signal direction, as tested in measurements at the South Pole [322]. The viewing angle can typically be reconstructed to within 1° [312, 315, 324]. The dominant uncertainty on the direction comes from the measurement of the signal polarization [312, 322, 324]. Polarization is generally measured better in shallow detector components because their orthogonal LPDA pairs provide equal sensitivity to both polarization states. For a shallow station, the capability to measure the polarization has been tested in-situ [322] and via measurements of cosmic rays [325].

The ability to measure the viewing angle and to combine all individual measurements to estimate the arrival direction was quantified in simulation studies using the forward folding technique [212, 312, 314, 324] and deep neural networks [300, 326]. The best resolution of the direction was obtained with a shallow detector station with a 68% quantile of 3°, which translates into an uncertainty of the zenith angle of $\sigma_{\theta_z} = 2°$. We adopt this angular resolution as the baseline in our forecasts below. Later, in Fig. 24, we explore how our results depend on the angular resolution.

Similar studies have estimated the uncertainty of the reconstructed shower energy [315, 317, 324]. They yield a resolution of approximately 0.1 in $\log_{10}(E_{\rm sh}^{\rm rec}/E_{\rm sh})$, where $E_{\rm sh}^{\rm rec}$ is the reconstructed shower energy and $E_{\rm sh}$ is the real shower energy, or roughly 30% on a linear scale in the energy range of interest. We adopt this energy resolution as the baseline in our forecasts below.

6.6.4 *Neutrino-induced event rates in IceCube-Gen2*

In a realistic experimental setting, only the shower energy is measured, not the energy of the neutrino that initiated it. Thus, in predicting the detected shower rate, we must account for the fact that a shower measured with a certain energy $E_{\rm sh}$ could have been initiated by any combination of neutrino energy, E_ν, and inelasticity, y, that satisfies $E_{\rm sh} = E_\nu y$ for NC interactions of all neutrino flavors and CC interactions of ν_μ and ν_τ, or $E_{\rm sh} = E_\nu$ for CC interactions of ν_e. See Section 6.6.1 for details. The relative contribution of each possible combination is weighed by the neutrino flux—which determines how many neutrinos of energy E_ν reach the detector—and by the differential cross section—which determines the chances that the interaction of a neutrino of energy E_ν has inelasticity y. (While the neutrino energy may be reconstructed from the measured shower energy, doing so requires making additional assumptions [311, 315], and is unnecessary for our goals, so we do not attempt that.)

Thus, the differential rate of showers induced in the radio array of IceCube-Gen2 by ν_α arriving at the detector with flux $\Phi^{\rm det}_{\nu_\alpha}$ after propagating inside Earth is

$$\frac{d^2 N_{\nu_\alpha}}{dE_{\rm sh} d\cos\theta_z} = 2\pi T n_t \int_0^1 dy \Bigg(\frac{E^{\rm NC}_{\nu_\alpha}(E_{\rm sh}, y)}{E_{\rm sh}} V^{\rm NC}_{{\rm eff},\nu_\alpha}(E_{\rm sh}, \cos\theta_z) \times \frac{d\sigma^{\rm NC}_{\nu_\alpha {\rm w}}(E_\nu, y)}{dy} \Phi^{\rm det}_{\nu_\alpha}(E_\nu, \cos\theta_z)|_{E_\nu = E^{\rm NC}_{\nu_\alpha}(E_{\rm sh}, y)} + {\rm NC} \to {\rm CC} \Bigg) \,, \quad (6.13)$$

where T is the exposure time of the detector, $n_t \equiv N_{\rm Av}\rho_{\rm ice}/M_{\rm ice}$ is the number density of water molecules in ice, $N_{\rm Av}$ is Avogadro's number, $\rho_{\rm ice} = 0.9168$ g cm^{-3} is the density of ice, and $M_{\rm ice} = 18.01528$ g mol^{-1} is the molar mass of water. Equation (6.13) accounts for the contributions of NC and CC interactions. On the right-hand side, the term $E^{\rm NC}_{\nu_\alpha}(E_{\rm sh}, y)/E_{\rm sh}$ re-scales the units of the flux from neutrino energy to shower energy. The effective volume, $V^{\rm NC}_{{\rm eff},\nu_\alpha}$, is the full-array volume described in Section 6.6.2. The cross section, $\sigma^{\rm NC}_{\nu_\alpha {\rm w}}$, is for neutrino DIS interaction on a water molecule (H_2O), *i.e.*, $\sigma^{\rm NC}_{\nu_\alpha {\rm w}} = 10\sigma^{\rm NC}_{\nu_\alpha p} + 8\sigma^{\rm NC}_{\nu_\alpha n}$, where $\sigma^{\rm NC}_{\nu_\alpha p}$ and $\sigma^{\rm NC}_{\nu_\alpha n}$ are the BGR18 $\nu_\alpha p$ and $\nu_\alpha n$ cross sections, respectively, and similarly for the CC cross sections [194]. In Eq. (6.13), the differential

shower rate on the left-hand side is evaluated at a shower energy $E_{\rm sh}$. This determines, on the right-hand side, the neutrino energy at which the integrand is evaluated, *i.e.*,

$$E^i_{\nu_\alpha}(E_{\rm sh}, y) = \begin{cases} E_{\rm sh}/y, & \text{for } \nu_\alpha \text{ NC} \\ E_{\rm sh}, & \text{for } \nu_e \text{ CC} \\ E_{\rm sh}/y, & \text{for } \nu_\mu \text{ and } \nu_\tau \text{ CC} \end{cases} , \tag{6.14}$$

for $i = \text{NC}, \text{CC}$. Equation (6.14) applies also to anti-neutrinos. (In our numerical solution of Eq. (6.13), we set the lower limit of the y integral to 10^{-8} instead of 0 to prevent the integral from diverging.)

The differential shower rate in Eq. (6.13) is the "true" shower rate. Because the detector measures energy and direction imperfectly, the true rate is unobservable. Instead, to produce our results, we use exclusively the "reconstructed" shower rate, *i.e.*, the rate expressed in terms of the reconstructed shower energy, $E^{\rm rec}_{\rm sh}$, and the reconstructed direction, $\theta^{\rm rec}_z$. These are the shower quantities that would be observed in a realistic experiment, after accounting for the measurement uncertainties. To do this, we fold the true shower rate with resolution functions in shower energy and direction, $R_{E_{\rm sh}}$ and R_{θ_z}, respectively, that capture the measurement precision of the detector.

For the resolution function in energy, we adopt a Gaussian function centered at the real shower energy, $E_{\rm sh}$, *i.e.*,

$$R_{E_{\rm sh}}(E^{\rm rec}_{\rm sh}, E_{\rm sh}) = \frac{\mathcal{N}_{E_{\rm sh}}}{\sqrt{2\pi}\sigma_{E_{\rm sh}}} e^{-\frac{(E^{\rm rec}_{\rm sh} - E_{\rm sh})^2}{2\sigma^2_{E_{\rm sh}}}} , \tag{6.15}$$

where the normalization constant,

$$\mathcal{N}_{E_{\rm sh}}(E^{\rm rec}_{\rm sh}) \equiv \frac{2}{1 + \text{erf}\left(\frac{E^{\rm rec}_{\rm sh}}{\sqrt{2}\sigma_{E_{\rm sh}}}\right)} , \tag{6.16}$$

ensures that the integral of $R_{E_{\rm sh}}$ from $E_{\rm sh} = 0$ to ∞ equals 1. The width of the resolution function is $\sigma_{E_{\rm sh}} = 10^{\sigma_\epsilon} E_{\rm sh}$, where σ_ϵ is the spread in the ratio $\epsilon \equiv \log_{10}(E^{\rm rec}_{\rm sh}/E_{\rm sh})$. Reference [315] reported approximately $\sigma_\epsilon = 0.1$, based on simulations performed for RNO-G; we take this value to be representative also of IceCube-Gen2, and use it to produce our results; see Section 6.6.3. References [317, 324] reported similar results for a shallow detector component in ARIANNA [317, 324]. The choice of σ_ϵ has little effect on our results, as long as it is under control, since the cross section is extracted mainly from the angular distribution of the showers, rather than from their energy distribution; see Section 6.3.3.

Table 1: Expected rates of neutrino-induced showers in the radio component of IceCube-Gen2, after $T = 10$ years of exposure time, for the benchmark UHE diffuse neutrino fluxes used in this analysis (see Section 6.4), and varying the νN DIS cross section $\sigma \equiv \sigma_{\nu_\alpha N}$, where $\alpha = e, \mu, \tau$. The cross section $\sigma_{\rm std}$ is the central BGR18 prediction [194] (see Section 6.3), against which we measure variations. The variation is the same for all flavors of ν_α and $\bar{\nu}_\alpha$. Possible flux types are: extrapolation to ultra-high energies (●), cosmogenic (■), source (◆), and cosmogenic + source (⬢). Results are obtained using the baseline choices for the detector resolution: shower energy resolution of $\sigma_\epsilon = 0.1$, with $\epsilon \equiv \log_{10}(E_{\rm sh}^{\rm rec}/E_{\rm sh})$, and angular resolution of $\sigma_{\theta_z} = 2^\circ$; see Section 6.6.4 for details. In this table, the shower rates shown are binned in a single bin of reconstructed shower energy, $10^7 \leq E_{\rm sh}^{\rm rec}/{\rm GeV} \leq 10^{10}$. Rates are all-sky, *i.e.*, summed over all values of reconstructed direction, $-1 \leq \cos\theta_z^{\rm rec} \leq 1$; we show separately the fraction of showers that are upgoing or near-horizontal, *i.e.*, with $\theta_z^{\rm rec} > 80^\circ$. (To produce our main results, instead we bin finely in reconstructed energy and direction; see Section 6.7.3.)

			Shower rate in IceCube-Gen2 radio array (10 yr)					
#	Type	UHE ν flux model	$\sigma = 0.1\sigma_{\rm std}$		$\sigma = \sigma_{\rm std}$		$\sigma = 4\sigma_{\rm std}$	
			All-sky	$\theta_z^{\rm rec} > 80^\circ$	All-sky	$\theta_z^{\rm rec} > 80^\circ$	All-sky	$\theta_z^{\rm rec} > 80^\circ$
1	●	IceCube HESE (7.5 yr) extrapolated [188]	0.12	62.58 %	0.73	36.86 %	2.57	29.23 %
2	●	IceCube ν_μ (9.5 yr) extrapolated [37]	4.09	57.42 %	26.90	35.34 %	98.13	29.41 %
3	■	Heinze *et al.*, fit to Auger UHECRs [174]	0.12	64.19 %	0.71	37.33 %	2.52	29.65 %
4	■	Bergman & van Vliet, fit to TA UHECRs [193]	45.29	51.00 %	332.34	33.74 %	1243.57	29.13 %
5	■	Rodrigues *et al.*, all AGN [179]	0.14	60.30 %	0.89	36.43 %	3.20	30.04 %
6	◆	Rodrigues *et al.*, all AGN [179]	17.33	60.94 %	107.16	36.62 %	385.97	30.11 %
7	■	Rodrigues *et al.*, HL BL Lacs [179]	3.32	51.90 %	24.24	34.08 %	89.89	29.40 %
8	⬢	Fang & Murase, cosmic-ray reservoirs [177]	8.25	54.48 %	57.41	34.59 %	211.27	29.33 %
9	◆	Fang *et al.*, newborn pulsars [175]	18.66	56.60 %	125.38	35.28 %	485.65	29.73 %
10	◆	Padovani *et al.*, BL Lacs [176]	9.41	61.28 %	57.85	36.67 %	207.58	30.00 %
11	⬢	Muzio *et al.*, max. extra p component [178]	7.93	51.62 %	56.55	33.57 %	213.28	28.60 %
12	⬢	Muzio *et al.*, fit to Auger & IceCube [180]	3.13	66.46 %	17.12	38.06 %	58.93	28.78 %

For the resolution function in direction, we adopt a Gaussian function centered at the real direction, θ_z, *i.e.*,

$$R_{\theta_z}(\theta_z^{\rm rec}, \theta_z) = \frac{\mathcal{N}_{\theta_z}}{\sqrt{2\pi}\sigma_{\theta_z}} e^{-\frac{(\theta_z^{\rm rec}-\theta_z)^2}{2\sigma_{\theta_z}^2}}, \tag{6.17}$$

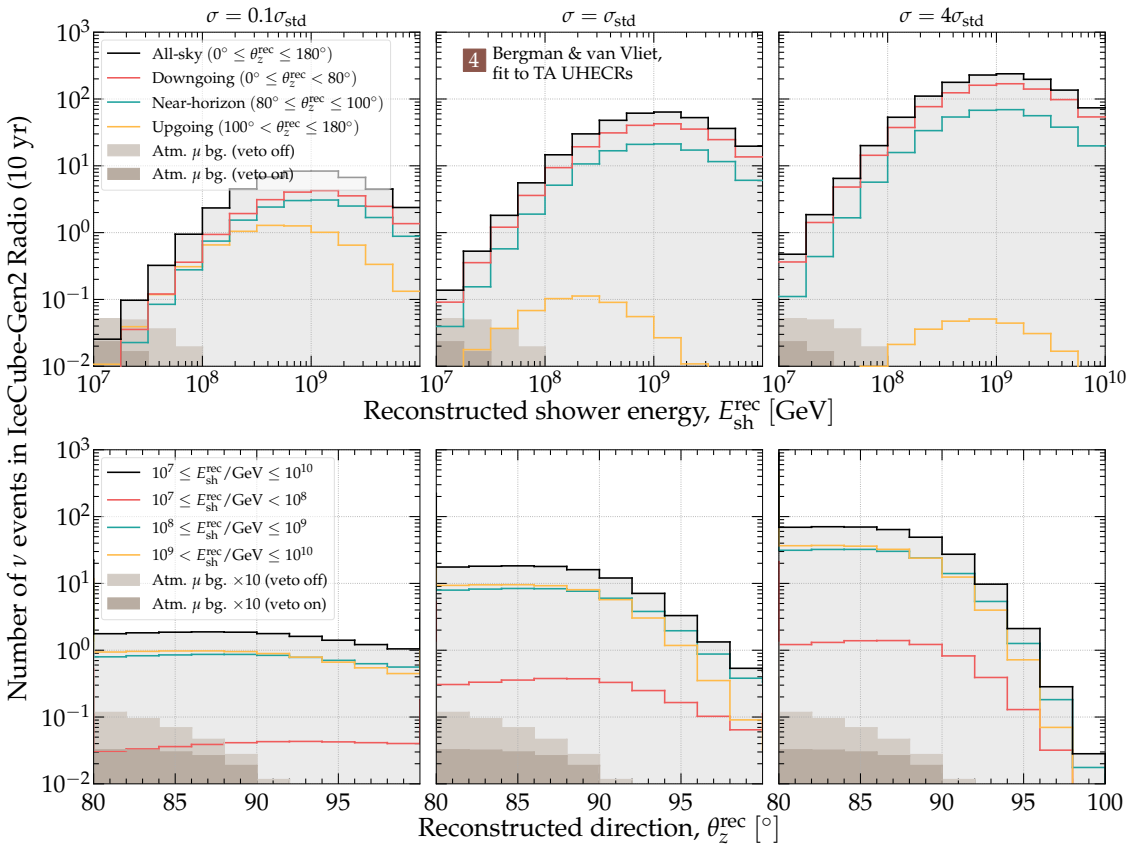

Figure 18: Mean expected distribution of neutrino-initiated showers in the radio component of IceCube-Gen2 after 10 years of exposure. For this plot, we assume the benchmark model 4 for the UHE diffuse neutrino flux [193] (see Fig. 8); to produce our results in the main text, we explore all flux models, 1–12 (see Section 6.4, Tables 1 and 2). Each column shows a different choice of the νN DIS cross section that affects the propagation of neutrinos through the Earth and their detection. The cross section $\sigma_{\rm std}$ is the central value of the BGR18 calculation [194], which we take as our baseline. See Section 6.6.4 for details about the calculation of shower rates. We include the background of showers due to atmospheric muons, which factors into our statistical analysis, computed using the hadronic interaction model SYBILL 2.3C [293]. (In the lower row of panels, the background is multiplied by a factor of 10 to make it visible.) In our analysis, we use exclusively the background after the application of the surface veto ("veto on"); in this plot, we show the case without the veto ("veto off") only for comparison.

where the normalization constant,

$$\mathcal{N}_{\theta_z}(\theta_z^{\rm rec}) \equiv \frac{2}{\operatorname{erf}\left(\frac{\pi-\theta_z^{\rm rec}}{\sqrt{2}\sigma_{\theta_z}}\right) + \operatorname{erf}\left(\frac{\theta_z^{\rm rec}}{\sqrt{2}\sigma_{\theta_z}}\right)}\,, \tag{6.18}$$

ensures that the integral of R_{θ_z} from $\theta_z = 0$ to π equals 1. We use $\sigma_{\theta_z} = 2°$ to produce our main results; see Section 6.3.3. In Section 6.8, we study the effect of varying σ_{θ_z} on measuring the νN cross section.

Folding the resolution functions, Eqs. (6.15)–(6.18), with the true shower rate, Eq. (6.13), yields the reconstructed shower rate, *i.e.*,

$$\frac{d^2 N_{\nu_\alpha}}{dE_{\rm sh}^{\rm rec} d\theta_z^{\rm rec}} = \int_{-1}^{+1} d\cos\theta_z \int_0^\infty dE_{\rm sh} \frac{d^2 N_{\nu_\alpha}}{dE_{\rm sh} d\cos\theta_z} \mathcal{R}_{E_{\rm sh}}(E_{\rm sh}^{\rm rec}, E_{\rm sh})\, \mathcal{R}_{\theta_z}(\theta_z^{\rm rec}, \theta_z)\,. \tag{6.19}$$

Finally, the total shower rate is the contribution from ν_α and $\bar{\nu}_\alpha$ of all flavors, *i.e.*,

$$\frac{d^2N_\nu}{dE_{\rm sh}^{\rm rec}d\theta_z^{\rm rec}} = \sum_{\alpha=e,\mu,\tau} \frac{d^2N_{\nu_\alpha}}{dE_{\rm sh}^{\rm rec}d\theta_z^{\rm rec}} + \nu_\alpha \to \bar{\nu}_\alpha \ . \tag{6.20}$$

We use Eq. (6.20) to forecast shower rates throughout our analysis, integrated in bins of $E_{\rm sh}^{\rm rec}$ and $\cos\theta_z^{\rm rec}$. In Section 6.7.3, we comment on the effect of the choice of binning on the measurement of the cross section.

Figure 17 shows the mean expected number of neutrino-induced showers for benchmark UHE neutrino flux model 4 [193] as illustration, broken down into the contribution of each interaction type and neutrino species. Because flux model 4 has comparable fluxes of each neutrino species at the surface of the Earth (see Fig. 9), the differences between the rates of different channels in Fig. 17 are due mainly to differences in the in-Earth propagation of the different species, the connection between neutrino and shower energy, Eq. (6.14), and the effective volumes for ν_e CC interactions and for all other interaction channels (see Fig. 16).

Figure 17 displays features that are common to all interaction channels and all benchmark flux models. Barring differences in the flux of the different species that reach the detector, the following observations hold generally. First, the dominant contribution comes from the CC interactions of ν_e and $\bar{\nu}_e$, the only two cases for which $E_{\rm sh} = E_\nu$; see Eq. (6.14). (In Fig. 17, there are more showers in the range 10^9–10^{10} GeV because those showers receive the full neutrino energy, and the flux model 4 peaks within that range; see Fig. 8.) Second, the NC interactions of all species, and the CC interactions of ν_μ, $\bar{\nu}_\mu$, ν_τ, and $\bar{\nu}_\tau$, contribute at about the same level, since $E_{\rm sh} = yE_\nu$ for all of them; see Eq. (6.14). Third, in all channels, because of in-Earth attenuation (see Section 6.5), events are mainly downgoing, *i.e.*, $0.2 \leq \cos\theta_z^{\rm rec} \lesssim 1$, and, to a lesser extent, near-horizontal, *i.e.*, $-0.2 \leq \cos\theta_z^{\rm rec} \leq 0.2$. Fourth, all channels have a deficit around $\cos\theta_z^{\rm rec} = 1$, because the neutrino interaction takes place almost always below the deepest antenna of the station, and all radio signals are emitted downward for vertical neutrino directions; see Fig. 16. Fifth, and finally, all channels have a deficit around $E_{\rm sh}^{\rm rec} = 10^7$ GeV, because the detector loses sensitivity quickly at low shower energies, where radio emission is weak; see Fig. 16.

Table 1 shows that the IceCube-Gen2 all-sky shower rate grows with the νN cross section, regardless of the choice of benchmark flux model. On the one hand, for all values of the cross section, the shower rate is dominated by downgoing showers, with $\theta_z^{\rm rec} \leq 80^\circ$, as expected from

Section 6.3.3. On the other hand, the fraction of near-horizontal and upgoing showers ($\theta_z^{\rm rec} > 80°$) decreases with the cross section. These two observations reveal that, in the all-sky shower rate, the main dependence on the cross section comes from its role in the detector, rather than in the in-Earth attenuation of the neutrino flux; see Eq. (6.1) for a simplified picture. Table 1 confirms what Eq. (6.1) professed: as the attenuation becomes more important, with rising cross section, the rate of near-horizontal and upgoing showers decreases. This is where the sensitivity to the cross section comes from. Table 1 shows that the changes in the shower rate with the cross section are roughly comparable for all benchmark flux models; differences between them are due to their different energy spectra.

Figure 18 illustrates the behavior seen in Table 1 for one benchmark flux model; other models behave similarly. The shape of the shower distribution in $E_{\rm sh}^{\rm rec}$ is largely insensitive to the value of the cross section: changes in the cross section merely scale the distribution down—if the cross section is smaller—or up—if the cross section is larger. This is because the all-sky shower rate is dominated by downgoing showers, initiated by neutrinos whose flux is unattenuated due to traveling a short distance inside Earth. Equation (6.1) shows that for downgoing showers, because there is little attenuation, the rate scales roughly linearly with the cross section. In contrast, the shape of the shower distribution in $\cos\theta_z^{\rm rec}$ is strongly affected by the value of the cross section. Equation (6.1) shows that, due to the exponential attenuation, a smaller cross section mitigates in-Earth attenuation and flattens the distribution in $\cos\theta_z^{\rm rec}$, while a larger cross section enhances the attenuation and tilts the distribution in $\cos\theta_z^{\rm rec}$. This exponential angular dependence of the shower rate on the cross section—rather than the linear dependence of the all-sky shower rate—is where most of the sensitivity to the cross section comes from. The tilting of the angular distribution becomes stronger the larger the value of $\theta_z^{\rm rec}$, *i.e.*, the longer the distance neutrinos travel inside the Earth. However, for upgoing neutrinos, the flux is nearly fully attenuated, even for the most optimistic diffuse flux models. Therefore, in practice, the sensitivity to the cross section comes from the angular distribution of showers coming from around the horizon. We pay special attention to them later, in Section 6.7.3, by binning them in fine angular bins.

6.7 MEASURING THE CROSS SECTION

We forecast the capability of IceCube-Gen2 to measure the UHE νN DIS cross section by means of its effect on the predicted shower rates. Because of the degeneracy that exists between the cross section and the neutrino flux normalization when computing shower rates (see Section 6.3.3.2), our forecasts are always for their simultaneous measurement. We use the methods introduced in Section 6.6.4 to generate samples of showers for different choices of their values. We perform the analysis below separately for each of the UHE neutrino flux models 1–12 introduced in Section 6.4.

6.7.1 *Overview*

For a choice of flux model, we start by generating the "real" shower sample, *i.e.*, a sample of showers distributed and binned in $E_{\rm sh}^{\rm rec}$ and $\cos\theta_z^{\rm rec}$, computed using the "real" values of the cross section and flux normalization. For the cross section, the real value is given by the central value of the BGR18 DIS calculation, $\sigma_{\rm std}$. For the flux normalization, the real value, $\Phi_{0,\rm std}$, is given by the model flux evaluated at a reference energy of $E_{\nu,0} = 10^8$ GeV. The resulting real shower sample is the mean expected sample predicted for IceCube-Gen2. Later, in Section 6.7.4, we use a statistical procedure to assess how well we can recover the real values of the cross section and flux normalization in a realistic experimental setting. As part of that procedure, we generate test shower samples using values of the cross section, $\sigma_{\nu_\alpha N}$, and flux normalization, Φ_0, different from the real values, and compare those shower samples to the real one, including the presence of a non-neutrino background.

To generate test shower samples, we parametrize deviations from the real value of the νN DIS cross section, within the range $E_\nu = 10^7$–10^{10} GeV, via

$$f_\sigma \equiv \sigma/\sigma_{\rm std}\ . \tag{6.21}$$

We consider only energy-independent modifications of the cross section, as in Ref. [60], so f_σ is constant in energy. Changing f_σ shifts the value of the cross section up or down from the central BGR18 value. The same value of f_σ applies to all flavors of ν_α and $\bar{\nu}_\alpha$, and to interactions on protons

($N = p$) and neutrons ($N = n$). The real shower sample is computed using $f_\sigma = 1$. Later, in Section 6.7.4,we allow its value to float generously, from 0.01 to 100, and generate a large number of test shower distributions for its different values.

Changing f_σ affects the neutrino flux that reaches the detector—by changing the propagation through the Earth (see Section 6.5)—and the cross section at the detection (see Section 6.6.4). For each choice of f_σ, we compute both effects. In our analysis, changing f_σ affects only the νN DIS cross section off the nucleon partons; the remaining, sub-leading neutrino interaction channels that act during neutrino propagation through the Earth (see Section 6.5) remain unchanged. Section 6.9 comments on possible generalizations.

Similarly, for each choice of flux model out of models 1–12, we parametrize deviations from the real value of the flux normalization, via

$$f_\Phi \equiv \Phi_0 / \Phi_{0,\text{std}} \ , \tag{6.22}$$

where the value of $\Phi_{0,\text{std}}$ is unique to each flux model. Changing f_Φ shifts the flux up or down from its central value, but the shape of the neutrino spectrum, flavor composition, and ν *vs.* $\bar{\nu}$ content are unchanged. The real shower sample is computed using $f_\Phi = 1$. The same value of f_Φ applies to all flavors of ν_α and $\bar{\nu}_\alpha$. Later, in Section 6.7.4, we allow its value to float generously, and generate a large number of test shower distributions for its different values. We vary f_Φ indirectly: for a given choice of flux model out of 1–12, we allow the value of $E^2_{\nu,0}\Phi_0$ to float from 10^{-12} to 10^{-7} GeV cm^{-2} s^{-1} sr^{-1}, and compute f_Φ for each value of $E^2_{\nu,0}\Phi_0$. Section 6.9 comments on possible generalizations of this procedure.

6.7.2 *Non-neutrino backgrounds*

In the radio component of IceCube-Gen2, in addition to neutrino-initiated events, we expect a background of irreducible non-neutrino-induced events that could mimic a neutrino signal. There are two main such backgrounds: in-ice showers induced by high-energy atmospheric muons created by cosmic-ray interactions in the atmosphere [213], and air-shower cores, *i.e.*, cores of showers that start in the atmosphere, induced mainly by cosmic rays, and that continue developing downwards in the ice [327]. The latter lead to in-ice Askaryan radiation that can be reflected

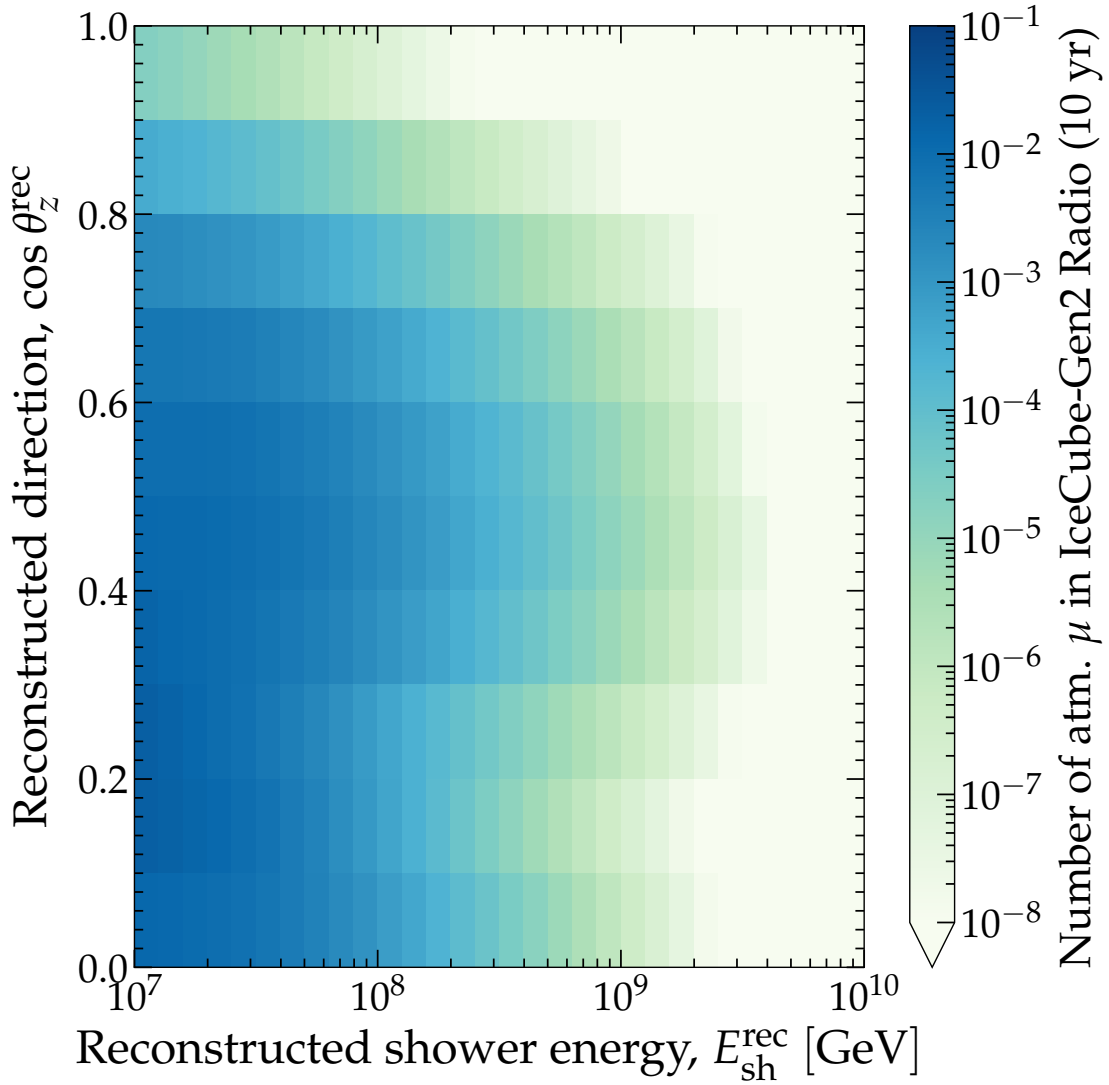

Figure 19: Mean expected number of background showers initiated by high-energy atmospheric muons in the baseline design of the IceCube-Gen2 radio array in 10 years of exposure time. The energy and angular resolution are the same as the baseline choices for neutrino-initiated events, *i.e.*, $\sigma_\epsilon = 0.1$ and $\sigma_{\theta_z} = 2^\circ$, respectively. The hadronic interaction model used is SYBILL 2.3C [293]. The background rates in this plot and in our analysis are after the application of a cosmic-ray veto used to suppress the background. See the main text for details.

back upwards by reflection layers that are known to be present in deeper ice. In our forecasts, we account only for the background of showers due to atmospheric muons, by generating their expected distribution in reconstructed energy and direction, as described below. We do not account for the background of cosmic-ray air-shower cores, since their estimates are presently uncertain, but comment on them in Section 6.9.

Figure 19 shows the mean distribution of muon-induced shower events in the radio component of IceCube-Gen2 [77, 213, 214]; see also Fig. 18. We estimate it using the hadronic interaction model

SYBILL 2.3C [293] and apply a veto coming from the detection of atmospheric muons by a surface array of cosmic-ray detector tanks, that helps to mitigates the rate. We expect roughly 0.2 showers per year in the range 10^4–10^{11} GeV, and < 0.1 showers per year in the range 10^7–10^{10} GeV relevant for our forecasts. These rates are subject to significant uncertainties, due mainly to the high-energy muon flux, but the ability to measure the cross section in IceCube-Gen2 will not be affected by the uncertainties; we comment on this below. The background of showers from atmospheric muons is direction- and energy-dependent. Figure 18 shows that most of the showers are in the range 10^7–10^9 GeV; thus, the highest-energy end of the shower spectrum is nearly free from this background. Since it is unlikely that a muon produced in the atmosphere reaches the detector from below the horizon, the background for $\theta_z > 90^\circ$ is zero (this changes slightly after applying angular smearing below).

Similarly to how we use the reconstructed neutrino-induced shower rate (see Section 6.6.4) in our analysis, we also use the reconstructed rate of muon-induced showers; this is what Fig. 19 shows. We compute it in the same way: by convolving the true rate of muon-induced showers with the resolution functions in Eqs. (6.15)–(6.18), and expressing the result in terms of $E_{\rm sh}^{\rm rec}$ and $\cos\theta_z^{\rm rec}$. At all times, we use the same energy and angular resolution for muon-induced showers as for neutrino-induced showers. As a result, a tiny fraction of the muon-induced showers leak into the highest energies and into directions just below the horizon, *i.e.*, for $\theta_z^{\rm rec} \gtrsim 90^\circ$; see Fig. 18.

6.7.3 *Choice of shower binning*

To produce our forecasts, we bin the real and test shower samples (see above) in fine bins of $E_{\rm sh}^{\rm rec}$ and $\cos\theta_z^{\rm rec}$. Accordingly, in our statistical analysis we use a binned likelihood function; see Section 6.7.4. The bins of reconstructed shower energy and direction that we use are equal in size to or larger than the width of the detector energy and angular resolution, *i.e.*, σ_{θ_z} and $\sigma_{E_{\rm sh}}$, respectively, from Eqs. (6.15) and (6.17). Section 6.9 comments on the possible future use of an unbinned likelihood.

When binning in $\cos\theta_z^{\rm rec}$, we pay special attention to Earth-skimming neutrinos, which have the strongest sensitivity to the cross section; see Section 6.3.3. For downgoing showers, we expect a

large rate; but, since they are largely unattenuated by their passage through Earth, they do not carry a significant angular dependence induced by the cross section. Thus, for them we use a single bin covering $\theta_z^{\rm rec} \in [0°, 80°]$. For horizontal and near-horizontal showers, our region of interest, we use ten bins, equally spaced between $\theta_z^{\rm rec} = 80°$ and 100°, each with a bin size equal to the angular resolution of the detector, σ_{θ_z}. To produce our main results, we use the baseline angular resolution of $\sigma_{\theta_z} = 2°$; later, we explore alternative choices (see Fig. 24). For upgoing showers, of which there are few due to the attenuation of the flux inside Earth, we use two large angular bins: one for $\theta_z^{\rm rec} \in [100°, 110°]$, which is populated only if the flux is high and the cross section is low (see Fig. 18), and one for $\theta_z^{\rm rec} \in [110°, 180°]$, which is typically nearly empty. For upgoing showers, using finer binning would lead to a large number of empty, uninformative bins.

When binning in $E_{\rm sh}^{\rm rec}$, we use twelve bins equally spaced in logarithmic scale ranging from $\log_{10}(E_{\rm sh}^{\rm rec}/{\rm GeV}) = 7$ to 10. Even though in our analysis we allow only for energy-independent re-scaling of the cross section from its predicted central value (see Section 6.7.1), the distribution of showers in energy still matters when extracting the cross section, for three reasons. First, during neutrino propagation inside the Earth an energy-independent re-scaling of the cross section affects the flux attenuation differently at different energies, due to the non-linear dependence on energy of the regeneration of neutrinos in NC interactions and ν_τ regeneration; see Fig. 11. Second, the distribution of showers in energy reflects the distribution of neutrino energies in the diffuse flux. Third, showers from the background of atmospheric muons are concentrated at low energies: above a few times 10^7 GeV, there are nearly none, so binning in energy enhances the statistical power of the neutrino-induced showers in that range. Naturally, the choice of energy binning is relevant only when the predicted number of showers is relatively large. If shower rate is low, like for benchmark flux models 1, 3, and 5, we have checked that the choice of $E_{\rm sh}^{\rm rec}$ binning does not affect cross-section measurements.

6.7.4 *Statistical analysis*

To produce our forecasts, we use a Bayesian statistical analysis. Section 6.7.1 outlined the procedure; below, we present it in detail. We carry the procedure separately for each UHE neutrino flux model, 1–12 (see Section 6.4).

First, for a given choice of flux model we generate the real shower sample (r), *i.e.*, the mean expected number of showers assuming the real values $f_\sigma = 1$ and $f_\Phi = 1$ (see Section 6.7.1), binned in $E_{\rm sh}^{\rm rec}$ and $\cos\theta_z^{\rm rec}$ as described in Section 6.7.3. In the i-th bin in $E_{\rm sh}^{\rm rec}$ and the j-th bin in $\cos\theta_z^{\rm rec}$ of the real shower sample, the mean number of neutrino-induced showers is $\bar{N}_{\nu,ij}^{(r)}$. To this bin, we associate a Poisson probability distribution, with mean $\bar{N}_{\nu,ij}^{(r)}$, of observing $N_{\nu,ij}^{(r)}$ showers in a particular realization of the shower distribution, *i.e.*,

$$\mathcal{P}_{\nu,ij}\left(N_{\nu,ij}^{(r)}\right) = \frac{\left(\bar{N}_{\nu,ij}^{(r)}\right)^{N_{\nu,ij}^{(r)}} e^{-\bar{N}_{\nu,ij}^{(r)}}}{N_{\nu,ij}^{(r)}!} \,. \tag{6.23}$$

Similarly, in each bin, the mean number of background muon-induced showers is $\bar{N}_{\mu,ij}^{(r)}$, and we associate to it a Poisson probability distribution, given by Eq. (6.23) but with $\bar{N}_{\nu,ij}^{(r)} \to \bar{N}_{\mu,ij}^{(r)}$ and $N_{\nu,ij}^{(r)} \to N_{\mu,ij}^{(r)}$, of observing $N_{\mu,ij}^{(r)}$ muon-induced showers in a particular realization of the shower distribution. Thus, in a particular *observed* realization of the real shower distribution, the total number of showers in the bin is $N_{{\rm obs},ij} = N_{\nu,ij}^{(r)} + N_{\mu,ij}^{(r)}$, where the neutrino and muon contributions are sampled from their respective probability distributions.

Next, for the same choice of flux model, we generate test shower samples (t) for values of f_σ and f_Φ that are in general different from their real values. In each bin, the mean expected numbers of neutrino-induced and muon-induced showers are, respectively, $\bar{N}_{\nu,ij}^{(t)}(\boldsymbol{\theta})$ and $\bar{N}_{\mu,ij}^{(t)}(\boldsymbol{\theta})$, where we use $\boldsymbol{\theta} \equiv (f_\sigma, f_\Phi)$ as shorthand. The total mean expected number of showers in this bin is $\bar{N}_{{\rm test},ij}(\boldsymbol{\theta}) = \bar{N}_{\nu,ij}^{(t)}(\boldsymbol{\theta}) + \bar{N}_{\mu,ij}^{(t)}(\boldsymbol{\theta})$.

Given a specific random realization of the real shower distribution, generated following the above procedure, we quantify its compatibility with the mean test shower distribution expected for a particular choice of $\boldsymbol{\theta}$, in each bin, via the likelihood function

$$\mathcal{L}_{ij}(\boldsymbol{\theta}) = \frac{\bar{N}_{{\rm test},ij}(\boldsymbol{\theta})^{N_{{\rm obs},ij}} e^{-\bar{N}_{{\rm test},ij}(\boldsymbol{\theta})}}{N_{{\rm obs},ij}!} \,. \tag{6.24}$$

The full likelihood function is the product of all the partial likelihood functions, *i.e.*,

$$\mathcal{L}(\boldsymbol{\theta}) = \prod_{i=1}^{N_{E_{\rm sh}^{\rm rec}}} \prod_{j=1}^{N_{\theta_z^{\rm rec}}} \mathcal{L}_{ij}(\boldsymbol{\theta}) \,, \tag{6.25}$$

where $N_{E_{\rm sh}^{\rm rec}}$ and $N_{\theta_z^{\rm rec}}$ are, respectively, the number of bins in $E_{\rm sh}^{\rm rec}$ and $\theta_z^{\rm rec}$; see Section 6.7.3 for details. The posterior probability distribution is

$$\mathcal{P}(\boldsymbol{\theta}) = \mathcal{L}(\boldsymbol{\theta})\pi(\boldsymbol{\theta}) \,, \tag{6.26}$$

where $\pi(\boldsymbol{\theta}) \equiv \pi(f_\sigma)\pi(f_\Phi)$, $\pi(f_\sigma)$ is the prior on f_σ, and $\pi(f_\Phi)$ is the prior on f_Φ.

We use wide priors in $\log_{10} f_\sigma$ and $\log_{10} f_\Phi$ to facilitate exploring large possible deviations from the real values of $f_\sigma = 1$ and $f_\Phi = 1$. The priors are flat to avoid introducing unnecessary bias. For $\log_{10} f_\sigma$, the prior spans the interval from -2 and 2; this range covers all reasonable modifications of the cross section. For $\log_{10} f_\Phi$, the prior spans a different interval for each flux model. For a given flux model, it is defined by varying the flux at $E_{\nu,0} = 10^8$ GeV from $E_{\nu,0}^2 \Phi(E_{\nu,0}) = 10^{-12}$ to 10^{-7} GeV cm^{-2} s^{-1} sr^{-1} and using Eq. (6.22) to compute f_Φ. The low end of this interval corresponds, in practice, to an unobservable flux. The high end exceeds the upper limits on the flux from IceCube and Auger (see Fig. 8). However, this does not put our analysis in tension: the IceCube and Auger limits were obtained under the assumption that the νN cross section has its nominal value ($f_\sigma = 1$) while, in our analysis, when we explore large reductions of the cross section ($f_\sigma \ll 1$), they can be traded off for large enhancements of the flux while keeping the number of showers unchanged; see Section 6.3.3.

For a particular random realization of the real shower distribution, we compute the posterior, Eq. (6.26), as a function of f_σ and f_Φ. We generate a large number of different random realizations of the real shower distribution using the above prescription; for each, we compute the associated posterior. Since our goal is to produce forecasts for the average sensitivity of IceCube-Gen2, we take the arithmetic average, $\langle \mathcal{P} \rangle$, of all the posteriors thus generated. This is equivalent to marginalizing over the Poisson distribution in each bin of the real shower distribution. In this way, our forecasts reflect the average sensitivity of the detector, taking into account statistical fluctuations. In an actual detection in IceCube-Gen2, and assuming that $f_\sigma = 1$ and $f_\Phi = 1$ are indeed the real values, the posterior computed with real data would be one of the random realizations that we averaged over.

Below, to produce our forecasts, we maximize $\langle \mathcal{P} \rangle$ with respect to f_σ and f_Φ, and find their best-fit values and credible intervals. We report results either as two-dimensional posteriors (see Figs. 20 and Fig. A1), or as one-dimensional posteriors obtained by marginalizing the full posterior over one of the two parameters (see Table 2 and Fig. A2), *i.e.*, $\langle \mathcal{P}(f_\sigma) \rangle_{f_\sigma} = \int df_\Phi \langle \mathcal{P}(f_\sigma, f_\Phi) \rangle$ for f_σ, and equivalently for f_Φ.

6.8 RESULTS

Below, to produce our main results, we use the baseline design of the IceCube-Gen2 radio array, *i.e.*, 144 hybrid (deep + shallow) stations plus 169 shallow-only stations, the baseline detector energy resolution, $\sigma_\epsilon = 0.1$, and angular resolution, $\sigma_{\theta_z} = 2^\circ$, and $T = 10$ years of exposure time. We state explicitly when we vary these parameters.

Figure 20 shows our results for the simultaneous measurement of the cross section and flux normalization for a selection of benchmark UHE neutrino flux models that is representative of the full variety explored in our analysis; see Fig. 8. Appendix A.1 contains similar results for all benchmark flux models. In Fig. 20, the elongated shape of the two-dimensional posteriors follows from the partial degeneracy between the cross section and the flux normalization: the number of showers depends on their product; see Eq. (6.1). The posteriors are narrower for flux models with a higher associated mean expected shower rate, *i.e.*, in Fig. 20, for flux models 4 ("Bergman & van Vliet, fit to TA UHECRs") and 6 ("Rodrigues *et al.*, all AGN"). This is because, in those cases, the number of horizontal showers is large enough to partially break the degeneracy between cross section and flux; in Eq. (6.1), this happens via the exponential attenuation term.

Figure 20 reveals an asymmetry between the region of high flux and small cross section in the upper-left corner—which is disfavored—and the region of low flux and large cross section in the lower-right corner—which is allowed. The asymmetry becomes more evident for lower-flux models. This preference for low flux and large cross section stems from the effect of the cross section on the shower distribution, as illustrated in Fig. 18 for flux model 4. A small cross section ($f_\sigma \lesssim 1$) implies that the in-Earth attenuation is small and, therefore, the flux at the detector, and the angular distribution of the associated showers, are closer to isotropic. In contrast, a high cross

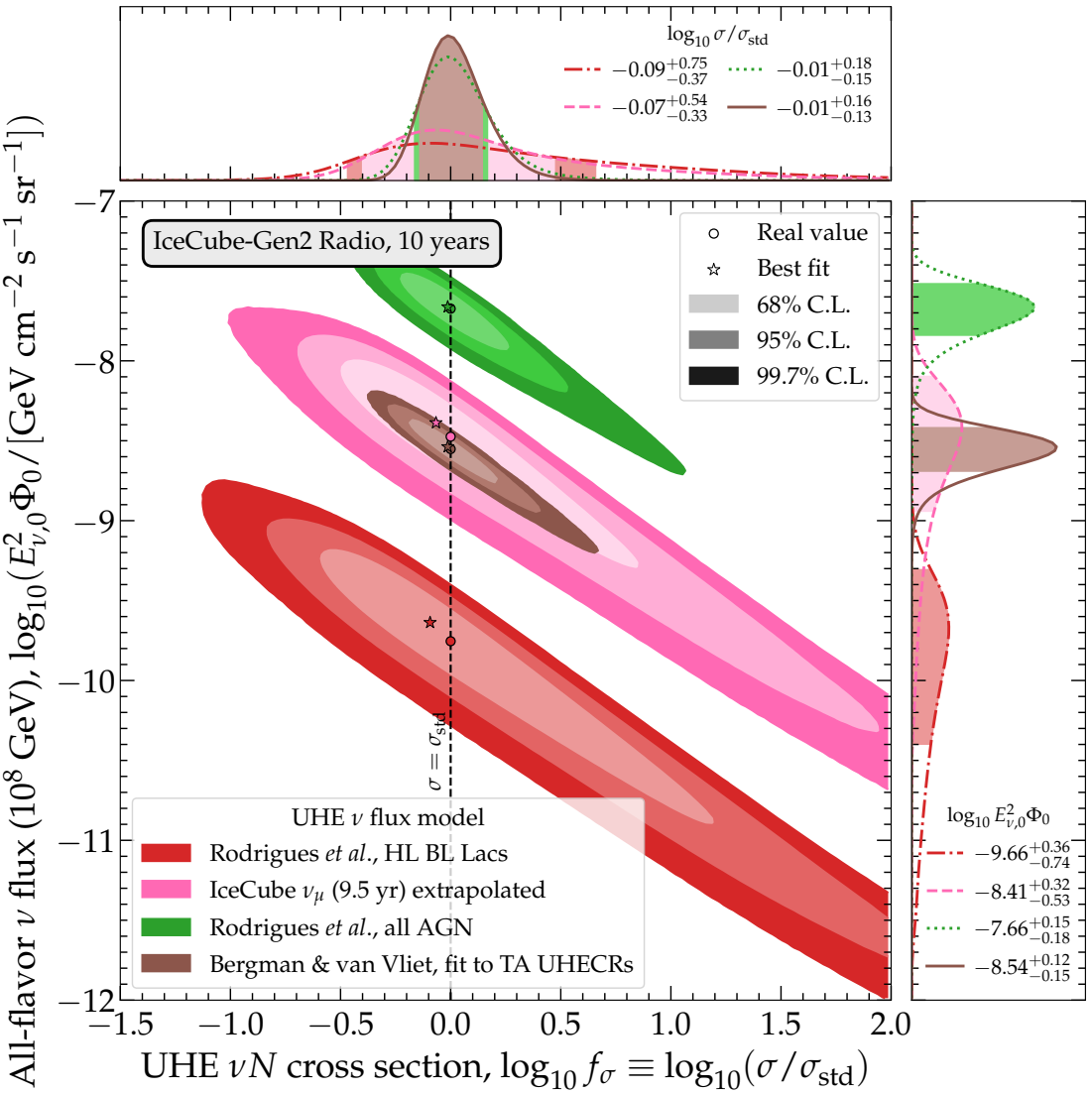

Figure 20: Mean expected capability of the radio component of IceCube-Gen2 to jointly measure the UHE νN DIS cross section and the diffuse neutrino flux normalization, for representative benchmark flux models 2, 4, 6, and 7 (see Fig. 8), shown as two-dimensional posteriors. Results account for the background of showers induced by atmospheric muons; see Section 6.7.2. Each posterior is the average over 10^6 random realizations of the shower distribution, binned in reconstructed shower energy and direction; see Section 6.7.4. Results are for the baseline detector design with 144 hybrid (shallow + deep) stations plus 169 shallow-only stations, angular resolution of $\sigma_{\theta_z} = 2°$, energy resolution of $\sigma_\epsilon = 0.1$, and $T = 10$ years of exposure. See Fig. A1 for similar results for all flux models, Table 2 and Fig. A2 for marginalized one-dimensional parameter ranges and posteriors, and the main text for details.

section ($f_\sigma \gtrsim 1$) implies a tilted angular distribution, with a sharp drop of the rate around the horizon. For the real values of the cross section and flux normalization, $f_\sigma = 1$ and $f_\Phi = 1$, the predicted near-horizontal shower rate is low: for most fluxes, it is only about one shower per bin in 10 years (exceptionally, for flux model 4, the highest among the benchmarks, there is a handful of near-horizontal showers). Therefore, high values of $f_\sigma \gtrsim 1$, which also result in a sharp drop, are favored over $f_\sigma \lesssim 1$; the asymmetry in Fig. 20 reflects this.

Figure 21 shows that the sensitivity to f_σ and f_Φ comes predominantly from near-horizontal and horizontal showers, since they are the ones initiated by neutrinos that undergo significant, but not complete, attenuation inside the Earth. Using only downgoing showers reveals the underlying degeneracy between cross section and flux in the calculation of shower rates (see Section 6.3.3), but is unable to break it. In short, downgoing showers, more numerous, help in the discovery of the diffuse UHE neutrino flux, while near-horizontal showers, more rare, help to jointly perform studies beyond flux discovery, like cross-section measurements.

Figure 22 shows that, using the baseline array design—made up of 144 hybrid (shallow + deep) plus 169 shallow-only stations—the precision in the measured values f_σ and f_Φ is dominated by shallow stations. The caveat to this is that in our analysis we assume that the angular resolution of all detected showers is the same, whereas in reality there will be differences. For instance, detection in deep antennas is expected to yield poorer resolution (see Section 6.6.3), which would further boost the importance of shallow stations. Section 6.9 comments on future improvements of the analysis in this direction.

Table 2 shows the one-dimensional marginalized ranges of f_σ and f_Φ for all the benchmark flux models. The results show that the radio component of IceCube-Gen2 could indeed jointly measure f_σ and f_Φ, to varying precision, as long as at least a few tens of showers are detected in 10 years. Appendix A.1 shows the corresponding one-dimensional marginalized posteriors.

We classify the results in Table 2 in three groups, according to the size of the flux and its associated shower rate. First, for low-flux models 1, 3, and 5, we expect fewer than one shower in 10 years and so no measurement is possible. Second, for medium-flux models 2, 7, 8, 10, 11, and 12, we expect tens of events; with them, we can measure f_σ to within 50–180% and f_Φ to within 70–110%, depending on the flux model. Third, for high-flux models 4, 6, and 9, we expect 100–300 events; with them, we can measure f_σ and f_Φ to within 40%. Table 2 reveals that these groups are not dominated by a single flux type; rather, different flux types—extrapolated, cosmogenic, source, and cosmogenic + source (see Section 6.4)—are represented in all groups.

Table 2 reveals important nuance associated to the shape of the UHE neutrino spectrum. For instance, even though flux model 12 has a lower shower rate than flux model 7, it leads to more accurate measurements of f_σ and f_Φ. Figure 8 shows that model 12 peaks at lower energies than

model 7. Since the νN cross section grows with energy, this implies that in model 12 neutrinos are less attenuated by their passage through Earth, and so more of them reach the detector from near-horizontal directions. Conversely, in model 7 neutrinos are higher-energy, so they are more strongly attenuated and a relatively larger number of them are downgoing. This, again, highlights the importance of Earth-skimming showers to perform studies beyond flux discovery.

We have tested that the capability of IceCube-Gen2 to measure the cross section is not limited by the uncertainty in the background shower rate of atmospheric muons. We did this by repeating our analysis using a rate of muon-induced showers five times higher than the one in Fig. 19. The results are practically indistinguishable from those in Table 2. There are three reasons for this. First, for the benchmark flux models for which the cross section can be measured, the rate of muon-induced showers is tiny compared to the rate of neutrino-induced showers. Second, muon-induced showers are concentrated at lower energies, leaving the higher energies background-free. Third, muon-induced showers affect almost exclusively downgoing bins, whereas the sensitivity to the cross section comes from bins around the horizon.

In our analysis, we set the real values of the cross section and flux normalization to be $f_\sigma = 1$ and $f_\Phi = 1$; see above. However, Table 2 shows that, for all flux models, their average best-fit values have a consistent bias toward $f_\sigma \lesssim 1$ and $f_\Phi \gtrsim 1$ (except for low-flux models 1, 3, and 5, for which f_Φ is compatible with zero due to the low shower rate). The bias toward an average best-fit $f_\sigma \lesssim 1$, though slight, stems from the interplay in shower rates between the single bin that contains downgoing showers—whose mean expected shower rate is relatively high—and the multiple bins that contain horizontal and near-horizontal showers—whose mean expected shower rates are relatively low. As a result, the Poisson probability distribution of the rate, Eq. (6.23), of the single downgoing bin is rather symmetric, while Poisson probability distributions of the horizontal bins are rather asymmetric. Therefore, in any one of the random realizations of the shower distribution that we generate as part of our statistical analysis (see Section 6.7.4), in the downgoing bin under-fluctuations and over-fluctuations relative to the mean shower rate are equally likely, while in the horizontal bins under-fluctuations are more likely than over-fluctuations. As a result, on average, under-fluctuations in the all-sky shower rate are more likely than over-fluctuations. Because lower shower rates correspond to smaller values of the cross section, via Eq. (6.1), the best-fit value of

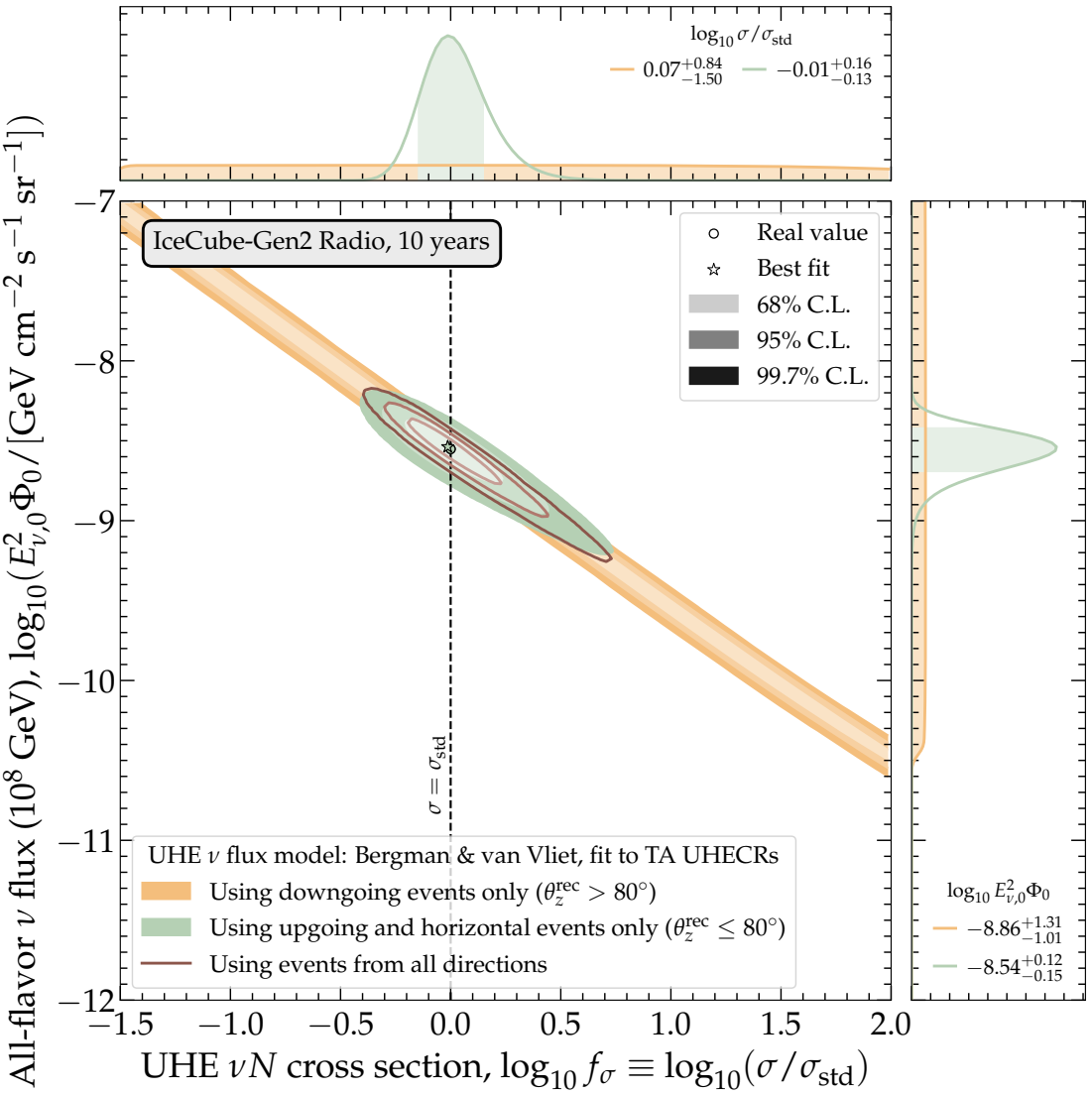

Figure 21: Same as Fig. 20, but for benchmark flux model 4 alone, and showing results using only downgoing showers and only upgoing plus horizontal showers.

$f_\sigma \lesssim 1$ on average. Nevertheless, within 68% C.L., the inferred values of f_σ and f_Φ are compatible with their real ones (again, except for the low-flux models). Further, their best-fit values approach their real values closer the higher the mean expected shower rate, and the longer the exposure time; see Fig. 23.

Figure 4 places our results in the context of existing cross-section measurements, including in IceCube, by showcasing a selection of three optimistic, representative benchmark flux models, 2, 4, and 5. In the best-possible scenario, *i.e.*, for flux model 4 ("Bergman & van Vliet, fit to TA UHECRs"), after 10 years we could be able to measure the cross section to within the theory uncertainty of the BGR18 prediction [194]. For lower, but still detectable, flux models, 4 shows

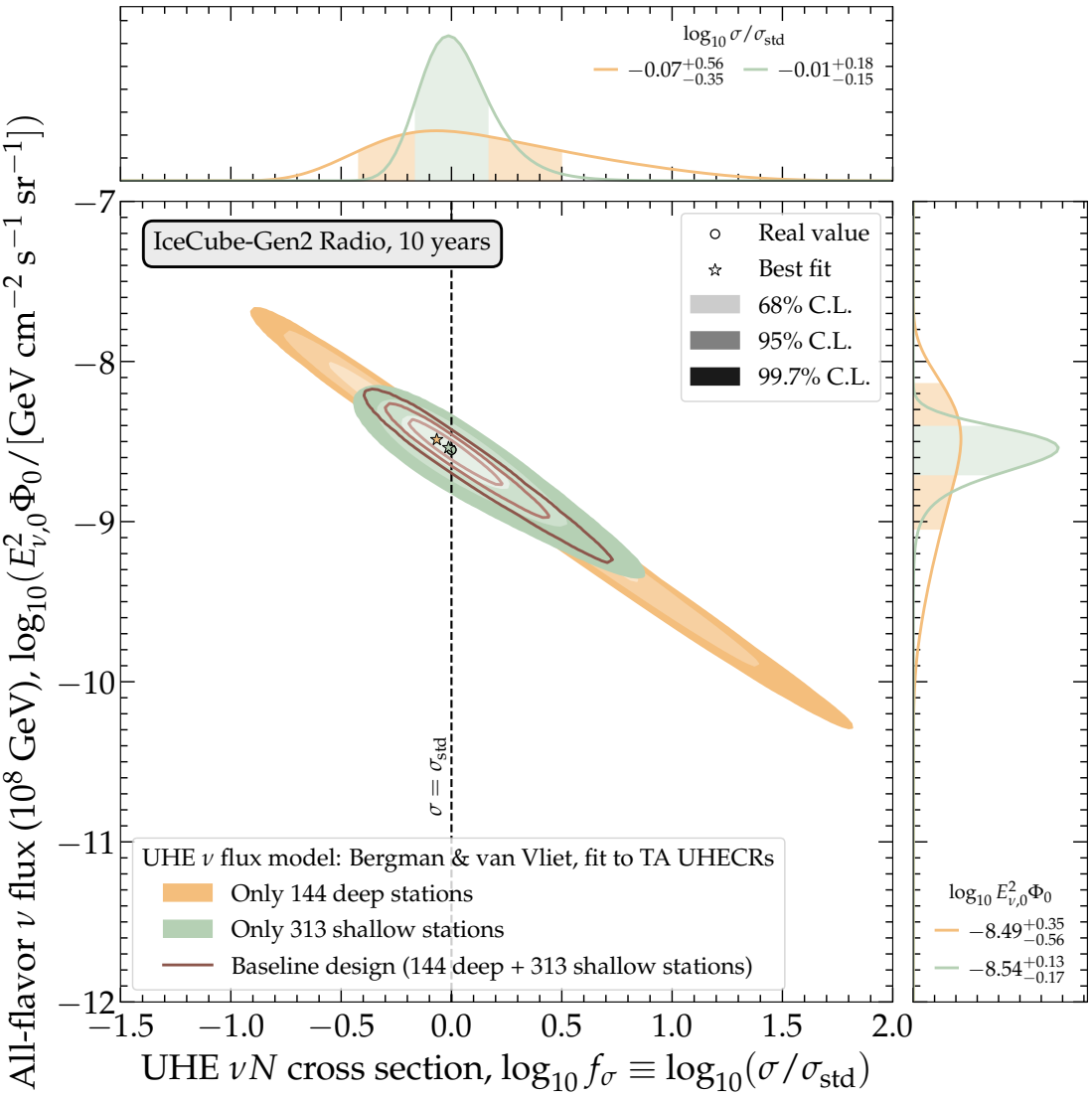

Figure 22: Same as Fig. 20, but for benchmark flux model 4 alone, and showing results using only the deep and shallow stations of the baseline array design.

that the measurement worsens, but remains informative. In particular, for flux model 2 ("IceCube ν_μ flux (9.5 yr), extrapolated to UHE")—a conservative benchmark based on the known TeV–PeV diffuse neutrino flux—the cross section could be measured to roughly the same accuracy at ultra-high energies as it is currently measured in the TeV–PeV range. Overall, medium-flux and high-flux models (see above) offer enough accuracy to test a diversity of proposed deviations of the cross section, due to new physics, *e.g.*, large extra dimensions [204], electroweak sphalerons [200], or to non-perturbative effects in the nucleon structure, *e.g.*, color glass condensate [201]; see Fig. 2 in Ref. [190] for an example.

Table 2: Expected rates of neutrino-induced showers and measurement capability of the cross section and flux normalization in the radio component of IceCube-Gen2, after $T = 10$ years of exposure time, for the benchmark UHE diffuse neutrino fluxes used in this analysis; see Section 6.4. Possible flux types are: extrapolation to ultra-high energies (●), cosmogenic (■), source (◆), and cosmogenic + source (⬢). Measurement capabilities are expressed in terms of $f_\sigma \equiv \sigma/\sigma_{\rm std}$ for the cross section, and $f_\Phi \equiv \Phi_0/\Phi_{0,\rm std}$ for the flux normalization at a neutrino energy of 10^8 GeV. The real values are $f_\sigma = 1$ and $f_\Phi = 1$. Results are obtained using the baseline choices for the detector resolution: shower energy resolution of $\sigma_\epsilon = 0.1$, with $\epsilon \equiv \log_{10}(E_{\rm sh}^{\rm rec}/E_{\rm sh})$, and angular resolution of $\sigma_{\theta_z} = 2^\circ$; see Section 6.6.4 for details. The shower rates shown are all-sky, *i.e.*, summed over all values of reconstructed direction, $-1 \leq \cos\theta_z^{\rm rec} \leq 1$, and binned in a single bin of reconstructed shower energy, $10^7 \leq E_{\rm sh}^{\rm rec}/{\rm GeV} \leq 10^{10}$. However, all-sky rates are only referential, and in the statistical analysis used to infer the cross section and flux normalization, we use instead binned shower rates; see Section 6.7.4 for details. For the inferred cross section and flux normalization, we show the best-fit values and 68% credible intervals of their one-dimensional marginalized posteriors. The statistical procedure returns results for $\log_{10} f_\sigma$ and $\log_{10} f_\Phi$; we show the corresponding results in terms of f_σ and f_Φ to facilitate their interpretation.

#	Type	UHE ν flux model	All-sky shower rate (10 yr)	Inferred cross section		Inferred flux normalization	
				$\log_{10} f_\sigma$	f_σ	$\log_{10} f_\Phi$	f_Φ
1	●	IceCube HESE (7.5 yr) extrapolated [188]	0.73	$-0.39^{+1.12}_{-1.01}$	$0.41^{+4.96}_{-0.37}$	$-1.16^{+0.99}_{-1.04}$	$0.07^{+0.61}_{-0.07}$
2	●	IceCube ν_μ (9.5 yr) extrapolated [37]	26.90	$-0.07^{+0.54}_{-0.33}$	$0.85^{+2.10}_{-0.45}$	$+0.06^{+0.32}_{-0.53}$	$+1.15^{+1.25}_{-0.81}$
3	■	Heinze *et al.*, fit to Auger UHECRs [174]	0.71	$-1.75^{+2.23}_{-0.20}$	$0.02^{+3.70}_{-0.01}$	$-1.11^{+1.35}_{-1.07}$	$0.08^{+1.66}_{-0.07}$
4	■	Bergman & van Vliet, fit to TA UHECRs [193]	332.34	$-0.01^{+0.16}_{-0.13}$	$0.98^{+0.44}_{-0.25}$	$+0.01^{+0.12}_{-0.15}$	$1.02^{+0.33}_{-0.30}$
5	■	Rodrigues *et al.*, all AGN [179]	0.89	$-1.45^{+2.14}_{-0.16}$	$0.04^{+4.86}_{-0.01}$	$-1.15^{+1.19}_{-0.90}$	$0.07^{+1.02}_{-0.06}$
6	◆	Rodrigues *et al.*, all AGN [179]	107.16	$-0.01^{+0.18}_{-0.15}$	$0.98^{+0.50}_{-0.29}$	$+0.01^{+0.15}_{-0.18}$	$1.02^{+0.42}_{-0.35}$
7	■	Rodrigues *et al.*, HL BL Lacs [179]	24.24	$-0.09^{+0.75}_{-0.37}$	$0.81^{+3.76}_{-0.47}$	$+0.09^{+0.36}_{-0.74}$	$1.23^{+1.59}_{-1.01}$
8	⬢	Fang & Murase, cosmic-ray reservoirs [177]	57.41	$-0.04^{+0.36}_{-0.26}$	$0.91^{+1.18}_{-0.41}$	$+0.03^{+0.25}_{-0.33}$	$1.07^{+0.83}_{-0.57}$
9	◆	Fang *et al.*, newborn pulsars [175]	125.38	$-0.01^{+0.19}_{-0.16}$	$0.98^{+0.54}_{-0.30}$	$+0.01^{+0.17}_{-0.18}$	$1.02^{+0.49}_{-0.35}$
10	◆	Padovani *et al.*, BL Lacs [176]	57.85	$-0.01^{+0.24}_{-0.21}$	$0.98^{+0.72}_{-0.37}$	$+0.02^{+0.20}_{-0.25}$	$1.05^{+0.61}_{-0.46}$
11	⬢	Muzio *et al.*, max. extra p component [178]	56.55	$-0.04^{+0.39}_{-0.28}$	$0.91^{+1.33}_{-0.43}$	$+0.03^{+0.27}_{-0.38}$	$1.07^{+0.92}_{-0.62}$
12	⬢	Muzio *et al.*,fit to Auger & IceCube [180]	17.12	$-0.04^{+0.48}_{-0.36}$	$0.91^{+1.84}_{-0.51}$	$+0.05^{+0.32}_{-0.49}$	$1.12^{+1.22}_{-0.76}$

Figure 23 shows the expected improvement in the measurements over time, for selected medium-flux and high-flux benchmark models. In the most optimistic scenario, for flux model 4 (“Bergman & van Vliet, fit to TA UHECRs"), the 2.5-year uncertainty in the inferred value of the cross section, f_σ, of 75 %, is already comparable to the baseline 10-year uncertainty, of 35 %. The 20-year

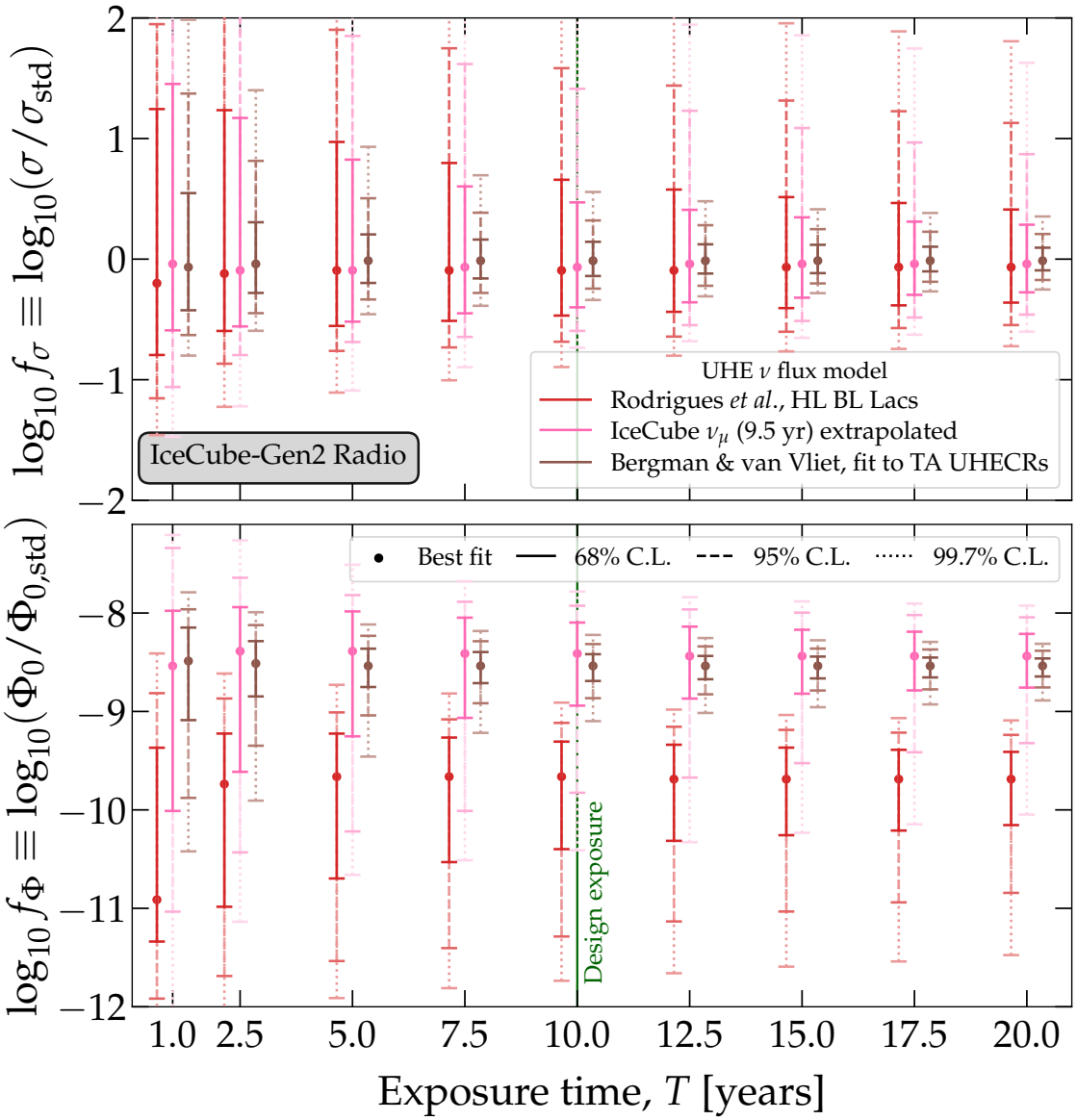

Figure 23: Evolution with exposure time of the precision in the forecast measurement of the UHE νN cross section (*top*) and the UHE neutrino flux normalization (*bottom*) in the radio component of IceCube-Gen2, for benchmark flux models 2, 4, and 7; see Fig. 8. See the main text for details.

uncertainty, of 22 %, is smaller than the BGR18 theory uncertainty shown in Fig. 4. Results for model 2 ("IceCube ν_μ flux (9.5 yr), extrapolated to UHE") are comparable. At short exposure times, increased exposure leads to drastic improvements in the measurement uncertainty because the measurement is dominated by statistical uncertainties. At long exposure times, improvements slow down, as the measurement becomes increasingly dominated by systematic uncertainties, *i.e.*, the energy and angular detector resolution and, to a lesser degree, the background of atmospheric muons.

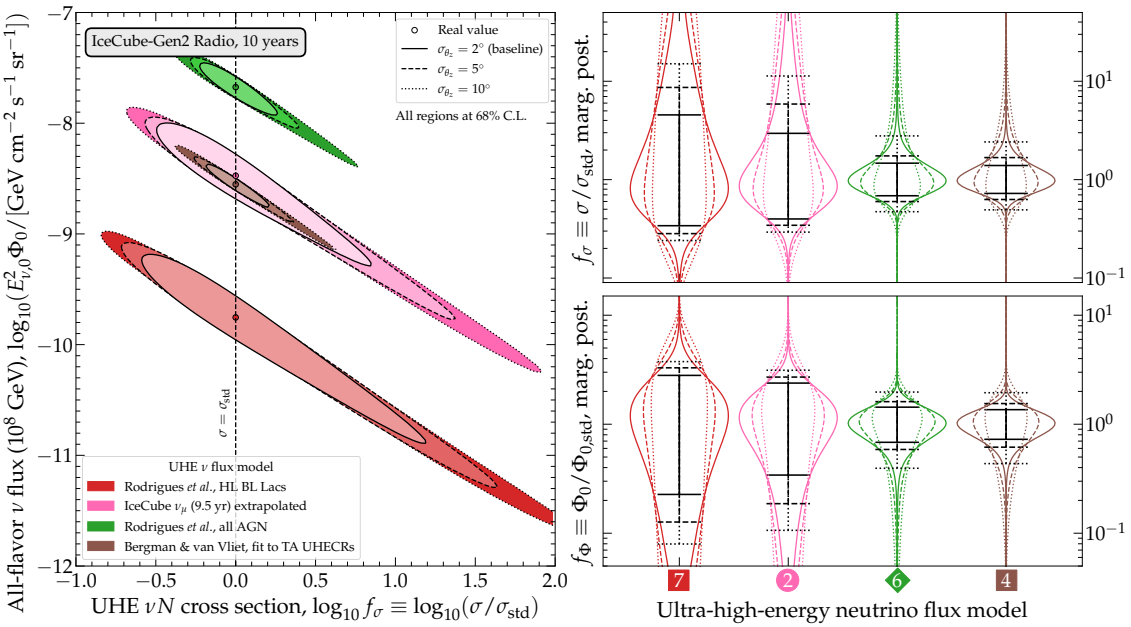

Figure 24: Impact of the detector angular resolution, σ_{θ_z}, on the measurement of the νN DIS cross section and flux normalization, for the benchmark UHE neutrino flux models 2, 4, 6, and 7; see Fig. 8. See Section 6.7.3 for details about the choice of binning.

Figure 24 shows that angular resolution, σ_{θ_z}, is key to making precise measurements of f_σ and f_Φ, especially in medium-flux models where the degeneracy between them is more resilient on account of a lower shower rate. A good angular resolution allows the detector to distinguish between similar arrival directions around the horizon, where the joint sensitivity to f_σ and f_Φ comes from; see Sections 6.6.4 and 6.7. In Fig. 24, we repeat our analysis, but for different choices of values of σ_{θ_z}. For each choice, we set the size of the angular bins used for horizontal and near-horizontal showers, with $\theta_z^{\rm rec} \in [80°, 100°]$, equal to σ_{θ_z}. Figure 24 shows, *e.g.*, for flux model 4 ("Bergman & van Vliet, fit to TA UHECRs"), that using a resolution of $\sigma_{\theta_z} = 5°$ yields $f_\sigma = 0.94^{+0.73}_{-0.31}$ and $f_\Phi = 1.06^{+0.49}_{-0.44}$, and using $\sigma_{\theta_z} = 10°$ yields $f_\sigma = 0.88^{+1.54}_{-0.38}$ and $f_\Phi = 1.14^{+1.28}_{-0.64}$, an increase of 50% and 178% in the uncertainty of f_σ and of 41% and 191% in the uncertainty of f_Φ, respectively, compared to the baseline results with $\sigma_{\theta_z} = 2°$ from Table 2. Results for other flux models change similarly.

6.9 FUTURE DIRECTIONS

When generating our forecasts above, we have used state-of-the-art predictions and dedicated simulations to describe the incoming UHE neutrino flux, its propagation through Earth, and its

detection in the radio component of IceCube-Gen2, and to jointly measure the cross section and flux normalization. Yet, there are potential improvements to be implemented in future, revised versions of our calculation. None of them represent a fundamental limitation of our present analysis. Below, we present possible future improvements, listed roughly in ascending order of implementation challenge, with the hope of sparking progress in various directions:

Raising the maximum neutrino energy in in-Earth propagation.— To compute the propagation of UHE neutrinos through the Earth, we have used NUPROPEARTH [209, 210], based on the state-of-the-art BGR18 νN DIS scattering cross section [194]; see Section 6.3.1 However, the version of NUPROPEARTH that we used was unable to propagate neutrinos beyond energies of 10^{10} GeV. Fortunately, for the majority of the benchmark flux models 1–12, the flux beyond 10^{10} GeV contributes marginally to the shower rate; see Fig. 8. Only for models 4 and 11 we expect that contribution to be slightly more sizeable. We recommend raising the maximum allowed neutrino energy in future versions of NUPROPEARTH.

Including the LPM effect in the relation between neutrino and shower energies.— The LPM effect is included in the NURADIOMC simulations of ν_e-induced CC showers and radio propagation that we use to generate the detector effective volume; see Section 6.6.4. However, the energy-dependent relevance of the LPM is not accounted for in the relation between neutrino energy, E_ν, and shower energy, $E_{\rm sh}$, Eq. (6.14), because a parametrization of it was not available at the time of writing. As a result, for ν_e-initiated CC showers, we have assumed that $E_{\rm sh} = E_\nu$ at all energies, whereas in reality the LPM should make $E_{\rm sh} < E_\nu$ at the highest energies. This may be improved in future work by building a suitable parametrization from dedicated simulations.

Including the contribution of secondary leptons in the effective volumes for ν_μ- and ν_τ-initiated CC showers.— When generating the effective volumes for ν_μ- and ν_τ-initiated CC showers, we have ignored the contribution of the radio emission coming from showers induced by the secondary charged leptons, *i.e.*, the final-state muons and tauons in the CC interactions, due to the additional computational expense involved in simulating them and in parametrizing the relation between neutrino to shower energy in the presence of secondary interactions; see Section 6.6.4. Reference [213] showed that they may enhance the shower rate by up to 25%, which makes our results above conservative. Their contribution may be included in future work via dedicated simulations.

Improving the modeling of the angular resolution.— To obtain our results, we assumed the same angular resolution for all detected showers; see Section 6.8. However, in reality, the angular resolution of a detected shower depends on its event quality, and on which detector component measured it, *i.e.*, only the shallow one, only the deep one, or multiple components in coincidence. With a better modelling of the expected experimental uncertainties, our analysis can be redone using different resolution functions depending on the event class. Further, we have only considered the resolution in zenith angle, not in azimuth angle; the latter might be relevant when analyzing real shower events, with definite celestial coordinates.

Using an unbinned likelihood analysis.— In our analysis above, we binned the expected IceCube-Gen2 showers in reconstructed shower energy and direction (see Section 6.7.3), and we used a binned likelihood function, Eq. (6.25), to infer the values of the νN cross section and the neutrino flux normalization. We chose the bin sizes to be no smaller than the detector energy and angular resolution. Yet, when inferring the cross section and flux normalization from actual future data detected by IceCube-Gen2, with each shower carrying its own energy and direction resolution, an unbinned likelihood would be preferable, in the style of IceCube TeV–PeV cross-section measurements in Refs. [61, 63]. Such unbinned prescription may also be used in forecasts of the cross-section measurement, with modifications of our above procedure.

Including the background of cosmic ray-induced showers.— Section 6.7.2 stated that the two main non-neutrino backgrounds in the radio array of IceCube-Gen2 are showers induced by atmospheric muons, which we account for in our analysis, and air-shower cores propagating into the ice, which we do not account for, since their rate is still largely unknown. Early estimates of this background put its rate anywhere between a handful and tens of showers per year, before the application of any cuts or of a surface veto that could mitigate them. If these estimates are accurate, and if vetoes do not mitigate the rate significantly, then they might render cross-section measurements in even medium-flux models unfeasible. Ongoing work should clarify the relevance of this background.

Including nuclear effects in the cross section.— To obtain our results, we have used the BGR18 cross section built using free-nucleon PDFs. However, the nucleons with which neutrinos interact are bound in heavy nuclei; this modifies the PDFs and, therefore, the νN DIS cross section. Reference [209] showed that using nuclear-corrected PDFs in in-Earth propagation could modify

the fraction of neutrinos that reach the detector by more than 50%, especially at high energies. This is comparable to or greater than the measurement precision that we have forecast; see, *e.g.*, 4. This should motivate future forecasts of UHE cross-section measurement to devote more attention to the effect of nuclear corrections.

Using flavor identification.— Figure 14 shows that the flavor ratios at the detector carry information about the νN cross section. For instance, comparing the tau-flavor ratio *vs.* the electron-flavor or muon-flavor ratios could give us information about the effect of the cross section on ν_τ regeneration. More generally, flavor ratios have the potential to explore a variety of new neutrino physics; see, *e.g.*, Refs. [190, 191, 267, 328–330]. Presently, however, flavor identification in neutrino radio-detection is still uncertain, though preliminary results on identifying showers from ν_μ and ν_τ CC interactions [213, 214] and from ν_e CC interactions [300] are promising. Even if flavor identification is not readily available in IceCube-Gen2, its all-flavor data could be combined with data collected by other planned neutrino telescopes that are predominantly sensitive to UHE ν_τ [82, 83], *i.e.*, AugerPrime [162], BEACON [153], EUSO-SPB [161], GRAND [72], POEMMA [74], PUEO [75], SKA [331], TAMBO [73], TAROGE-M [159], TAx4 [332], and Trinity [81, 333], in order to compute the tau-flavor ratio.

Looking for energy-dependent new physics in the cross section.— In our analysis above, we have looked for energy-independent modifications of the Standard Model νN DIS cross section. However, if there are beyond-the-Standard-Model contributions to the cross section, they may instead be energy-dependent and possibly even localized only within a narrow energy window. In particular, UHE neutrinos could allow us to probe new νN resonant interactions via new heavy mediators with masses up to, roughly, $(m_q/\text{GeV})^{0.5} \times 100$ TeV, where m_q is the mass of the quark involved in the interaction. Reference [192] explored the effect of new energy-dependent contributions to the νN cross section, and of resonant contributions to the neutrino-electron cross section, in the context of GRAND, POEMMA and Trinity. For IceCube-Gen2, attempting to explore energy-dependent modifications of the νN cross section within the same sophisticated end-to-end framework that we have developed above quickly escalates the complexity of the tasks involved, and is best left for future work.

Jointly measuring the νN cross section, flux normalization, and spectral shape.— In our analysis above, we forecast the joint measurement of the νN cross section and flux normalization, but kept the shape of the neutrino energy spectrum fixed to that of one of the benchmark flux models 1–12 taken from the literature; see Section 6.4. While this procedure provides us already with useful information about the capability to measure the cross section, ultimately we would also like the shape of the neutrino energy spectrum to be determined from data, rather than assumed. To do this, future studies could exploit the fact that the sensitivity to the cross section comes almost exclusively from showers around the horizon; see Fig. 21. This suggests that we may use the large number of downgoing, unattenuated showers to measure the shape of the neutrino energy spectrum.

6.10 SUMMARY AND OUTLOOK

Measuring the neutrino-nucleon (νN) cross section at ultra-high neutrino energies, above 100 PeV, offers novel insight into the deep structure of protons and neutrons, and sensitivity to potentially transformative new physics. Yet, it hinges on using ultra-high-energy (UHE) neutrinos of cosmic origin, long sought, but so far undiscovered. Fortunately, upcoming neutrino telescopes, currently under planning and testing, will have a realistic chance of discovering them in the next 10–20 years, even if their flux is low, as is expected. Accordingly, we have put forward the first detailed forecasts of the capabilities of IceCube-Gen2 [39], one of the leading upcoming neutrino telescopes, to measure the UHE νN cross section. We have endeavored to make our forecasts complete, robust, and realistic. Our results are encouraging.

The sensitivity to the UHE νN cross section stems from the strong directional dependence of the UHE neutrino flux that reaches the detector after propagating through Earth. Due to significant νN interactions underground, UHE neutrinos only reach the detector from above—where they undergo nearly no interactions before reaching the detector—and from directions around the horizon—where significant interactions imprint the νN cross section on the angular dependence of the flux. It is from these latter Earth-skimming neutrinos that the sensitivity to the UHE νN cross section comes from.

In our forecasts, we have used state-of-the-art ingredients at every stage. For the νN cross section, we adopted as a baseline the recent BGR18 deep-inelastic-scattering (DIS) calculation [194]. For the fluxes of UHE neutrinos, we explored a wide variety of predictions [37, 174–180, 188, 193], including extrapolations of the known IceCube TeV–PeV fluxes to ultra-high energies, cosmogenic neutrinos, neutrinos produced inside cosmic-ray sources, and self-consistent models of joint production of the latter two. We treat each neutrino species separately, ν_e, $\bar{\nu}_e$, ν_μ, $\bar{\nu}_\mu$, ν_τ, and $\bar{\nu}_\tau$. For the neutrino propagation through Earth, we compute νN DIS plus sub-dominant interactions, via NUPROPEARTH [209]. For detection, we focus on the radio-detection of neutrino-initiated showers. We use the same simulation tools as the IceCube-Gen2 Collaboration, NURADIOMC [211] and NURADIORECO [212], to simulate neutrino interactions in the detector, ensuing particle showers, emission of coherent radio signals—Askaryan radiation—its propagation in the Antarctic ice, and its detection in the radio stations. We account for the detector resolution in shower energy and direction, and for the background of showers from atmospheric muons.

To properly represent the significant uncertainty in the predicted neutrino flux, in our forecasts we have jointly extracted the cross section and the neutrino flux normalization. To do this, we used a Bayesian statistical approach that accounts for random fluctuations in the number of expected detected showers. We report results in terms of mean sensitivity, averaged over many random realizations of the predicted shower distributions.

We find that it may be possible to measure the UHE νN cross section to within 50% of the BGR18 prediction within 10 years of exposure of IceCube-Gen2, as long as at least a few tens of neutrino-induced showers are detected in this period; see Fig. 4. In the most optimistic case, we expect that comparable precision could be achieved within 5 years; see Fig. 23. By far, the largest systematic uncertainty in our forecasts comes from the UHE neutrino flux. Regardless, the level of precision that may be achieved is enough to test the standard prediction of the νN DIS cross section [194], to look for non-linear effects in the nucleon structure [195–198], color-glass condensates [199], and sphalerons [200], and to identify deviations introduced by a host of new-physics models [192, 204–208].

Our forecasts are comprehensive, but we have identified areas where further work is needed. Most pressing are estimating the effect of the background of showers induced by cosmic rays,

improved modelling of reconstruction uncertainties based on individual event quality, and extending our analysis to let both the neutrino flux normalization *and* the shape of the neutrino energy spectrum be inferred from data. Thanks to the flexibility of our calculation framework, these improvements can be easily incorporated. Work in these directions is ongoing.

We provide our forecasts in the hope of informing the design choices of IceCube-Gen2 and other upcoming neutrino telescopes. Ultimately, we hope that detailed forecasts like ours provide guidance to tap into their full potential for fundamental-physics research.

6.11 CRITICAL OUTLOOK

In this section, we delve into the critical aspects of our research, presenting both an overview of our main findings and the limitations we have encountered, along with future perspectives for improvement. The main text of the published research paper already includes similar discussions in Sections 6.9 and 6.10. In this section we summarize those discussions and focus on a critical view of the results from a state-of-the-art perspective and how this has been updated since the results were first published.

6.11.1 *Overview and main findings*

Our research has utilized leading-edge predictions and dedicated simulations to elucidate the characteristics of ultra-high-energy (UHE) neutrinos, specifically those in the 100 PeV–10 EeV energy range. We have comprehensively accounted for UHE neutrino flux uncertainty, described its propagation through Earth, and its detection in UHE neutrino telescopes, in particular, the radio component of IceCube-Gen2. Ultimately, we report the first forecast of joint measurements of the cross section and flux normalization at ultra-high energies. Our findings showcase significant progress in several key areas:

- We used state-of-the-art tools to model the UHE neutrino interaction with matter inside Earth, providing crucial insights into the perspectives of the first observation of an UHE neutrino.

Additionally, we have explore the effect of the Earth in the neutrino flux attenuation for cross section values that deviate from that of the Standard Model prediction.

- Our work lays the foundation for measuring the νN cross section at ultra-high energies, offering the potential to validate the standard predictions and explore new physics. Furthermore, it provides a reference for quantifying the potential of a future neutrino telescope in terms physical observables, such as the neutrino-nucleon cross section.

- We have developed a Bayesian statistical approach that accounts for the uncertainties in the predicted atmospheric background content and which averages over multiple realizations of the observed signal shower distribution, enhancing the robustness of our results.

6.11.2 *Limitations and future perspectives*

While our work has yielded promising results, it is important to acknowledge its limitations and outline future directions for improvement. We summarize the directions pointed out in more detail in Section 6.9 and refer to recent developments in those directions when available:

1. *Raising the maximum neutrino energy:* We recommend increasing the maximum allowed neutrino energy in future versions of NUPROPEARTH to expand our understanding of UHE neutrinos beyond 10^{10} GeV.

2. *Incorporating LPM effect:* Future work should incorporate the Landau-Pomeranchuk-Migdal (LPM) effect into the relationship between neutrino and shower energies to provide a more accurate representation, especially at the highest energies. A recent study has exploited deep neutral networks to account for the impact of the LPM effect in the shower development for electron neutrino CC interactions [334].

3. *Secondary leptons:* The contribution of secondary charged leptons in effective volumes for ν_μ and ν_τ initiated CC showers should be included in future simulations to refine our results. A recent work focused on the Askaryan Radio Array showed that these secondaries could make up to 30% of the total number of events in a radio-based UHE neutrino detector [335].

4. *Improved angular resolution:* Enhancing the modeling of angular resolution, considering event quality and azimuth angle, can lead to more precise measurements.

5. *Unbinned likelihood analysis:* Transitioning to an unbinned likelihood analysis for cross-section measurements, similar to IceCube TeV–PeV cross-section measurements, can provide better insights. This limitation was later addressed in Ref. [336], and discussed in Ch. 8 of this thesis, by implementing an unbinned analysis framework. This paves the road for a future implementation of an event-by-event angular and energy resolution, eventually solving the issue pointed out in the previous item.

6. *Cosmic ray-induced showers:* Addressing the background of cosmic ray-induced showers, particularly air-shower cores propagating into the ice, is crucial for more accurate cross-section measurements. Recent progress has been achieved on improving the characterization of the radio signal triggered by developing cosmic ray initiated showers in in-ice Askaryan radio detectors [337].

7. *Nuclear effects in cross section:* Future studies should explore the impact of nuclear effects on the νN cross section to account for modifications in neutrino detection.

8. *Flavor identification:* Efforts to improve flavor identification in neutrino radio-detection and combining data from different neutrino telescopes can advance our understanding of UHE neutrinos.

9. *Energy-dependent new physics:* Exploring energy-dependent modifications of the νN cross section and potential resonant interactions can provide insights into new physics. In Ref. [336] we came closer to explore energy-dependent effects by inferring the νN cross section in three different energy bins, one for each energy decade between 10^7 and 10^{10} GeV.

10. *Jointly measuring cross section, flux, and spectral shape:* Future research should aim to simultaneously measure the νN cross section, flux normalization, and spectral shape to refine our understanding of UHE neutrinos. This was the central problem addressed in Ref. [336]. We found that such measurement is possible modeling the neutrino flux with a piecewise cubic hermite interpolating polynomial or with a piecewise analysis, see Ch. 8 for more details.

In addition to the limitations and future opportunities for improvement pointed out in the manuscript, the nominal configuration of radio stations for IceCube-Gen2 has been updated since the publication of this work [338]. The latest design has a similar total effective volume, and the validity of the results in our work is preserved. Furthermore, the computational and statistical methods developed in this work can be adapted to new configurations of the radio component of IceCube-Gen2, or in general any UHE neutrino telescope (see Fig. 22). The updated detector configuration might not be final and improvements are constantly being implemented as we improve our understanding of in-ice Askaryan neutrino detection. For that purpose, detailed research works as the ones presented in this thesis are used as reference.

In summary, our research has paved the way for significant advancements in the study of UHE neutrinos and the measurement of the νN cross section at a new energy frontier. Despite the challenges and limitations, the prospects for exploring new physics and refining our knowledge in this field are promising. Further work in the outlined directions will continue to expand our understanding of astroparticle physics.

7

UHE NEUTRINO FLUX DISCOVERY POTENTIAL

Based on: **Víctor B. Valera Baca**, Mauricio Bustamante, Christian Glaser, *Near-future discovery of the diffuse flux of ultra-high-energy cosmic neutrinos*, Phys. Rev. D 107, 043019, arXiv:2210.03756

ABSTRACT Ultra-high-energy (UHE) neutrinos, with EeV-scale energies, carry with them unique insight into fundamental open questions in astrophysics and particle physics. For fifty years, they have evaded discovery, but maybe not for much longer, thanks to new UHE neutrino telescopes, presently under development. We capitalize on this upcoming opportunity by producing state-of-the-art forecasts of the discovery of a diffuse flux of UHE neutrinos in the next 10–20 years. By design, our forecasts are anchored in often-overlooked nuance from theory and experiment; we gear them to the radio array of the planned IceCube-Gen2 detector. We find encouraging prospects: even under conservative analysis choices, most benchmark UHE neutrino flux models from the literature may be discovered within 10 years of detector exposure—many sooner—and may be distinguished from each other. Our results validate the transformative potential of next-generation UHE neutrino telescopes.

7.1 INTRODUCTION

Ultra-high-energy (UHE) neutrinos, with energies in the EeV scale (1 EeV $\equiv 10^{18}$ eV), were first predicted in the late 1960s [65], as a natural consequence [27, 28] of the interaction of UHE cosmic rays (UHECRs), with comparable energies, and cosmological photon fields, like the cosmic microwave background. They are the most energetic neutrinos expected to be produced from standard particle processes, at least 10–100 times more energetic than the TeV–PeV neutrinos discovered by the IceCube neutrino telescope [34, 35, 37, 184–186, 188] (there may be higher-energy

neutrinos made in exotic processes [29, 339–341], but we do not consider them). UHE neutrinos provide unique insight into long-standing open problems in astrophysics—what are the most energetic astrophysical sources in the Universe—and particle physics—how do neutrinos, in particular, and fundamental physics, in general, behave at the highest energies [82, 83, 125, 187, 189–191, 216, 342, 343]. Yet, despite efforts, they remain undiscovered; however, maybe not for much longer.

Over the last fifty years, UHE neutrinos have received considerable attention from experiment and theory. Progress, while steady, has been challenging: past and present experiments have placed upper limits on their flux [66–69, 150], but even the tightest present-day limits [66, 67] leave vast swathes of the space of UHE neutrino flux models unconstrained; see Fig. 26. On the experimental front, the main challenge is that the flux of UHE neutrinos is possibly tiny [344, 345]. This motivates the need to build larger neutrino telescopes and explore more suitable detection strategies [83]. On the theory front, the main challenge is that predictions of the UHE neutrino flux are uncertain because they depend on properties of UHECRs and their sources, which are known only uncertainly, such as the evolution with redshift of the source number density, the UHECR mass composition, the UHECR acceleration mechanism, including the maximum cosmic-ray energies achievable, and the neutrino production mechanism, among others; for details, see, *e.g.*, Refs. [171–174, 255]. This motivates the need to consider a host of competing, representative flux predictions [174–180, 193]. We tackle both challenges.

Upcoming UHE neutrino telescopes, presently in different stages of planning, design, and prototyping, and built around different detection strategies, will have a real chance of discovering UHE neutrinos in the next 10–20 years, *even if their flux is low* [83, 216, 343]. We carve out this opportunity by providing the most detailed forecasts, to our knowledge, of the prospects of discovering a diffuse flux of UHE neutrinos. Our results, even under conservative analysis choices, are encouraging.

To include realistic experimental nuance, we gear our forecasts to the radio array of IceCube-Gen2 [39] ("IceCube-Gen2 Radio" in our figures), the planned high-energy upgrade of IceCube, whose target UHE neutrino flux sensitivity is among the best [83]. The array will instrument Antarctic ice with radio antennas that look for radio signals emitted by showers induced by UHE

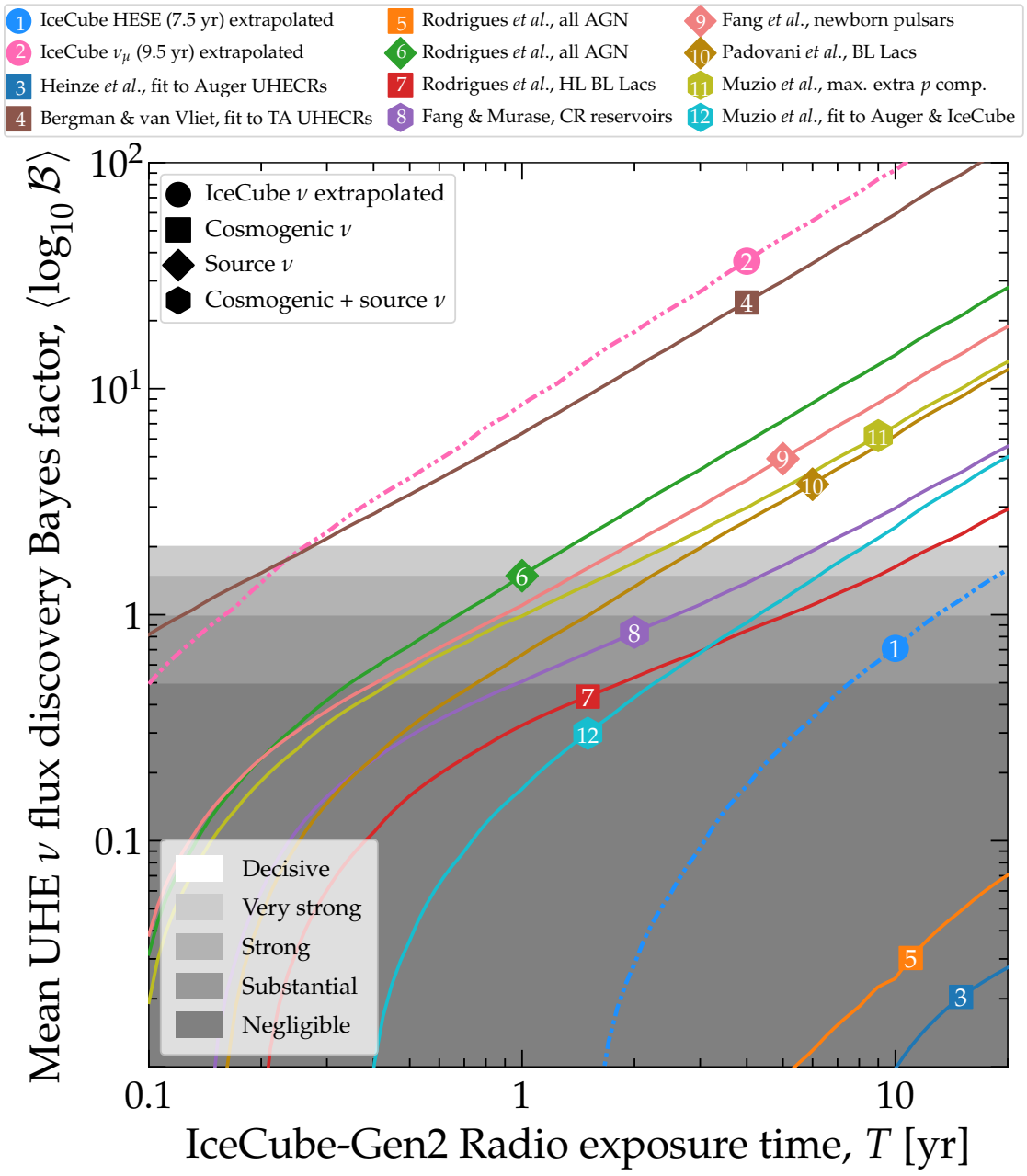

Figure 25: Discovery potential of benchmark diffuse ultra-high-energy (UHE) neutrino flux models 1–12 [37, 174–180, 188, 193] (Fig. 26) in the radio array of IceCube-Gen2. The background to discovery consists of atmospheric muons [77, 213], for all models, plus the tentative UHE tail of the IceCube 9.5-year through-going ν_μ flux [37], for models 3–12; see Section 7.4.5. All analysis choices are baseline and conservative; see Table 4 and Section 7.5.2.1. *Decisive discovery may be achievable for most flux models after only a handful of years.* See the main text, especially Sections 7.5.1 and 7.5.2.2, for details.

neutrinos [165, 166, 304], a technique tested by ARA [68] and ARIANNA [69] (and by ANITA [150], from the air). RNO-G [84], currently under deployment, will serve as a pathfinder for the radio array of IceCube-Gen2. To make our forecasts comprehensive, we consider a large number of benchmark UHE neutrino flux models that span the full allowed space of models, in size and shape, from optimistic to pessimistic [37, 174–180, 188, 193].

To produce our forecasts, we adopt the same flow of calculations as Ref. [346]. For each UHE neutrino flux model, we propagate it through the Earth, computing neutrino interactions with matter along the way, and model its detection in the radio array of IceCube-Gen2. We use the same state-of-the-art ingredients at every stage of the calculation as Ref. [346]: in the choice of diffuse UHE neutrino flux models (Section 7.2), the UHE neutrino-nucleon cross section, the propagation of neutrinos through the Earth (Section 7.3), the neutrino detection, including the emission, propagation, and detection of radio signals in ice, and the neutrino and non-neutrino backgrounds (Section 7.4). See Section II of Ref. [346] for an overview. Further, our forecasts account for random statistical fluctuations in the predicted event rates (Sections 7.5 and 7.6). Below, we expand on all of the above.

Figure 25 shows our main results: the discovery prospects of the benchmark UHE neutrino flux models, computed under our baseline analysis choices, chosen to be largely conservative. Because our statistical analysis is Bayesian, we report the flux discovery potential—and, later, the potential to tell apart different flux models—via Bayes factors. Figure 25 reveals encouraging prospects: *conservatively, most benchmark UHE neutrino flux models may be discovered after only a handful of years*. Later, we show that less conservative analysis choices, still well-motivated, lead to even better prospects.

The overarching goal of our detailed forecasts is to help map the potential science reach that upcoming UHE neutrino telescopes will usher in in the next 10–20 years. We make our forecasts realistic by factoring in nuance, from experiment and theory, that is often considered only partially, or not at all. We present our methods in considerable detail so that they can be readily adapted to produce forecasts for other upcoming UHE neutrino telescopes. We hope that they help to assess and compare the complementary capabilities of competing designs.

This paper is organized as follows. Section 7.2 presents the benchmark diffuse UHE neutrino flux models that we use in our forecasts. Section 7.3 sketches the effects of neutrino propagation inside Earth on them. Section 7.4 introduces the method that we use to compute neutrino-induced event rates and the backgrounds that we consider. Section 7.5 contains forecasts of the discovery potential of the benchmark flux models. Section 7.6 contains forecasts of the separation between different

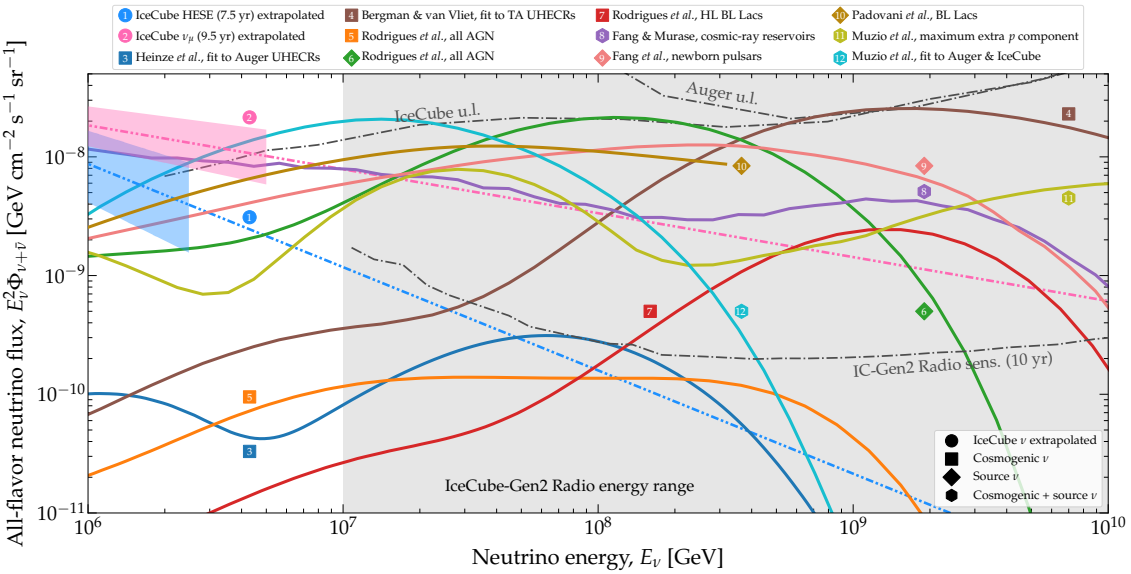

Figure 26: Benchmark diffuse ultra-high-energy neutrino flux models [37, 174–180, 188, 193] used here to assess the flux discovery capabilities of the radio array of IceCube-Gen2 [39] ("IceCube-Gen2 Radio"). These flux models are representative of the breadth of theoretical predictions in the literature. The upper limits on the flux are from IceCube [66] and the Pierre Auger Observatory [67]. The shaded region indicates the approximate neutrino energy range to which the radio array of IceCube-Gen2 will be sensitive. In this figure, fluxes are all-flavor, *i.e.*, summed over all neutrino flavors, but our analysis treats individually the flux of each neutrino species, ν_e, ν_μ, ν_τ, $\bar{\nu}_e$, $\bar{\nu}_\mu$, and $\bar{\nu}_\tau$. See Fig. 6 in Ref. [346] for a breakdown of the flux of each neutrino species for each flux model. See Section 7.2 for details.

benchmark flux models. Section 7.7 outlines possible directions for future work. Section 7.8 summarizes and concludes.

7.2 ULTRA-HIGH-ENERGY NEUTRINOS

Ultra-high-energy neutrinos [27], with energies above 100 PeV, are expected to be produced in the interaction of UHECRs [28, 65], with energies up to 10^{12} GeV, with matter and radiation, inside the UHECR sources (*source* neutrinos), outside them and en route to Earth (*cosmogenic* neutrinos), or both. See Ref. [83] for a review.

The interaction of UHECR protons on matter (pp) and radiation ($p\gamma$) produces a short-lived $\Delta(1232)$ resonance that decays into charged pions. Upon decaying, they produce high-energy neutrinos, via $\pi^+ \to \mu^+ + \nu_\mu$, followed by $\mu^+ \to e^+ + \nu_e + \bar{\nu}_\mu$, and their charge-conjugated processes. Each final-state neutrino carries, on average, 5% of the energy of the parent proton. En route to Earth, neutrino oscillations change the flavor composition of the flux, *i.e.*, the relative

content of ν_e, ν_μ, and ν_τ in it. (Our benchmark UHE neutrino flux models below account for this change; more on this later.)

In realistic neutrino production models, including in some of our benchmark UHE neutrino flux models below, different production channels become accessible or dominant at different energies. In $p\gamma$ interactions, neutrino production occurs via resonances heavier than $\Delta(1232)$ at intermediate energies, and via multi-pion production at high energies [256–258]. In pp interactions, the pion multiplicity changes with energy and affects the neutrino yield [130]. The physical conditions inside the sources may affect neutrino production, too. For instance, neutrino energies might be damped by strong magnetic fields that cool intermediate charged particles—protons, pions, muons—via synchrotron radiation [104, 133, 259, 260], or by UHECR interactions in dense source environments [262, 263].

For UHE neutrinos produced in pp interactions, their energy spectrum is a power law that follows the power-law spectrum of the parent protons, and that may extend to low neutrino energies [177]. For UHE neutrinos produced in $p\gamma$ interactions, their energy spectrum is determined by the spectra of the parent protons and photons. Because the photon spectrum is typically peaked around a characteristic energy, the resulting neutrino energy spectrum is also peaked, at an energy set by the energy requirements to produce a Δ resonance.

Figure 26 shows the energy spectra of the benchmark UHE neutrino flux models 1–12 [37, 174–180, 188, 193] that we use in our forecasts below. They span predictions from optimistic to pessimistic. The wide variety in their size and shape is indicative of the present-day spread of the flux predictions available in the literature, and reflects large extant uncertainties in the properties of UHECRs and of their sources [29, 125]. The benchmark flux models in Fig. 26 are the same ones that Ref. [346] used to forecast the measurement of the UHE neutrino-nucleon cross section. Below, we only sketch the main features of the models; we defer to Ref. [346] for a detailed overview, and to the original Refs. [37, 174–180, 188, 193] for full details.

Our benchmark UHE neutrino flux models are grouped in four classes, depending on the origin of the flux:

(a) **UHE extrapolation of the IceCube neutrino flux ("IceCube ν extrapolated", ● models 1 and 2):** These are unbroken extrapolations to ultra-high-energies of the power-law ($\propto E_\nu^{-\gamma}$) neutrino flux measured by IceCube in the TeV–PeV range.

Flux model 1 ("IceCube HESE (7.5 yr) extrapolated") extrapolates the soft-spectrum flux ($\gamma = 2.87$) of the IceCube 7.5-year HESE analysis [188].

Flux model 2 ("IceCube ν_μ (9.5 yr) extrapolated") extrapolates the hard-spectrum flux ($\gamma = 2.37$) of the IceCube 9.5-year through-going ν_μ analysis [37].

[In our forecasts below, we consider flux models 1 or 2, augmented with a high-energy cut-off (Section 7.4.5.2), as a background to the discovery of the other flux models, 3–12; see Section 7.5.1. Section 7.5.2.9 forecasts the discovery of flux models 1 and 2 themselves.]

(b) **Models of cosmogenic neutrinos ("Cosmogenic ν", ■ models 3–5, 7):** These are models of cosmogenic neutrinos made either by a population of nondescript sources of UHECRs, or by known classes of potential UHECRs sources.

Flux model 3 [174] ("Heinze *al.*, fit to Auger UHECRs") considers UHECRs produced by nondescript sources, and fits their flux and mass composition to recent UHECR observations by the Pierre Auger Observatory [275, 276]. (References [172, 173] predict similar fluxes using similar procedures and data.)

Flux model 4 [193]) ("Bergman & van Vliet, fit to TA UHECRs") is produced similarly to flux model 3, but using instead recent UHECR observations by the Telescope Array (TA) [278, 279]. (Reference [280] predicts a similar flux.) Flux model 3 is significantly smaller than flux model 4 because Auger observations favor a heavier UHECR mass composition at the highest energies, and because the fit of the UHECR spectrum to Auger data favors a lower cosmic-ray maximum rigidity [172–174] than the fit to TA data.

Flux model 5 [179] ("Rodrigues *et al.*, all AGN") is the cosmogenic neutrino flux expected from the full population of active galactic nuclei (AGN), which are taken to be UHECR accelerators, including low- and high-luminosity BL Lacs and flat-spectrum radio quasars. The resulting UHECR flux is fit to Auger data [275], and the associated cosmogenic neutrino flux satisfies the

IceCube upper limit on the UHE neutrino flux [66]. We adopt the maximum allowed predicted cosmogenic neutrino flux from the entire AGN population (Fig. 2 in Ref. [179]).

Flux model 7 [179] ("Rodrigues *et al.*, HL BL Lacs") isolates the contribution of high-luminosity (HL) BL Lacs to the cosmogenic neutrino flux of model 5.

(c) **Models of UHE neutrinos made inside astrophysical sources ("Source ν", ◆ models 6, 9, 10):** These are models based on more detailed descriptions of the physical properties of known UHECR and neutrino source classes.

Flux model 6 [179] ("Rodrigues *et al.*, all AGN") is the counterpart source neutrino flux to the cosmogenic flux model 5. We adopt the maximum allowed predicted source neutrino flux from the entire AGN population (Fig. 2 in Ref. [179]).

Flux model 9 [175] ("Fang *et al.*, newborn pulsars") is the neutrino flux predicted from newborn, fast-spinning pulsars with intense surface magnetic fields that may accelerate UHECRs in the pulsar wind. UHECR pp interactions on the surrounding supernova ejecta produce neutrinos. We adopt the flux prediction from Ref. [175] for which the number density of pulsars evolves with redshift following the star formation rate. (We include only the contribution of neutrinos made inside the pulsar environment.)

Flux model 10 [176] ("Padovani *et al.*, BL Lacs") is the neutrino flux produced by $p\gamma$ interactions inside the jets of BL Lacs, computed within the framework of the simplified view of blazars. Following Ref. [291], the ratio of the neutrino intensity to the gamma-ray intensity, a key parameter of the model [176], is set to $Y_{\nu\gamma} = 0.13$ to satisfy the present IceCube upper limit on the UHE neutrino flux [66].

(d) **Models of joint cosmogenic and UHE source neutrinos ("Cosmogenic + source ν", ⬢ models 8, 11, 12):** These are multi-messenger models that aim to explain the joint production of UHECRs and TeV–EeV neutrinos.

Flux model 8 [177] ("Fang & Murase, cosmic-ray reservoirs") is the flux of UHE neutrinos produced, via pp and $p\gamma$ interactions, by UHECRs accelerated in the jets of radio-loud AGN embedded in galaxy clusters that act as cosmic-ray reservoirs, within a grand-unified multi-

messenger model. The predicted UHECR flux and mass composition are fit to Auger data [288] and the predicted TeV–PeV neutrino flux, to IceCube data [186, 289].

Flux model 11 [178] ("Muzio *et al.*, maximum extra p component") is the neutrino flux produced in $p\gamma$ interactions within the UFA15 multi-messenger framework [292], where the UHECR flux and mass composition are fit to Auger data. The model includes a sub-dominant UHECR pure-proton component beyond 10^9 GeV that enhances the UHE neutrino flux. We adopt the maximum allowed neutrino flux from the joint single-mass UFA15 plus pure-proton components, computed using the SYBILL 2.3C [293] hadronic interaction model (Fig. 9 in Ref. [178]).

Flux model 12 [180] ("Muzio *et al.*, fit to Auger & IceCube") is the neutrino flux produced in $p\gamma$ interactions within the UFA15 multi-messenger framework, and in pp interactions of UHECRs in the source environment. The UHECR flux and mass composition are fit to Auger data, and the neutrino flux is fit to the IceCube TeV–PeV neutrino flux [243, 294]. We adopt the best-fit total neutrino flux, "UHECR ν" plus "Non-UHECR ν", from Fig. 1 in Ref. [180]).

In each UHE neutrino flux model above, we treat individually the flux of each neutrino species, ν_e, ν_μ, ν_τ, $\bar{\nu}_e$, $\bar{\nu}_\mu$, $\bar{\nu}_\tau$. To compute the flavor composition at Earth, after oscillations, we follow the same detailed prescription as in Ref. [346], based on recent values of the neutrino mixing parameters from the NUFIT 5.0 [268, 269] global fit to neutrino oscillation data. See Section 7.4.5.2 for a sketch of our prescription (in the particular context of flux models 1 and 2 as background fluxes) and Ref. [346] for full details of the flavor composition of each flux model. We maintain the individual treatment of the flux of each neutrino species during their propagation through the Earth (Section 7.3) and when computing their contribution to the predicted event rate (Section 7.4). However, we conservatively assume no capability to distinguish events made by different flavors in the radio array of IceCube-Gen2.

7.3 PROPAGATING NEUTRINOS THROUGH EARTH

Once UHE neutrinos arrive at the surface of the Earth, they propagate underground toward the detector, from all directions. Because the neutrino-matter cross section grows with energy (see

below), for UHE neutrinos interactions with matter underground are significant, and attenuate the flux of neutrinos that reaches the detector. The attenuation is energy- and direction-dependent: the higher the energy and the longer the distance traveled by a flux of neutrinos inside the Earth, the stronger it is attenuated. The attenuation is also flavor-dependent: ν_τ are relatively less affected compared to ν_e and ν_μ. In our forecasts, we account in detail for the in-Earth propagation of UHE neutrinos from the surface of the Earth to the radio array of IceCube-Gen2. Below, we elaborate.

At neutrino energies above a few GeV, the leading neutrino interaction channel is neutrino-nucleon (νN) deep inelastic scattering (DIS) [217, 218, 220]. In it, a neutrino scatters off of one of the partons, *i.e.*, a quark or a gluon, inside a nucleon, N, *i.e.*, a proton or a neutron. The final-state parton promptly hadronizes into final-state hadrons, X. A neutral-current (NC) DIS interaction, mediated by a Z boson, produces in addition a final-state neutrino, *i.e.*, $\nu_\alpha + N \to \nu_\alpha + X$ ($\alpha = e, \mu, \tau$). A charged-current (CC) DIS interaction, mediated by a W boson, produces in addition instead a final-state charged lepton, *i.e.*, $\nu_\alpha + N \to l_\alpha + X$. The νN DIS cross section has been measured at sub-TeV neutrino energies by a variety of accelerator neutrino experiments [42–59]; in the few-TeV range, by FASER [347] (and the upcoming FASERν [183]), and in the TeV–PeV range, using IceCube data [60, 61, 63]. At higher energies, the cross section is predicted [134, 194, 203, 205, 221, 225–229] and may be measured in upcoming UHE neutrino telescopes [192, 215, 346, 348].

Computing the UHE νN DIS cross section requires knowing the parton distribution functions in protons and neutrons, which are measured in lepton-hadron collisions, and extrapolating them beyond the regime where they have been measured. (Concretely, it requires extrapolating them to values of Bjorken-x—the fraction of nucleon momentum carried by the interacting parton—beyond the measured ones.) At ultra-high energies, the NC and CC νN cross sections, $\sigma^{\rm NC}_{\nu N}$ and $\sigma^{\rm CC}_{\nu N}$, respectively, grow roughly $\propto E_\nu^{0.36}$ [134], are essentially equal for all flavors of ν_α and $\bar{\nu}_\alpha$, and $\sigma^{\rm NC}_{\nu N} \approx \sigma^{\rm CC}_{\nu N}/3$. Below, to produce our forecasts, we adopt the state-of-the-art BGR18 calculation of the νN DIS cross sections [194] in the propagation and detection of neutrinos. The BGR18 is built using recent experimental results and sophisticated next-to-leading-order calculations, including the major corrections described in Appendix B4 of Ref. [194]; for details, see Ref. [194] andRef. [236], for a summary, see Ref. [346].

In a DIS interaction, the final-state hadrons receive a fraction y—the inelasticity—of the neutrino energy, and the final-state lepton receives the remaining fraction $(1-y)$. In each interaction, the value of y is randomly sampled from a probability density that is proportional to the differential DIS cross sections, $d\sigma_{\nu N}^{\rm NC}/dy$ and $d\sigma_{\nu N}^{\rm CC}/dy$. At the energies relevant for our work, the average value of y is about 0.25 [221]. However, because the distribution of values of y has a large spread (see Fig. 4 in Ref. [346]), when propagating neutrinos through the Earth below (and also when computing the event rates that they induce, in Section 7.4.4), we do it by using the distributions of y, separately for NC and CC DIS, rather than by using its average value.

Inside the Earth, NC interactions shift the UHE neutrino flux to lower energies, by regenerating lower-energy neutrinos, while CC interactions dampen the flux altogether, by replacing neutrinos with charged leptons. The one exception is the CC interaction of ν_τ: in them, the final-state tauon may propagate for some distance inside the Earth before decaying and generating a new, high-energy ν_τ. As a result of this "ν_τ regeneration," the flux of ν_τ is less attenuated than that of ν_e and ν_μ.

The severity of the effects of in-Earth propagation on the neutrino flux varies with neutrino energy, E_ν, and direction, expressed via the zenith angle, θ_z, measured from the South Pole, where IceCube-Gen2 will be located. Higher energies and directions corresponding to longer path lengths inside the Earth yield more severe effects. To illustrate this, we use a simplified calculation of the number of neutrino-induced events in the detector, $N_\nu^{\rm simp}$, similar to the one in Ref. [61], *i.e.*,

$$N_\nu^{\rm simp}(E_\nu,\theta_z) \propto \Phi_\nu(E_\nu)\sigma_{\nu N}(E_\nu)e^{-L(\theta_z)/L_{\nu N}(E_\nu,\theta_z)}\,, \tag{7.1}$$

where Φ_ν is the neutrino flux at the surface of the Earth, $\sigma_{\nu N}$ is the νN cross section (for this simplified calculation, it is the sum of NC and CC cross sections), $L(\theta_z)$, defined as,

$$L(\theta_z) = \sqrt{\left(R_\oplus^2 - 2R_\oplus d\right)\cos^2\theta_z + 2R_\oplus d} - (R_\oplus - d)\cos\theta_z, \tag{7.2}$$

is the distance traveled inside the Earth by a neutrino with incoming direction θ_z, where $R_\oplus = 6371$ km is the radius of Earth, d is the detector depth, approximately 200 m for the radio array of IceCube-Gen2, $L_{\nu N} \equiv (\sigma_{\nu N} n_N)^{-1}$ is the neutrino mean free path inside the Earth along this direction, and n_N is the average number density of nucleons along this direction, based on knowledge of the internal matter density of Earth (more on this later). (We use Eq. (7.1) only for illustration; later we describe the detailed calculation with which we produce our results.)

Equation (7.1) accounts for flux attenuation during in-Earth propagation, via the exponential dampening term, but ignores the regeneration of lower-energy neutrinos. Even so, it embodies essential features of the propagation and detection of high-energy and ultra-high-energy neutrinos. Upgoing neutrinos ($\cos\theta_z < 0$), *i.e.*, neutrinos that reach the detector from below after traveling underground a distance of up to the diameter of the Earth, are more strongly attenuated than downgoing ($\cos\theta_z > 0$) and horizontal neutrinos ($\cos\theta_z \approx 0$). For UHE neutrinos, the attenuation is so strong that virtually no upgoing neutrinos reach the detector (see Fig. A2 in Ref. [61]), unless the neutrino flux at the surface is extraordinarily large; *e.g.*, benchmark flux model 4 in Figs. 26, 27, and 28. This means that our forecasts below, which factor in the contribution of neutrinos from all directions, are driven primarily by downgoing and horizontal neutrinos.

Further, Eq. (7.1) shows that while flux attenuation is $\propto e^{-\sigma_{\nu N}}$, the rate of neutrino interactions in the detector is $\propto \sigma_{\nu N}$. The interplay between these competing effects is accentuated at high energies, where the cross section is larger: a larger cross section makes the already tiny flux of upgoing neutrinos vanish, which has little marginal effect, but it appreciably increases the number of downgoing and horizontal neutrinos detected.

Finally, Eq. (7.1) reveals important nuance in the rate of neutrino interactions, which is $\propto \Phi_\nu \sigma_{\nu N}$. In a realistic setting, given that neither the UHE neutrino flux nor the UHE νN cross section have been measured so far, or that they are known only uncertainly at best, the detection of a number of neutrinos $N_\nu^{\rm simp}$ implies a degeneracy between Φ_ν and $\sigma_{\nu N}$ [205, 244–247]. Reference [346] accounted for the uncertainty on Φ_ν and $\sigma_{\nu N}$ when forecasting the potential of IceCube-Gen2 to measure the UHE νN cross section. Here, we account for the uncertainty on the UHE νN cross section when forecasting the potential of IceCube-Gen2 to discover benchmark UHE neutrino flux models 1–12, and to distinguish between them. As in Ref. [346], we do so via the energy-independent scaling parameter $f_\sigma \equiv \sigma_{\nu N}/\sigma_{\nu N}^{\rm std}$, where $\sigma_{\nu N}^{\rm std}$ is the central BGR18 prediction [194]. The nominal value is $f_\sigma = 1$, and the value of f_σ is common to the NC and CC cross sections. Values of $f_\sigma \neq 1$ scale the central BGR18 cross section up or down, but do not affect its energy dependence.

The effect of changing f_σ on the flux attenuation is most evident in neutrinos that reach the detector from around the horizon, *i.e.*, $80^\circ \lesssim \theta_z \lesssim 120^\circ$, for which flux attenuation is present

but milder than for upgoing neutrinos. Changing f_σ affects the directional distribution of events induced by horizontal neutrinos: a larger value of f_σ sharpens the drop in the event rate from horizontal to upgoing neutrinos, while a smaller value softens it. These effects are intrinsic to our event-rate calculation in Section 7.4.4; Ref. [346] illustrates them explicitly. Below, as part of our statistical methods in Sections 7.5.1 and 7.6.1, we allow the value of f_σ to float in fits to predicted mock event rates in IceCube-Gen2. When doing so, for a given test value of f_σ, we modify equally the cross section used in in-Earth propagation and in neutrino detection.

While Eq. (7.1) is useful to understand the essential features of in-Earth propagation, in our forecasts we propagate neutrinos inside the Earth in a more detailed manner, using the state-of-the-art Monte Carlo code NUPROPEARTH [209, 210]. NUPROPEARTH propagates neutrinos accounting for the leading contribution from CC and NC νN DIS, using the BGR18 cross sections, and for the subdominant contribution of other neutrino-matter interaction channels that, taken together, can attenuate the flux attenuation by up to an additional 10% [209]. It also includes $\bar{\nu}_e$ scattering on atomic electrons, via the Glashow resonance [242, 243], ν_τ regeneration, energy losses of intermediate tauons, and the regeneration of lower-energy neutrinos in NC interactions. It takes the internal matter density profile of Earth to be that of the Preliminary Reference Earth Model [295], given as a set of concentric layers of different densities and mass compositions. Reference [209] has a full description of NUPROPEARTH; for a summary, see Ref. [346].

Thus, to compute neutrino-induced event rates below, in Section 7.4.4, we first propagate the fluxes of ν_e, ν_μ, ν_τ, $\bar{\nu}_e$, $\bar{\nu}_\mu$, and $\bar{\nu}_\tau$ separately, from the surface of the Earth to the simulated surface of the radio array of IceCube-Gen2 (Section 7.4.3), for multiple neutrino energies and across multiple directions. Figures 10 and 11 in Ref. [346] illustrate the resulting neutrino fluxes at the detector. (Later, when computing neutrino-induced event rates in Section 7.4.4, the energy and angular dependence of the effective volume of IceCube-Gen2 that we use represents the detector response only, not the effect of in-Earth propagation on the neutrino fluxes.)

7.4 FORECASTING ULTRA-HIGH-ENERGY NEUTRINO EVENT RATES

7.4.1 *Overview of the experimental landscape*

In high-energy neutrino telescopes, neutrinos of TeV-scale energies and above interact with the detector medium—ice, air, rock—predominantly via νN DIS; see Section 7.4.4. Final-state products interact with the medium, or decay, and initiate high-energy particle showers. As a shower develops, charged particles within it emit electromagnetic radiation, in the optical, ultraviolet, or radio wavelengths, depending on the neutrino energy and on the medium where the shower develops. Neutrino telescopes target this emission using a variety of techniques, which we overview below; for a comprehensive review, see Refs. [82, 83]. From the properties of the detected electromagnetic emission, neutrino telescopes infer the neutrino energy, direction, and flavor, with varying degrees of precision.

Present TeV–PeV neutrino telescopes—IceCube [34], ANTARES [349], Baikal NT-200 [350]—instrument large bodies of water or ice to detect the optical Cherenkov light emitted by showers, initiated mostly by ν_e and ν_τ, and tracks, initiated mostly by ν_μ. IceCube is the largest among them: it consists of about 1 km^3 of Antarctic ice instrumented by thousands of photomultipliers at depths of 1.5–2.5 km. IceCube discovered [34, 35] and regularly observes TeV–PeV cosmic neutrinos [37, 188], but may not be large enough to either discover UHE neutrinos, of EeV-scale energies, whose predicted flux may conceivably be significantly smaller [172–174, 344, 345], or to observe a large number of them. Indeed, currently the most constraining upper limits on the flux of UHE neutrinos come from IceCube [66] and the Pierre Auger Observatory [67]; see Fig. 26. Future in-ice and in-water optical neutrino telescopes—Baikal-GVD [147], the optical array of IceCube-Gen2 [39], KM3NeT [40], P-ONE [41], TRIDENT [148]—will be as large or larger than IceCube, and so will have higher detection rates, but will remain mainly sensitive in the TeV–PeV range.

In the search for UHE neutrinos, the main limitation of optical detection is the attenuation length of light in ice or water, of 100–200 m [351], which forces optical neutrino telescopes to use relatively dense arrays of photomultipliers. Scaling the arrays up to the size required to achieve sensitivity to a conceivably tiny UHE neutrino flux is technically and financially challenging. Instead, for UHE

neutrinos, a variety of alternative techniques exist that can monitor a larger detection volume using more sparse instrumentation. They target the particles, light, and radio emission from the showers initiated by UHE neutrinos in the atmosphere, in ice, or from space [82, 83]. Large arrays of surface particle detectors, like Auger [67] and the proposed TAMBO [73], are sensitive to showers from Earth-skimming neutrinos [352]. Atmospheric imaging telescopes, like the Telescope Array [353], the Cherenkov Telescope Array (CTA) [354], under construction, and the proposed Trinity [355] and Ashra NTA [356], target the Cherenkov and fluorescence light from neutrino-initiated extensive air showers, from different vantage points on the surface. The proposed POEMMA [74] satellites target Cherenkov emission from space, while the proposed ANDIAMO [357] aims for acoustic neutrino detection in water.

In recent years, the technique of radio-detection of UHE particles, including neutrinos, has matured. Because the attenuation length of radio is roughly 1 km in ice and negligible in air [304], radio-based neutrino telescopes can monitor large detector volumes using sparse arrays of radio antennas. We focus on them below.

7.4.2 *Radio-detection of UHE neutrinos*

Reference [166] first proposed using radio emission from showers initiated by high-energy neutrinos as a means to detect them. In a dense, transparent, and dielectric medium, like ice, as the shower develops it accumulates an excess of electrons on the shower front that can reach 20–30% over the number of electrons plus positrons [166] at shower maximum, after which the charge imbalance fades away. The time-varying excess charge produces a nanosecond-long pulse, known as *Askaryan radiation* [165] with a frequency content of approximately 100 MHz–1 GHz. For a comprehensive introduction to the in-ice radio-detection technique, see Ref. [358].

Pioneering experiments established the viability of the radio-detection of UHE neutrinos. ANITA [150] was a balloon-borne detector that targeted radio emission from extensive air showers. ARA [68] and ARIANNA [69], and RICE [359] before them, are underground antenna arrays in Antarctica that target the radio emission from neutrino-initiated showers in ice. (They, and other ra-

dio detectors like AERA [360], CODALEMA [361], LOPES [362], LOFAR [363], and Tunka-Rex [364], also look for UHECRs that interact in the atmosphere.)

In spite of their larger effective volume, these experiments have not yet been able to discover EeV neutrinos. Thus, a number of radio-based neutrino telescopes currently in planning—BEACON [153], GRAND [72], the radio array of IceCube-Gen2 [39, 77], PUEO [75], RET [365], RNO-G [84], TAROGE [366]—aim to do so by using larger detectors and refined techniques.

The main advantage of the radio-detection technique is the long attenuation length of radio waves in ice: up to 1.5 km at the South Pole [310, 367], and roughly 1 km in Greenland [368, 369], *vs.* 100–200 m for optical signals [39, 351]. This makes it possible to build larger detectors by placing a smaller number of radio antennas sparsely distributed, covering a larger area, and reaching a flux sensitivity that would be technically and economically more demanding with an optical detector.

Below, we gear our forecasts to the radio array of IceCube-Gen2, one of the detectors in an advanced stage of planning and that envisions one of the best target flux sensitivities [83]. IceCube-Gen2 [39] will be located in Antarctica, at the same site as IceCube, and will include an extension of the optical array aimed at high-statistics measurements in the TeV–PeV range, and a new underground radio antenna array aimed at discovering EeV neutrinos. RNO-G [84], in Greenland, presently under construction, has an order-of-magnitude smaller sensitivity than foreseen for IceCube-Gen2, but will field-test its design features. In our forecasts, we model in detail the propagation of radio signals in ice, and their detection in antennas with the capabilities envisioned in the IceCube-Gen2 baseline design [39, 77]. This allows us to make forecasts that include experimental nuance.

7.4.3 *IceCube-Gen2*

The planned design of IceCube-Gen2 [39] includes an underground radio array that spans a total surface area of 500 km^2. The baseline design of the array [77], which we adopt for our work, consists of 313 stations, each containing a cluster of antennas, and separated by 1–2 km from each other. Because the stations are located far apart from each other, they function largely as

stand-alone detectors, *i.e.*, they have nearly independent effective volumes, unlike the strings of digital optical modules used in optical detectors, a number of which typically need to be triggered by the same shower in order to claim detection. Thus, the total effective volume of the radio array grows roughly linearly with the number of stations.

The radio stations contain shallow antennas, buried close to the surface, and deep antennas, buried up to 200 m in the ice [39, 77]. The final design of the stations and of the array is still evolving. Placing antennas deeper in the ice increases the sky coverage, whereas shallow antennas have a field of view of that is more concentrated around the horizon [358]. This is because signal trajectories bend downward in the upper 200 m of the ice sheet due to a changing refraction index that restricts the region of ice that can be effectively monitored. In our forecasts, we adopt the current baseline design of 169 stations containing only shallow antennas and 144 stations containing both shallow and deep antennas [77].

Regarding the angular resolution of the detector, the ability to reconstruct the incoming direction of detected events is different for shallow and deep antennas. Shallow antennas have good angular resolution, expected to be as good as 3° [314, 324], which translates into 2° when projected on the zenith angle. Deep antennas have, on average, worse angular resolution due to the more limited ability to measure the horizontal signal polarization component [312]. Presently, the development of algorithms to reconstruct the energy and direction of detected events is still in an early stage; future improvements are possible. To reflect this, below we repeat our analysis for different assumptions of angular resolution. For our baseline results, in Section 7.5.2.2, we assume a zenith angle resolution of $\sigma_{\theta_z} = 2^\circ$ for each radio station; see Table 4. (We assume a common resolution of shallow and deep antennas.) This is optimistic, but not unrealistic given likely improvements in reconstruction methods foreseen for the next decade, especially via the use of deep learning [370]. In Section 7.5.2.7, we present results for a poorer resolution of $\sigma_{\theta_z} = 5^\circ$ and 10°. Angular resolution is especially important to break the degeneracy between flux and cross section described in Section 7.3. It is also key to discovering point sources of UHE neutrinos; see Refs. [371, 372].

Regarding the energy resolution of the detector, current estimates of the resolution of the shower energy are of a factor of two, *i.e.*, a standard deviation of 0.3 on logarithmic scale, or better [315,

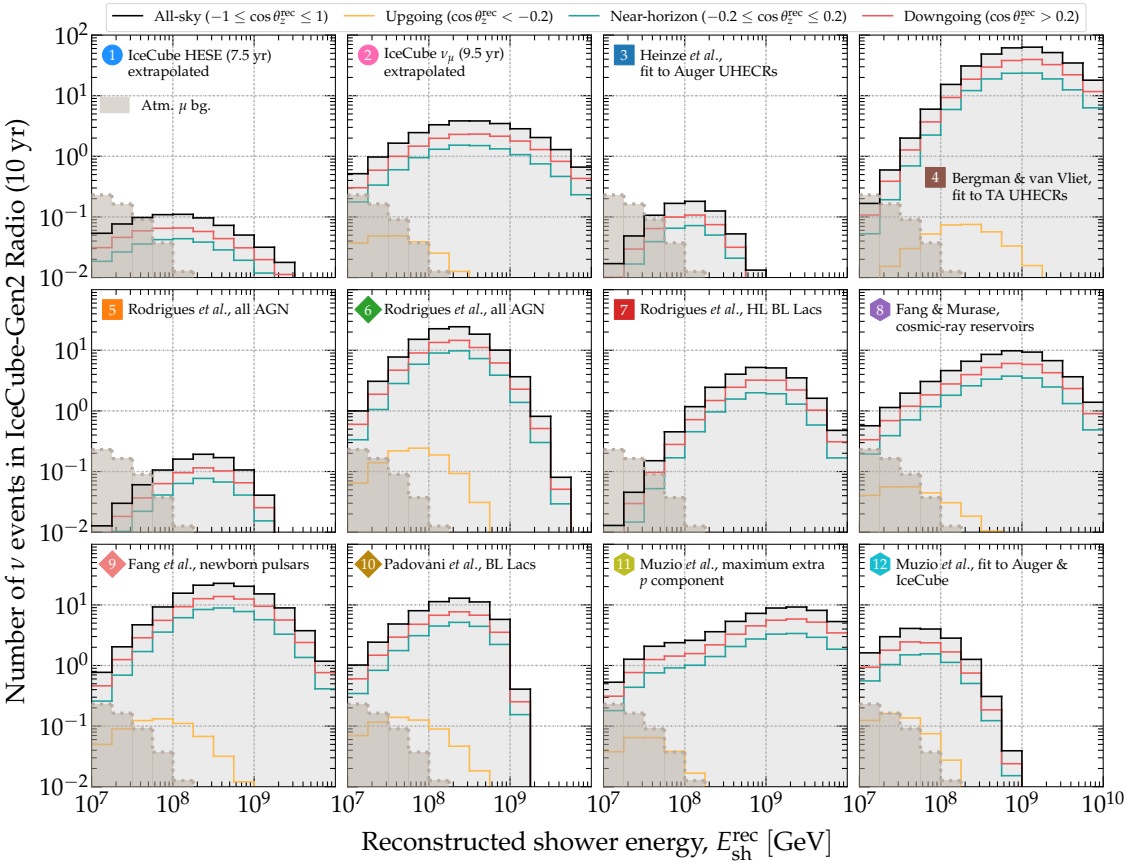

Figure 27: Mean distribution of events in reconstructed shower energy, $E_{\rm sh}^{\rm rec}$, expected in the radio array of IceCube-Gen2 after 10 years of exposure, for the benchmark UHE neutrino flux models 1–12 from Fig. 26. Figure 28 shows the corresponding distribution in reconstructed direction. The neutrino-induced event rates are computed using the methods from Section 7.4.4 and, in this plot (and also in Figs. 28 and 36), by adopting our baseline analysis choices (see Table 4 and Section 7.5.2.2); in particular, the energy resolution is $\sigma_\epsilon = 0.1$ and angular resolution is $\sigma_{\theta_z} = 2^\circ$. Figures 25 and 38 show, respectively, the associated baseline flux discovery potential and flux model separation. Table 3 shows the corresponding all-sky mean integrated event rates (however, to obtain our main results, in Sections 7.5 and 7.6, we use binned event rates). We include the baseline background of atmospheric muons (see Section 7.4.5.1), but not the background of the UHE tail of the high-energy IceCube neutrino flux (see Section 7.4.5.2), though both enter our analysis; see Sections 7.5.1 and 7.6.1.

317, 324, 370], and as good as 30%, *i.e.*, a standard deviation of 0.1 on logarithmic scale, for certain conditions [315]. For our baseline results, in Section 7.5.2.2, we assume an uncertainty of $\sigma_\epsilon = 0.1$ on the logarithm of the reconstructed shower energy; see Table 4. In Section 7.5.2.7, we present results for a poorer energy resolution of $\sigma_\epsilon = 0.5$ and 1.0. Energy resolution is especially important to distinguish between signal and background event distributions (see Fig. 27), and between predictions from alternative UHE neutrino flux models (Section 7.6).

Later, we describe in detail how the predicted event rates in IceCube-Gen2 are affected by the angular and energy resolution of the detector, in connection to Eq. (7.5).

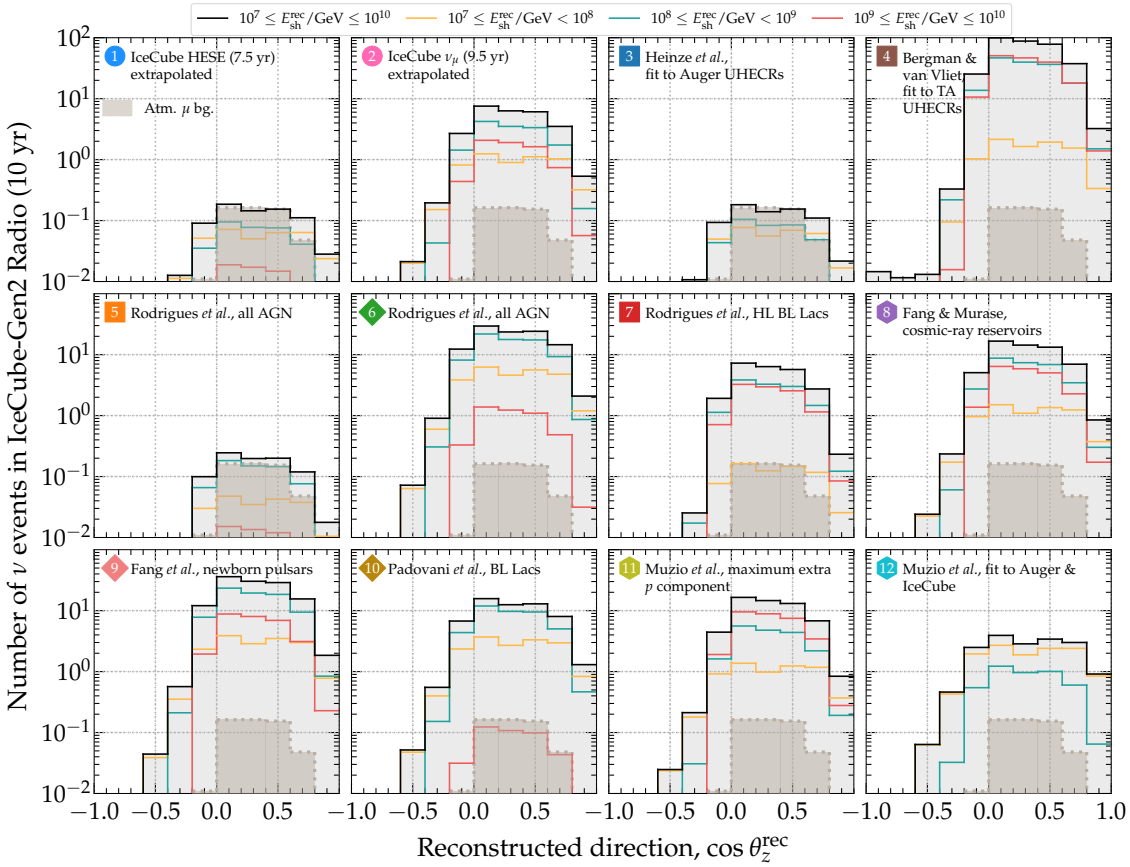

Figure 28: Mean distribution of events in reconstructed direction, $\cos\theta_z^{\rm rec}$, expected in the radio array of IceCube-Gen2 after 10 years of exposure, for the benchmark UHE neutrino flux models 1–12 from Fig. 26. Figure 27 shows the corresponding distribution in reconstructed shower energy. The neutrino-induced event rates are computed using the methods from Section 7.4.4 and, in this plot (and also in Figs. 27 and 36), by adopting our baseline analysis choices (see Table 4 and Section 7.5.2.2); in particular, the energy resolution is $\sigma_\epsilon = 0.1$ and angular resolution is $\sigma_{\theta_z} = 2^\circ$. Figures 25 and 38 show, respectively, the associated baseline flux discovery potential and flux model separation. The uniform binning in this plot is only for illustration; the binning used in our statistical analysis is finer for events around the horizon ($80^\circ \leq \theta_z^{\rm rec} \leq 100^\circ$) and coarser for downgoing ($\theta_z^{\rm rec} < 80^\circ$) and upgoing directions ($\theta_z^{\rm rec} > 100^\circ$); it is described in Section 7.5.2.1. Table 3 shows the corresponding all-sky mean integrated event rates (however, to obtain our main results, in Sections 7.5 and 7.6, we use binned event rates). We include the baseline background of atmospheric muons (see Section 7.4.5.1), but not the background of the UHE tail of the high-energy IceCube neutrino flux (see Section 7.4.5.2), though both enter our analysis; see Sections 7.5.1 and 7.6.1.

7.4.4 *Computing event rates*

To forecast neutrino-induced event rates in the radio array of IceCube-Gen2, we follow the same methods introduced in Ref. [346]. We sketch them below, and defer to Ref. [346] for details. While we make our predictions particular to neutrino radio-detection IceCube-Gen2, our methods can be adapted to other neutrino telescopes, radio-based or otherwise; see Section 7.7.

In-ice, radio-based neutrino telescopes, like ARA [68], ARIANNA [69], RNO-G [84], and IceCube-Gen2 [39], measure the energy deposited in the ice by particle showers that emit Askaryan radiation [165]. In a shower initiated by a neutrino-nucleon (νN) DIS event, the shower energy, $E_{\rm sh}$, is a fraction of the parent neutrino energy, E_ν. The value of the fraction depends on the flavor of the interacting neutrino and on whether the interaction is NC or CC; we elaborate on this below. See also Section 7.3 for the effect of DIS in neutrino propagation inside Earth.

In the NC DIS interaction initiated by any flavor of ν_α or $\bar{\nu}_\alpha$ ($\nu_\alpha + N \to \nu_\alpha + X$, $\alpha = e, \mu, \tau$), only the final-state hadrons, X, shower. The final-state hadrons receive a fraction y—the inelasticity—of the parent neutrino energy, while the final-state neutrino, which escapes without interacting, receives the remaining fraction $1 - y$; so, in this case, $E_{\rm sh} = yE_\nu$. In the CC DIS interaction initiated by a ν_e or $\bar{\nu}_e$ ($\nu_e + N \to e + X$), the showers initiated by the final-state electron and hadrons both radiate, so the full neutrino energy is transmitted to the shower, *i.e.*, $E_{\rm sh} = E_\nu$. Finally, in the CC DIS interaction initiated by a ν_μ, ν_τ, $\bar{\nu}_\mu$, or $\bar{\nu}_\tau$ ($\nu_\alpha + N \to \alpha + X$, $\alpha = \mu, \tau$), the shower initiated by the final-state hadrons dominates the radiation; so, in this case, $E_{\rm sh} = yE_\nu$. (There is an additional sub-dominant contribution to the shower rate, of up to 20%, coming from showers initiated by the final-state muons and tauons [213, 214]. However, as in Ref. [346], we do not account it in our simulations because it is computationally taxing to include. This makes our forecasts below conservative.) In summary, for a given shower energy $E_{\rm sh}$, the neutrino energy is

$$E^i_{\nu_\alpha}(E_{\rm sh}, y) = \begin{cases} E_{\rm sh}/y, & \text{for } \nu_\alpha, i = \text{NC} \\ E_{\rm sh}, & \text{for } \nu_e\,, i = \text{CC} \\ E_{\rm sh}/y, & \text{for } \nu_\mu \text{ and } \nu_\tau, i = \text{CC} \end{cases} . \tag{7.3}$$

As during in-Earth neutrino propagation (Section 7.3), in each DIS interaction in the detector the value of y is sampled at random from a probability distribution that is proportional to the energy-dependent differential νN cross section, $d\sigma^{\rm NC}_{\nu_\alpha}/dy$ for NC interactions and $d\sigma^{\rm CC}_{\nu_\alpha}/dy$ for CC interactions; see Eq. (7.4) below. In our forecasts, we use the inelasticity distribution built from the BGR18 UHE νN cross section [194]; see Fig. 4 in Ref. [346].

After a νN DIS event, Askaryan radiation propagates through the ice, attenuating en route to the detector, and, upon reaching it, may or may not trigger the antennas, depending on the shower energy and direction, the characteristics of the antenna, and the size and geometry of the detector

array. We account for these features via dedicated Monte Carlo simulations of neutrino-induced shower production, propagation, and detection using the same state-of-the-art computational tools as the IceCube-Gen2 Collaboration, NURADIOMC [211] and NURADIORECO [212]. These simulations characterize the expected detector response; we describe it via the detector effective volumes, $V^{\rm NC}_{{\rm eff},\nu_\alpha}$ and $V^{\rm CC}_{{\rm eff},\nu_\alpha}$ below, which depend on the energy and direction of the shower.

In our forecasts, we adopt the same simulated effective volumes introduced in Ref. [346]. First, we simulate separately the effective volumes for NC and CC interactions of a shallow and a deep detector station; see Fig. 12 in Ref. [346]. The shallow-station components are triggered by requiring a time-coincident high-and-low threshold crossing of two out of four LPDA antennas in an optimized trigger bandwidth [320]. The deep-station components are triggered by an interferometric phased array installed at a depth of 200 m [319]. These are the trigger settings foreseen for IceCube-Gen2 [77]. We simulate the interactions, for NC and CC separately, in several cubic kilometers of ice surrounding the antennas, of a large number of neutrinos with different energies and from different directions, and the ensuing production and propagation of showers and Askaryan radiation. We keep record of which showers trigger the antennas and are deemed as detected. With this, we compute the effective volume as the fraction of showers that are detected times the simulated detector volume.

Second, we scale up the effective volumes obtained for the single detector component up to the size of the array to obtain the full-detector volumes, $V^{\rm NC}_{{\rm eff},\nu_\alpha}$ and $V^{\rm CC}_{{\rm eff},\nu_\alpha}$, by multiplying the effective volume of a single component times their total number in the array. To do that, we adopt the baseline array design of Ref. [77], *i.e.*, 144 hybrid stations, each containing a shallow component and a deep component, plus 169 shallow-only stations; see Fig. 13 in Ref. [346]. Equation (7.4) shows the role of the effective volume in the calculation of event rates. Unlike common practice, the energy and direction dependence of the effective volume that we use stem exclusively from the detector response, not from the neutrino propagation through the Earth. We account for the latter in the neutrino flux that reaches the detector, $\Phi^{\rm det}_{\nu_\alpha}$, computed as described in Section 7.3.

The differential rate of showers induced by the NC and CC interactions of ν_α is the convolution of the effective volume, the differential cross section, and the neutrino flux at the detector, *i.e.*,

$$\frac{d^2N_{\nu_\alpha}}{dE_{\rm sh}d\cos\theta_z} = 2\pi T n_t \int_0^1 dy \Bigg(\frac{E^{\rm NC}_{\nu_\alpha}(E_{\rm sh},y)}{E_{\rm sh}} V^{\rm NC}_{{\rm eff},\nu_\alpha}(E_{\rm sh},\cos\theta_z) \times \frac{d\sigma^{\rm NC}_{\nu_\alpha {\rm w}}(E_\nu,y)}{dy} \Phi^{\rm det}_{\nu_\alpha}(E_\nu,\cos\theta_z)|_{E_\nu = E^{\rm NC}_{\nu_\alpha}(E_{\rm sh},y)} + {\rm NC}\to{\rm CC} \Bigg) , \quad (7.4)$$

where T is the detector exposure time, $n_t \equiv N_{\rm Av}\rho_{\rm ice}/M_{\rm ice}$ is the number density of water molecules in ice, $N_{\rm Av}$ is Avogadro's number, $\rho_{\rm ice} = 0.9168$ g cm^{-3} is the density of ice, and $M_{\rm ice} = 18.01528$ g mol^{-1} is the molar mass of water. On the right-hand side of Eq. (7.4), the term $E^{\rm NC}_{\nu_\alpha}/E_{\rm sh}$, and its CC equivalent, transforms the energy scale from neutrino energy to shower energy; it is given by Eq. (7.3). The differential cross section is for neutrino DIS on one molecule of water (H_2O), *i.e.*, $\sigma^{\rm NC}_{\nu_\alpha w} = 10\sigma^{\rm NC}_{\nu_\alpha p} + 8\sigma^{\rm NC}_{\nu_\alpha n}$, where $\sigma^{\rm NC}_{\nu_\alpha p}$ and $\sigma^{\rm NC}_{\nu_\alpha n}$ are the $\nu_\alpha p$ and $\nu_\alpha n$ BGR18 cross sections [194], respectively, and similarly for CC interactions. The event rate induced by $\bar{\nu}_\alpha$ is the same as for ν_α, *i.e.*, Eq. (7.4), but changing the cross section to $\sigma^{\rm NC}_{\bar{\nu}_\alpha {\rm w}}$, which, at ultra-high energies, is nearly equal to $\sigma^{\rm NC}_{\nu_\alpha {\rm w}}$ (also true for CC interactions; see Fig. 3 in Ref. [346]), and the flux to $\Phi^{\rm det}_{\bar{\nu}_\alpha}$.

Equation (7.4) computes the event rate in terms of the true shower energy, $E_{\rm sh}$, and the true shower direction, θ_z. We account for the limited energy and angular resolution of the detector by using energy and angular resolution functions, and by expressing the event rate in terms of reconstructed shower energy, $E^{\rm rec}_{\rm sh}$, and reconstructed direction, $\theta^{\rm rec}_z$. The energy resolution function, $\mathcal{R}_{E_{\rm sh}}$, is a Gaussian probability density function of $\log_{10} E^{\rm rec}_{\rm sh}$, centered at the true shower energy, $\log_{10} E_{\rm sh}$, with a width $\sigma_{E_{\rm sh}} \equiv 10^{\sigma_\epsilon} E_{\rm sh}$, where $\epsilon \equiv \log_{10}(E^{\rm rec}_{\rm sh}/E_{\rm sh})$. For our baseline results (Table 4), we set $\sigma_\epsilon = 0.1$ as discussed above. The angular resolution function, $\mathcal{R}_{\theta_z}$, is a Gaussian probability density function of $\theta^{\rm rec}_z$, centered at the true direction, θ_z, with a width of σ_{θ_z}. For our baseline results (Table 4), we set $\sigma_{\theta_z} = 2^\circ$ as discussed above. In Section 7.5.2.7, we show the impact on our results of varying the values of σ_ϵ and σ_{θ_z}. Reference [346] contains explicit definitions of the resolution functions.

Thus, the differential event rate of showers induced by ν_α, in terms of reconstructed energy and direction, is

$$\frac{d^2N_{\nu_\alpha}}{dE^{\rm rec}_{\rm sh}d\theta^{\rm rec}_z} = \int_{-1}^{+1} d\cos\theta_z \int_0^\infty dE_{\rm sh} \frac{d^2N_{\nu_\alpha}}{dE_{\rm sh}d\cos\theta_z} \mathcal{R}_{E_{\rm sh}}(E^{\rm rec}_{\rm sh},E_{\rm sh})\, \mathcal{R}_{\theta_z}(\theta^{\rm rec}_z,\theta_z) \, . \quad (7.5)$$

The CC interaction of ν_e and $\bar{\nu}_e$ dominates the event rate, since these are the two cases for which $E_{\rm sh} = E_\nu$. The NC interaction of each species, and the CC interaction of ν_μ, ν_τ, $\bar{\nu}_\mu$, and $\bar{\nu}_\tau$ each contributes at roughly the same level. For details, see Fig. 14 in Ref. [346]. To be conservative in our forecasts, we do not assume that flavor identification will be possible, though there are promising early results [214, 300]. Accordingly, we use only the total event rate induced by all flavors of ν_α and $\bar{\nu}_\alpha$, *i.e.*,

$$\frac{d^2N_\nu}{dE_{\rm sh}^{\rm rec}d\theta_z^{\rm rec}} = \sum_\alpha^{e,\mu,\tau}\left(\frac{d^2N_{\nu_\alpha}}{dE_{\rm sh}^{\rm rec}d\theta_z^{\rm rec}} + \frac{d^2N_{\bar{\nu}_\alpha}}{dE_{\rm sh}^{\rm rec}d\theta_z^{\rm rec}}\right) . \tag{7.6}$$

Below, as part of our analysis, we compute event rates in bins of reconstructed energy and direction; to do so, we integrate Eq. (7.6) in $E_{\rm sh}^{\rm rec}$ and $\theta_z^{\rm rec}$ inside each bin. For our baseline results, we use 12 bins of $E_{\rm sh}^{\rm rec}$, evenly distributed in logarithmic scale from 10^7 GeV to 10^{10} GeV, and 13 bins of $\theta_z^{\rm rec}$, with a denser coverage around the horizon; see Table 4 and Section 7.5.2.1 for details.

Figure 27 shows the mean predicted energy distribution of events after 10 years of exposure in the radio array of IceCube-Gen2, for the benchmark flux models 1–12 introduced in Section 7.2 and Fig. 26. Because of the severe in-Earth attenuation of UHE neutrinos, the event rate is dominated by downgoing events and, to a lesser extent, by near-horizontal events. For each flux model, the shape of the event energy distribution traces the shape of its corresponding neutrino energy spectrum from Fig. 26. Later, in Section 7.6, this feature will allow us to distinguish between different flux models. For all flux models, below $E_{\rm sh}^{\rm rec} = 10^7$ GeV the event rates dip because the effective volume decreases at low neutrino energies as a result of Askaryan radiation weakening.

Figure 28 shows the corresponding mean predicted angular distribution of events for the benchmark flux models. (The angular binning used in Fig. 28 is for illustrative purposes only. Our analysis uses a finer binning around the horizon; see Table 4 and Section 7.5.2.1.) Above the horizon, *i.e.*, $\cos\theta_z^{\rm rec} > 0$, where in-Earth attenuation is small or negligible, the angular event distribution primarily traces the angular dependence of the effective volume. At the horizon and below it, *i.e.*, $\cos\theta_z^{\rm rec} < 0$, the angular distribution has a sharp cut-off due to the strong in-Earth attenuation. Only flux models with a large normalization, *i.e.*, models 2, 4, 6–12, overcome the suppression and yield a handful of events below the horizon. In contrast to the energy distribution of the events, where differences between flux models are evident, differences in the angular distribution between flux models are mild.

The event rates computed using Eqs. (7.4)–(7.6) and shown in Figs. 27 and 28 are the mean expected rates. In a specific experimental observation, the number of events in each bin will be an integer value, and might deviate appreciably from the mean, especially when it has a low value. Therefore, later, as part of our statistical analyses in Sections 7.5.1 and 7.6.1, we account for random statistical fluctuations around the mean.

7.4.5 *Backgrounds*

Below, in Sections 7.5 and 7.6, we forecast the potential to discover the benchmark UHE neutrino flux models 1–12, and to distinguish between them, factoring in the contamination from background that may mimic the events induced by the flux models. We account for two expected sources of background—atmospheric muons and the potential UHE tail of the IceCube neutrino flux—and comment on the pressing need to characterize a third likely source of background—air-shower cores.

7.4.5.1 *Atmospheric muons*

High-energy muons produced in the interaction of UHECRs in the atmosphere may trigger in-ice showers whose Askaryan radiation is expected to generate a small, but irreducible background for UHE neutrino searches [213]. We estimate the rate of muon-induced events in the radio array of IceCube-Gen2 using the hadronic interaction model SYBILL 2.3C [293] and applying a surface veto that mitigates its effect by detecting the air shower that accompanies the muon. This is the same prescription that was used to compute the muon background in Refs. [346, 372]. In our forecasts below, the background of atmospheric muons affects all benchmark flux models 1–12.

Figures 27 and 28 show the resulting energy and angular distribution of muon-induced events in the radio array of IceCube-Gen2. They are concentrated at the lowest energies, $E_{\rm sh}^{\rm rec} \lesssim 10^8$ GeV, and in downgoing directions, $\cos\theta_{\rm z}^{\rm rec} \gtrsim 0$, since muons cannot penetrate far inside Earth. The irreducible all-sky integrated rate of muon-induced events above 10^8 GeV, *i.e.*, that cannot be vetoed by the surface veto, is lower than 0.1 events per year. Hence, atmospheric muons represent an obstacle only to the discovery of an UHE neutrino flux that is small and that peaks at low

Table 3: Expected mean rates of neutrino-induced events in the radio array of IceCube-Gen2, after exposure time T, for the benchmark UHE diffuse neutrino flux models used in this analysis (see Section 7.2 and Fig. 26), time needed for their decisive discovery, $T^{\rm disc}$, *i.e.*, for the mean discovery Bayes factor $\langle \mathcal{B}^{\rm disc} \rangle > 100$ (see Section 7.5.1), and mean number of events induced by them until the time of their decisive discovery, $N_\nu^{\rm disc}$. Flux models with blank entries (–) are not expected to be discovered within 20 years. Entries marked with an asterisk (*) signal that the background includes only atmospheric muons (see Sections 7.4.5.1 and 7.5.2.9); unmarked entries include in addition the background from the UHE tail of the IceCube high-energy neutrino flux (see Section 7.4.5.2). Flux types are (Section 7.2): extrapolation to ultra-high energies (●), cosmogenic (■), source (◆), and cosmogenic + source (⬢). Results in this table are obtained using our baseline analysis choices (Table 4 and Section 7.5.2.1). Figure 25 shows the continuous evolution of $\langle \mathcal{B}^{\rm disc} \rangle$ with T; this table shows only snapshots. Results for alternative analysis choices are in Sections 7.5.2.3–7.5.2.9. The event rates shown are all-sky, *i.e.*, summed over all reconstructed directions, $-1 \leq \cos\theta_z^{\rm rec} \leq 1$, and grouped in a single bin of reconstructed shower energy, $10^7 \leq E_{\rm sh}^{\rm rec}/{\rm GeV} \leq 10^{10}$. However, all-sky rates are only illustrative; the statistical analysis with which we compute $\langle \mathcal{B}^{\rm disc} \rangle$ uses instead binned event rates; see Section 7.5.1 for details.

#	Type	UHE ν flux model	All-sky integrated event rate, N_ν			Decisive flux discovery ($\langle \mathcal{B}^{\rm disc} \rangle > 100$)	
			$T = 1$ yr	$T = 3$ yr	$T = 10$ yr	$T^{\rm disc}$ [yr]	$N_\nu^{\rm disc}$
1	●	IceCube HESE (7.5 yr) extrapolated [188]	0.07	0.22	0.73	$> 20^\star$	–
		... with cut-off at $E_{\nu,\rm cut}^{\rm HE} = 500$ PeV	0.05	0.14	0.45	$> 20^\star$	–
		... with cut-off at $E_{\nu,\rm cut}^{\rm HE} = 100$ PeV	0.02	0.07	0.22	$> 20^\star$	–
		... with cut-off at $E_{\nu,\rm cut}^{\rm HE} = 50$ PeV	0.01	0.04	0.13	$> 20^\star$	–
2	●	IceCube ν_μ (9.5 yr) extrapolated [37]	2.69	8.07	26.90	0.26*	0.70*
		... with cut-off at $E_{\nu,\rm cut}^{\rm HE} = 500$ PeV	1.02	3.06	10.20	1.05*	1.07*
		... with cut-off at $E_{\nu,\rm cut}^{\rm HE} = 100$ PeV	0.35	1.04	3.47	4.97*	1.74*
		... with cut-off at $E_{\nu,\rm cut}^{\rm HE} = 50$ PeV	0.18	0.53	1.75	11.10*	2.00*
3	■	Heinze *et al.*, fit to Auger UHECRs [174]	0.07	0.21	0.71	> 20	–
4	■	Bergman & van Vliet, fit to TA UHECRs [193]	33.23	99.70	332.34	0.28	9.30
5	■	Rodrigues *et al.*, all AGN benchmark [179]	0.09	0.27	0.89	> 20	–
6	◆	Rodrigues *et al.*, all AGN benchmark [179]	10.72	32.15	107.16	1.31	14.04
7	■	Rodrigues *et al.*, HL BL Lacs [179]	2.42	7.27	24.24	13.03	31.53
8	⬢	Fang & Murase, cosmic-ray reservoirs [177]	5.74	17.22	57.41	6.16	35.36
9	■	Fang *et al.*, newborn pulsars [175]	12.54	37.61	125.38	1.89	23.70
10	■	Padovani *et al.*, BL Lacs [176]	5.79	17.34	57.85	3.07	17.78
11	■	Muzio *et al.*, maximum extra p component [178]	5.66	19.97	56.55	2.48	5.97
12	⬢	Muzio *et al.*, fit to Auger & IceCube [180]	1.71	5.14	17.12	8.05	13.77
–	–	Atmospheric muon background (baseline)	0.05	0.16	0.54	–	–

neutrino energies, *e.g.*, benchmark flux models 1, 3, and 9; Section 7.5.2 shows this in detail. In Appendix B.3 we comment on the effect on the flux discovery potential of not using a surface veto; in that case, the discovery potential is only degraded mildly.

The muon background shown in Figs. 27 and 28 constitutes our baseline analysis choice; see Section 7.5.2.1, and Tables 4 and 5 for a full list of analysis choices. Below, we produce our main results using it. In Section 7.5.2.3, we show that even if our baseline muon-induced background was a significant underestimation of its true size, this would only erode mildly the prospects of discovering most of our benchmark UHE neutrino flux models. (However, in Section 7.5.2.3, we only change the normalization of the atmospheric muon flux, not the shape of its energy spectrum. If the energy spectrum of atmospheric muons were to extend to higher energies than in our baseline prescription of it, the conclusions about its importance in our forecasts might change.)

7.4.5.2 *UHE tail of the IceCube high-energy neutrino flux*

Presently, using roughly ten years of data, IceCube has found that the diffuse flux of high-energy cosmic neutrinos that it measures spans the neutrino energy range from about 10 TeV to at least a few PeV [37, 188]. In the PeV range, data is sparse because the neutrino energy spectrum falls steeply with energy. As a result, it is presently unknown whether the flux measured at TeV–PeV energies extends to ultra-high energies, beyond 100 PeV and, if so, what the size and shape of its spectrum is at those energies.

In Fig. 26, benchmark UHE neutrino flux models 1 and 2 are straightforward UHE extrapolations of two IceCube TeV–PeV power-law flux measurements [37, 188], without any high-energy suppression (more on this later). They illustrate that if the UHE tail of the IceCube high-energy neutrino flux is large enough to trigger events in the radio array of IceCube-Gen2, it would constitute a background to the discovery of UHE neutrino flux models. In our forecasts below, the background from the UHE tail of the IceCube high-energy neutrino flux affects benchmark flux models 3–12. (In Section 7.5.2.9, we study separately the discovery of the UHE tail of the IceCube high-energy neutrino flux itself.)

Currently, the TeV–PeV neutrino flux seen by IceCube is described well as a simple power law $\propto E_\nu^{-\gamma}$. Two properties of the TeV–PeV neutrino flux determine whether its UHE tail may be

detectable in UHE neutrino telescopes: the value of the spectral index, γ, and whether the flux is further suppressed, relative to the simple power law, at or above the few-PeV scale.

Regarding the spectral index, its value depends on the set of IceCube events that is used to perform the fit. The neutrino spectrum is harder ($\gamma \approx 2.37$) when derived from a fit to 9.5 years of through-going muon tracks [37], created by ν_μ that interact outside the detector and make muons that cross it. The spectrum is softer ($\gamma \approx 2.87$) when derived from a fit to 7.5 years of High Energy Starting Events (HESE), created by neutrinos of all flavors that interact inside the detector [188]. In the TeV–PeV range, these results are compatible with each other within 1σ [188]. However, because a harder spectrum falls more slowly with energy, its UHE tail is more likely to be prominent and trigger events in the radio array of IceCube-Gen2. In our forecasts, we explore different values of the spectral index (and of the corresponding normalization of the flux), motivated by IceCube results; see Sections 7.5.2.1 and 7.5.2.4, and Tables 4 and 5.

Regarding the possible further suppression of the IceCube flux in the few-PeV range, it is unknown whether the flux extends beyond a few PeV as a simple power law, or whether it is suppressed by an exponential cut-off $e^{-E_\nu / E^{\rm HE}_{\nu,{\rm cut}}}$ at a cut-off energy $E^{\rm HE}_{\nu,{\rm cut}}$ of a few PeV or more. A lower value of the cut-off energy implies a smaller UHE tail of the flux, and a lower contribution of it as a background in the radio array of IceCube-Gen2. Currently, there is no significant evidence for the existence of a cut-off: a recent analysis using 7.5 years of HESE events [188] strongly disfavors the presence of an exponential cut-off below 370 TeV and finds no substantial evidence for a cut-off above 1.6 PeV. However, the measurement is hampered by the paucity of events in the PeV range. In our forecasts, we explore different possibilities for the value of the cut-off energy, representative of our present and possible future knowledge of it; see Sections 7.5.2.1 and 7.5.2.5, and Tables 4 and 5.

We model the background flux of high-energy (HE) $\nu_\alpha + \bar{\nu}_\alpha$ as an exponentially suppressed power law, *i.e.*,

$$\Phi^{\rm HE}_{\nu_\alpha+\bar{\nu}_\alpha}(E_\nu) = f_{\alpha,\oplus}\Phi^{\rm HE}_0 \left(\frac{E_\nu}{100\ {\rm TeV}}\right)^{-\gamma} e^{-\frac{E_\nu}{E^{\rm HE}_{\nu,{\rm cut}}}}, \tag{7.7}$$

where $f_{\alpha,\oplus}$ is the ratio of the flux of $\nu_\alpha + \bar{\nu}_\alpha$ to the all-flavor flux and $\Phi^{\rm HE}_0$ is the normalization of the all-flavor flux. The flux shape in Eq. (7.7) is the same one used by searches for an exponential suppression performed by the IceCube Collaboration, *e.g.*, in Refs. [37, 188]. Equation (7.7) makes

the typical simplifying assumption that the fluxes of neutrinos of all flavors share common values of γ and $E^{\rm HE}_{\nu,{\rm cut}}$, and that the flux of ν_α and $\bar{\nu}_\alpha$ are equal, *i.e.*, $\Phi_{\nu_\alpha} = \Phi_{\bar{\nu}_\alpha} = \Phi_{\nu_\alpha+\bar{\nu}_\alpha}/2$, which is expected from neutrino production in pp interactions [130] and, at high energies, in $p\gamma$ interactions [256–258].

For the flavor composition, $f_{\alpha,\oplus}$, in Eq. (7.7), we adopt the canonical scenario where high-energy neutrinos come from the decay of pions produced in pp and $p\gamma$ interactions in astrophysical sources (S). Thus, at production, the flavor composition is approximately $\left(f_{e,{\rm S}}, f_{\mu,{\rm S}}, f_{\tau,{\rm S}}\right) = (1/3, 2/3, 0)$. Oscillations en route to Earth change the flavor composition into $f_{\alpha,\oplus} = \sum_\beta^{e,\mu,\tau} P_{\beta\alpha} f_{\beta,{\rm S}}$, where $P_{\beta\alpha} \equiv \sum_{i=1}^3 |U_{\alpha i}|^2 |U_{\beta i}|^2$ is the average flavor-transition probability for $\nu_\alpha \to \nu_\beta$ [266], and $\mathbf{U}$ is the Pontecorvo-Maki-Nagawa-Sakata (PMNS) mixing matrix. We evaluate the PMNS matrix using the present-day best-fit values of the mixing parameters from the NuFit 5.0 global fit to oscillation data [268, 269]. This yields flavor ratios at Earth ($\oplus$) close to equipartition [267, 329], *i.e.*,

$$\left(f_{e,\oplus}, f_{\mu,\oplus}, f_{\tau,\oplus}\right) = (0.298 : 0.359 : 0.342)\,. \tag{7.8}$$

These are the flavor ratios that we use to evaluate Eq. (7.7). (These are also the flavor ratios with which we build the benchmark UHE neutrino flux models that originally lacked detailed flavor composition; see Ref. [346] for details.) We neglect uncertainties on $f_{\alpha,\oplus}$ that stem from uncertainties in the mixing parameters. References [267, 346] showed that by the time that IceCube-Gen2 is operating, in the 2030s, precise measurement of the mixing parameters in upcoming oscillation experiments DUNE [271], Hyper-Kamiokande [272], JUNO [273], and the IceCube Upgrade [373], will have rendered the uncertainty on the predicted values of $f_{\alpha,\oplus}$ negligible. (The issue of inferring the flavor composition at the neutrino sources is related, but separate [267, 374].)

For the all-flavor flux normalization, $\Phi_0^{\rm HE}$, and the spectral index, γ, in Eq. (7.7), we consider three possibilities based on their best-fit values reported in IceCube analyses (see also Section 7.5.2.1, and Tables 4 and 5):

- **Hard flux motivated by the 9.5-year through-going ν_μ analysis [37]:** We set $\Phi_0^{\rm HE} = \Phi_{\nu_\mu+\bar{\nu}_\mu,0}/f_{\mu,\oplus}$, where $\Phi_{\nu_\mu+\bar{\nu}_\mu,0} = 1.44\times10^{-18}$ GeV^{-1} cm^{-2} s^{-1} sr^{-1} is the best-fit value of the normalization of the $\nu_\mu + \bar{\nu}_\mu$ flux in Ref. [37], and $\gamma = 2.37$. This is the hardest background neutrino flux that we consider: it induces the largest background event rate.

To be conservative, we adopt it as our baseline analysis choice. (Without a cut-off, *i.e.*, for $E^{\rm HE}_{\nu,{\rm cut}} \to \infty$, this background matches flux model 2.)

- **Intermediate flux motivated by the 9.5-year through-going ν_μ analysis:** We keep the same normalization as for the case of the hard flux above, but change the spectral index to $\gamma = 2.50$.

- **Soft flux motivated by the 7.5-year HESE analysis [188]:** For this neutrino background scenario, we set $\Phi_0^{\rm HE} = 6.37 \times 10^{-18}\ {\rm GeV}^{-1}\ {\rm cm}^{-2}\ {\rm s}^{-1}\ {\rm sr}^{-1}$ and $\gamma = 2.87$. This is the softest background neutrino flux that we consider: it induces the smallest background event rate. (Without a cut-off, *i.e.*, for $E^{\rm HE}_{\nu,{\rm cut}} \to \infty$, this background matches flux model 1.)

We make the reasonable assumption that, by the time that IceCube-Gen2 is operating the values of $\Phi_0^{\rm HE}$ and γ will be known precisely from measurements in TeV–PeV neutrino telescopes [83]. Thus, in our forecasts we neglect the uncertainty on their values, and use only their present-day best-fit values. Below, Sections 7.5.2.2 and 7.6.2 show results for our baseline choice of a hard background high-energy neutrino flux; Section 7.5.2.4 and Appendix B.1 show results for the two alternative choices.

For the cut-off energy, $E^{\rm HE}_{\nu,{\rm cut}}$, in Eq. (7.7), we assume that its value lies between 10^7 GeV and 10^{12} GeV. For our conservative baseline forecasts, we assume complete ignorance of its value in the statistical analysis to reflect the present-day scenario; see Section 7.5.2.1 and Table 4. The lack of knowledge of the size and shape of the UHE tail of the high-energy neutrino flux encumbers the discovery of benchmark UHE neutrino flux models 3–12 and the separation between them. For our forecasts made with alternative analysis choices, we assume limited and precise knowledge of the value of $E^{\rm HE}_{\nu,{\rm cut}}$; see Section 7.5.2.5. There, we show that our current ignorance of $E^{\rm HE}_{\nu,{\rm cut}}$ erodes, but does not destroy, the potential to discover benchmark flux models.

Some of the benchmark UHE neutrino flux models we consider predict a sizable flux of neutrinos at $\lesssim 10$ PeV, around the high-energy end of current IceCube measurements; this is the case for models 6 and 8–12 (see Fig. 26). In these cases, adding the high-energy tail of the IceCube flux may naively seem to overshoot present-day IceCube flux measurements below 10 PeV. We argue that this is not necessarily the case: in the 1–10 PeV energy range, present-day IceCube measurements are rather limited, with only a handful of events detected so far. This is reflected in the fluxes inferred from the IceCube HESE and through-going muon analyses in Fig. 26: they stop at about

2 PeV and 5 PeV, respectively, and their allowed bands are rather wide. This allows for additional flux components to coexist with the high-energy tail of the IceCube flux, like the flux models that we study.

We compute event rates induced by the UHE tail of the IceCube high-energy neutrino flux using the same methods introduced in Section 7.4.4.

7.4.5.3 *Air-shower cores*

In addition to the two sources of background described above, a likely third one is the background from air-shower cores [327, 375, 376]. These are cores of particle showers initiated by cosmic-ray interactions in the atmosphere, that develop downwards and penetrate the ice, where they may trigger detectable Askaryan radiation. Reflection layers in the deep ice [376] may then reflect the radiation upwards, resulting in signals that mimic those expected from neutrinos. Presently, the estimates of the size and shape of this background are uncertain. (Reference [376] contains early results on this front.) Thus, we do not account for it in our forecasts below. Nevertheless, as in Ref. [346], we point out that characterizing the background of air-shower cores, and possibly minimizing its effect, is a pressing issue in assessing the science reach of upcoming in-ice UHE neutrino telescopes.

7.5 DIFFUSE FLUX DISCOVERY POTENTIAL

Below, we answer the question of how long it would take to discover benchmark flux models 1–12 (see Fig. 26) in the radio array of IceCube-Gen2. The UHE neutrino diffuse flux discovery potential of the detector represents its ability to distinguish between a signal induced by a diffuse UHE neutrino flux model plus background, *i.e.*, the *signal hypothesis*, *vs.* a signal induced by background only, *i.e.*, the *background-only hypothesis*. We compute the discovery potential via a Bayesian statistical comparison of the two hypotheses, accounting for random statistical fluctuations in the predicted rate of detected events and for uncertainties in key analysis ingredients. Later, in Section 7.6, we use similar methods to distinguish between different neutrino flux models, *i.e.*, between different signal hypotheses.

Because of the degeneracy between the neutrino flux and the νN cross section (Section 7.3), and because both the event rates induced by the signal—*i.e.*, one of the flux models (Section 7.2)—and the background—*i.e.*, atmospheric muons and the UHE tail of the IceCube high-energy neutrino flux (Section 7.4.5)—scale roughly linearly with the cross section (see Eq. (7.1)), in our treatment below we account for the uncertainty on the cross section when computing the flux discovery potential. Reference [346] used similar methods to address the related issue of simultaneously measuring the UHE neutrino flux and the UHE νN cross section.

7.5.1 *Statistical analysis*

For a given choice of UHE neutrino flux model, $\mathcal{M}_{\rm UHE}$, out of models 3–12 in Fig. 26, and for a given choice of the background UHE tail of the IceCube high-energy neutrino flux (Section 7.4.5.2), $\mathcal{M}_{\rm HE}$, we quantify the discovery potential on the basis of a likelihood function binned in reconstructed shower energy and direction. For the signal hypothesis (s+bg), this is

$$\mathcal{L}^{(\rm s+bg)}_{\mathcal{M}_{\rm UHE},\mathcal{M}_{\rm HE}}(\boldsymbol{\theta}) = \prod_{i=1}^{N_{E^{\rm rec}_{\rm sh}}} \prod_{j=1}^{N_{\theta^{\rm rec}_z}} \mathcal{L}^{(\rm s+bg)}_{\mathcal{M}_{\rm UHE},\mathcal{M}_{\rm HE},ij}(\boldsymbol{\theta}) \,, \tag{7.9}$$

and for the background-only hypothesis (bg), this is

$$\mathcal{L}^{(\rm bg)}_{\mathcal{M}_{\rm HE}}(\boldsymbol{\theta}) = \prod_{i=1}^{N_{E^{\rm rec}_{\rm sh}}} \prod_{j=1}^{N_{\theta^{\rm rec}_z}} \mathcal{L}^{(\rm bg)}_{\mathcal{M}_{\rm HE},ij}(\boldsymbol{\theta}) \,, \tag{7.10}$$

In Eqs. (7.9) and (7.10), $\boldsymbol{\theta} \equiv (\log_{10} f_\sigma, \log_{10}(E^{\rm HE}_{\nu,\rm cut}/\rm GeV))$ represents the free parameters on which the neutrino-induced event rate depends, *i.e.*, the νN cross section (Section 7.3), $f_\sigma \equiv \sigma_{\nu N}/\sigma^{\rm std}_{\nu N}$, and the cut-off energy of the background IceCube high-energy neutrino flux (Section 7.4.5.2), $E^{\rm HE}_{\nu,\rm cut}$. The number of bins of $E^{\rm rec}_{\rm sh}$ is $N_{E^{\rm rec}_{\rm sh}}$ and the number of bins of $\cos\theta^{\rm rec}_z$ is $N_{\theta^{\rm rec}_z}$. (Because flux models 1 and 2 represent a particular realization of the background UHE tail of the IceCube high-energy neutrino flux—*i.e.*, one where the cut-off energy $E^{\rm HE}_{\nu,\rm cut} \to \infty$, we forecast their discovery separately from models 3–12, in Section 7.5.2.9. Specifically, for them we only consider as background the atmospheric muons.)

The total likelihood in Eqs. (7.9) and (7.10) is the product of partial likelihoods over all bins of reconstructed energy and direction. The partial likelihood in bin ij compares the predicted (pred) average event rate in the radio component of IceCube-Gen2, computed following the procedure

in Section 7.4.4, *vs.* a particular realization of the observed (obs) event rate, $N_{\text{obs},ij}$. To account for possibly low event rates, we take the partial likelihood to be Poissonian. For the signal hypothesis, it is

$$\mathcal{L}^{(\text{s+bg})}_{\mathcal{M}_{\text{UHE}},\mathcal{M}_{\text{HE}},ij}(\boldsymbol{\theta}) = \frac{N^{(\text{s+bg})}_{\text{pred},ij}(\boldsymbol{\theta})^{N_{\text{obs},ij}} e^{-N^{(\text{s+bg})}_{\text{pred},ij}(\boldsymbol{\theta})}}{N_{\text{obs},ij}!} \,, \tag{7.11}$$

where the predicted event rate, $N^{(\text{s+bg})}_{\text{pred},ij}$, is due to the UHE neutrino flux model being tested (Section 7.2), $N^{\mathcal{M}_{\text{UHE}}}_{\nu,ij}$, the background from the UHE tail of the IceCube high-energy neutrino flux (Section 7.4.5.2), $N^{\mathcal{M}_{\text{HE}}}_{\nu,ij}$, and the background of atmospheric muons (Section 7.4.5.1), $N_{\mu,ij}$, *i.e.*,

$$N^{(\text{s+bg})}_{\text{pred},ij}(\boldsymbol{\theta}) = N^{\mathcal{M}_{\text{UHE}}}_{\nu,ij}(f_\sigma) + N^{\mathcal{M}_{\text{HE}}}_{\nu,ij}(f_\sigma, E^{\text{HE}}_{\nu,\text{cut}}) + N_{\mu,ij} \,. \tag{7.12}$$

Similarly, for the background-only hypothesis, the partial likelihood is

$$\mathcal{L}^{(\text{bg})}_{\mathcal{M}_{\text{HE}},ij}(\boldsymbol{\theta}) = \frac{N^{(\text{bg})}_{\text{pred},ij}(\boldsymbol{\theta})^{N_{\text{obs},ij}} e^{-N^{(\text{bg})}_{\text{pred},ij}(\boldsymbol{\theta})}}{N_{\text{obs},ij}!} \,, \tag{7.13}$$

where the predicted event rate, $N^{(\text{bg})}_{\text{pred},ij}$, is due solely to the background, *i.e.*,

$$N^{(\text{bg})}_{\text{pred},ij}(\boldsymbol{\theta}) = N^{\mathcal{M}_{\text{HE}}}_{\nu,ij}(f_\sigma, E^{\text{HE}}_{\nu,\text{cut}}) + N_{\mu,ij} \,. \tag{7.14}$$

Thus, the likelihood function in Eq. (7.11) represents the probability that the observed event rate is due to the signal hypothesis, computed for a given UHE neutrino flux model $\mathcal{M}_{\text{UHE}}$ out of models 3-12, and the likelihood function in Eq. (7.13) represents the probability that it is due to the background-only hypothesis. Broadly stated, the UHE neutrino flux model will be more easily discoverable when the former is higher than the latter.

When computing the likelihood, Eqs. (7.11)–(7.14), we sample the value of the observed event rate, $N_{\text{obs},ij}$, at random from a Poisson distribution with central value equal to $N^{(\text{s+bg})}_{\text{pred},ij}(\boldsymbol{\theta}^\star)$, where $\boldsymbol{\theta}^\star$ represents the set of real parameter values of the model, *i.e.*, $f_\sigma = 1$ and $E^{\text{HE}}_{\nu,\text{cut}}$ fixed at a value between 10^7 and 10^{12} GeV, with the specific value depending on the scenario we are testing. To account for statistical fluctuations, we perform the sampling many times. We elaborate on this below.

For the signal hypothesis, the posterior probability distribution associated to the likelihood in Eq. (7.9) is

$$\mathcal{P}^{(\text{s+bg})}_{\mathcal{M}_{\text{UHE}},\mathcal{M}_{\text{HE}}}(\boldsymbol{\theta}) = \frac{\mathcal{L}^{(\text{s+bg})}_{\mathcal{M}_{\text{UHE}},\mathcal{M}_{\text{HE}}}(\boldsymbol{\theta})\pi(\boldsymbol{\theta})}{\mathcal{Z}^{(\text{s+bg})}_{\mathcal{M}_{\text{UHE}},\mathcal{M}_{\text{HE}}}} \,, \tag{7.15}$$

where $\pi(\boldsymbol{\theta}) \equiv \pi(\log_{10} f_\sigma)\pi(\log_{10}(E^{\rm HE}_{\nu,{\rm cut}}/{\rm GeV}))$ is the prior on the model parameters; we expand on them in Section 7.5.2. The normalization factor in Eq. (7.15),

$$\mathcal{Z}^{(\rm s+bg)}_{\mathcal{M}_{\rm UHE},\mathcal{M}_{\rm HE}} = \int d\boldsymbol{\theta} \mathcal{L}^{(\rm s+bg)}_{\mathcal{M}_{\rm UHE},\mathcal{M}_{\rm HE}}(\boldsymbol{\theta})\pi(\boldsymbol{\theta}) \,, \tag{7.16}$$

is the statistical evidence, *i.e.*, the likelihood fully marginalized over the space of model parameters. For the background-only hypothesis, the posterior and evidence, $\mathcal{P}^{(\rm bg)}_{\mathcal{M}_{\rm HE}}$ and $\mathcal{Z}^{(\rm bg)}_{\mathcal{M}_{\rm HE}}$, are computed as in Eqs. (7.15) and (7.16), but using $\mathcal{L}^{(\rm bg)}_{\mathcal{M}_{\rm HE}}$ instead, *i.e.*,

$$\mathcal{P}^{(\rm bg)}_{\mathcal{M}_{\rm HE}}(\boldsymbol{\theta}) = \frac{\mathcal{L}^{(\rm bg)}_{\mathcal{M}_{\rm HE}}(\boldsymbol{\theta})\pi(\boldsymbol{\theta})}{\mathcal{Z}^{(\rm bg)}_{\mathcal{M}_{\rm HE}}} \tag{7.17}$$

and

$$\mathcal{Z}^{(\rm bg)}_{\mathcal{M}_{\rm HE}} = \int d\boldsymbol{\theta} \mathcal{L}^{(\rm bg)}_{\mathcal{M}_{\rm HE}}(\boldsymbol{\theta})\pi(\boldsymbol{\theta}) \,. \tag{7.18}$$

We report the discovery potential of the UHE neutrino flux model $\mathcal{M}_{\rm UHE}$ via the ratio of the statistical evidence of the signal and background-only hypotheses, *i.e.*, the *discovery* Bayes factor,

$$\mathcal{B}^{\rm disc}_{\mathcal{M}_{\rm UHE},\mathcal{M}_{\rm HE}} = \frac{\mathcal{Z}^{(\rm s+bg)}_{\mathcal{M}_{\rm UHE},\mathcal{M}_{\rm HE}}}{\mathcal{Z}^{(\rm bg)}_{\mathcal{M}_{\rm HE}}} \,. \tag{7.19}$$

The Bayes factor represents the preference for the signal hypothesis over the background-only hypothesis. Following convention, we ascribe qualitative significance to its value using Jeffreys' table [377]: $10^0 \leq \mathcal{B} < 10^{0.5}$ represents negligible evidence for the signal hypothesis; $10^{0.5} \leq \mathcal{B} < 10^1$, moderate evidence; $10^1 \leq \mathcal{B} < 10^{1.5}$, strong evidence; $10^{1.5} \leq \mathcal{B} < 10^2$, very strong evidence; and $\mathcal{B} \geq 10^2$, decisive evidence. In our discussion below we focus mainly on flux discovery with decisive evidence.

To compute the statistical evidence, we use UltraNest [378], an efficient Bayesian nested-importance sampler [379, 380]. UltraNest integrates Eqs. (7.16) and (7.18) numerically and reports the result of each as $\ln \mathcal{Z} \pm \Delta \ln \mathcal{Z}$, where $\Delta \ln \mathcal{Z}$ is the numerical error of the integral. With it, we compute the numerical error on the Bayes factor in Eq. (7.19) as

$$\Delta \ln \mathcal{B}^{\rm disc}_{\mathcal{M}_{\rm UHE},\mathcal{M}_{\rm HE}} = \sqrt{\left(\Delta \ln \mathcal{Z}^{(\rm s+bg)}_{\mathcal{M}_{\rm UHE},\mathcal{M}_{\rm HE}}\right)^2 + \left(\Delta \ln \mathcal{Z}^{(\rm bg)}_{\mathcal{M}_{\rm HE}}\right)^2} \,. \tag{7.20}$$

For a given choice of UHE neutrino flux model, $\mathcal{M}_{\rm UHE}$, and background high-energy neutrino flux, $\mathcal{M}_{\rm HE}$, we account for the effect of random statistical fluctuations in the observed event rate by repeating the above procedure $N_{\rm samples} = 10^4$ times. Each time, we draw a different random

realization of the distribution of the observed event rate across all bins, $N_{\mathrm{obs},ij}$, as explained above. For each random realization, we compute the discovery Bayes factor and its error as in Eqs. (7.16) and (7.20).

Below, when presenting results, the value of the Bayes factor that we report is always the average over all random realizations, $\langle \log_{10} \mathcal{B}^{\mathrm{disc}}_{\mathcal{M}_{\mathrm{UHE}},\mathcal{M}_{\mathrm{HE}}} \rangle$. Specifically, it is the weighted arithmetic mean of $\log_{10} \mathcal{B}^{\mathrm{disc}}_{\mathcal{M}_{\mathrm{UHE}},\mathcal{M}_{\mathrm{HE}}}$ (equal to the weighted geometric mean of $\mathcal{B}^{\mathrm{disc}}_{\mathcal{M}_{\mathrm{UHE}},\mathcal{M}_{\mathrm{HE}}}$), *i.e.*,

$$\langle \log_{10} \mathcal{B}^{\mathrm{disc}}_{\mathcal{M}_{\mathrm{UHE}},\mathcal{M}_{\mathrm{HE}}} \rangle = \frac{1}{\ln 10} \frac{\sum_{i=1}^{N_{\mathrm{samples}}} w_i \ln \mathcal{B}^{\mathrm{disc}}_{\mathcal{M}_{\mathrm{UHE}},\mathcal{M}_{\mathrm{HE}},i}}{\sum_{i=1}^{N_{\mathrm{samples}}} w_i} \,, \tag{7.21}$$

where $\mathcal{B}^{\mathrm{disc}}_{\mathcal{M}_{\mathrm{UHE}},\mathcal{M}_{\mathrm{HE}},i}$ is the Bayes factor computed in the i-th random realization and the weight, w_i, is

$$w_i = \left(\Delta \ln \mathcal{B}^{\mathrm{disc}}_{\mathcal{M}_{\mathrm{UHE}},\mathcal{M}_{\mathrm{HE}},i} \right)^{-2} \,, \tag{7.22}$$

where $\Delta \ln \mathcal{B}^{\mathrm{disc}}_{\mathcal{M}_{\mathrm{UHE}},\mathcal{M}_{\mathrm{HE}},i}$ is the error on the Bayes factor computed in the same realization. (Computing the weighted arithmetic mean of $\log_{10} \mathcal{B}^{\mathrm{disc}}_{\mathcal{M}_{\mathrm{UHE}},\mathcal{M}_{\mathrm{HE}}}$, instead of the weighted arithmetic mean of $\mathcal{B}^{\mathrm{disc}}_{\mathcal{M}_{\mathrm{UHE}},\mathcal{M}_{\mathrm{HE}}}$, avoids the bias that the mean Bayes factor would otherwise have towards non-representative large values resulting from the pull of the relatively few random realizations that yield significantly larger Bayes factors.) In Appendix B.4 we comment on the spread of the distribution of values of the Bayes factor obtained from the different random realizations of the observed event rate, and how much they may deviate from the mean value.

In some cases scenarios, the sum of the UHE tail of the IceCube high-energy neutrino flux plus the UHE flux model 3–12 may exceed the present-day experimental upper limits from IceCube and Auger shown in Fig. 26. However, those limits were derived assuming a fixed value of the UHE neutrino-nucleon cross section while in our analysis the cross section is a free parameter with a wide prior around its standard prediction. This means that for choices of the cross section that are different from the ones used by IceCube and Auger in computing their limits, those limits need not apply to our results. Beyond that, we do not attempt to incorporate the lack of observation of UHE neutrinos by IceCube and Auger in our analysis, since doing so would required modeling those two detectors to compute event rates for each of our flux predictions, which is beyond the scope of this work.

Parameter	Baseline analysis choice		
	Description	Location in text of results	
		Flux discovery	Flux separation
Atmospheric muon background (Section 7.4.5.1)	SYBILL 2.3C, mitigated by surface veto	Section 7.5.2.2 Fig. 25	Section 7.6.2 Fig. 38
Background UHE tail of the IceCube high-energy neutrino flux, $\mathcal{M}_{\mathrm{HE}}$ (Section 7.4.5.2)	*Hard flux*: UHE extrapolation of the flux from 9.5-yr IceCube track analysis ($\gamma = 2.37$)	Section 7.5.2.2 Fig. 25	Section 7.6.2 Fig. 38
Prior on the cut-off energy of the UHE tail of the IceCube high-energy ν flux, $E^{\mathrm{HE}}_{\nu,\mathrm{cut}}$ (Section 7.4.5.2)	Flat prior on $\log_{10}(E^{\mathrm{HE}}_{\nu,\mathrm{cut}}/\mathrm{GeV})$ between 5 and 12, followed by averaging of Bayes factor over $E^{\mathrm{HE}}_{\nu,\mathrm{cut}}$	Section 7.5.2.2 Fig. 25	Section 7.6.2 Fig. 38
Prior on the neutrino-nucleon cross section, f_σ (Section 7.3)	Flat prior on $\log_{10} f_\sigma$ from -1 to 2	Section 7.5.2.2 Fig. 25	Section 7.6.2 Fig. 38
Detector energy resolution, σ_ϵ, and angular resolution, σ_{θ_z} (Section 7.4.4)	$\sigma_\epsilon = 0.1$ $\sigma_{\theta_z} = 2^\circ$	Section 7.5.2.2 Fig. 25	Section 7.6.2 Fig. 38

Table 4: Baseline analysis choices used to forecast the flux discovery potential (Section 7.5) and flux model separation (Section 7.6) in the radio array of IceCube-Gen2, and location in the text of corresponding results. See Section 7.5.2.1 for an overview and Table 5 for alternative choices.

7.5.2 *Results*

7.5.2.1 *Baseline analysis choices*

Section 7.5.2.2 shows our main results for the flux discovery potential. To produce them, we adopt baseline analysis choices for the atmospheric muon background, the high-energy neutrino background, including the prior on the value of its cut-off energy, the detector energy and angular resolution, and the prior on the neutrino-nucleon cross section. (Later, in Section 7.6, when comparing flux models, we keep the same baseline choices.) *Our baseline analysis choices, chosen to be largely conservative, lead to promising results for the flux discovery potential.*

Sections 7.5.2.3–7.5.2.6 show results obtained under well-motivated alternative analysis choices. Different alternative choices may expedite or delay decisive flux discovery, but do not change our main conclusion: fluxes that may be discovered within 20 years of exposure time under the baseline analysis choices remain discoverable.

Parameter	Alternative analysis choices		
	Description	Location in text of results	
		Flux discovery	Flux separation
Atmospheric muon background (Section 7.4.5.1)	Baseline $\times 10$, $\times 100$, $\times 1000$	Section 7.5.2.3 Fig. 30	–
Background UHE tail of the IceCube high-energy neutrino flux, $\mathcal{M}_{\rm HE}$ (Section 7.4.5.2)	*Soft flux*: UHE extrapolation of the 7.5-yr IceCube HESE flux ($\gamma = 2.87$) / *Intermediate flux*: $\gamma = 2.50$	Section 7.5.2.4 Figs 31 and B1	Appendix B.1 Fig. B2
Prior on the cut-off energy of the UHE tail of the IceCube high-energy ν flux, $E^{\rm HE}_{\nu,{\rm cut}}$ (Section 7.4.5.2)	Wide Gaussian prior and delta-function prior centered on $\log_{10}(E^{\rm HE}_{\nu,{\rm cut}}/{\rm GeV}) = 8$	Section 7.5.2.5 Fig. 32	–
Prior on the neutrino-nucleon cross section, f_σ (Section 7.3)	Wide Gaussian prior and delta-function prior centered on central value of BGR18 prediction, $\log_{10} f_\sigma = 0$	Section 7.5.2.6 Fig. 33	–
Detector energy resolution, σ_ϵ, and angular resolution, σ_{θ_z} (Section 7.4.4)	$\sigma_\epsilon = 0.5, 1.0$ $\sigma_{\theta_z} = 5^\circ, 10^\circ$	Section 7.5.2.7 Figs. 34, B3, B4	Appendix B.2 Figs. B5 and B6

Table 5: Alternative analysis choices used to forecast the flux discovery potential (Section 7.5) and flux model separation (Section 7.6) in the radio array of IceCube-Gen2, and location in the text of associated content. See Section 7.5.2.1 for an overview and Table 4 for baseline choices.

Tables 4 and 5 summarize our baseline and alternative analysis choices, and show where in the text to find associated content. Below we elaborate on our choices:

- *Atmospheric muon background*: Our baseline choice is the event rate computed using the hadronic interaction model SYBILL 2.3C, mitigated by applying a surface veto [214]; see Section 7.4.5 for details. Section 7.5.2.3 shows results obtained under a substantially larger atmospheric muon background; with them, the discovery potential shrinks only mildly.

- *Background UHE tail of the IceCube high-energy neutrino flux, $\mathcal{M}_{\rm HE}$*: Our baseline choice is to adopt a flux motivated by the 9.5-year IceCube through-going track analysis [37] introduced in Section 7.4.5.2. This choice is conservative because, due to its hard spectral index ($\gamma = 2.37$), this flux may extend to higher energies compared to alternative, softer spectra, and so yields a larger background to the discovery of UHE neutrino flux models 3–12. Section 7.5.2.4 shows results for the less conservative, softer high-energy neutrino spectra introduced in Section 7.4.5.2, motivated by alternative IceCube results; with them, the discovery potential improves appreciably.

- *Prior on the cut-off energy of the UHE tail of the IceCube high-energy neutrino flux background, $E^{\rm HE}_{\nu,\rm cut}$*: Our baseline choice for $\pi(\log_{10}(E^{\rm HE}_{\nu,\rm cut}/\text{GeV}))$ in Eq. (7.16) is a flat distribution between $\log_{10}(E^{\rm HE}_{\nu,\rm cut}/\text{GeV}) = 7$ and 12. In addition, in our baseline analysis we average the mean Bayes factor, Eq. (7.21), over all possible real values of $\log_{10}(E^{\rm HE}_{\nu,\rm cut}/\text{GeV})$, and report the result of that. These choices of prior and averaging are conservative and reflect our present-day ignorance on the existence and position of a cut-off in the IceCube high-energy neutrino flux. Section 7.5.2.4 shows results obtained using alternative, informed priors that reflect possible evidence of a cut-off found in upcoming measurements of the high-energy neutrino flux; with them, the discovery potential improves significantly.

- *Prior on the neutrino-nucleon cross section, f_σ*: Our baseline choice for $\pi(\log_{10} f_\sigma)$ in Eq. (7.16) is a flat distribution between $\log_{10} f_\sigma = -1$ and 2. This choice is conservative because it ignores the pull from theory towards the central value of the BGR18 [194] prediction, *i.e.*, towards $\log_{10} f_\sigma = 0$, when fitting to mock data. (Nevertheless, we always use $\log_{10} f_\sigma = 0$ as the true value to generate the mock observed event rate against which we fit; see Section 7.5.1.) Our choice of a baseline wide prior reflects the current lack of direct measurement of the UHE neutrino-nucleon cross section. Such a wide prior may even encompass new-physics modifications to the cross section (see, *e.g.*, Ref. [61]); the fact that it may be possible to discover most flux models even under such a loose prior (Fig. 25) is encouraging. Section 7.5.2.6 shows results for alternative informed priors on $\log_{10} f_\sigma$; their use expedites decisive flux discovery by up to a factor of roughly 3 compared to the baseline expectation, depending on the flux model.

- *Detector energy resolution, σ_ϵ, and angular resolution, σ_{θ_z}*: Our baseline choices for the resolution on the reconstructed shower energy and reconstructed zenith angle are, respectively, $\sigma_\epsilon = 0.1$ and $\sigma_{\theta_z} = 2^\circ$. These choices are motivated by dedicated simulations [212, 312, 314, 315, 317, 324, 326, 370]; see Section 7.4.4 for details. The detector energy and angular resolution affect the event rate computed via Eq. (7.5) and determine the energy and angular binning used to compute the likelihood, Eqs. (7.9) and (7.10). For the baseline energy binning, we use 12 bins equally spaced in logarithmic scale from $E^{\rm rec}_{\rm sh} = 10^7$ GeV to 10^{10} GeV. For the angular binning, we use a single large bin for downgoing events, from $\theta^{\rm rec}_z = 0^\circ$ to 80°; 10 bins of

size 2° from 80° to 100°; and two large bins for upgoing events, one from 100° to 110°, and another one from 110° to 180°. Section 7.5.2.7 shows results for alternative choices of poorer detector resolution, and their associated binning; with them, the discovery potential shrinks for poorer energy resolution—mainly because of features in the energy spectrum become unresolved—and for poorer angular resolution—mainly because the uncertainty in the νN cross section is allowed to have a larger impact.

We keep the design of the IceCube-Gen2 radio array fixed to the baseline design of Ref. [77], as described in Section 7.4.3. We describe the detector response via the energy- and direction-dependent effective volumes generated from dedicated simulations of radio generation, propagation, and detection from Ref. [346]; see Section 7.4.4 and Ref. [346] for details. We adopt this detector design to make concrete forecasts, but the final design remains under consideration at the time of writing.

We do not explore alternative detector designs in our forecasts, since doing so requires running intensive simulations for each design choice. However, we discuss detector-related features that may inform the design of upcoming detectors: the impact of detector energy and angular resolution (Section 7.5.2.7), the importance of the detector response being sensitive to Earth-skimming neutrinos (Section 7.5.2.8), and the impact of using an air-shower surface array veto to mitigate the atmospheric muon background (Appendix B.3).

7.5.2.2 *Baseline discovery potential of the benchmark UHE neutrino flux models*

Even under conservative analysis choices, IceCube-Gen2 should be able to claim decisive evidence for the discovery of most of the benchmark UHE neutrino fluxes models after one decade of operation.

Figure 25 shows our main result: the evolution with exposure time of the mean discovery Bayes factor in the radio array of IceCube-Gen2, for the UHE neutrino flux models 1–12 from Fig. 26, computed as detailed in Section 7.5.1 and under our baseline analysis choices from Section 7.5.2.1. The figure reveals promising prospects, in spite of our baseline analysis choices being conservative. Alternative, less conservative choices of background and priors may hasten discovery; we explore them later. For flux models 3–12, we include as background of atmospheric muons and the UHE tail of the IceCube high-energy neutrino spectrum; see Section 7.5.1. For flux models 1 and 2—

unbroken UHE extrapolations of the IceCube TeV–PeV neutrino flux [37, 188]—we include only the background of atmospheric muons; see Section 7.5.2.9.

Figure 25 sorts flux models 1–12 into three classes, depending on the time it takes for them to be discovered with decisive evidence: models discoverable within 1 year (models 2, 4, 6, 9, 11), models discoverable in 1–10 years (models 7, 8, 10, 12), and models that are not discoverable within 20 years (models 3 and 5). Flux model 1, the UHE extrapolation of the 7.5-year IceCube HESE flux [188], can be discovered with very strong evidence after 20 years. This classification conveys in detail what Fig. 26 shows roughly: fluxes above the IceCube-Gen2 sensitivity are discoverable within 10 years; fluxes below are not. Lowering the discovery threshold to “very strong" or “strong" evidence expedites flux discovery; however, fluxes that are not discoverable remain as such.

At short exposure times, the predicted event rate, made up of signal plus background events, Eq. (7.12), for most benchmark UHE neutrino flux models is low and observations are compatible with the background-only hypothesis. (The exception is flux model 4, the highest among all benchmark models, which is compatible with the signal hypothesis even at short exposure times.) With growing exposure time, the larger predicted event rates enhance the contrast between the alternative hypothesis. Then the observations become more compatible with the signal hypothesis in our statistical analysis; see Section 7.5.1 for details.

The growth rate of the flux discovery Bayes factor in Fig. 25 results from the interplay of two factors: the size of the predicted event rate, integrated across all energies and directions, induced by the UHE neutrino flux model—*i.e.*, larger rates lead to larger Bayes factors—and the shape of the event rate induced by the UHE neutrino flux model—*i.e.*, flux models whose energy spectrum peaks at high energies, far from the background concentrated at $E_{\rm sh}^{\rm rec} \lesssim 10^8$ GeV (see Fig. 27), lead to larger Bayes factors. This explains the difference in the growth rate of the Bayes factor in Fig. 25 at short and long exposure times. We elaborate below.

At short exposure times, Fig. 25 shows that the Bayes factor grows fast. There, the growth is dominated by the notable difference between the energy distributions of the event rates induced by the signal and the background; see Fig. 27. Differences between their angular distributions are smaller and contribute weakly to the growth rate; see Fig. 28. Because our analysis is binned

in energy and direction (see the likelihood functions in Eqs. (7.9) and (7.10)), it is able to resolve differences in the energy distributions of the signal hypothesis *vs.* the background-only hypothesis even if their associated events rate are low, *i.e.*, even at low exposure times. [For flux models 10 and 12, whose energy spectra peak at lower energies, closer to the background, the Bayes factor grows more slowly because distinguishing between them is harder. This subtle feature is most clearly seen by comparing flux models 10 and 11: their integrated event rates are similar (see Table 3), but the rate for flux model 10 peaks at significantly lower energies than for flux model 11 (see Fig. 27).]

At longer exposure times, Fig. 25 shows that the Bayes factor grows more slowly. There, the growth rate is dominated by the large difference in integrated event rate induced by the signal and by the background; see Table 3. At large exposure times, the posterior distributions, Eqs. (7.15) and (7.17), become narrow due to the lessening of the impact of random statistical fluctuations. As a result, the Bayes factor, Eq. (7.19), is dominated by the peak value of the posteriors. The event rate, $N_{\mathrm{obs},ij}$, grows linearly with time for all flux models; see Eq. (7.4). Therefore, the logarithm of the likelihood function, Eq. (7.11), also grows linearly with time, and so does the logarithm of the discovery Bayes factor, Eq. (7.19), as seen in Fig. 25. (For flux model 12, this growth regime is reached beyond 20 years, so it is not seen in Fig. 25.)

Figure 29 illustrates the roles that binning events in reconstructed energy and direction have on the UHE neutrino flux discovery potential. Binning in energy allows our statistical analysis to distinguish between the energy distributions of events induced by the UHE neutrino flux model *vs.* events induced by the atmospheric muon background—which are concentrated at low energies—and by the UHE tail of the IceCube high-energy neutrino flux—when it has a low cut-off energy, $E^{\mathrm{HE}}_{\nu,\mathrm{cut}}$, compared to the energy at which the UHE neutrino flux model 3–12 peaks. Binning in direction allows our statistical analysis to break the innate degeneracy between neutrino flux and cross section described in Section 7.3 and, by doing so, to claim a higher evidence for the discovery of the UHE neutrino flux model 3–12. This is especially true when using a flat prior on the cross section, *i.e.*, when there is little to no knowledge of the cross section and, thus, a larger degeneracy with the neutrino flux; see Section 7.5.2.6.

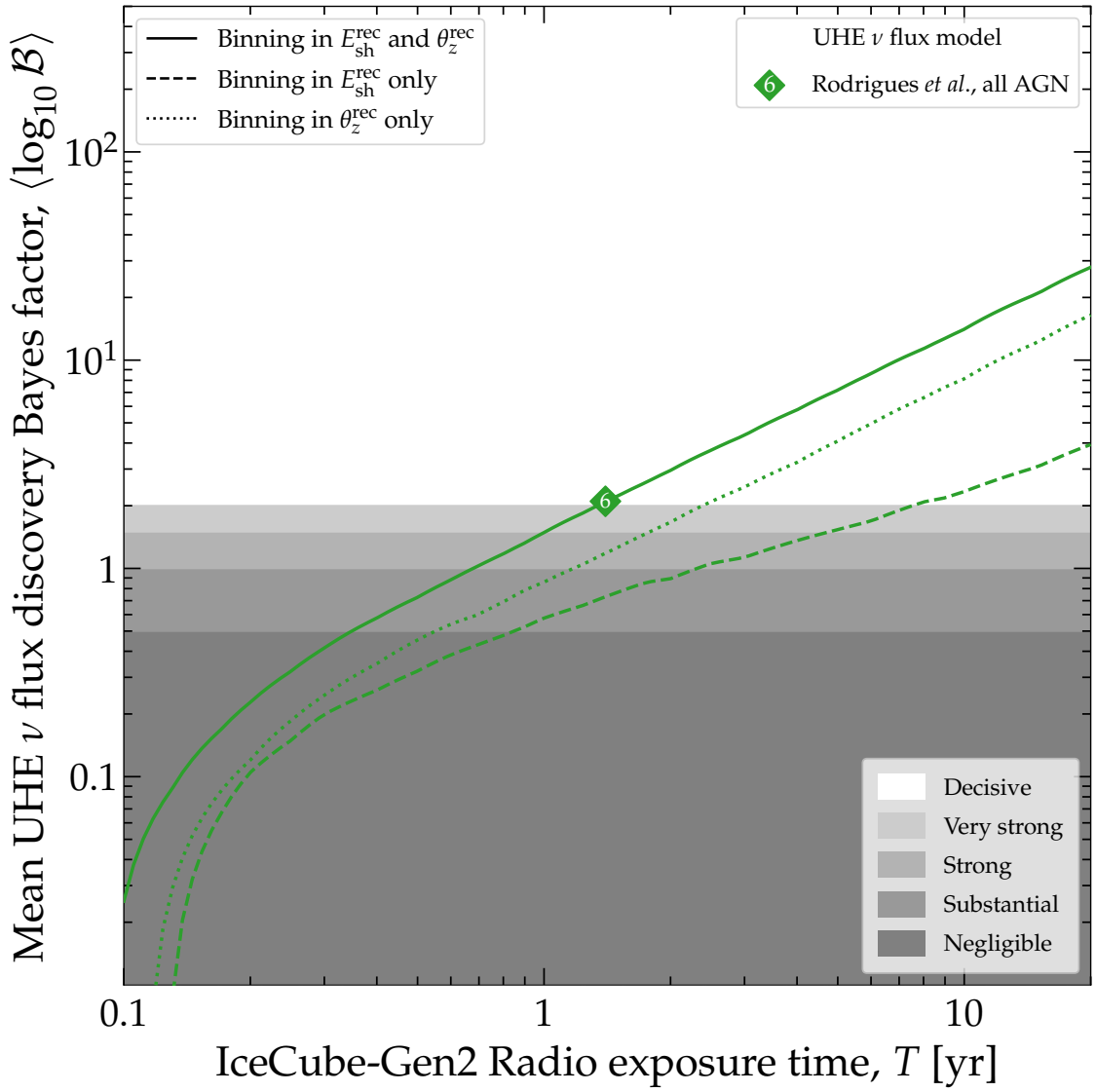

Figure 29: Impact of binning the detected events only in reconstructed shower energy, E_{sh}^{rec}, only in reconstructed direction, θ_z^{rec}, and in both, on the discovery potential of the UHE neutrino flux model 6 [179]. Results are for our conservative baseline assumption of a flat prior on the νn cross section, f_σ—representing little to no prior knowledge of the cross section. *In the absence of precise knowledge of the νN cross section, early flux discovery hinges on using both the energy and, especially, angular distribution of events.* See Section 7.5.2.2 for details.

7.5.2.3 *Impact of the atmospheric muon background*

The UHE flux discovery potential of IceCube-Gen2 is robust against large uncertainties in the predicted size of the muon background, because it is concentrated mainly at the lowest energies, i.e., $E_{sh}^{rec} \lesssim 10^8$ GeV.

Figure 30 shows that artificially increasing the size of the atmospheric muon background only impacts mildly the UHE neutrino flux discovery potential. (We comment on the impact of changes to the shape of the energy spectrum of the atmospheric muon background later.) To single out

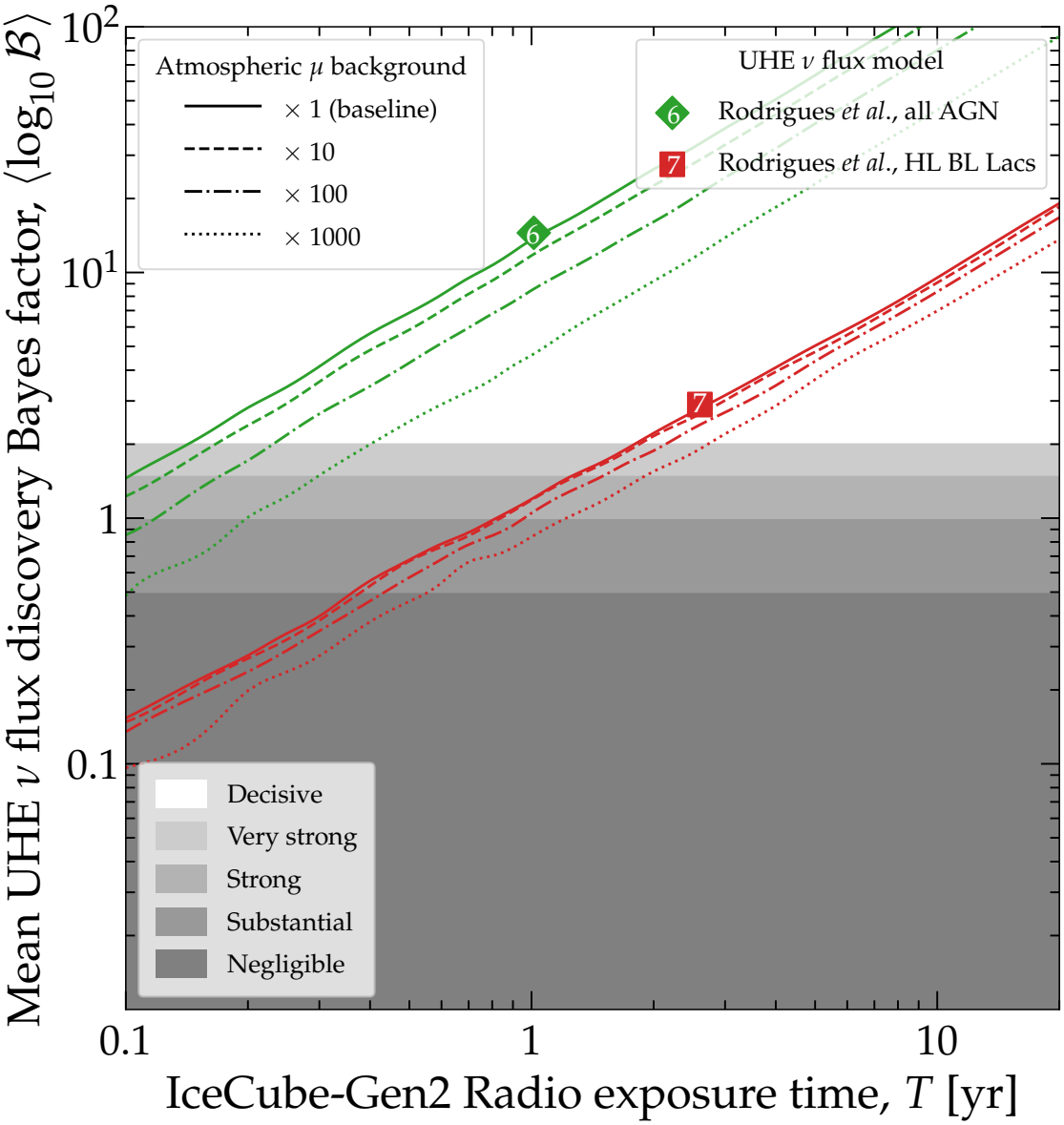

Figure 30: Impact of an enlarged atmospheric muon background on the flux discovery potential of UHE neutrino flux models 6 and 7 [179]; see Fig. 26. Results for other flux models are similar. For this plot only, the cut-off energy of the high-energy neutrino flux background is fixed at $E^{\mathrm{HE}}_{\nu,\mathrm{cut}} = 10$ PeV, so that the main background is from atmospheric muons. All other analysis choices are baseline; see Table 4 and Section 7.5.2.1. *Even a thousand-fold increase in the muon background over its baseline expectation reduces the discovery potential only mildly.* See Section 7.5.2.3 for details.

the impact of the atmospheric muon background, in Fig. 30 we mitigate the contribution to the background from the UHE tail of the IceCube high-energy flux by fixing its cut-off energy to a relatively low value of $E^{\mathrm{HE}}_{\nu,\mathrm{cut}} = 10$ PeV. (In most other results, we let the value of $E^{\mathrm{HE}}_{\nu,\mathrm{cut}}$ float generously; see Section 7.5.2.1.) Even a hefty thousand-fold increase in the muon background over its baseline expectation (see Section 7.4.5), which yields an integrated mean yearly rate of fewer than 100 detected muon events, only delays discovery of flux model 6 [179] by about three

months and of flux model 7 [179] by about one year. The illustrative choice of $E^{\rm HE}_{\nu,{\rm cut}} = 10$ PeV is conservative: a higher value would increase the contribution of the UHE tail of the IceCube high-energy neutrino flux to the background and reduce the relative contribution of the muon background, weakening further its impact on the flux discovery potential.

The mild impact that a larger muon background has on the flux discovery potential is due to the difference in the energy and angular distributions of events induced by the muon background and events induced by a UHE neutrino flux model 3–12; see Figs. 27 and 28. Events induced by the muon background lie at low energies, $E^{\rm rec}_{\rm sh} \lesssim 10^8$ GeV, and above the horizon, but not in downgoing directions, *i.e.*, they lie at $0 \lesssim \cos\theta^{\rm rec}_z \lesssim 0.8$. In contrast, events induced by the UHE neutrino flux reach higher energies, may be downgoing, but may also come from just below the horizon, especially if the flux is large. Because our analysis (Section 7.5.1) is binned in energy and direction, it is sensitive to the above differences in the distributions, which renders the flux discovery potential largely insensitive to increases in the size of the muon background.

The flux discovery potential is robust to changes in the size of the atmospheric muon background, but may not be so to changes in the shape of its event energy distribution. In particular, a muon-induced event energy distribution that extends to $E^{\rm rec}_{\rm sh} \gtrsim 10^8$ GeV would hinder the discovery of flux models that peak at neutrino energies above 10^8 GeV that, under our baseline choice for the muon background, are expected to be discoverable.

We have checked that replacing our baseline muon background, produced using the SYBILL 2.3C [293] hadronization model, with the central value of the predicted muon backgrounds computed in Ref. [213] using the EPOS-LHC [381] or QGSJET-II-04 [382] hadronization models, has negligible impact on the flux discovery potential. However, that exploration is not exhaustive, and may not be representative of all possible variations in the shape of the muon-induced event energy spectrum. Hence, analyses beyond the scope of this work should account, within their statistical procedures, for the impact that the systematic uncertainties in the hadronization model, and in the size, shape, and mass composition of the parent UHECR energy spectrum have on the energy spectrum of atmospheric muons. Reference [188] contains a recent implementation of this in an IceCube analysis.

In reality, a factor-of-100 or factor-of-1000 underestimation of the muon background, like the ones in Fig. 30, is unlikely. However, such a large contribution could come from other, non-muon and non-neutrino backgrounds, like air-shower cores; see Section 7.4.5.3 for details. Its size and shape are presently uncertain, but it may conceivably extend to higher energies than the muon background; see Ref. [327] for early estimates. What Fig. 30 suggests is that, even in such a case, a non-neutrino background that is relatively well characterized in energy and direction, even if large in size, may have limited impact on the UHE neutrino flux discovery potential.

7.5.2.4 *Impact of the background UHE tail of the IceCube high-energy neutrino flux, $\mathcal{M}_{\rm HE}$*

The UHE neutrino flux discovery potential of IceCube-Gen2 may be enhanced significantly if the background from the UHE tail of the IceCube high-energy neutrino flux is small, i.e., if its energy spectrum is soft and consistent with the IceCube 9.5-year HESE analysis.

Figure 31 shows the impact on the flux discovery potential of the radio array of IceCube-Gen2 of adopting a different choice for the UHE tail of the IceCube high-energy neutrino background (Section 7.4.5.2). These are extrapolations to ultra-high energies of the power-law neutrino fluxes measured by IceCube in the TeV–PeV range, suppressed by a high-energy cut-off, *i.e.*, $\propto E_\nu^{-\gamma} e^{-E_\nu/E_{\nu,\rm cut}^{\rm HE}}$, following Eq. (7.7). We compare the three possibilities introduced in Section 7.4.5.2: our baseline choice of a hard spectrum (spectral index of $\gamma = 2.37$) motivated by the 9.5-year IceCube through-going ν_μ analysis [37], an intermediate spectrum ($\gamma = 2.50$) with the same flux normalization, and a soft spectrum ($\gamma = 2.87$) motivated by the 7.5-year IceCube HESE analysis [188]. Here we study the impact of the choice of the normalization and spectral index of the background neutrino flux; in Section 7.5.2.5, we study the impact of our degree of ignorance of $E_{\nu,\rm cut}^{\rm HE}$.

Figure 31 shows that using the softer spectrum may expedite decisive flux discovery significantly: for flux models 6 and 7, decisive discovery is reduced roughly from 1.3 and 13 years, respectively, to 4 months and 1.2 years. This is because a softer UHE tail of IceCube high-energy neutrino flux corresponds to a lower background. Figure 31 also shows that the improvement stems predominantly from the shape of the spectrum, rather than from its size, *viz.*, when comparing the results using the hard and intermediate background spectra, which share the same flux normalization (see Section 7.4.5.2).

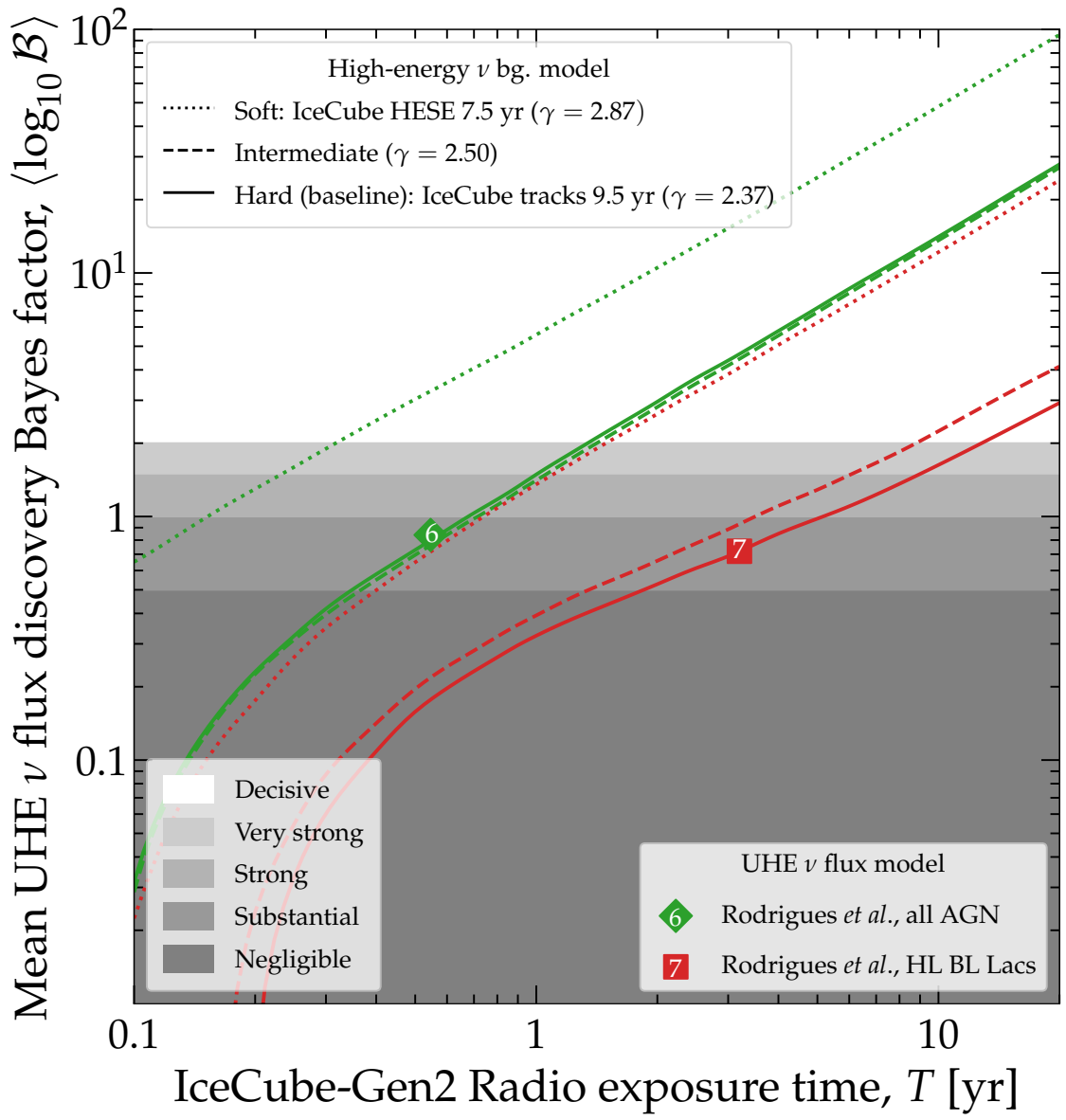

Figure 31: Impact of the choice of high-energy neutrino flux, whose UHE tail constitutes a potential background at ultra-high energies, on the flux discovery potential of UHE neutrino flux models 6 and 7 [179]; see Fig. 26. All other analysis choices are baseline; see Table 4 and Section 7.5.2.1. The hard and soft background fluxes are UHE extrapolations of the IceCube through-going track [37] and HESE [188] results, respectively; we also show an intermediate case. In all cases, the background flux has a high-energy exponential cut-off; see Section 7.4.5. Results for other flux models are similar. *A softer UHE tail of the high-energy neutrino flux background may expedite the discovery of an UHE flux model appreciably, by months or years.* See Section 7.5.2.4 for details.

Changes to the background UHE tail of the IceCube high-energy neutrino flux differ from changes to the atmospheric muon background (Section 7.5.2.3) mainly in two aspects. First, if the cut-off energy is known to be $E^{\mathrm{HE}}_{\nu,\mathrm{cut}} \gtrsim 10^8$ GeV or if, as in our baseline treatment, its value is unknown but allowed to be possibly high, then the UHE tail of the IceCube high-energy neutrino

flux constitutes the dominant background contribution; see Section 7.4.5. Therefore, changes to it naturally affect the flux discovery potential significantly.

Second, unlike the atmospheric muon background, the background from the UHE tail of the IceCube high-energy neutrino flux depends on the νN cross section, *i.e.*, on f_σ. Because our baseline analysis allows the value of f_σ to float (Section 7.5.2.1), this grants the UHE tail of the IceCube high-energy neutrino flux, when computed under the background-only hypothesis, the freedom to find values of f_σ with which it can reproduce closely the observed rate (supplemented, at low energies, by the sub-dominant atmospheric muon background). (Section 7.5.2.6 explains in detail how a larger or smaller cross section affects internally the statistical analysis.) Letting the value of f_σ float leads to larger values of the posterior and evidence in the background-only hypothesis, Eqs. (7.17) and (7.18), and, consequently, lower values of the Bayes factor, Eq. (7.19), and to a longer exposure time required to claim decisively the discovery of a given UHE neutrino flux model 3–12. In Section 7.5.2.6 we explore how the impact of the IceCube high-energy neutrino flux is reduced by more precise prior knowledge of f_σ.

7.5.2.5 *Impact of the prior on the cut-off energy of the UHE tail of the IceCube high-energy neutrino flux background*, $E^{\rm HE}_{\nu,{\rm cut}}$

The UHE neutrino flux discovery potential of IceCube-Gen2 may be significantly enhanced by even limited knowledge of the ultra-high-energy tail end of the high-energy neutrino flux, i.e., of its cut-off energy.

Figure 32 shows the impact that the choice of prior on the cut-off energy of the background UHE tail of the IceCube high-energy neutrino flux, $\pi(\log_{10}(E^{\rm HE}_{\nu,{\rm cut}}/{\rm GeV}))$ in Eqs. (7.15)–(7.18), has on the UHE neutrino flux discovery potential. We compare results obtained using our conservative baseline analysis choice of a flat prior, followed by an average of the Bayes factor over the real value of the cut-off energy (see Section 7.5.2.1), against results obtained using two alternative, informed priors: a wide Gaussian prior and a Dirac δ-function prior. These alternatives reflect, respectively, the possible outcome of limited and precise measurement of the tail end of the high-energy neutrino flux by present and future TeV–PeV neutrino telescopes, *e.g.*, IceCube, IceCube-Gen2 [39], via its optical array, KM3NeT [40], Baikal-GVD [147], P-ONE [41], TAMBO [73], TRIDENT [148], Trinity [355], or a combination of detectors [78].

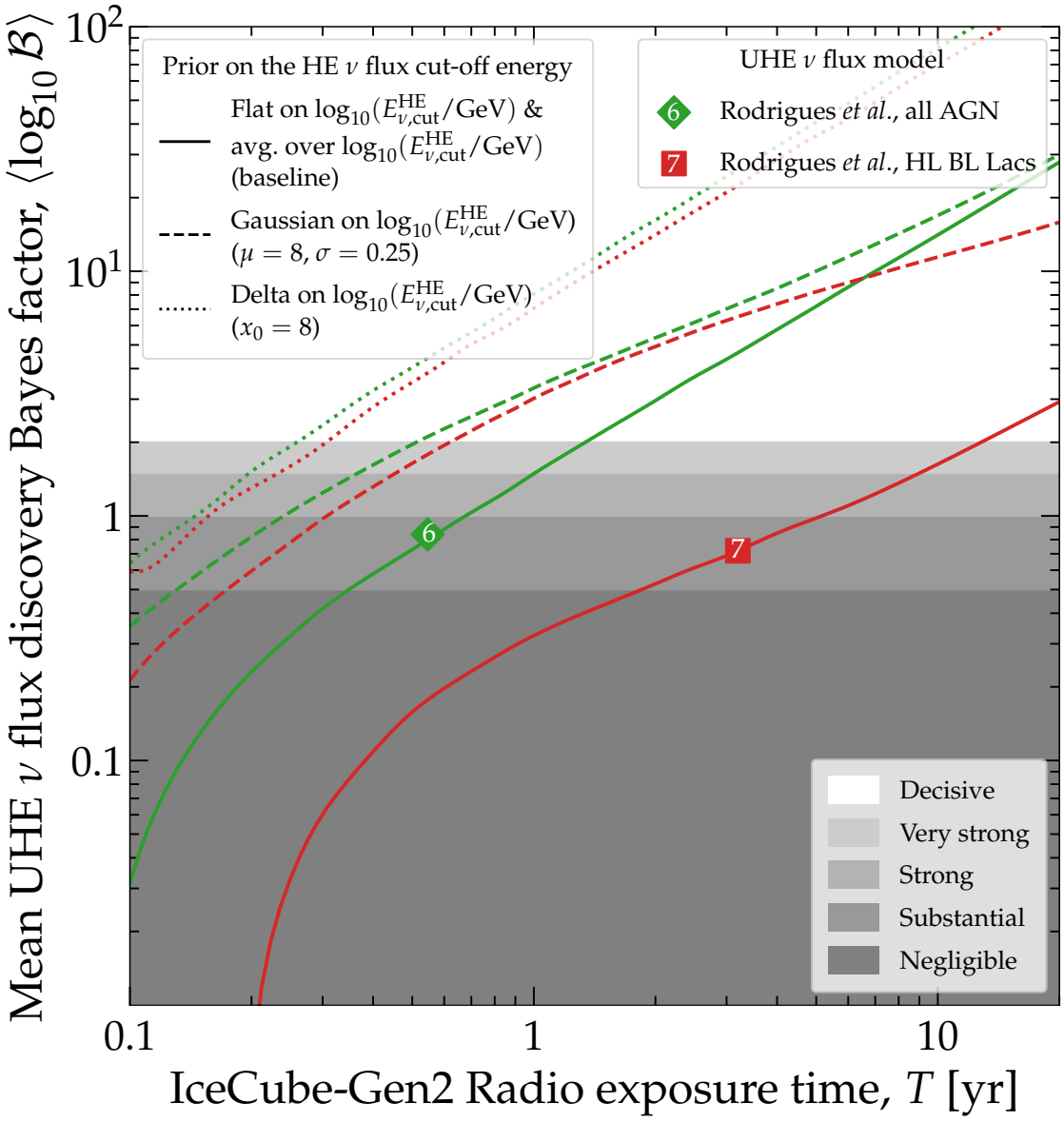

Figure 32: Impact of the choice of prior on the cut-off energy of the UHE tail of the background IceCube high-energy neutrino flux, $E^{\rm HE}_{\nu,\rm cut}$, on the flux discovery potential of UHE neutrino flux models 6 and 7 [179]; see Fig. 26. All other analysis choices are baseline; see Table 4 and Section 7.5.2.1. The baseline choice of a flat prior followed by an average of the Bayes factor over the value of the cut-off energy is conservative and represents complete ignorance of $E^{\rm HE}_{\nu,\rm cut}$. A wide Gaussian prior and delta-function prior, both centered at $E^{\rm HE}_{\nu,\rm cut} = 100$ PeV, represent limited and precise knowledge of its value, respectively. Results for other flux models are similar. *Even limited evidence for the existence and value of a cut-off in the UHE tail of the IceCube high-energy neutrino flux, possibly gathered in upcoming astrophysical TeV–PeV neutrino measurements, may significantly expedite UHE neutrino flux discovery.* See Section 7.5.2.5 for details.

In Fig. 32, as illustration, we choose the real value of the cut-off energy to be $E^{\rm HE}_{\nu,\rm cut} = 100$ PeV; for the Gaussian prior, we choose a width of 0.25 in $\log_{10}(E^{\rm cut}_{\nu,\rm cut}/\rm GeV)$. In both cases, the analysis is the same as the one described in Section 7.5.1, with the exception of using a different prior on $\log_{10}(E^{\rm cut}_{\nu,\rm cut}/\rm GeV)$ and, unlike the baseline analysis choice, of not averaging the Bayes factor over

the real value of $\log_{10}(E^{\rm cut}_{\nu,{\rm cut}}/{\rm GeV})$ anymore, since when using informed priors we are no longer in a situation of complete ignorance of the value of the cut-off energy.

Figure 32 shows that using informed priors on $\log_{10}(E^{\rm cut}_{\nu,{\rm cut}}/{\rm GeV})$ brings significant improvement to the UHE flux discovery potential. Because the UHE tail end of the IceCube high-energy neutrino flux is the dominant background in our analysis (see Section 7.4.5), understanding it better, as reflected by using informed priors on $\log_{10}(E^{\rm cut}_{\nu,{\rm cut}}/{\rm GeV})$, significantly improves the separation between the signal and background-only hypotheses. In Fig. 32, the improvement is striking for flux model 7. Using our conservative baseline prior on the cut-off energy, we would need about 10 years of exposure time to decisively discover flux model 7. In contrast, using the wide Gaussian prior reduces the exposure time needed to about 7 months, and using the δ-function prior reduces it to about 4 months. Similar improvements are achievable for the other benchmark UHE neutrino flux models 1–12.

This significant reduction in the exposure time required for UHE flux discovery highlights the importance of the simultaneous development and deployment of neutrino telescopes that operate in the high-energy (TeV–PeV) and ultra-high-energy ($>$ 100 PeV) ranges, and their combined observations [82, 83, 189, 190].

7.5.2.6 *Impact of the prior on the neutrino-nucleon cross section, f_σ*

The UHE neutrino flux discovery potential of IceCube-Gen2 may be enhanced moderately by limited knowledge of the UHE neutrino-nucleon cross section, especially at low exposure times, and substantially enhanced by precise knowledge of it, for any exposure time.

Ultra-high-energy neutrinos can be used to measure the UHE deep-inelastic-scattering neutrino-nucleon (νN) cross section, σ. Reference [346] made detailed forecasts of this for IceCube-Gen2, based on the same detector design, effective volume, and calculation framework that we use here; see also Refs. [215, 348] for complementary forecasts. In Ref. [346], the best-fit value and uncertainty on σ were determined using a statistical analysis similar to the one we introduced in Section 7.5.1: after 10 years, as long as at least a few tens of events are detected, the UHE νN cross section may be measured to within 50% of its BGR18 prediction [194]. Here, while our goal is not to measure the νN cross section, we nevertheless account for the important effect that it has on

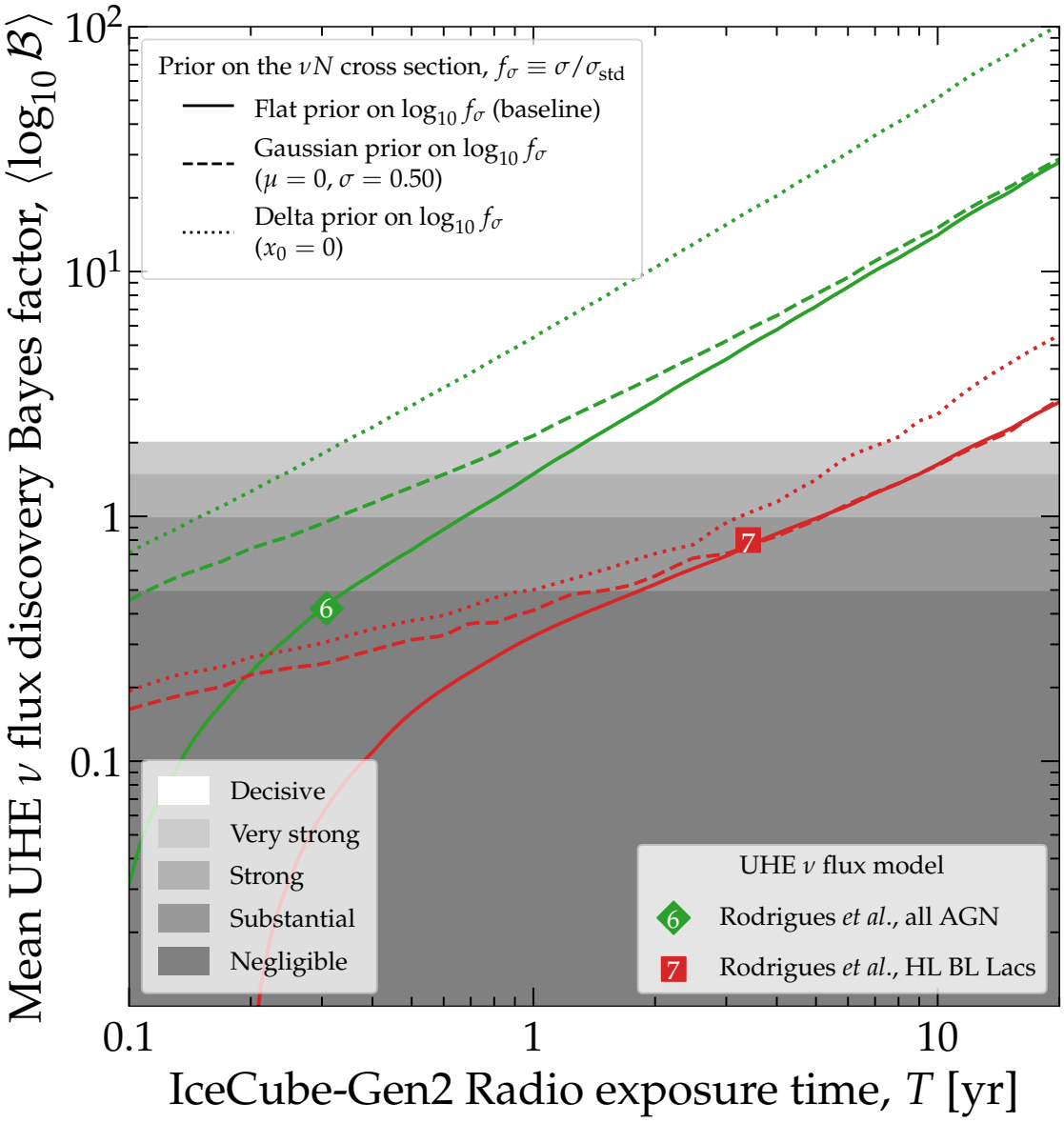

Figure 33: Impact of the choice of prior on the UHE neutrino-nucleon (νN) cross section, $f_\sigma \equiv \sigma/\sigma_{\rm std}$, on the flux discovery potential of UHE neutrino flux models 6 [179] and 7 [179]; see Fig. 26. All other analysis choices are baseline; see Table 4 and Section 7.5.2.1. Here, σ is the cross section, whose value is allowed to float in the statistical procedure, and $\sigma_{\rm std}$ is its BGR18 prediction [194]. The baseline choice of a flat prior on $\log_{10} f_\sigma$ is conservative and represents complete ignorance of f_σ. A wide Gaussian prior and delta-function prior, both centered at the central BGR18 prediction of $\log_{10} f_\sigma = 0$, represent limited and precise knowledge of its value, respectively. Results for other flux models are similar. *Using even a limited informed prior on f_σ expedites flux discovery, especially at low exposure times, where the event rate may be low; at long exposure times, where the event rate is higher, only a precise informed prior helps.* See Section 7.5.2.6 for details.

the discovery Bayes factor, via the prior $\pi(\log_{10} f_\sigma)$, where $f_\sigma \equiv \sigma/\sigma_{\rm std}$ (Section 7.5.1). Below, we show how.

Figure 33 shows the impact that the choice of prior has on the UHE neutrino flux discovery potential. We compare results obtained using our conservative baseline analysis choice of a flat

prior on $\log_{10} f_\sigma$ (see Section 7.5.2.1), against results obtained using two alternative, informed priors: a wide Gaussian prior, with a half-decade width, and a Dirac δ-function prior, both centered on the central value of the BGR18 prediction of the νN cross section, *i.e.*, on $\log_{10} f_\sigma = 0$.

Figure 33 shows that using informed priors expedites flux discovery. The improvements over the baseline expectations when using the wide Gaussian prior are moderate at short exposure times and negligible at long exposure times. The improvements when using the δ-function prior are substantial for any exposure time. For both informed priors, improvements are more evident at short exposure times, where signal event rates are lower, which makes separating them from background event rates more challenging. At longer exposure times, where event rates are higher and the separation is clearer even when f_σ is known uncertainly, there is sizable improvement only when using the δ-function prior. For example, using our conservative baseline prior on the cross section, we would need roughly 1.3 years of exposure time to decisively discover flux model 6. In contrast, using the wide Gaussian prior reduces the exposure time needed to about 1 year, and using the δ-function prior reduces it to about 4 months. Similar improvements are achievable for the other benchmark UHE neutrino flux models.

There is nuanced insight to be gained from how the νN cross section affects the flux discovery potential; we describe it below. Changing the cross section affects the neutrino-induced event rate, Eq. (7.4), in two ways. (The illustrative simplified event-rate calculation, Eq. (7.1), also captures these features, as described in Section 7.3.)

First, a larger or smaller cross section, respectively, increases or decreases the interaction rate of neutrinos in the detector. This affects the total event rate, *i.e.*, the rate integrated over all reconstructed energies and directions. See Ref. [346] for a detailed study.

Second, a larger or smaller cross section, respectively, strengthens or weakens the attenuation of the neutrino flux as it propagates through the Earth. This affects the angular distribution of neutrino-induced events: a larger cross section induces a steeper decline in the event rate around the horizon, *i.e.*, at $\theta_z^{\rm rec} \approx 90^\circ$, since upgoing neutrinos are attenuated more strongly. Reference [346] showed that the sensitivity to the cross section stems from events coming from around the horizon, where in-Earth attenuation is significant, but not overbearing.

It is from the interplay of the above two effects that more precise prior knowledge of f_σ leads to a larger UHE neutrino flux discovery potential. Since information about the cross section is extracted from the angular dependence of the event rate around the horizon, a detector angular resolution that allows us to resolve this accurately is essential (more on this in Section 7.5.2.7).

Further, because the νN cross section grows with neutrino energy, flux models that peak at low energies are less attenuated inside the Earth *vs.* flux models that peak at high energies. Figure 27 illustrates this: the relative contributions of upgoing events and downgoing events resemble each other more closely for flux models that peak at low energy, *e.g.*, models 10 and 12, than for flux models that peak at high energy, *e.g.*, models 4 and 7. Thus, for flux models that peak at low energies, the relatively larger number of events at the horizon and below it helps to pin down f_σ. This impacts the evolution of the discovery Bayes factor with exposure time: flux models that peak at low energy but have a relatively low integrated event rate reach Bayes factors as high or higher than flux models that predict larger integrated event rates. For example, Fig. 25 shows that, after a few years, flux model 12 can be discovered with a significance comparable to flux models 7 and 8, even though it only yields about 70% and 30% of their event rates, respectively; see Table 3.

7.5.2.7 *Impact of the detector energy resolution, σ_ϵ, and angular resolution, σ_{θ_z}*

The UHE neutrino flux discovery potential of IceCube-Gen2 may be appreciably weakened by poor detector energy resolution—which impairs resolving signal vs. background features in the event energy distribution—and poor angular resolution—which preserves the innate degeneracy between neutrino flux and νN cross section

Figure 34 shows the impact that the detector resolution in reconstructed shower energy, σ_ϵ, where $\epsilon \equiv \log_{10}(E_{\rm sh}^{\rm rec}/E_{\rm sh})$, and the reconstructed zenith angle, σ_{θ_z}, have on the UHE neutrino flux discovery potential. The detector resolution affects the computation of event rates via Eq. (7.5); see Section 7.4.4 for details. Figure 34 shows that alternative choices of the energy and angular resolution, poorer than the baseline choices, delay UHE flux discovery, but may not prevent it.

Poorer energy resolution lessens the difference between the distributions in reconstructed energy of the signal and background events (see Fig. 27 for a comparison *vs.* the muon background); see Section 7.5.2.2. Thus, a significantly poorer energy resolution may appreciably weaken the UHE

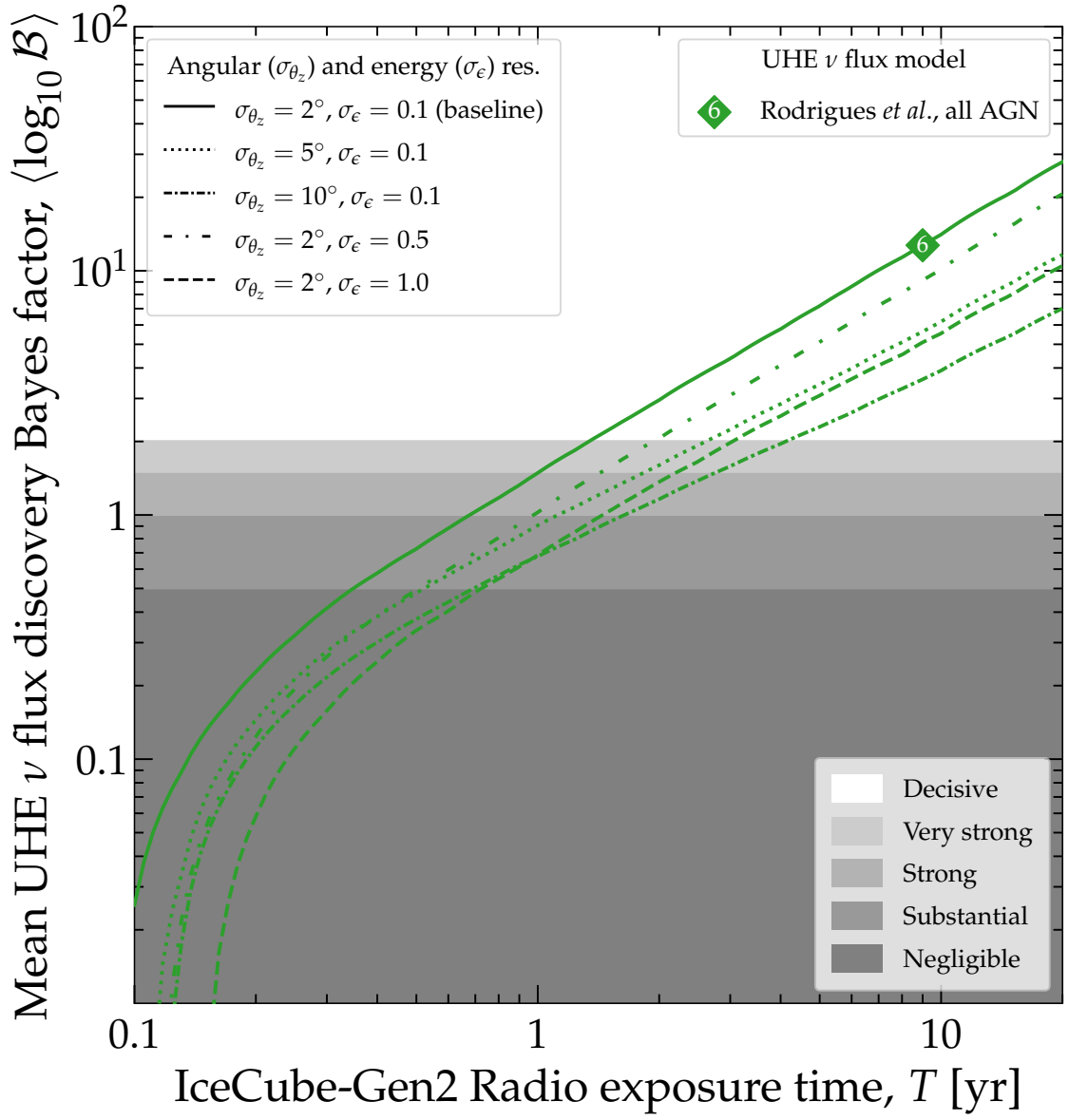

Figure 34: Impact of the resolution of the radio array of IceCube-Gen2 in measuring reconstructed energy, σ_ϵ, and reconstructed direction, σ_{θ_z}, on the flux discovery potential of UHE neutrino flux model 6 [179]; see Fig. 26. All other analysis choices are baseline; see Table 4 and Section 7.5.2.1. Results for other flux models are similar; see Figs. B3 and B4 in Appendix B.2. *Poorer detector resolution delays flux discovery, but does not prevent it; energy resolution has a stronger impact, because it weakens the distinction between the energy distributions of signal and background.* See Section 7.5.2.7 for details.

flux discovery potential. Figure 34 shows that, under our baseline choices of detector resolution, with $\sigma_\epsilon = 0.1$, *i.e.*, one-tenth of a decade in shower energy, flux model 6 may be decisively discovered in roughly 1.3 years. With $\sigma_\epsilon = 0.5$, *i.e.*, a resolution of half a decade in shower energy, decisive discovery is delayed to roughly 2 years. With $\sigma_\epsilon = 1$, *i.e.*, a resolution of a full decade in shower energy, it is delayed to roughly 3 years. Similar delays occur for the other benchmark UHE neutrino flux models 3–12; see Fig. B3 in Appendix B.2. The delays are substantially longer for the

flux models with the lowest event rates, for which the separation between signal and background events is more challenging *i.e.*, models 1, 3, 5, 7, and 12; see Fig. 27 and Table 3. (When changing σ_ϵ, we change the binning in reconstructed energy accordingly. For $\sigma_\epsilon = 0.1$, 0.5, and 1, we use, respectively, 30, 6, and 3 bins equally spaced in logarithmic scale from $E_{\rm sh}^{\rm rec} = 10^7$ GeV to 10^{10} GeV.)

Poorer angular resolution lessens the difference between the distributions in reconstructed direction of the signal and background events; see Fig. 28 for a comparison *vs.* the muon background. However, this has only a mild impact on the flux discovery potential. The dominant impact comes instead from the fact that, since our baseline results assume no prior knowledge of the νN cross section, *i.e.*, a flat prior on $\log_{10} f_\sigma$, poorer angular resolution preserves the innate degeneracy between the neutrino flux and the cross section, illustrated in Eq. (7.1). Ordinarily, the degeneracy would be broken by comparing the angular distribution of events coming from around the horizon, but a poor angular resolution obfuscates this. For details, see Section 7.3 and, especially, the discussion in connection to Fig. 29 in Sections 7.5.2.2 and 7.5.2.6. (Separately, angular resolution is critical for discovering point sources of UHE neutrinos [371, 372] and important when measuring the UHE neutrino-nucleon cross section [205, 215, 346, 348]).

Figure 34 shows that, under our baseline choices of detector resolution, with $\sigma_{\theta_z} = 2^\circ$, flux model 6 may be decisively discovered in roughly 1.3 years. With $\sigma_{\theta_z} = 5^\circ$ and 10°, decisive discovery is delayed to roughly 2.5 and 4 years, respectively. Similar delays occur for the other benchmark UHE neutrino flux models 3–12; see Fig. B4 in Appendix B.2. As for the case of poorer energy resolution, the delays are longer for the flux models with the lowest event rates. (When changing σ_{θ_z}, we change the binning in reconstructed direction accordingly. For $\sigma_{\theta_z} = 2^\circ$, 5°, and 10°, we use, respectively, 10, 4, and 2 equally spaced bins for events around the horizon, *i.e.*, from $\theta_z^{\rm rec} = 80^\circ$ to 100°. We leave the binning of downgoing and upgoing events unchanged).

In our forecasts, we have considered a common detector angular and energy resolution for all of the events. However, in a real experiment every event will be reconstructed, in general, with a different angular and energy error. Future, revised versions of our analysis should include this event-by-event treatment [336].

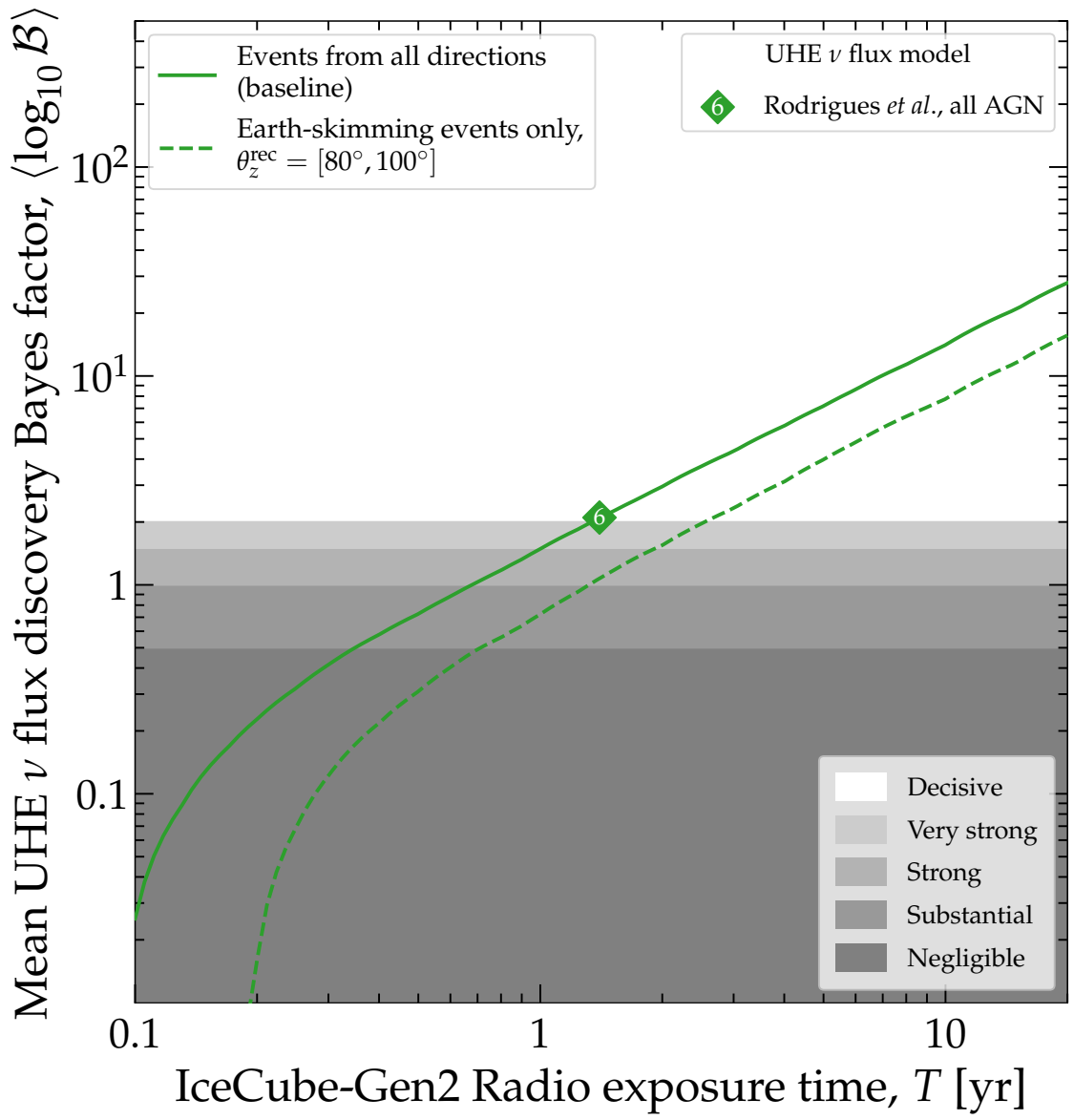

Figure 35: Flux discovery potential of the UHE neutrino flux model 6 [179] computed using events from all directions *vs.* using only Earth-skimming, or horizontal, events. All other analysis choices are baseline; see Table 4 and Section 7.5.2.1. Results for other flux models are similar. *Earth-skimming events are largely responsible for the flux discovery potential, so optimizing a detector to observe them is a sensible strategy.* See Section 7.5.2.8 for details.

7.5.2.8 *Importance of Earth-skimming events*

Most of the UHE neutrino flux discovery potential comes from Earth-skimming events, i.e., events that reach the detector from around the horizon ($\theta_z^{\text{rec}} \approx 90°$).

Section 7.3 showed that the flux of Earth-skimming, or horizontal, *i.e.*, $\theta_z^{\text{rec}} \approx 90°$, neutrinos is attenuated by neutrino-matter interactions inside the Earth, but is not obliterated by them, unlike upgoing events, and so they induce a sizable number of events in the detector. In contrast,

downgoing neutrinos reach the detector mostly unattenuated, and the number of neutrinos reaching the detector is much larger. Figures 27 and 28 show these features for the UHE neutrino flux models 1–12.

Because the design of IceCube-Gen2 is still under consideration, its final form might conceivably have a response to downgoing and horizontal events that is different from that of the baseline design [77] that we have adopted; see Section 7.4.3 for details on it. Further, other UHE neutrino telescopes presently under planning target mainly Earth-skimming events induced by ν_τ, *i.e.*, Ashra-NTA [356], AugerPrime [162], BEACON [153], EUSO-SPB2 [383], GCOS [384], GRAND [72], POEMMA [74], PUEO [75], RET [365], TAROGE [366], TAx4 [385], TAMBO [73], Trinity [355]; see Ref. [83] and Fig. 53 in Ref. [82] for an overview. This prompts us to study the importance that Earth-skimming events have in our forecasts of flux discovery potential.

Figure 35 shows, for flux model 6, the extreme case where our forecasts use only Earth-skimming events, with $\theta_z^{\rm rec} = [80^\circ, 100^\circ]$, which make up roughly 35% of the all-sky event rate. To understand this result, consider naively that if events from all directions were equally relevant for flux discovery, then using a subset of only one third of them, with randomly chosen directions, should delay flux discovery by roughly a factor of 3. However, Fig. 35 shows that using only Earth-skimming events delays the decisive flux discovery of flux model 6, which takes 1.31 years in our baseline predictions (Table 3), by only about 1.5 years, rather than by the naive expectation of about 2.6 years. This is because flux discovery stems largely from resolving the angular distribution of Earth-skimming events, especially if the νN cross section is unknown; see Sections 7.5.2.6 and 7.5.2.7 for details.

To further illustrate the point above, we imagine an extreme alternative design of the radio array of IceCube-Gen2 that detects exclusively Earth-skimming events, but preserves the same total effective volume, integrated over all energies and directions, as our baseline design. That alternative design should detect roughly three times as many events as are used in the result in Fig. 35 based on Earth-skimming events only. Increasing the event rate by a factor of 3 is equivalent to increasing the exposure time by the same factor. Because, at long exposure times, the discovery Bayes factor grows linearly with time (Section 7.5.2.2), the alternative detector design could claim decisive flux discover a factor-of-3 sooner than the baseline result using Earth-skimming events only in Fig. 35, *i.e.*, a reduction from about 3 years to 1 year. In turn, this would be a reduction of

about 30% compared to the 1.3 years needed for decisive flux discovery in our baseline forecast in Fig. 35 using events from all directions. This demonstrates that optimizing the detector response to detect Earth-skimming *vs.* downgoing events is a strategy that merits exploration.

7.5.2.9 *Discovering the UHE tail end of the IceCube high-energy neutrino flux*

The UHE tail of the IceCube high-energy neutrino flux, based the hard-spectrum ($\gamma = 2.37$) flux measured in through-going ν_μ, may be decisively discovered within 10 years of exposure of the radio array of IceCube-Gen2, even if suppressed by a low-energy cut-off at 50 PeV.

So far, we have forecast the discovery potential of UHE neutrino flux models 3–12, and considered the UHE tail of the IceCube high-energy neutrino flux as a background to their discovery, together with the background of atmospheric muons; see Section 7.5.1. Here, we forecast instead the discovery of the UHE tail of the IceCube high-energy neutrino flux by itself, and consider atmospheric muons as a background to their discovery. Following the discussion in Section 7.4.5.2, we expect that to discover the UHE tail of the high-energy neutrino flux, it must have a hard spectrum, *i.e.*, a value of the spectral index, γ, not too far from 2, and a cut-off energy, *i.e.*, $E^{\rm HE}_{\nu,{\rm cut}}$, in the tens of PeV, or no cut-off at all. If these conditions are met, the UHE tail of the high-energy neutrino flux could induce a sizable number of neutrino events in the radio array of IceCube-Gen2 and in other UHE neutrino telescopes, and become detectable over the atmospheric muon background. Below we quantify this.

Figure 36 compares, for different choices of the cut-off energy, the mean expected event rate induced by our alternative soft-spectrum choice and our baseline hard-spectrum choice for the UHE tail of the IceCube high-energy neutrino flux introduced in Section 7.4.5.2. They are based respectively, on the flux measured in the 7.5-year HESE analysis [188], with $\gamma = 2.87$, and in the 9.5-year through-going ν_μ analysis [37] by the IceCube Collaboration, with $\gamma = 2.37$, both augmented by a high-energy exponential cut-off, Eq. (7.7). When without a cut-off, *i.e.*, with $E^{\rm HE}_{\nu,{\rm cut}} \to \infty$, they correspond to our benchmark UHE neutrino flux models 1 and 2, respectively.

Figure 36 shows that lower values of $E^{\rm HE}_{\nu,{\rm cut}}$ reduce the integrated event rate and, especially, the event rate at high energies, thus concentrating events at low energies, and making their energy distribution resemble that of the atmospheric muon background. Below we show how this erodes

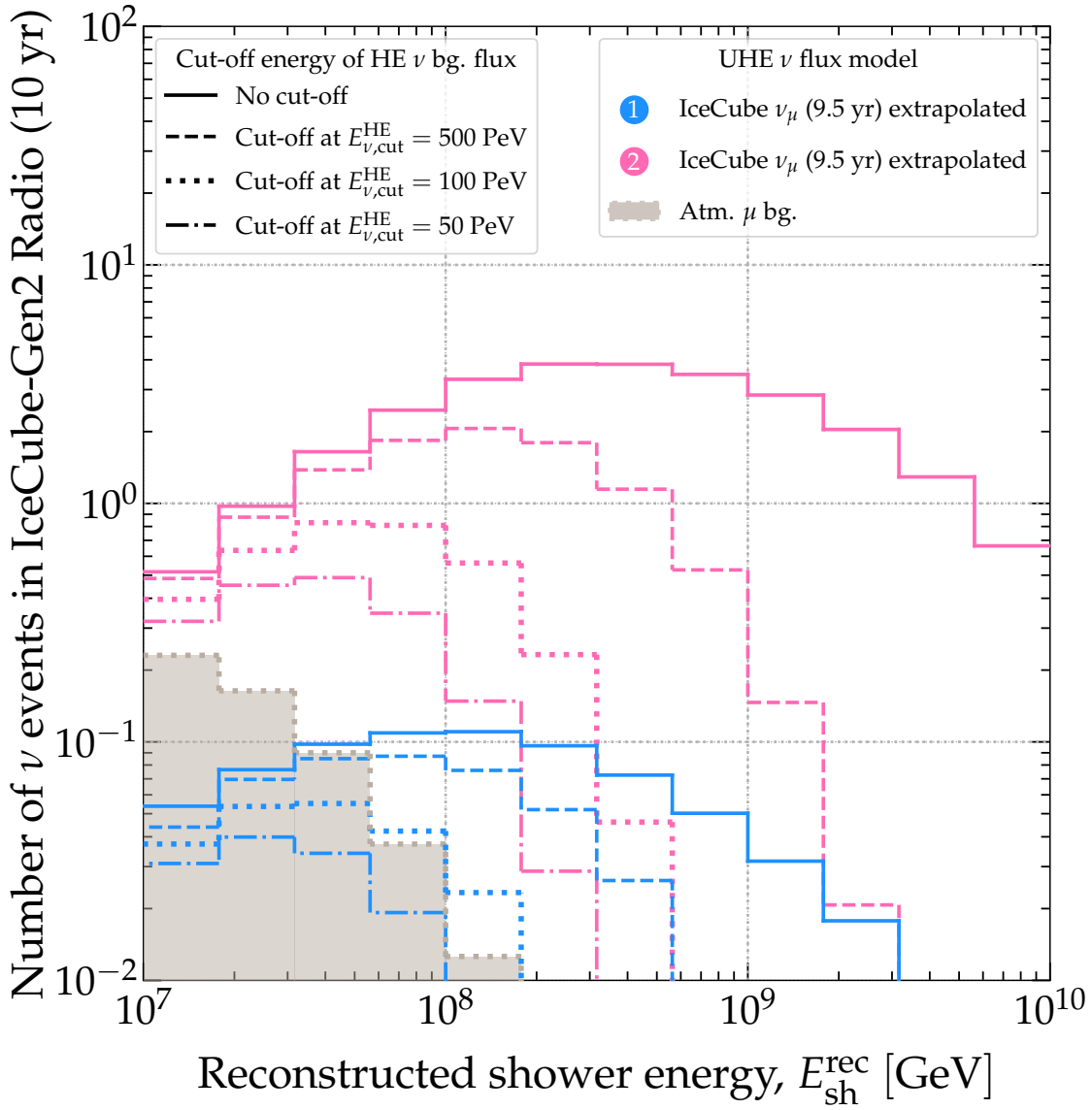

Figure 36: Mean event distribution in reconstructed shower energy, E^{rec}_{sh}, expected in the radio array of IceCube-Gen2 after 10 years of exposure for flux models 1 and 2, *i.e.*, the UHE extrapolation of the IceCube high-energy neutrino flux from the 7.5-year HESE [188] and 9.5-year through-going muon analyses [37], respectively (see Fig. 26), augmented with a high-energy exponential cut-off at energy $E^{HE}_{\nu,cut}$; see Eq. (7.7). Event rates are computed using the procedure from Section 7.4.4, and under our baseline analysis choices; see Section 7.5.2.1. See Table 3 for integrated event rates, Fig. 37 for the associated flux discovery potential, and Section 7.5.2.9 for details.

their prospects of being discovered. Table 3 shows event rates for flux models 1 and 2, for different choices of the cut-off energy. Flux model 1 yields, on average, fewer than one event in 10 years, and versions of it with a cut-off yield even less. Flux model 2 yields, on average, about 27 events in 10 years, and about 2 events even with an early cut-off at 50 PeV.

Figure 37 shows the impact that the value of $E^{HE}_{\nu,cut}$ has on the discovery potential of the UHE tail of the IceCube high-energy neutrino flux. As expected from Fig. 36, lower values of $E^{HE}_{\nu,cut}$

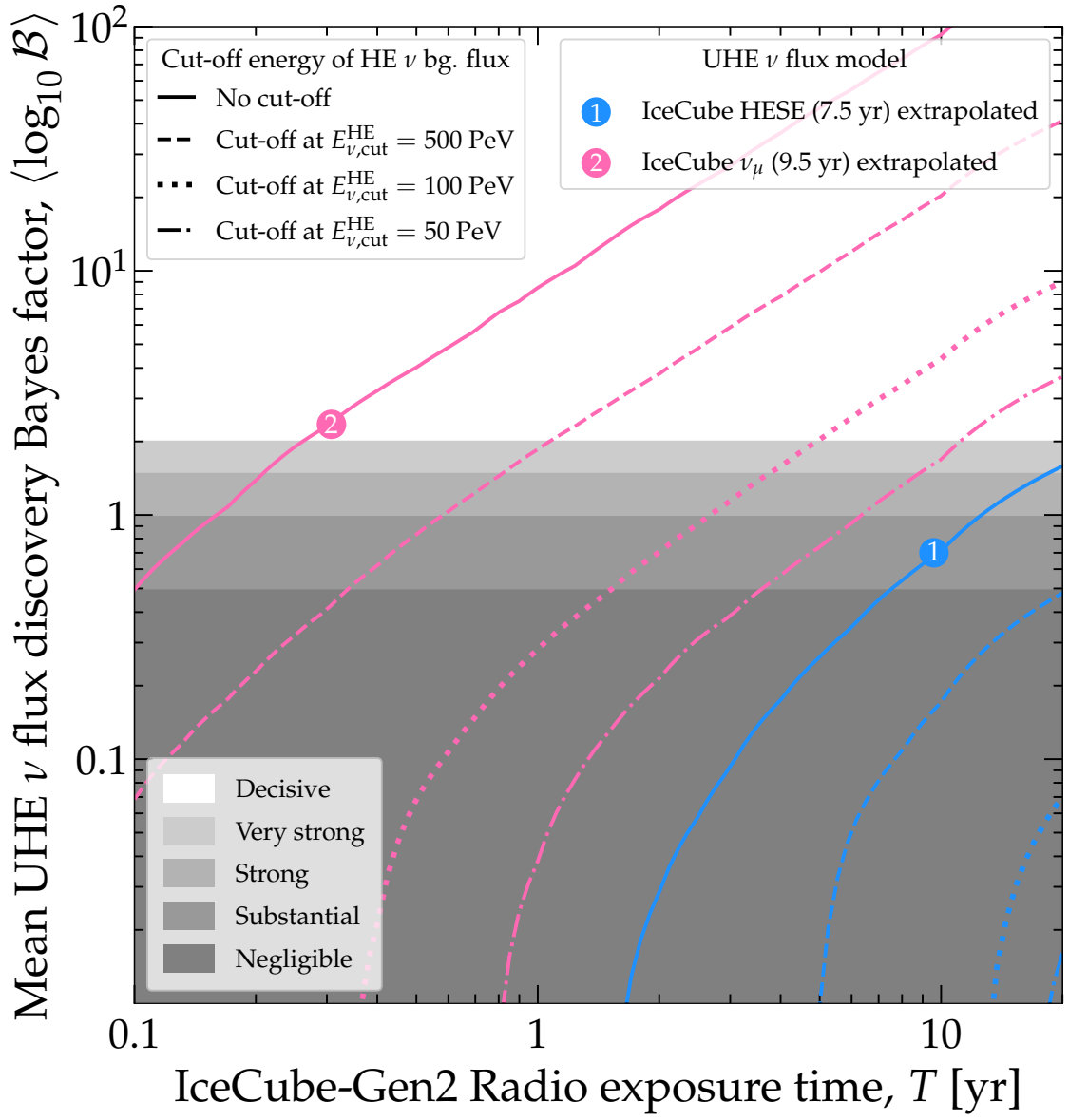

Figure 37: Impact of the cut-off energy, $E^{\rm HE}_{\nu,\rm cut}$, on the discovery potential of flux model 2, *i.e.*, the UHE extrapolation of the high-energy flux from the IceCube 9.5-year through-going muon analysis [37], augmented by a high-energy exponential cut-off at energy $E^{\rm HE}_{\nu,\rm cut}$; see Eq. (7.7). Unlike our baseline procedure, in this plot we do not average the Bayes factor over the real value of $E^{\rm HE}_{\nu,\rm cut}$, since it is assumed to be known; however, we still use our baseline flat prior on $\log_{10}(E^{\rm HE}_{\nu,\rm cut}/\text{GeV})$ when computing the posterior, Eq. (7.15). For this plot only, the sole background to flux discovery is from atmospheric muons. All other analysis choices are baseline; see Table 4 and Section 7.5.2.1. See Fig. 36 and Table 3 for the event rates and Section 7.5.2.9 for details.

hinder discovery. To compute the flux discovery Bayes factor in this case, we follow the same procedure introduced in Section 7.5.1, but using only atmospheric muons for the background, *i.e.*, using $N^{(\rm s+bg)}_{\rm pred},ij(\boldsymbol{\theta}) = N^{\rm HE}_{\nu,ij}(\boldsymbol{\theta}) + N_{\mu,ij}$ instead of Eq. (7.12) for the signal hypothesis and $N^{(\rm bg)}_{\rm pred},ij = N_{\mu,ij}$ instead of Eq. (7.14) for the background-only hypothesis. In addition, unlike our baseline prescription (Section 7.5.2.1), when the value of $E^{\rm HE}_{\nu,\rm cut}$ is fixed at 50, 100, or 500 PeV, we no longer

average the Bayes factor over it. Figure 37, and also Fig. 25, show that in the absence of a cut-off flux model 2 could be discovered decisively within 4 months. The presence of a cut-off delays its discovery, but does not preclude it: for a high cut-off at $E_{\nu,\mathrm{cut}}^{\mathrm{HE}} = 500$ PeV, the flux may be discovered decisively within 1 year, and even for a low cut-off at 50 PeV, it may still be discovered after roughly 10 years. Flux model 2, without a cut-off, may be discovered with very strong evidence after 20 years, but versions of it with a cut-off are undiscoverable.

Figure 37 posits the intriguing possibility of using the IceCube high-energy neutrino flux to calibrate the response of UHE neutrino telescopes, which is known uncertainly. If the value of the cut-off energy of the IceCube flux can be measured or constrained by complementary measurements in detectors with high sensitivity in the energy range of 1–10 PeV, like the optical array of IceCube-Gen2 [39], TAMBO [73], or Trinity [355], then it may be possible to make informed predictions about the contribution of its UHE tail to the event rate in UHE neutrino telescopes. However, there is an unavoidable trade-off: a low cut-off energy would be easier to characterize with 1–10 PeV telescopes, but it would also imply a low event rate in the UHE range (that is, in the absence of other contributions, like UHE neutrino flux models 3–12).

7.5.2.10 *Summary*

Our forecasts—Figs. 25 and 37, and in Table 3—tempered by design by important nuance from theory and experiment, reveal promising prospects for the discovery of an UHE neutrino flux in the first decade of operation of IceCube-Gen2. Several of our benchmark UHE neutrino flux models (Section 7.2) may even be decisively discovered within 5 years of detector exposure.

Less conservative, but still reasonable and well-motivated alternative analysis choices may hasten or delay decisive flux discovery within a decade, but are unlikely to preclude discovery. *This renders our forecasts robust against analysis choices.* In summary, the impact of the different analysis choices on the UHE neutrino flux discovery potential is as follows:

- The size of the atmospheric muon background has only a mild impact—as long as it only affects the lowest energy bins, as predicted by current hadronic models. See Section 7.5.2.3.

- The normalization and, especially, the spectral index of the UHE tail of the background IceCube high-energy neutrino flux has a large impact; a softer spectrum yields a smaller background, which hastens the discovery of UHE neutrino flux models 3–12. See Section 7.5.2.4.

- Using an informed prior on the cut-off energy of the background UHE tail of the IceCube high-energy neutrino flux, $E^{\rm HE}_{\nu,{\rm cut}}$, may significantly hasten flux discovery, even if the prior is based on limited knowledge. See Section 7.5.2.5.

- Using an informed prior on the UHE νN cross section, f_σ, may hasten flux discovery moderately, if the prior is based on limited knowledge, or substantially, if it is based on precise knowledge. See Section 7.5.2.6.

- Poor detector resolution on shower energy, σ_ϵ, and zenith angle, σ_{θ_z}, may appreciably delay flux discovery. See Section 7.5.2.7.

- Because Earth-skimming events, with $\theta_z^{\rm rec} = [80^\circ, 100^\circ]$, provide most of the UHE neutrino flux discovery potential, a detector with a total effective volume equivalent to that of our baseline design, but focused on the horizontal directions, could enhance discovery opportunities. See Section 7.5.2.8.

Finally, we also found that the UHE tail of the IceCube high-energy neutrino flux, augmented with a high-energy cut-off, Eq. (7.7)—which is typically a background for the discovery of other flux models—may itself be discovered. Depending on the value of the cut-off energy, which determines the UHE event rate induced by this flux, discovery may occur within months, if the cut-off energy is high, or years, if it is low. See Section 7.5.2.9.

7.6 FLUX MODEL SEPARATION

In Section 7.5, we discussed the UHE neutrino flux discovery potential of benchmark flux models 1–12. Here we tackle a related question: how well can two UHE neutrino flux models be experimentally distinguished from each other? To answer it, we consider two hypotheses: the *true signal hypothesis*, built assuming knowledge of which is the “true" neutrino flux model, and the *test signal hypothesis*, built for alternative, “test" models. Below, we forecast how well these hypotheses can

be experimentally distinguished in the radio array of IceCube-Gen2. We focus on benchmark flux models 3–12. Like in Section 7.5, we account for the background from atmospheric muons and the UHE tail of the IceCube high-energy neutrino flux, for random statistical fluctuations in the event rate, and for the uncertainty in analysis parameters. We adopt the same baseline analysis choices as for the flux discovery potential (Table 4 and Section 7.5.2.1), but limit our exploration of alternative analysis choices to the effect of different choices for the background UHE tail of the IceCube high-energy neutrino flux (Appendix B.1) and of the detector energy and angular resolution (Appendix B.2).

7.6.1 *Statistical analysis*

We model the statistical analysis used for model separation closely after the analysis used for flux discovery introduced in Section 7.5.1. For a given choice of the true UHE neutrino flux, $\mathcal{M}^{\text{true}}_{\text{UHE}}$, of the test UHE neutrino flux, $\mathcal{M}^{\text{test}}_{\text{UHE}}$, and of the background UHE tail of the IceCube high-energy neutrino flux, $\mathcal{M}_{\text{HE}}$, we compute the likelihood function under the true and test hypotheses, $\mathcal{L}^{(\text{s+bg})}_{\mathcal{M}^{\text{true}}_{\text{UHE}},\mathcal{M}_{\text{HE}}}$ and $\mathcal{L}^{(\text{s+bg})}_{\mathcal{M}^{\text{test}}_{\text{UHE}},\mathcal{M}_{\text{HE}}}$, respectively, using Eq. (7.9). The true and test flux is any of the benchmark flux models 3–12; see Section 7.2 and Fig. 26. When computing these likelihood functions we sample the value of the observed event rate in each energy and angular bin, $N_{\text{obs},ij}$, at random from a Poisson distribution with central value $N^{(\text{s+bg})}_{\text{pred},ij}$ equal to the event rate predicted by the true UHE neutrino flux model, using Eq. (7.12), which includes the background of atmospheric muons and the UHE tail of the IceCube flux. We use the same random realization to compute the likelihood functions under the true and test hypotheses. (Like before, we repeat this procedure using many random realizations; we explain this below.)

We compute the corresponding statistical evidence, $\mathcal{Z}^{(\text{s+bg})}_{\mathcal{M}^{\text{true}}_{\text{UHE}},\mathcal{M}_{\text{HE}}}$ and $\mathcal{Z}^{(\text{s+bg})}_{\mathcal{M}^{\text{test}}_{\text{UHE}},\mathcal{M}_{\text{HE}}}$, using Eq. (7.16), and, with them, the *model separation* Bayes factor,

$$\mathcal{B}^{\text{sep}}_{\mathcal{M}^{\text{true}}_{\text{UHE}},\mathcal{M}^{\text{test}}_{\text{UHE}},\mathcal{M}_{\text{HE}}} = \frac{\mathcal{Z}^{(\text{s+bg})}_{\mathcal{M}^{\text{true}}_{\text{UHE}},\mathcal{M}_{\text{HE}}}}{\mathcal{Z}^{(\text{s+bg})}_{\mathcal{M}^{\text{test}}_{\text{UHE}},\mathcal{M}_{\text{HE}}}} \,, \tag{7.23}$$

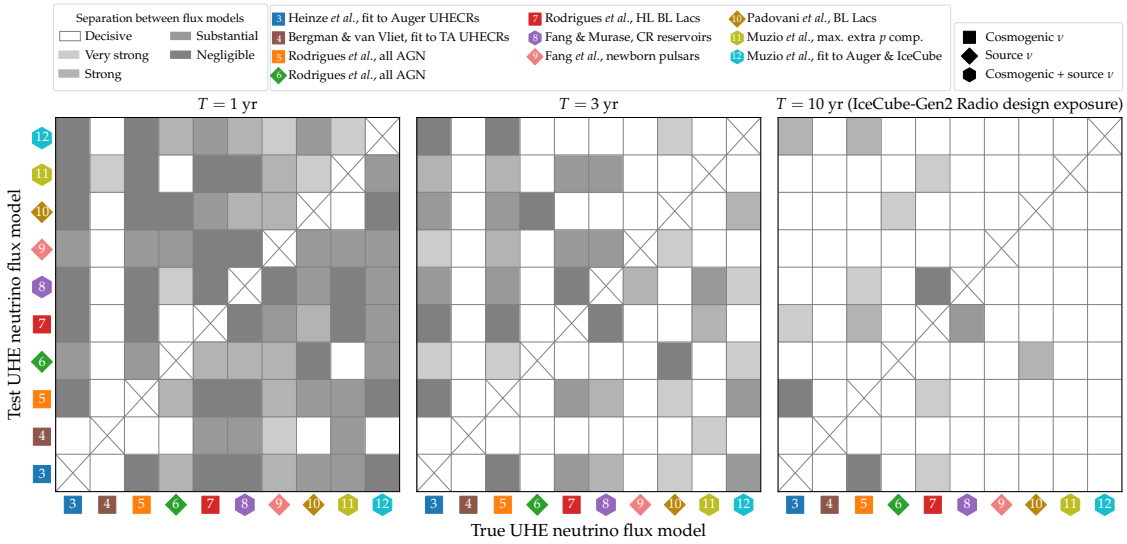

Figure 38: Confusion matrix showing the experimental separation between true and test UHE neutrino flux models in the radio array of IceCube-Gen2, after an exposure time T. The true flux model determines the observed event rate, and they are contrasted against event-rate predictions from the test models. The color coding shows the mean model separation Bayes factor, $\langle \mathcal{B}^{\text{sep}}_{\mathcal{M}^{\text{true}}_{\text{UHE}},\mathcal{M}^{\text{test}}_{\text{UHE}},\mathcal{M}_{\text{HE}}} \rangle$, accounting for the background from atmospheric muons and from the UHE tail of the high-energy neutrino spectrum, and interpreted qualitatively using Jeffreys' table [377] (Section 7.5.1). All analysis choices are baseline; see Table 4 and Section 7.5.2.1. *After 10 years, the majority of UHE neutrino flux models that are discoverable (see Section 7.5.2.2), can also be distinguished from each other; yet, some discoverable flux models with similar energy spectra can still be confused with each other.* See Section 7.6 for details, and Appendices B.1 and B.2 for results obtained under alternative analysis choices.

via which we report the model separation potential between two UHE neutrino flux models. It represents the preference for the true signal hypothesis over the test signal hypothesis, given an observed event rate.

Like we did for the flux discovery Bayes factor in Section 7.5.1, we use UltraNest [378] to find the statistical evidence under the true and test hypotheses, compute the model separation Bayes factor for $N_{\text{samples}} = 10^4$ different random realizations of the observed event rate for each choice of $\mathcal{M}^{\text{true}}_{\text{UHE}}$, $\mathcal{M}^{\text{test}}_{\text{UHE}}$, and $\mathcal{M}_{\text{HE}}$, and report only the mean Bayes factor, averaged over all the realizations, $\langle \mathcal{B}^{\text{sep}}_{\mathcal{M}^{\text{true}}_{\text{UHE}},\mathcal{M}^{\text{test}}_{\text{UHE}},\mathcal{M}_{\text{HE}}} \rangle$, computed similarly to Eq. (7.21).

7.6.2 *Results*

Figure 38 shows the *confusion matrix* for 1, 3, and 10 years of detector exposure time. In each matrix, the horizontal axis shows the true UHE neutrino flux models, $\mathcal{M}^{\text{true}}_{\text{UHE}}$, which we use to generate the observed rate, and the vertical axis shows the test UHE neutrino flux models, $\mathcal{M}^{\text{test}}_{\text{UHE}}$. Each

entry in the confusion matrix represents the value of the model separation Bayes factor, Eq. (7.23), interpreted qualitatively according to Jeffreys' table [377]; see Section 7.5.1 for details.

Figure 38 shows that, as expected, at short exposure times most UHE neutrino flux models cannot be distinguished from each other. (The exceptions are flux model 4 and, to a lesser extent, flux model 6, which have the highest event rates; see Table 3.) This is because at short exposure times the observed event rate is generally low, so features in the energy and angular distribution of the observed events are resolved poorly, or not at all. Model separation is further marred by the relatively large random statistical fluctuations that affect low event rates.

At longer exposure times, the observed event rate grows, features in the energy and angular event distribution become better resolved and more robust against random fluctuations. Consequently, the observed features can be more cleanly contrasted against the features predicted by different flux models, and the true model may be more easily distinguished from others. Accordingly, Fig. 38 shows that after 10 years most of the flux models that can be discovered (see Section 7.5.2.2) can also be distinguished from each other with at least strong evidence, and many with decisive evidence. There are a few exceptions. For instance, flux models 7 and 8 remain easy to confuse even after 10 years, because the energy spectrum of model 7, supplemented by the background of the UHE tail of the IceCube high-energy neutrino flux, resembles the energy spectrum of model 8. Naturally, flux models that yield low event rates and that are not expected to be discovered within a decade, *i.e.*, models 1, 3, and 5 (see Fig. 25), cannot be distinguished from each other.

A subtle feature of the confusion matrix is that it is nearly, but not exactly, symmetric along its diagonal. This is because, when comparing a pair of true and test flux models, the observed event rate and the size of its statistical fluctuations are computed using the true flux model, while the predicted event rate is computed using the test flux model. As a result, at short exposure times, when event rates are low and affected significantly by fluctuations, swapping the roles of the true and test flux models impacts the size of the fluctuations significantly. This, in turn, impacts the model separation Bayes factor appreciably, and is reflected in the asymmetry of the confusion matrix. At longer exposure times, when event rates are higher and more robust to fluctuations, swapping the true and test flux models does not impact the Bayes factor as much. Consequently, the confusion matrix becomes more symmetric with exposure time.

The results for flux model separation above were obtained using our baseline analysis choices (see Table 4 and Section 7.5.2.1); specifically, using a hard spectrum for the UHE tail of the IceCube high-energy neutrino flux, detector angular resolution of $\sigma_{\theta_z} = 2^\circ$, and detector energy resolution of $\sigma_\epsilon = 0.1$. Appendix B.1 contains confusion matrices generated instead using our soft and intermediate choices of the spectrum for the background UHE tail of the IceCube high-energy flux, introduced in Section 7.4.5.2. Figure B2 shows appreciable improvement in the flux model separation when switching from the baseline hard to the soft background flux.

Appendix B.2 contains confusion matrices generated using poorer choices of detector angular and energy resolution. Figure B6 shows that poorer angular resolution has little effect on flux model separation. This is because the angular distributions of events for all flux benchmark models are comparable. Figure B5 shows, in contrast, that poorer energy resolution strongly erodes flux model separation. This is because most of the model separation power stems from the differences between the event energy distributions of the different flux models. For an energy resolution of a decade in shower energy, *i.e.*, $\sigma_\epsilon = 1.0$, model separation is largely unfeasible, except for flux model 4 due to its high event rate. This reveals that, while good detector energy resolution is important for flux discovery (see Section 7.5.2.7), it is essential for flux model separation.

7.7 FUTURE DIRECTIONS

To produce our forecasts of the UHE neutrino flux discovery potential and model separation above, we used state-of-the-art detector simulations and theoretical input. Yet, there are potential improvements that could be implemented in future revisions. None of them represents a fundamental limitation of our present analysis.

Since our calculation framework is similar to that of Ref. [346], it shares potential directions of future improvement identified in that work: raising the maximum neutrino energy in in-Earth propagation, including the Landau–Pomeranchuk–Migdal effect in the relation between neutrino and shower energies, including the contribution of secondary leptons in the detector effective volumes for ν_μ- and ν_τ-initiated CC showers, improving the modeling of angular resolution, using an unbinned likelihood analysis rather than a binned one, including the background of

air-shower cores, including nuclear effects in the cross section, using flavor identification, and jointly measuring the νN cross section, flux normalization and spectral shape. See Ref. [346] for details. Work is ongoing on several of these fronts.

Below, we present additional potential future improvements that are directly relevant to the present work, listed roughly in order of implementation challenge.

Characterizing the UHE tail of the IceCube high-energy neutrino flux.— In our forecasts, we found that the main background to the discovery of flux model 3–12, and the separation between them, may be from the UHE tail of the IceCube high-energy neutrino flux, especially if it has a hard energy spectrum and a high cut-off energy; see Section 7.4.5. In our results, we factored in already the large uncertainty in the position of the cut-off energy, but not the uncertainties on the flux normalization and spectral index. Instead, we fixed them to their current best-fit values, which is reasonably motivated: by the time that the radio array IceCube-Gen2 gathers sufficient UHE data to perform the above analyses, it is likely that the TeV–PeV range of the flux will have been precisely characterized, by IceCube, the optical array of IceCube-Gen2, or by a combination of neutrino telescopes [78]. Even then, it is foreseeable that the UHE tail of the IceCube high-energy neutrino flux will be known imprecisely due to the paucity of UHE events. Thus, factoring in the full uncertainty on the shape of the UHE tail, not only from the cut-off energy, but also from its normalization and spectral index, may weaken future revised forecasts.

Reconstructing the UHE neutrino energy spectrum.— When computing the UHE neutrino flux discovery potential of benchmark flux models 1–12, we did not quantify how well their neutrino energy spectrum could be reconstructed. Yet, doing this is critical to being able to claim flux discovery and model separation without the theory bias that comes from working with a limited collection of flux models that, while representative of the model parameter space, is evidently not exhaustive. Work in reconstructing the normalization and spectral shape of the UHE neutrino flux using a generic parametrization of the UHE neutrino flux, and in addition to jointly measure the νN cross section, is ongoing [336].

Applying our analysis methods to other UHE neutrino telescopes.— To make concrete forecasts that represent realistic experimental nuance, we geared them to IceCube-Gen2, presently in advanced planning stages. Yet, it is straightforward to apply our analysis methods to compute event rates,

flux discovery potential, and flux model separation to other UHE neutrino telescopes [83], radio-based or otherwise, without large alteration. Section 7.4 shows that the particulars of the detector affect the calculation via the detector geometry, *i.e.*, when computing where neutrinos hit the detector after propagating inside the Earth, and in the modeling of the detector response via the energy- and direction-dependent effective volume. Given the same information for a different UHE neutrino telescope, our methods can be repeated.

Informing the design of the radio array of IceCube-Gen2 and of other detectors.— Conversely, our methods can be used to optimize the design of the IceCube-Gen2 detector—or any future detector—based on its potential to discover the UHE neutrino flux, in terms of effective volume, energy resolution, and angular resolution.

Combining the optical and radio arrays of IceCube-Gen2.— We focused our forecasts exclusively on the radio array of IceCube-Gen2. Yet, the planned design of IceCube-Gen2 [39] includes also a large extension of the optical array that is expected to characterize in detail the TeV–PeV neutrino flux beyond the capabilities of IceCube. Because the optical array will be sensitive to neutrinos with up to roughly 10 PeV, using it in combination with the radio array could enhance the discovery potential of UHE neutrino flux models that peak at relatively low energies, and the separation between flux models that differ primarily at low energies. References [321, 386] have early results in this direction.

7.8 SUMMARY AND OUTLOOK

Ultra-high-energy (UHE) neutrinos, with EeV-scale energies, represent the ultimate high-energy neutrino frontier [65, 387]. Sought unsuccessfully for the past half-century, there is a real chance of finally discovering them in the next 10–20 years, thanks to new large-scale UHE neutrino telescopes presently under development [83]. Their discovery would reveal key insight into extant questions in astrophysics and particle physics [82, 83, 125, 187, 189–191, 216, 342, 343].

So far, existing forecasts of the discovery of UHE neutrinos, and general-purpose methods to produce them, while pioneering, have of necessity lacked detail. Still, further work from theory and phenomenology is needed to accurately forecast the discovery potential of upcoming detectors.

In dialogue with ongoing experimental development, these forecasts will help map out near-future capabilities and may inform design choices and science programs of upcoming detectors.

Our work addresses this need. We have produced detailed forecasts of the discovery of a diffuse flux of UHE neutrinos, aimed at upcoming UHE neutrino telescopes. (The discovery of point sources of UHE neutrinos is addressed elsewhere, *e.g.*, in Refs. [371, 372].) To make our forecasts realistic, robust, and useful, we factor in nuance that previous works either considered partially or not at all. By design, and inasmuch as possible, our forecasts are anchored in detailed theory and experimental considerations. Despite being tempered by them, we have found encouraging prospects.

On the theory front, since the diffuse flux of UHE neutrinos is predicted uncertainly, we have considered a large number of competing benchmark predictions [37, 174–180, 188, 193], built on diverse assumptions, that span the allowed parameter of flux models presently allowed, from optimistic to pessimistic; see Fig. 26. The models include extrapolations of the TeV–PeV IceCube neutrino flux to ultra-high energies [37, 188], cosmogenic neutrinos [174, 179, 193], neutrinos made in astrophysical sources [175, 176, 179], and combinations of the latter two [177, 178, 180].

On the experimental front, we have used state-of-the-art ingredients to compute the propagation of neutrinos through the Earth (Section 7.3), of neutrino-induced event rates at the detector (Section 7.4.4), including dedicated simulations of the detector response, and of neutrino and atmospheric muon backgrounds (Section 7.4.5). We factored in the uncertainty in the UHE neutrino-nucleon cross section, which affects neutrino in-Earth propagation and detection. We made our forecasts concrete by focusing on UHE neutrino detection in the envisioned radio array of IceCube-Gen2 [39], whose target sensitivity is among the best [83]. We produced forecasts using a Bayesian statistical approach, and reported them via Bayes factors that account for random statistical fluctuations in the predicted event rates (Section 7.5.1).

In our baseline results, we adopted conservative analysis choices for the detector capabilities, backgrounds, and neutrino-nucleon cross section (Table 4 and Section 7.5.2.1). With them, and even after accounting for the above experimental nuance, *we found (Fig. 25) that most of our benchmark UHE neutrino diffuse flux models may be discovered decisively (i.e., with a Bayes factor larger than 100) within ten years of operation of the radio array of IceCube-Gen2; most of them, within a handful of years and*

some, within a few months. On average, discoverable flux models are expected to induce roughly 10–300 events with energies from 10 PeV to 10 EeV per decade (Table 3). Discovery may be claimed sooner at a lower statistical significance, or by adopting alternative analysis choices (Table 5). Flux models with less than one event per decade will remain undiscovered; these include, *e.g.*, some cosmogenic neutrino flux models fit to the heavy UHECR mass composition measured by Auger [174].

We found that the potential UHE tail of the IceCube TeV–PeV neutrino flux may be the dominant background to discovering the benchmark flux models. In some cases, knowing the precise energy where the background IceCube neutrino flux cuts off may reduce the time needed for the discovery of an UHE neutrino flux model from several years to a few months (Section 7.5.2.5). This stresses the need for a precise understanding of the size and shape of the high-energy tail of the IceCube neutrino flux. Detectors that will target the tens-of-PeV range, like TAMBO [73], Trinity [355], and the optical array of IceCube-Gen2 [39], should prove valuable. The UHE tail of the IceCube flux may itself be discovered in the radio array of IceCube-Gen2 within 10 years, provided its spectrum is hard [37] and its cut-off is beyond 50 PeV (Section 7.5.2.9). This opens up the possibility that the IceCube flux span the TeV–EeV range and that it could be used as a calibration flux bridging TeV–PeV-scale telescopes and EeV-scale telescopes.

Finally, we have found that, in the event of UHE neutrino flux discovery, it should be possible within 10 years to distinguish between nearly all our competing benchmark flux models (Section 7.6). The power to separate competing flux predictions stems from the differences in the energy distribution of the events that they induce.

We provide our forecasts and methods in the hope of complementing ongoing work in the planning and building of UHE neutrino telescopes. We encourage experimental collaborations to adopt our methods, or similar ones; or, alternatively, to make publicly available the simulated response function of their detectors. In light of our findings, the coming decades have a real chance to bring transformative progress to astroparticle physics.

7.9 CRITICAL OUTLOOK

We provide a critical outlook on the results and implications of our study, focusing on the key findings, limitations, and future perspectives. The main text of the published research paper already includes similar discussions in Sections 7.8 and 7.7. We summarize those discussions and focus on a critical view of the results from a state-of-the-art perspective and how this has been updated since the results were first published.

7.9.1 *Overview and main findings*

The results of our work are encouraging. Even with conservative assumptions about detector capabilities and background noise, our findings suggest that many UHE neutrino flux models could be decisively discovered within a decade of operation of IceCube-Gen2. Some might even be discovered within months. This rapid progress could be achieved by better understanding the high-energy tail of the IceCube neutrino flux. Instruments designed for the tens-of-PeV energy range could play a crucial role. Additionally, the UHE tail of the IceCube flux could be observed within a decade, potentially serving as a calibration source for telescopes spanning a wide energy range. Our research aims to contribute to the advancement of astroparticle physics and encourages collaboration among experimental scientists to adopt our methods for future discoveries.

Among the key findings of this work are the following:

- The importance of an accurate characterization of the UHE tail of the IceCube astrophysical neutrino flux.
- The effect of varying the energy and angular resolution on the UHE neutrino flux discovery potential. In particular, when distinguishing among different flux models, the energy resolution is the most relevant quantity, while for the case of separating a signal from a background contribution, both quantities have a similar impact.
- Earth-skimming neutrinos are the ones that carry the most valuable information, as they help to break the degeneracy between the neutrino flux and the νN cross section.

- The effect of the size of the atmospheric muon background on the discovery potential is small, in particular when compared with the impact of the background component of the UHE tail of the HE neutrino flux. This is mainly because, in our work, the atmospheric muon background spectral shape is fixed. Furthermore, the muon background contamination is localized in the lowest energy bins which leaves the high-energy bins background-free.

7.9.2 *Limitations and future perspectives*

To generate our forecasts regarding the potential discovery of ultra-high-energy (UHE) neutrino flux and model separation, we employed leading-edge detector simulations and theoretical inputs. While our analysis is robust, there are areas for potential improvement in future revisions. These potential enhancements do not fundamentally limit our present analysis.

The calculation framework for this work is similar to that presented in Ch. 6; therefore, many of the limitations and potential direction for improvement also apply in the context of this work (see Sec. 6.11). In the following we focus on the additional potential improvement relevant for this work.

1. *Characterizing the UHE tail of the iceCube high-energy neutrino flux:* Our forecasts indicate that the primary background to discovering certain flux models may come from the UHE tail of the IceCube high-energy neutrino flux, especially if it exhibits a hard energy spectrum and a high cut-off energy. While we accounted for the uncertainty in the cut-off energy, we did not consider uncertainties in the flux normalization and spectral index. Future revisions should explore the full range of uncertainty in the shape of the UHE tail, encompassing cut-off energy, normalization, and spectral index. Furthermore, the results in this analysis must be revisited as more data becomes available in the upcoming years and the characterization of the high-energy astrophysical neutrino flux improves.

2. *Reconstructing the UHE neutrino energy spectrum:* In our calculations of the UHE neutrino flux discovery potential, we did not assess how accurately the energy spectrum of UHE neutrinos could be reconstructed. This is crucial for claiming flux discovery and model separation without theoretical bias. Our recent work in Ref. [336] and discussed in this thesis in Ch. 8

focuses on reconstructing the normalization and spectral shape of the UHE neutrino flux, using a generic parametrization, and jointly measuring the neutrino-nucleon cross section. These results maybe used as a starting point for an improved characterization of the UHE neutrino flux discovery potential with reduced theoretical bias.

3. *Applying our analysis methods to other UHE neutrino telescopes:* While our analysis was tailored to IceCube-Gen2, it can be extended to other UHE neutrino telescopes, including radio-based ones. The neutrino event rates computation and the statistical analyses in this work have pushed the development of highly-optimized computational tools. Ongoing efforts aim to make these tools public an easy to adapt for a diverse set of neutrino telescopes.

4. *Informing detector design:* Conversely, our methods can play a vital role in optimizing the design of future detectors, including the radio array of IceCube-Gen2, by assessing their potential for UHE neutrino flux discovery in terms of effective volume, energy resolution, and angular resolution. The computational tools mentioned in the previous item are now available for the internal use of the IceCube-Gen2 Collaboration, and they are expected to be used as a reference for optimizing the radio antennas trigger and the detector configuration.

5. *Combining optical and radio arrays:* While our forecasts focused on the radio array of IceCube-Gen2, the planned IceCube-Gen2 design includes a substantial extension of the optical array. Combining data from both arrays could enhance the potential for discovering UHE neutrino flux models with lower energy peaks and improve the separation between models with differences primarily at lower energies. Our work presented in Ch. 8 confirms the need of a combined analysis. Figure 27 shows that the region between 10^7 and 10^8 GeV has a low number of neutrino events due to the limited sensitivity of the radio component of IceCube-Gen2 in this region. The optical array would help alleviate this limitations. Furthermore, other planned detectors, such as TAMBO [388], target this particular region would contribute too.

These potential future improvements not only strengthen the foundations of UHE neutrino research but also contribute to the advancement of astroparticle physics and the optimization of future detector facilities.

8

JOINT MEASUREMENT OF THE NEUTRINO FLUX AND NEUTRINO-NUCLEON CROSS SECTION

Based on: **Víctor B. Valera Baca**, Mauricio Bustamante, Olga Mena, *Joint measurement of the ultra-high-energy neutrino spectrum and cross section*, arXiv:2308.07709

ABSTRACT Soon, a new generation of neutrino telescopes, presently under planning, will target the discovery of ultra-high-energy (UHE) neutrinos of cosmic origin, with energies higher than 100 PeV, that promise unique insight into astrophysics and particle physics. Yet, predictions of the UHE neutrino flux and interaction cross section—whose measurement is co-dependent—are laden with significant uncertainty that, if unaddressed, could misrepresent the capabilities to measure one or the other. To address this, we advocate for the joint measurement of the UHE neutrino spectrum and neutrino-nucleon cross section, including of their energy dependence, without assuming prior knowledge of either. We illustrate our methods by adopting empirical parametrizations of the neutrino spectrum, in forecasts geared to the planned radio array of the IceCube-Gen2 neutrino telescope. We warn against using simple parametrizations—a simple power law or one augmented with an exponential cut-off—that might fail to capture features of the spectrum that are commonplace in the predictions. We argue instead for the use of flexible parametrizations—a piecewise power law or an interpolating polynomial—that ensure accuracy. We report loose design targets for the detector energy and angular resolution that are compatible with those under present consideration.

8.1 INTRODUCTION

For over fifty years [65], ultra-high-energy (UHE) neutrinos, with EeV-scale energies (1 EeV $\equiv 10^{18}$ eV)—have evaded detection. At long last, this might change in the next decade, thanks to new, larger neutrino telescopes. Yet, because much is unknown about them, planning for their discovery has unavoidably involved making informed assumptions; notably, regarding the size of the UHE neutrino flux and interaction cross section, and their dependence on neutrino energy. Below, we show that these assumptions can be abandoned—and should be abandoned—if we are to tap into the unbiased joint sensitivity to astrophysics and particle physics that the next generation of UHE neutrino telescopes will offer.

Ultra-high-energy neutrinos are produced in the interaction of ultra-high-energy cosmic rays (UHECRs) with radiation or matter, either inside extragalactic cosmic-ray accelerators, or during the long propagation of UHECRs to Earth [83]. They are the most energetic neutrinos expected, 10–100 times more so than the TeV–PeV neutrinos discovered by the IceCube neutrino telescope that are the most energetic ones detected to date [37, 188]. They carry insight into long-standing open questions in astrophysics [189]—what are the sources of UHECRs—and fundamental physics [190]—how do neutrinos, and particle physics broadly, behave at the highest energies.

The existence of UHE neutrinos is all but guaranteed, since it relies on the existence of UHECRs and cosmological radiation fields, both of which are observed. However, they are rare; so much so that, so far, they remain undiscovered in spite of the fact that the neutrino-nucleon cross section, which fixes the probability of detecting UHE neutrinos, is expected to be larger at ultra-high energies [134, 205, 217, 218, 220, 221, 250]. Searches for UHE neutrinos have placed increasingly tighter upper limits on their diffuse flux [66–68, 389], which means that existing neutrino telescopes are likely too small to discover them. In parallel, predictions of the UHE neutrino flux have grown in sophistication, but still vary significantly in size and shape (see, *e.g.*, Refs. [172–180, 193, 255, 344, 345] and Fig. 2 in Ref. [390]), because they rely on properties of UHECRs and their sources, which are only known uncertainly [29, 125].

In view of this, in the next 10–20 years a new generation of UHE neutrino telescopes, presently under planning and construction [82, 83], will target the discovery of UHE neutrinos even if their

flux is tiny. They adopt new detection strategies, or extend proven ones, to monitor detector volumes larger than present-day telescopes—Baikal-GVD [391] (following Baikal NT-200 [392]), KM3NeT [40] (following ANTARES [393]), and IceCube [35]—which use in-ice and in-water optical Cherenkov detection. Techniques under consideration include the detection of neutrino-initiated showers via their radio emission in ice, in IceCube-Gen2 [39], RNO-G [84], and RET-N [152] (following ARA [157] and ARIANNA [69]), or in the atmosphere, in BEACON [153], GRAND [72], PUEO [75] (following ANITA), and TAROGE-M [394]; via their Cherenkov emission in the atmosphere, like Ashra NTA [356], CTA [354], EUSO-SPB [383], SKA [331], TAx4 [395], Trinity [333], and, from space, POEMMA [74]; and via their particle showers at ground level, like AugerPrime [162].

In preparation, previous works have forecast the potential of upcoming detectors to discover the diffuse flux of UHE neutrinos [390] (and also UHE neutrino point sources [371, 372]), and to measure, for the first time, the UHE neutrino-nucleon cross section [215, 346, 348]. The forecasts are encouraging. However, they rely on key simplifying assumptions: they fix either the UHE neutrino flux—its normalization or energy spectrum—the neutrino-nucleon cross section—its size or energy dependence—or both. Adopting these assumptions does not invalidate the conclusions reached by these works, though they may have cast them in an overly optimistic light, since these quantities are ultimately unknown and must be measured. More importantly, they may have unwittingly downplayed the capability of upcoming neutrino telescopes to make joint measurements of the UHE neutrino flux and cross section, including of their energy dependence, unencumbered by assumptions on one or the other, and with little theoretical bias.

An earnest analysis of UHE neutrinos, one that conveys the true capabilities of upcoming neutrino telescopes, should strive to jointly measure the neutrino spectrum and the energy dependence of the neutrino-nucleon cross section. For the first time, we provide forecasts of such an analysis. We show that this should be feasible under realistic experimental setups, so as to motivate upcoming experimental endeavors to embrace their full potential.

Figure 39 shows a condensed view of our main results; we defer details to later. We gear our results to UHE neutrino radio-detection in IceCube-Gen2 because it is one of the largest planned telescopes; we model it in state-of-the-art detail [346]. Based on plausible detector performance

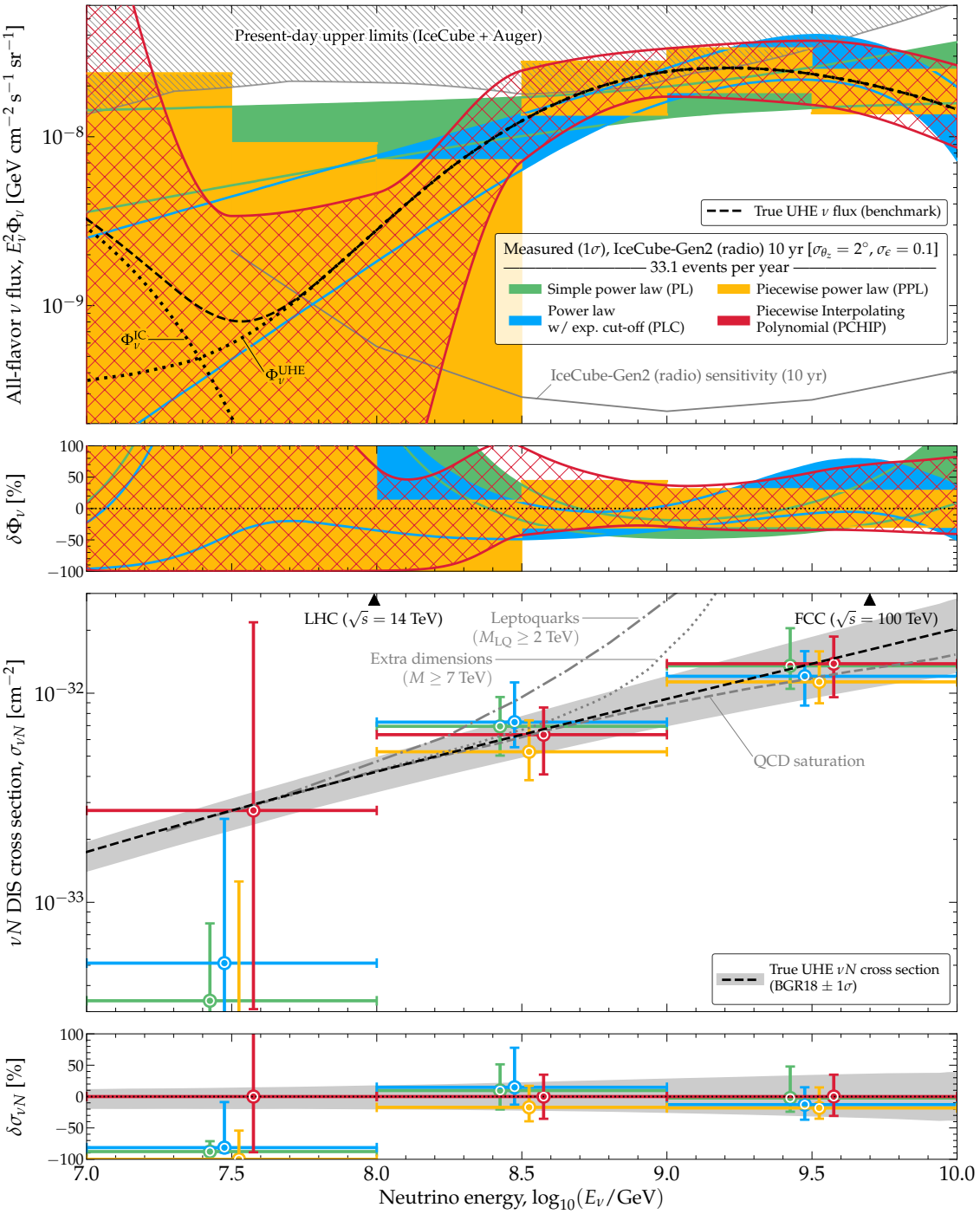

Figure 39: ***Projected joint measurement of the ultra-high-energy (UHE) neutrino flux and neutrino-nucleon deep-inelastic scattering cross section in the radio array of IceCube-Gen2.*** We show results for our benchmark UHE neutrino flux (Sec. 8.3.2), computed using four fit models of the neutrino spectrum: PL, PLC, PPL, and PCHIP (Sec. 8.5.1). *Top two panels*: UHE neutrino flux, and relative error between the measured and true flux, $\delta\Phi_\nu = (\Phi_\nu - \Phi_\nu^{\rm true})/\Phi_\nu^{\rm true}$. Present-day upper limits on the flux are from IceCube [66] and Auger [67]. The projected sensitivity of IceCube-Gen2 is from Ref. [396]. *Bottom two panels:* UHE neutrino-nucleon cross section, and relative error between the measured and true [194] cross section, $\delta\sigma_{\nu N} = (\sigma_{\nu N} - \sigma_{\nu N}^{\rm true})/\sigma_{\nu N}^{\rm true}$. Central values are offset horizontally for clarity. See Sec. 8.7 and Fig. 41 for details.

and energy and angular resolution, Fig. 39 shows that it should be possible to jointly measure the UHE neutrino spectrum and the energy dependence of the cross section, both with a relative uncertainty of tens of percent, enough to reconstruct the spectrum closely—which can provide astrophysical insight—and to identify potential deviations of the cross section from its standard prediction—which can provide particle-physics insight.

There are, however, three caveats; we address them in detail later. First, such joint measurement requires a detection rate of at least a handful of UHE neutrinos per year; ideally, of a few tens. However, this is not unique to our work; it is also true for previous forecasts of flux discovery [390] and cross-section measurement [215, 346, 348]. Second, Fig. 39 shows that measurements below 100 PeV are poor; this is because there UHE neutrino telescopes become less efficient. This showcases the need for complementarity between UHE neutrino telescopes and telescopes sensitive to PeV-scale neutrinos [39, 83, 321]. Third, for our measurements to be accurate, *i.e.*, centered on the true values of the flux and cross section, it is critical when contrasting test *vs.* true UHE neutrino energy spectra to use a parametrization of the test spectra that is flexible enough to capture the features of the true spectrum. Otherwise, precision may be high but accuracy low.

The rest of this paper is organized as follows. Section 8.2 presents the synopsis, context, and tenet of our work. Section 8.3 overviews general features of the UHE neutrino flux and introduces our benchmark flux model. Section 8.4 describes the method we use to estimate event rates. Section 8.5 introduces the models of the UHE neutrino flux and cross section that we adopt in our fits to simulated observations. Section 8.6 introduces our statistical methods. Section 8.7 shows results using different analysis choices. Section 8.8 summarizes.

8.2 SYNOPSIS, CONTEXT, AND TENET

8.2.1 *Measuring the neutrino flux and cross section*

Upon reaching the Earth, high-energy cosmic neutrinos travel from its surface, through its interior, to the detector, over distances of up to the diameter of the Earth. Along the way, they interact with underground matter—predominantly via neutrino-nucleon (νN) deep inelastic scattering

(DIS) [60–63]—and, as a result, their flux is attenuated. Roughly, the attenuation factor is $e^{-\sigma_{\nu N} L}$, where $\sigma_{\nu N}$ is the νN DIS cross section and L is the distance traveled by the neutrinos inside Earth. Thus, the flux of neutrinos that reach a detector from below, after traveling through thousands of kilometers inside the Earth, is more severely attenuated than the flux of neutrinos that reach it from above, after traveling through only a few kilometers of matter. Because the νN cross section grows with neutrino energy [217, 218, 220], the attenuation is more severe the higher the neutrino energy.

The neutrino flux, Φ_ν, and the νN cross section determine the number of neutrinos detected upon reaching the detector. Roughly, this is $N_\nu \sim \Phi_\nu \sigma_{\nu N} e^{-\sigma_{\nu N} L}$. This illustrates an essential aspect of our plight: for a given number of detected neutrinos, there is a degeneracy between the flux and cross section that is broken only by the exponential dampening term, as long as it is sufficiently different from unity. It is, in fact, from this interplay that the measurement of the νN cross section stems; we outline this below. Yet, when the cross section is too high—at the highest energies—the attenuation nearly fully dampens the flux. (We use the above expression only for illustration; later, in Sec. 8.4, we produce our results using detailed computations of neutrino propagation inside the Earth and detection.)

Below about 10 TeV—below the energies relevant to our work—the cross section is small enough for Earth to be largely transparent to neutrinos, regardless of their arrival directions to the detector, *i.e.*, $e^{-\sigma_{\nu N} L} \approx 1$. Between about 100 TeV and a few PeV—still below our energies of interest—the cross section grows to appreciably attenuate the flux of neutrinos that reach the detector from below, *i.e.*, $e^{-\sigma_{\nu N} L} \lesssim 1$ from below and $e^{-\sigma_{\nu N} L} \approx 1$ from above. Above 100 PeV—the energies relevant to our work—the attenuation is severe across most arrival directions, *i.e.*, $e^{-\sigma_{\nu N} L} \ll 1$ from below $e^{-\sigma_{\nu N} L} \lesssim 1$ from above and from horizontal directions. See Fig. A2 in Ref. [61] for an illustration. Later, we show how dwindling event rates are a challenge to UHE measurements.

Our goal is to measure the UHE neutrino flux and νN cross section—and to do it jointly. For TeV–PeV neutrinos, these measurements are performed regularly using IceCube data, though seldom jointly (more on this below). Given a sample of detected neutrinos, to measure the flux responsible for it, analyses undo the effect of in-Earth attenuation and, to measure the cross section, analyses compare the flux attenuation along different directions. Below, we outline the methods

used to measure the TeV–PeV neutrino flux and cross section. At ultra-high energies, the methods are similar, but have important differences that motivate our analysis choices.

8.2.2 *Today: TeV–PeV measurements*

Measuring the neutrino flux.—To infer the flux of TeV–PeV cosmic neutrinos by undoing the effect of in-Earth attenuation, analyses require knowledge of the νN cross section, at least within its theoretical uncertainty, and an ansatz for the neutrino spectrum. For the former, there are multiple predictions [134, 194, 203, 205, 221, 225–230, 250, 397]. For the latter, the nominal assumption, motivated by astrophysical considerations, is a power-law spectrum, $\Phi_\nu \propto E_\nu^{-\gamma}$, where E_ν is the neutrino energy. The values of the flux normalization and the spectral index, γ, are allowed to float and are fixed in a fit to data that contrasts predicted event rates *vs.* observed ones. Numerous analyses using IceCube data have used this procedure to measure the diffuse flux of astrophysical and atmospheric neutrinos [34, 35, 37, 184–186, 188, 294, 398–401].

At present, there is no strong preference from data for alternative choices of the TeV–PeV neutrino spectrum—a broken power law, a power law with an exponential cut-off, or a log-parabola; see, *e.g.*, Refs. [37, 188, 402]. Another, more flexible choice, trades the use of a single spectrum over the full energy range of the analysis for a piecewise spectrum that is $\propto E_\nu^{-2}$ inside multiple, relatively narrow energy bins, each one carrying its own independent, floating normalization. The greater shape flexibility of a piecewise power-law spectrum grants the analysis sensitivity to narrow energy features that would otherwise be missed by using a rigid spectral shape. We explore this choice ourselves later in our UHE forecasts (Sec. 8.5.1).

Measuring the νN cross section.—The measurement of the νN cross section stems from comparing the number of neutrinos of different energies detected along different arrival directions to the detector, which reflects how much the flux has been attenuated by propagating underground [205, 207, 244–247]. Based on this method, Refs. [60–63] used IceCube neutrinos to pioneer measurements of the TeV–PeV νN DIS cross section.

However, most of these cross-section analyses made simplifying assumptions that restricted their purview. Reference [60] measured only the normalization of the νN cross section, while

keeping its energy dependence fixed to a standard prediction [250]. Reference [63] measured the energy dependence of the cross section, but did so by assuming a common neutrino power-law flux that spans the full energy range of the analysis. Reference [62] performed a related analysis, extracting the average inelasticity (see Sec. 8.4.1) of νN DIS interactions.

Joint measurements.—To the best of our knowledge, a joint measurement of the TeV–PeV neutrino flux and cross section, including of their energy dependence, has only been performed in full in Ref. [61], using publicly available IceCube data [184, 403–405]. This analysis extracted the flux and cross section in separate energy bins, and provided the first measurement of the energy dependence of the cross section above 10 TeV. Because the flux and cross section were measured independently in each bin, the results did not rely on assumptions of their behavior across a wide energy range, which could be either questionable or too constraining. This conferred the analysis sensitivity to the potential presence of narrow features in the energy spectrum—such as bumps that could hint at the origin of the neutrinos [402]—or in the cross section—which could hint at deviations from standard predictions [61]. (A later analysis [63] measured the cross section also in multiple energy bins, but assumed instead a common neutrino flux across them.)

8.2.3 *This work: upcoming UHE measurements*

The upcoming access to ultra-high neutrino energies motivates making suitable analysis choices from the start.

The severe attenuation of the UHE neutrino flux inside the Earth shrinks not only the size of the available sample of detected events, but, more importantly, the range of neutrino directions from which we can compare the relative in-Earth attenuation to infer the νN cross section. Further, the regeneration of lower-energy neutrinos via neutral-current interactions and ν_τ charged-current interactions [209, 406]—relatively unimportant at lower energies—becomes important at ultra-high energies. This renders the measurement of the neutrino flux and cross section at ultra-high energies especially susceptible to mismodeling their energy dependence.

With this in mind, we adopt three guiding principles when forecasting measurements:

MAKE JOINT MEASUREMENTS We measure jointly the UHE neutrino flux and νN cross section, and without fixing one when measuring the other. In our statistical methods (Sec. 8.6), we adopt broad and uninformative priors on the flux and cross-section model parameters to avoid introducing bias.

MEASURE THE ENERGY-DEPENDENT $\sigma_{\nu N}$ To be sensitive to the potential presence of narrow features in the νN cross section or changes in its growth rate with energy—*e.g.*, coming from extra dimensions [407], leptoquarks [408], or QCD saturation [229]—we measure the cross section in multiple energy bins; see Fig. 39.

MEASURE THE NEUTRINO SPECTRUM Given the large variety in the shapes of competing predictions of the UHE neutrino spectrum (Sec. 8.3), we favor flexible parametrizations when attempting to measure it from data. Later (Sec. 8.7), we show that adopting too rigid a parametrization leads to poor accuracy in the measurements; see Fig. 39.

We build an analysis based on these principles, gearing our forecasts to the radio-detection of UHE neutrinos in IceCube-Gen2 [39]. Our forecasts are based on methods introduced in Ref. [346], and validated in Refs. [372, 390, 409].

Our goal is not to provide an exhaustive exploration of the capability to measure the UHE neutrino flux and cross section; for that, see Refs. [346, 390]. It is to bring attention to the need to measure them jointly, and to make suitable analysis choices when doing so. Accordingly, later we produce forecasts assuming a relatively large benchmark UHE neutrino flux, based off of Ref. [193], that yields about 33 detected events per year (Sec. 8.3), which allows us to illustrate clearly our methods; see Fig. 39.

In reality, the rate of detected events may be appreciably lower. In that case, we might be tempted to adopt simpler analysis choices rather than follow our guiding principles above, which involve more informative, albeit complex, choices. Granted, if only a handful of events were detected over the full observation campaign, simpler analysis choices would likely be preferable—*e.g.*, using a simple power-law spectrum and measuring the cross-section normalization but not its energy dependence.

However, we show below that maintaining simpler analysis choices when the event rate is higher would be detrimental. Adopting too rigid a parametrization of the neutrino spectrum

might unknowingly incur not only in its misreconstruction but also in that of the cross section (Sec. 8.7). Still, choosing flexible parametrizations, with more model parameters, entails reducing the precision with which each parameter is measured: selecting for accuracy comes at the cost of sacrificing some precision. We deem this trade-off tolerable.

8.3 ULTRA-HIGH-ENERGY NEUTRINOS

8.3.1 *Overview*

Ultra-high-energy neutrinos, with energies in excess of 100 PeV, are expected to be produced in the interaction of UHECRs, of EeV-scale energies, with matter or radiation, *i.e.*, in pp interactions [130] or $p\gamma$ interactions [256–258], respectively. The interactions may occur inside the UHECR sources, purportedly extragalactic cosmic-ray accelerators—in which case neutrinos are dubbed *source neutrinos*—or during the propagation of UHECRs after leaving the sources, upon their scattering on the cosmic microwave background and the extragalactic background light—in which case they are dubbed *cosmogenic neutrinos*. These interactions produce high-energy charged pions that decay into high-energy neutrinos, *i.e.*, $\pi^+ \to \mu^+ + \nu_\mu$, followed by $\mu^+ \to e^+ + \nu_e + \bar{\nu}_\mu$, and their charge-conjugated processes. Each neutrino carries about 5% of the energy of the parent proton. Other production processes contribute, too, their importance growing with neutrino energy [256–258].

Broadly stated, the energy spectrum of UHE neutrinos made in pp interactions is a power law $\propto E_\nu^{-\gamma}$ inherited from the power-law spectrum of the parent UHECR protons, with $2 \lesssim \gamma \lesssim 3$. In contrast, the energy spectrum of UHE neutrinos made in $p\gamma$ interactions peaks at a characteristic energy set by the kinematic condition to produce the $\Delta(1232)$ resonance that decays into charged pions. The shape of the spectrum, especially for source neutrinos, may be further affected by energy losses and gains of the parent cosmic rays and charged secondary particles [259–261]. The normalization of the UHE neutrino flux depends on the properties of the UHECRs—their mass composition, spectrum, and maximum energy—and of their sources—mainly, their distribution in redshift. The joint production of UHE source and cosmogenic neutrinos often considers both pp

and $p\gamma$ interactions; their predicted spectra are superpositions of a power law and a bump-like spectrum; *e.g.*, Refs. [177, 178, 180].

Regarding the flavor composition of UHE neutrinos, *i.e.*, the proportions of ν_e, ν_μ, and ν_τ in their total flux, the canonical expectation comes from the decay of high-energy pions (see above). At the neutrino sources (S), the flavor composition from pion decay is $(f_{e,\mathrm{S}}, f_{\mu,\mathrm{S}}, f_{\tau,\mathrm{S}}) = (1/3, 2/3, 0)$, where $f_{\alpha,\mathrm{S}} \equiv (\Phi_{\nu_\alpha,\mathrm{S}} + \Phi_{\bar{\nu}_\alpha,\mathrm{S}})/\Phi_\mathrm{S}$ ($\alpha = e, \mu, \tau$), $\Phi_{\nu_\alpha,\mathrm{S}}$ is the flux of ν_α, $\Phi_{\bar{\nu}_\alpha,\mathrm{S}}$ is the flux of $\bar{\nu}_\alpha$, and $\Phi_\mathrm{S} \equiv \sum_\alpha (\Phi_{\nu_\alpha,\mathrm{S}} + \Phi_{\bar{\nu}_\alpha,\mathrm{S}})$ is the total neutrino flux. Because of flavor mixing during propagation, the corresponding canonical flavor composition at Earth ($\oplus$), computed using the best-fit values of the neutrino mixing parameters [268, 269], is of near flavor equipartition: $(f^\pi_{e,\oplus}, f^\pi_{\mu,\oplus}, f^\pi_{\tau,\oplus}) \approx (0.298, 0.359, 0.342)$ [267] (see also Ref. [329]). By the years 2030–2040, for which we forecast, the uncertainties on the flavor composition at Earth are at the per-mille level [267, 346], and we ignore them. Other neutrino production processes or the physical conditions at the sources might affect the flavor composition, including in energy-dependent manners (see Fig. 5 in Ref. [346]), and so might new neutrino physics [83, 328, 329, 410, 411], though we do not consider those possibilities here.

In our forecasts of joint measurement of the UHE neutrino flux and cross section, we use the diffuse neutrino flux, made up of the contributions of all neutrino sources distributed across all redshifts, and which we take to be precisely isotropic. It includes, in principle, contributions of source neutrinos and cosmogenic neutrinos; however, we make no attempt to tell these contributions apart. The diffuse flux affords the largest expected rates of detected events. In addition, the diffuse flux provides neutrinos from all arrival directions—which we need to make the measurements (Sec. 8.2.1)—unlike UHE neutrinos from point sources [372], which are confined to come from the directions of a limited number of sources.

Presently, because the identity of the UHECR sources and the UHECR production processes are unknown, there is a large spread in the UHE neutrino flux predictions, in shape and size. Figure 2 in Ref. [390] illustrates the current status of the flux predictions.

Regarding the neutrino spectrum, differences between competing predictions stem from different choices of the parent proton spectrum, target photon spectrum inside sources, and source properties such as magnetic field intensity. For instance, models of neutrino production via $p\gamma$ interactions

predict spectra that peak at 10^7 GeV [180], 10^8 GeV [179], or 10^9 GeV [389], with varying width of the spectrum around the peak value. The spectrum might even have multiple peaks [180].

Regarding the flux normalization, differences between competing predictions stem from the large uncertainty in the properties of UHECRs and their sources. Heavier UHECR mass composition, steeper energy spectrum, and lower maximum energy—such as those favored by Pierre Auger Observatory (Auger) observations [25, 26, 253]—lead to a lower neutrino flux. The converse—favored by Telescope Array (TA) observations [412, 413]—holds, too. For details, see *e.g.*, Refs. [172–174, 255, 414]. As a result, flux predictions range from being as high as to saturate the present-day upper limits [66, 67] (see Fig. 39) and as low as to be practically undetectable [344, 345, 390].

Given the breadth of predictions of the UHE neutrino flux, we build our analysis methods later so that they are able to handle their variety of shape and size. We achieve this by adopting flexible parametrizations of the spectrum, which we describe later (Sec. 8.5.1).

8.3.2 *Benchmark UHE neutrino flux*

To illustrate our methods of joint measurement of the UHE neutrino flux and cross section, we adopt a benchmark model of the UHE neutrino flux that is representative of the breadth of flux predictions outlined above. Following Ref. [390], our benchmark flux is the sum of two flux components, shown in Fig. 39: an UHE flux prediction, $\Phi_{\nu_\alpha}^{\text{UHE}}$, plus the UHE tail of the IceCube flux, $\Phi_{\nu_\alpha}^{\text{IC}}$, *i.e.*, $\Phi_{\nu_\alpha} = \Phi_{\nu_\alpha}^{\text{UHE}} + \Phi_{\nu_\alpha}^{\text{IC}}$. When computing event rates due to our benchmark flux (Sec. 8.4.2), we use the flux of each neutrino species separately, and assume equal proportions of neutrinos and anti-neutrinos of each flavor. We describe each flux component below.

For the first component of our benchmark flux, $\Phi_{\nu_\alpha}^{\text{UHE}}$, we adopt the prediction of the cosmogenic neutrino flux from Ref. [389], generated by fitting the UHECR flux generated by a population of nondescript UHECR sources to observations by TA; see also Ref. [346] for an overview. Because TA favors a relatively light UHECR mass composition at the highest energies [413], the resulting cosmogenic neutrino flux is high—as high as is presently allowed by upper limits [66, 67]. The flavor composition evolves with neutrino energy, but stays close to the canonical expectation from pion decay; see Fig. 6 in Ref. [346]. (This flux component is flux model 4 in Refs. [346, 390].) This

flux component is the dominant one: it yields about 33.1 events per year in the radio array of IceCube-Gen2, within 10^7–10^{10} GeV, computed using the methods that we introduce in Sec. 8.4.2; see Table I of Ref. [390] for detailed event rates.

For the second component of our benchmark flux, $\Phi^{\rm IC}_{\nu_\alpha}$, we adopt an extrapolation to ultra-high energies of the TeV–PeV astrophysical neutrino power-law flux inferred by IceCube using 9.5 years of through-going ν_μ [37]. We augment it with an exponential cut-off at $E_{\nu,\rm IC} = 10^8$ GeV to explore the likely scenario where $\Phi^{\rm IC}_{\nu_\alpha}$ dies off at ultra-high energies and $\Phi^{\rm UHE}_{\nu_\alpha}$ takes over. Thus, the second flux component is $\Phi^{\rm IC}_{\nu_\alpha} = (f^\pi_{\alpha,\oplus}/f^\pi_{\mu,\oplus})(\Phi_{\nu_\mu+\bar\nu_\mu}/2)(E_\nu/100\ \text{TeV})^{-\gamma_{\rm IC}} e^{-E_\nu/E_{\nu,\rm IC}}$, where $\Phi_{\nu_\mu+\bar\nu_\mu} = 1.44\times10^{-18}\ \text{GeV}^{-1}\ \text{cm}^{-2}\ \text{s}^{-1}\ \text{sr}^{-1}$ is the best-fit normalization of the $\nu_\mu+\bar\nu_\mu$ flux (dividing it by 2 splits it evenly between ν_μ and $\bar\nu_\mu$) and $\gamma_{\rm IC} = 2.37$ is the best-fit spectral index, both from Ref. [37]. The prefactor $(f^\pi_{\alpha,\oplus}/f^\pi_{\mu,\oplus})$ converts the flux of ν_μ into the flux of ν_α, using the flavor ratios from Sec. 8.3.1. By itself, the second flux component yields a mean rate of only about 0.35 events per year (see Table I of Ref. [390]). Regardless, they should not be ignored because they are concentrated in the low end of the IceCube-Gen2 energy range, whereas events from the first flux component are concentrated at higher energies. (The background of atmospheric muons that we consider (Sec. 8.4.3) is similarly concentrated at low energies; see Fig. 40.)

(Basing instead the second component of our benchmark flux on the IceCube neutrino flux inferred from 7.5 years of High Energy Starting Events (HESE)—a steeper power law with spectral index of around 2.87—would have contributed a negligible rate of 0.22 events in 10 years; see Table I and Fig. 12 in Ref. [390].)

8.4 UHE NEUTRINO DETECTION

8.4.1 *Neutrino propagation inside Earth*

After neutrinos arrive at Earth, they propagate underground, from the surface of the Earth to the detector, IceCube-Gen2, located in South Pole, over distances of up to the diameter of the Earth. Along the way, they interact with underground Earth matter, which modifies the flux that reaches the detector depending on neutrino energy, direction, and flavor [60–63, 134, 205, 209, 215, 346,

348, 390]. In our analysis, we account for these effects using state-of-the-art calculations of the neutrino-matter cross sections and of neutrino propagation inside Earth. We present an overview below, and defer to Refs. [209, 346, 390] for details.

At the energies of interest, the neutrino interaction on matter is typically νN DIS. In a scattering event, the interacting neutrino scatters off of one of the partons—a quark or a gluon—of a nucleon, N—a proton or a neutron—and breaks it up into final-state hadrons, X. The interaction is either neutral-current (NC), *i.e.*, $\nu_\alpha + N \to \nu_\alpha + X$, where the final-state neutrino has lower energy than the incoming neutrino, or charged-current (CC), *i.e.*, $\nu_\alpha + N \to l_\alpha + X$, where l_α is a charged-current lepton of flavor α. Anti-neutrinos undergo the same processes, charge-conjugated; at ultra-high energies, the $\bar{\nu}N$ and νN DIS cross sections are very similar.

The final-state hadrons receive a fraction $0 \leq y \leq 1$, the inelasticity, of the energy of the incoming neutrino, while the final-state lepton receives the remaining fraction $1 - y$. The inelasticity distributions, $d\sigma^{\rm NC}_{\nu N}/dy$ and $d\sigma^{\rm CC}_{\nu N}/dy$, where $\sigma^{\rm NC}_{\nu N}$ and $\sigma^{\rm CC}_{\nu N}$ are the NC and CC cross sections, are energy-dependent and relatively broad; see, *e.g.*, Fig. 4 in Ref. [346]. At ultra-high energies, the average value of the inelasticity is $\langle y \rangle \approx 0.25$ [221]; however, we compute neutrino interactions during propagation using the y distributions, not their averages.

Because the νN DIS cross sections grow with energy, roughly $\propto E_\nu^{0.36}$ at ultra-high energies [134], the νN interactions of UHE neutrinos significantly modify the flux that reaches the detector. While NC interactions shift the neutrino flux to lower energies, CC interactions deplete it. Broadly stated, the net effect is an exponential attenuation of the neutrino flux, more prominent the higher the energy and the longer the distance traveled inside Earth (Sec. 8.2.1); see, *e.g.*, Figs. A1 and A2 of Ref. [61], Fig. 4.1 of Ref. [209], and Fig. 9 of Ref. [346]. As a result, at ultra-high energies, the flux of upgoing neutrinos, *i.e.*, those coming from $\theta_z \gtrsim 90^\circ$ (θ_z is the zenith angle measured from the South Pole) is nearly fully attenuated when it reaches the detector. In contrast, the flux of neutrinos arriving from downgoing ($\theta_z \gtrsim 90^\circ$) and horizontal ($\theta_z \approx 90^\circ$) directions is appreciably, though not fully attenuated. It is from these directions that UHE neutrinos may be discovered [372, 390] and their cross section measured [205, 215, 244, 346, 348]. Our joint measurement of the UHE neutrino energy spectrum and cross section stems from neutrinos from these directions (Sec. 8.7).

In our work, we propagate UHE neutrinos inside the Earth using the same procedure as in Refs. [346, 372, 390]. We use NUPROPEARTH [209, 210], a state-of-the-art Monte-Carlo neutrino propagation code. For the underground matter density of the Earth, we use the Preliminary Reference Earth Model [295], including variations in the chemical composition with depth. For the UHE νN DIS cross sections, NUPROPEARTH adopts the recent BGR18 calculation [194] and accounts for sub-leading neutrino interactions, for the important Glashow resonance of $\bar{\nu}_e$ on atomic electrons, and for the regeneration of ν_τ via repeated CC interactions; see Ref. [209] for details and Ref. [346] for a summary. We propagate the fluxes of ν_e, $\bar{\nu}_e$, ν_μ, $\bar{\nu}_\mu$, ν_τ, and $\bar{\nu}_\tau$ separately. Unlike the fluxes at the surface of the Earth, the fluxes that reach the detector, $\Phi^{\rm det}_{\nu_\alpha}$ and $\Phi^{\rm det}_{\bar{\nu}_\alpha}$, are no longer isotropic. For each neutrino flavor, initial energy, and direction, we propagate 10^7 neutrinos using NUPROPEARTH, as in Refs. [346, 354, 390, 409]. For the geometry of the radio array of IceCube-Gen2, our detector of choice, we use the cylindrical volume model introduced in Ref. [346].

8.4.2 *Neutrino radio-detection in IceCube-Gen2*

In the planned radio array of IceCube-Gen2 [39], UHE neutrinos will be detected via their interaction with nucleons in the ice, which initiates a particle shower whose electromagnetic component emits coherent, impulsive radio signals. The radio emission, known as Askaryan radiation [165], is due to the dipole formed between the shower axis and the excess of negative charges that accumulate on the front of the shower as it propagates. IceCube-Gen2 will be instrumented with radio antennas buried in the ice, capable of detecting this signal. From it, it will be possible to reconstruct the shower direction and energy, which are proxies for the direction and energy of the interacting neutrino. To compute neutrino-initiated event rates, we use the methods and detector description introduced in Ref. [346], to which we defer for details. Below, we only outline them.

The relation between the neutrino energy, E_ν, and the ensuing shower energy, $E_{\rm sh}$, depends on the neutrino flavor and on whether the interaction is NC or CC DIS. For NC interactions of neutrinos of all flavors and CC interactions of ν_μ and ν_τ, $E_\nu^{\rm NC} = E_{\rm sh}/y$, since only the final-state hadrons radiate [213]. For CC interactions of ν_e, $E_\nu^{\rm CC} = E_{\rm sh}$, since both the final-state charged

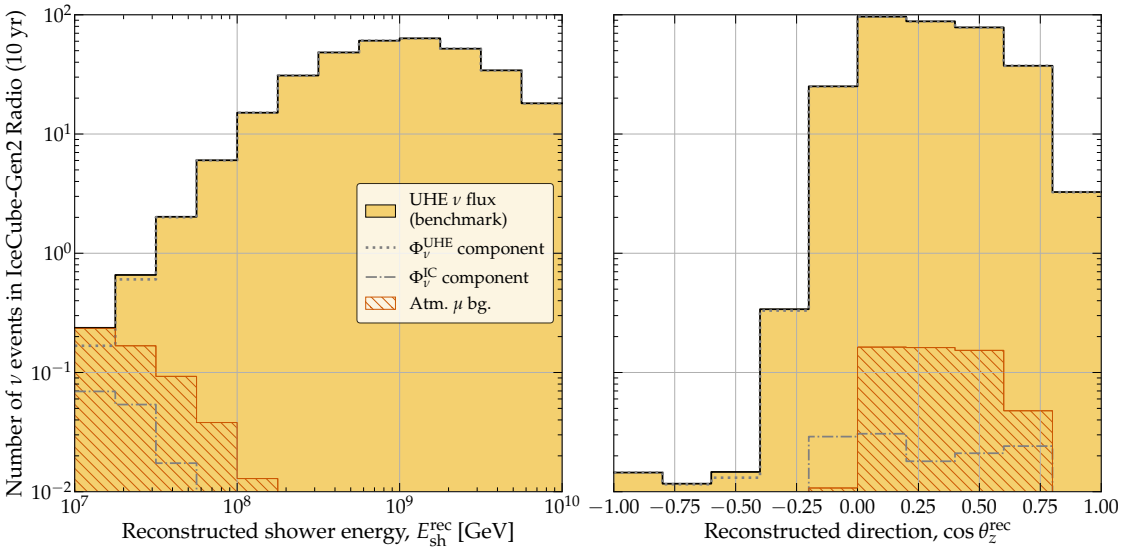

Figure 40: ***Mean expected number of events detected in the radio array of IceCube-Gen2 induced by our benchmark neutrino flux model.*** The benchmark neutrino flux is described in Sec. 8.3.2 and shown in Fig. 39. It consists of a cosmogenic flux component, $\Phi_\nu^{\rm UHE}$, from Ref. [389], and the UHE tail of the diffuse flux inferred from the IceCube 9.5-year ν_μ analysis [37], augmented by an exponential cut-off at 100 PeV, $\Phi_\nu^{\rm IC}$. Event rates are computed using our baseline choices for the detector energy resolution, $\sigma_\epsilon = 0.1$, and angular resolution, $\sigma_{\theta_z} = 2^\circ$. The background of high-energy atmospheric muons is computed using the baseline prescription of the muon flux. See Sec. 8.4.2 for the computation of neutrino-induced event rates and Sec 8.4.3, for that of event rates induced by atmospheric muons. *Left:* Events distributed in reconstructed energy. *Right:* Events distributed in reconstructed direction.

electron and hadrons radiate. Like during in-Earth propagation, the inelasticity, y, is distributed following the differential cross section (Sec. 8.4.1). At ultra-high energies, the y distributions of ν_α and $\bar{\nu}_\alpha$ of all flavors are equal.

The detector response is expressed via simulated effective detector volumes, $V_{{\rm eff},\nu_\alpha}^{\rm NC}$ and $V_{{\rm eff},\nu_\alpha}^{\rm CC}$, for NC and CC interactions, respectively. They are the same for ν_α and $\bar{\nu}_\alpha$. The effective volumes that we use were introduced in Ref. [346], and used also in Refs. [372, 390, 409]. They are generated in simulations of neutrino interaction, and of the ensuing radio emission and propagation in ice, employing the same tools used by the IceCube-Gen2 Collaboration, NuRadioReco [211] and NuRadioMC [212]. We adopt the same baseline detector configuration as in Refs. [346, 396], made up of a combination of shallow and deep radio stations. The effective volumes vary with the shower direction, θ_z, shower energy, $E_{\rm sh}$, and neutrino flavor; see Fig. 13 in Ref. [346] for an illustration.

The differential rate of events [346] initiated by ν_α is

$$\frac{d^2N_{\nu_\alpha}}{dE_{\rm sh}d\cos\theta_z} = 2\pi T n_t \int_0^1 dy \Bigg(\frac{E^{\rm NC}_{\nu_\alpha}(E_{\rm sh},y)}{E_{\rm sh}} V^{\rm NC}_{{\rm eff},\nu_\alpha}(E_{\rm sh},\cos\theta_z) \times \frac{d\sigma^{\rm NC}_{\nu_\alpha {\rm w}}(E_\nu,y)}{dy} \Phi^{\rm det}_{\nu_\alpha}(E_\nu,\cos\theta_z)|_{E_\nu = E^{\rm NC}_{\nu_\alpha}(E_{\rm sh},y)} + {\rm NC} \to {\rm CC} \Bigg) \,, \quad (8.1)$$

where T is the exposure time, n_t is the number density of water molecules in ice, and $d\sigma^{\rm NC}_{\nu_\alpha {\rm w}}/dy$ is the νN NC cross section on a water molecule, made up of 10 protons and 8 neutrons. The event rate due to $\bar{\nu}_\alpha$ is the same as Eq. (8.1), but changing $\Phi^{\rm det}_{\nu_\alpha} \to \Phi^{\rm det}_{\bar{\nu}_\alpha}$, $d\sigma^{\rm NC}_{\nu_\alpha {\rm w}}/dy \to d\sigma^{\rm NC}_{\bar{\nu}_\alpha {\rm w}}/dy$, and $d\sigma^{\rm CC}_{\nu_\alpha {\rm w}}/dy \to d\sigma^{\rm CC}_{\bar{\nu}_\alpha {\rm w}}/dy$.

We account for the capability of the detector to reconstruct the shower energy and arrival direction by smearing the above differential event rate using the energy and angular resolution functions. The detector reports the reconstructed shower energy, $E^{\rm rec}_{\rm sh}$, and direction, $\theta^{\rm rec}_z$, of the events. For the energy resolution function, $\mathcal{R}_{E_{\rm sh}}(E^{\rm rec}_{\rm sh}, E_{\rm sh})$, we use a Gaussian function of $\log_{10} E^{\rm rec}_{\rm sh}$, centered at the true shower energy, $\log_{10} E_{\rm sh}$, with a width of $\sigma_{E_{\rm sh}} \equiv 10^{\sigma_\epsilon} E_{\rm sh}$, where $\epsilon \equiv \log_{10}(E^{\rm rec}_{\rm sh}/E_{\rm sh})$; we choose $\sigma_\epsilon = 0.1$ for our baseline results [315, 317, 324]. For the angular resolution function, $\mathcal{R}_{\theta_z}(\theta^{\rm rec}_z, \theta_z)$, we use a Gaussian function on the zenith angle with a width of $\sigma_{\theta_z} = 2^\circ$, which approximates the expected point spread function of the radio array of IceCube-Gen2 of $\sigma_\Omega = 3^\circ$ [212, 312, 314, 324]. Reference [346] contains full definitions of the resolution functions. We integrate over the real values of shower energy and direction to obtain the differential event rate in terms of measured quantities,

$$\frac{d^2N_{\nu_\alpha}}{dE^{\rm rec}_{\rm sh}d\theta^{\rm rec}_z} = \int_{-1}^{+1} d\cos\theta_z \int_0^\infty dE_{\rm sh} \frac{d^2N_{\nu_\alpha}}{dE_{\rm sh}d\cos\theta_z} \mathcal{R}_{E_{\rm sh}}(E^{\rm rec}_{\rm sh}, E_{\rm sh})\, \mathcal{R}_{\theta_z}(\theta^{\rm rec}_z, \theta_z) \,, \quad (8.2)$$

and similarly for $\bar{\nu}_\alpha$. In Sec. 8.7.6 we comment on the effect that the energy and angular resolution have on our results. We use the neutrino differential event rate due to ν_α and $\bar{\nu}_\alpha$ of all flavors, obtained by adding their individual contributions,

$$\frac{d^2N_\nu}{dE^{\rm rec}_{\rm sh}d\theta^{\rm rec}_z} = \sum_{\alpha=e,\mu,\tau} \left(\frac{d^2N_{\nu_\alpha}}{dE^{\rm rec}_{\rm sh}d\theta^{\rm rec}_z} + \frac{d^2N_{\bar{\nu}_\alpha}}{dE^{\rm rec}_{\rm sh}d\theta^{\rm rec}_z} \right) . \quad (8.3)$$

Figure 40 shows the binned distribution of the mean number of events for our benchmark UHE neutrino flux (Sec. 8.3.2), computed using Eq. (8.3). The all-sky, energy-integrated event rate, within $E^{\rm rec}_{\rm sh} \in [10^7, 10^{10}]$ GeV, is about $\mathcal{N}_\nu = 33.1$ events per year. The event distribution peaks around 10^9 GeV because that is where the flux peaks and where the detector effective volume is larger.

8.4.3 *Atmospheric muon background*

Separately, we compute the rate of events induced by the background of high-energy atmospheric muons, $d^2N_\mu/dE_{\rm sh}^{\rm rec}d\theta_z^{\rm rec}$. To compute it, we follow the procedure introduced in Ref. [346], using the same energy and angular resolution as for neutrino-initiated events above. Like in Refs. [346, 372, 390], we adopt the calculation of the atmospheric muon background from Refs. [77, 213, 214], based on the hadronic interaction model SYBILL 2.3C [293], accounting for the detector response, and mitigated by a surface array of cosmic-ray detectors that acts as veto. Figure 15 in Ref. [346] shows the effect of the veto on event rates.

Figure 40 shows the baseline prediction of the rate of muon-induced events (see also Figs. 15 and 16 in Ref. [346], and Table I and Figs. 4, 5 in Ref. [390]). The muon background is small—on average, we expect $\mathcal{N}_\mu = 0.54$ events in 10 years in the range $E_{\rm sh}^{\rm rec} \in [10^7, 10^{10}]$ GeV—is concentrated in the lower end of this range and is exclusively downgoing. In spite of its small size, we do not ignore it because it can be relevant if the contribution of neutrino-initiated events is low—due to a low neutrino flux—and concentrated at low energies. We make no attempt to distinguish the contribution of neutrino-initiated events from that muon-initiated events. References [372, 390] explored the related issue of the influence of the muon background on the discovery of UHE neutrinos and the measurement of the UHE cross section.

(A potential second source of background events in the radio array of IceCube-Gen2 is due to the cores of particle showers initiated by cosmic rays in the atmosphere, which may penetrate the ice and continue to develop, producing Askaryan radiation alike that of neutrinos [327]. We do not include this background in our analysis because presently estimates of it are uncertain, though work is ongoing in improving and mitigating them.)

8.5 FIT MODELS OF THE UHE NEUTRINO FLUX AND CROSS SECTION

Table 6 shows a summary of the free parameters of the models of the UHE neutrino flux, νN DIS cross section, and atmospheric muon background that we adopt, and our choice of priors for them. We explore models that are relatively simple and that allow us to measure the flux and cross section

in varying detail, though our focus is on flexible models that allow to measure the shape of the neutrino spectrum. Below, we describe them; later, we use them in our statistical methods (Sec. 8.6) to produce our forecasts (Sec. 8.7).

8.5.1 *UHE neutrino flux*

We make forecasts using four competing models of the UHE neutrino spectrum: a simple power law (PL), a power law with an exponential cut-off (PLC), a piecewise power law (PPL), and a Piecewise Cubic Hermite Interpolating Polynomial (PCHIP). Each model has a different set of parameters, $\boldsymbol{f}_\Phi$, that describe the neutrino spectrum; we present them below. In our forecasts (Sec. 8.6) we find values for $\boldsymbol{f}_\Phi$ via fits to projected observations in IceCube-Gen2. The choice of flux model impacts the quality of the measurement of not only the neutrino spectrum, but also of the νN cross section.

By construction, the fluxes of ν_α and $\bar{\nu}_\alpha$ that we use are identical at the surface of the Earth, *i.e.*, $\Phi_{\nu_\alpha} = \Phi_{\bar{\nu}_\alpha}$; hence the factor of 2 in the flux definitions, Eqs. (8.4)–(8.7) below. We assume a common spectral shape for neutrinos of all flavors. The flavor composition at Earth, $f_{\alpha,\oplus}$, is fixed to the best-fit prediction for the year 2040 [267, 390] (Sec. 8.3). The above assumptions are common and reasonable simplifications. In reality, each species of UHE neutrino could have a spectrum of its own; see, *e.g.*, flux models 3–7 and 12 in Fig. 6 of Ref. [346].

Power law (PL).—The UHE ν_α spectrum is

$$\Phi_{\nu_\alpha}(E_\nu, \boldsymbol{f}_\Phi) = \frac{f^\pi_{\alpha,\oplus}}{2} \Phi_0 \left(\frac{E_\nu}{10\ \text{PeV}} \right)^{-\gamma} . \tag{8.4}$$

The free parameters are the flux normalization at 10 PeV, Φ_0, and the spectral index, γ, *i.e.*, $\boldsymbol{f}_\Phi \equiv (\Phi_0, \gamma)$. In analyses of IceCube TeV–PeV neutrinos, a simple power law is the standard and often marginally preferred shape for the diffuse neutrino spectrum; see, *e.g.*, Refs. [37, 188]. (Yet, present-day uncertainties might conceal additional spectral features; see, *e.g.*, Refs. [260, 402].) For UHE neutrinos, most predictions of the spectrum have a structure richer than a simple power law; see Fig. 6 in Ref. [346] and Fig. 2 in Ref. [390]. We use the PL model largely as a baseline against which to compare the other flux models.

Power law with exponential cut-off (PLC).—The UHE ν_α spectrum is

$$\Phi_{\nu_\alpha}(E_\nu, \boldsymbol{f}_\Phi) = \frac{f^\pi_{\alpha,\oplus}}{2} \Phi_0 \left(\frac{E_\nu}{10\ \text{PeV}}\right)^{-\gamma} e^{-\frac{E_\nu}{E_\text{cut}}} \,. \tag{8.5}$$

The free parameters are the flux normalization at 10 PeV, Φ_0, the spectral index, γ, and the cut-off energy, E_cut, *i.e.*, $\boldsymbol{f}_\Phi \equiv (\Phi_0, \gamma, E_\text{cut})$. In analyses of IceCube TeV–PeV neutrinos, present-day IceCube observations do not strongly disfavor a PLC diffuse neutrino spectrum with a cut-off in the multi-PeV range [37]. For UHE neutrinos, a large number of theoretical flux predictions resemble a PLC, albeit some of only roughly; see Fig. 2 in Ref. [390].

Piecewise power law (PPL).—The UHE ν_α spectrum is

$$\Phi_{\nu_\alpha}(E_\nu, \boldsymbol{f}_\Phi) = \frac{f^\pi_{\alpha,\oplus}}{2} \left(\frac{E_\nu}{10\ \text{PeV}}\right)^{-2.0} \times \begin{cases} \Phi_1, & 10^7 \leq E_\nu/\text{GeV} < 10^{7.5} \\ \Phi_2, & 10^{7.5} \leq E_\nu/\text{GeV} < 10^8 \\ \Phi_3, & 10^8 \leq E_\nu/\text{GeV} \leq 10^{8.5} \\ \Phi_4, & 10^{8.5} \leq E_\nu/\text{GeV} < 10^9 \\ \Phi_5, & 10^9 \leq E_\nu/\text{GeV} < 10^{9.5} \\ \Phi_6, & 10^{9.5} \leq E_\nu/\text{GeV} \leq 10^{10} \end{cases} . \tag{8.6}$$

The free parameters are the six flux normalization constants, Φ_i ($i = 1, \ldots, 6$), one for each of the six half-decade energy bins between 10 PeV and 10 EeV, *i.e.*, $\boldsymbol{f}_\Phi \equiv (\Phi_1, ..., \Phi_6)$. In analyses of IceCube TeV–PeV neutrinos, this parametrization is often employed to infer the neutrino spectrum [37]. We use half-decade bins because this bin size is larger than our baseline choice for energy resolution of 10% per energy decade (Sec. 8.4.2). Six bins is also about the minimum number needed to capture the main features of the neutrino spectrum.

Piecewise Cubic Hermite Interpolating Polynomial (PCHIP).—A PCHIP is a shape-preserving interpolating function that uses monotonic cubic splines anchored at nodes with predefined positions [415]. In our case, we use it to interpolate the UHE neutrino energy spectrum based off of seven flux nodes $f_{\Phi,i} \equiv \log_{10}[E^2_{\nu,i}\Phi_{\nu_\alpha}(E_{\nu,i})]$ ($i = 1, \ldots, 7$), located at seven fixed values of the neutrino energy, $E_{\nu,i}$, equally spaced in logarithmic scale between 10^7 and 10^{10} GeV. For given values of $\boldsymbol{f}_\Phi \equiv (f_{\Phi,1}, \ldots, f_{\Phi,7})$, we construct the PCHIP, $\varphi(E_\nu, \boldsymbol{f}_\Phi)$, and, with it, the flux of ν_α, as

$$\Phi_{\nu_\alpha}(E_\nu, \boldsymbol{f}_\Phi) = \frac{f^\pi_{\alpha,\oplus}}{2} \frac{10^{\varphi(E_\nu, \boldsymbol{f}_\Phi)}}{E^2_\nu} \,. \tag{8.7}$$

Among the flux models that we consider, a PCHIP has the greatest flexibility to reproduce various shapes of neutrino spectra, because it has no set shape, but instead molds itself into the one that best fits experimental observations, as opposed to the PL and PLC models, which have a predetermined shape. It is closer to the PPL model, but has greater flexibility owing to using cubic splines. Later (Sec. 8.6) we find that, indeed, a PCHIP offers comparative advantages over the other tree flux models that we consider to jointly reconstruct the UHE neutrino flux and cross section (Sec. 8.7). Similarly to the PPL flux model, we use seven PCHIP nodes because this is about the minimum number needed to capture the main features of the neutrino spectrum.

8.5.2 *UHE νN DIS cross section*

We model the UHE νN DIS cross section based on the BGR18 calculation [194], $d\sigma_0/dy$. We allow for deviations from it inside each energy decade from 10^7 to 10^{10} GeV, via the free shift parameters $f_{\sigma,1}$, $f_{\sigma,2}$, and $f_{\sigma,3}$, *i.e.*,

$$\frac{d\sigma(E_\nu, y, f_{\sigma,i})}{dy} = \frac{d\sigma_0(E_\nu, y)}{dy} \times \begin{cases} 10^{f_{\sigma,1}}, & 10^7 \leq E_\nu/\text{GeV} < 10^8 \\ 10^{f_{\sigma,2}}, & 10^8 \leq E_\nu/\text{GeV} < 10^9 \\ 10^{f_{\sigma,3}}, & 10^9 \leq E_\nu/\text{GeV} \leq 10^{10} \end{cases} . \tag{8.8}$$

When $f_{\sigma,1} = f_{\sigma,2} = f_{\sigma,3} = 0$, Eq. (8.8) matches the BGR18 calculation. In our forecasts (Sec. 8.6), we find values for $\boldsymbol{f}_\sigma \equiv (f_{\sigma,1}, f_{\sigma,2}, f_{\sigma,3})$ via fits to projected observations. This parametrization of the UHE cross section is akin to the one used to measure the TeV–PeV cross section in Refs. [61, 63] and to forecast the measurement of the UHE cross section in Ref. [348].

Previous works [346, 390] based on the same event-rate calculation framework that we use here (Sec. 8.4.2) parametrized instead the UHE cross section with a single floating parameter across 10^7–10^{10} GeV (see also Ref. [215]), akin to what was used in the first measurement of the TeV–PeV cross section [60]. There are two advantages to using multiple bins instead, as in Eq. (8.8). First, it allows us not only to measure the energy dependence of the cross section, but also to find potential narrow nonstandard features in it, or to identify changes in its growth rate with energy that only

turn on at a threshold energy; see Fig. 39. Second, it ensures that the cross-section measurement uncertainty that we report for each energy decade reflects the statistical power of that decade, and is not artificially driven by the power of a different energy region that has a higher event rate. Figure 39 illustrates this: the cross section is measured more precisely in the higher energy bins, where the event rate is higher, than in the lowest energy bin, where it is lower.

In our analysis, a change in the νN DIS cross section affects the calculation of neutrino-induced event rates at two stages: during neutrino propagation inside the Earth and in the interaction of neutrinos inside the detector. (During propagation inside the Earth, we leave non-DIS sub-leading neutrino interactions [209, 210, 346] unchanged.) Using the parametrization of the cross section in Eq. (8.8) makes computing neutrino propagation and detection more nuanced. As neutrinos propagate underground, their energies are lowered via neutrino regeneration in NC interactions or, for ν_τ, in CC interactions. As a result, for example, a neutrino that enters the Earth with an energy in the 10^9–10^{10} GeV decade and, therefore, interacts initially with a cross section scaled by $f_{\sigma,3}$, could eventually lose enough energy to lie in the 10^8–10^9 GeV decade, at which point it would interact instead with a cross section scaled by $f_{\sigma,2}$. Further energy losses might lower the energy into the 10^7–10^8 GeV decade, at which point the neutrino would interact with a cross section scaled by $f_{\sigma,1}$.

However, keeping track of how the relevant cross-section shift parameter changes during neutrino propagation inside the Earth would be a computationally demanding task within NUPROPEARTH (see Sec. 8.4.1). We deal with this in a simplified manner. For given values of the scaling parameters, before starting to propagate a neutrino of a certain energy inside the Earth, we select what energy decade it falls in and pick out the cross-section scaling parameter associated to it, $f_{\sigma,1}$, $f_{\sigma,2}$, or $f_{\sigma,3}$. Then we propagate the neutrino inside the Earth assuming that the value of that shift parameter is common to all shift parameters. The shift parameters are made equal only for the sake of speeding up the propagation, though. At the end of propagation, the neutrino interacts inside the detector with a cross section scaled by $f_{\sigma,1}$, $f_{\sigma,2}$, or $f_{\sigma,3}$—no longer taken to be equal—depending on what its final energy is.

The error we incur in by adopting the above simplification is small. Since the average νN DIS inelasticity at ultra-high energies is $\langle y \rangle \approx 0.25$, a neutrino retains about 75% of its energy in each

NC interaction it undergoes. This means that a neutrino would need to undergo eight consecutive NC interactions for its final energy to be one tenth of its original energy; this is as many interactions as it can undergo before falling into a lower energy decade. Given that $\sigma_{\nu N}^{\rm NC} \approx \sigma_{\nu N}^{\rm CC}/3$ [194], the probability of a neutrino undergoing eight consecutive NC without disappearing due to a CC interaction is $(1/4)^8 \approx 0.002\%$. Since for each neutrino flavor, energy, and direction we propagate 10^7 neutrinos through the Earth, only about 150 of those would have propagated with an incorrect cross-section shift parameter.

8.5.3 *Atmospheric muon background*

We model the background of muon-induced events based on its baseline prescription (Sec. 8.4.3), but allowing for its rescaling via the free parameter f_μ, *i.e.*,

$$\frac{dN_\mu^2}{dE_{\rm sh}^{\rm rec} d\theta_z^{\rm rec}} \to \frac{f_\mu}{\mathcal{N}_\mu} \frac{dN_\mu^2}{dE_{\rm sh}^{\rm rec} d\theta_z^{\rm rec}} \,, \tag{8.9}$$

where $\mathcal{N}_\mu$ is the baseline rate of all-sky, energy-integrated muons. The parameter f_μ is the rescaled rate of muon-induced events; if $f_\mu = \mathcal{N}_\mu$, we recover the baseline prescription. In our forecasts (Sec. 8.6) we find its value via fits to projected observations.

Like in Refs. [346, 390], we only allow for changes in the normalization of the atmospheric muon flux—including large ones, up to $f_\mu = 100$ (Table 6)—but not in the shape of its energy spectrum. Were the muon spectrum to extend to higher energies than in its baseline prescription, into the region where the UHE neutrino flux is expected to be larger, its influence in our forecasts might change. Exploring that possibility requires dedicated studies beyond the scope of this paper.

8.6 STATISTICAL METHODS

To produce our forecasts of joint measurement of the UHE neutrino spectrum and cross section, we adopt a Bayesian approach based on generating and analyzing a large number of mock event samples that represent the expected response of the radio array of IceCube-Gen2.

We generate a mock observed event sample by assuming our benchmark model for the UHE neutrino flux (Sec. 8.3.2) and the BGR18 νN DIS cross section; we refer to them as the *true flux* and *true cross section* below and in Fig. 39. Using the procedure described in Sec. 8.4, we compute the mock differential event rate of neutrino-initiated events, Eq. (8.3), to which we add the rate of events initiated by atmospheric muons (Sec. 8.4.3). We interpret the differential event rate as a joint probability distribution function in $E_{\rm sh}^{\rm rec}$ and $\theta_z^{\rm rec}$, from which we randomly sample mock observed events. Then we compare that observed event sample *vs.* an event sample generated using test values of the flux and cross-section parameters, adopting for them the fit models described in Sec. 8.5. We repeat this procedure many times, so as to average over all possible realizations of the observed event sample.

Below we describe the procedure step-by-step in detail to facilitate its independent implementation. We carry it out separately for each choice of flux fit model—PL, PLC, PPL, and PCHIP.

1. Taking our benchmark flux (Sec. 8.3.2) as the true neutrino flux and the BGR18 νN cross section (Sec. 8.4.1) as the true cross section, *i.e.*, $f_{\sigma,1} = f_{\sigma,2} = f_{\sigma,3} = 0$ in Eq. (8.8), compute the differential rate of observed neutrino-induced events, Eq. (8.3), and the baseline rate of muon-induced events, Eq. (8.9) with $f_\mu = \mathcal{N}_\mu$, and, with them, the total differential observed event rate,

$$\frac{d^2N_{\rm sh}}{dE_{\rm sh}^{\rm rec}d\theta_z^{\rm rec}} = \frac{d^2N_\nu}{dE_{\rm sh}^{\rm rec}d\theta_z^{\rm rec}} + \frac{d^2N_\mu}{dE_{\rm sh}^{\rm rec}d\theta_z^{\rm rec}} \,. \tag{8.10}$$

   (Figure 40 shows these distributions, though only summed over all energies or over all directions.) Later steps in the calculation (2–11) contrast samples of observed events drawn

1 All the priors are uniform within their corresponding ranges.

2 We show true values only when they are available. For the flux parameters, they refer to our benchmark UHE neutrino flux (Sec. 8.3.2).

3 The units of $E_\nu^2\Phi_\nu$ are 10^{-8} GeV cm^{-2} s^{-1} sr^{-1}. In practice, for speed-up, we centered the prior of each $f_{\Phi,i}$ ($i = 1,\ldots,7$) at its true value. However, because the prior is flat and wide, this choice does not affect our results.

Table 6: ***Free model parameters, their priors, and true values.*** The flux parameters are different for each of the four flux fit models: PL, PLC, PPL, and PCHIP. The cross-section parameters and the atmospheric muon parameter are the same regardless of the choice of flux fit model. See Section 8.5 for details.

Flux fit model	Free model parameter					
	Symbol	Units	Description	Prior range[1]	True value[2]	Ref.
			Flux parameters, f_Φ			
PL	Φ_0	$\mathrm{GeV}^{-1}\ \mathrm{cm}^{-2}\ \mathrm{s}^{-1}\ \mathrm{sr}^{-1}$	Flux norm. at 10 PeV	$[10^{-27}, 10^{-19}]$	···	Eq. (8.4)
	γ	···	Spectral index	[0, 5]	···	
PLC	Φ_0	$\mathrm{GeV}^{-1}\ \mathrm{cm}^{-2}\ \mathrm{s}^{-1}\ \mathrm{sr}^{-1}$	Flux norm. at 10 PeV	$[10^{-27}, 10^{-19}]$	···	Eq. (8.5)
	γ	···	Spectral index	[0, 5]	···	
	E_{cut}	GeV	Cut-off energy	$[10^6, 10^{11}]$	···	
PPL	Φ_1	$\mathrm{GeV}^{-1}\ \mathrm{cm}^{-2}\ \mathrm{s}^{-1}\ \mathrm{sr}^{-1}$	E_ν^{-2} flux norm., 10^7–$10^{7.5}$ GeV	$[0, 10^{-19}]$	···	Eq. (8.6)
	Φ_2	$\mathrm{GeV}^{-1}\ \mathrm{cm}^{-2}\ \mathrm{s}^{-1}\ \mathrm{sr}^{-1}$	…$10^{7.5}$–10^8 GeV	$[0, 10^{-19}]$	···	
	Φ_3	$\mathrm{GeV}^{-1}\ \mathrm{cm}^{-2}\ \mathrm{s}^{-1}\ \mathrm{sr}^{-1}$	…10^8–$10^{8.5}$ GeV	$[0, 10^{-19}]$	···	
	Φ_4	$\mathrm{GeV}^{-1}\ \mathrm{cm}^{-2}\ \mathrm{s}^{-1}\ \mathrm{sr}^{-1}$	…$10^{8.5}$–10^9 GeV	$[0, 10^{-19}]$	···	
	Φ_5	$\mathrm{GeV}^{-1}\ \mathrm{cm}^{-2}\ \mathrm{s}^{-1}\ \mathrm{sr}^{-1}$	…10^9–$10^{9.5}$ GeV	$[0, 10^{-19}]$	···	
	Φ_6	$\mathrm{GeV}^{-1}\ \mathrm{cm}^{-2}\ \mathrm{s}^{-1}\ \mathrm{sr}^{-1}$	…$10^{9.5}$–10^{10} GeV	$[0, 10^{-19}]$	···	
PCHIP	$f_{\Phi,1}$	···	$\mathrm{Log}_{10}(E_\nu^2 \Phi_\nu)$ at 10^7 GeV^3	[-13, -3]	-8.49	Eq. (8.7)
	$f_{\Phi,2}$	···	… at $10^{7.5}$ GeV	[-13, -3]	-9.09	
	$f_{\Phi,3}$	···	… at 10^8 GeV	[-13, -3]	-8.55	
	$f_{\Phi,4}$	···	… at $10^{8.5}$ GeV	[-13, -3]	-7.91	
	$f_{\Phi,5}$	···	… at 10^9 GeV	[-13, -3]	-7.61	
	$f_{\Phi,6}$	···	… at $10^{9.5}$ GeV	[-13, -3]	-7.63	
	$f_{\Phi,7}$	···	… at 10^{10} GeV	[-13, -3]	-7.84	
			Cross section parameters, f_σ			
All	$f_{\sigma,1}$	···	$\sigma_{\nu N}$ shift, 10^7–10^8 GeV	[-2, 2]	0	Eq. (8.8)
	$f_{\sigma,2}$	···	… 10^8–10^9 GeV	[-2, 2]	0	
	$f_{\sigma,3}$	···	… 10^9–10^{10} GeV	[-2, 2]	0	
			Atmospheric muon background parameter, f_μ (nuisance)			
All	f_μ	···	Number atm. μ	[0, 100]	···	Eq. (8.9)

from this distribution against test samples generated using test choices of the flux and cross-section parameters.

2. Compute the probability distribution function of observed events,

$$\mathcal{P}(E_{\rm sh}^{\rm rec}, \theta_z^{\rm rec}) = \frac{1}{\mathcal{N}_{\rm obs}} \frac{d^2 N_{\rm sh}(E_{\rm sh}^{\rm rec}, \theta_z^{\rm rec})}{dE_{\rm sh}^{\rm rec} d\theta_z^{\rm rec}} \,, \tag{8.11}$$

where $\mathcal{N}_{\rm obs} = \mathcal{N}_\nu + \mathcal{N}_\mu$ is the all-sky, energy-integrated mean number of observed events. For our choice of true neutrino flux, $\mathcal{N}_\nu = 33.1$ neutrino-initiated events per year (Sec. 8.4.2). For the baseline computation of the atmospheric muon background, $\mathcal{N}_\mu = 0.054$ muon-initiated events per year (Sec. 8.4.3).

3. Randomly sample the number of observed events, $N_{\rm obs}$, from a Poisson distribution whose central value is equal to the mean expectation, $\mathcal{N}_{\rm obs}$. Then generate a sample of $N_{\rm obs}$ detected events, $\{e_i\}_{i=1}^{N_{\rm obs}}$, each consisting of a pair of reconstructed energy and direction, $e_i \equiv (E_{{\rm sh},i}^{\rm rec}, \theta_{z,i}^{\rm rec})$, whose values are randomly sampled from Eq. (8.11).

4. For the chosen flux fit model—PL, PLC, PPL, or PCHIP—generate a random variate of the model parameters, $\boldsymbol{\theta} \equiv (\boldsymbol{f}_\Phi, \boldsymbol{f}_\sigma, f_\mu)$ (Sec. 8.5). (In practice, we sample the parameter values from prior distributions; more on this later.)

5. Compute the isotropic flux of ν_α and $\bar{\nu}_\alpha$ at the surface of the Earth, $\Phi_{\nu_\alpha}(E_\nu, \boldsymbol{f}_\Phi) = \Phi_{\bar{\nu}_\alpha}(E_\nu, \boldsymbol{f}_\Phi)$.

6. Propagate separately ν_e, $\bar{\nu}_e$, ν_μ, $\bar{\nu}_\mu$, ν_τ, and $\bar{\nu}_\tau$ from the surface of the Earth to IceCube-Gen2 (Sec. 8.4), using the νN DIS cross section modified by the parameters $\boldsymbol{f}_\sigma$, Eq. (8.8). The resulting fluxes at the detector are no longer isotropic, *i.e.*, $\Phi_{\nu_\alpha}^{\rm det}(E_\nu, \cos\theta_z, \boldsymbol{f}_\Phi, \boldsymbol{f}_\sigma)$, and similarly for $\bar{\nu}_\alpha$.

7. Compute the corresponding differential rate of neutrino-induced events in the radio array of IceCube-Gen2 (Sec. 8.4), $d^2 N_\nu(\boldsymbol{f}_\Phi, \boldsymbol{f}_\sigma)/dE_{\rm sh}^{\rm rec} d\theta_z^{\rm rec}$, Eq. (8.3). In doing so, the parameters $\boldsymbol{f}_\sigma$ also modify the νN DIS cross section used at detection.

8. Compute the differential rate of events induced by atmospheric muons, re-scaled by the factor f_μ, $d^2 N_\mu(f_\mu)/dE_{\rm sh}^{\rm rec} d\theta_z^{\rm rec}$, Eq. (8.9).

9. Integrate the differential event rates to find the all-sky, energy-integrated number of events due to neutrinos, $N_\nu(\boldsymbol{f}_\Phi, \boldsymbol{f}_\sigma)$, and muons, $N_\mu(f_\mu) = f_\mu$. The total number of events is $N(\boldsymbol{\theta}) \equiv N_\nu(\boldsymbol{f}_\Phi, \boldsymbol{f}_\sigma) + f_\mu$.

10. Compute the fraction of events in the sample that is due to neutrinos (*i.e.*, the signal), $\mathcal{F}_\nu(\boldsymbol{\theta}) \equiv N_\nu(\boldsymbol{f}_\Phi, \boldsymbol{f}_\sigma)/N(\boldsymbol{\theta})$, and the fraction that is due to muons (*i.e.*, the background), $\mathcal{F}_\mu(\boldsymbol{\theta}) \equiv f_\mu/N(\boldsymbol{\theta})$.

11. For the i-th event in the sample, e_i, compute the partial likelihood

$$\mathcal{L}_i(\boldsymbol{\theta}) = \mathcal{F}_\nu(\boldsymbol{\theta}) p_\nu(e_i|\boldsymbol{f}_\Phi, \boldsymbol{f}_\sigma) + \mathcal{F}_\mu(\boldsymbol{\theta}) p_\mu(e_i|f_\mu) \,, \tag{8.12}$$

where the probability density of this event being due to a neutrino is

$$p_\nu(e_i|\boldsymbol{f}_\Phi, \boldsymbol{f}_\sigma) = \frac{1}{N_\nu(\boldsymbol{f}_\Phi, \boldsymbol{f}_\sigma)} \left.\frac{d^2 N_\nu(\boldsymbol{f}_\Phi, \boldsymbol{f}_\sigma)}{dE_{\rm sh}^{\rm rec} d\theta_z^{\rm rec}}\right|_{E_{{\rm sh},i}^{\rm rec}, \theta_{z,i}^{\rm rec}} \,,$$

and the probability density of it being due to a muon is

$$p_\mu(e_i|f_\mu) = \frac{1}{f_\mu} \left.\frac{d^2 N_\mu(f_\mu)}{dE_{\rm sh}^{\rm rec} d\theta_z^{\rm rec}}\right|_{E_{{\rm sh},i}^{\rm rec}, \theta_{z,i}^{\rm rec}} \,. \tag{8.13}$$

Compute Eq. (8.12) for each of the $N_{\rm obs}$ events in the sample.

12. Compute the unbinned extended Poisson likelihood for the full event sample,

$$\mathcal{L}\left(\{e_i\}_{i=1}^{N_{\rm obs}}|\boldsymbol{\theta}\right) = \frac{e^{-N(\boldsymbol{\theta})} N(\boldsymbol{\theta})^{N_{\rm obs}}}{N(\boldsymbol{\theta})!} \prod_{i=1}^{N_{\rm obs}} \mathcal{L}_i(\boldsymbol{\theta}) \,. \tag{8.14}$$

We use an unbinned likelihood to avoid our results depending on our choice of bin size.

13. Using Bayes' theorem, compute the corresponding posterior probability density,

$$\mathcal{P}\left(\{e_i\}_{i=1}^{N_{\rm obs}}|\boldsymbol{\theta}\right) = \frac{\mathcal{L}\left(\{e_i\}_{i=1}^{N_{\rm obs}}|\boldsymbol{\theta}\right)\pi(\boldsymbol{\theta})}{\mathcal{Z}\left(\{e_i\}_{i=1}^{N_{\rm obs}}\right)} \,, \tag{8.15}$$

where $\pi(\boldsymbol{\theta}) \equiv \pi(\boldsymbol{f}_\Phi)\pi(\boldsymbol{f}_\sigma)\pi(f_\mu)$ is the prior distribution on the model parameters. For each parameter, we use a wide, uniform prior, and we assume no correlations between them; see Table 6. The denominator in Eq. (8.15) is the model evidence, and is obtained by integrating the numerator over the whole model parameter space of $\boldsymbol{\theta}$. We compute it using UltraNest [378], an efficient importance nested sampler [379, 380].

14. Keeping the same observed event sample, repeat steps 4–13 for many different random variates $\boldsymbol{\theta}$, using UltraNest, until the parameter space has been thoroughly explored, and the posterior has been evaluated throughout it.

15. Repeat steps 3–14, for 10^4 random observed event samples. After that, compute the posterior averaged over all the realizations of observed event samples, $\bar{\mathcal{P}}(\boldsymbol{\theta})$, which we use to make our forecasts. We maximize it to compute the best-fit values of the model parameters, and we integrate it to find their credible intervals.

8.7 RESULTS

8.7.1 *General trends*

Figure 41 (also Fig. 39) illustrates our forecasts of the joint measurement of the UHE neutrino spectrum and νN DIS cross section in the radio array of IceCube-Gen2. We show results assuming each of our four neutrino spectrum fit models in turn (Sec. 8.5.1)—PL, PLC, PPL, and PCHIP—and adopting for the true UHE neutrino flux our benchmark flux from Sec. 8.3.2. To produce our main forecasts, we assume baseline energy and angular resolution of $\sigma_\epsilon = 0.1$ and $\sigma_{\theta_z} = 2^\circ$, respectively (Sec. 8.4). Later, we explore the impact of alternative choices.

There are common trends shared by the four sets of results. At intermediate energies, from 100 PeV to 1 EeV, the measurements are most precise, though not necessarily accurate—except for PCHIP, for which results are always accurate. At low and high energies, the measurements worsen due to low event rates. At low energies, in the tens of PeV, this is due to the small effective volume of the radio array of IceCube-Gen2, since Askaryan emission weakens [304]. This stresses the need for complementary measurements at tens of PeV, *e.g.*, by the optical component of IceCube-Gen2 [39], TAMBO [73, 388], or Trinity [333, 416]. At high energies, above 1 EeV, the measurements worsen because our benchmark flux model decreases, which is representative of flux predictions. Longer detector exposure improves the accuracy of the measurements, and more slowly, their precision; we show results for 3, 10, and 20 years.

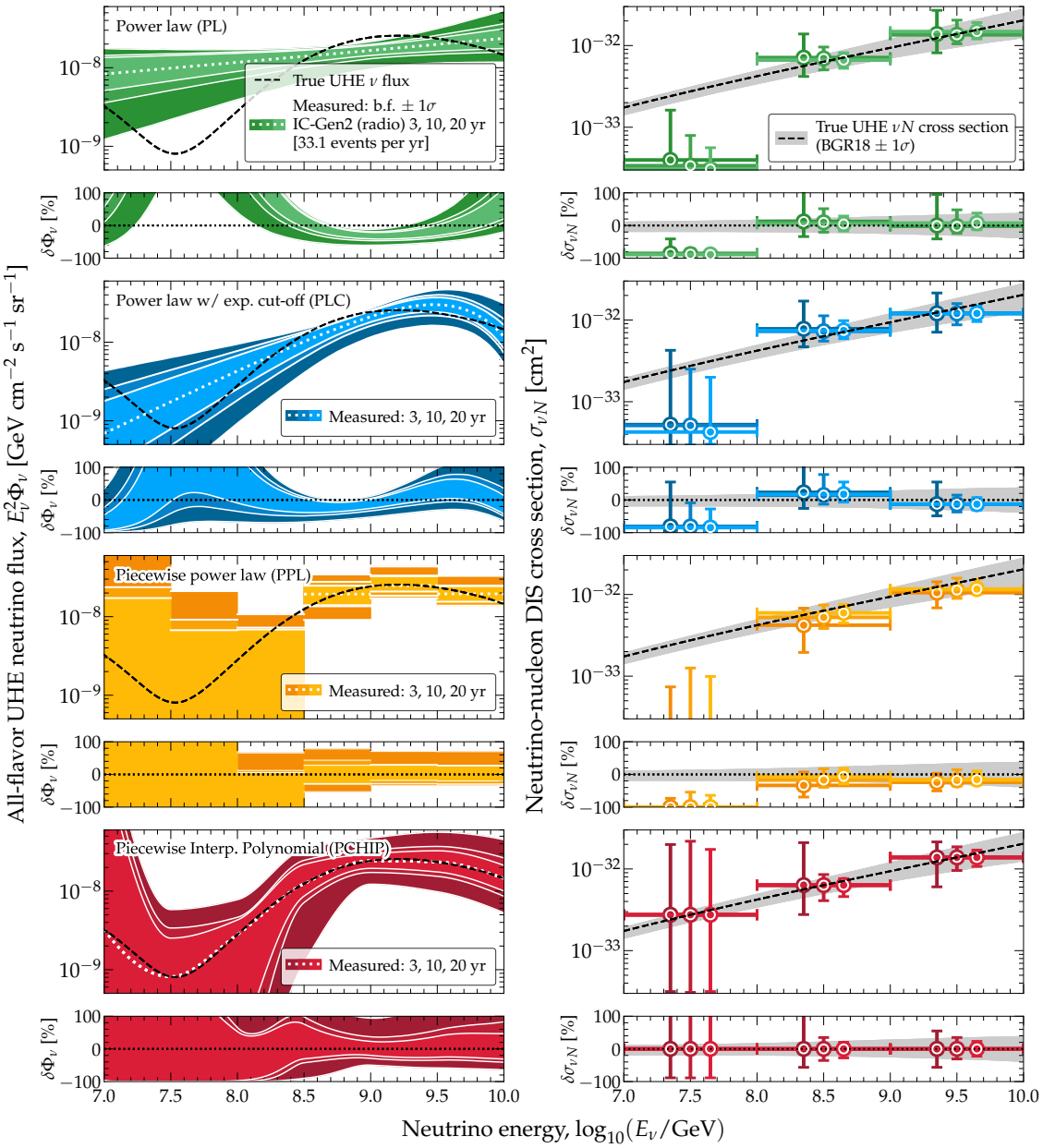

Figure 41: ***Forecasts of the joint measurement of the UHE neutrino energy spectrum and the neutrino-nucleon cross section.*** Each row shows the performance of using one of our models of the neutrino spectrum (Sec. 8.5.1) in a fit to simulated observed event samples in the radio array of IceCube-Gen2 (Sec. 8.4), after 3, 10, and 20 years of exposure. *Left column:* Measured neutrino energy spectrum. The true UHE neutrino flux is our benchmark flux, representative of theoretical predictions (Sec. 8.3). *Right column:* Measured neutrino-nucleon cross section, reconstructed in three decade-wide energy bins. The true cross section is the BGR18 model [194]. *The PL and PLC flux models yield high precision—due to their having a small number of free parameters—but low accuracy—due to their rigid shape. The PPL and PCHIP flux models yield comparable precision but superior accuracy—due to their flexible shape.* See Sec. 8.7 for details.

8.7.2 *Power law (PL)*

Figure 41 shows that, as expected, the PL flux model is too simple and rigid to capture the features of our benchmark flux, *i.e.*, the dip around $10^{7.5}$ GeV and the bump around 10^9 GeV, even after 20

years of exposure. After 10 or 20 years, the spectrum is reconstructed with high precision—due to the low number of flux model parameters—but with atrocious accuracy: the allowed flux band overestimates the true neutrino flux at low energies by about one order of magnitude and at high energies by about 100%, and underestimates it by tens of percent at intermediate energies.

This, in turn, affects the accuracy of the joint measurement of the cross section. Because of the partial degeneracy between flux and cross section in the computation of event rates (Sec. 8.2.1), when the measured flux is too high relative to its true value, the measured cross section is too low relative to its own. Figure 41 shows that this trade-off is flagrant in the lowest energy decade, where the measured cross section is offset from its true value by about 100%, regardless of the exposure time. In the intermediate and high energy decades, the cross section can be measured within tens of percent after 10–20 years.

Given that all but the barest predictions posit UHE neutrino spectra with shapes more complex than a power law (see Fig. 2 in Ref. [390]), using the PL model in the fits would knowingly run a high risk of misreconstructing the flux and cross section. ***Lacking prior knowledge of the true shape of the UHE neutrino spectrum, we recommend against using the PL model.***

8.7.3 *Power law with exponential cut-off (PLC)*

Figure 41 shows that the PLC flux model performs marginally better than the PL model, but retains its main shortcomings. Like with the PL model, the flux is measured precisely—less so due to having one more parameter than the PL model—but inaccurately. At low energies, like for the PL model, flux reconstruction is particularly inaccurate because the event rate drops. At intermediate and high energies, it is more accurate than for the PL model because the exponential cut-off in the PLC model makes it possible to fit the bump-like spectrum of the true flux. Regarding the cross section, the PLC model performs similarly to the PL model: it undershoots the cross section at the lowest energies, and measures it to within tens of percent at intermediate and high energies, centered close to its true value.

Were the true neutrino spectrum more closely a power law with a bump-like feature on top of it, like in the prediction of Ref. [177] (flux model 8 in Ref. [390]), then the PLC flux model would

perform better. ***Like for the PL model, lacking prior knowledge of the true shape of the energy spectrum, we recommend against using the PLC model. Yet, if pressed to use a flux model with a low number of free parameters, PLC is preferable to PL.***

8.7.4 *Piecewise power law (PPL)*

Figure 41 shows that the PPL flux model is able to reconstruct the shape of our benchmark neutrino spectrum with a precision comparable to that of the PL and PLC models at intermediate and high energies, but with higher accuracy. At low energies, where our benchmark flux is low, the model allows only to place upper limits on it. Regarding the cross section, the PPL model also roughly matches the precision of the PL and PLC models in the intermediate and high energy decades, but undershoots the true cross section in the lowest energy decade by about 100%.

Unlike the PL and PLC models, and similarly to the PCHIP model below, the PPL model does not impose a fixed shape on the neutrino energy spectrum across the entire energy range. The PPL model has the flexibility to reconstruct diverse shapes of the neutrino spectrum. The width of each E_ν^{-2} energy segment in the PPL prescription, Eq. (8.6), limits how closely the true shape of the energy spectrum can be approximated, and the precision with which the flux can be measured. Using more PPL energy segments in the PPL would allow for a finer reconstruction of the shape of the energy spectrum, but could also worsen the measurement precision by introducing more free model parameters to fit.

Lacking prior knowledge of the true shape of the neutrino energy spectrum, we recommend using the PPL model to ensure sensitivity to the large variety of possible spectrum shapes. However, in energy ranges with low event rates, PPL might only set upper limits on the flux and might report values of the cross section significantly offset from the real ones.

8.7.5 *Piecewise Cubic Hermite Interpolating Polynomial (PCHIP)*

Figure 41 shows that the PCHIP flux fit model outperforms the other models in accuracy, at all energies, while approximating their precision at intermediate and high energies. The superiority

of PCHIP rests not from achieving higher precision, but from guaranteeing accuracy: the best-fit flux and cross section measured using PCHIP are always centered on their true values, even at low exposure times.

The neutrino spectrum is measured accurately across the full energy range. For a low exposure of 3 years, the measurement precision is worse than that of the other flux fit models, on account of the larger number of model parameters of the PCHIP model. But, after 10–20 years, the precision becomes comparable to that of the other models at intermediate and high energies, reaching 50%–25%. At low energies, it is worse due to the paucity of events, comparable to that of the PPL model.

The cross section is also measured accurately across all energy decades. In the intermediate and high energy decade, after 10–20 years, the measurement precision is comparable to that of the other flux fit models. In the low energy decade, the precision is significantly worse; there, similarly to the PPL model, the lack of a rigid spectrum shape means that the few events that are available are insufficient to make a precise measurement.

Given the guaranteed accuracy of the PCHIP flux fit model, and its precision on par with other models, we recommend using it, especially if at least a few tens of events are available.

8.7.6 *Impact of the energy and angular resolution*

In Secs. 8.7.2–8.7.5, we generated our main results using the baselines values of $\sigma_{\theta_z} = 2^\circ$ and $\sigma_\epsilon = 0.1$ for the angular and energy resolution of the detector (Sec. 8.4), the same ones used in related forecasts [346, 390] based on similar techniques as here. However, the capabilities of upcoming UHE neutrino telescopes are still under development, including those of IceCube-Gen2, so we explore the effect on our results of changing the detector resolution, focusing on the PCHIP flux model.

Figure 42 shows the effect of changing the detector resolution on the measurement of the neutrino spectrum. Poorer angular resolution worsens the precision moderately, but poorer energy resolution, even one slightly poorer than the baseline, significantly distorts the reconstructed energy spectrum. This is because it becomes harder to infer the energy spectrum when features in

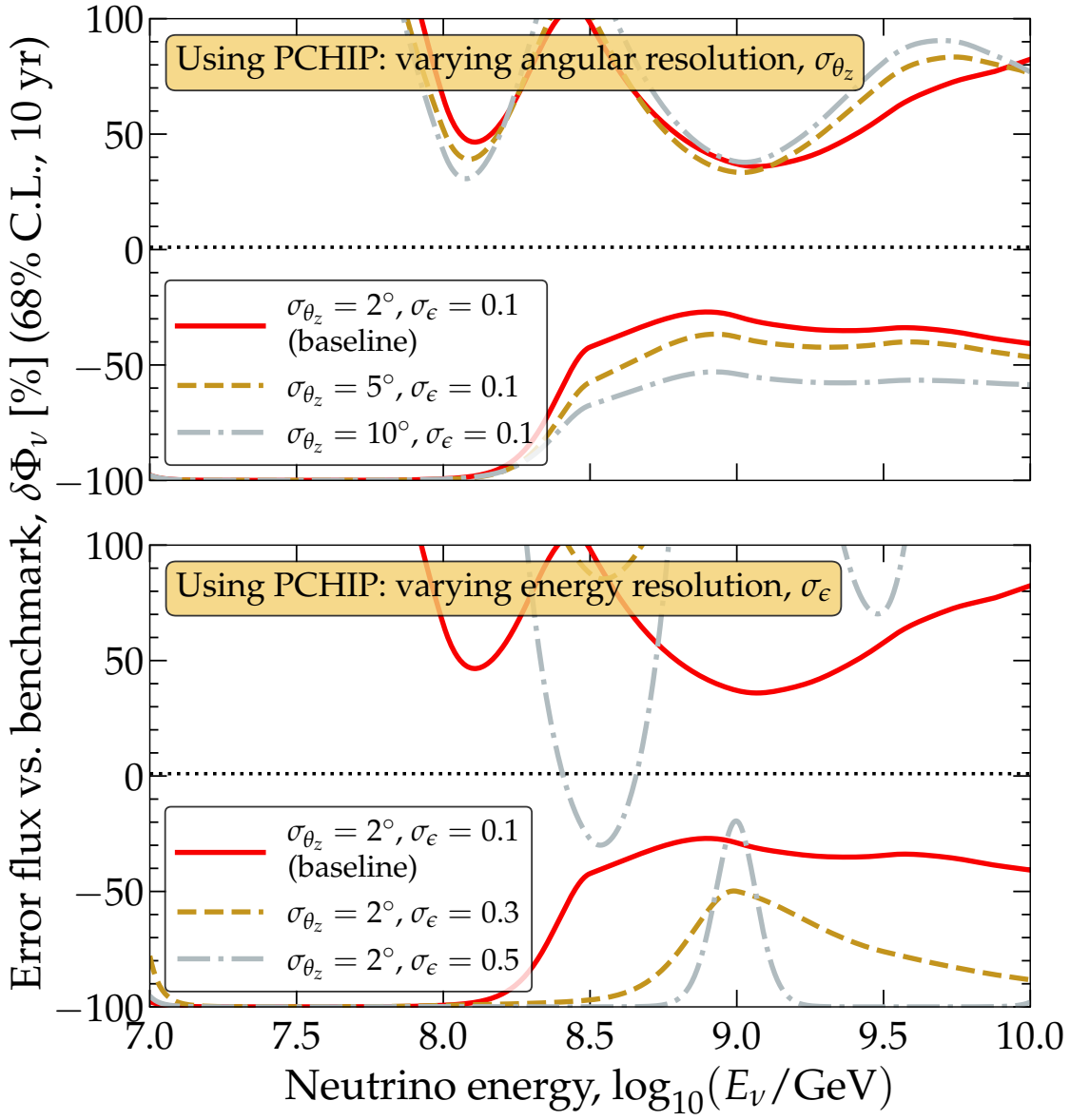

Figure 42: ***Relative error in the measurement of the UHE neutrino flux, for varying detector resolution.*** The detector is the radio array of IceCube-Gen2. The comparison is between the flux measured using the PCHIP flux fit model, Eq. (8.7), and our benchmark neutrino flux (Sec. 8.3.2). *Top:* Varying the detector angular resolution. *Bottom:* Varying the detector energy resolution. See Sec. 8.4.2 for how the detector resolution affects the computation of event rates, and Sec. 8.7.6 for details.

the energy distribution are washed out by poor energy resolution. This sets a loose design target of $\sigma_\epsilon \approx 0.1$ (see Sec. 8.4.3 for a definition) for the detector energy resolution needed in order to measure the UHE neutrino spectrum using a flexible parametrization such as PCHIP.

Figure 43 shows the effect of changing the detector resolution on the measurement of the cross section. Poorer angular resolution worsens the precision appreciably across all energy decades. This is especially evident in the results for $\sigma_{\theta_z} = 10°$. Given that the measurement of the cross section stems from comparing the attenuation of the neutrino flux from different near-horizontal

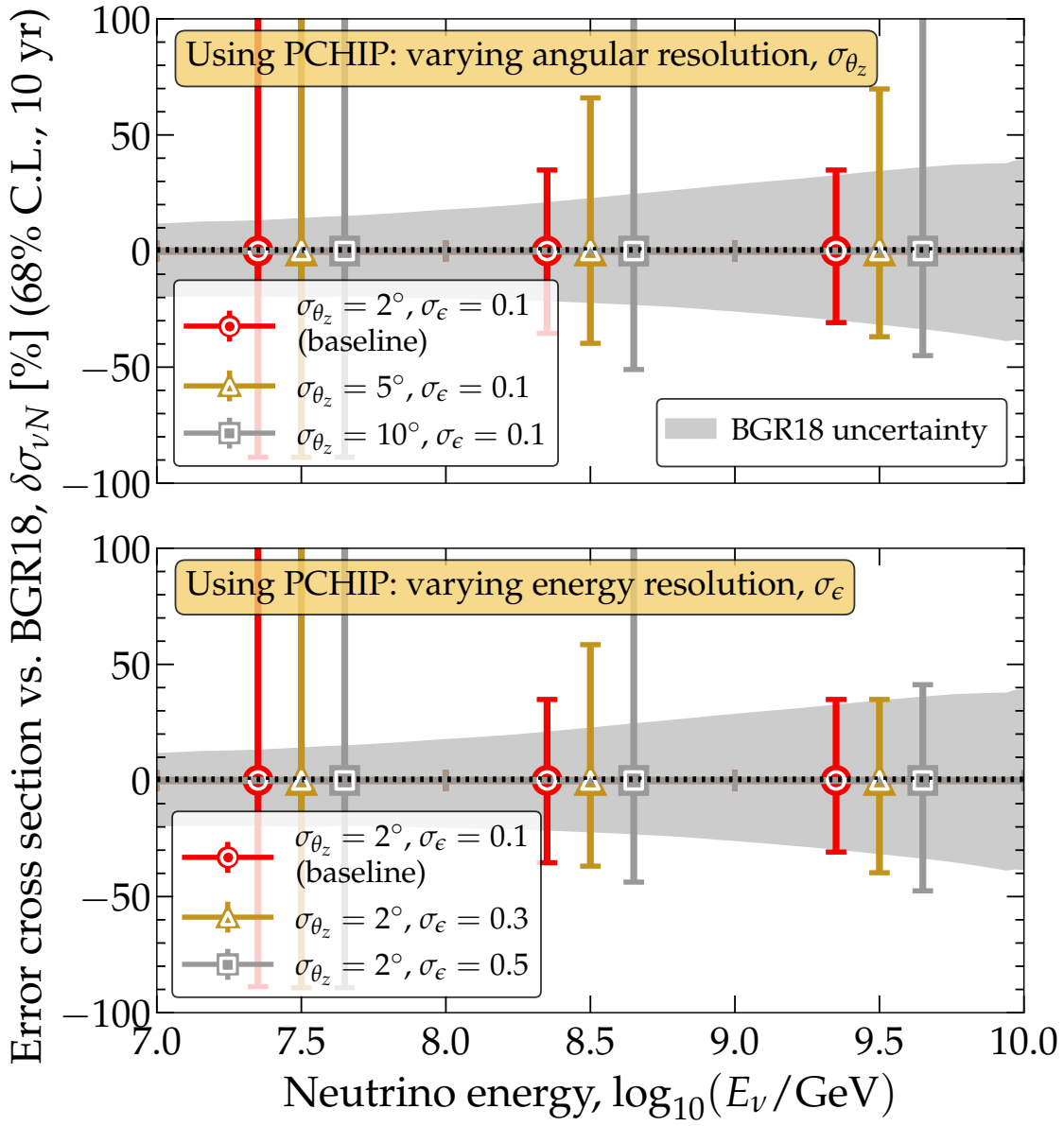

Figure 43: ***Relative error in the measurement of the UHE νN DIS cross section, for varying detector resolution.*** Same as Fig. 42, but the comparison is between the measured cross section, Eq. (8.8), (assuming the PCHIP flux fit model, Eq. (8.7)) and the BGR18 calculation of the cross section [194]. *Top:* Varying the detector angular resolution. *Bottom:* Varying the detector energy resolution. See Sec. 8.7.6 for details.

directions, about $\pm 5°$ around the horizon [346], a resolution of $10°$ dramatically reduces the measurement precision.

The impact of poorer energy resolution on the cross section is more nuanced. In the lowest energy decade, its impact does not fundamentally change the outcome obtained using the baseline resolution, since measurements are already limited by low event rates. In the intermediate and high energy decades, where the event rate is higher, the impact of poorer angular resolution is more

evident. The intermediate energy decade is more affected by it as a result of the misreconstruction of the energy spectrum, as shown in Fig. 42. This sets a loose design target of $\sigma_{\theta_z} \approx 2^\circ$ and $\sigma_\epsilon \approx 0.1$ in order to measure the energy dependence of the cross section.

Conveniently, the loose design targets for the detector resolution that we have found above—around our baseline choices of $\sigma_\epsilon = 0.1$ and $\sigma_{\theta_z} = 2^\circ$—are the same ones that would enable in the radio array of IceCube-Gen2, and other UHE neutrino telescopes, the discovery of the diffuse flux of UHE neutrinos and distinguishing between competing flux predictions [390], measuring the UHE νN cross section normalization [346], finding point sources of UHE neutrinos [372], and looking for the decay of heavy dark matter into UHE neutrinos [409].

8.8 SUMMARY AND OUTLOOK

The discovery of ultra-high-energy (UHE) neutrinos, with energies in excess of 100 PeV, would bring insight into long-standing open questions in astrophysics and particle physics. In preparation for the near-future discovery opportunities brought about by upcoming UHE neutrino telescopes, we have introduced methods to jointly measure two essential, but so-far-unknown quantities: the UHE neutrino flux and the neutrino-nucleon cross section, including their dependence with neutrino energy, and without prior knowledge of either. Achieving this would unlock in earnest the potential of UHE neutrino telescopes to perform measurements unhampered, inasmuch as possible, by preconceptions of the size and shape of the flux and cross section that, especially for the former, are laden with large uncertainty from theory.

Our methods are of general applicability; we have presented them at length to facilitate their implementation. We have illustrated them via forecasts of the capabilities of the planned radio array of the IceCube-Gen2 neutrino telescope, based on state-of-the-art simulations of it.

In light of the large variety of shape and size in the predictions of the UHE neutrino flux, we have focused on flexible parametrizations of the neutrino spectrum that can capture this variety, aiming for measurement precision and accuracy, but favoring the latter over the former. We explored four analysis models for the shape of the neutrino spectrum: two with rigid shape—a power law (PL)

and a power law with an exponential cut-off (PLC)—and two with flexible, adaptable shape—a piecewise power law (PPL) and a Piecewise Cubic Hermite Interpolating Polynomial (PCHIP).

The PL and PLC flux models, while appealing in concept due to their simplicity, are unable to capture features of the neutrino spectrum—dips and bumps, stemming from the neutrino production processes—that are commonplace in theory predictions. They achieve relatively high precision but atrocious accuracy, both in measuring the neutrino spectrum and the cross section. This underscores the necessity for more nuanced and adaptable flux models.

The PPL and PCHIP flux models provide the required flexibility, though at the cost of introducing more free model parameters. PPL stands out for its inherent flexibility, capable of accommodating a diverse range of spectrum shapes, though its accuracy is moderated by the challenges posed by low event rates. PCHIP affords yet greater flexibility, but with unwavering accuracy, even when confronted with low event rates. To use flexible flux models, like PCHIP, the detector requires a resolution of about 10% per energy decade in the energy of detected events and about 2° in the direction of detected events. Conveniently, these loose design targets roughly match the projected performance of the radio array of IceCube-Gen2 presently under study.

Access to a new energy regime motivates revisiting analysis choices. We present our methods and forecasts of the joint measurement of the UHE neutrino spectrum and neutrino-nucleon cross section with the goal of exploiting the full potential of UHE neutrino telescopes.

8.9 CRITICAL OUTLOOK

In this section, we provide a critical outlook on the results and implications of our study, focusing on the key findings, limitations, and future perspectives. The main text of the published research paper already includes similar discussions in Sections 8.8. In this section we summarize those discussions and focus on a critical view of the results from a state-of-the-art perspective and how this has been updated since the results were first published.

8.9.1 *Overview and main findings*

The results presented in this study offer valuable insights into the capabilities and limitations of UHE neutrino telescopes, specifically focusing on the radio array of IceCube-Gen2. We have employed innovative methods to jointly infer the UHE neutrino energy spectrum and the neutrino-nucleon cross section, allowing for a deeper understanding of these elusive particles.

We studied four models for the reconstruction of the UHE neutrino flux. The first one, the power law (PL) model, is motivated by the preferred fit of the astrophysical neutrino data in the TeV–PeV energy range. The hypothesis was that since at ultra-high energies the neutrino fluxes are not expected to follow a simple power law, then this model would result in a poor measurement. Our results confirmed this hypothesis. The PL model, while simple, fails to accurately capture the features of the UHE neutrino spectrum, resulting in imprecise measurements, especially at low and high energies. On top of that, an inaccurate reconstruction of the neutrino flux yields an inaccurate reconstruction of the νN cross section. Therefore, the PL model is not recommend, since the true spectrum shape is unknown.

The next model we explored is the power law with exponential cut-off (PLC). In astrophysical particle production models, a cut-off is connected with the maximum energy that a cosmic factory can achieve. The PLC model performs slightly better than the PL model but still suffers from accuracy issues, particularly at low and high energies. It is a more reasonable choice than PL but should be used cautiously in the absence of prior knowledge about the spectrum.

Next, we study the piecewise power law (PPL) model, another neutrino flux parametrization commonly used in the TeV–PeV range. The PPL model has the advantage of providing a larger degree of flexibility in capturing various spectrum shapes, resulting in improved accuracy compared to PL and PLC models. However, at low event rates, it may provide only upper limits on the flux. This issue could eventually be resolved with the implementation of the event contribution from the IceCube-Gen2 optical array at lower energies.

Finally, the piecewise cubic Hermite interpolating polynomial (PCHIP) model emerges as the preferred flux model, as it consistently delivers accurate measurements across all energy ranges. It balances precision and accuracy and is recommended, especially when a sufficient number of

events are available. The PCHIP model is capable of reconstructing any neutrino flux spectral shape, acknowledging the statistical limitations that a small flux manifest and translating them into a larger but accurate error band.

For all the cases, our forecasts indicate that the measurements of the UHE neutrino spectrum and the cross section are most precise at intermediate energies (100 PeV to 1 EeV). The accuracy tends to decrease at both low and high energy extremes. The precise measurements at intermediate energies follows from a combination of a relatively high neutrino flux and a large detector effective volume. At the lowest energies, the measurement worsens because the effective volume is in smaller, while at the highest energies the neutrino flux decreases.

8.9.2 *Limitations and future perspectives*

While our study has provided insights into UHE neutrino measurements, several limitations and future perspectives warrant consideration. The most evident one is the impact of the detector resolution. Our findings highlight the crucial role of detector characteristics, in particular the angular and energy resolution. The choice of angular and energy resolution significantly affects measurement precision and accuracy. We recommend aiming for detectors with resolutions close to the suggested targets to maximize their scientific potential.

A promising future development is the inclusion of neutrino flavor composition sensitivity. Throughout this study we fixed the neutrino flavor ratios to that of photo-hadronic production, both for the neutrino flux that generates the observed signal and the model we used to fit the observation. In reality, the UHE neutrino flux could deviate from this assumption. Modern methods for flavor reconstruction in in-ice radio neutrino detectors are currently under development [417]. Such information could be exploited in the future to extract the neutrino flavor composition from the data.

This work has built upon the methods and results presented in Chapters 6 and 7. It has implemented some of recommendations presented in the conclusions of those studies and patched their weaknesses. Nevertheless, we can point to some future directions that would be worth following.

- *Extension to other UHE neutrino telescopes:* While we have focused on IceCube-Gen2, our analysis methods can be applied to other UHE neutrino telescopes with straightforward modifications.

- *Optimizing detector designs:* The accuracy of measurements depends on the design of UHE neutrino detectors. Our methods can be used to optimize detector designs in terms of effective volume, energy resolution, and angular resolution.

- *Combining optical and radio arrays:* Future research should explore the synergies between different detector components. Combining the capabilities of the radio array and optical array, as planned in IceCube-Gen2, could enhance the discovery potential for various UHE neutrino flux models [418].

In conclusion, our study has paved the way for advanced UHE neutrino measurements, offering guidance on flux models and detector resolutions. To unlock the full potential of UHE neutrino telescopes, ongoing research efforts should focus on improving our understanding of UHE neutrino spectra, optimizing detector designs, and exploring synergies between different detector components.

Part III

PHYSICS OPPORTUNITIES WITH UHE NEUTRINOS

9

DETECTING POINT SOURCES OF UHE NEUTRINOS

Based on: Damiano F. G. Fiorillo, Mauricio Bustamante, **Víctor B. Valera Baca**, *Near-future discovery of point sources of ultra-high-energy neutrinos*, JCAP03(2023)026, arXiv:2205.15985

ABSTRACT Upcoming neutrino telescopes may discover ultra-high-energy (UHE) cosmic neutrinos, with energies beyond 100 PeV, in the next 10–20 years. Finding their sources would identify guaranteed sites of interaction of UHE cosmic rays, whose origin is unknown. We search for sources by looking for multiplets of UHE neutrinos arriving from similar directions. Our forecasts are state-of-the-art, geared at neutrino radio-detection in IceCube-Gen2. They account for detector energy and angular response, and for critical, but uncertain backgrounds. Sources at declination of -45° to 0° will be easiest to discover. Discovering even one steady-state source in 10 years would imply that the source has an UHE neutrino luminosity at least larger than about 10^{43} erg/s (depending on the source redshift evolution). Discovering no transient source would disfavor transient sources brighter than 10^{53} erg as dominant. Our results aim to inform the design of upcoming detectors.

9.1 INTRODUCTION

Where do ultra-high-energy cosmic rays (UHECRs) come from? They are the most energetic particles known—nuclei with energies in excess of 10^{12} GeV—yet their origin remains unknown sixty years after their discovery [19, 29, 125, 419]. As long as it does, our understanding of the high-energy Universe will be incomplete.

The sources of UHECRs are purportedly extragalactic cosmic particle accelerators located Mpc–Gpc away from Earth [421–431], though none has been irrefutably identified. Searches for sources

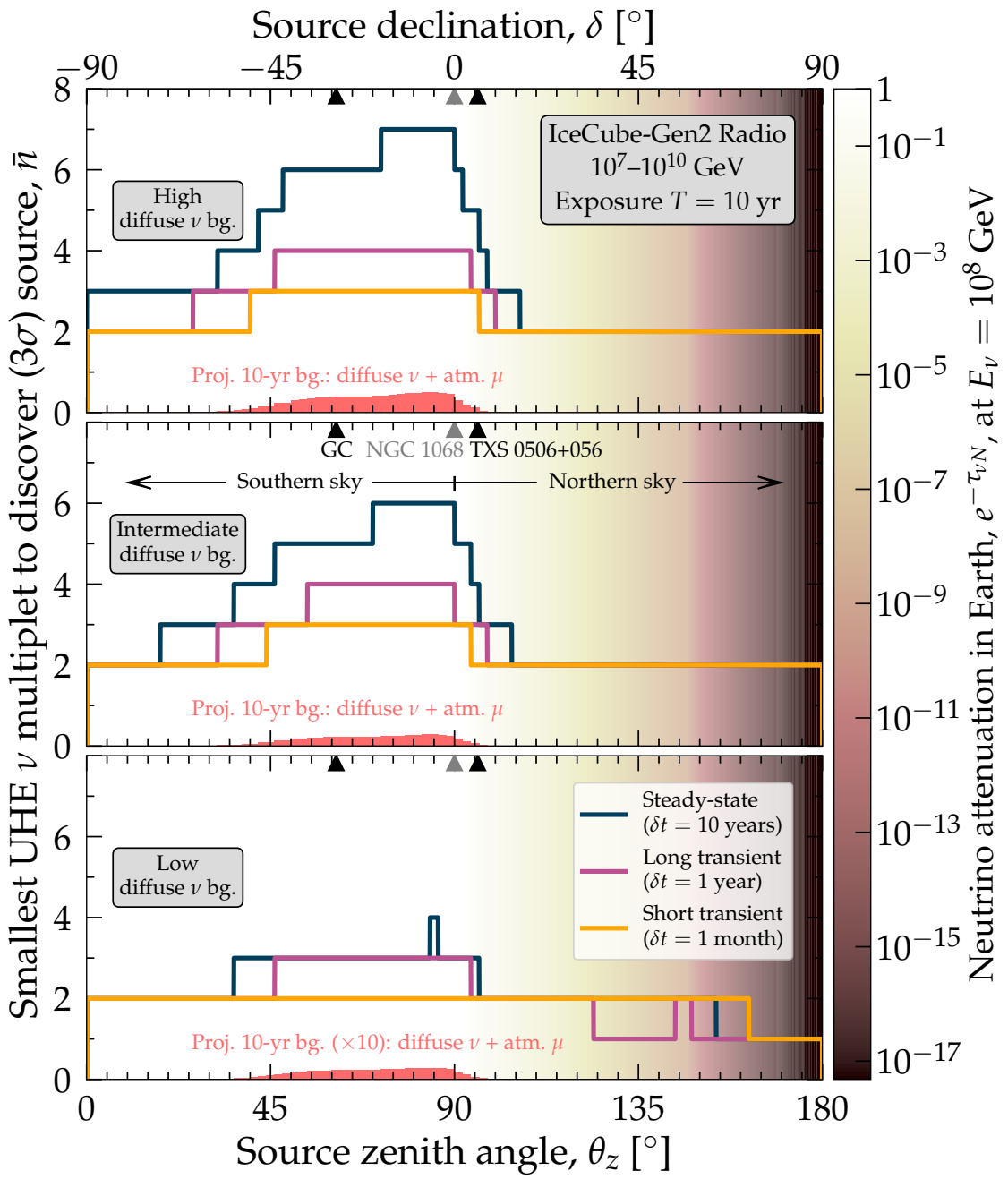

Figure 44: Smallest UHE multiplet needed for the IceCube-Gen2 radio array to discover an UHE neutrino source, steady-state or transient, with global significance of 3σ, for three choices of the unknown background diffuse UHE neutrino flux: high (*top*), intermediate (*center*), and low (*bottom*). For each, we show the projected 10-year rate of background events with reconstructed shower energy of 10^7–10^{10} GeV. The shading shows the in-Earth attenuation coefficient $e^{-\tau_{\nu N}}$ for 100-PeV neutrinos, where $\tau_{\nu N}$ is the optical depth to neutrino-nucleon (νN) scattering; smaller values of it represent stronger attenuation. For this plot, we use a detector angular resolution of $\sigma_{\theta_z} = 2°$ and our baseline radio array design. We include positions of promising sources: the Galactic Center (GC), Seyfert galaxy NGC 1068 [420], and blazar TXS 0506+056 [36]. See the main text for details and Appendix C.5 for 5σ results.

based on the detection of UHECRs are fundamentally limited: UHECR trajectories bend in cosmic magnetic fields [432–439] and, at EeV-scale energies, UHECRs rarely reach us from beyond 100 Mpc due to their scattering off cosmic photon backgrounds [27, 28]. Searches based on the detection of

gamma rays are similarly limited: PeV gamma rays emitted by UHECR sources get re-processed into the GeV–TeV range, where they are easily confused with backgrounds [91, 440–442]; EeV gamma rays, more resilient, remain undiscovered [443–447].

Neutrinos are free from these limitations [83, 164, 189, 190]. They are made in the interaction of UHECRs with matter and radiation in the UHECR sources, and during UHECR propagation to Earth; they receive a sizable fraction of the parent proton energy [130, 133, 256, 257, 387, 448]. Unlike UHECRs, neutrinos are electrically neutral, so they point back to their sources, and, unlike UHECRs and gamma rays, they only interact weakly, so they are not damped by interactions en route to Earth. Thus, detecting them may neatly reveal the positions of UHECR interaction sites in the sky.

In the last decade, the IceCube neutrino telescope discovered high-energy cosmic neutrinos, with TeV–PeV energies [34, 35, 184–188], that revealed the first likely sources of UHECRs with tens of PeV [36, 420, 449, 450]. However, it is unknown whether these are also the long-sought sources of EeV-scale UHECRs. To answer this definitively, we need *ultra-high-energy* (UHE) neutrinos, beyond 100 PeV. Yet, they are rare, and remain undiscovered [66–68, 80, 150, 160, 168, 353, 451–466] since their prediction in the 1960s [27, 28].

Fortunately, upcoming UHE neutrino telescopes have a real chance of discovering them in the next 10–20 years, even if their flux is low [83, 164, 189, 390]. We capitalize on this by making state-of-the-art forecasts of the UHE source discovery via UHE *neutrino multiplets*, *i.e.*, clusters of neutrinos from similar positions in the sky, indicative of a source. We gear our forecasts to IceCube-Gen2 [39], one of the leading upcoming neutrino telescopes, expected to start operations in the 2030s.

We provide methods and baseline forecasts to inform the aims and designs of upcoming UHE neutrino telescopes. We frame our results in terms of two questions: what is the size of the smallest UHE multiplet needed to claim source discovery, and what would source discovery, or lack thereof, imply for the population of UHE sources.

Figure 44 shows our answer to the first question. The variation with source position reflects the angular distribution of background events, which itself reflects the in-Earth neutrino attenuation and detector response. Results depend strongly on the size of the diffuse UHE neutrino flux,

presently unknown, which is the main background that the source search must overcome: a higher background demands larger multiplets. Later, in 46, we show our answer to the second question above.

Pioneering work explored the prospects of discovering point sources of high-energy [467–473] and UHE neutrinos [371]. Our methods add key features that enhance its usefulness to realistic UHE source searches. Individually, they lead to sizeable improvements; together, they lead to powerful advances.

First, we avoid introducing source-model bias by making the diffuse UHE neutrino flux equal to different plausible choices, rather than modeling it as coming from the same source population responsible for the multiplets. Second, we account for the atmospheric muon background, recently found to matter for UHE neutrino radio-detection [213]. Third, we account for critical, but often-overlooked features in source searches, *e.g.*, neutrino propagation through Earth, the energy- and direction-dependent detector response, and its energy and angular resolution [346]. Fourth, though our methods apply generally, we ground our forecasts in the radio-detection of neutrinos in IceCube-Gen2, via state-of-the-art simulations of neutrino interactions, the ensuing particle showers, and the emission, propagation, and detection of radio signals [211].

Refs. [371, 472] use the sky-wide distribution of the angular separation of neutrino pairs to detect the presence of point sources; Ref. [472] used them also to locate sources, though not UHE ones. Unlike them, we tessellate the sky to rely only on local information and use multiplets—not only pairs—*mainly* to locate point sources. Appendix C.1 extends our methods to resemble Ref. [371]. Our approach is analytic, complementary to the Monte Carlo approach used by Ref. [474] for TeV–PeV neutrinos.

9.2 DETECTING UHE NEUTRINOS

We compute the propagation of UHE neutrinos inside Earth and their detection in IceCube-Gen2 as in Ref. [346]. Below, we sketch the methods; for details, see Appendix C.2 and Ref. [346].

We model UHE neutrino propagation through the Earth using the state-of-the-art code NUPROPEARTH [209, 210]. The detector response is modeled via its effective volume, Fig. 13 in Ref. [346],

simulated using the same tools, NuRadioMC [211] and NuRadioReco [212], as the IceCube-Gen2 Collaboration. For our main results, we adopt the baseline design of the IceCube-Gen2 radio array from Ref. [396]: 313 detector stations, made up of 169 shallow stations and 144 hybrid, *i.e.*, shallow plus deep, stations with complementary response. Appendix C.3 contains results for alternative designs; our conclusions are broadly unaffected. Our choices of detector resolution are informed by simulations [212, 300, 312, 314, 315, 317, 324, 326, 346]; they are the same as in Ref. [346].

9.3 BACKGROUNDS

The main challenge to multiplet searches is that, underlying the UHE neutrinos from point sources, we expect a diffuse background of UHE neutrinos and atmospheric muons whose random over-fluctuations may mimic multiplets from point sources. Later, we show how our methods overcome this.

The diffuse flux of UHE neutrinos is likely composed of cosmogenic neutrinos [27, 28, 65], made in UHECR interactions en route to Earth, and of neutrinos from unresolved sources. There are numerous flux predictions for both [172–180, 193], and upper limits [66–68, 80, 150, 160, 168, 353, 451–466] come chiefly from IceCube [66] and Auger [67]. Rather than adopting a particular prediction, we set the diffuse UHE neutrino flux to benchmark levels representative of current and future detector sensitivity: the current IceCube upper limit on the energy flux $E_\nu^2 \Phi_\nu$ (*high*) [66], and versions of it shifted down to 10^{-8} (*intermediate*) and 10^{-9} GeV cm^{-2} s^{-1} sr^{-1} (*low*). Each represents a future possibility for the largest allowed diffuse UHE neutrino flux, either a flux measurement or an upper limit. We conservatively do not perform a spectral analysis in energy. The above benchmark fluxes yield roughly 520, 297, and 30 events all-sky, respectively, in 10 years of IceCube-Gen2; see Appendix C.4.

The diffuse neutrino flux is isotropic, but the angular distribution of the event rate is not. Fewer events come from directly above the detector ($\theta_z \lesssim 45°$), due to weaker detector response, and from below the detector ($\theta_z \gtrsim 95°$), due to in-Earth neutrino attenuation, than from slant and horizontal directions ($45° \lesssim \theta_z \lesssim 95°$). We also account for a background of atmospheric muons,

which is however negligible; see Appendix C.4. Because of the anisotropic event rate, source discovery prospects vary across the sky.

9.4 DISCOVERING SOURCES

The first question that we address is how large should a detected multiplet be to claim that it is due to a point source, and not to an over-fluctuation of the background.

We tessellate the sky into $N_{\rm pixels}$ square pixels that approximate the circular error regions expected from shallow detector stations [396]. The width in zenith angle of each pixel is σ_{θ_z}, the detector angular resolution. The width in azimuth is chosen so that the solid angle of each pixel equals that of a cone of apex angle $2\sigma_{\theta_z}$. In the i-th pixel, we compute the mean number of background-induced events, μ_i, expected after an exposure time T, following the procedure sketched above.

The *local* p-value p of detecting a multiplet of more than n_i events in the i-th pixel, *i.e.*, the probability that a multiplet is due to background alone, is $p(\mu_i, n_i) = \sum_{k=n_i}^{+\infty} (\mu_i^k/k!) e^{-\mu_i}$. But this does not account for the look-elsewhere effect: even if p is small—so that a background fluctuation is unlikely—the probability that an excess with this p-value occurs anywhere in the sky may be large. Therefore, in our forecasts we use instead the *global* p-value $P(p)$, *i.e.*, the probability that a multiplet with local p-value p occurs in any of the pixels, *i.e.*,

$$P(p) = 1 - \prod_{i=1}^{N_{\rm pixels}} \left(1 - \sum_{k=\bar{n}_i(p)}^{\infty} \frac{\mu_i^k}{k!} e^{-\mu_i} \right) . \tag{9.1}$$

Appendix C.1 contains the derivation of 9.1. Roughly, $P \sim N_{\rm pixels} p$, provided $p \ll N_{\rm pixels}^{-1}$. Given a target global p-value $\bar{P}$, we invert 9.1 to find the local p-value $\bar{p}$ and the size of the smallest multiplet in each pixel needed to reach it, $\bar{n}_i(\bar{p})$. We report this in 44 and in Appendix C.1. For transient sources, with an emission period of duration $\delta t \ll T$, *e.g.*, a flaring blazar or gamma-ray burst, we modify this procedure to account for a look-elsewhere effect in time; see Appendix C.1.

Figure 44 shows the smallest multiplet needed to claim source discovery at 3σ, *i.e.*, with $\bar{P} = 0.003$, in $T = 10$ yr of exposure time, for our three background neutrino diffuse fluxes. In all cases, sources located above IceCube-Gen2 ($\theta_z \lesssim 45°$), where the background is smallest, may be discovered by detecting a doublet or triplet, regardless of the choice of benchmark. However,

detection is unlikely in these directions because the detector effective volume is small. In contrast, sources located closer to the horizon ($45^\circ \lesssim \theta_z \lesssim 95^\circ$), where the background is largest, require larger multiplets, as large as a heptaplet for the high background benchmark. Yet, detection is promising in these directions because the effective volume is larger and in-Earth attenuation is mild.

Steady-state sources, like starburst galaxies, are active during the full exposure time, T. Searches for them accumulate larger background and require larger multiplets to claim discovery. Long- and short-duration transient sources, like blazar flares and tidal disruption events, respectively, are active for a fraction of that time, δt. Searches for them require smaller multiplets. For very-short-duration transients, like gamma-ray bursts, doublets or triplets are always enough, regardless of source position and background level; see Appendix C.6.

Our results are significantly affected by the angular resolution of the detector. Figure 44 uses $\sigma_{\theta_z} = 2^\circ$. Better angular resolution allows for finer sky pixels and a smaller contribution of the background in each of them. Using $\sigma_{\theta_z} = 5^\circ$ roughly doubles the size of the multiplets needed to claim discovery; see Appendix C.3.

Our results are tentatively robust to the choice of the design of the IceCube-Gen2 radio array. Figure 44 uses our baseline design described above. At least for two alternative designs, our general observations hold; see Appendix C.3. Our claim stems from a non-exhaustive exploration of array designs. Stronger claims require further simulation work, which is ongoing [396].

9.5 MULTIPLETS FROM A POPULATION OF UHE SOURCES

Next we show what we can learn about the UHE neutrino source populations with the detection or absence of a multiplet. We compute how likely it is to discover a source from a given source population. Following what seminal Refs. [468, 471] did for TeV–PeV neutrino sources, we consider a population of identical UHE sources distributed in redshift, z. For steady-state sources, we describe the population using the neutrino luminosity emitted by a source, L_ν, and the local source number density, $n_0 \equiv n(z = 0)$. The parameter L_ν, in particular, significantly depends on the internal parameters of the source and on the chemical composition of the UHECRs. For

transient sources, we use the energy emitted by a source in neutrinos, E_ν, and the local source burst rate, $\mathcal{R}_0 \equiv \mathcal{R}(z=0)$. All sources in a population share the same value of L_ν or E_ν. Each source emits neutrinos with a broken power-law spectrum that approximates neutrino production via proton-photon interactions [475–478]. The neutrino emissivity, $L_\nu n(z)$ or $E_\nu \mathcal{R}(z)$, follows the star-formation rate [471, 479]. Fixing the values of the source population parameters fixes the neutrino flux coming from that source class.

Let us denote the number density per comoving volume as $n(z) = n_0 f(z)$, where $n_0 \equiv n(z=0)$ is the local number density and $f(z)$ describes the evolution with redshift z. We set $f(z)$ to be equal to the star-formation rate [471, 479], normalized so that $f(z=0) = 1$. (For specific source classes, the redshift evolution of the sources might differ, *e.g.*, for FSRQs [283] and BL Lacs [284]. We examine how this impacts our results in Appendix C.7.) For simplicity, we assume that all the sources in a given population have the same broken-power-law neutrino spectrum,

$$\frac{dN_\nu}{dEdt} \propto \left[a \left(\frac{E}{E_0} \right)^{\alpha} + (1-a) \left(\frac{E}{E_0} \right)^{\beta} \right]^{-1} , \tag{9.2}$$

normalized so that $\int_0^\infty dE E(dN_\nu/dEdt) = L_\nu$. For transient sources, the equivalent parametrization is in terms of the total number of neutrinos injected in the burst, dN_ν/dE, normalized to the total energy of the burst, *i.e.*, $\int_0^\infty dE E(dN_\nu/dE) = E_\nu$ To produce our results, we choose $\alpha = 1$, $\beta = 3$, $a = 0.8$, and $E_0 = 10^8$ GeV, which approximates a neutrino energy spectrum that peaks inside the energy range where the IceCube-Gen2 radio array is sensitive. Inside one pixel, the probability distribution of sources in redshift is

$$p_{\rm src}(z) = \frac{\delta\Omega\, n_0\, f(z) r^2(z)}{H(z) N_{\rm src}} , \tag{9.3}$$

where $\delta\Omega$ is the solid angle of a pixel, $r(z)$ is the comoving distance, and $H(z)$ is the Hubble parameter. We assume a ΛCDM cosmology, with Hubble constant $H_0 = 67.4$ km s^{-1} Mpc^{-1}, and adimensional energy density parameters $\Omega_m = 0.315$, $\Omega_\Lambda = 0.685$ [264]. Finally, the mean number of sources in each pixel is

$$N_{\rm src} = \int_0^\infty dz\, \frac{n_0\, f(z)\, \delta\Omega\, r^2(z)}{H(z)} . \tag{9.4}$$

Below, we detail how we compute the constraints on the source population parameters that we show in the main text. The procedure consists of three steps: computing the contribution of the

diffuse background in each pixel, computing the distribution of the number of events in each pixel, and computing constraints on the source populations.

9.5.1 *Contribution of the diffuse background in each pixel*

The normalization and angular distribution of the neutrino-induced event rate from a source depends on the source redshift, source luminosity, and zenith angle of the pixel in which the source is located. Formally, it also depends on the neutrino energy spectrum, since different neutrino energy spectra are affected differently by their propagation through the Earth. However, because our analysis groups events in a single energy bin, it is largely insensitive to the shape of the neutrino energy spectrum. A source at redshift z produces a mean number of events $s_i(z)$ in the i-th pixel. The number of events from this source in different pixels is different because of different effects of in-Earth attenuation and because of the angular response of the detector. We account for these differences by assuming that $s_i(z) = \kappa_s B_i$, where B_i is the mean number of events expected from a particular choice of the diffuse isotropic UHE neutrino background (see Appendix C.4), and κ_s is a proportionality constant that we determine below. We compute the proportionality constant between s_i and B_i using the following procedure:

- First, we compute B_i in each pixel, following our sophisticated procedure from Appendix C.2. We pick either of our benchmark background isotropic UHE neutrino fluxes—low, intermediate, or high; see C5. All of them yield the same angular distribution of events; they differ only in the normalization of the event rate;

- From the projected 90% C.L. sensitivity to the diffuse UHE neutrino flux of the radio array of IceCube-Gen2 reported in Ref. [396], we extract the energy-dependent effective area, $A'_{\rm eff}(E)$, following Eq. (C.1) in Ref. [478]. The treatment in Ref. [478] is geared to the sensitivity to point sources, expressed in GeV cm^{-2} s^{-1}. To extract the effective area from the sensitivity to the diffuse flux, measured in GeV cm^{-2} s^{-1} sr^{-1}, we include an additional factor of 4π in the denominator of Eq. (C.1) in Ref. [478];

- Because the effective area extracted above corresponds to a different detector array design than the ones we use, the event rate computed using it does not match the event rate computed following our procedure from Appendix C.2. To fix this, we scale the effective area by an energy-independent factor κ_A, defined implicitly as $A_{\rm eff}(E) = \kappa_A A'_{\rm eff}(E)$, and chosen so that the all-sky rate computed using $A_{\rm eff}$ for our chosen background model (see below) matches $\sum_{i=1}^{N_{\rm pixels}} B_i$. (We use this workaround only when computing constraints on the source population. When computing the smallest multiplets needed to claim source discovery, we use directly our procedure from Appendix C.2);

- The effective area that we extracted from Ref. [396] is for a diffuse isotropic neutrino flux; the angular response of the detector has already been averaged over all the sky. Therefore, with this effective area we compute the mean number of events from a source at redshift z when the source direction is averaged over all the sky. For a steady-state source, this is

$$\langle s(z)\rangle = \frac{T}{4\pi r^2(z)} \int_0^\infty \frac{dN_\nu}{dEdt}[E(1+z)]A_{\rm eff}(E)dE \,, \tag{9.5}$$

  where $T = 10$ years is the exposure time. For a transient source, it is

$$\langle s(z)\rangle = \frac{1}{4\pi r^2(z)} \int_0^\infty \frac{dN_\nu}{dE}[E(1+z)]A_{\rm eff}(E)dE \,; \tag{9.6}$$

- Finally, we compute κ_s, the proportionality constant between $s_i(z)$ and B_i by requiring that the average of $s_i(z)$ over all pixels, $\kappa_s \sum_{j=1}^{N_{\rm pixels}} B_j/N_{\rm pixels}$, matches 9.5 or 9.6, which yields

$$s_i(z) = \frac{\langle s(z)\rangle N_{\rm pixels}}{\sum_{j=1}^{N_{\rm pixels}} B_j} B_i \,. \tag{9.7}$$

The mean number of events in the i-th pixel is

$$\langle n_i\rangle = N_{\rm src} \int_0^\infty dz\; p_{\rm src}(z) s_i(z) + b_i \,, \tag{9.8}$$

where the first term is due to point sources, calculated following the above procedure and the second term, b_i, is due to the background of cosmogenic neutrinos, unresolved sources, and atmospheric muons. The value of b_i is fixed by requiring that the mean event rate per pixel is saturated by the background, *i.e.*, $\langle n_i\rangle = B_i$.

9.5.2 *Computing the distribution of the number of events in each pixel*

Next, we compute the probability distribution of the number of events n_i, detected, in the i-th pixel. This is given by the convolution of the Poisson distribution of the number of sources, σ_i, centered around the mean number of sources per pixel, $N_{\rm src}$, from 9.4; the probability density, $p_{\rm src}(z_\alpha)$, from 9.3, for the source number α in this pixel, with redshift z_α, where $\alpha = 1, \ldots, \sigma_i$; the Poisson distribution of the number of detected events, n_i, centered around the mean value $b_i + \sum_{\alpha=1}^{\sigma_i} s_i(z_\alpha)$. Altogether, the probability distribution is

$$P_i(n_i) = \sum_{\sigma_i=0}^{\infty} \frac{N_{\rm src}^{\sigma_i} e^{-N_{\rm src}}}{\sigma_i!} \prod_{\alpha=1}^{\sigma_i} \int_0^\infty p_{\rm src}(z_\alpha) dz_\alpha \frac{(b_i + \sum_{\alpha=1}^{\sigma_i} s_i(z_\alpha))^{n_i}}{n_i!} e^{-b_i - \sum_{\alpha=1}^{\sigma_i} s_i(z_\alpha)} \,. \tag{9.9}$$

To simplify numerical evaluation, we find an analytical expression for $P_i(n_i)$ by computing its generating function, $\Phi_i(x) = \sum_{n_i=0}^{\infty} P_i(n_i) x^{n_i}$. The sum over n_i can then be performed explicitly, *i.e.*,

$$\Phi_i(x) = \exp\left[b_i(x-1) + N_{\rm src} \left(\int_0^\infty dz \; p_{\rm src}(z) e^{s_i(z)(x-1)} - 1 \right) \right] \,. \tag{9.10}$$

Thus, by the definition of the generating function, the probability distribution is

$$P_i(n_i) = \frac{1}{n_i!} \left[\frac{d^{n_i} \Phi_i(x)}{dx^{n_i}} \right]_{x=1} \,. \tag{9.11}$$

Below, when finding constraints on the source population, we use 9.11 to compute numerically the probability of detecting n_i events in the i-th pixel.

9.5.3 *Computing constraints on the source populations*

Finally, we set constraints on the source population parameters, *i.e.*, on n_0 and L_ν for steady-state sources, or $\mathcal{R}_0$ and E_ν for transient sources; see the main text. When setting constraints on the source population, our underlying assumption is of source discovery with a global significance of 5σ. Requiring this fixes the size of the smallest multiplet needed to claim source discovery in each pixel, $n_{i,5\sigma}$; see Fig. 1 in the main text. Therefore, the probability that no source is discovered in the i-th pixel is

$$Q_i = \sum_{n_i=0}^{n_i = n_{i,5\sigma} - 1} P_i(n_i) \,. \tag{9.12}$$

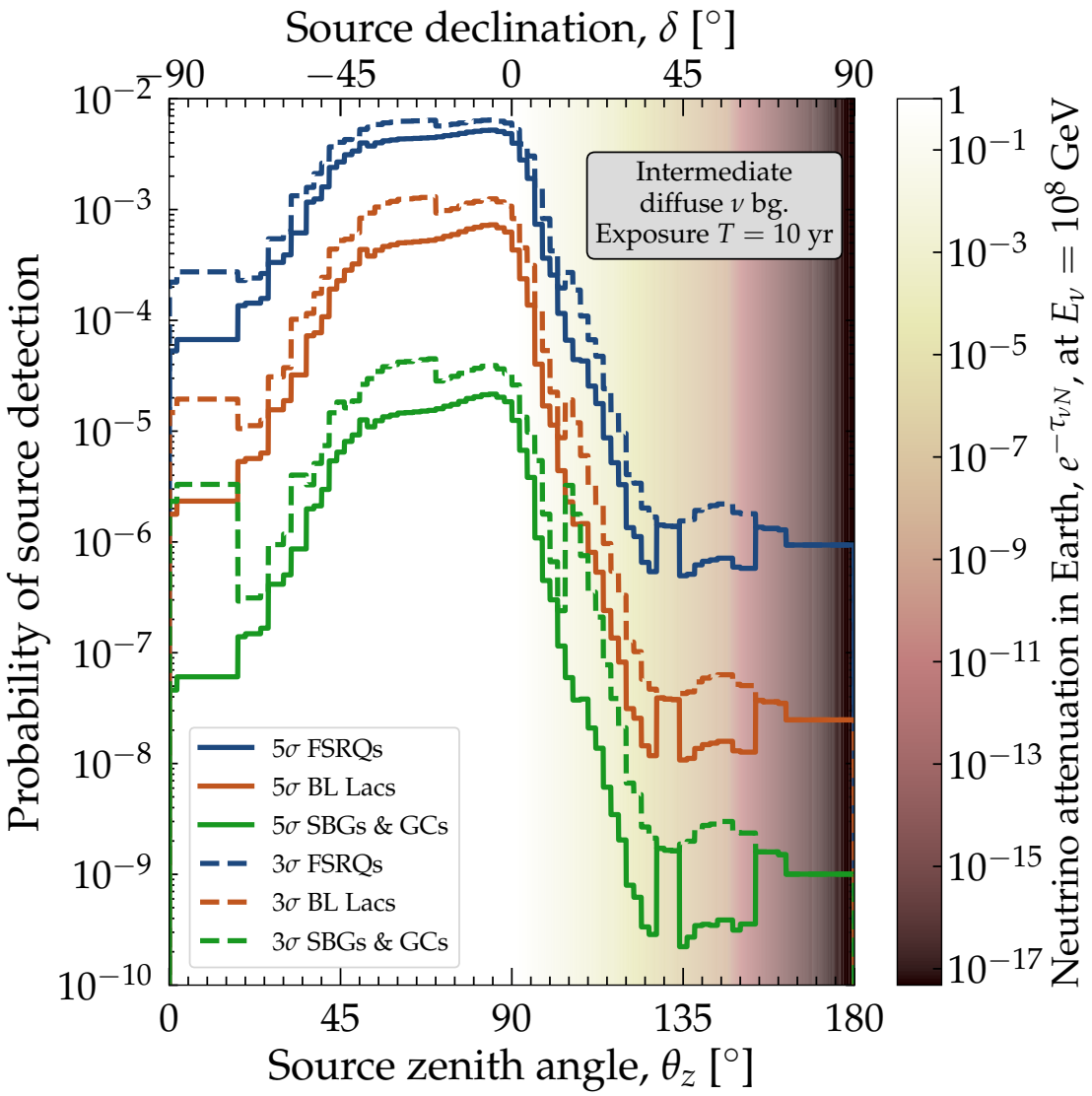

Figure 45: Probability of source discovery in each pixel in the sky, at 3σ and 5σ, for three candidate classes of steady-state UHE neutrino sources: FSRQs, BL Lacs, and SBGs & GCs. For this plot, the detector angular resolution is $\sigma_{\theta_z} = 2°$, and we use our baseline array design and intermediate benchmark diffuse neutrino flux. The large jumps at high zenith angles are due to statistical fluctuations in the multiplet size needed for detection.

With this, the probability that no source is discovered anywhere in the sky is simply the product of Q_i over all pixels, *i.e.*,

$$\mathcal{Q} = \prod_{i=1}^{N_{\text{pixels}}} Q_i \,. \tag{9.13}$$

We now use this probability to identify the regions of parameter space which are expected to lead to the discovery of point sources.

9.5.4 *Results*

Figure 46 shows the constraints that we set on UHE source populations based on 9.13, assuming our intermediate benchmark UHE diffuse background.

The first constraint comes from demanding that the neutrino flux from each class saturates the background diffuse neutrino flux. Doing this fixes the values of L_ν and E_ν; the values of n_0 and $\mathcal{R}_0$ are from Ref. [189, 471]. Tables 7 and 8 shows the values of the population parameters of each source class for our three benchmark background fluxes. In Ref. [471], the values of n_0 and $\mathcal{R}_0$ were obtained under the assumption of a model-dependent scaling between the high-energy neutrino and gamma-ray luminosity, which we do not apply (however, see Appendix C.7 for a similar treatment of FSRQs as that of Ref. [471]). Further, for some of the source classes that we show, UHE neutrino production may not even be expected at all. We forego a discussion of the different models of UHE neutrino production in the different candidate source classes, which is not our goal. Since all the candidate source classes in 46 are treated on equal footing, without modeling the physical conditions and neutrino production mechanisms particular to each, the values of the population parameters in it should be taken merely as indicative.

The second constraint comes from demanding that each class either yields at least one 5σ source discovery, or none, with 90% probability. The blue region would be excluded by the lack of 5σ source discovery, and is obtained by demanding $\mathcal{Q} < 0.1$. The second region would be excluded by the discovery, at 5σ, of at least one source, and is obtained by demanding $\mathcal{Q} > 0.9$. Figure C10, in Appendix C.6, shows equivalent results for our low and high benchmarks.

Versions of 46 for TeV–PeV sources were shown, *e.g.*, in Refs. [189, 468, 471]; to our knowledge, 46 shows for the first time multiplet-based constraints for UHE sources.

For steady-state sources, if none is discovered after 10 years, only bright, rare source classes would be disfavored as individually dominant. While 46 may suggest that FSRQs would be excluded, in reality some candidate source classes, like TDEs, FSRQs and BL Lacs, have a redshift evolution that is quite different from the star-formation rate. Appendix C.7 illustrates this. Conversely, if even one source is discovered, most known candidate source classes would be excluded.

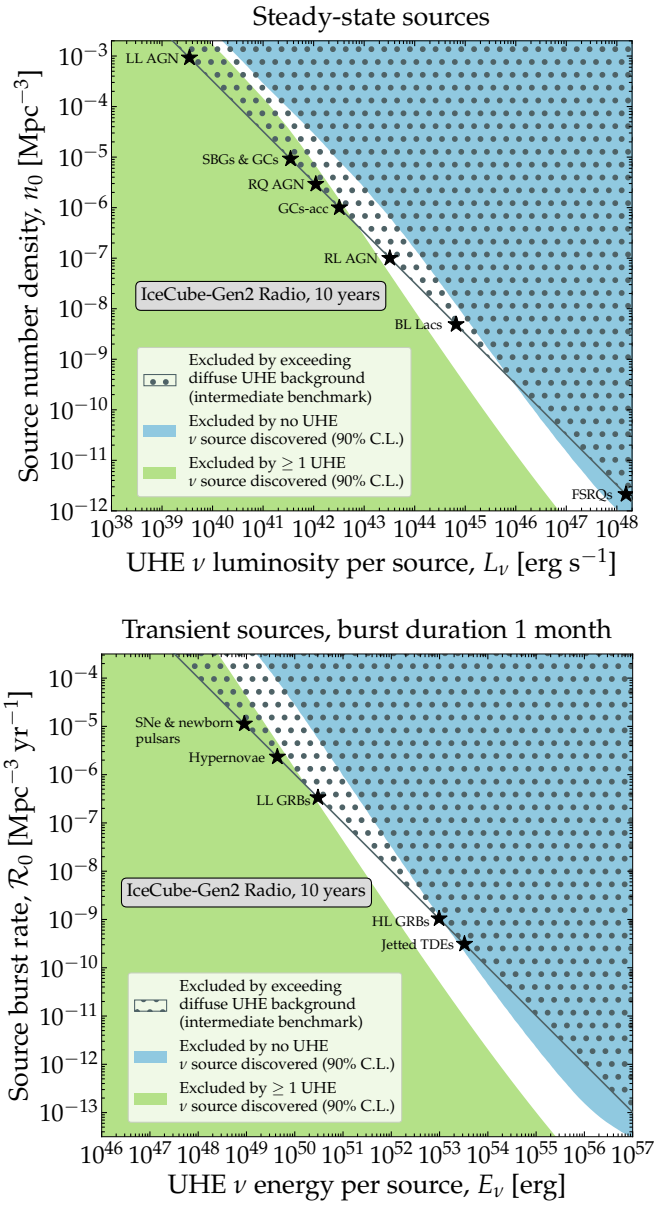

Figure 46: Constraints on candidate classes of steady-state (*top*) and transient (*bottom*) UHE neutrino sources, from the discovery or absence of UHE multiplets, *i.e.*, of UHE neutrino sources, in the radio array of IceCube-Gen2 after 10 years of exposure. We showcase promising candidate source classes: low-luminosity active galactic nuclei [480, 481] (LL AGN), starburst galaxies [482–487] & galaxy clusters [488–490] (SBGs & GCs), radio-quiet AGN [491] (RQ AGN), accretion shocks in galaxy clusters [109, 492, 493] (GCs-acc), radio-loud AGN [103, 477, 494] (RL AGN), BL Lacertae AGN [179, 495] (BL Lacs), flat-spectrum radio quasars [495–498] (FSRQs), supernovae [499–504] & newborn pulsars [175, 505] (SNe & newborn pulsars), hypernovae [502, 506], low-luminosity gamma-ray bursts [507, 508] (LL GRBs), high-luminosity GRB [104, 106, 509–511] (HL GRBs), and jetted tidal disruption events [115, 512–518] (jetted TDEs). For each, the value of n_0 or $\mathcal{R}_0$ is from Refs. [189, 471]; the value of L_ν or E_ν is chosen to saturate the background UHE neutrino diffuse flux; for this plot, we fix it to our intermediate benchmark. Appendix C.6 contains results using our low and high benchmarks. In the hatched region, the flux from the source population exceeds the background diffuse flux. See the Appendix 9.5 for the values of the source-population parameters.

Source class	n_0 [Mpc^{-3}]	L_ν [erg s^{-1}] (low ν bg.)	L_ν [erg s^{-1}] (interm. ν bg.)	L_ν [erg s^{-1}] (high ν bg.)
LL AGN	9.2×10^{-4}	3.5×10^{38}	3.5×10^{39}	6.1×10^{39}
SBGs & GCs	9.2×10^{-6}	3.5×10^{40}	3.5×10^{41}	6.1×10^{41}
RQ AGN	2.9×10^{-6}	1.1×10^{41}	1.1×10^{42}	1.9×10^{42}
GCs-acc	1.0×10^{-6}	3.2×10^{41}	3.2×10^{42}	5.6×10^{42}
RL AGN	1.0×10^{-7}	3.2×10^{42}	3.2×10^{43}	5.6×10^{43}
BL Lacs	4.9×10^{-9}	6.6×10^{43}	6.6×10^{44}	1.2×10^{45}
FSRQs	2.1×10^{-12}	1.5×10^{47}	1.5×10^{48}	2.7×10^{48}

Table 7: Steady-state source population parameters used for the benchmark source classes in the main text. The effective local number density, n_0, for each class is obtained from Ref. [471]. The UHE neutrino luminosity, L_ν, is fixed for each source class by demanding that the UHE neutrino flux from it saturates the diffuse UHE neutrino background. Results are for our low, intermediate, and high benchmark diffuse UHE neutrino background; see Appendix C.4.

Source class	$\mathcal{R}_0$ [Mpc^{-3} yr^{-1}]	E_ν [erg] (low ν bg.)	E_ν [erg] (interm. ν bg.)	E_ν [erg] (high ν bg.)
SNe & newborn pulsars	1.1×10^{-5}	9.0×10^{47}	9.0×10^{48}	1.6×10^{49}
Hypernovae	2.3×10^{-6}	4.4×10^{48}	4.4×10^{49}	7.6×10^{49}
LL GRBs	3.4×10^{-7}	3.0×10^{49}	3.0×10^{50}	5.3×10^{50}
HL GRBs	1.0×10^{-9}	9.8×10^{51}	9.8×10^{52}	1.7×10^{53}
Jetted TDEs	3.1×10^{-10}	3.3×10^{52}	3.3×10^{53}	5.7×10^{53}

Table 8: Transient source population parameters used for the benchmark source classes in the main text. The effective local burst rate, $\mathcal{R}_0$. for each class is from Ref. [189] (see also Ref. [519]). The energy emitted as UHE neutrinos, E_ν, is fixed for each source class by demanding that the UHE neutrino flux from it saturates the diffuse UHE neutrino background. Results are for our low, intermediate, and high benchmark diffuse UHE neutrino background; see Appendix C.4.

For transient sources, the situation is reversed. If none is discovered, the brightest transients, with total energy per source larger than 10^{53} erg, would be disfavored: these include GRBs and TDEs, which are known candidates for UHECR acceleration. Conversely, if even one transient source is discovered, it would be a strong indication in favor of these source classes. TDEs have a negative redshift evolution; however, we show in Appendix C.7 that accounting for their correct evolution does not change results significantly.

Our conclusions for steady-state sources are broadly unaffected by the size of the background diffuse neutrino flux: the precise parameter-space regions excluded depend on the background, but we find similar results for our low, intermediate, and high benchmarks. For transients, we find that a diffuse background much lower than 10^{-9} GeV cm^{-2} s^{-1} sr^{-1} would disfavor source discovery even for very bright sources. If the background diffuse neutrino flux is comparable to the projected 10-year IceCube-Gen2 sensitivity [396], our conclusions are taken to their natural extreme. Steady-state source discovery would disfavor all possible source classes; no discovery would disfavor none. Transient source discovery would disfavor dim, abundant classes; no discovery would disfavor bright, rare ones. On the other hand, if the diffuse flux is below the IceCube-Gen2 sensitivity, the possibility of observing point sources is evidently reduced dramatically. See Appendix C.6 for details.

9.6 SUMMARY AND OUTLOOK

Discovering UHE neutrinos, beyond 100 PeV, is key to finding the origin of UHECRs. We have shown that IceCube-Gen2 may discover them within 10 years of operation via searches for UHE multiplets. Their discovery—and also their absence—would place powerful constraints on the population of UHE sources. Our forecasts are state-of-the-art in the propagation and radio-detection of UHE neutrinos, and in the backgrounds that muddle source discovery.

For steady-state sources, if even one is discovered, most candidate classes would be disfavored as individually dominant; if none is, only bright, rare sources would be disfavored. For transient sources, if none is discovered, all candidate classes with total injected energy larger than 10^{53} erg would be disfavored as individually dominant. In any case, comparable contributions from multiple source classes might remain viable [473].

Our conclusions are broadly robust against different choices of the background level—currently unknown—the effective volume of the detector array—tentatively, contingent on further simulation work—and the detector energy resolution—since conservatively we do not use the event energy spectrum in our work—but are sensitive to the detector angular resolution. We recommend upcoming UHE telescopes [39, 69, 71, 72, 74, 84, 153, 159, 162, 316, 355, 356, 383, 384, 520,

521] to target a zenith-angle resolution of about 2°. Auspiciously, the requirements that grant IceCube-Gen2 sensitivity to source discovery via multiplets also grant it sensitivity to simultaneous measurement of the diffuse UHE neutrino flux and the neutrino-nucleon cross section [346, 348].

Finally, the identification of point sources belonging to specific classes will be greatly helped by comparison with specific source catalog and dedicated point source searches. Further, source identification could be eased by looking at the unbinned angular distribution of UHE neutrinos, rather than identifying multiplets in the binned angular distribution as we do here.

In the next 10–20 years, we will have an opportunity to complete our picture of the high-energy Universe. We provide advanced tools and forecasts to help realize it.

9.7 CRITICAL OUTLOOK

This section analyzes the key findings and limitations of this study. It also provides insights into the future perspectives and potential advancements in the field of neutrino astronomy.

9.7.1 *Overview and main findings*

The central accomplishment of this work lies in the establishment of constraints on candidate classes of UHE neutrino sources, steady-state and transient. These constraints are instrumental in unraveling the enigma of UHECRs.

We have considered source populations inspired by the characteristic properties of promising candidates, including low-luminosity AGN, starburst galaxies, galaxy clusters, radio-quiet AGN, accretion shocks in galaxy clusters, radio-loud AGN, BL Lacertae AGN, flat-spectrum radio quasars, supernovae, newborn pulsars, hypernovae, low-luminosity gamma-ray bursts, high-luminosity GRBs, and jetted tidal disruption events.

Our constraints on these sources are derived from by the requirement that the UHE neutrino flux from each source class saturates the background UHE neutrino diffuse flux. Our constraints are on the effective local number density (n_0) and UHE neutrino luminosity (L_ν or E_ν).

Our work shows the impact of the diffuse UHE neutrino flux on discoverting point sources of UHE neutrinos. We find that discovering point sources is possible even when the diffuse flux is large. The angular resolution of the neutrino detector plays a pivotal role in determining the sensitivity to point sources..

We offer recommendations for upcoming UHE telescopes. We suggest that they should aim for a zenith-angle resolution of approximately 2°, to enhance source identification and facilitate measurements related to the diffuse UHE neutrino flux and neutrino-nucleon cross section. In-air neutrino radio detectors, such as GRAND, plan to achieve a sub-degree angular resolution [72], which would further improve the discovery prospects.

9.7.2 *Limitations and future perspectives*

While the study provides valuable insights into UHE neutrino astroparticle physics, several limitations and areas for future research should be considered:

1. *Limited Physical Modeling:* The study treats candidate source classes on equal footing without detailed modeling of the physical conditions and neutrino production mechanisms specific to each class. Future research could delve into more detailed modeling to refine population parameters.

2. *Background Uncertainty:* The study acknowledges the uncertainty in the background UHE neutrino flux. Future work should aim to reduce this uncertainty and refine source constraints accordingly.

3. *Source Catalogs:* To enhance source identification, future research should consider comparing the results of this study with specific source catalogs and dedicated point source searches.

4. *Unbinned Angular Distribution:* The study identifies multiplets in the binned angular distribution of UHE neutrinos. Future research could explore the unbinned angular distribution as an alternative method for source identification.

5. *Advancements in Detector Technology:* As detector technology continues to advance, future telescopes may offer even higher angular resolution and sensitivity, opening up new possibilities for astroparticle physics research.

In summary, the study provides a valuable foundation for understanding UHE neutrino sources and their constraints. Future research should address the limitations and uncertainties mentioned above, leveraging advanced technology and modeling techniques to further advance our knowledge of the high-energy Universe.

10

DARK MATTER

Based on: Damiano F. G. Fiorillo, **Víctor B. Valera Baca**, Mauricio Bustamante, Walter Winter, *Searches for dark matter decay with ultra-high-energy neutrinos endure backgrounds*, arXiv:2307.02538

ABSTRACT Next-generation ultra-high-energy (UHE) neutrino telescopes, presently under planning, will have the potential to probe the decay of heavy dark matter (DM) into UHE neutrinos, with energies in excess of 10^7 GeV. Yet, this potential may be deteriorated by the presence of an unknown background of UHE neutrinos, cosmogenic or from astrophysical sources, not of DM origin and seemingly large enough to obscure the DM signature. We show that leveraging the angular and energy distributions of detected events safeguards future searches for DM decay against such backgrounds. We focus on the radio-detection of UHE neutrinos in the planned IceCube-Gen2 neutrino telescope, which we model in state-of-the-art detail. We report promising prospects for the discovery potential of DM decay into UHE neutrinos, the measurement of DM mass and lifetime, and limits on the DM lifetime, despite the presence of a large background, without prior knowledge of its size and shape.

10.1 INTRODUCTION

About 85% of the matter in the Universe is dark, not interacting electromagnetically nor strongly. Evidence for dark matter (DM) comes from velocity dispersion and rotation curves in galaxies and galaxy clusters [525–529], gravitational lensing measurements in galaxy clusters and collisions of galaxy clusters [530, 531], the cosmic microwave background (CMB) anisotropy, and the large-scale structure of the Universe [532–536]. Because this evidence relates to the gravitational effect that DM

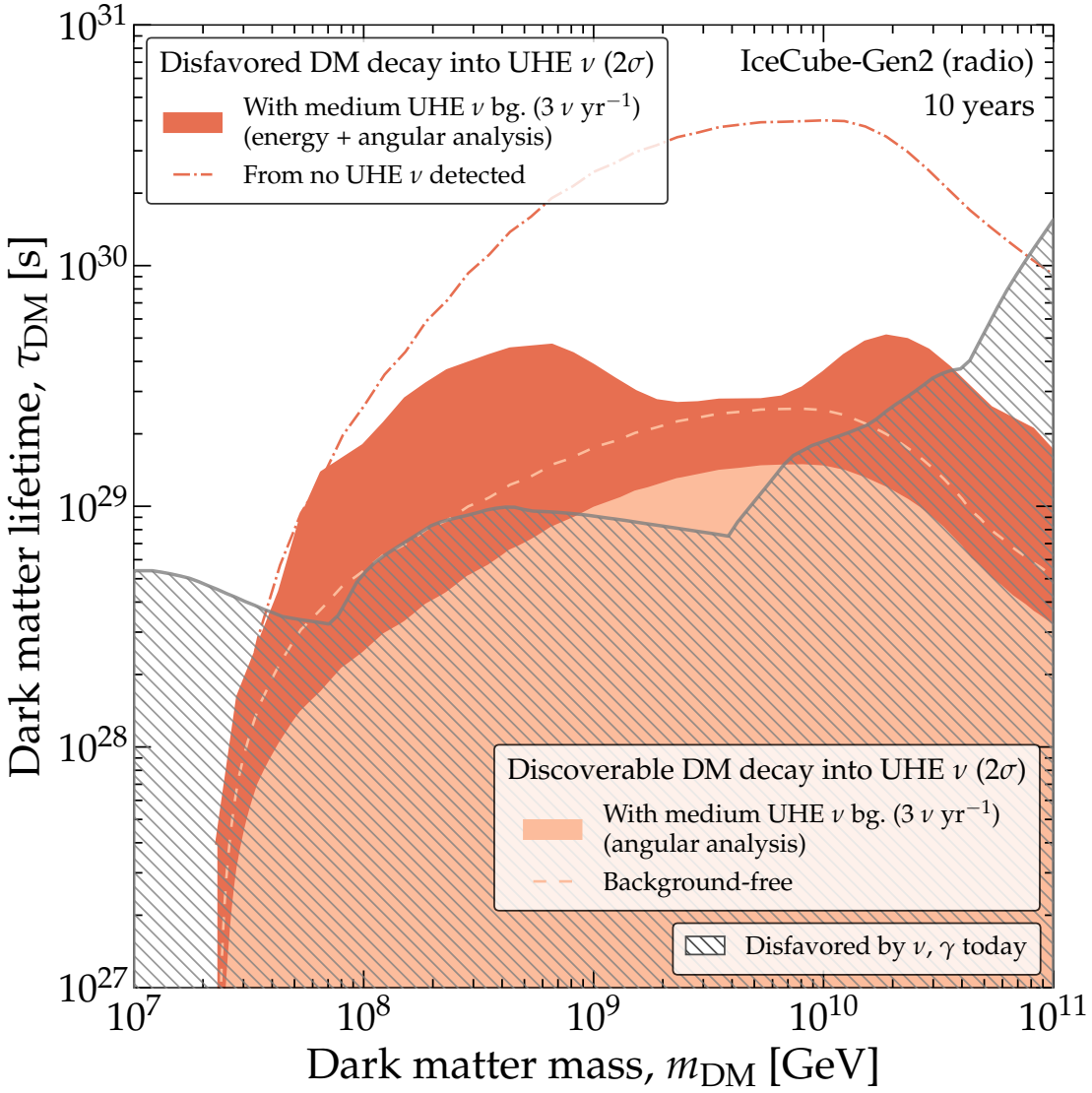

Figure 47: ***Forecasts of discovery and constraints of dark matter decay into UHE neutrinos in the radio array of IceCube-Gen2.*** *Dark matter (DM) decay can be discovered or constrained even in the presence of a medium-sized non-DM cosmogenic background flux of UHE neutrinos (Fig. 48).* Forecasts are based on state-of-the-art projected samples of detected events with energies over 10^7 GeV, use baseline choices of the detector angular and (logarithmic) energy resolution, $\sigma_\Omega = 3^\circ$ and $\sigma_\epsilon = 0.1$, and assume no knowledge of the non-DM neutrino background in the analysis of projected data. For discovery, forecasts use the angular distribution of events; for constraints, their joint angular and energy distribution. This figure assumes the Navarro-Frenk-White density profile for Galactic DM. Existing lower limits on the DM lifetime are from neutrino and gamma-ray searches in IceCube [522], KASCADE-Grande [446], the Telescope Array [447], and the Pierre Auger Observatory [523]; see Ref. [524]. See Sec. 10.4 for details on discovery (especially Figs. 53–56) and Sec. 10.5 for details on bounds (especially Figs. 57 and 58).

has on the visible Universe, it provides little guidance to understand other possible interactions between DM and Standard-Model particles that could reveal its nature.

The absence of such guidance has spurred a broad program to understand the nature of DM, from theory and experiment. From theory, diverse candidates have been proposed as DM constituents;

see, *e.g.*, Ref. [537] for a historical review. These include novel particles, such as weakly interacting massive particles [538, 539], axions [540], Majorons [541–543], and sterile neutrinos [544], and non-particle candidates, such as primordial black holes [545]. From experiment, searches for these candidates follow four complementary strategies: collider searches, which attempt to produce DM in high-energy particle collisions; direct DM searches, which look for Galactic DM scattering on dense detector targets; astrophysical searches, which look for the impact that DM would have on cosmic particles; and indirect DM searches, which look for products of DM self-annihilation or decay.

We focus on indirect searches for the decay of heavy DM particles, with masses in excess of 10 PeV, into neutrinos. Our choice is motivated by upcoming experimental capabilities (more on this later) that, for the first time, could allow us to probe DM decay using ultra-high-energy (UHE) neutrinos, with energies in excess of 10 PeV. (We do not consider DM self-annihilation because, for heavy DM, its cross section is strongly constrained by unitarity bounds [546–548].)

Already in the last decade, the breadth of DM indirect searches widened after the discovery by the IceCube neutrino telescope of high-energy neutrinos of cosmic origin, with energies between 10 TeV and 10 PeV [34, 35, 184–188]. In fact, initially the discovery led to speculation that heavy DM decaying to neutrinos could explain their flux in the 10–100 TeV range [549–559]. Nowadays, more conventional astrophysical explanations are favored [560–562], but IceCube observations still set competitive bounds on the DM lifetime and self-annihilation cross section for DM masses below 10 PeV [146, 524, 563]. These bounds are complementary to the ones obtained from gamma-ray observations in a similar mass range; see, *e.g.*, Refs. [524, 564]

In the next decade, a host of new neutrino telescopes, presently in different stages of planning, design, and prototyping, will target the long-sought discovery of UHE neutrinos, between 100 PeV and 10 EeV, that were first predicted in 1969 [65]. They include AugerPrime [162], BEACON [153], EUSO-SPB2 [383], GCOS [384], GRAND [72], POEMMA [74], PUEO [521], RNO-G [84], TAROGE [159], and the radio array of IceCube-Gen2, the envisioned upgrade of IceCube [39]. Ultra-high neutrinos will bring new insight into astrophysics [83, 189, 565] and fundamental physics [83, 164, 190, 191, 565, 566]. In particular, they will allow us to test the decay of heavier DM particles, with masses from 10 PeV to 100 EeV; see, *e.g.*, Refs. [524, 548, 567].

However, the capacity of UHE neutrino telescopes to probe DM decay critically depends on an unknown quantity: the diffuse flux of UHE neutrinos that do not originate from DM decay, and that acts as a background to DM searches. If this background is large, it could obscure more subtle signatures of neutrinos from DM decay. These background neutrinos—hereafter dubbed "non-DM neutrinos"—are expected from the interaction of ultra-high-energy cosmic-ray (UHECRs) with ambient matter or radiation inside the extragalactic astrophysical sources where they are accelerated—*i.e.*, *astrophysical* neutrinos—or with cosmic photon backgrounds during their propagation to Earth—*i.e.*, *cosmogenic* neutrinos [27, 28, 65]. We expand on them later (Sec 10.2.1).

The situation is worsened by the large variety, in size and shape, in the current theoretical predictions of UHE astrophysical and cosmogenic neutrino fluxes; see, *e.g.*, Fig. 2 in Ref. [390]. Without a firm estimate of the non-DM UHE neutrino background, it would seem that the mere discovery of UHE neutrinos may be insufficient to establish whether they originate from DM decay or not. Were the possibility of a background of non-DM UHE neutrinos ignored, the evidence for or against DM decay could be interpreted erroneously.

We show that these difficulties can be overcome by leveraging known differences between the distributions in energy and arrival directions of UHE neutrinos from DM decay and non-DM UHE neutrinos. Regarding energy, neutrinos from DM decay are produced predominantly at an energy of $E_\nu \sim m_{\rm DM}/2$, where $m_{\rm DM}$ is the mass of the DM particle, whereas the spectrum of non-DM neutrinos is expected to be relatively extended in energy. Regarding direction, the flux of neutrinos from DM decay should peak towards the Galactic Center (GC), where DM is concentrated, whereas the diffuse flux of non-DM neutrinos is expected to be isotropic. The above features are essential and generic to UHE neutrinos of DM and non-DM origin alike, and are broadly present in models of their fluxes. By relying on them, our methods apply broadly, regardless of the specific nature of the DM particle, of the relative size of the fluxes of neutrinos from DM decay and of non-DM neutrinos, and of the specific shape of the energy spectrum of non-DM neutrinos.

Our strategy is similar to studies of the decay of TeV–PeV DM that use IceCube data (see, *e.g.*, Ref. [563]), but has one important advantage. In the TeV–PeV range, it is possible that non-DM astrophysical processes produce an excess of neutrinos towards the GC that could obfuscate a signal of neutrinos from DM decay [38, 568–580]. In contrast, in the UHE range, we expect no

astrophysical process to produce neutrinos towards the GC, making the search for DM decay cleaner.

We gear our forecasts to the radio-detection of UHE neutrinos in IceCube-Gen2, since it is among the largest upcoming neutrino telescopes under consideration and is presently in an advanced stage of planning. We model neutrino detection via the same state-of-the-art simulations used in Refs. [346, 372, 390], which account for UHE neutrino propagation inside Earth, detector geometry, energy- and direction-dependent detector response, and energy and angular detector resolution.

Figure 47 summarizes our main findings; we defer details to later. They are two-fold: on the discovery of DM decay and on lower limits on the DM lifetime. For the first time, we report robust discovery prospects for UHE neutrinos from DM decay, *i.e.*, the values of DM mass and lifetime that would allow us not only to detect UHE neutrinos, but also to claim that they originate from DM decay, at least partially. In Fig. 47, the presence of about 30 neutrinos from DM decay in a 10-year event sample, would allow us to claim their DM origin. Separately, we find that while the background of non-DM UHE neutrinos weakens the lower limits on DM lifetime, an energy and angular analysis mitigates this weakening, keeping the limits competitive with present-day ones, at worst.

The overarching message of our results is that, despite our ignorance of the background of astrophysical and cosmogenic UHE neutrinos, the discovery of UHE neutrinos will constitute a sensitive probe of heavy DM decay. We present our results and methods to inform future forecasts and searches.

This paper is structured as follows. In Sec. 10.2 we discuss the main features of DM and non-DM neutrino production, and highlight the models that we choose as benchmark for this work. In Sec. 10.3 we describe how we compute UHE neutrino-induced event rates at IceCube-Gen2. In Sec. 10.4 we obtain the prospects of IceCube-Gen2 for the discovery of DM neutrinos. In Sec. 10.5 we forecast bounds on the DM lifetime if no evidence for DM decay is found. In Sec. 10.6, we conclude.

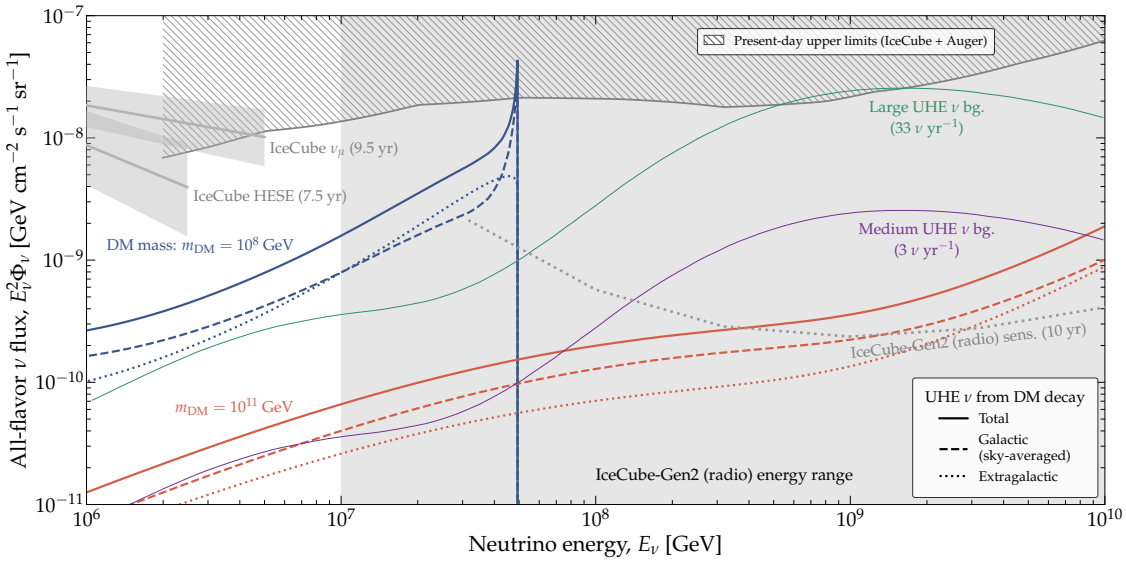

Figure 48: ***Diffuse flux of UHE neutrinos from DM decay and non-DM background flux.*** The flux from the decay of a DM particle, χ, into neutrinos (*i.e.*, $\chi \to \nu + \bar{\nu}$) is shown for illustrative choices of the DM mass, $m_{\rm DM} = 10^8$ GeV and 10^{11} GeV, and of the DM lifetime, $\tau = 10^{29}$ s, and computed following Sec. 10.2.2. Later, we vary the values of the DM mass and lifetime in our forecasts. The neutrino flux from DM decay is separated into its sky-averaged Galactic component and its isotropic extragalactic component. (We do not show in this figure the primary-neutrino contribution to the Galactic component, since it is a singular monochromatic line at $E_\nu = m_{\rm DM}/2$, but we include it in our calculations; see Sec. 10.2.2.) The two non-DM isotropic UHE neutrino fluxes are the benchmarks that we use in our work. The large benchmark flux is the cosmogenic neutrino flux predicted by Bergman & van Vliet [193] based on cosmic-ray data from the Telescope Array [278, 279]. The medium benchmark flux is 10% of that. The projected sensitivity of the radio array of IceCube-Gen2 is from Ref. [396]. Present-day upper limits on the flux of UHE neutrinos are from IceCube [66] and the Pierre Auger Observatory [67]. For comparison, we show the tail end of the present-day IceCube measurements of TeV–PeV neutrinos [37, 188]. See Sec. 10.2 for details.

10.2 FLUXES OF UHE NEUTRINOS

The diffuse flux of UHE astrophysical and cosmogenic neutrinos, itself a target of discovery [83, 164, 189, 390], could be a background to searches for the diffuse flux of UHE neutrinos from DM decay. Fortunately, these fluxes differ in their distributions in energy and direction. In energy, the non-DM background neutrino flux is spread out, while that of neutrinos from DM decay is more concentrated. In direction, the non-DM background neutrino flux is isotropic, while that of neutrinos from DM decay peaks towards the Galactic Center. We review these features below; later (Secs. 10.4 and 10.5), we use them to distinguish between the fluxes.

10.2.1 *UHE astrophysical and cosmogenic neutrinos*

UHE neutrinos are expected from the interaction of UHECR protons, with energies $E_p \gtrsim 100$ PeV, with ambient matter [130, 387, 448] or radiation [256, 257, 387], inside the extragalactic astrophysical sources where they are accelerated—*i.e.*, *astrophysical* neutrinos—or with cosmic photon backgrounds during their propagation in extragalactic space—*i.e.*, *cosmogenic* neutrinos. These interactions produce high-energy pions, and other intermediate particles, that promptly decay into high-energy neutrinos via $\pi^- \to \mu^- + \bar{\nu}_\mu$, followed by $\mu^- \to e^- + \bar{\nu}_e + \nu_\mu$, and their charge-conjugated processes, where each neutrino has energy $E_\nu \simeq E_p/20$.

We focus on the diffuse UHE neutrino flux, *i.e.*, the sum of the UHE neutrino emission—astrophysical or cosmogenic—from all sources, across all redshifts. The cosmogenic neutrino flux is isotropic, since extragalactic magnetic fields scramble the trajectories of neutrino-producing UHECRs; see Fig. 50. The angular distribution of the astrophysical neutrino flux reflects that of the neutrino sources in the sky. Because UHE neutrino sources are in all likelihood extragalactic, we assume that they are isotropically distributed, and so the diffuse neutrino flux from them is isotropic, too. The discovery of the diffuse flux of astrophysical and cosmogenic neutrinos is one of the main goals of the next generation of neutrino telescopes [83, 189, 346, 390]. (The associated discovery of point sources of UHE neutrinos is explored in Refs. [371, 372, 472].) Yet, in our work, they represent a background to the discovery of neutrinos from DM decay.

Cosmogenic neutrinos were first proposed in the late 1960s [65], as a natural consequence of the interaction of UHECRs on the CMB [27, 28]. They constitute a nearly guaranteed contribution in the UHE neutrino range, since their production only relies on the existence of UHECRs and of the CMB (and also of the extragalactic background light). The flux of cosmogenic neutrinos depends on the properties of UHECRs—their spectrum, maximum energies, and mass composition—and of their sources—their distribution in redshift. Because these properties are known uncertainly [125], the flux predictions vary widely, in size and shape; see, *e.g.*, Refs. [37, 172–180, 188, 193, 255, 344, 345].

Astrophysical UHE neutrinos are produced inside astrophysical sources. In this case, the target photons need not be the CMB, but low-energy photons present in the environments in which

UHECRs are injected. Flux predictions are made more complex because they depend also on the physical conditions inside the sources, including the shape of the photon spectra, the matter density, and the geometry of the neutrino production region. Numerous models have been proposed for various candidate source classes, including active galactic nuclei (AGN) [103, 176, 179, 477, 480, 481, 491, 494–498], gamma-ray bursts (GRBs) [104, 507–511, 581, 582], newborn pulsars [175, 505], and tidal disruption events (TDEs) [115, 512–518, 583]. In some models, the diffuse astrophysical neutrino flux can be comparable or larger than the cosmogenic neutrino flux; *e.g.*, Ref. [179].

Thus, there is a large number of competing theoretical predictions of the cosmogenic and astrophysical UHE neutrino flux; see Fig. 2 in Ref. [390] and Fig. 6 in Ref. [346] for an overview. The range of predicted UHE neutrino fluxes spans several orders of magnitude. The highest flux predictions [193] would yield about 30 events per year in the radio array of IceCube-Gen2, making them easily discoverable; the lowest [174, 179], less than one event in 10 years, making them undiscoverable (see Fig. 1 and Table I in Ref. [390] for details).

Most flux predictions share some common features; *e.g.*, they can be roughly described as a power-law flux—from neutrino production via proton-matter interactions—a bump-like flux—from neutrino production via proton-photon interactions—or a combination of both. The resemblance between different flux predictions is largely superficial, since they differ in a number of important assumptions, *i.e.*, the identity of the neutrino sources, the physical conditions in the region of neutrino production, the neutrino production mechanism, and the UHECR observations on which the neutrino predictions are based. Regardless, in our forecasts below, we pivot on these superficial similarities and choose a benchmark background flux of UHE neutrinos that is representative of the range of theoretical predictions.

Figure 48 shows the two illustrative flux predictions that we select as benchmark "non-DM" UHE neutrino background for our analysis. They represent a large background and an intermediate one; later, we complement them with a null-background scenario. We base both on the cosmogenic neutrino flux predicted by Bergman & van Vliet [193] by fitting the simulated UHECR energy spectrum and mass composition at Earth to recent data from the Telescope Array (TA) [278, 279]. (This is flux model 4 in Refs. [346, 390].) Because TA data favors a light UHECR mass composition

and high maximum rigidity, the resulting cosmogenic neutrino flux is large: Fig. 48 shows that it saturates the present-day upper limits from IceCube [66] and the Pierre Auger Observatory [67].

LARGE NON-DM BACKGROUND This is the full cosmogenic neutrino flux predicted by Bergman & van Vliet [193], which yields about 33 events per year in the radio array of IceCube-Gen2; see Figs. 3 and 4 and Table I in Ref. [390], and Fig. 51 below. Because this is as large a flux of UHE neutrinos as is allowed by present-day upper limits (Fig. 48), it is about the largest background of non-DM UHE neutrinos that we could face in a search for DM decay.

INTERMEDIATE NON-DM BACKGROUND This is the Bergman & van Vliet cosmogenic flux scaled down to 10% of its size, which yields about 3 events per year in the radio array of IceCube-Gen2.

NULL BACKGROUND The ideal scenario for the discovery of UHE neutrinos from DM is the absence of non-DM UHE neutrinos. This has been the scenario adopted in previous forecasts of DM decay into UHE neutrinos [567, 584]. We maintain it here as a baseline against which we compare our forecasts including a non-DM background.

Figure 48 shows the all-flavor background flux, but when computing event rates (Sec. 10.3) we sum the individual contributions of the fluxes of ν_e, $\bar{\nu}_e$, ν_μ, $\bar{\nu}_\mu$, ν_τ, and $\bar{\nu}_\tau$ for this model, as shown in Fig. 6 in Ref. [346].

For the purpose of discovering neutrinos from DM decay, what matters is not whether the non-DM UHE neutrino background is cosmogenic or astrophysical, but rather that its angular and energy distributions are different from those of the flux of neutrinos from DM decay (Sec. 10.1). We point out these differences explicitly in Sec. 10.2.3. Admittedly, in choosing a benchmark non-DM UHE neutrino background, we make a specific choice of the shape of its energy spectrum. This choice is necessary to be able to generate simulated samples of detected events (Sec. 10.3). However, when analyzing these samples (Secs. 10.5 and 10.4), we do not assume knowledge of the size or shape of the non-DM background, but instead let them vary, just as an analysis of real detected data would.

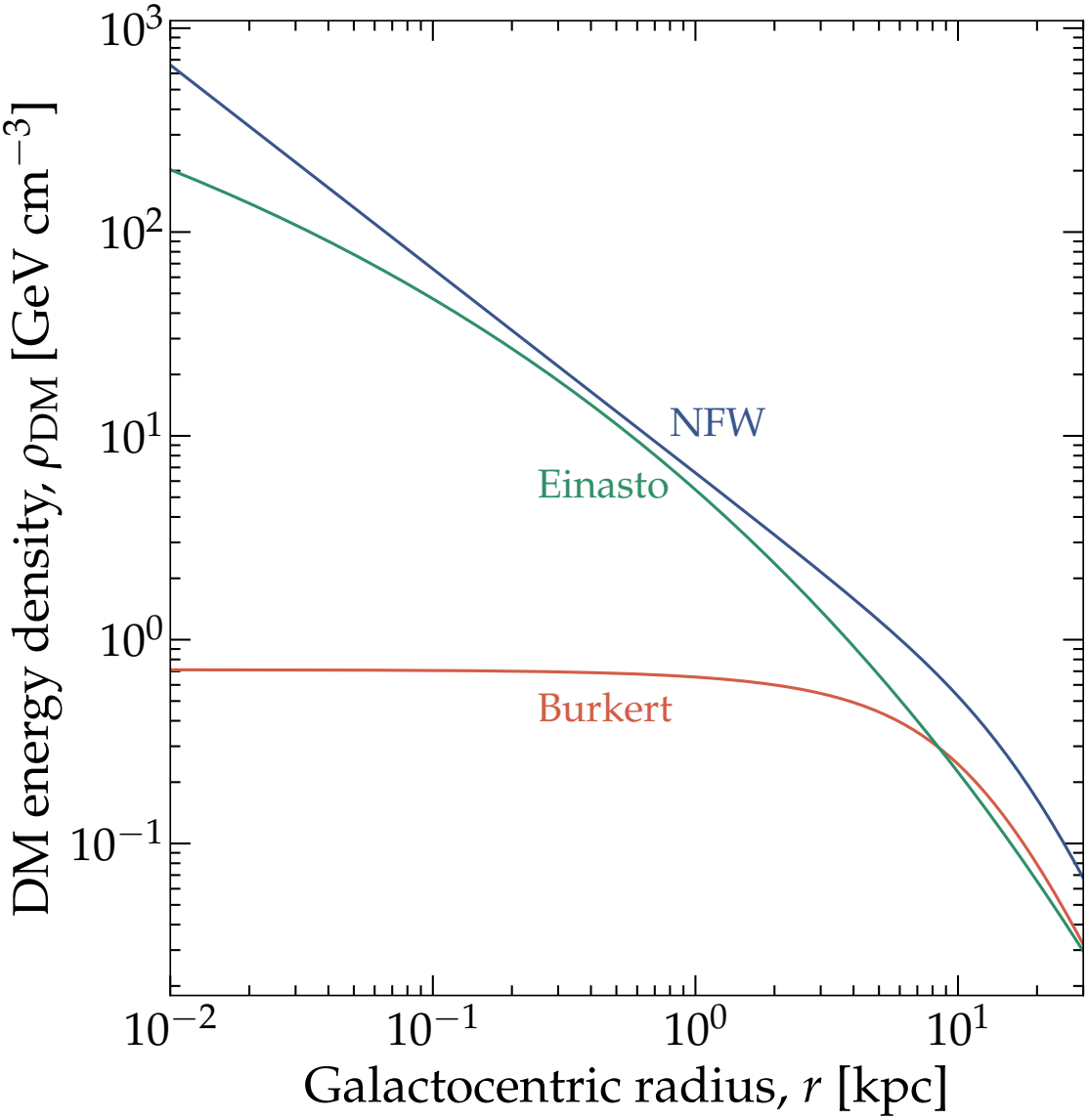

Figure 49: ***Profiles of Galactic dark matter density.*** For the Navarro-Frenk-White (NFW) profile [585], we use Eq. (10.3). For the Einasto [586] and Burkert [587] profiles, we use the parametrizations and parameter choices from Ref. [588]; see Eq. (10.4). Our main results for DM discovery (Figs. 53, 55, 56, and D1) and bounds (Figs. 57, 58, and D2) are generated assuming the NFW profile. Results generated assuming the Einasto profile (not shown) are similar. Figures 54 and 59 contrast results obtained assuming the NFW and Burkert profiles.

10.2.2 *UHE neutrinos from dark matter decay*

The decay of a heavy DM particle, χ, with mass $m_{\rm DM} \gtrsim 10^7$ GeV, into Standard Model particles, leads to the production of high-energy neutrinos. The yield of neutrinos depends on the channels by which the DM particle decays. If the DM particle decays primarily into neutrinos, *i.e.*, $\chi \to \bar{\nu}\nu$, the resulting neutrino flux has a primary contribution that is monoenergetic at $E_\nu = m_{\rm DM}/2$. We

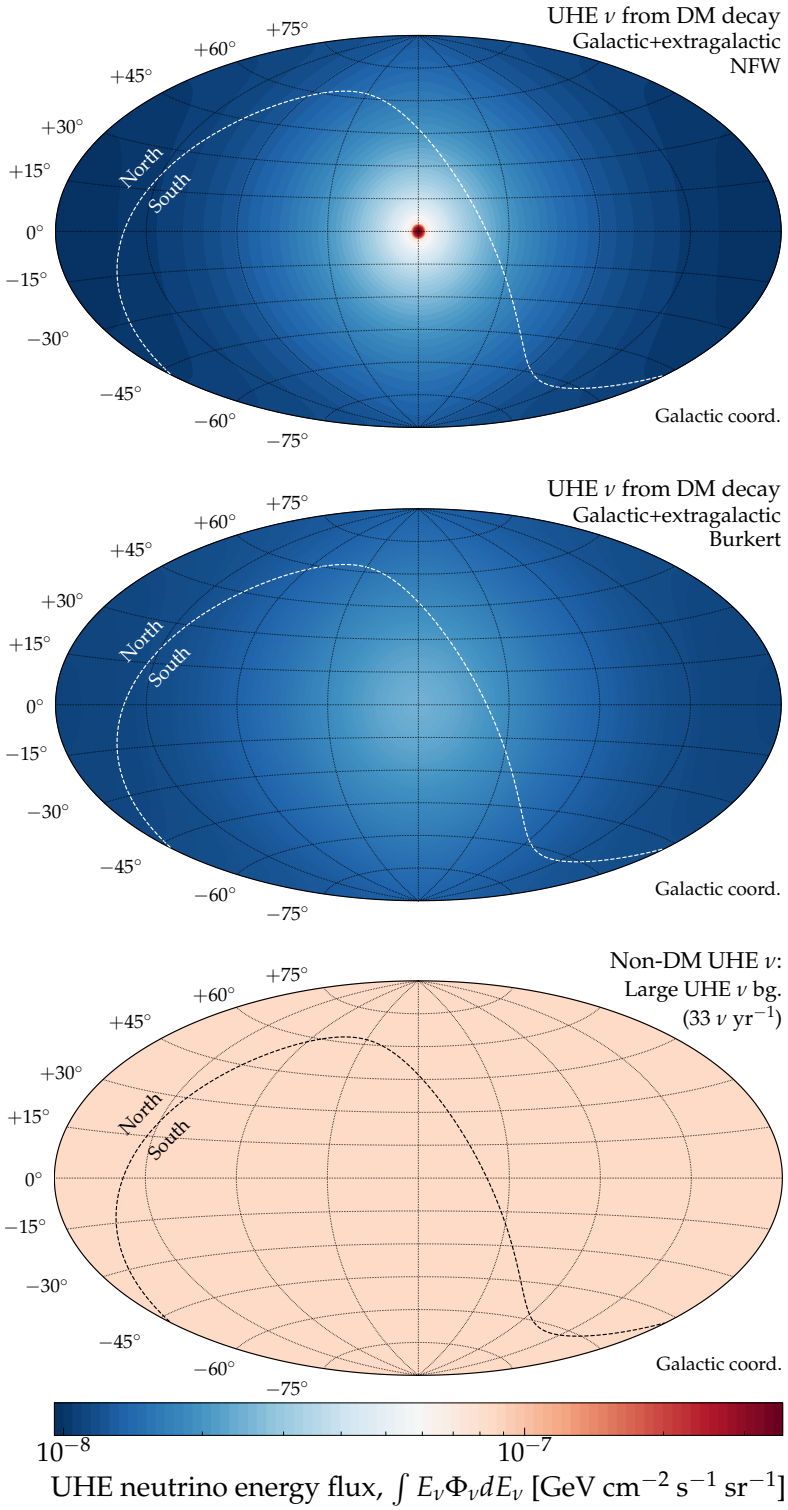

Figure 50: ***Angular distribution of the diffuse flux of UHE neutrinos.*** *Top:* Neutrinos from DM decay, for an NFW profile. We show the distribution computed using illustrative values of DM mass and lifetime, $m_{\rm DM} = 10^8$ GeV and $\tau_{\rm DM} = 10^{29}$ s, but for other values the angular distribution is very similar. *Center:* Same for a Burkert profile. *Bottom:* Neutrinos from the non-DM isotropic background of UHE neutrinos. The flux is isotropic, so the sky map is shaded uniformly. We show the distribution from our large benchmark background, *i.e.*, the cosmogenic neutrino flux by Bergman & van Vliet [193], but for other choices of the isotropic background flux the angular distribution is very similar.

neglect the spread of the energy spectrum due to the thermal velocity of DM, since it is small [589, 590]. A secondary contribution comes from electroweak corrections, generated from the emission, by the decay products, of off-shell W and Z bosons that promptly decay into neutrinos; this contribution is present even if DM does not primarily decay to neutrinos. In our analysis, we consider the neutrino flux made up of both primary and secondary contributions.

The electroweak corrections unavoidably give rise to gamma rays, electrons, positrons, protons, and anti-protons that are also amenable to indirect detection. Upper limits on their flux indirectly constrain the associated neutrino flux. Notably, for most decay channels (*e.g.*, for hadronic decay channels such as $\chi \to \bar{b}b$), the present-day upper limits on the gamma-ray flux are so strong that the projected limits on the associated UHE neutrino flux are comparable or weaker; see, *e.g.*, Ref. [584] (see also Ref. [591] for a comparison of the bounds from gamma-ray and cosmic-ray measurements). However, for leptonic (*e.g.*, $\chi \to \bar{\tau}\tau$) and neutrinophilic (*i.e.*, $\chi \to \bar{\nu}\nu$) decay channels, in the DM mass range $m_{\rm DM} = 10^7$–10^{10} GeV, the bounds from UHE neutrinos may be comparable or stronger than the present-day bounds from gamma rays. For this reason, we focus exclusively on the neutrinophilic decay channel, $\chi \to \bar{\nu}\nu$. We assume equal branching ratios for the decay into each of the three flavors, $\chi \to \bar{\nu}_e\nu_e$, $\chi \to \bar{\nu}_\mu\nu_\mu$, and $\chi \to \bar{\nu}_\tau\nu_\tau$. We treat the flux of ν_e, $\bar{\nu}_e$, ν_μ, $\bar{\nu}_\mu$, ν_τ, and $\bar{\nu}_\tau$ separately; later, we propagate each through the Earth (Sec. 10.3.1) and compute its contribution to the detected event rate (Sec. 10.3.2).

We compute the neutrino spectra numerically, using the public code `HDMSpectra` [592], which evolves the particle showers initiated by DM decay, including in detail electroweak corrections, and yields the final-state products of shower evolution. The neutrino spectra from DM decay are notoriously hard to compute precisely, since the emission of soft collinear $W^\pm$ bosons leads to logarithmically enhanced terms $\propto \log^2(m_{\rm DM}/m_W)$, where m_W is the mass of the W boson, that need to be resummed [593]; `HDMSpectra` accounts for this. Thus, from `HDMSpectra` we obtain dN_{ν_α}/dE_ν and $dN_{\bar{\nu}_\alpha}/dE_\nu$ ($\alpha = e, \mu, \tau$), the number of ν_α and $\bar{\nu}_\alpha$ emitted in a single DM decay per unit energy. These spectra include also the primary monoenergetic contributions at $E_\nu = m_{\rm DM}/2$.

The diffuse flux of neutrinos that reach the Earth is due to DM decays that occur inside the Galaxy (Gal) and in extragalactic space (EG), *i.e.*,

$$\frac{d\Phi_{\nu_\alpha}}{dE_\nu d\Omega_\nu} = \frac{d\Phi^{\rm Gal}_{\nu_\alpha}}{dE_\nu d\Omega_\nu} + \frac{d\Phi^{\rm EG}_{\nu_\alpha}}{dE_\nu d\Omega_\nu} \,, \tag{10.1}$$

where Ω_ν is the solid angle. To compute the Galactic contribution, we integrate the neutrino spectrum from a single DM decay over the spatial distribution of DM in the Milky Way. This makes the Galactic neutrino flux anisotropic, since it traces the density of Galactic DM. To compute the extragalactic contribution, we integrate the neutrino spectrum from a single DM decay over the cosmological distribution of DM. This makes the extragalactic neutrino flux isotropic.

The Galactic contribution of ν_α is

$$\frac{d\Phi^{\rm Gal}_{\nu_\alpha}}{dE_\nu d\Omega_\nu} = \frac{dN_{\nu_\alpha}}{dE_\nu}\int_0^\infty \frac{\rho_{\rm DM}(s,b,l)}{4\pi\tau_{\rm DM} m_{\rm DM}} ds \,, \tag{10.2}$$

where s is the distance measured from the Earth, b and l are Galactic latitude and longitude and parametrize the neutrino incoming direction, $\tau_{\rm DM}$ is the DM lifetime, and $\rho_{\rm DM}$ is the density profile of DM in the Galaxy.

Figure 49 shows competing models of the Galactic DM density profiles. The "cuspy" Navarro-Frenk-White (NFW) [585] profile—obtained from a numerical fit to N-body simulations of structure formation—and Einasto [586] profile—originally proposed to describe stellar systems and later extended to fit the DM halo—peak towards the GC. The "puffy" Burkert profile [587]—obtained by a fit to the DM distribution in dwarf galaxies—instead plateaus to a core towards the GC. We pick the NFW and Burkert profiles as representative of the two extremes of the "cusp *vs.* core" uncertainty in Galactic DM profiles. To produce our main results, in Figs. 53, 55, 56, D1, 57, 58, and D2, we adopt the NFW profile; in Figs. 57, 58, and D2, we contrast them against results obtained assuming the Burkert profile. For the NFW profile, we use [588]

$$\rho^{\rm NFW}_{\rm DM}(s,b,l) = \frac{\rho_0}{\left(\frac{r(s,b,l)}{r_c}\right)\left(1+\frac{r(s,b,l)^2}{r_c^2}\right)} \,, \tag{10.3}$$

where $\rho_0 = 0.33$ GeV cm^{-3}, $r_c = 20$ kpc, and $r(s,b,l) = \sqrt{s^2 + R_s^2 - 2sR_s\cos b\cos l}$ is the Galacto-centric radius, with $R_s = 8.5$ kpc. For the Burkert profile, we use

$$\rho^{\rm Burkert}_{\rm DM}(s,b,l) = \frac{\rho_s}{\left(1+\frac{r(s,b,l)}{r_s}\right)\left(1+\frac{r(s,b,l)^2}{r_s^2}\right)} \,, \tag{10.4}$$

with $\rho_s = 0.712$ GeV cm^{-3} and $r_s = 12.67$ kpc [588].

The extragalactic contribution of ν_α is

$$\frac{d\Phi^{\rm EG}_{\nu_\alpha}}{dE_\nu d\Omega_\nu} = \frac{\Omega_{\rm DM}\rho_c}{4\pi\tau_{\rm DM} m_{\rm DM}}\int_0^\infty \frac{dz}{H(z)}\left.\frac{dN_{\nu_\alpha}}{dE_\nu}\right|_{E_\nu(1+z)} \,, \tag{10.5}$$

where z is the redshift, $\rho_c = 4.79 \times 10^{-6}$ GeV cm^{-3} is the critical density of the Universe, $\Omega_{\rm DM} = 0.265$ is the fraction of energy density of the Universe in the form of DM, $H(z) = H_0\sqrt{\Omega_\Lambda + \Omega_m(1+z)^3}$ is the Hubble parameter, $H_0 = 1.08 \times 10^{-28}$ cm^{-1} h is the Hubble constant, with $h = 0.674$, $\Omega_\Lambda = 0.685$ is the vacuum energy density, and $\Omega_m = 0.315$ is the matter energy density. The right-hand side of Eq. (10.5) is evaluated at an energy $E_\nu(1+z)$ to compensate for the cosmological expansion.

Figure 48 shows the resulting diffuse energy spectrum of UHE neutrinos from DM decay, integrated over all sky directions, for two benchmark values of the DM mass, and separated into the Galactic and extragalactic components only for illustration. The main features of the energy spectrum are a spike of neutrinos close to the energy $E_\nu = m_{\rm DM}/2$, and a power-law tail at lower energies, from electroweak corrections and, in the case of the extragalactic component, from redshifting. The dominant component of the flux is the Galactic one, due to the nearby DM overdensity in the GC. However, at energies close to the spike, a pile-up of neutrinos from the direct decay $\chi \to \bar{\nu}\nu$, redshifted to lower energies, causes the extragalactic contribution to dominate instead in a narrow energy range. Because we assume DM decay into neutrinos of all flavors with equal branching ratios (see above), the all-flavor flux in Fig. 48 is split evenly among the three flavors and among neutrinos and anti-neutrinos.

10.2.3 *Non-DM neutrinos vs. neutrinos from DM decay*

The essential differences between the background flux of UHE non-DM neutrinos and the flux of UHE neutrinos from DM decay are in their energy spectrum and in their angular distribution in the sky.

ENERGY SPECTRUM Figure 48 shows that the energy spectrum of our benchmark non-DM background flux—which is typical of many flux predictions—is more spread out around its maximum compared to the energy spectrum of neutrinos from DM decay, which peaks sharply at $E_\nu = m_{\rm DM}/2$. Yet, because of the spread of the latter towards lower energies due to redshifting (compounded, later, by the limited energy resolution of the detector), the differences in spectral shape are not as marked. While the lack of a bump-like feature in the

observed spectrum of UHE neutrinos would disfavor DM decay, its observation could be attributed either to DM decay or to a non-DM background flux. Accordingly, the energy spectrum is not the driving factor to discover DM decay (Sec. 10.4), but supplements angular information to set constraints (Sec. 10.5).

ANGULAR DISTRIBUTION Figure 50 shows the angular distribution of the total diffuse flux of UHE neutrinos, integrated over energy. This reveals the critical difference between non-DM and DM neutrinos: the flux of non-DM neutrinos is isotropic, while the flux of DM neutrinos peaks towards the GC, where, under the NFW profile, it is about a factor 20 larger than in the rest of the sky. This contrast is the main driving factor to discover DM decay and place constraints on it. For the puffier Burkert profile, the contrast is milder, which weakens both prospects, as we show later. In either case, because the GC is in the Southern Hemisphere, neutrinos from DM decay coming from this direction are not attenuated by their passage through Earth before reaching IceCube-Gen2 (Sec. 10.3.1), making it particularly sensitive to this signal.

Below (Sec. 10.3), we show that the above differences between the fluxes are mirrored, albeit imperfectly, by corresponding differences in the energy and angular distributions of detected events.

10.3 DETECTION OF UHE NEUTRINOS

To make realistic forecasts of probes of DM decay into UHE neutrinos, we compute in detail their propagation inside the Earth and their radio-detection in our detector of choice, the radio array of IceCube-Gen2.

10.3.1 *Neutrino propagation inside the Earth*

Upon reaching Earth, UHE neutrinos propagate from its surface, through its interior, to the detector, IceCube-Gen2, situated at the South Pole. While propagating, neutrinos interact with matter underground. Because the neutrino-nucleon cross section, $\sigma_{\nu N}$, grows with neutrino energy

(at ultra-high energies, roughly as $\sigma_{\nu N} \propto E_\nu^{0.363}$ [134]), these interactions appreciably attenuate the flux of neutrinos that reaches the detector. Roughly, neutrino interactions attenuate the flux via an exponential dampening factor $e^{-\sigma_{\nu N} L}$, where L is the distance traveled underground. Thus, the attenuation grows with neutrino energy and with distance traveled.

At ultra-high energies, neutrinos interact with nucleons predominantly via deep inelastic scattering (DIS) [60–63, 217, 218, 220]. In it, the incoming neutrino scatters off of a parton—a quark or a gluon—of a nucleon are rest, N—a proton or a neutron ($N = p, n$). The interaction is neutral-current (NC) if mediated by a Z boson, *i.e.*, $\nu_\alpha + N \to \nu_\alpha + X$ ($\alpha = e, \mu, \tau$), where X represents final-state hadrons, or charged-current (CC) if mediated by a W boson, *i.e.*, $\nu_\alpha + N \to \alpha + X$. The NC neutrino-nucleon cross section, $\sigma^{\rm NC}_{\nu_\alpha N}$, is about 1/3 of the CC cross section, $\sigma^{\rm CC}_{\nu_\alpha N}$. At these energies, the cross sections on proton and on neutron are very similar, and the cross sections for different neutrino flavors are nearly equal. When propagating neutrinos inside the Earth, and also when computing detected event rates (Sec. 10.3.3), we treat separately the NC and CC interactions of neutrinos of different flavor, each with its own cross section.

In a DIS interaction, the final-state hadrons receive a fraction y—the inelasticity—of the energy of the interacting neutrino. The final-state leptons receive the remaining fraction, $(1 - y)$. The inelasticity follows a probability distribution given by the differential cross sections, either $d\sigma^{\rm NC}_{\nu_\alpha N}/dy$ or $d\sigma^{\rm CC}_{\nu_\alpha N}/dy$. The distributions peak at $y = 0$, but they are broad, and depend on the neutrino energy; see, *e.g.*, Fig. 4 in Ref. [346].

Thus, as neutrinos propagate inside the Earth, NC interactions shift the neutrino flux to lower energies, while CC interactions deplete the flux. (For ν_τ, the consecutive CC neutrino interactions and decays of the ensuing tauons—known as "ν_τ regeneration"—appreciably counteract the flux dampening; see, *e.g.*, Fig. 8 in Ref. [346].) At ultra-high energies, the flux of upgoing neutrinos, with $\theta_z > 90^\circ$, where θ_z is the zenith angle measured from the South Pole, is nearly fully attenuated by the time it reaches the detector. On the contrary, the flux of downgoing ($\theta_z < 90^\circ$) and horizontal ($\theta_z \approx 90^\circ$) neutrinos is attenuated appreciably, but is not completely depleted. For illustration, see, *e.g.*, Fig. A2 in Ref. [61], Ref. [209], and Figs. 10 & 11 in Ref. [346]. This makes the detection of UHE neutrinos more likely from these directions, provided there is sufficient detector response, which is the case for our modeling of IceCube-Gen2; we elaborate on this in Secs. 10.3.2 and 10.3.3.

We compute the propagation of UHE neutrinos inside the Earth as in Refs. [346, 372, 390], using the sophisticated propagation code NUPROPEARTH [209, 210]. It uses the recent BGR18 neutrino-nucleon DIS cross sections [537], the same ones that we use in Sec. 10.3.3 to compute the rate of detected events. NUPROPEARTH also accounts for ν_τ regeneration, for energy losses of intermediate leptons during propagation, and for subleading neutrino interactions that, taken together, increase the flux attenuation by approximately an extra 10%. For the density profile of matter inside the Earth, we adopt the Preliminary Reference Earth Model [295], with an added layer of surface ice 3 km thick to represent Antarctica, and account also for the radial change in the chemical composition of underground matter [209]. Finally, we model the volume of the neutrino detector—the radio array of IceCube-Gen2—as a cylinder of radius 12.6 km and height 1.50 km, buried vertically 100 m underground at the South Pole; see Fig. 7 in Ref. [346].

In summary, given a flux of neutrinos at the surface of the Earth, from DM decay or from the non-DM background neutrino flux, we propagate it across many different directions to the detector. We propagate separately the fluxes of ν_e, $\bar{\nu}_e$, ν_μ, $\bar{\nu}_\mu$, ν_τ, and $\bar{\nu}_\tau$;. Below, we use their fluxes at the detector, $\Phi^{\rm det}_{\nu_\alpha}$ and $\Phi^{\rm det}_{\bar{\nu}_\alpha}$, to compute neutrino-induced event rates.

10.3.2 *UHE neutrino radio-detection at IceCube-Gen2*

Reference [166] first proposed using the radio emission from UHE particles as a means to detect them. Upon reaching the detector volume, an UHE neutrino may scatter off a nucleon in ice and produce a shower of high-energy particles. As the shower travels, it accumulates an excess of electrons in its front that, after reaching shower maximum, is emitted as an impulsive coherent radio pulse, known as Askaryan radiation [165]. For details, see Ref. [304, 358]. Because radio travels in ice subject only to mild attenuation, it may be detected using a sparse underground array of radio antennas, which makes it feasible to instrument a large volume that makes up for the potentially tiny fluxes of incoming UHE neutrinos.

This is the strategy adopted by the planned radio array of IceCube-Gen2 [39]. Of the proposed UHE neutrino telescopes [83, 164, 594], the radio array of IceCube-Gen2 is among the largest and

in an advanced stage of planning [39]. Thus, we gear our forecasts to it. However, our methods can be readily adapted to other upcoming UHE neutrino telescopes [83, 164, 594].

To compute realistic projected event rates at the radio array of IceCube-Gen2, we follow the detailed procedure introduced in Ref. [346], which uses an estimated detector response based on state-of-the-art simulations. This has been used already to forecast the measurement of the UHE neutrino-nucleon cross section [346], the discovery of UHE neutrino point sources [372], and the discovery of the diffuse flux of UHE neutrinos [390]. Below, we only sketch the procedure and introduce necessary modifications to it; we defer to Ref. [346] for details.

Upon reaching the detector volume, after propagating through the Earth (Sec. 10.3.1), an UHE ν_α of energy E_ν interacts with a nucleon at rest, N, typically via DIS (see above). The ensuing particle shower has an energy $E_{\rm sh}$, a fraction of the parent neutrino energy. For showers initiated by the NC DIS of ν_α or $\bar{\nu}_\alpha$ of any flavor, only the final-state hadrons radiate [213], so $E_{\rm sh} = yE_\nu$. For showers initiated by the CC DIS of a ν_e or $\bar{\nu}_e$, both the final-state electron and hadrons radiate, so $E_{\rm sh} = E_\nu$. For showers initiated by the CC DIS of ν_μ, $\bar{\nu}_\mu$, ν_τ, or $\bar{\nu}_\tau$, only the final-state hadrons radiate, so $E_{\rm sh} = yE_\nu$. As during propagation, at detection the value of the inelasticity follows $d\sigma^{\rm NC}_{\nu_\alpha}/dy$ and $d\sigma^{\rm CC}_{\nu_\alpha}/dy$, for which we adopt the BGR18 [537] calculation; see Fig. 4 in Ref. [346].

The detector response is represented by its effective volume, which we treat separately for NC and CC showers, $V^{\rm NC}_{{\rm eff},\nu_\alpha}$ and $V^{\rm CC}_{{\rm eff},\nu_\alpha}$. The effective volume depends on the shower energy and on the direction of the incoming neutrino. It is generated by simulating the interaction of neutrinos in the detector volume, followed by the generation of Askaryan radiation, its propagation in ice, including changes in the index of refraction of ice with depth, and its detection in the two types of radio antennas envisioned in the array. For the simulations we use NuRadioReco [211] and NuRadioMC [212], the same tools used by the IceCube-Gen2 Collaboration. We adopt the same array design consisting of a combination of shallow and deep radio stations as in Ref. [346]. The effective volume is least sensitive around 10^7 GeV, grows with shower energy, and is relatively less sensitive for downgoing neutrinos ($\cos\theta_z \approx 1$); see Fig. 13 in Ref. [346]. (Unlike common practice, the detector volume does not contain the effect of the attenuation of the neutrino flux underground. This is contained separately, in $\Phi^{\rm det}_{\nu_\alpha}$.)

The differential event rate is obtained by convolving the neutrino flux that reaches the detector (Sec. 10.3.1), $\Phi^{\rm det}_{\nu_\alpha}$, the effective volume, and the neutrino-nucleon cross section. For ν_α, after an exposure time T, this is

$$\frac{d^2N_{\nu_\alpha}}{dE_{\rm sh}d\cos\theta_z d\phi} = Tn_t \int_0^1 dy \Bigg(\frac{E^{\rm NC}_{\nu_\alpha}(E_{\rm sh},y)}{E_{\rm sh}} V^{\rm NC}_{{\rm eff},\nu_\alpha}(E_{\rm sh},\cos\theta_z) \times \frac{d\sigma^{\rm NC}_{\nu_\alpha {\rm w}}(E_\nu,y)}{dy} \Phi^{\rm det}_{\nu_\alpha}(E_\nu,\cos\theta_z)|_{E_\nu = E^{\rm NC}_{\nu_\alpha}(E_{\rm sh},y)} + {\rm NC}\to{\rm CC} \Bigg) \,, \quad (10.6)$$

where $d\sigma^{\rm NC}_{\nu_\alpha {\rm w}}/dy$ is the cross section for interaction with water, made up of 10 protons and 8 neutrons, and n_t is the number density of water molecules in ice. The event rate due to $\bar\nu_\alpha$ is the same as Eq. (10.6), but changing $\Phi^{\rm det}_{\nu_\alpha} \to \Phi^{\rm det}_{\bar\nu_\alpha}$, $d\sigma^{\rm NC}_{\nu_\alpha}/dy \to d\sigma^{\rm NC}_{\bar\nu_\alpha}/dy$, and $d\sigma^{\rm NC}_{\nu_\alpha}/dy \to d\sigma^{\rm CC}_{\bar\nu_\alpha}/dy$. At these energies the cross sections for ν_α and $\bar\nu_\alpha$ are nearly indistinguishable; see Ref. [537] and Fig. 3 in Ref. [346]. Equation (10.6) generalizes the original procedure in Ref. [346] by allowing the flux and the event rate to vary not only with zenith angle, θ_z, but also with azimuth, ϕ. This allows our analysis to be sensitive to an excess of UHE neutrinos from the decay of DM towards the GC.

As in Ref. [346], we smear the event rate using the detector energy and angular resolution, and use for our forecasts the event rate in terms of the reconstructed shower energy, $E^{\rm rec}_{\rm sh}$, and reconstructed direction, $\Omega^{\rm rec}$, *i.e.*,

$$\frac{d^2N_{\nu_\alpha}}{dE^{\rm rec}_{\rm sh}d\Omega^{\rm rec}} = \int dE_{\rm sh} \int d\Omega \frac{d^2N_{\nu_\alpha}(E_{\rm sh},\theta_z,\phi)}{dE_{\rm sh}d\Omega} \times R_{E_{\rm sh}}(E^{\rm rec}_{\rm sh},E_{\rm sh}) R_\Omega(\mathbf{n}^{\rm rec},\mathbf{n}) \,, \quad (10.7)$$

where $d\Omega = \sin\theta_z d\theta_z d\phi$ and $d\Omega^{\rm rec} = \sin\theta^{\rm rec}_z d\theta^{\rm rec}_z d\phi^{\rm rec}$ are the real and reconstructed differential solid angles, and $\mathbf{n}$ and $\mathbf{n}^{\rm rec}$ are the real and reconstructed shower directions. We model the energy resolution via a Gaussian function in $\epsilon \equiv \log_{10}(E^{\rm rec}_{\rm sh}/E_{\rm sh})$, *i.e.*,

$$R_{E_{\rm sh}}(E^{\rm rec}_{\rm sh},E_{\rm sh}) = \sqrt{\frac{2}{\pi}} \frac{\exp\left[-\frac{(E^{\rm rec}_{\rm sh}-E_{\rm sh})^2}{2\sigma^2_{E_{\rm sh}}}\right]}{\sigma_{E_{\rm sh}}\left[1+{\rm Erf}\left(\frac{E^{\rm rec}_{\rm sh}}{\sqrt{2}\sigma_{E_{\rm sh}}}\right)\right]} \,, \quad (10.8)$$

where $\sigma_{E_{\rm sh}} = 10^{\sigma_\epsilon} E_{\rm sh}$. As baseline, we fix $\sigma_\epsilon = 0.1$, based on simulations performed for UHE neutrino radio-detection at the RNO-G neutrino telescope [315], which we take as representative of IceCube-Gen2, too. We model the angular resolution via a Gaussian function of the angle between true and reconstructed direction, *i.e.*,

$$R_\Omega(\mathbf{n}^{\rm rec},\mathbf{n}) = \frac{\sigma^2}{2\pi(1-e^{-2/\sigma^2})} \exp\left(\frac{\mathbf{n}\cdot\mathbf{n}_{\rm rec}}{\sigma^2}\right) \,, \quad (10.9)$$

with a common width of $\sigma_{\theta_z} = \sigma_\phi =\equiv \sigma_\Omega$ in zenith and azimuth. As baseline, we fix $\sigma_\Omega = 3^\circ$, similar to what Ref. [346] adopted for the zenith-angle resolution. References [346, 390] explored the effect of varying the energy and angular resolution on the event rate.

To produce our forecasts, we use the all-flavor event rate of ν_α and $\bar{\nu}_\alpha$, *i.e.*,

$$\frac{d^2N_\nu}{dE_{\rm sh}^{\rm rec}d\Omega^{\rm rec}} = \sum_{\alpha=e,\mu,\tau}\left(\frac{d^2N_{\nu_\alpha}}{dE_{\rm sh}^{\rm rec}d\Omega^{\rm rec}} + \frac{d^2N_{\bar{\nu}_\alpha}}{dE_{\rm sh}^{\rm rec}d\Omega^{\rm rec}}\right) . \tag{10.10}$$

Conservatively, we do not assume that radio-detection at IceCube-Gen2 will be able to distinguish between events initiated by different flavors; however, there is promising ongoing work in this direction [213, 214, 300].

10.3.3 *Expected event rates*

Using the methods above, we compute event rates for the flux of UHE neutrinos from DM decay and for the non-DM background flux of UHE neutrinos. For the former, the event rate depends on the DM mass and lifetime. For the latter, it depends on our choice of background flux. As illustration, below we show event rates for the fluxes in Fig. 48; later, when producing results, we compute event rates for many more cases.

Figure 51 shows the all-sky differential event rate in reconstructed shower energy. The event energy spectra reflect the features of the underlying neutrino energy spectra in Fig. 48, though smoothed out by the detector energy resolution, which complicates distinguishing between them in our forecasts later (see also Sec. 10.2.3). Further, while the neutrino energy spectrum from DM decay with $m_{\rm DM} = 10^8$ GeV and the spectrum of the large non-DM benchmark flux are comparable in Fig. 48, in Fig. 51 the event rate for the former is appreciably smaller than that for the latter. This is because the effective volume falls at low energies, where the spectrum from DM decay peaks; see Sec. 10.3.2.

Figure 52 shows sky maps of the angular distribution of the energy-integrated event rate, for neutrinos from DM decay and for the background neutrinos. The angular distribution of events is anisotropic, even when it is due to an isotropic neutrino flux, like the background flux. The radio array of IceCube-Gen2 is mostly sensitive to zenith angles between 45° and 90°. At larger zenith angles, Earth attenuation strongly reduces the chances of neutrino detection, whereas at

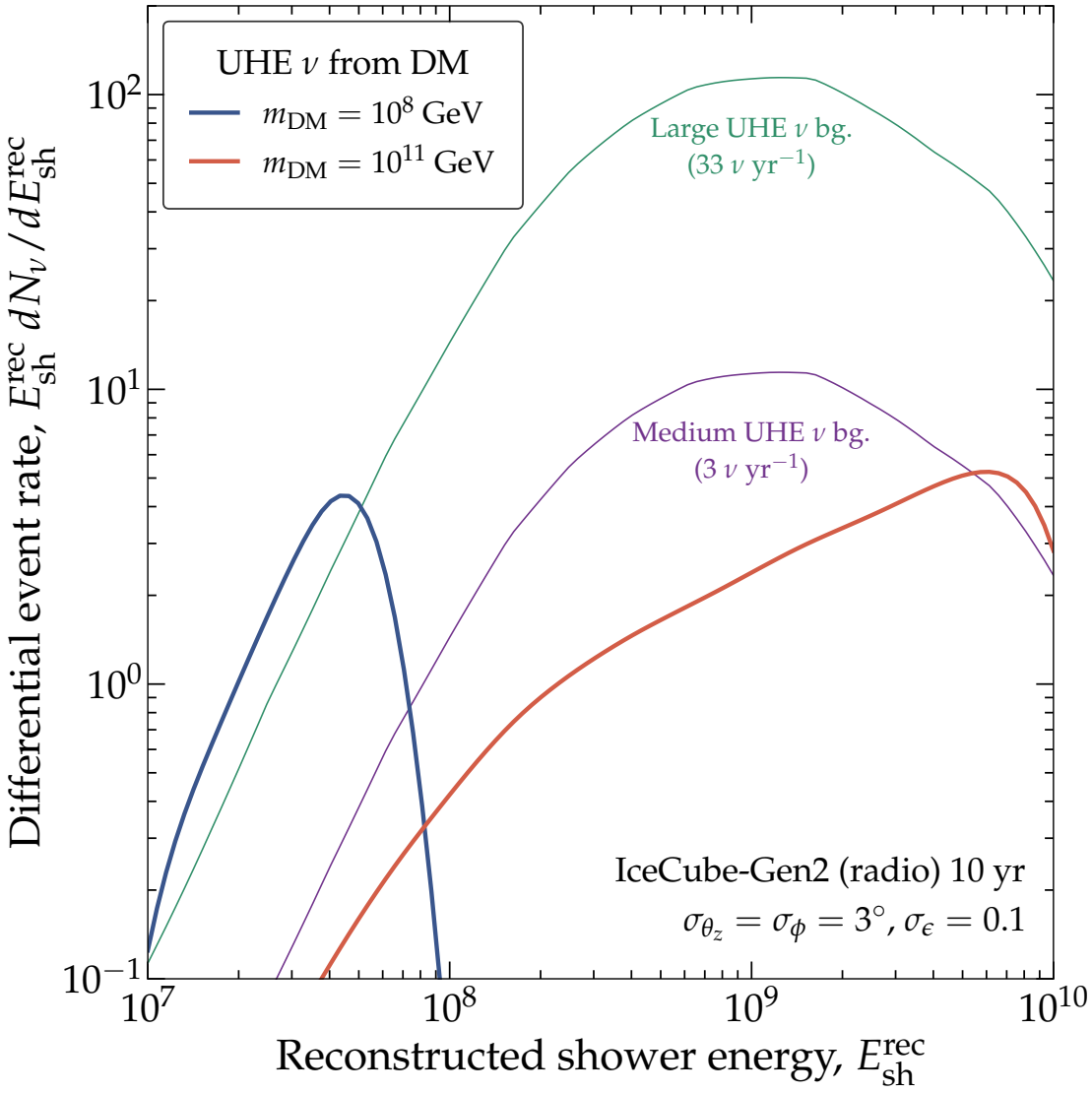

Figure 51: ***Differential rate of neutrino-induced events in the radio array of IceCube-Gen2.*** We show results obtained for the same illustrative choices of the flux from DM decay and the non-DM background flux as in Fig. 48. The event rate is computed using Eq. (10.10), using baseline choices of the detector angular and (logarithmic) energy resolution, $\sigma_\Omega = 3^\circ$ and $\sigma_\epsilon = 0.1$. This figure shows the direction-averaged energy distribution of events; Fig. 52 shows the angular event distribution. See Sec. 10.3 for details.

smaller zenith angles the effective volume is smaller. For this reason, most of the events come from declinations between -45° and 0°. (The two bright zenith bands in the skymaps, easily visible for neutrinos from DM decay, are due to features in the response of the two types of antennas that the radio array is made of; see Fig. 12 in Ref. [346].)

The sky maps in Fig. 52 illustrate the combined effect of the three sources of angular dependence in our calculation: from the neutrino flux itself, from the propagation of neutrinos through the Earth, and from the detector effective volume. The latter two, together with the angular resolution of the detector, smooth out any natural anisotropy in the neutrino flux. Nevertheless, Fig. 52 shows

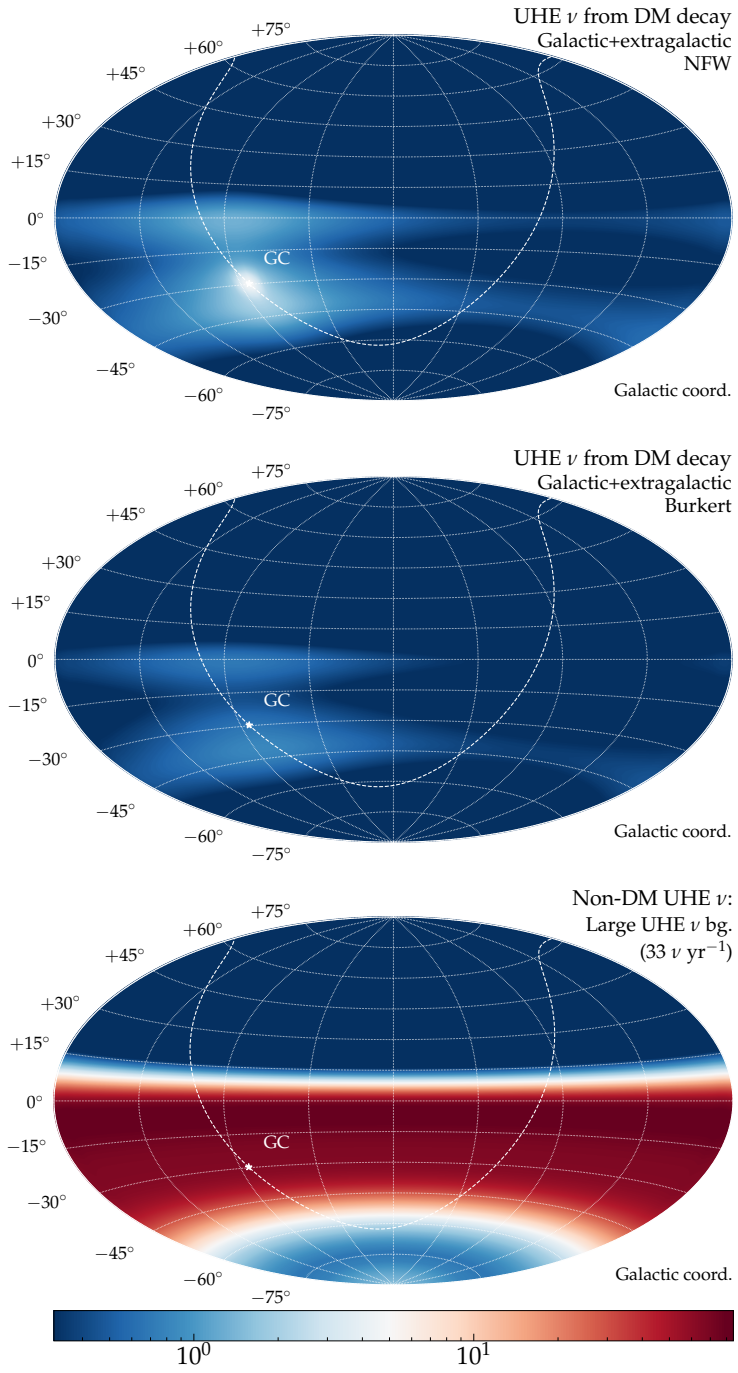

Figure 52: ***Angular distribution of detected events in the radio array of IceCube-Gen2.*** We use the same illustrative fluxes as in Fig. 50. *Top:* Neutrinos from DM decay for an NFW profile. *Center:* Same for a Burkert profile. *Bottom:* Neutrinos from the non-DM isotropic background of UHE neutrinos. The angular dependence is due both to the angular distribution of the flux (Fig. 50) and the angular response of the detector (Fig. 13 in Ref. [346]). The event rate is computed using Eq. (10.10), using baseline choices of the detector angular and (logarithmic) energy resolution, $\sigma_\Omega = 3°$ and $\sigma_\epsilon = 0.1$. This figure shows the energy-integrated angular distribution of events; Fig. 51 shows the energy distribution. See Sec. 10.3 for details.

that the excess of neutrinos from DM decay towards the GC survives into the angular distribution of events, though it is more spread out. The excess is more concentrated for the NFW profile than for the Burkert profile, reflecting their fluxes from Fig. 52.

10.4 DISCOVERY PROSPECTS FOR DARK MATTER DECAY

The decay of heavy DM into UHE neutrinos may be discovered even in the presence of sizable non-DM neutrino backgrounds, by using the angular distribution of detected events, in 10 years of exposure of the radio array of IceCube-Gen2 (Fig. 53). However, a puffy Galactic DM density profile may weaken the discovery prospects (Fig. 54). Upon discovery, the DM mass and lifetime, and the flux of neutrinos from its decay, may be accurately and precisely measured by using also the energy distribution of events (Figs. 55 and 56).

10.4.1 *Overview*

The distinct angular distribution of UHE neutrinos from DM decay—peaked towards the GC—provides a smoking-gun signature of their origin when compared to the isotropic flux of astrophysical and cosmogenic neutrinos. Yet, so far, the usefulness of this difference has gone underused or ignored in forecasts of searches for DM decay in UHE neutrino telescopes; see, *e.g.*, Ref. [584]. In contrast, our methods embrace it. Unlike previous forecasts, we use this angular difference to not only claim the discovery of UHE neutrinos with a *possible* origin in DM decay, but to *assert* their DM origin in the presence of a non-DM neutrino background, *i.e.*, to firmly discover UHE neutrinos from DM decay.

However, a sensible DM discovery claim requires a sufficiently large excess towards the GC. Added to that, if there is a large isotropic background of non-DM neutrinos, it could wash out the excess of neutrinos from DM decay, weakening the discovery claim.

In our forecasts below, we quantify the above statements in two ways. First (Sec. 10.4.2), we find the values of the mass and lifetime of DM needed to discover UHE neutrinos from its decay, in the presence of a non-DM neutrino background. For this, we use only the angular distribution of

detected events in the radio array of IceCube-Gen2. Second (Sec. 10.4.3), in the event of discovery, we illustrate the accuracy with which the DM mass and lifetime could be measured. For this, we use the joint angular and energy distribution of events.

10.4.2 *Discovery prospects*

We forecast the regions of DM mass and lifetime where UHE neutrinos from DM decay could be discovered. Figure 53 (also Fig. D1) shows our results.

10.4.2.1 *Statistical methods*

We produce discovery forecasts by analyzing projected samples of detected events. To be conservative, we use only their angular distribution, summed over all energies, since it is in it that the critical difference between the flux of neutrinos from DM decay and the non-DM neutrino background manifests (Sec. 10.2.3). Later (Sec. 10.5), we derive upper limits using also their energy distribution. We build our forecasts using the maximum likelihood technique and report mean discovery prospects based on Asimov data samples.

Each event sample is the sum of events due to neutrinos from DM decay, dependent on the DM mass, $m_{\rm DM}$, and lifetime, $\tau_{\rm DM}$, and events from the background of non-DM neutrinos, rescaled by a flux normalization, $\mathcal{N}_\Phi$, *i.e.*,

$$\frac{dN_\nu(\boldsymbol{\vartheta})}{d\Omega^{\rm rec}} = \frac{dN_\nu^{\rm DM}\left(m_{\rm DM}, \tau_{\rm DM}\right)}{d\Omega^{\rm rec}} + \mathcal{N}_\Phi \frac{dN_\nu^{\rm bg}}{d\Omega^{\rm rec}} \,, \tag{10.11}$$

where $\boldsymbol{\vartheta} \equiv \{m_{\rm DM}, \tau_{\rm DM}, \mathcal{N}_\Phi\}$. For the non-DM background, we show forecasts obtained under the three benchmark scenarios presented in Sec. 10.2.1: a large flux set to the cosmogenic flux by Bergman & van Vliet [193], a medium flux that is 10% of that, and a null background; see Fig. 48. The large and medium benchmark backgrounds have the same angular distribution of events (see Fig. 52 and also Fig. 4 in Ref. [390]); they only differ in the total number of events (Fig. 51).

Based on a projected event sample, we compare two hypotheses: the DM hypothesis, where the angular distribution of events is best explained by the presence of a DM decay component on top of a background non-DM component *vs.* the null hypothesis, where it is best explained by the presence of only the background non-DM component. In both cases, the background flux

normalization, $\mathcal{N}_\Phi$, is left free to vary to best fit the data. Hence, when analyzing a simulated event sample, we obtain results that do not require prior knowledge of the true background flux. We do this separately for each of the three above choices of the simulated background flux, and for a wide range of true values of the DM and lifetime.

First, for a particular choice of the true DM mass and lifetime, $m_{\rm DM}$ and $\tau_{\rm DM}$, and using the true value of the flux normalization, $\mathcal{N}_\Phi = 1$, we compute the projected *observed* sample of $N_{\rm evts}$ events, each with reconstructed direction $\Omega_i^{\rm rec}$ sampled from the distribution $dN_\nu(m_{\rm DM}, \tau_{\rm DM}, \mathcal{N}_\Phi = 1)/d\Omega^{\rm rec}$. Later, we use a test statistic that is averaged over all possible random realizations of the number of events and of the distribution of reconstructed directions of the events.

Then, based on this observed sample, we evaluate an unbinned likelihood function at different test values of the model parameters, $\boldsymbol{\vartheta}' \equiv (m'_{\rm DM}, \tau'_{\rm DM}, \mathcal{N}'_\Phi)$, *i.e.*,

$$\mathcal{L}(\boldsymbol{\vartheta}'; \{\Omega_i^{\rm rec}\}) = e^{-N_\nu(\boldsymbol{\vartheta}')} \prod_{i=1}^{N_{\rm evts}} \left.\frac{dN_\nu(\boldsymbol{\vartheta}')}{d\Omega^{\rm rec}}\right|_{\Omega_i^{\rm rec}} , \tag{10.12}$$

where $N_\nu(\boldsymbol{\vartheta}') \equiv \int (dN_\nu(\boldsymbol{\vartheta}')/d\Omega^{\rm rec}) d\Omega^{\rm rec}$ is the all-sky event rate. In the comparison, we let the test values of $m'_{\rm DM}$, $\tau'_{\rm DM}$, and $\mathcal{N}'_\Phi$ float as free parameters, as they would in a test based on real experimental data. Under the null hypothesis, where there is no DM decay contribution because DM is stable (*i.e.*, $\tau_{\rm DM} \to \infty$), the likelihood reduces to

$$\mathcal{L}_{\rm bg}(\mathcal{N}'_\Phi; \{\Omega_i^{\rm rec}\}) \equiv \lim_{\tau'_{\rm DM} \to \infty} \mathcal{L}(\boldsymbol{\vartheta}'; \{\Omega_i^{\rm rec}\}) , \tag{10.13}$$

where the right-hand side no longer depends on the test values $m'_{\rm DM}$ and $\tau'_{\rm DM}$.

For a specific choice of the true values of $m_{\rm DM}$ and $\tau_{\rm DM}$, the test statistic depends on the angular distribution of the associated random observed event sample. To account for the possible different realizations of the observed sample, we average the logarithm of the likelihood functions, Eqs. (10.12) and (10.13), over all possible realizations. The probability to observe a total number of $N_{\rm evts}$, over the full sky, $\mathcal{P}(N_{\rm evts}|N_\nu)$, is given by a Poisson distribution with a mean value equal to the mean all-sky event rate, $N_\nu \equiv N_\nu(m_{\rm DM}, \tau_{\rm DM}, \mathcal{N}_\Phi = 1)$. The probability to sample an event with

reconstructed direction $\Omega_i^{\rm rec}$ from this distribution is $\mathcal{P}(\Omega_i^{\rm rec}) \equiv (1/N_\nu)(dN_\nu/d\Omega^{\rm rec})|_{\Omega_i^{\rm rec}}$. Thus, the likelihood function, Eq. (10.12), averaged over all possible realizations of the event sample, is

$$\begin{aligned}\langle \ln \mathcal{L}(\boldsymbol{\vartheta}')\rangle_{m_{\rm DM},\tau_{\rm DM}} &= \sum_{N_{\rm evts}=0}^{\infty} \mathcal{P}\left[N_{\rm evts}|N_\nu(m_{\rm DM},\tau_{\rm DM},\mathcal{N}_\Phi=1)\right] \\ &\quad \times \int d\Omega_1^{\rm rec}\cdots\int d\Omega_{N_{\rm evts}}^{\rm rec} \\ &\quad \prod_{i=1}^{N_{\rm evts}} \mathcal{P}(\Omega_i^{\rm rec}|m_{\rm DM},\tau_{\rm DM},\mathcal{N}_\Phi=1)\ln\mathcal{L}\left[\boldsymbol{\vartheta}', \left\{\Omega_j^{\rm rec}\right\}_{j=1}^{N_{\rm evts}}\right] ,\end{aligned} \tag{10.14}$$

and, similarly, the average log-likelihood under the null hypothesis, in which only background non-DM neutrinos are present, Eq. (10.13), is

$$\langle \ln \mathcal{L}_{\rm bg}(\mathcal{N}_\Phi')\rangle_{m_{\rm DM},\tau_{\rm DM}} \equiv \lim_{\tau_{\rm DM}'\to\infty} \langle \ln \mathcal{L}(\boldsymbol{\vartheta}')\rangle_{m_{\rm DM},\tau_{\rm DM}} , \tag{10.15}$$

We average the log-likelihood, rather than the likelihood, to prevent the averaging procedure from prescribing exceedingly large averaging weights to random realizations that have associated large likelihood values. This corresponds to obtaining the results for an Asimov data sample [595], in which the observed distribution of events exactly coincide with the expected one.

To compare the two hypotheses, we use as a test statistic the average log-likelihood ratio, *i.e.*,

$$\begin{aligned}\langle \Lambda(m_{\rm DM},\tau_{\rm DM})\rangle &= \min_{\mathcal{N}_\Phi'}\left[-2\langle \ln \mathcal{L}_{\rm bg}(\mathcal{N}_\Phi')\rangle_{m_{\rm DM},\tau_{\rm DM}}\right] \\ &\quad - \min_{\boldsymbol{\vartheta}'}\left[-2\langle \ln \mathcal{L}(\boldsymbol{\vartheta}')\rangle_{m_{\rm DM},\tau_{\rm DM}}\right] .\end{aligned} \tag{10.16}$$

According to Wilks' theorem [596], in the asymptotic limit of a large data sample, this quantity follows a χ^2 distribution with two degrees of freedom, corresponding to the difference between the dimensions of the parameter spaces of the two competing hypotheses. We adopt it in our forecasts since, for 10 and 20 years of detector exposure, and for the neutrino fluxes that we adopt, they are based on a large number of events. Hence, below, when $\langle\Lambda\rangle > 6$, we claim discovery of DM neutrinos at the 2σ confidence level (C.L.); when $\langle\Lambda\rangle > 11.5$, we claim it at 3σ C.L.

10.4.2.2 *Results*

Figure 53 shows the regions of DM mass and lifetime, obtained with the above methods, where DM can be discovered at $\geq 2\sigma$. We show results for our three benchmark choices of non-DM UHE neutrino background flux (Sec. 10.2.1)—null, medium, and large. The results in Fig. 53 convey three key messages.

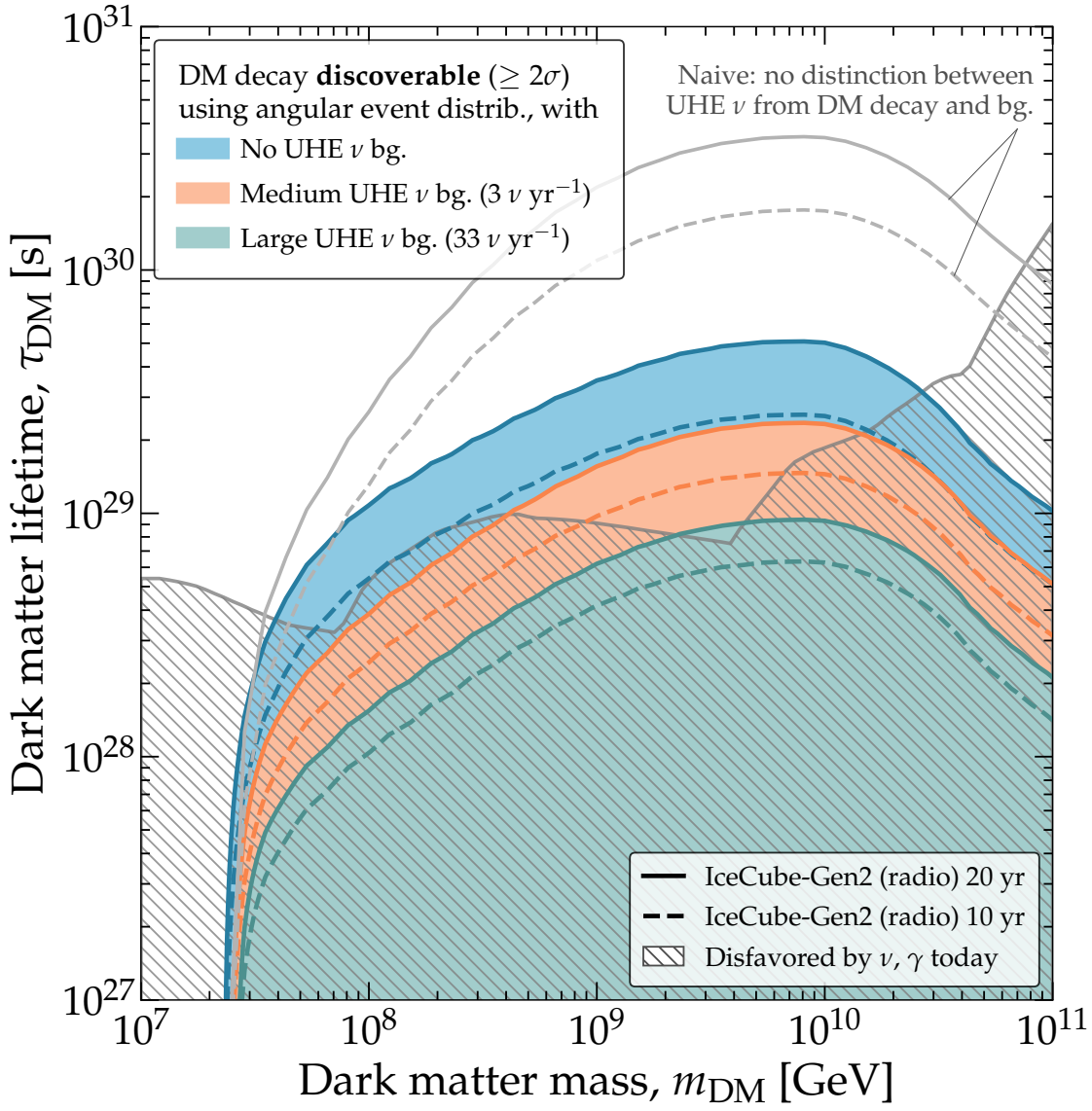

Figure 53: ***Discovery prospects of UHE neutrinos from DM decay in the radio array of IceCube-Gen2.*** Forecasts are for three benchmark choices of the background flux of non-DM UHE neutrinos (*i.e.*, cosmogenic): null, medium, and large (Sec. 10.2.1), based on the cosmogenic neutrino flux by Bergman & van Vliet [193] (fig. 48). The forecasts use only the angular distribution of events, summed over all reconstructed energies $E_{\rm sh}^{\rm rec} \geq 10^7$ GeV. They use baseline choices of the detector angular and (logarithmic) energy resolution, $\sigma_\Omega = 3^\circ$ and $\sigma_\epsilon = 0.1$; see Sec. 10.3.2. This figure assumes the NFW density profile for Galactic DM. Existing lower limits on the DM lifetime are the same as in Fig. 47. In this figure, results are for discovery at $\geq 2\sigma$; see Fig. D1 for results at $\geq 3\sigma$. *Even in the presence of a medium-sized background, DM discovery might be possible.* See Sec. 10.4.2 for details.

First, while a large part of the parameter space in Fig. 53 is already disfavored by present-day neutrino and gamma-ray searches, upcoming UHE neutrino telescopes will extend the search to longer DM lifetimes, roughly above 10^{29} s, that are unreachable with present-day experiments. This aspect of our results agrees with previous works; see, *e.g.*, Refs. [524, 584]). Yet, for the first

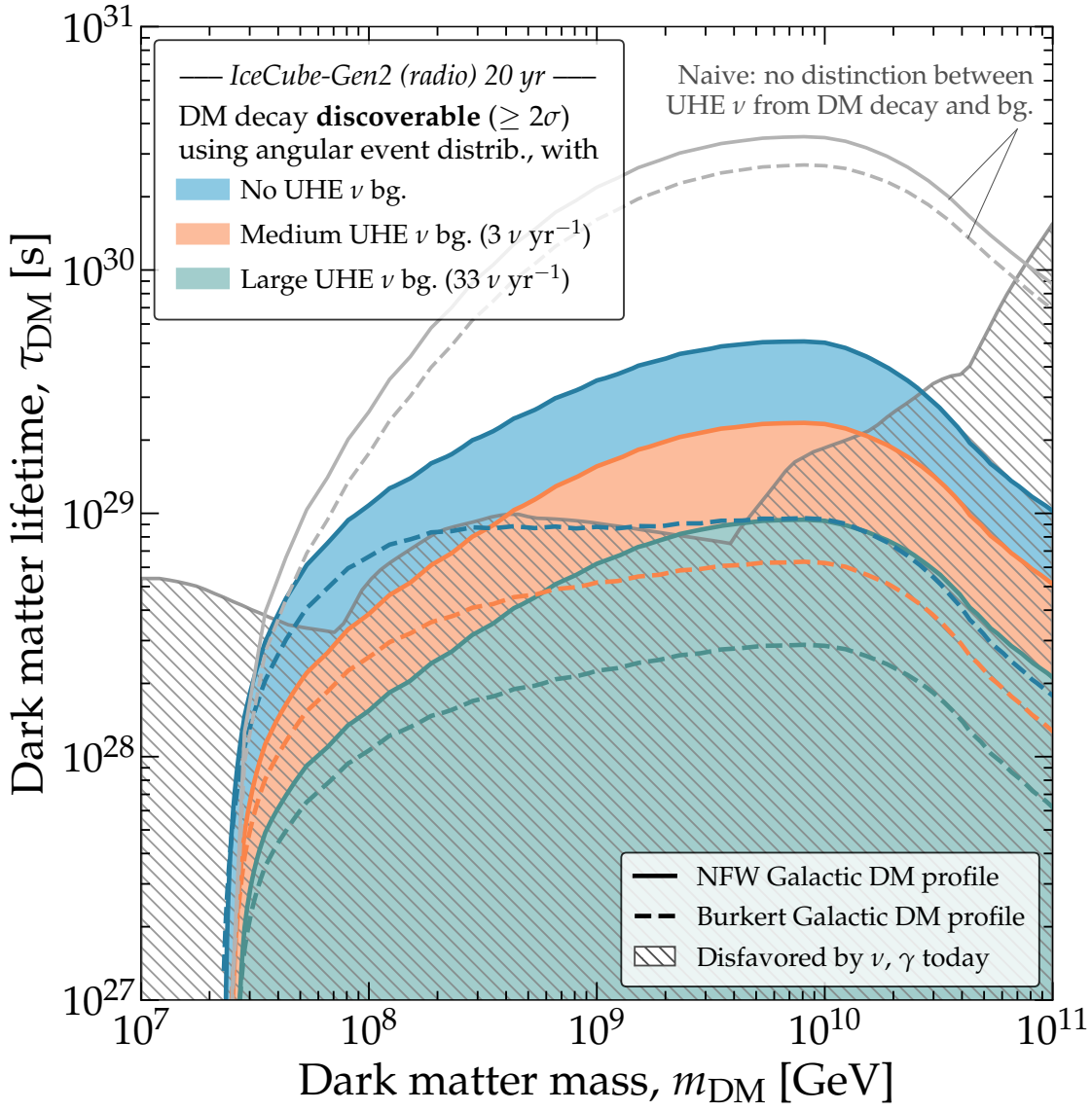

Figure 54: ***Discovery prospects of UHE neutrinos from DM decay for NFW vs. Burkert Galactic DM profiles.*** Same as Fig. 53, but comparing results obtained using the NFW *vs.* Burkert Galactic DM density profiles (Fig. 49). Results are for discovery at $\geq 2\sigma$ after 20 years; see Fig. D3 for more results using the Burkert profile. Existing lower limits on the DM lifetime are the same as in Fig. 47, and computed assuming the NFW profile [524]. *If the Galactic DM profile is "puffy", like the Burkert profile, discovery of DM becomes barely feasible, and only if there is no isotropic non-DM UHE neutrino background.* See Sec. 10.4.2 for details.

time, we fortify the claim by showing that it holds even in the presence of a medium-sized isotropic background flux of non-DM UHE neutrinos.

Second, Fig. 53 shows the significant difference between *detecting* events, which a priori may or may not be due to DM decay, and *claiming* that those events are produced by DM decay. Earlier forecasts of UHE neutrino detection from DM decay [584] had only investigated the maximum lifetime needed to detect neutrinos from DM decay, without identifying their origin. We show a version of these forecasts in Fig. 53, generated by demanding that DM decay yields at least one

event over the full sky, background-free, with a probability larger than 95% (or 99.7% in Fig. D1). As expected, this weaker criterion leads to overly long lifetimes being discoverable: compared to our results using the angular distribution of events, lifetimes longer by at least one order of magnitude could be detected without actually leading to a DM discovery. Thus, hereafter the main observations and conclusions of our work are based exclusively on forecasts made using the angular—and energy (in Secs. 10.4.3 and 10.5)—distribution of events.

Third, Fig. 53 shows that, while the discovery prospects are best when background-free, as expected, the presence of a medium-size background only degrades the reach of discoverable DM lifetimes by a factor of about 2. In other words, ***UHE neutrinos retain the potential to reveal DM decay even in the presence of a sizable isotropic background of non-DM origin***. This is true also for discovery at 3σ; see Fig. D1.

Figure 54 shows that, however, our prospects for discovery of DM decay are contingent on the Galactic DM density profile being cuspy, *i.e.*, markedly pronounced towards the GC. Swapping the cuspy NFW profile for the puffy Burkert profile reduces the region amenable for discovery by about one order of magnitude, pushing it into the region of DM mass and lifetime that is already disfavored, and rendering discovery all but unfeasible. A subtle point is that the present-day disfavored region shown in Fig. 54 was computed, in Ref. [524], assuming the NFW profile. Assuming the Burkert instead would push down the disfavored region, leaving slightly more room for discovery under the Burkert profile; we do not attempt this recalculation here. Yet, the bottom line holds: for realistic choices of the detector angular resolution, like the $\sigma_\Omega = 3^\circ$ that we adopt, ***the discovery of DM decay into UHE neutrinos will be likely only if the Galactic DM density profile is cuspy***.

10.4.3 *Measuring dark matter mass and lifetime*

In the event of the discovery of DM decay into UHE neutrinos, we forecast how well the DM mass and lifetime could be inferred. Figure 55 shows our results.

10.4.3.1 *Statistical methods*

Above (Sec. 10.4.2), we showed that to claim the discovery of DM decay into UHE neutrinos it was enough to use the angular distribution of events. In the event of discovery, inferring the DM lifetime also relies mainly on the angular distribution events; concretely, as before, on its excess towards the GC. Because the DM lifetime determines the normalization of the neutrino flux from DM decay, its value can be inferred from the magnitude of the excess. However, inferring the DM mass requires the energy distribution of events, too. Using it allows us to infer the DM mass by looking for the distinct bump-like feature imprinted by DM decay on the neutrino spectrum, which peaks at $E_\nu = m_{\rm DM}/2$; see Figs. 48 and 51. Thus, below, we extend the statistical methods from Sec. 10.4.2.1 to include also the energy of the detected events.

First, we generate the *true* event sample, *i.e.*, the one that we assume will be detected. We use a procedure similar to the one we used to compute discovery prospects (Sec. 10.4.2), but extended to included also the energy distribution of events. To illustrate our method, we choose $m_{\rm DM} = 3.5 \times 10^9$ GeV and $\tau_{\rm DM} = 1.19 \times 10^{29}$ s as true values; these are representative of the discoverable region under our benchmark medium non-DM in Fig. 53. We use for the non-DM background UHE neutrino flux the same three benchmarks (Sec. 10.2.1) that we used earlier to make discovery forecasts—null, medium, and large. In analogy to Eq. (10.11), the true distribution is

$$\frac{dN_\nu^{\rm true}(m_{\rm DM}, \tau_{\rm DM})}{dE_{\rm sh}^{\rm rec} d\Omega^{\rm rec}} = \frac{dN_\nu^{\rm DM}(m_{\rm DM}, \tau_{\rm DM})}{dE_{\rm sh}^{\rm rec} d\Omega^{\rm rec}} + \frac{dN_\nu^{\rm bg}}{dE_{\rm sh}^{\rm rec} d\Omega^{\rm rec}} \,. \tag{10.17}$$

From it, we randomly sample $N_{\rm evts}$ events, each with reconstructed energy $E_{{\rm sh},i}^{\rm rec}$ and direction $\Omega_i^{\rm rec}$. Later, for each choice of $m_{\rm DM}$ and $\tau_{\rm DM}$, we average our test statistic over all possible random realizations of the event samples.

Then we compare the true event sample to *test* event samples, generated for many different test values of DM mass and lifetime, in order to find which ones fit best. To produce test event samples, we generalize what we did to compute discovery prospects and adopt a generic model of the non-DM background neutrino energy spectrum. We parametrize it as a piecewise (pw) spectrum

$\propto E_\nu^{-2}$, with three independent normalization constants, $\mathcal{N}_{\Phi,1}$, $\mathcal{N}_{\Phi,2}$, $\mathcal{N}_{\Phi,3}$, in three decades of neutrino energy, from 10^7 GeV to 10^{10} GeV. For ν_α, this is

$$\Phi_{\nu_\alpha}^{\mathrm{bg-pw}}(E_\nu) = \frac{f_{\alpha,\oplus}}{2E_\nu^2} \times \begin{cases} \mathcal{N}_{\Phi,1}, & 10^7 \leq E_\nu/\mathrm{GeV} < 10^8 \\ \mathcal{N}_{\Phi,2}, & 10^8 \leq E_\nu/\mathrm{GeV} < 10^9 \\ \mathcal{N}_{\Phi,3}, & 10^9 \leq E_\nu/\mathrm{GeV} \leq 10^{10} \end{cases} , \tag{10.18}$$

where, for the flavor composition at Earth, we adopt the one from the canonical expectation of neutrino production via the pion decay chain (Sec. 10.2.1), computed using recent best-fit values of the neutrino mixing parameters [268, 597], $f_{e,\oplus} = 0.298$, $f_{\mu,\oplus} = 0.359$, and $f_{\tau,\oplus} = 0.342$, from Ref. [267], *i.e.*, close to flavor equipartition (see also, *e.g.*, Ref. [329]). Since we make forecasts for 10–20 years, when the values of the mixing parameters will likely be known precisely [346], we neglect the small uncertainties in these predictions; see Eqs. (7)–(9) in Ref. [346] . The fluxes of ν_α and $\bar{\nu}_\alpha$ are identical; this is ensured by the factor of 2 in the denominator of Eq. (10.18).

We adopt this background flux model to analyze projected event samples using a phenomenological prescription of the non-DM neutrino background that is as agnostic as possible regarding the shape of its energy spectrum and its origin. Our strategy resembles one that would be used by future analyses based on real experimental observations. Indeed, similar flux models are used by the IceCube Collaboration to analyze present-day data [37, 188]. Using the piecewise background flux, we compute the associated differential event spectrum, $dN_\nu^{\mathrm{bg-pw}}/dE_{\mathrm{sh}}^{\mathrm{rec}}d\Omega^{\mathrm{rec}}$, using the methods from Sec. 10.3.2. Thus, the total differential test event spectrum is

$$\frac{dN_\nu^{\mathrm{test}}(\boldsymbol{\vartheta}')}{dE_{\mathrm{sh}}^{\mathrm{rec}}d\Omega^{\mathrm{rec}}} = \frac{dN_\nu^{\mathrm{DM}}(m'_{\mathrm{DM}},\tau'_{\mathrm{DM}})}{dE_{\mathrm{sh}}^{\mathrm{rec}}d\Omega^{\mathrm{rec}}} + \frac{dN_\nu^{\mathrm{bg-pw}}(\mathcal{N}'_{\Phi,1},\mathcal{N}'_{\Phi,2},\mathcal{N}'_{\Phi,3})}{dE_{\mathrm{sh}}^{\mathrm{rec}}d\Omega^{\mathrm{rec}}} , \tag{10.19}$$

where now $\boldsymbol{\vartheta}' \equiv (m'_{\mathrm{DM}},\tau'_{\mathrm{DM}},\mathcal{N}'_{\Phi,1},\mathcal{N}'_{\Phi,2},\mathcal{N}'_{\Phi,3})$.

In analogy to Eq. (10.12), we evaluate an unbinned likelihood function at different test values of the model parameters, $\boldsymbol{\vartheta}'$, *i.e.*,

$$\mathcal{L}_{\mathrm{mea}}(\boldsymbol{\vartheta}', \left\{E_{\mathrm{sh},i}^{\mathrm{rec}}, \Omega_i^{\mathrm{rec}}\right\}) = e^{-N_\nu^{\mathrm{test}}(\boldsymbol{\vartheta}')} \prod_{i=1}^{N_{\mathrm{evts}}} \left.\frac{dN_\nu^{\mathrm{test}}(\boldsymbol{\vartheta}')}{dE_{\mathrm{sh}}^{\mathrm{rec}}d\Omega^{\mathrm{rec}}}\right|_{E_{\mathrm{sh},i}^{\mathrm{rec}},\Omega_i^{\mathrm{rec}}} , \tag{10.20}$$

where N_ν^{test} is the all-sky number of events with energies $E_{\mathrm{sh}}^{\mathrm{rec}} \geq 10^7$ GeV. As before (Sec. 10.4.2), for a specific choice of the true values of m_{DM} and τ_{DM} and of the non-DM background neutrino flux, we average the logarithm of the above likelihood over all possibly random realizations of the observed event sample. In analogy to Eq. 10.14, this yields $\langle \ln \mathcal{L}_{\mathrm{mea}}(\boldsymbol{\vartheta}') \rangle_{m_{\mathrm{DM}},\tau_{\mathrm{DM}}}$. Finally, to infer

the values of the DM mass and lifetime, we profile the likelihood over the test parameters and, in analogy to Eq. 10.16, define the test statistic

$$\begin{aligned}\langle \Lambda_{\rm mea}(m_{\rm DM}, \tau_{\rm DM})\rangle \;=\; & \min_{\mathcal{N}'_{\Phi,1},\mathcal{N}'_{\Phi,2},\mathcal{N}'_{\Phi,3}} \\ & \times \left[-2\langle \ln \mathcal{L}_{\rm mea}(m'_{\rm DM}=m_{\rm DM}, \tau'_{\rm DM}=\tau_{\rm DM}, \mathcal{N}'_{\Phi,1}, \mathcal{N}'_{\Phi,2}, \mathcal{N}'_{\Phi,3})\rangle_{m_{\rm DM},\tau_{\rm DM}}\right] \\ & - \min_{\boldsymbol{\vartheta}'} \left[-2\langle \ln \mathcal{L}_{\rm mea}(\boldsymbol{\vartheta}')\rangle_{m_{\rm DM},\tau_{\rm DM}}\right] \,. \end{aligned} \tag{10.21}$$

As in Sec. 10.4.2, based on Wilks' theorem, this test statistic follows a χ^2 distribution with two degrees of freedom. Below, we use it to infer allowed regions of $m_{\rm DM}$ and $\tau_{\rm DM}$ at difference confidence levels.

10.4.3.2 *Results*

Figure 55 illustrates that, in the event of discovery of DM decay into UHE neutrinos, IceCube-Gen2 may infer the values of the DM mass and lifetime responsible for the discovered signal. In Fig. 55, we show results obtained using our illustrative choice for the true DM and mass lifetime (see above). To illustrate the influence of a non-DM isotropic background flux of UHE neutrinos, we compare results obtained assuming no background *vs.* assuming our medium benchmark background (Sec. 10.2.1).

Our results confirm our expectation (Sec. 10.4.3.1) that using the energy distribution of events grants us sensitivity to the DM parameters. For the choice of DM mass and lifetime in Fig. 55, and similar ones, their values can be inferred with an accuracy of a factor of 2–3. In the presence of the medium background, the accuracy degrades only slightly compared to the null-background case. A larger background degrades the accuracy further, but does not preclude measurement; it may, however, reduce the precision with which the DM mass is inferred (see below).

While the accuracy on the DM mass is only weakly degraded by the presence of a background, the precision on it suffers more appreciably. In the absence of a background, the best-fit value of the DM mass matches its true value. In the presence of a medium-size background, its best-fit value is offset from the real one. This stems from our choice of the three-piece background flux, Eq. 10.18, to analyze projected event samples. On the one hand, this flux prescription frees us from having to rely on specific theoretical predictions of the UHE astrophysical or cosmogenic neutrino flux. On the other hand, because it is rather coarse—with decade-wide flux normalization

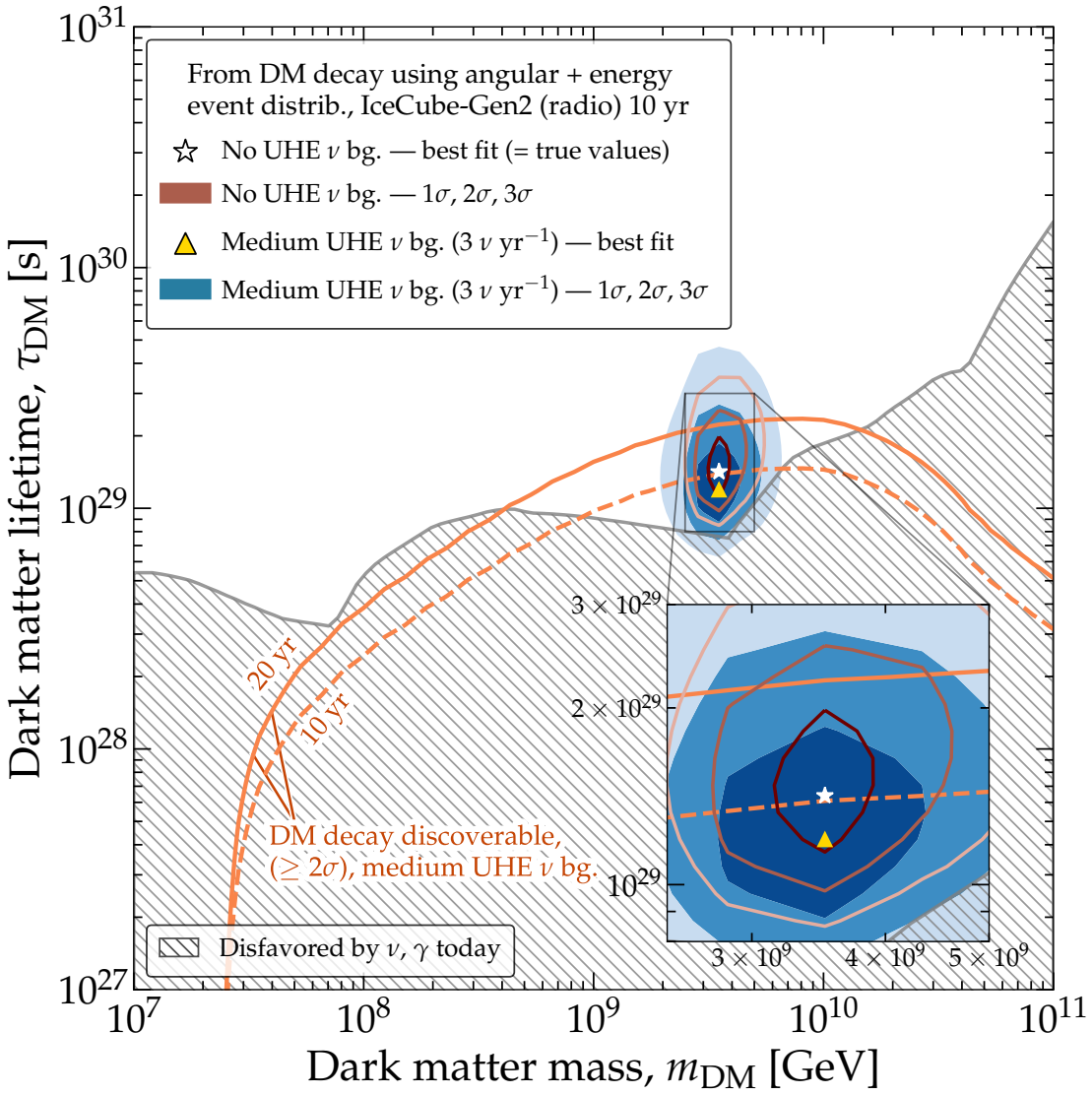

Figure 55: ***DM mass and lifetime inferred from detecting UHE neutrinos from DM decay in the radio array of IceCube-Gen2.*** Results are generated for an illustrative choice of the true values of the DM mass and lifetime, $m_{\rm DM} = 3.5 \times 10^9$ GeV and $\tau_{\rm DM} = 1.19 \times 10^{29}$ s, which are representative of what is discoverable with 10 years of detector exposure and allowed by present-day limits (Fig. 53). Forecasts are for two choices of the background isotropic flux of non-DM UHE neutrinos: null and medium (Sec. 10.2.1), *i.e.*, 10% of the cosmogenic flux by Bergman & van Vliet [193] (Fig. 48). The forecasts use the joint angular and energy distribution of events, and baseline choices of the detector angular and (logarithmic) energy resolution, $\sigma_\Omega = 3^\circ$ and $\sigma_\varepsilon = 0.1$; see Sec. 10.3.2. This figure assumes the NFW density profile for Galactic DM. Existing lower limits on the DM lifetime are the same as in Fig. 47. *In the event of DM discovery, the DM mass and lifetime may be measured with reasonable accuracy and precision.* See Sec. 10.4.3 for details.

constants—it fails to reproduce closely the shape of the background neutrino energy spectrum, Fig. 48. Even so, the mismatch between the best-fit and true values is small; they are consistent within 1σ. Future analyses could mitigate this loss of precision by adopting a more finely binned version of the piecewise background flux.

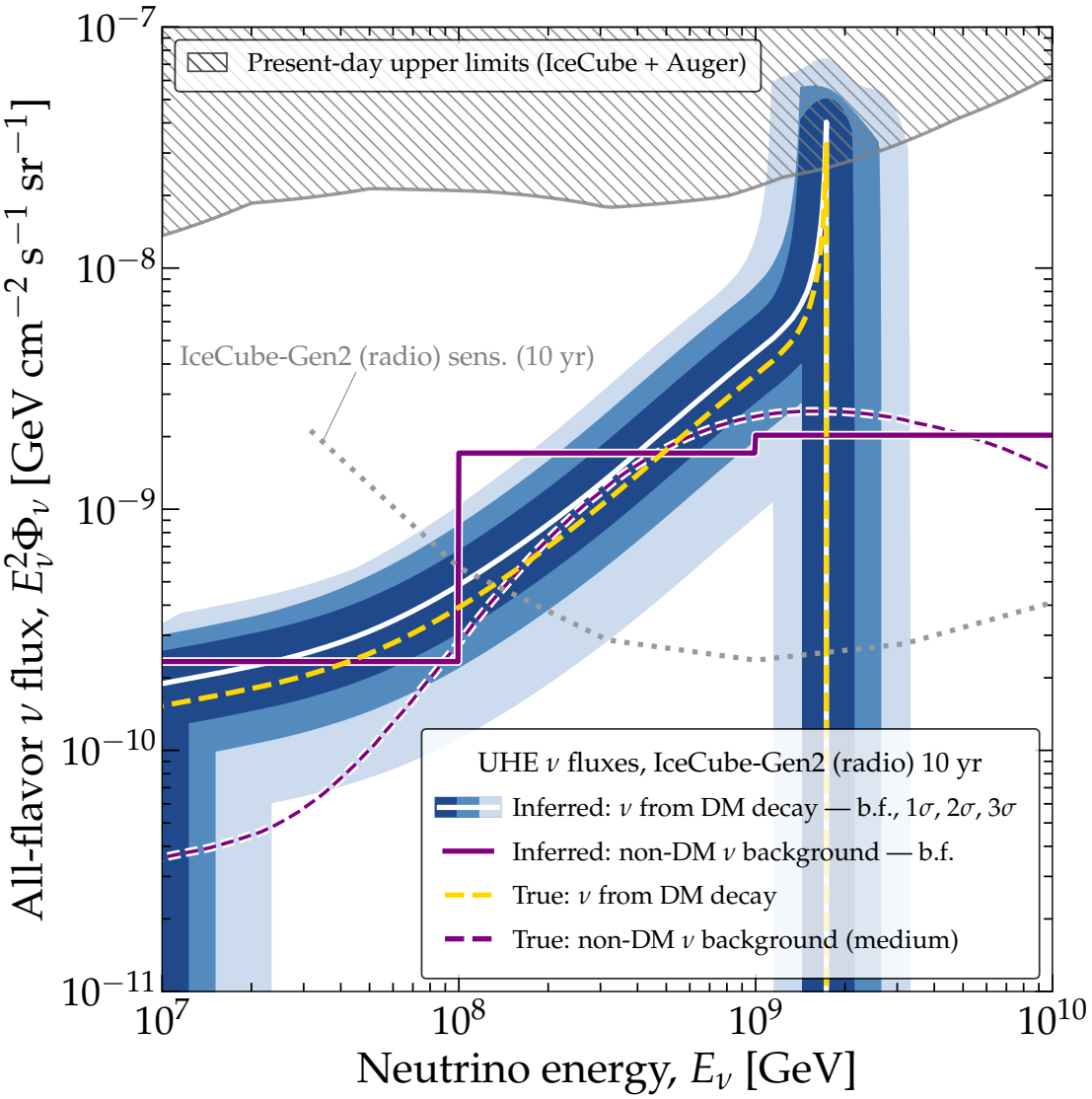

Figure 56: ***Inferred flux of UHE neutrinos using the radio array of IceCube-Gen2.*** The flux of neutrinos from DM decay, sky-averaged, and the isotropic background flux are shown separately. The true values of the DM mass and lifetime are the same as used in Fig. 55. The allowed band of neutrino flux from DM decay corresponds to the allowed regions of inferred DM mass and lifetime from Fig. 55. The forecast assumes our medium-sized benchmark background flux of non-DM UHE neutrinos (Sec. 10.2.1), *i.e.*, 10% of the cosmogenic neutrino flux by Bergman & van Vliet [193] (Fig. 48), or about 3 background events detected per year. This figure assumes the NFW density profile for Galactic DM. Existing upper limits on the flux of UHE neutrinos are from IceCube [66] and Auger [67]. The projected sensitivity of the radio array of IceCube-Gen2 is from Ref. [396]. *Even using a coarse model for the UHE neutrino flux background (Eq. 10.18), the flux of neutrinos from DM decay may be reconstructed with reasonable accuracy and precision.* See Sec. 10.4.3 for details.

Thus, the DM mass and lifetime can be accurately inferred, even in the presence of a non-DM isotropic background flux of UHE neutrinos, by analyzing jointly the angular and energy distribution of events. In doing so, there is essentially no degeneracy between the flux of UHE neutrinos from DM decay and the unknown background flux of UHE astrophysical and cosmogenic

neutrinos, since in our procedure the former is determined almost exclusively by neutrinos from the GC, while the latter is determined by neutrinos from every direction.

Figure 56 shows the corresponding allowed regions of the sky-averaged diffuse flux of UHE neutrinos from DM. The approximate factor-of-2 uncertainty on the DM lifetime translates into an uncertainty of similar size on the flux normalization. The mismatch between the best-fit and true vales of the DM mass translates into a mismatch between the low-energy tails of secondary neutrinos from electroweak corrections in their corresponding fluxes. Figure 56 shows also that our piecewise background flux model, Eq. 10.18, is able to match the true background flux reasonably well, within the limitations of its coarse shape, except in the lowest energy bin, where the match is poor because due to the background flux dipping well below the sensitivity of the radio array of IceCube-Gen2, thus leading to low event rates. There, results could be improved by a combined analyses of TeV–PeV and UHE neutrinos detected, respectively, by the optical and radio arrays of IceCube-Gen2 [39, 321].

10.5 PROJECTED BOUNDS ON DARK MATTER DECAY

The lifetime of heavy DM that decays into UHE neutrinos may be bound even in the presence of sizable non-DM neutrino backgrounds, by using the joint angular and energy distribution of detected events, in 10 years of exposure of the radio array of IceCube-Gen2 (Fig. 57). Even when using the largest possible allowed background, the bounds on the DM lifetime remain competitive or better than present-day bounds (Fig. 58).

10.5.1 *Overview*

Absent evidence for UHE neutrinos from DM decay, it may still be possible to place competitive bounds on the DM lifetime, even in the presence of a sizable non-DM isotropic UHE neutrino background flux. Like for the discovery of DM decay (Sec. 10.4), below we gear our results for radio-detection at IceCube-Gen2, but our methods and, broadly stated, our conclusions are applicable to next-generation UHE neutrino telescopes in general.

References [524, 567, 584] reported projected bounds for DM decay into UHE neutrinos, including via their radio-detection at IceCube-Gen2. We improve on those in two ways. First, we use a significantly more detailed calculation of event rates in IceCube-Gen2, based on state-of-the-art simulations of neutrino propagation, interaction, and radio-detection (Sec. 10.3). Like for the discovery of DM decay, this is key to generating reliable angular and energy event distributions, which our analysis uses to discriminate against the background. Second, unlike previous works, we forecast bounds in the presence of a sizable non-DM isotropic UHE neutrino background flux. Reference [584] did consider the presence of a potential background, but discriminated against it simply by counting only neutrinos with energy smaller than $m_{\rm DM}/2$. In contrast, we use a full-fledged angular and energy analysis to produce our bounds.

10.5.2 *Statistical methods*

Unlike our earlier analyses to discover DM decay and infer the DM mass and lifetime (Sec. 10.4), to place bounds on DM decay we assume that the *true*, observed event distributions are due solely to the non-DM isotropic background flux of UHE neutrinos, and we contrast *test* event distributions expected from DM decay against it. For the non-DM background flux, we use our two medium and large benchmark fluxes (Sec. 10.2.1), based off of the cosmogenic neutrino flux by Bergman & van Vliet [193]. Our main conclusions hold for other choices of background, and we point out below what features of our results are due to our specific benchmark choices.

Further, unlike when computing discovery prospects (Sec. 10.4.2), when setting bounds below we use not only the angular distribution of events, but also their energy distribution. We demand that the energy distribution of events lacks features that are characteristic of the energy spectrum of neutrinos from DM decay, *i.e.*, a clustering of events with similar energies that reflects an underlying bump-like shape of the spectrum (Sec. 10.2.2). Admittedly, this is a broad, conservative criterion: it discriminates against the flux of neutrinos from DM decay, but also against any astrophysical or cosmogenic flux that has a bump-like feature in its spectrum, of which there are many proposals, including our benchmark background fluxes; see, *e.g.*, Fig. 2 in Ref. [390].

For a given choice of the non-DM neutrino background, we compute the true, observed event distribution,

$$\frac{dN_\nu^{\rm true}}{dE_{\rm sh}^{\rm rec} d\Omega^{\rm rec}} = \frac{dN_\nu^{\rm bg}}{dE_{\rm sh}^{\rm rec} d\Omega^{\rm rec}} \,, \tag{10.22}$$

using the methods from Sec. 10.3.3. From it, we sample random realizations of the observed event sample, consisting of a random number $N_{\rm evts}$ of events, each with reconstructed energy and direction, $E_{{\rm sh},i}^{\rm rec}$ and $\Omega_i^{\rm rec}$.

Then, for a choice of the DM mass $m_{\rm DM}$ and lifetime $\tau_{\rm DM}$, we compare the true event rate *vs.* the test event rate expected from DM decay, $dN_\nu^{\rm test}(\boldsymbol{\vartheta}')/dE_{\rm sh}^{\rm rec} d\Omega^{\rm rec}$, given by Eq. 10.19 evaluated at test parameters $\boldsymbol{\vartheta}' \equiv (m'_{\rm DM} = m_{\rm DM}, \tau'_{\rm DM} = \tau_{\rm DM}, \mathcal{N}'_{\Phi,1}, \mathcal{N}'_{\Phi,2}, \mathcal{N}'_{\Phi,3})$. This test event rate is computed using the same piecewise background UHE neutrino spectrum, Eq. 10.18, that we used to infer the DM mass and lifetime (Sec. 10.4.3).

Like when computing discovery forecasts, we compare the true (*i.e.*, background-only) and test (*i.e.*, background plus DM) hypotheses via an unbinned likelihood, given by Eq. 10.20, *i.e.*,

$$\mathcal{L}_{\rm full}(\boldsymbol{\vartheta}', \left\{E_{{\rm sh},i}^{\rm rec}, \Omega_i^{\rm rec}\right\}) = e^{-N_\nu^{\rm test}(\boldsymbol{\vartheta}')} \prod_{i=1}^{N_{\rm evts}} \frac{dN_\nu^{\rm test}(\boldsymbol{\vartheta}')}{dE_{\rm sh}^{\rm rec} d\Omega^{\rm rec}}\bigg|_{E_{{\rm sh},i}^{\rm rec}, \Omega_i^{\rm rec}} \,, \tag{10.23}$$

which relies on the full available information on the events, *i.e.*, their joint angular and energy distribution.

In addition, to highlight the role of the angular and energy information in placing bounds, we compute separately analyses that use limited information. An analysis that relies only on angular information uses a likelihood where the event rate is integrated across all reconstructed energies from 10^7 GeV to 10^{10} GeV, *i.e.*,

$$\mathcal{L}_{\rm ang}(\boldsymbol{\vartheta}', \{\Omega_i^{\rm rec}\}) = e^{-N_\nu^{\rm test}(\boldsymbol{\vartheta}')} \prod_{i=1}^{N_{\rm evts}} \left(\int dE_{\rm sh}^{\rm rec} \frac{dN_\nu^{\rm test}(\boldsymbol{\vartheta}')}{dE_{\rm sh}^{\rm rec} d\Omega^{\rm rec}} \right)\bigg|_{\Omega_i^{\rm rec}} \,. \tag{10.24}$$

An analysis that relies only on energy information uses a likelihood where the event rate is all-sky, *i.e.*,

$$\mathcal{L}_{\rm en}(\boldsymbol{\vartheta}', \left\{E_{{\rm sh},i}^{\rm rec}\right\}) = e^{-N_\nu^{\rm test}(\boldsymbol{\vartheta}')} \prod_{i=1}^{N_{\rm evts}} \left(\int d\Omega^{\rm rec} \frac{dN_\nu^{\rm test}(\boldsymbol{\vartheta}')}{dE_{\rm sh}^{\rm rec} d\Omega^{\rm rec}} \right)\bigg|_{E_{{\rm sh},i}^{\rm rec}} \,. \tag{10.25}$$

And, finally, an analysis that relies only on the all-sky number of events of all energies uses

$$\mathcal{L}_{\rm count}(\boldsymbol{\vartheta}') = e^{-N_\nu^{\rm test}(\boldsymbol{\vartheta}')} \left[N_\nu^{\rm test}(\boldsymbol{\vartheta}')\right]^{N_{\rm evts}} \,. \tag{10.26}$$

Like for the DM discovery prospects before, we compute projected bounds on the DM mass and lifetime using an Asimov event sample. In analogy to Eq. 10.14, we average the above

likelihood functions over all possible random realizations of the observed events, sampled from the underlying event distribution due to the non-DM background, $dN_\nu^{\rm true}/dE_{\rm sh}^{\rm rec}d\Omega^{\rm rec}$. This yields the average functions $\langle \ln \mathcal{L}_{\rm full}\rangle$, $\langle \ln \mathcal{L}_{\rm ang}\rangle$, $\langle \ln \mathcal{L}_{\rm en}\rangle$, and $\langle \ln \mathcal{L}_{\rm count}\rangle$. In analogy to Eq. 10.15, we define likelihood functions computed under the background-only hypothesis, *e.g.*,

$$\langle \ln \mathcal{L}_{\rm full,bg}\left(\mathcal{N}'_{\Phi,1},\mathcal{N}'_{\Phi,2},\mathcal{N}'_{\Phi,3}\right)\rangle = \lim_{\tau'_{\rm DM}\to\infty}\langle \ln \mathcal{L}_{\rm full}\left(m'_{\rm DM},\tau'_{\rm DM},\mathcal{N}'_{\Phi,1},\mathcal{N}'_{\Phi,2},\mathcal{N}'_{\Phi,3}\right)\rangle\,, \tag{10.27}$$

where the right-hand side no longer depends on the DM mass and lifetime. Similar expressions apply for the other likelihood functions, *i.e.*, $\langle \mathcal{L}_{\rm ang,bg}\rangle$, $\langle \mathcal{L}_{\rm en,bg}\rangle$, $\langle \mathcal{L}_{\rm count,bg}\rangle$.

To place bounds, we follow Ref. [595] and define a test statistic that compares the true hypothesis—that there is no DM neutrino flux—and test hypothesis—that there is a DM neutrino flux with parameters $m_{\rm DM}$ and $\tau_{\rm DM}$. *E.g.*, for the full analysis,

$$\begin{aligned}\langle \Lambda_{\rm full}(m_{\rm DM},\tau_{\rm DM})\rangle \;=\; & -2\,\min_{\mathcal{N}'_{\Phi,1},\mathcal{N}'_{\Phi,2},\mathcal{N}'_{\Phi,3}} \\ & \times\Big[\langle \ln \mathcal{L}_{\rm full}\left(m_{\rm DM},\tau_{\rm DM},\mathcal{N}'_{\Phi,1},\mathcal{N}'_{\Phi,2},\mathcal{N}'_{\Phi,3}\right)\rangle - \\ & \quad \langle \ln \mathcal{L}_{\rm full,bg}\left(\mathcal{N}'_{\Phi,1},\mathcal{N}'_{\Phi,2},\mathcal{N}'_{\Phi,3}\right)\rangle\Big] \\ & \times\,\Theta\left[\hat{\tau}_{\rm DM}-\tau_{\rm DM}\right]\,,\end{aligned} \tag{10.28}$$

where Θ is the Heaviside function and $\hat{\tau}_{\rm DM}(m_{\rm DM})$ is the value of the DM lifetime that, for a fixed value of the DM mass, $m_{\rm DM}$, maximizes the likelihood function $\langle \ln \mathcal{L}_{\rm full}\rangle$. Similar expressions apply for the other analyses, *i.e.*, $\langle \Lambda_{\rm ang}\rangle$, $\langle \Lambda_{\rm en}\rangle$, $\langle \Lambda_{\rm count}\rangle$. With this definition, under the null hypothesis where neutrinos from DM decay exist, the test statistic should be distributed according to a half-χ^2 distribution with one degree of freedom. Hence, below, we place limits on the DM lifetime at the 2σ C.L. when $\langle \Lambda_{\rm full}\rangle > 2.7$, and similarly for the other analyses.

10.5.3 *Results*

Figure 57 shows the resulting projected bounds on the DM lifetime, obtained by adopting our benchmark medium non-DM UHE neutrino background. We extract two main observations from it.

First, Fig. 57 shows that the existence of a sizable non-DM neutrino background appreciably weakens the bounds, compared to those obtained by plainly demanding that no UHE neutrino

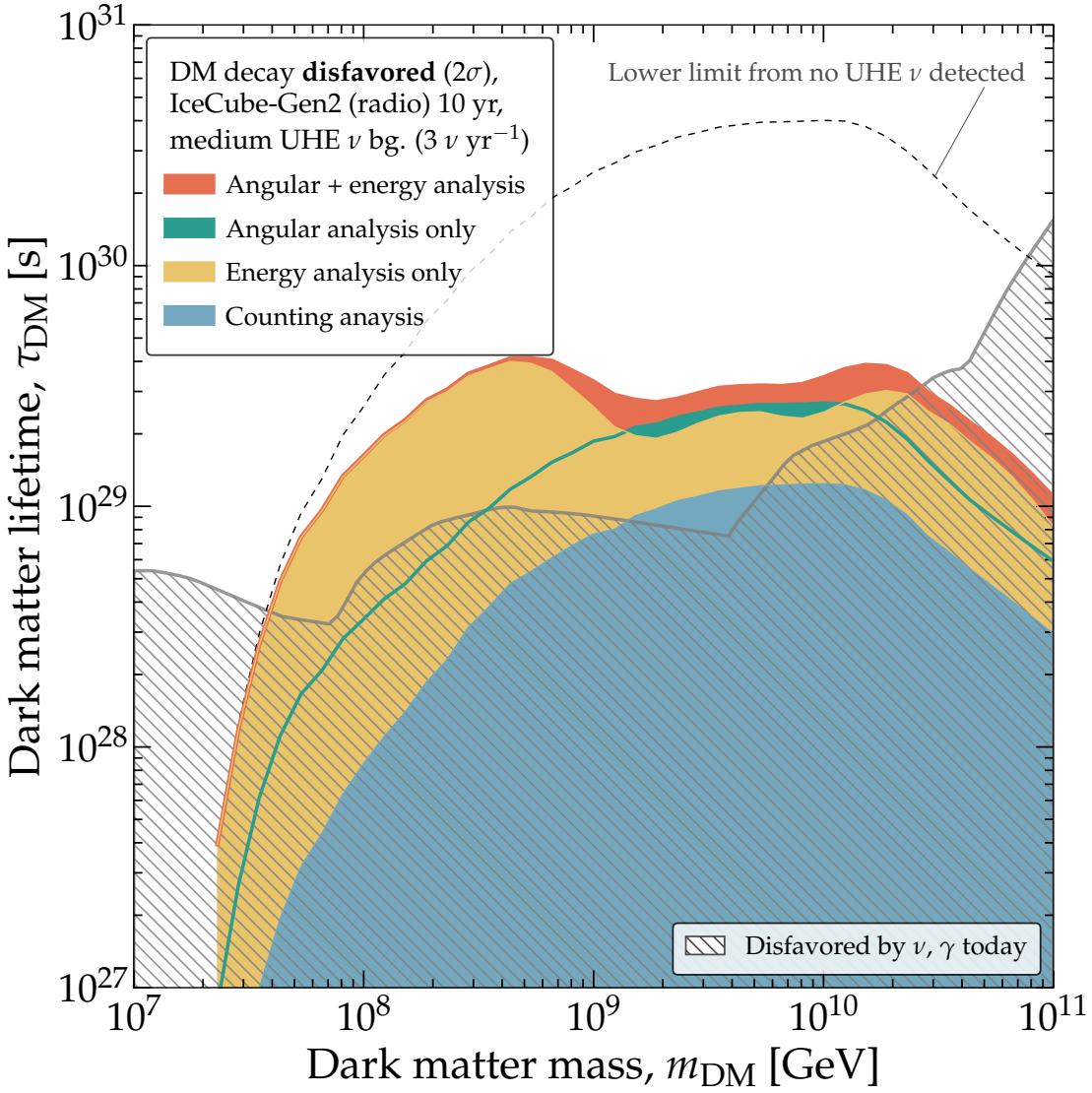

Figure 57: ***Projected lower limits on the DM mass and lifetime from a search for UHE neutrinos in the radio array of IceCube-Gen2.*** The limits are placed in the absence of detection of neutrinos from DM decay, assuming a medium-sized benchmark non-DM isotropic background flux of UHE neutrinos, *i.e.*, 10% of the cosmogenic neutrino flux by Bergman & van Vliet [193]; see Fig. 48. We show bounds obtained using the joint angular and energy distribution of events—our main results—only the angular or only the energy distribution, and only counting the all-sky rate of events of all energies. The bounds obtained using energy information dip between 10^9 and 10^{10} GeV, where our benchmark background neutrino energy spectrum peaks and may mimic the spectrum of neutrinos from DM decay. We adopt baseline choices of the detector angular and (logarithmic) energy resolution, $\sigma_\Omega = 3^\circ$ and $\sigma_\epsilon = 0.1$; see Sec. 10.3.2. For comparison, we show limits obtained if no UHE neutrinos are detected at 2σ. This figure assumes the NFW density profile for Galactic DM. Existing lower limits on the DM lifetime are the same as in Fig. 47. *Even in the presence of a sizable non-DM isotropic background flux of UHE neutrinos, using the angular and energy distributions of events keeps the projected lower limits on DM lifetime comparable to, or better than present-day ones.* See Fig. D2 for results obtained using a large UHE neutrino background. See Sec. 10.5 for details.

is detected, which are representative of most previous analyses in the literature. (In Fig. 57, the null-detection curve also corresponds to a value of the test statistic of 2.7, which implies a mean

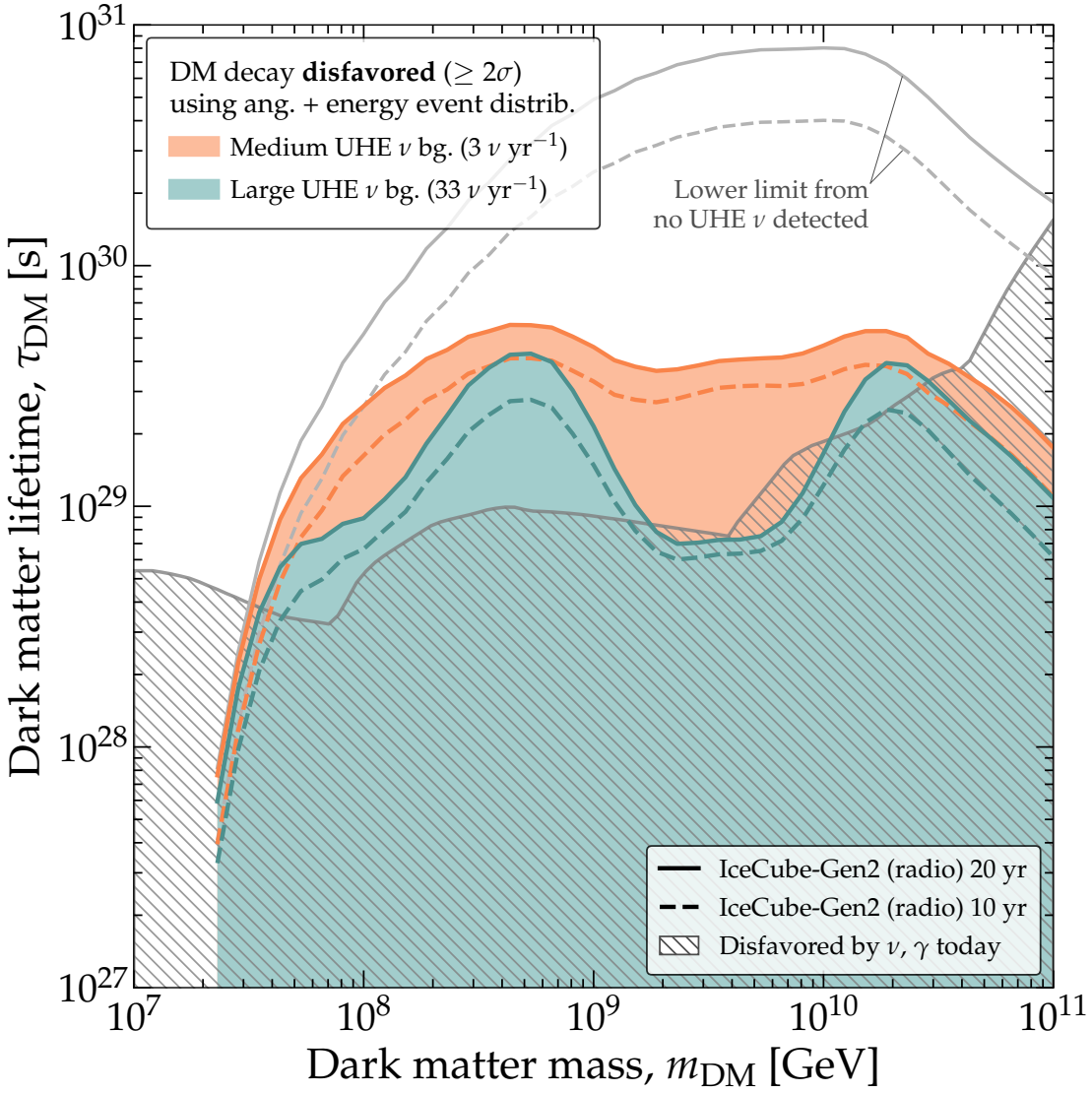

Figure 58: ***Projected lower limits on the DM lifetime for different choices of non-DM UHE neutrino background.*** Same as Fig. 57, but showing only results obtained from the joint angular and energy analysis. We compare results obtained using our medium and large benchmark background isotropic fluxes of non-DM neutrinos (Fig. 48), and using 10 years and 20 years of detector exposure. The limit on DM lifetime is degraded for values of the DM mass that yield neutrino spectra that peak at energies where our benchmark background neutrino spectrum also peaks, *i.e.*, between 10^9 and 10^{10} GeV. This figure assumes the NFW density profile for Galactic DM. *The presence of a sizable non-DM isotropic background flux of UHE neutrinos will degrade the lower limits that can be placed on the DM lifetime, but only within a window of values of the DM mass.* See Sec. 10.5 for details.

number of detected events of 1.35.) Blatantly, when using only a counting analysis, the bounds that we obtain are up to 40 times weaker than bounds obtained from demanding that no neutrino is detected. In reality, how much the bounds are weakened will depend on the actual size and shape of the non-DM background. Still, our results serve as a reminder that projected bounds on the DM lifetime reported in the literature may be optimistic.

Second, Fig. 57 shows that using the angular and energy event distributions mitigates how much the bounds are weakened. Depending on the DM mass, they improve the bounds compared to the counting analysis by a factor of 2–10. This holds even when adopting our benchmark large background instead; see Fig. D2. Overall, using the angular and energy distributions allows projected bounds to remain competitive with present-day ones.

The angular and energy information complement each other. Using the energy distribution strongly improves the bounds at low and high DM masses. In the intermediate region, between 10^9 GeV and 10^{10} GeV, bounds that use energy information weaken because this is where our benchmark background neutrino spectrum peaks (Fig. 48) and where it may be misconstrued as being due to DM decay; see the discussion in Sec. 10.5.2. This is counteracted by using angular information: in the 10^9–10^{10} GeV range, where the detector response is largest (see Fig. 13 in Ref. [346]), the isotropic neutrino background induces a number of events large enough for the analysis to reject an excess towards the GC from DM decay. Figure 57 shows the result of this interplay for our particular choice of non-DM background; in reality, the specifics will depend on the actual size and shape of the background.

Figure 58 shows that using our large benchmark non-DM UHE neutrino background instead—ten times larger than the medium one—weakens the bounds by only a factor of roughly 2, except in the range 10^9–10^{10} GeV, where the bounds weaken by a factor of up to 6, but even so remain roughly competitive with present-day ones. This represents promising prospects: ***the background flux we use here [193] is as large as allowed by the present-day IceCube [66] and Auger [67] upper limits. Yet, even with this aggressive choice of background, our projected bounds in Fig. 58 remain comparable or better than present-day ones.***

Figure 59 shows that, naturally, the bounds degrade when using the Burkert Galactic DM profile instead of the NFW profile. Because the Burkert profile is puffier, the bounds derived from the analysis of the angular distribution of events are weakened, so most of the limit-setting power comes from the energy distribution of events instead; see also Fig. D4. Still, the energy analysis sets bounds using the Burkert profile that are only a factor-of-2 worse than using the NFW profile. Thus, given our extant imperfect knowledge of the Galactic DM profile—in particular,

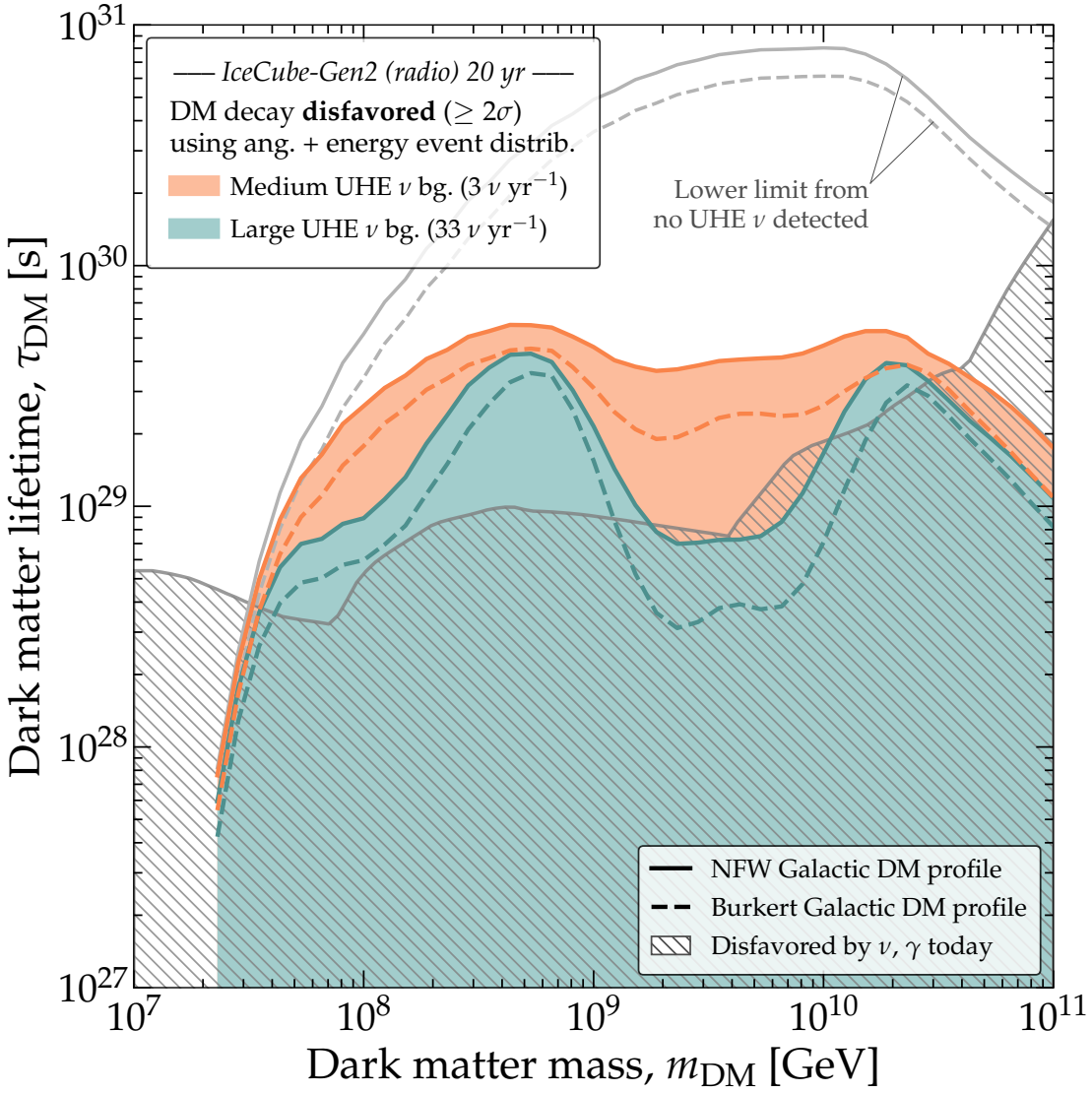

Figure 59: ***Projected lower limits on the DM lifetime for NFW vs. Burkert Galactic DM profiles.*** Same as Fig. 58, but comparing results obtained using the NFW *vs.* Burkert Galactic DM density profiles (see Fig. 49). In this figure, results are for discovery at $\geq 2\sigma$ after 20 years; see Fig. D4 for more results using the Burkert profile. *If the Galactic DM profile is "puffy", like the Burkert profile, bounds weaken by a factor of roughly 2, compared to a "cuspy" DM profile, like NFW.* See Sec. 10.5 for details.

given the possibility of a puffy DM profile—leveraging the interplay between energy and angular information is key.

10.6 SUMMARY AND OUTLOOK

In the next decade, ultra-high-energy (UHE) neutrino telescopes, presently in planning, will deliver a new way to look for heavy dark matter (DM), with masses in excess of 10^7 GeV, via its decay

into UHE neutrinos, with energies in excess of 10^7 GeV. To properly harness this potential, it is critical to disentangle the signatures of UHE neutrinos of DM decay origin from the signatures of UHE neutrinos of astrophysical and cosmogenic origin—long-sought but still undiscovered—that act as a background to DM searches. Failure to do so may incur in steep misrepresentation when claiming discovery of DM decay, inferring the DM mass and lifetime in the event of discovery, or setting bounds on the DM mass and lifetime otherwise. The task is complicated by the fact that the size and shape of the non-DM neutrino background is unknown, that the number of detected events may be small, and that the direction- and energy-measurement capabilities of the detectors are limited.

Even so, we have shown, by means of detailed forecasts, that these obstacles are surmountable. Key to that is to examine the energy and angular distributions of the detected UHE neutrinos. They grant us access to the essential differences between the diffuse neutrino fluxes from DM decay and from the non-DM background: in energy, the former is concentrated around the DM mass, while the latter is more spread out (Fig. 48), and, in direction, the former is concentrated around the Galactic Center (GC)—where DM is abundant—while the latter is isotropic (Fig. 50). In our forecasts, we look for these differences in projected observations.

We have geared our forecasts to the radio-detection of UHE neutrinos in the envisioned IceCube-Gen2 neutrino telescope, which we simulate using state-of-the-art methods, including experimental nuance that dull the above differences between the fluxes. Our findings are promising: these differences survive an analysis under realistic experimental conditions (Figs. 51, 52). ***Therefore, while the existence of a non-DM UHE neutrino background, even the largest presently allowed, weakens claims of discovery of DM decay or bounds on it, it does not necessarily preclude them.*** Still, the limit-setting potential and, particularly, the discovery potential, are contingent to the Galactic DM profile peaking markedly towards the GC (Figs. 54 and 59).

Regarding the discovery of DM decay, we have shown that DM with mass between 10^8 GeV and 10^{10} GeV and lifetime of roughly 10^{29} s should be discoverable after 10 years of operation of the radio array of IceCube-Gen2, even in the presence of a medium-sized non-DM neutrino background that yields about 3 events per year (Fig. 53). This is conservatively achieved using only the angular distribution of detected events. Under a larger background, of about 33 events

per year, discovery becomes unfeasible in the face of existing bounds on the DM lifetime. Our discovery forecasts depend only mildly on the shape of the energy spectrum of the non-DM neutrino background—whose size we let float in our analyses—and depend mainly on the total number of events.

In the event of discovery, the DM mass and lifetime could be measured with reasonable accuracy and precision (Fig. 55), depending on their true values, and the flux of UHE neutrinos from DM decay could be similarly inferred (Fig. 56). Importantly, this result is robust: when inferring the values of the DM parameters—and also when setting bounds on them (see below)—we analyze the simulated event samples *without* assuming knowledge of the shape and size of the energy spectrum of the non-DM neutrino background.

If discovery is not possible, we will be able to place lower limits on the DM lifetime, which we forecast. Using the joint angular and energy distribution of events allows us to constrain the presence of bump-like energy spectra and excesses towards the Galactic Center even under challenging, but plausible scenarios where the energy spectrum of the non-DM neutrino background is medium-sized and whose bump-like energy spectrum inconveniently resembles that of neutrinos from DM decay (Fig. 57). Even in the presence of a large bump-like non-DM background, using the energy distribution of events safeguards the limits on the DM lifetime for DM masses sufficiently far from the peak of the non-DM flux (Fig. 58). Overall, we forecast lower limits on the DM lifetime that are comparable to, or better than, existing limits from gamma rays and TeV–PeV neutrinos.

While our forecasts are geared to the detection of UHE neutrinos in the radio array of IceCube-Gen2, our conclusions apply generally to planned neutrino telescopes of comparable size, radio-based and otherwise, and our methods can be readily adapted to them. In particular, detectors with an envisioned high angular resolution, like GRAND, could be better at discovering or discriminating against an excess of events towards the GC [567].

It seems that, fortunately, the potential of next-generation UHE neutrino telescopes to probe heavy DM decay may be safeguarded against sizable unknown neutrino backgrounds.

10.7 CRITICAL OUTLOOK

This section analyzes the key findings and limitations of this study. It also provides insights into the future perspectives and potential advancements in the search for dark matter signatures.

10.7.1 *Overview and main findings*

Our research identified promising paths for the detection and study of heavy dark matter through its potential decay into ultra-high-energy neutrinos. Through detailed forecasts and simulations, we demonstrated that the challenges posed by an unknown background of non-DM UHE neutrinos can be surmountable, and the prospects for discovery and measurement of dark matter properties are encouraging.

The key findings of this study include:

- The ability to discover dark matter decay for masses between 10^8 GeV and 10^{10} GeV and lifetimes around 10^{29} s with the radio array of IceCube-Gen2, even in the presence of a medium-sized non-DM neutrino background.
- The feasibility of measuring the dark matter mass, lifetime, and UHE neutrino flux in the event of discovery, providing valuable insights into the nature of DM particles.
- The robustness of lower limits on the DM lifetime, which remain competitive with existing limits even when faced with challenging scenarios involving a significant non-DM neutrino background.

10.7.2 *Limitations and future perspective*

Some aspects and challenges deserve attention in future research on this topic:

- *Characterization of Non-DM Neutrino Background:* It is essential to continue efforts to refine our understanding of the non-DM UHE neutrino background. This involves improving our

knowledge of its energy spectrum and spatial distribution. More precise measurements of astrophysical sources and cosmic ray interactions could contribute to this characterization.

- *Galactic DM Profile:* The sensitivity of DM detection and lower limit setting depends significantly on the assumed Galactic DM profile. Future studies should explore the implications of different DM density profiles, considering both the NFW and Burkert profiles as this study does, to account for uncertainties in this aspect.

- *Angular Resolution:* As detector technologies advance, the angular resolution of UHE neutrino telescopes may improve. Investigating how an improved angular resolution impacts the discrimination between DM decay signals and non-DM backgrounds is an avenue for future exploration.

- *Energy Calibration and Spectrum:* Ongoing advancements in energy calibration and the ability to reconstruct neutrino energy spectra accurately will be critical for disentangling the energy distributions of DM and non-DM neutrinos effectively.

- *Different Neutrino Detection Techniques:* While this research focuses on radio-detection in IceCube-Gen2, exploring the capabilities and limitations of other detection techniques and proposed neutrino telescopes (e.g., GRAND) is vital for a comprehensive assessment of the field.

- *Statistical Methods:* Development and refinement of statistical methods for robustly distinguishing DM signals from backgrounds will be essential. Exploring Bayesian techniques, machine learning approaches, and refined likelihood analyses can enhance sensitivity.

In summary, this work provides a strong foundation for the pursuit of DM detection via UHE neutrinos. Addressing these critical aspects and challenges will further advance the field, enabling more robust and sensitive searches for heavy DM decay in the coming years.

Part IV

SUMMARY AND CONCLUSIONS

11

CONCLUSION

We have explored the transformative potential of UHE neutrinos. This work was motivated by the near-future availability of UHE neutrino telescopes with realistic discovery prospects in the next 10–20 years. Our research journey has taken us through a series of investigations, each contributing to our understanding in the fields of particle physics and neutrino astronomy. In this concluding chapter, we summarize the key findings and overarching contributions of this work.

11.1 SUMMARY OF KEY FINDINGS

11.1.1 *Discovering the first EeV neutrinos*

In Chapter 7, we embarked on a comprehensive exploration of the physics opportunities presented by UHE neutrinos, in particular in the energy range between 10 PeV to 10 EeV. By leveraging state-of-the-art simulations and detailed theoretical treatment, we provided insights into the potential discovery of a diffuse flux of UHE neutrinos within the next 10–20 years. Our findings underscored the transformative potential of next-generation UHE neutrino telescopes, with encouraging prospects for discovering benchmark UHE neutrino flux models, even under conservative analysis choices.

This detailed investigation identified some key features as the most relevant for optimizing the discovery prospects of an UHE neutrino flux within one decade of exposure. The key findings from this research included:

- The importance of characterizing the UHE tail of the astrophysical neutrino flux.
- The impact of energy and angular resolution on UHE neutrino flux discovery potential.

- The significance of Earth-skimming neutrinos in breaking degeneracies in flux and cross-section measurements.
- The limited effect of atmospheric muon background on discovery potential due to its spectral shape and localization.

Our work in Chapter 7 laid a robust foundation for advancing astroparticle physics and encouraged collaboration among experimental scientists to adopt our methods for future discoveries.

11.1.2 *UHE Neutrino Spectrum and Neutrino-Nucleon Cross Section Measurement*

Chapters 6 and 8 presented our efforts in pursuing a joint measurement of the UHE neutrino spectrum and neutrino-nucleon cross section. Chapter 6 presented a relatively simple parametrization of the neutrino flux and the cross section that was only sensitive to energy-independent deviations.It was this study that allowed us to build the foundations of the numerical and computational tools that were later exploited for more complex analyses. Furthermore, the results in Ch. 6, together with those in Ch. 7, motivated us to pursue a more ambitious goal: a simultaneous reconstruction of the UHE neutrino flux and energy-dependent νN cross section with little implicit theory bias in the flux and cross-section models.

Chapter 8 explored various neutrino flux parametrizations and their impact on the precision and accuracy of measurements. Notably, we introduced the PCHIP model as a preferred flux model, capable of reconstructing any neutrino flux spectral shape with a balance of precision and accuracy. We showcase its capabilities by comparing its performance to that of simpler parametrizations, such as simple power-law, commonly used in the PeV–TeV energy range.

The key findings of this venture can be summarized in the following:

- The demonstration of the potential of UHE neutrinos to unlock a new frontier for particle physics explorations.
- The identification of the PCHIP model as a versatile and accurate flux parametrization.
- Recommendations for optimizing detector designs and the potential benefits of combining optical and radio arrays.

Our research in Chapters 6 and 8 highlighted the importance of refining flux models, optimizing detector configurations, and exploring synergies between detector components for precise UHE neutrino measurements.

11.1.3 *Search for Sources of UHE Neutrinos*

Chapter 9 undertook the task of forecasting the discovery of point sources of UHE neutrinos. This goal is closely connected with the central ambition in astroparticle physics of finding the sources of UHECRs. By looking for multiplets of UHE neutrinos arriving from similar directions, we aimed to identify potential point sources. Our research offered valuable insights into the constraints on steady-state and transient source classes.

The key contributions and findings in Ch. 9 include:

- The identification of promising candidate source classes, ranging from active galactic nuclei to hypernovae.
- The use of the projected discovery of multiplets, or lack thereof, to place constraints on the properties of populations of UHE neutrino sources.
- Recommendations for future UHE neutrino telescopes, including target angular resolution.

Chapter 9 provided the first search for UHE neutrino point sources based on realistic detector detail, establishing a solid foundation for these kind of searches in the near future once multiple UHE neutrino telescope come online.

11.1.4 *Physics Opportunities with Ultrahigh-Energy Neutrinos*

Chapter 10 ventured into the realm of dark matter. It provided the first forecast for the detection of DM decaying into UHE neutrinos that uses detailed, realistic experimental capabilities. This chapter addressed the challenges posed to the discovery of heavy dark matter by an unknown background of non-DM UHE neutrinos and demonstrated the feasibility of detecting DM decay signatures over this background. We found enouraging for discovering DM decay, measuring

DM mass and lifetime, and setting limits on DM lifetime. This study on the connection between UHE neutrinos and dark matter is representative of the potential of UHE neutrinos for hunting for evidence of physics beyond the Standard Model..

The list of key findings from this study include:

- The ability to discover DM decay for a range of masses and lifetimes despite the presence of a non-DM neutrino background.
- The feasibility of measuring the DM mass and lifetime, providing insights into the nature of DM particles.

Chapter 10 laid the groundwork for the robust pursuit of DM detection via UHE neutrinos and highlighted areas for future research.

11.2 CLOSING REMARKS

In conclusion, our journey through the world of ultrahigh-energy neutrinos and their potential for astrophysical discoveries has been both enlightening and challenging. Our work has made significant strides in understanding the prospects of discovering the UHE neutrino flux, UHE neutrino source searches, and the pursuit of dark matter detection.

As we peer into the future, the mysteries of the high-energy Universe beckon us to continue our exploration. With advancements in technology and through interdisciplinary research, we are poised to unlock even more profound insights with the collective efforts of researchers from diverse fields.

The path ahead is filled with exciting possibilities, and the knowledge gained from this thesis will serve as a solid foundation for future endeavors in the evolving field of astroparticle physics.

Part V

APPENDICES

A

APPENDIX: UHE νN CROSS SECTION MEASUREMENTS

A.1 POSTERIOR DISTRIBUTIONS FOR ALL BENCHMARK UHE NEUTRINO FLUX MODELS

In the main text we used twelve benchmark UHE neutrino flux models to make our forecasts of cross-section measurements; see Section 6.4. For all of them, we showed expected shower rates in IceCube-Gen2 in Table 1 and one-dimensional marginalized posteriors of f_σ and f_Φ in Table 2, but we showed two-dimensional posteriors of f_σ and f_Φ only for four of them, models 2, 4, 6, and 7, in 20.

Figure A1 shows the two-dimensional posteriors of f_σ and f_Φ for all benchmark flux models, for the same baseline detector parameters as in 20. From top to bottom and left to right, results are arranged in order of increasing sensitivity, from the most pessimistic to the most optimistic scenarios.

Figure A2 shows the corresponding one-dimensional marginalized posteriors of f_σ and f_Φ. The 68% C.L. ranges in this figure match those shown in Table 2.

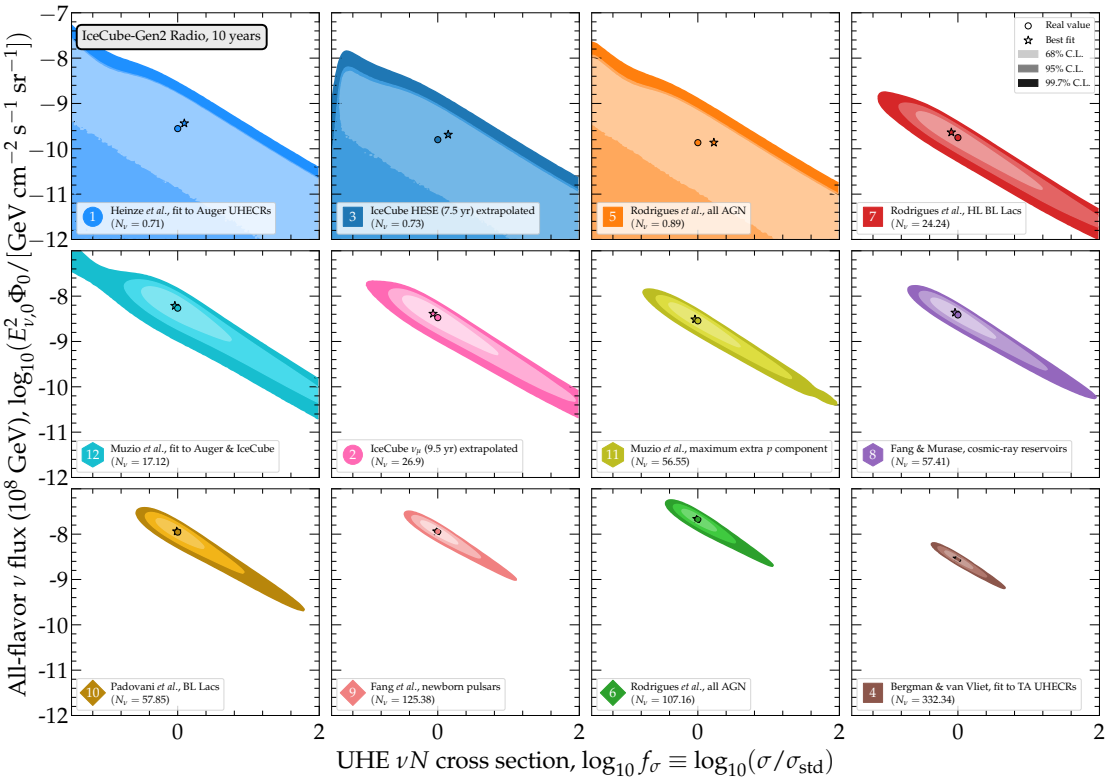

Figure A1: Same as 20 in the main text, but for all the benchmark UHE neutrino flux models adopted in our analysis; see Section 6.4.

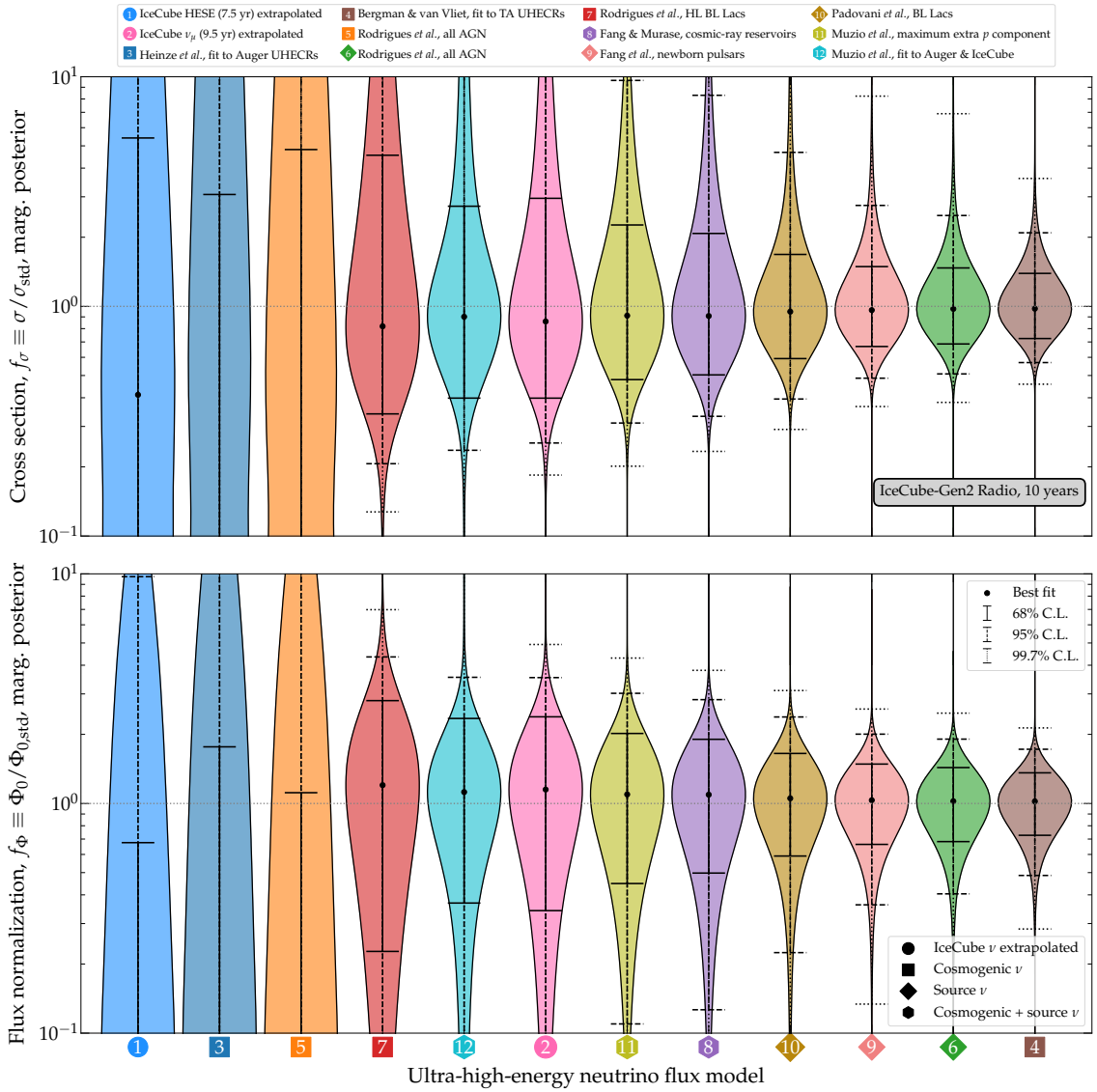

Figure A2: One-dimensional marginalized posteriors of the UHE νN cross section, f_σ, and the UHE neutrino flux normalization, f_Φ, for all the benchmark UHE neutrino flux models adopted in our analysis. See A1 for the corresponding two-dimensional posteriors and Table 2 for numerical values.

B

APPENDIX: UHE NEUTRINO FLUX DISCOVERY

B.1 IMPACT OF THE BACKGROUND UHE TAIL OF THE ICECUBE HIGH-ENERGY NEUTRINO FLUX ON ALL UHE NEUTRINO FLUX MODELS

Figure 31 in the main text showed, for benchmark UHE neutrino flux models 6 and 7 [179], the impact on the flux discovery potential of using our three choices of background UHE tail of the IceCube high-energy neutrino flux: hard-spectrum—our conservative baseline choice—intermediate, and soft-spectrum. See Section 7.4.5.2 for details.

Figure B1 extends the result to all flux models 3–12. The same conclusions as in Section 7.5.2.4 hold: using a softer background UHE tail of the IceCube high-energy neutrino flux may expedite flux discovery significantly. However, UHE neutrino flux models with meager event rates, like flux models 3 and 5 (see Table 3) remain undiscoverable regardless of the choice of background.

Figure 38 in the main text showed, for all benchmark UHE neutrino flux models, the confusion matrix representing the degree of separation between models achievable, after 1, 3, and 10 years of detector exposure. Those results were computed under our baseline choice of a hard-spectrum UHE tail of the IceCube high-energy neutrino flux.

Figure B2 shows the confusion matrix computed using also the intermediate- and soft-spectrum choices of the UHE tail of the IceCube high-energy neutrino flux, for a fixed exposure time of 3 years. Using a softer background appreciably improves the separation between UHE neutrino flux models 3–12, since it allows the features of their event energy distributions to be resolved more cleanly.

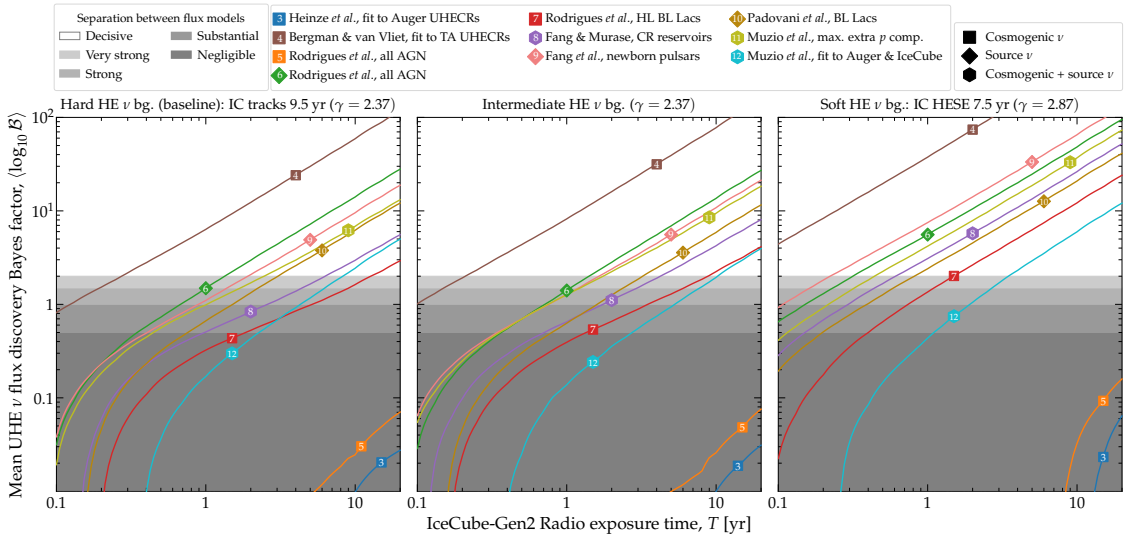

Figure B1: Discovery potential of benchmark UHE neutrino flux models 3–12 [174–180, 193] (see Fig. 26) in the radio array of IceCube-Gen2, for three different choices of the background UHE tail of the IceCube high-energy neutrino flux; see Section 7.4.5.2. All other analysis choices are baseline and conservative; see Table 4 and Section 7.5.2.1. UHE neutrino flux models 1 [188] and 2 [37]—the UHE extrapolation of the IceCube high-energy neutrino flux—are not included in this figure because in their analysis the sole background is from atmospheric muons; see Section 7.5.2.9. *Left:* Baseline choice of a hard-spectrum background, with spectral index $\gamma = 2.37$, motivated by the IceCube 9.5-year through-going ν_μ analysis [37]. Results match Fig. 25 in the main text. *Center:* Intermediate background, with the same normalization, but $\gamma = 2.50$. *Right:* Soft-spectrum background, with $\gamma = 2.87$, motivated by the IceCube 7.5-year HESE analysis [188]. See Appendix B.1 and Section 7.5.2.4 for details.

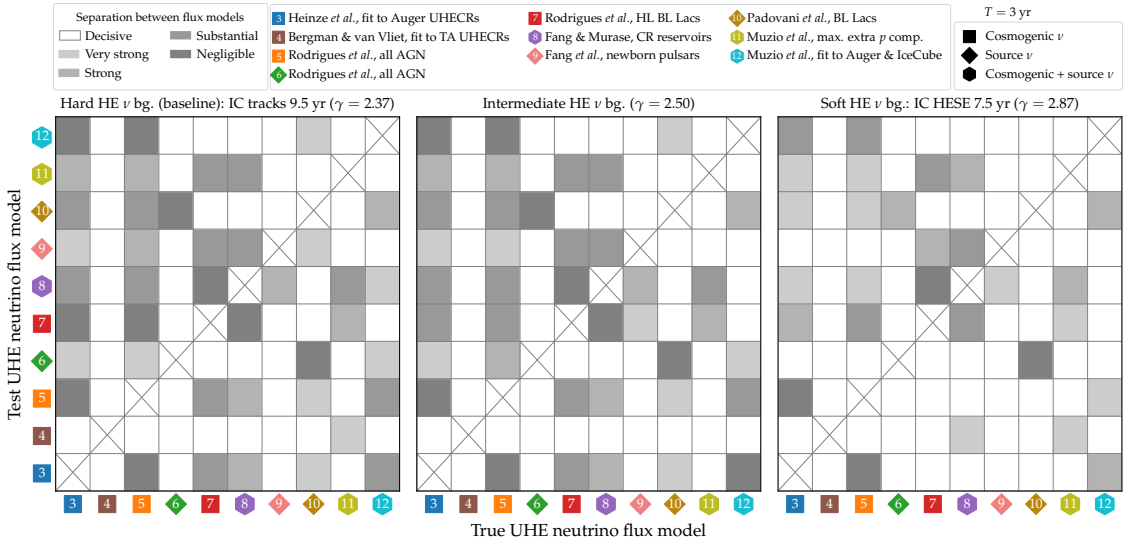

Figure B2: Confusion matrix showing the experimental separation between true and test UHE neutrino flux models 3–12 (see Fig. 26) in the radio array of IceCube-Gen2, after $T = 3$ years of detector exposure, computed using the same three choices for the background UHE tail of the IceCube high-energy neutrino flux as in Fig. B1; see Section 7.4.5.2. All other analysis choices are baseline and conservative; see Table 4 and Section 7.5.2.1. *Left:* Baseline choice of a hard-spectrum background. Results match Fig. 38 in the main text. *Center:* Intermediate background. *Right:* Soft-spectrum background. See Appendix B.1 and Section 7.6.2 for details.

B.2 IMPACT OF THE DETECTOR ANGULAR AND ENERGY RESOLUTION ON ALL UHE NEUTRINO FLUX MODELS

Figure 34 in the main text showed, for benchmark UHE neutrino flux model 6, the impact on the flux discovery potential of alternative choices of the detector energy and angular resolution. In connection to Fig. 34, in Section 7.5.2.7 we found that poorer energy resolution hinders flux discovery by diluting the features of the event energy spectrum and poorer angular resolution, by preserving the innate degeneracy between the UHE neutrino flux and cross section (see Section 7.3). Here we extend these results to all the benchmark UHE neutrino flux models 1–12. As for Fig. 34, when changing the energy and angular resolution, we change the size of the bins of reconstructed shower energy and reconstructed zenith angle commensurately; see Section 7.5.2.7.

Figures B3 and B4 show, respectively, the flux discovery potential for detector energy resolution of $\sigma_\epsilon = 0.1$ (our baseline choice), 0.5, and 1.0, and for detector angular resolution of $\sigma_{\theta_z} = 2^\circ$ (our baseline choice), 5°, and 10°, for the benchmark UHE neutrino flux models 3–12. The results are similar as for flux model 6 in Fig. 34.

Figures B6 and B5 show the confusion matrix representing flux model separation, after 3 years of detector exposure, for the same choices of detector angular and energy resolution, respectively, as Figs. B4 and B3. Since most of the power to separate between flux models comes from resolving the differences between their event energy distributions, model separation is affected more severely by poorer energy resolution than by poorer angular resolution.

Figure B4 shows a subtle feature: for some flux models, notably, for flux model 1, poorer angular resolution improves the discovery potential, which seems counter-intuitive. The reasons behind this behavior expose limitations associated to using a binned likelihood to compute the flux discovery potential (Section 7.5.1). In our prescription, the event rates of low UHE neutrino fluxes, like flux model 1, that predict fewer than one event in a decade of detector exposure (Table 3), are plagued by a large number of unpopulated event-rate bins in many of the random realizations of their mock observed event rates that we use to compute the mean discovery Bayes factor (Section 7.5.1). (High UHE neutrino fluxes are unaffected because they do not have unpopulated event bins.) When using poorer detector resolution in our forecasts, as in Fig. B4, our prescription

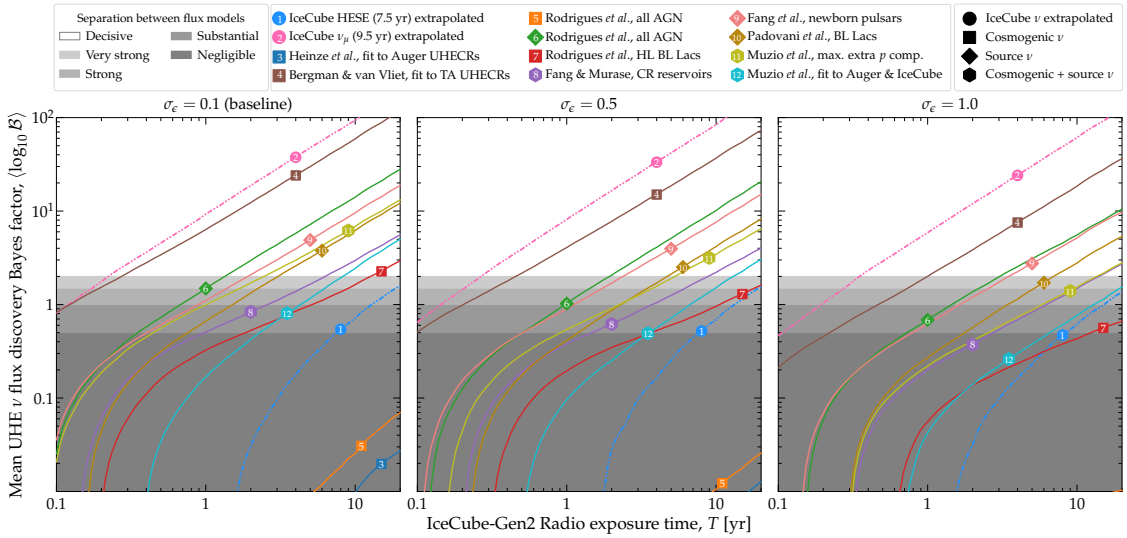

Figure B3: Impact of the resolution of the radio array of IceCube-Gen2 in measuring the reconstructed energy, $\sigma_\epsilon = 0.1$ (*left*, our baseline choice), 0.5 (*center*), and 1.0 (*right*), on the flux discovery potential of UHE neutrino flux models 1–12. All other analysis choices are baseline; see Table 4 and Section 7.5.2.1. See Appendix B.2 and Section 7.5.2.7 for details.

changes to using coarser event bins (Section 7.5.2.7). This reduces the number of unpopulated bins by merging formerly unpopulated with populated bins and this, in turn, improves the flux discovery potential of the low UHE neutrino flux models, as seen in Fig. B4 for flux model 1.

Figure B3 shows that, in contrast, when using poorer energy resolution the discovery potential of flux model 1 remains unchanged. There are two competing effects responsible for this. On the one hand, like with poorer angular resolution, using a poorer energy resolution induces coarser binning and improves discovery prospects. On the other hand, unlike with poorer angular resolution, using poorer energy resolution reduces the integrated event rate due to some events leaking out of the energy range of interest to our analysis, $E_{\text{sh}}^{\text{rec}} = 10^7$–$10^{10}$ GeV, on account of broader Gaussian energy resolution function; see Eq. (15) in Ref. [346]. These two effects balance each other out, leaving the discovery potential of flux model 1 unchanged.

Evidently, the above features are not physical, but rather limitations that stem from using a binned likelihood for scenarios of low event rates. In revised versions of our analysis [336], these limitations will be overcome by switching to an unbinned likelihood analysis.

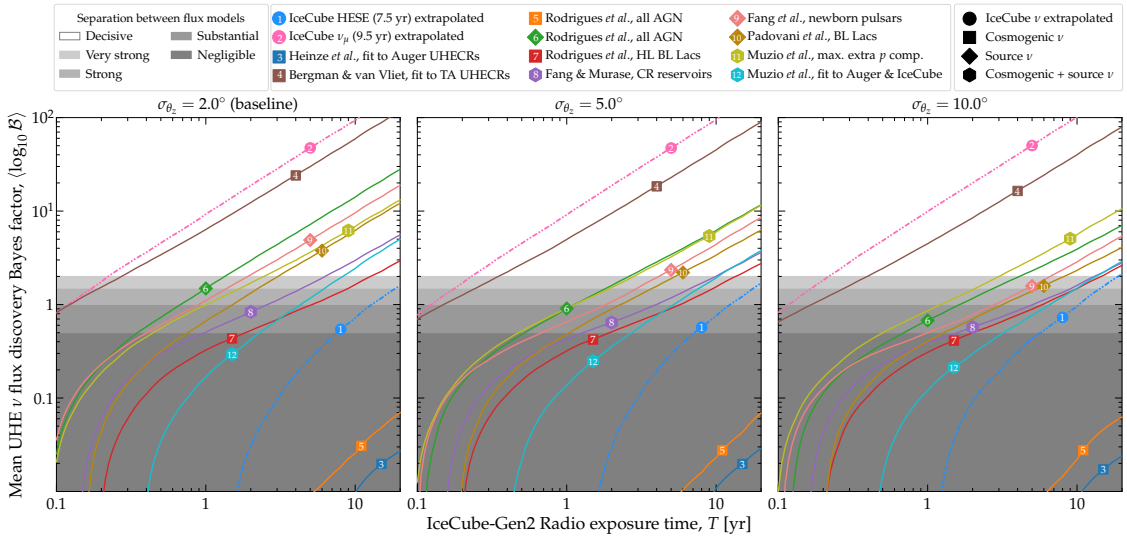

Figure B4: Impact of the resolution of the radio array of IceCube-Gen2 in measuring the reconstructed zenith angle, $\sigma_{\theta_z} = 2°$ (*left*, our baseline choice), 5° (*center*), and 10° (*right*), on the flux discovery potential of UHE neutrino flux models 1–12. All other analysis choices are baseline; see Table 4 and Section 7.5.2.1. See Appendix B.2 and Section 7.5.2.7 for details.

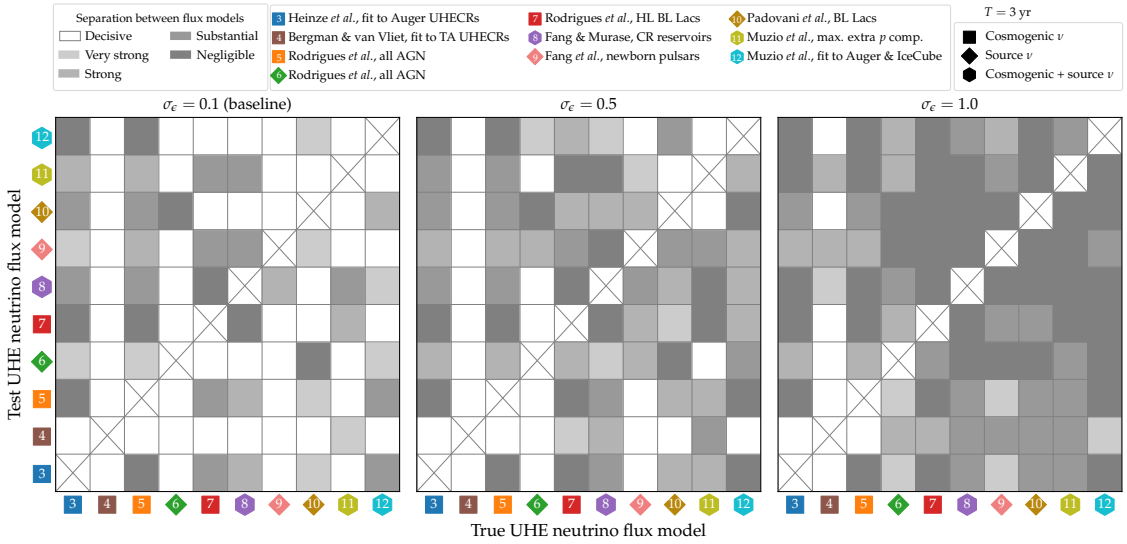

Figure B5: Impact of the resolution of the radio array of IceCube-Gen2 in measuring the reconstructed energy, $\sigma_\epsilon = 0.1$ (*left*, our baseline choice), 0.5 (*center*), and 1.0 (*right*), on the confusion matrix that represents the separation between true and test UHE neutrino flux models 3–12, after $T = 3$ years of detector exposure. All other analysis choices are baseline; see Table 4 and Section 7.5.2.1. The left panel coincides with Fig. 38 in the main text. See Appendix B.2 and Section 7.6 for details.

B.3 IMPACT OF THE SURFACE VETO ON THE FLUX DISCOVERY POTENTIAL

Section 7.5.2.3 found that increasing the normalization of the background of atmospheric muons has little impact on the flux discovery potential. (The same may not be true of changing the energy spectrum of the background.) Our baseline analysis choice for the atmospheric muon background

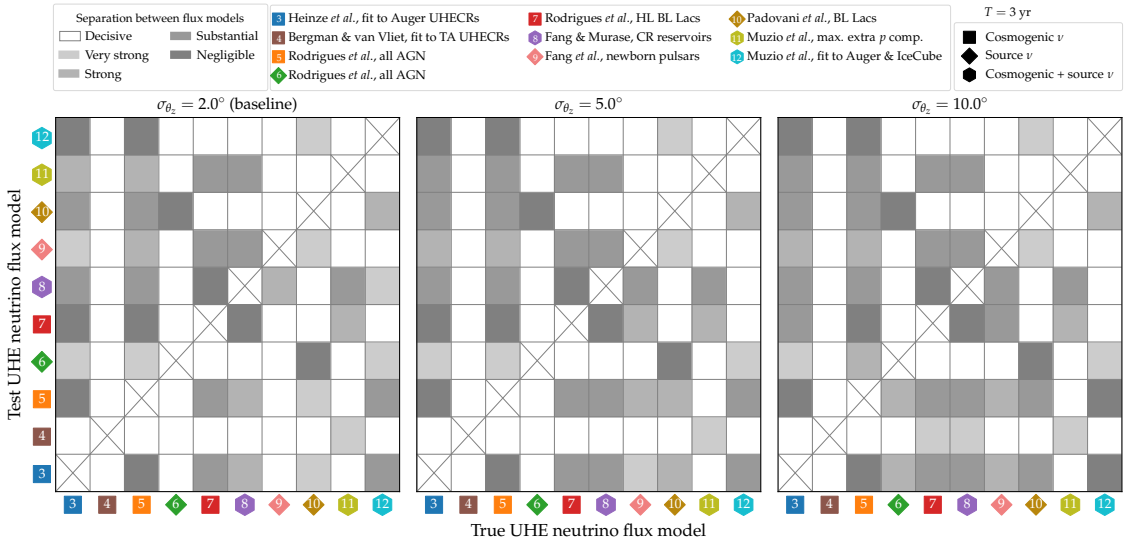

Figure B6: Impact of the resolution of the radio array of IceCube-Gen2 in measuring the reconstructed zenith angle, $\sigma_{\theta_z} = 2^\circ$ (*left*, our baseline choice), 5° (*center*), and 10° (*right*), on the confusion matrix that represents the separation between true and test UHE neutrino flux models 3–12, after $T = 3$ years of detector exposure. All other analysis choices are baseline; see Table 4 and Section 7.5.2.1. The left panel coincides with Fig. 38 in the main text. See Appendix B.2 and Section 7.6 for details.

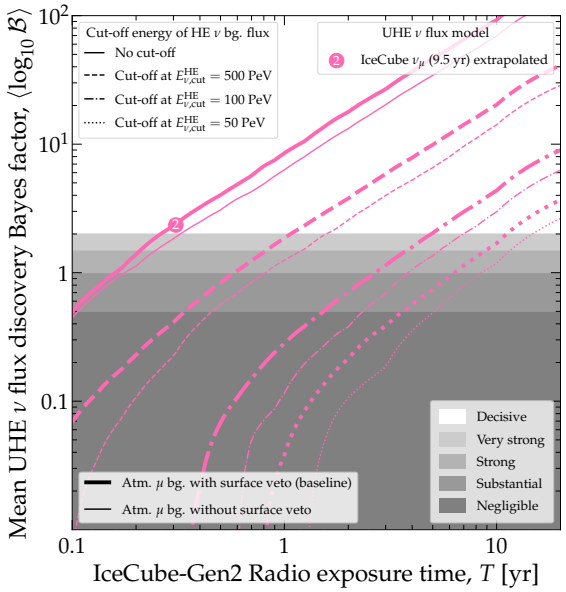

Figure B7: Same as Fig. 37 in the main text, for UHE neutrino flux model 2 [37] only, but showing the impact of using the veto of air-shower surface detectors to mitigate the background of atmospheric muons. All other analysis choices are baseline and conservative; see Table 4 and Section 7.5.2.1. See Appendix B.3 for details.

includes applying a veto from air-shower surface detectors to mitigate it, following Ref. [77]; see Section 7.4.5.1 for details. Removing the surface veto increases the background rate, especially at high energies, though not greatly; see Fig. 15 in Ref. [346]. Here we study the impact of the surface veto on our results; we focus on its impact on the discovery of flux model 2 [37], for which the only background is from atmospheric muons.

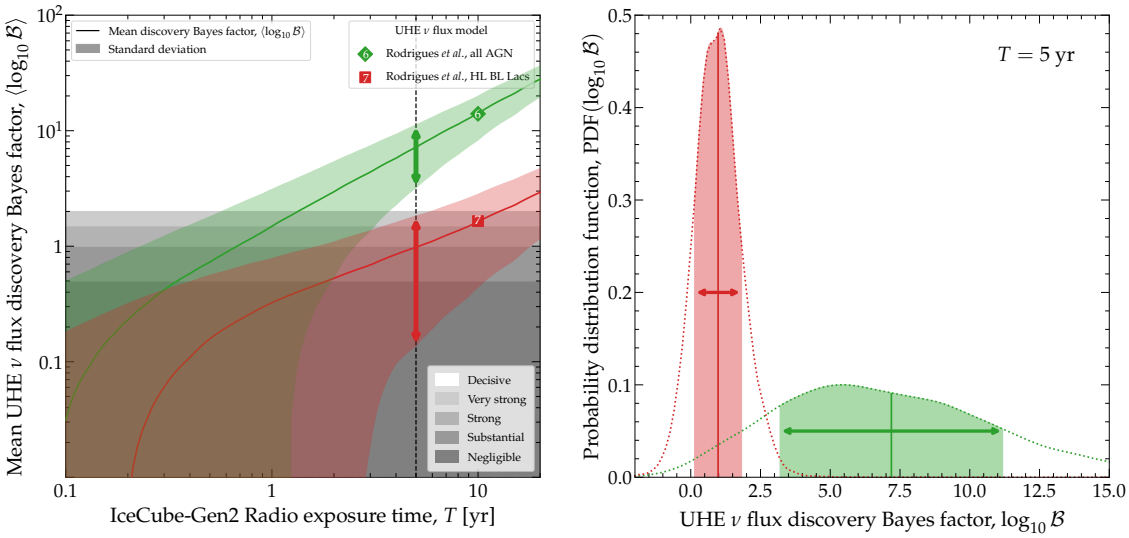

Figure B8: Mean and standard deviation of the discovery Bayes factor of benchmark UHE neutrino flux models 6 and 7 [179] (see Fig. 26). The mean is computed using Eq. (7.21); the standard deviation is built from many random realizations of the observed event rate in the radio array of IceCube-Gen2. *Left:* Evolution of the mean and standard deviation with detector exposure time. *Right:* Probability distribution functions of the Bayes factor after $T = 5$ years of detector exposure. See Appendix B.4 and Section 7.5.1 for details.

Figure B7 shows that switching off the surface veto shifts the discovery Bayes factor to longer exposure times. This delays the discovery of flux model 2, but only slightly. This weak impact is expected, since flux model 2—and our other benchmark UHE neutrino flux models (Section 7.2)—reach higher energies than the atmospheric muon background, even without the surface veto, and so can be clearly separated from it; see Fig. 27 and Fig. 15 in Ref. [346].

Thus, the discovery of flux model 2 with a high cut-off energy is only delayed by a few months, since in that case events induced by it reach $E_{\mathrm{sh}}^{\mathrm{rec}} \gg 10^8$ GeV, far from the atmospheric muon background that is concentrated at $E_{\mathrm{sh}}^{\mathrm{rec}} \lesssim 10^8$ GeV. The discovery of flux model 2 with a low cut-off energy is delayed longer; at worst, by a handful of years, for $E_{\nu,\mathrm{cut}}^{\mathrm{HE}} = 50$ PeV. Other UHE neutrino flux models with meager associated event rates, like flux models 1, 3, and 5, remain undiscoverable even if the surface veto is switched off. Overall, these results suggest that the surface veto, while helpful, might not be determinant for UHE neutrino flux discovery (barring a change in the atmospheric muon background that stretches it to higher energies; see Section 7.5.2.3).

B.4 STATISTICAL SIGNIFICANCE OF THE MEAN BAYES FACTOR

In the main text and other appendices, we reported our results in terms of the mean Bayes factor, Eq. (7.21), averaged over $N_{\text{samples}} = 10^4$ random realizations of the observed event rate, following the prescription in Section 7.5.1. Here, we examine the distribution of values of the discovery Bayes factor obtained in those random realizations, in order to assess how representative the mean value is of the underlying distribution.

Figure B8 shows the mean value and standard deviation of the discovery Bayes factor for two representative UHE neutrino flux models, models 6 and 7 [179]. For both models, the standard deviation is broad, especially at low exposure times, where event rates are low and more severely affected by random Poissonian fluctuations; see Section 7.5.1.

Figure B8, left, shows that within the standard deviation of the Bayes factor the detector exposure time needed for flux discovery can be significantly longer or shorter compared to the man, by up to years. In the case of flux model 7, decisive discovery may be unfeasible within 20 years if the observed Bayes factor lies close to the bottom of its standard deviation. UHE neutrino flux models with larger event rates have a smaller spread of their discovery Bayes factor, and so their discovery is more robust to statistical fluctuations, *viz.* flux models 6 *vs.* 7 in Fig. B8, left.

Figure B8, right, shows the corresponding probability distribution functions of the Bayes factor after 5 years of exposure. The distributions span several orders of magnitude in $\mathcal{B}$. This justifies our averaging procedure, introduced in Section 7.5.2.1, of reporting our results via the arithmetic mean of $\log_{10} \mathcal{B}$ or, equivalently, the geometric mean of $\mathcal{B}$, to avoid biasing the mean Bayes factor towards large, unrepresentative values. At longer exposure times, where event rates are higher, the probability distribution functions become more symmetric and narrower around the mean, mitigating our original need to avoid the above bias.

C

APPENDIX: UHE NEUTRINO POINT SOURCE DISCOVERY

C.1 DERIVATION OF THE PROBABILITIES TO DETECT MULTIPLETS

In the main text, we computed the size of the smallest multiplet required to claim detection of a source located at different positions in the sky, *i.e.*, in each pixel in the sky. For each pixel, we computed the global probability that one or more multiplets of that size appears anywhere in the sky as a result of random over-fluctuations of the diffuse background of UHE neutrinos and atmospheric muons. From the global probability, we computed the local p-value, in each pixel, that is required to claim source detection. Below, we derive the global probability and generalize it.

Reference [371] adopted a different, but related strategy to ours. They used the sky-wide distribution of the angular separation of detected neutrino pairs to reject the hypothesis of no point sources. This strategy does not directly lead to locating point sources, but has the well-suited for identifying the presence of a large number of dim point sources that might not be discovered individually. This is because a dim point source may produce a multiplet that is not large enough to claim lead to source discovery by itself, yet the detection of more than one such multiplet may reveal the subtle presence of point source, since it is unlikely that the pure diffuse background leads to sub-threshold fluctuations in the number of events in multiple pixels simultaneously. Reference [472] applied these methods to locate sources by ranking the pairs according to their statistical significance. Below, we extend our methods in a similar direction, using the combined information from more than one multiplet over all the sky. However, we do not use this extension to produce the results in the main text.

In the i-th pixel, the probability of detecting a multiplet of any size at less than the local p-value p is

$$\pi_i(p) = \sum_{k=\bar{n}_i(p)}^{\infty} \frac{\mu_i^k}{k!} e^{-\mu_i} \,, \tag{C.1}$$

where $\bar{n}_i(p)$ is the size of smallest multiplet required to claim detection at local p-value p, as defined in the main text. If the number of events were a continuous variable, $\pi_i(p)$ would be identically equal to p. However, because the number of events is a discrete quantity, $\pi_i(p)$ jumps discontinuously and is always less than or equal to p.

The probability $\pi_i(p)$ is local, in the sense that it involves a single pixel. To shift to a global description, *i.e.*, one that accounts for the full sky, we compute the probability for the detection of no multiplet anywhere in the sky, *i.e.*,

$$P_0(p) = \prod_{i=1}^{N_{\text{pixels}}} (1 - \pi_i(p)) \ , \tag{C.2}$$

where N_{pixels} is the number of pixels that tessellate the sky. The probability of detection of exactly one multiplet in the j-th pixel, and no multiplet in any other pixel, is

$$P_{1;j}(p) = \pi_j(p) \prod_{i\neq j, i=1}^{N_{\text{pixels}}} (1 - \pi_i(p)) \ . \tag{C.3}$$

From this, the probability of detection of exactly one multiplet in any of the pixels is

$$P_1(p) = \sum_{j=1}^{N_{\text{pixels}}} P_{1;j}(p) \ . \tag{C.4}$$

These results can be generalized to the case of multiple multiplets: the probability of detection of N_{mult} multiplets in the pixels $j_1, \ldots, j_{N_{\text{mult}}}$ is

$$P_{N_{\text{mult}};j_1,\ldots,j_{N_{\text{mult}}}}(p) = \pi_{j_1}(p) \ldots \pi_{j_{N_{\text{mult}}}}(p) \prod_{i\neq(j_1,\ldots,j_{N_{\text{mult}}}),i=1}^{N_{\text{pixels}}} (1 - \pi_i(p)) \ , \tag{C.5}$$

and the probability of detection of N_{mult} in any of the pixels is

$$P_{N_{\text{mult}}}(p) = \sum_{j_1=1}^{N_{\text{pixels}}} \sum_{j_2\neq j_1, j_2=1}^{N_{\text{pixels}}} \cdots \sum_{j_{N_{\text{mult}}}\neq(j_1,\ldots,j_{N_{\text{mult}}-1}), j_{N_{\text{mult}}}=1}^{N_{\text{pixels}}} P_{N_{\text{mult}};j_1,\ldots,j_{N_{\text{mult}}}}(p) \ . \tag{C.6}$$

The functions $P_0(p), P_1(p), \ldots, P_{N_{\text{mult}}}(p)$ represent how likely it is to detect $0, 1, \ldots, N_{\text{mult}}$ multiplets over all sky, each at local p-value p. Using them, we define the probabilities $P_{\geq n}(p)$ of detecting at least n multiplets in the pure-background case. The probability $P_{\geq 0}(p) = 1$ identically. The remaining probabilities are computed recursively via

$$P_{\geq n}(p) = P_{\geq n-1}(p) - P_{n-1}(p) \ . \tag{C.7}$$

The probabilities $P_{\geq n}(p)$ allow us to define the global p-values for the rejection of the pure-background hypothesis, accounting for the look-elsewhere effect. In particular, if n multiplets

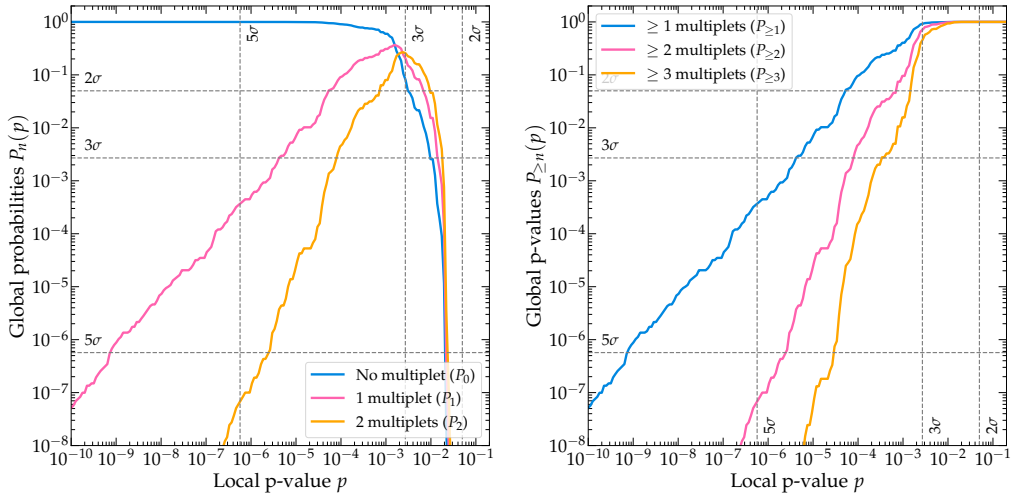

Figure C1: Global probabilities, $P_n(p)$ (*left*), and p-values, $P_{\geq n}$ (*right*), in the IceCube-Gen2 radio array, as functions of the local p-value p, for the first few multiplets. The diffuse UHE neutrino background is our benchmark intermediate background; see Appendix C.4. The radio array design is our baseline design (see main text), the detector angular resolution is our $\sigma_{\theta_z} = 2^\circ$, and the exposure time is $T = 10$ years. See Appendix C.1 for details.

are detected, each with a local p-value smaller than p, the global p-value is $P_{\geq n}(p)$. Indeed, the definition adopted for the global p-value in the main text coincides with $P_{\geq 1}(p)$.

Figure C1 shows the functions $P_n(p)$ and $P_{\geq n}(p)$ for the first few values of n, assuming our intermediate benchmark diffuse UHE neutrino background; see Appendix C.4. For very small local p-values p, the probability of detecting a multiplet anywhere in the sky is negligible, *i.e.*, $P_0(p) \approx 1$. At larger values of p, it becomes increasingly likely that one or more multiplets are detected anywhere in the sky, due to the large number of pixels. For our baseline choice of detector angular resolution of $\sigma_{\theta_z} = 2^\circ$ (see the main text), there are $N_{\text{pixels}} \approx 3400$ pixels. Hence, the threshold value of p at which the probability of detecting one multiplet, $P_1(p)$, becomes significantly large is between 10^{-4} and 10^{-3}, of the order of $1/N_{\text{pixels}}$.

Correspondingly, the global p-values for diffuse background rejection in the case of 1, 2, and 3 detected multiplets, shown in Fig. C1, monotonically increase with p. Further, the global p-value at a fixed value of p decreases monotonically with the number of detected multiplets. This means that, for a fixed global confidence level, if the sky contains more multiplets, then a larger value of p is sufficient to claim background rejection. For example, claiming a 5σ detection with a single multiplet requires $p \approx 10^{-9}$, whereas claiming it with two multiplets requires only $p \approx 10^{-6}$. Therefore, even if the two multiplets are detected with p-values that are insufficient to claim their

discovery as two individual point sources, we can still claim that there is at least one point source in the sky.

Above, in C.6, we implicitly assumed that, regardless of the number of multiplets detected, each multiplet was detected with the same p-value p. However, in data collected by a real experiment, it is unlikely that all multiplets have the same local p-value. In that situation, we can compute the global p-value for the hypothesis that no point source is present in any pixel as

$$P_{\text{global}} = \prod_{i=1}^{N_{\text{pixels}}} \sum_{k=n_i^{\text{obs}}}^{\infty} \frac{\mu_i^k}{k!} e^{-\mu_i} \,, \tag{C.8}$$

where n_i^{obs} is the observed number of events in the i-th pixel. This approach amounts to a complementary, binned version of the method in Ref. [371]. However, it is only feasible a posteriori, with the data available. That is why, in our analysis, we focus on a simplified version where all multiplets have the same local p-value.

C.1.1 *Temporal look-elsewhere effect*

For transient sources, with a neutrino-emission period of duration δt, *e.g.*, a flaring blazar or gamma-ray burst, this procedure requires modification. If the detector exposure time $T \gg \delta t$, a look-elsewhere effect may also happen in time, *i.e.*, background over-fluctuations in any of the $N_{\delta t} \equiv T/\delta t$ time intervals may be misattributed to transient sources. To prevent this, we raise the number of pixels to $N_{\text{pixels}} \times N_{\delta t}$, scale the background event rate in each pixel by $1/N_{\delta t}$, and repeat the procedure introduced in the main text to claim source discovery.

C.2 RADIO-DETECTING ULTRA-HIGH-ENERGY NEUTRINOS IN ICECUBE-GEN2

To compute neutrino-induced event rates at the IceCube-Gen2 radio array, we follow the procedure introduced in Ref. [346]. Below, we sketch it; for details, we defer to Ref. [346].

After UHE cosmic neutrinos reach the surface of the Earth, they travel underground towards the detector, IceCube-Gen2, at the South Pole, across different directions. Underground, neutrinos interact with matter; as a result, their flux is attenuated and shifted to lower energies. These effects

grow with the matter column density traversed by the neutrinos on their way to the detector, *i.e.*, they depend on the neutrino direction. Downgoing neutrinos arrive at the detector from above, after traversing a small column density, and so are largely unattenuated. Upgoing neutrinos arrive at the detector from below, after traversing up to diameter of the Earth, and so their flux is attenuated to the point of being negligible. Earth-skimming neutrinos arrive at the detector from directions around the horizon, and so their flux is attenuated, but not fully; in general, it remains detectable.

The leading neutrino-matter interaction at ultra-high energies is neutrino-nucleon (νN) deep-inelastic scattering (DIS) [217–220]. An interaction can be neutral-current (NC)—when it is mediated by a Z boson, *i.e.*, $\nu_l + N \to \nu_l + X$, where X are final-state hadrons–or charged-current (CC), *i.e.*, $\nu_l + N \to l^- + X$—when it is mediated by a W boson. NC interactions shift neutrinos down to lower energies; CC interactions dampen the flux by removing neutrinos. At ultra-high energies, CC interactions of ν_τ may lead to "ν_τ regeneration," which makes ν_τ more likely to survive their passage through Earth [598–605]. We compute neutrino in-Earth propagation at next-to-leading order, for ν_α and $\bar{\nu}_\alpha$ ($\alpha = e, \mu, \tau$) separately, using the state-of-the-art tool NUPROPEARTH [209, 210]. For the internal matter density of Earth, we use the Preliminary Reference Earth Model [295].

Inside the detector, a neutrino interacts with a proton or neutron of the Antarctic ice, via νN DIS, triggering a high-energy particle shower that receives a fraction of the neutrino energy. As the shower develops, the charged particles in it emit a coherent radio signal—Askaryan radiation [165]. It offers a promising method of detecting UHE neutrinos [204], validated by laboratory measurements [169, 305, 306] and atmospheric shower measurements [304, 307–309]. Existing UHE neutrino telescopes—ARA [316], ARIANNA [69]—and upcoming ones—RNO-G [71], IceCube-Gen2 [39]—target it. Because radio waves have an attenuation length of roughly 1 km in ice [310], compared to the roughly 100 m for optical light applicable to optical-Cherenkov detectors like IceCube, a large detection volume can be monitored with sparser instrumentation. The simulated detector volume is a cylinder 1.50 km tall, its top lid, with an area of 500 km^2, buried 100 m underground [346].

Following Ref. [346], we model the IceCube-Gen2 response as the fraction of all the neutrino-initiated showers inside the geometric volume of the detector that trigger a signal and are recorded

as events, and we use this fraction to define an effective volume for the experiment. This effective volume depends on the energy deposited in the ice and on the direction of the incoming neutrino. The simulations are performed in Ref. [346], using the same tools as the IceCube-Gen2 Collaboration, NuRadioMC [211] and NuRadioReco [212]. Appendix C.3 details our baseline design of the radio array, and alternative designs. Different array designs have different effective volumes; we compute the effective separately volume for each. The resulting effective volumes do not include the impact of reconstruction efficiencies, since this is not presently available in public literature. This effect could somewhat reduce the total number of events and influence our results, but its importance is still under consideration.

Given a flux of ν_α at the detector, $\Phi^{\rm det}_{\nu_\alpha}$, the differential rate of neutrino-induced events, in shower energy and direction, is

$$\begin{aligned}\frac{d^2N_{\nu_\alpha}}{dE_{\rm sh}d\cos\theta_z} =& 2\pi T n_t \int_0^1 dy \left(\frac{E^{\rm NC}_{\nu_\alpha}(E_{\rm sh},y)}{E_{\rm sh}} V^{\rm NC}_{{\rm eff},\nu_\alpha}(E_{\rm sh},\cos\theta_z) \right. \\ & \left. \times \frac{d\sigma^{\rm NC}_{\nu_\alpha {\rm w}}(E_\nu,y)}{dy} \Phi^{\rm det}_{\nu_\alpha}(E_\nu,\cos\theta_z)\Big|_{E_\nu = E^{\rm NC}_{\nu_\alpha}(E_{\rm sh},y)} + {\rm NC}\to{\rm CC} \right) ,\end{aligned} \tag{C.9}$$

where T is the exposure time, $n_t \equiv N_{\rm Av}\rho_{\rm ice}/M_{\rm ice}$ is the number density of water molecules in ice, $N_{\rm Av}$ is Avogadro's number, $\rho_{\rm ice}$ is the density of ice, $M_{\rm ice}$ is the molar mass of water, and $\sigma_{\nu_\alpha {\rm w}}$ is the neutrino cross section on a water molecule. The integration over y accounts for the contribution of all possible initial neutrino energies E_ν that can produce a given shower energy $E_{\rm sh}$. To account for the resolution of the detector in measuring shower energy and direction, we rewrite the differential event rate in terms of measured quantities, *i.e.*, the reconstructed shower energy, $E^{\rm rec}_{\rm sh}$, and the reconstructed arrival direction, $\theta^{\rm rec}_z$. We use energy and direction resolution functions, $\mathcal{R}_{E_{\rm sh}}$ and $\mathcal{R}_{\theta_z}$, respectively, to cast the event rate in terms of measured quantities, *i.e.*,

$$\frac{d^2N_{\nu_\alpha}}{dE^{\rm rec}_{\rm sh}d\theta^{\rm rec}_z} = \int_{-1}^{+1} d\cos\theta_z \int_0^\infty dE_{\rm sh} \frac{d^2N_{\nu_\alpha}}{dE_{\rm sh}d\cos\theta_z} \mathcal{R}_{E_{\rm sh}}(E^{\rm rec}_{\rm sh},E_{\rm sh})\, \mathcal{R}_{\theta_z}(\theta^{\rm rec}_z,\theta_z) \,. \tag{C.10}$$

The energy and direction resolution functions are modeled as Gaussian functions centered at the real values of shower energy and direction, with widths σ_{θ_z} and $\sigma_{E_{\rm sh}}$, respectively. To produce our main results, we set $\sigma_{\theta_z} = 2^\circ$ and $\sigma_{E_{\rm sh}} = 10^{\sigma_\epsilon} E_{\rm sh}$, where $\sigma_\epsilon = 0.1$ is the spread in the ratio $\epsilon \equiv \log_{10}(E^{\rm rec}_{\rm sh}/E_{\rm sh})$. These values are chosen based on simulations [212, 300, 312, 314, 315, 317, 324, 326, 346]. To produce our results, we use the total event rate, summing C.10 over all flavors of neutrinos and anti-neutrinos. To obtain the expected number of events in a given energy and

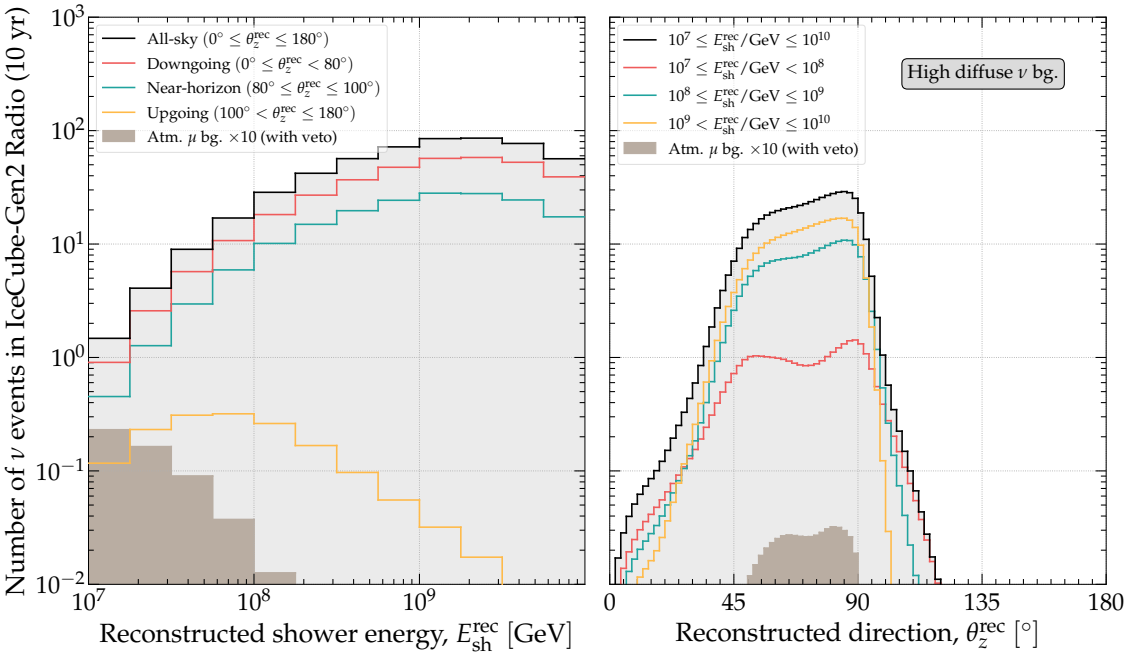

Figure C2: Distribution of events induced in IceCube-Gen2 by our high benchmark diffuse UHE neutrino diffuse model, in reconstructed shower energy (*left*) and direction (*right*), in $T = 10$ years of detector exposure time. Events are computed following the procedure in Appendix C.2. For this plot, we use our baseline design of the IceCube-Gen2 radio array, a detector shower energy resolution of 10% in logarithmic scale, and a detector angular resolution in zenith angle of $\sigma_{\theta_z} = 2^\circ$. See the main text and appendices C.2 and C.4 for details.

direction bin, we integrate the total rate over the range reconstructed shower energy and direction boundaries of the bin.

Figure C2 illustrates the event rate, binned in reconstructed shower energy and direction, assuming for the neutrino flux our high benchmark flux; see the main text and Appendix C.4. The event rates for our intermediate and low benchmarks are shifted-down versions of Fig. C2. To produce our results, we do not use the distribution of events in energy, only in direction; see Appendix C.4 for details.

C.3 IMPACT OF THE DETECTOR ANGULAR RESOLUTION AND THE RADIO ARRAY DESIGN

In the main text, we presented results obtained using our choice of baseline detector angular resolution and of the design of the IceCube-Gen2 radio array. The baseline detector angular resolution is $\sigma_{\theta_z} = 2^\circ$ in zenith angle [300]. The baseline design is composed of 144 hybrid stations

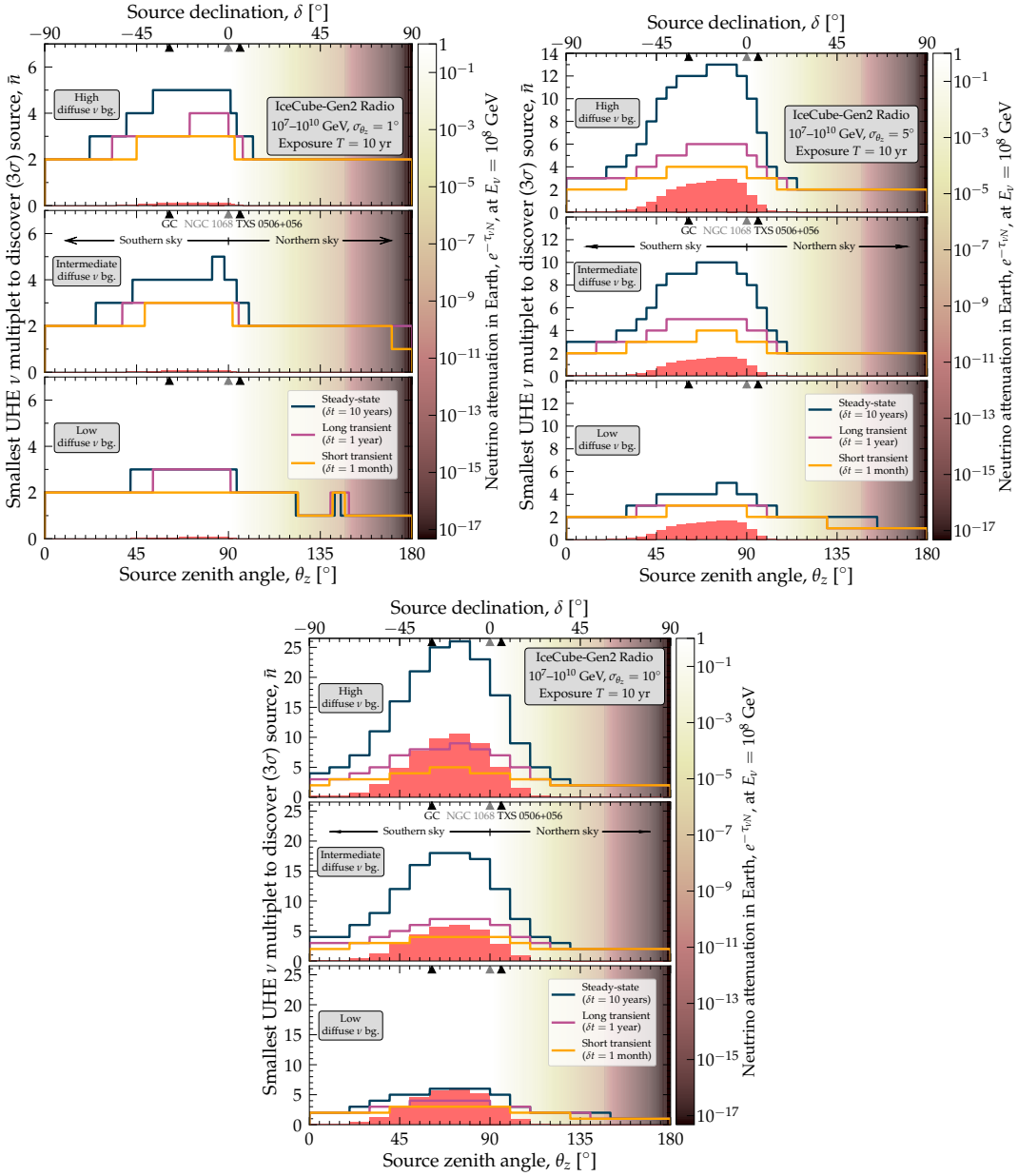

Figure C3: Same as Fig. 1 in the main text, but for different choices of the detector angular resolution: $\sigma_{\theta_z} = 1°$ (*top left*), 5° (*top right*), and 10° (*bottom*).

(shallow + deep components) plus 169 shallow-only stations [396]; the deep components are buried 200 m underground. In the main text, we commented on the effect on our results of using alternative choices of the angular resolution and the array design. Here we present these results.

Figure C3 shows the impact of varying the angular resolution on the smallest multiplet size needed to claim source discovery. For comparison, in the main text we obtained results using $\sigma_{\theta_z} = 2°$. The angular resolution has a dramatic impact on the results: worsening it implies tessellating the sky with larger pixels and a corresponding larger diffuse background in each of

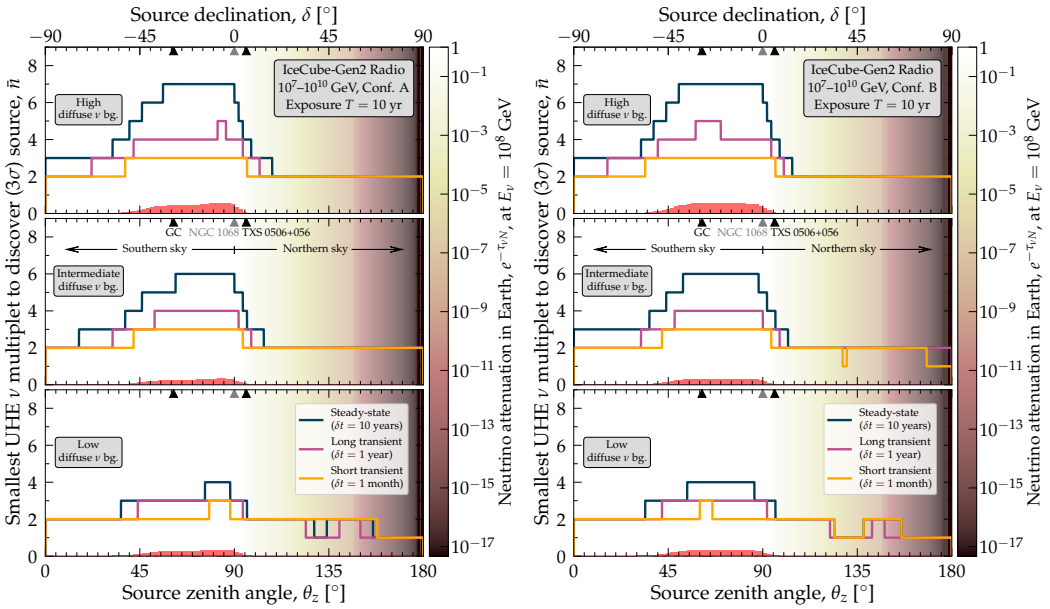

Figure C4: Same as Fig. 1 in the main text, but for two alternative designs of the IceCube-Gen2 radio array. See Appendix C.3 for details.

them, hindering claims of source discovery. For $\sigma_{\theta_z} = 5°$, discovering steady-state sources would require up to size-13 multiplets if the diffuse background is high. Transient sources would be more weakly affected: even for $\sigma_{\theta_z} = 10°$, short-duration transients may require at most a quintuplet or hexaplet to claim a detection.

Figure C4 shows the impact of using two alternative designs of the IceCube-Gen2 radio array on the smallest multiplet size to claim source discovery. We do not account for changes in the reconstruction efficiency of different array designs, since this information is presently not publicly available; see Appendix C.2. In the main text we used our baseline array design. Alternative array configuration A contains 361 shallow stations and 164 deep stations. Alternative array configuration B contains 208 hybrid stations only. The prospects for detection are weakly dependent on the choice of array design; for our three design choices, at most heptaplets are needed to claim source discovery. Because our exploration of alternative array designs is non-exhaustive, the weak dependence that we find should only be considered tentative. More simulation work is necessary to claim this definitively.

C.4 DIFFUSE ULTRA-HIGH-ENERGY NEUTRINO BACKGROUND

The diffuse UHE neutrino flux depends on the properties of UHECRs and their sources. Because these are known uncertainly, the diffuse UHE neutrino flux is predicted uncertainly, and there are many competing theory models [174–180, 193]. The diffuse UHE neutrino flux remains undiscovered, but there are upper limits on it, from IceCube [66] and Auger [67].

In our work, rather than adopting one of the above predictions for the diffuse UHE neutrino background, we adopt a flux that saturates, at each value of the neutrino energy, the IceCube upper limit [66]. This makes our background experiment-motivated rather than theory-motivated. To account for future improvements in the detector sensitivity, we consider the three benchmark neutrino diffuse flux levels introduced in the main text—the present-day IceCube upper limit (*high*) and two smaller ones (*intermediate* and *low*). See the main text for details. Because we do not use the energy distribution of the events, only their angular distribution, the specific shape of the neutrino energy spectrum that we adopt has no large consequence on our results. What matters is only the total number of events, integrated across all energies. The fact that our choice of spectral shape follows present-day upper limits and has no realistic theoretical counterpart does not impact our results significantly.

We take the diffuse neutrino flux to be isotropic at the surface of the Earth, in agreement with the expectation of a predominantly extragalactic origin. Neutrino propagation through the Earth makes the resulting distribution of neutrino-induced anisotropic; see Appendix C.2 and Fig. C5. For our three benchmarks, we assume approximate flavor equipartition at the surface of the Earth, *i.e.*, equal proportion of $\nu_e + \bar{\nu}_e$, $\nu_\mu + \bar{\nu}_\mu$, and $\nu_\tau + \bar{\nu}_\tau$ in the flux. This is the nominal expectations for high-energy neutrinos made in proton-proton and proton-photon interactions. Because in our analysis the neutrino-induced event rate is due to all flavors (see Appendix C.2) and we conservatively do not assume that flavor identification will be available, our results are only weakly sensitive to the precise flavor composition. Further, we assume that the flux is equally divided between neutrinos and anti-neutrinos. (At the highest energies, this may no longer be true, though we do not consider that possibility here; see, *e.g.*, Ref. [257, 346]). At these

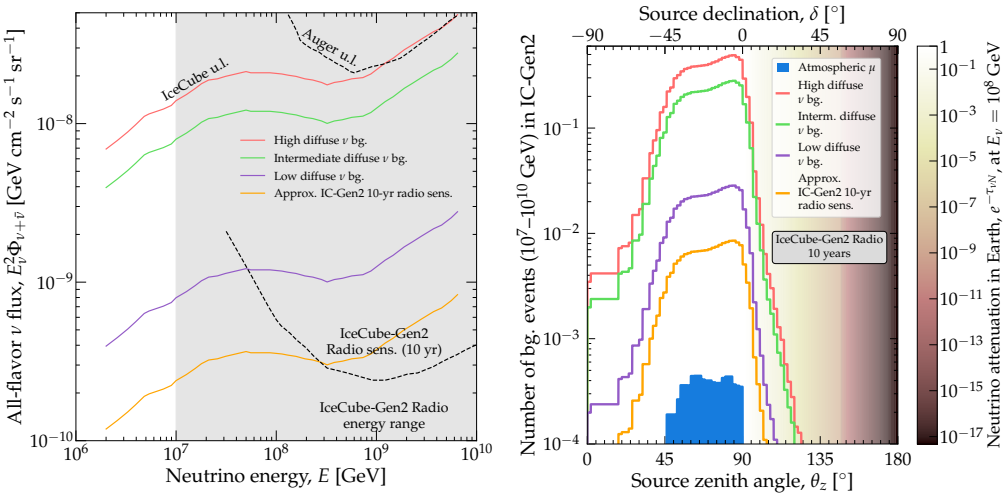

Figure C5: *Left:* Benchmark diffuse UHE neutrino flux models used in our work. For comparison, we include the IceCube-Gen2 radio array sensitivity [396], and the upper limit from Auger [67]. *Right:* Angular distribution of the events induced by the benchmark diffuse neutrino background models in $T = 10$ years of IceCube-Gen2 exposure time. For this plot, we use our baseline design of the IceCube-Gen2 radio array, and a detector angular resolution in zenith angle of $\sigma_{\theta_z} = 2°$; see the main text. The shading is the same as in Fig. 1 in the main text. See Appendix C.4 for details.

energies, the neutrino and anti-neutrino cross sections are nearly equal, so uncertainties in the neutrino-to-antineutrino ratio have no discernible impact on the event rate.

Figure C5 shows our three benchmark diffuse UHE neutrino fluxes and their associated number of neutrino-induced events expected at IceCube-Gen2, in each pixel of the sky, computed following the procedure in Appendix C.2. We include an additional benchmark flux that approximates the level of the projected 10-year sensitivity of the IceCube-Gen2 radio array [396]. Because diffuse flux is isotropic at the surface of the Earth, the angular distribution of the events reflects solely the effects of in-Earth propagation and the detector response. The number of events close to the horizon is larger than at higher declination because there the detector angular response is strongest, while in-Earth attenuation is mild, compared to the severe attenuation experienced by upgoing neutrinos.

Figure C2 shows details of the angular and energy distribution of events induced by our high benchmark diffuse UHE neutrino flux. In our analysis, we do not use the energy distribution of the events; rather, we group all events in a single bin of reconstructed energy, 10^7–10^{10} GeV. We show finer energy bins in Fig. C2 for illustration only. The energy dependence of the diffuse background model follows the energy spectrum of the IceCube upper limit, and is not theoretically motivated. In terms of number of events, this leads to a signal that is more pronounced near 10^9 GeV, mostly

because of the higher effective volume of the detector at these energies. A different, possibly more realistic energy spectrum of the background diffuse neutrino flux would lead to a different event energy distribution. However, as pointed out earlier, because our analysis does not use the event energy distribution when looking for multiplets, our results are not significantly impacted by specific choices of the neutrino energy spectrum.

The second background that we account for is due to atmospheric muons coming from extensive air showers initiated by cosmic-ray interactions in the atmosphere [213]. The number of events is highest at slant and near-horizontal directions, where the atmospheric muon flux is largest. We use the same muon background as Ref. [346], computed using the SYBILL 2.3C hadronic interaction model [293], mitigated by a surface veto, and subject to the same angular and energy resolution as neutrinos. The background of muon-induced events is < 0.1 per year, sub-dominant to the background of neutrino-induced events. Even without the veto mitigating the atmospheric muon rate, we still expect less than one muon-induced event per year [346]. Figures C5 and C2 show the energy and angular distribution of events induced by atmospheric muons, subject to the same angular and energy resolution as neutrino-induced events. For our benchmark background diffuse UHE neutrino fluxes, atmospheric muons are always sub-dominant in the total diffuse background, and influence weakly our results. In principle, their impact could be further reduced by using the information on the energy spectrum in our analysis. Since muons are produced by cosmic-ray interactions, their spectrum decreases steeply with energy, so their contribution is only relevant below 10^8 GeV. We conservatively do not use this information, but it could improve source-discovery prospects.

An additional background for UHE neutrino radio-detection may be due to the reflected cores of cosmic-ray showers [327]. However, because its size is still under study, we cannot yet assess its impact on source discovery.

C.5 SMALLEST MULTIPLET SIZE FOR 5σ DETECTION AND VERY SHORT TRANSIENTS

Figure 1 in the main text shows the smallest multiplet size required to claim source discovery at a 3σ significance. The largest multiplet, for steady-state sources, is a heptaplet.

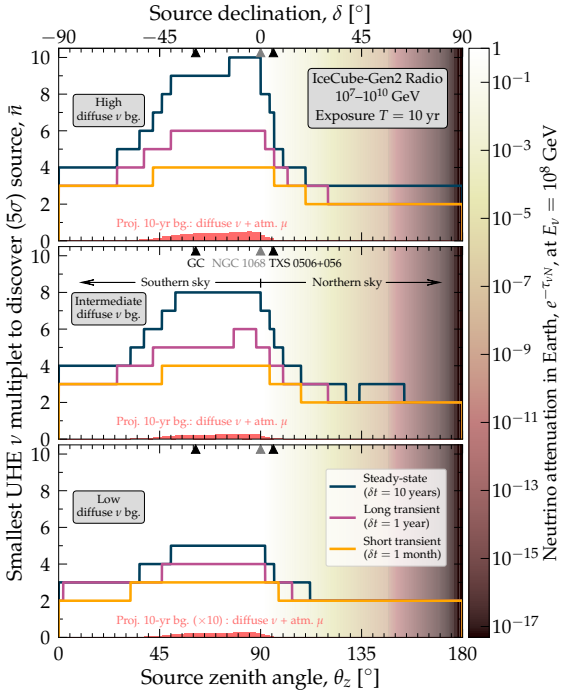

Figure C6: Same as Fig. 1 in the main text, but for source discovery at a global significance of 5σ.

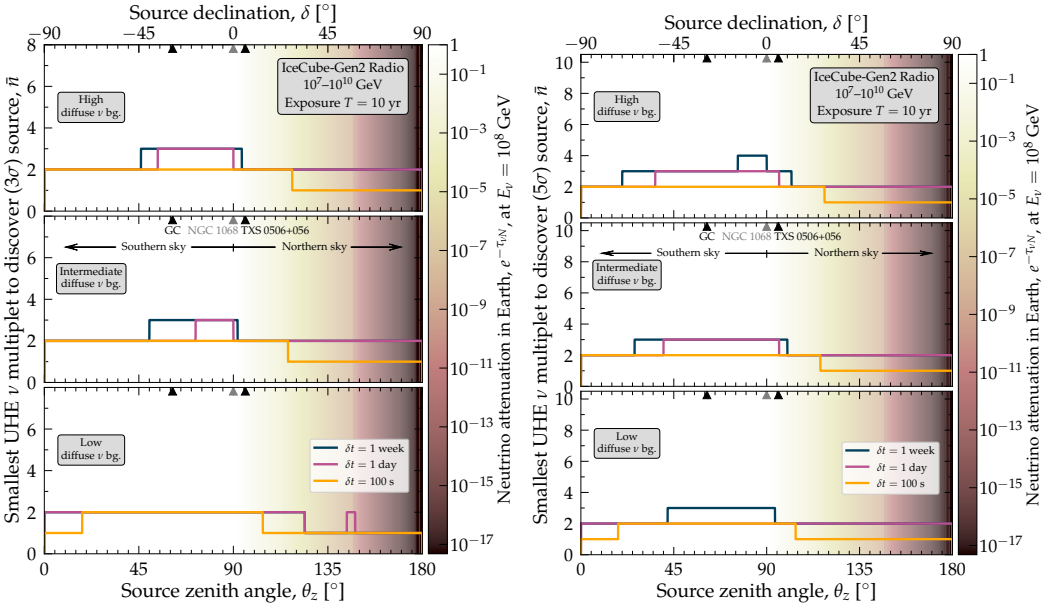

Figure C7: Same as Fig. 1 in the main text, but for very-short-duration transient sources, of duration $\delta t = 1$ week, 1 day, and 100 s. Results are for source discovery at 3σ (*left*) and 5σ (*right*) significance. The diffuse background is too small to be visible and, therefore, is not shown.

Figure C6 shows the smallest multiplet size required for a 5σ discovery. In this case, larger multiplets are needed to overcome the background by a larger margin: up to decaplets may be needed to discover steady-state sources.

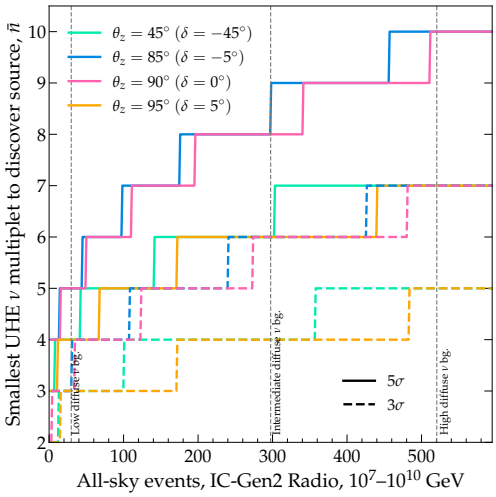

Figure C8: Threshold number of events for a detection as a function of the number of all-sky events. The predicted exposure time for the intermediate background model is shown in the top axis. The declination angle is fixed to four benchmark values of $\delta = -45°$ (green), $\delta = -5°$ (blue), $\delta = 0°$ (magenta), and $\delta = 5°$ (orange). We show the multiplet size for detection at 5σ (solid line) and 3σ (dashed line).

Figure C7 shows the smallest multiplet size needed to discover very-short-duration transient sources. Because the background accumulated over the source duration is tiny, source discovery is significantly easier: doublets or triplets are sufficient anywhere in the sky.

C.6 CONSTRAINTS ON SOURCE POPULATIONS FOR VARYING BACKGROUND

Figure C8 shows how the size of the smallest multiplet needed to claim source discovery varies with the all-sky number of background-induced events, which is proportional to the background diffuse UHE neutrino flux. A lower background means that smaller multiplets are needed to claim source discovery.

Figure C9 shows the probability of source discovery in each pixel, for our low and high benchmarks of the diffuse UHE neutrino background. Figure 45 shows the case for our intermediate benchmark. A larger diffuse background requires larger multiplets to claim source discovery. However, because in Figs. 45 and C9 the neutrino flux from each source class is chosen to saturate the diffuse background (see Tables 7 and 8), a larger diffuse background implies a higher chance of source discovery in every pixel.

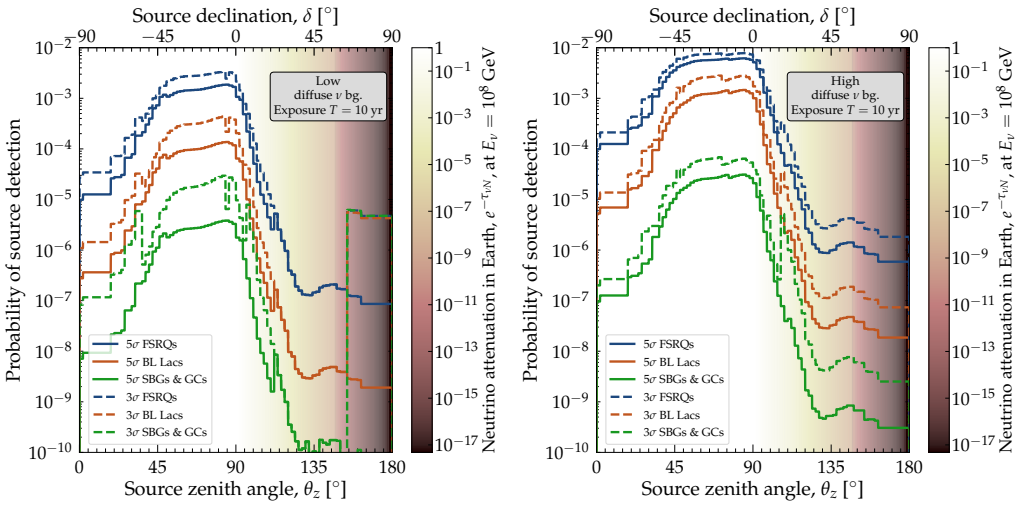

Figure C9: Same as Fig. 45, but using our benchmark low (*left*) and high (*right*) UHE neutrino background. See Appendix C.6 and the main text for details.

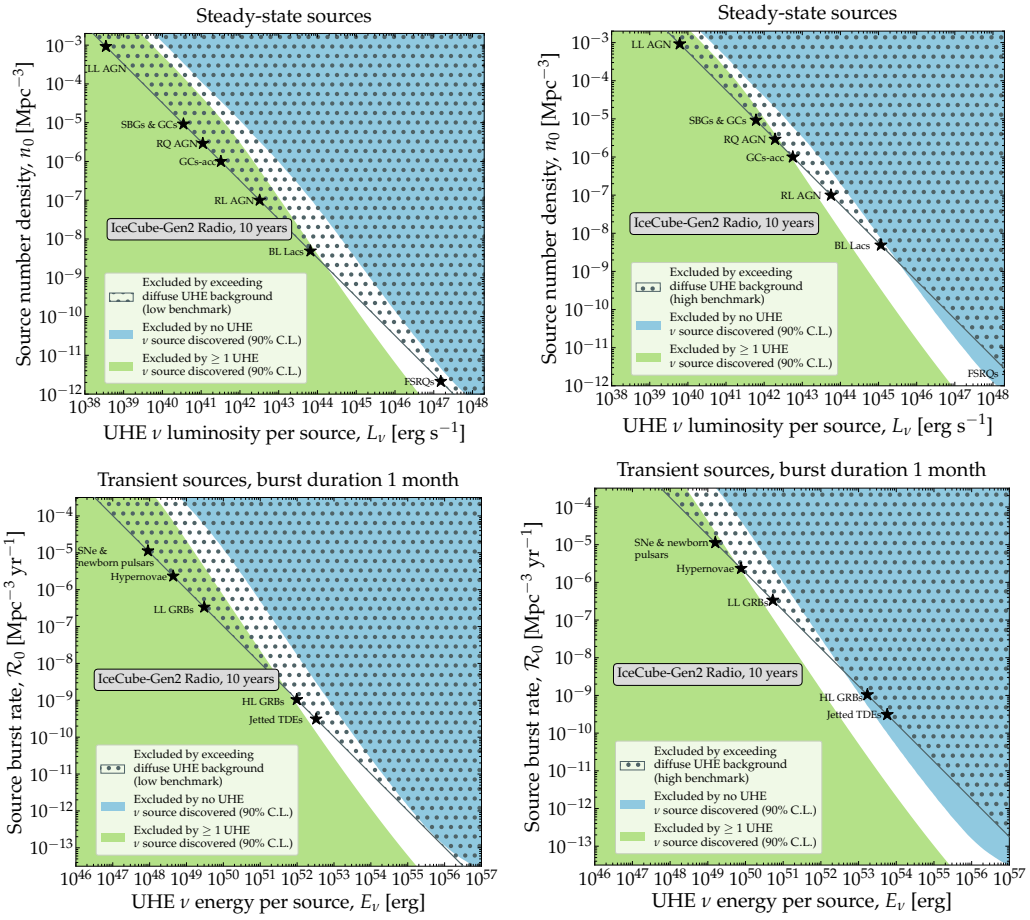

Figure C10: Same as Fig. 2 in the main text, but using our benchmark low (*left column*) and high (*right column*) UHE neutrino background, for steady-state sources (*top row*) and transient sources (*bottom row*). See the main text and Appendix C.6 for details.

Figure C10 shows the constraints on UHE neutrino sources, from the discovery or absence of UHE multiplets, for our benchmark low and high UHE neutrino background. In the main text,

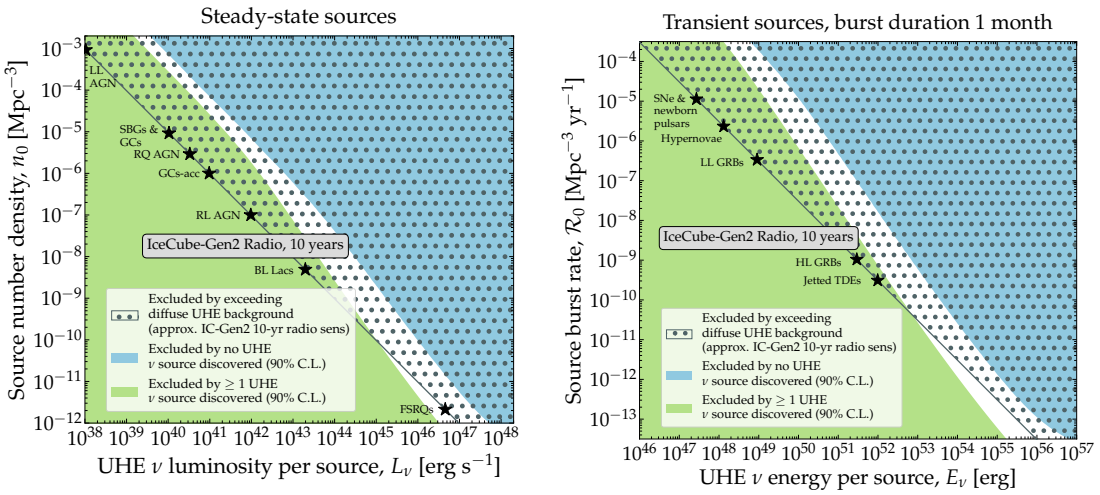

Figure C11: Same as Fig. 2 in the main text, but using an UHE neutrino background approximately coinciding with the IceCube-Gen2 radio array sensitivity [396]. See Appendix C.6 and the main text for details.

Fig. 2 shows constraints for our intermediate benchmark. Fig. C10 shows that the qualitative impact of the choice of background on the constraints is mild. For steady-state sources, regardless of the background, if even a single source is discovered, most known candidate source classes would be disfavored. Figure C10 reveals that this is especially true if the background is low, because then sources cannot be too bright without exceeding it. For transient sources, in the high-background case our conclusions are unchanged, whereas in the low-background case the absence of a detection would not disfavor the known source classes.

Figure C11 shows the constraints on the source population assuming an even lower background, one approximately at the same level as the projected 10-year sensitivity of the IceCube-Gen2 radio array sensitivity [396]; see Fig. C5. For such a low background, we expect about 9 events all-sky in 10 years of IceCube-Gen2 for our baseline array design. Indeed, in the case of no point-source discovery, Fig. C11 shows that point source discovery is not expected for any source class. It is entirely possible that the diffuse neutrino flux is lower even than our low benchmark model. In that, case the bounds obtained from the absence of point sources would be significantly weaker than the requirement of not exceeding the bounds on the diffuse neutrino flux.

C.7 IMPACT OF REDSHIFT AND LUMINOSITY EVOLUTION

The results shown in the main text are based on the assumption of sources having all the same luminosity in their rest frame, and evolving in redshift according to the star formation rate. While this may be a reasonable assumption for some of the sources we consider, it does not apply to some of the most promising candidates, including BL Lacs and TDEs, which have a negative evolution with redshift, and FSRQs, which have a significant luminosity evolution with redshift. Here we apply our methods to study how the results change by relaxing our assumptions on the evolution.

First, we focus on jetted TDEs. We extract their redshift evolution from Fig. 14 of Ref. [607], for a black hole mass of 10^6–10^7 solar masses. The projected constraints for this redshift evolution are shown for transient sources in Fig. C12. Compared to Fig. 46, which was generated assuming SFR redshift evolution, in Fig. C12 we find that jetted TDEs still lie in the regions where they could be excluded by the absence of multiplets, provided they saturate the diffuse flux for our intermediate diffuse background model. The question of whether TDEs are able to produce a

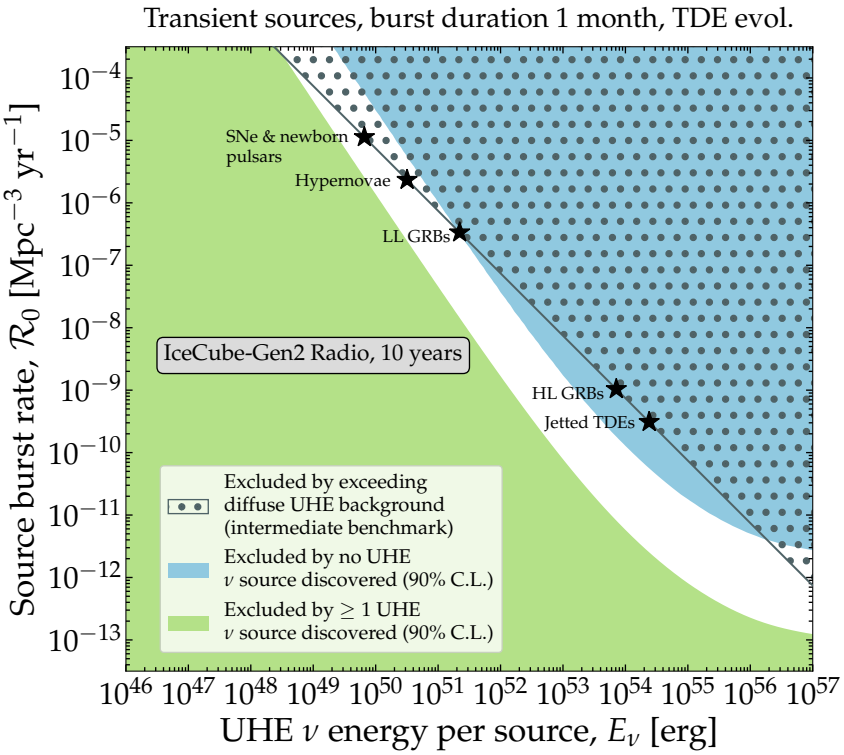

Figure C12: Same as Fig. 46 in the main text, for transient sources, but assuming a TDE-like redshift evolution for the number source density. See Appendix C.7 for details.

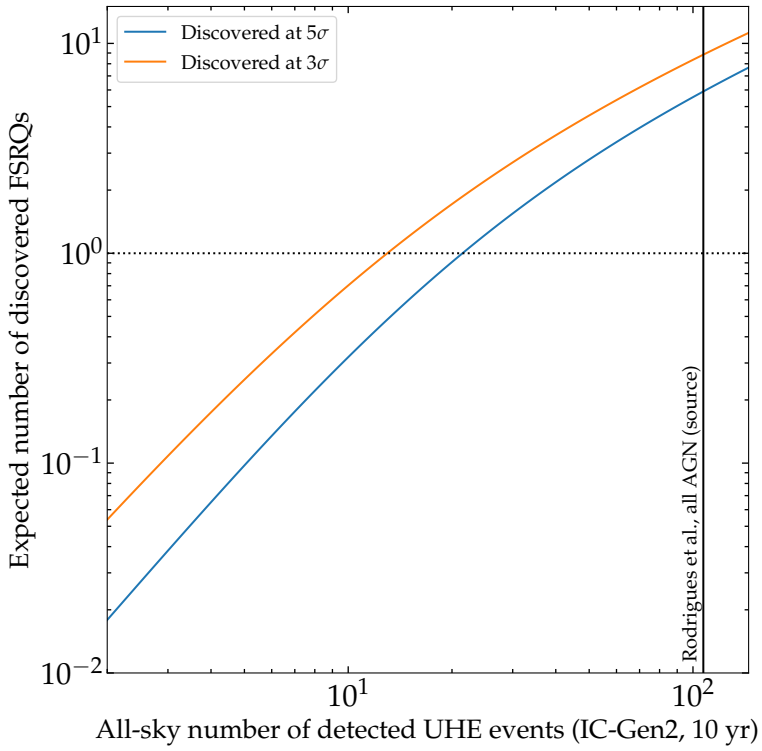

Figure C13: Expected number of FSRQ-like sources detected after 10 years of exposure in the IceCube-Gen2 radio array, as a function of the all-sky number of detected neutrino events. The neutrino luminosity is assumed to scale with the gamma-ray luminosity following Ref. [285]. We adopt the luminosity and redshift evolution of the source number density from Ref. [606]. For reference, we mark the threshold value of one detected source and the expected all-sky number of events for the blazar model of Ref. [179]. We show results for 3σ and 5σ detection.

diffuse flux comparable to the intermediate diffuse background model depends on their neutrino luminosity, depends on specifics of the neutrino production model [182, 515, 518, 583, 608]; we do not investigate this question here.

Next, we turn to the case of blazars. We focus on FSRQs only, since, as discussed in Refs. [179, 285], the UHE neutrino production from blazars is expected to be dominated by them (see also Refs. [495–498]). For a detailed treatment of FSRQs, a crucial element is the evolution with redshift of the luminosity distribution. Therefore, we change our approach compared to the main text in the following way: in place of Eq. 9.3, we use a correlated redshift and luminosity probability distribution extracted from Ref. [606]. For this calculation, the local source density is not a free parameter that we let float, but is determined by the distribution of blazars detected by *Fermi*-LAT. Therefore, throughout the rest of the calculation, all the averages over the redshift distribution become averages over the redshift *and* luminosity distribution. The distributions of Ref. [606] are in terms of the gamma-ray luminosity of FSRQs, whereas for the determination of the point source

sensitivity we need the neutrino luminosity. We assume that the two are related by an efficiency ϵ_ν, *i.e.*, $L_\nu = \epsilon_\nu(L_\gamma)L_\gamma$. We assume that the efficiency depends on the gamma-ray luminosity following the dependence found in Ref. [285], Fig. 15, for proton injection and advective escape. However, we let its normalization float. Finally, following the procedure described in the main text, we obtain the expected number of sources discovered in 10 years. This number depends on the normalization of the neutrino production efficiency: a higher efficiency leads to a larger diffuse neutrino flux, more events detected and, therefore, more sources discovered.

Figure C13 shows the expected number of detected sources as a function of the all-sky expected number of events. In this case, a point source can be discovered even if there are only 10–20 over the full sky, since the sources are especially bright. For the neutrino production model of Ref. [179], which predicts about 108 events over all sky, a sizable number of point source discoveries is expected.

D

APPENDIX: DARK MATTER DECAY INTO UHE NEUTRINOS

D.1 ADDITIONAL FIGURES

Without further ado, we include additional figures to complement those in the main text:

FIGURE D1 Discovery prospects at 3σ, for the NFW Galactic DM profile.

FIGURE D2 Lower limits on DM lifetime under a large background of non-DM UHE neutrinos, for the NFW profile.

FIGURE D3 Discovery prospects at $\geq 2\sigma$ and $\geq 3\sigma$, for the Burkert Galactic DM profile.

FIGURE D4 Lower limits on DM lifetime, for the Burkert Galactic DM profile.

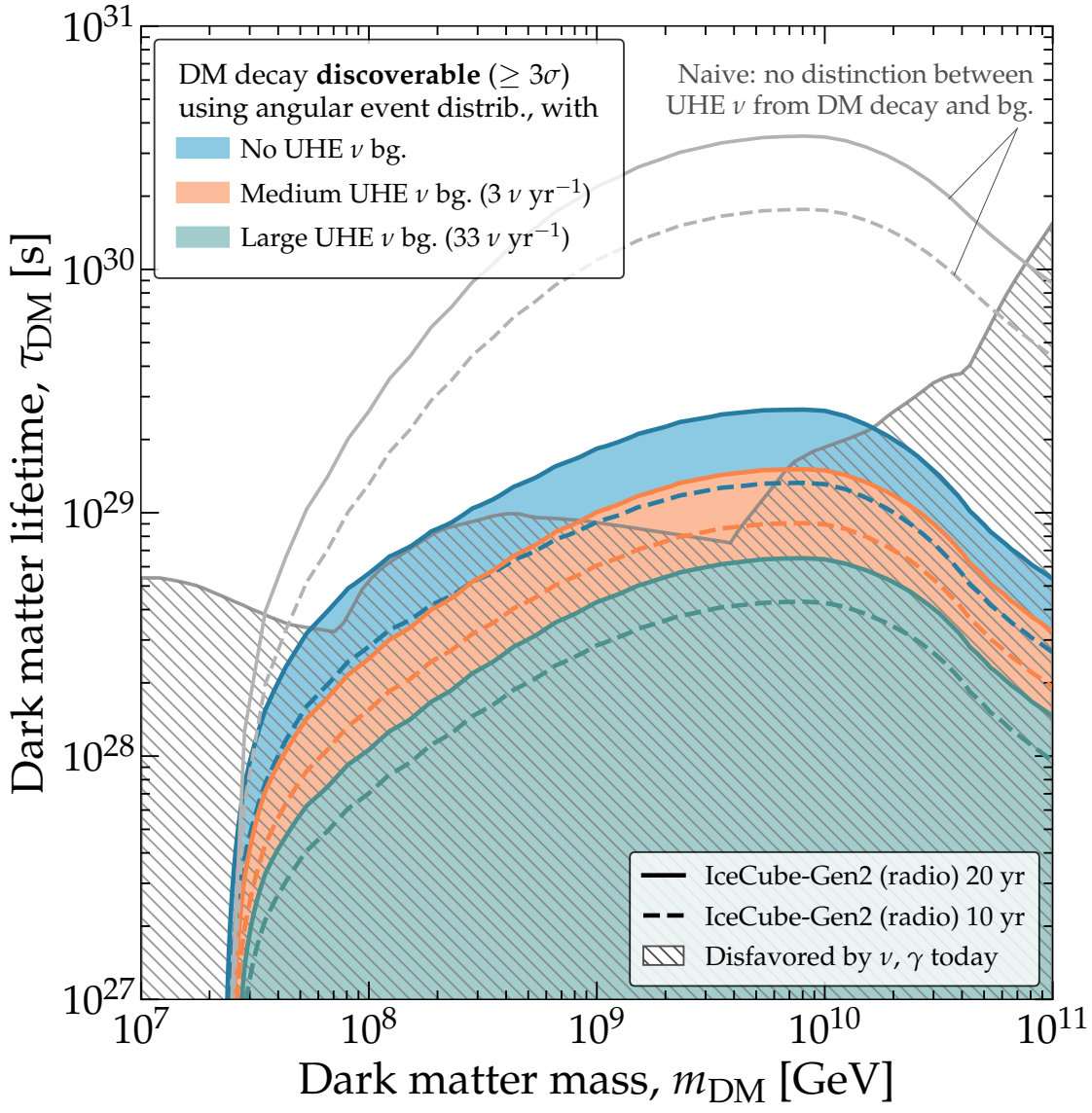

Figure D1: ***Discovery prospects for UHE neutrinos from DM decay, at*** $\geq 3\sigma$**.** Compare to Fig. 53, which is for $\geq 2\sigma$.

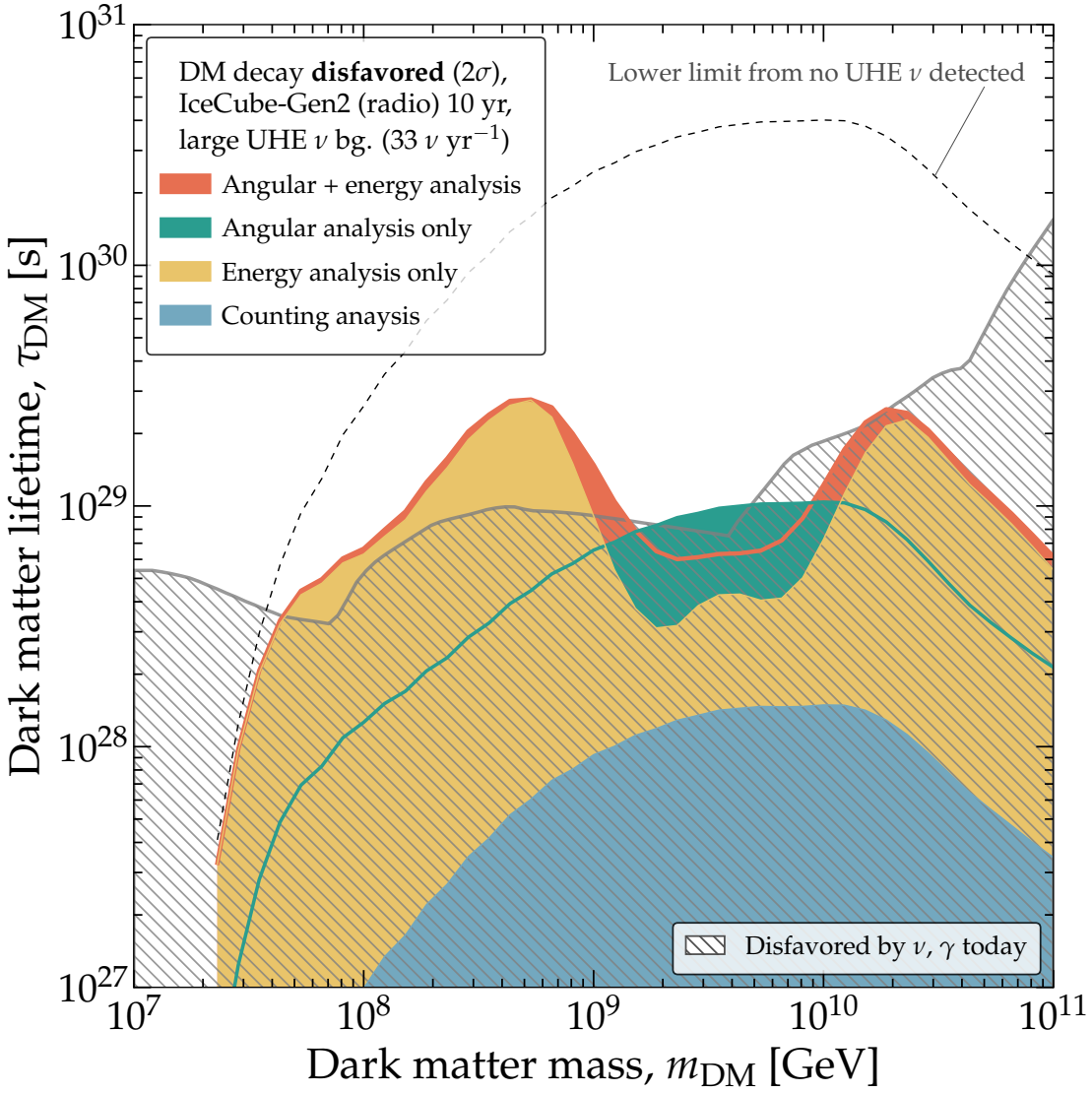

Figure D2: ***Projected lower limits on the DM lifetime, under a large background of non-DM UHE neutrinos.*** Same as Fig. D2, but assuming our large benchmark non-DM isotropic background flux of UHE neutrinos, *i.e.*, the cosmogenic neutrino flux by Bergman & van Vliet [193]. See Sec. 10.5 for details.

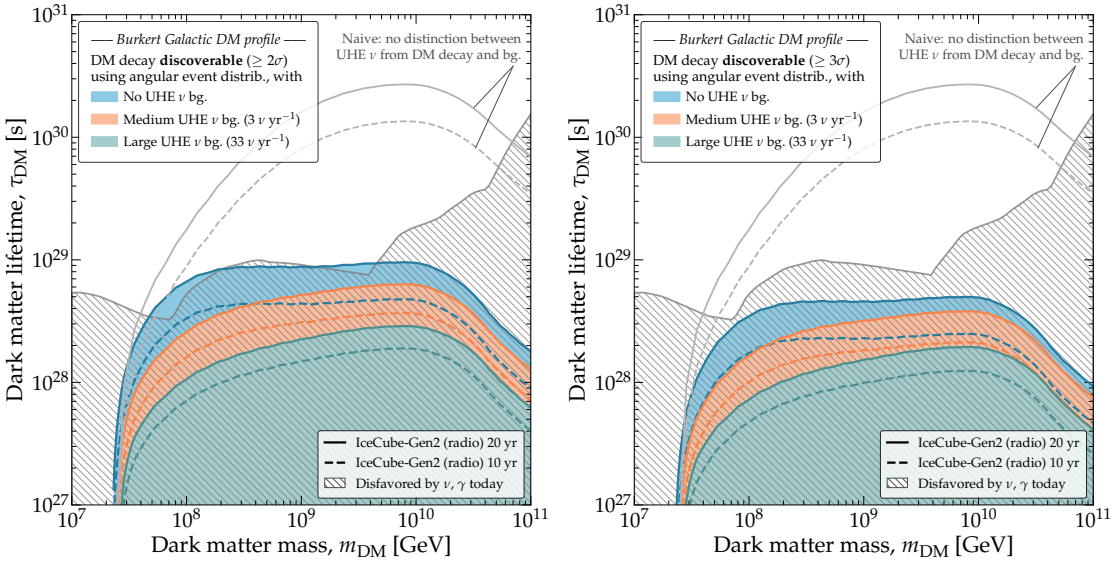

Figure D3: ***Discovery prospects for UHE neutrinos from DM decay, using a Burkert Galactic DM profile.*** *Left:* For discovery at $\geq 2\sigma$, to be compared with Fig. 53. *Right:* For discovery at $\geq 3\sigma$, to be compared with Fig. D1.

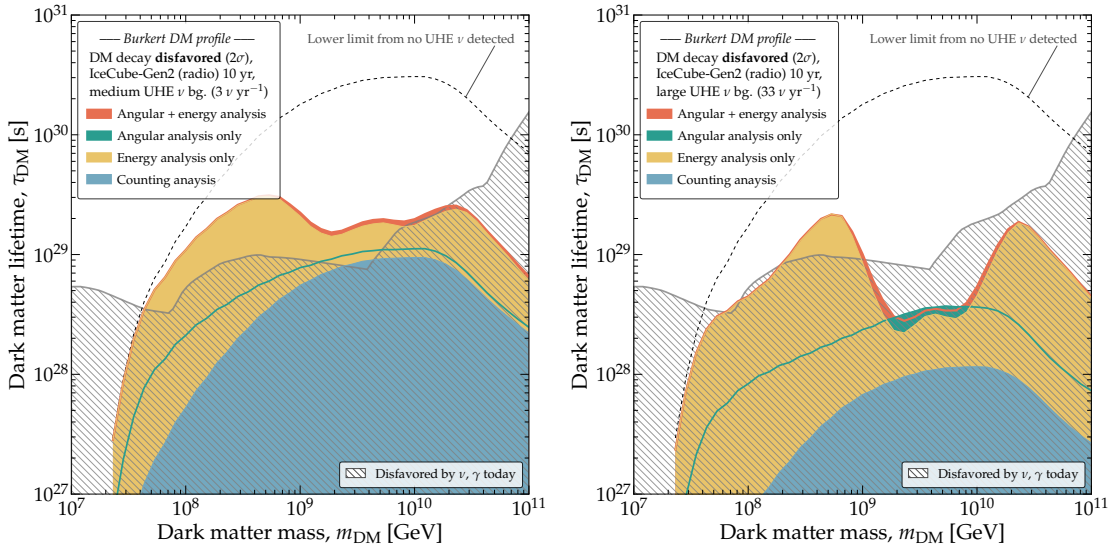

Figure D4: ***Projected lower limits on the DM lifetime, using a Burkert Galactic DM profile.*** *Left: For a medium background of non-DM UHE neutrinos, to be compared with Fig. 57. Right: For a large background of non-DM UHE neutrinos, to be compared with Fig. D2.*

BIBLIOGRAPHY

[1] Frederick Reines and Clyde L. Cowan. "The neutrino". In: *Nature* 178 (1956), pp. 446–449. DOI: 10.1038/178446a0.

[2] Ziro Maki, Masami Nakagawa, and Shoichi Sakata. "Remarks on the unified model of elementary particles". In: *Prog. Theor. Phys.* 28 (1962), pp. 870–880. DOI: 10.1143/PTP.28.870.

[3] B. Pontecorvo. "Neutrino Experiments and the Problem of Conservation of Leptonic Charge". In: *Zh. Eksp. Teor. Fiz.* 53 (1967), pp. 1717–1725.

[4] B. T. Cleveland et al. "Measurement of the solar electron neutrino flux with the Homestake chlorine detector". In: *Astrophys. J.* 496 (1998), pp. 505–526. DOI: 10.1086/305343.

[5] John N. Bahcall. "Solar neutrinos. I: Theoretical". In: *Phys. Rev. Lett.* 12 (1964), pp. 300–302. DOI: 10.1103/PhysRevLett.12.300.

[6] R. Davis. "Solar neutrinos. II: Experimental". In: *Phys. Rev. Lett.* 12 (1964), pp. 303–305. DOI: 10.1103/PhysRevLett.12.303.

[7] John N. Bahcall and Roger K. Ulrich. "Solar Models, Neutrino Experiments and Helioseismology". In: *Rev. Mod. Phys.* 60 (1988), pp. 297–372. DOI: 10.1103/RevModPhys.60.297.

[8] K. S. Hirata et al. "Observation of B-8 Solar Neutrinos in the Kamiokande-II Detector". In: *Phys. Rev. Lett.* 63 (1989), p. 16. DOI: 10.1103/PhysRevLett.63.16.

[9] Y. Fukuda et al. "Measurements of the solar neutrino flux from Super-Kamiokande's first 300 days". In: *Phys. Rev. Lett.* 81 (1998). [Erratum: Phys.Rev.Lett. 81, 4279 (1998)], pp. 1158–1162. DOI: 10.1103/PhysRevLett.81.1158. arXiv: hep-ex/9805021.

[10] Y. Fukuda et al. "Evidence for oscillation of atmospheric neutrinos". In: *Phys. Rev. Lett.* 81 (1998), pp. 1562–1567. DOI: 10.1103/PhysRevLett.81.1562. arXiv: hep-ex/9807003.

[11] Q. R. Ahmad et al. "Direct evidence for neutrino flavor transformation from neutral current interactions in the Sudbury Neutrino Observatory". In: *Phys. Rev. Lett.* 89 (2002), p. 011301. DOI: 10.1103/PhysRevLett.89.011301. arXiv: nucl-ex/0204008.

[12] K. Eguchi et al. "First results from KamLAND: Evidence for reactor anti-neutrino disappearance". In: *Phys. Rev. Lett.* 90 (2003), p. 021802. DOI: 10.1103/PhysRevLett.90.021802. arXiv: hep-ex/0212021.

[13] K. Hirata et al. "Observation of a Neutrino Burst from the Supernova SN 1987a". In: *Phys. Rev. Lett.* 58 (1987). Ed. by K. C. Wali, pp. 1490–1493. DOI: 10.1103/PhysRevLett.58.1490.

[14] R. M. Bionta et al. "Observation of a Neutrino Burst in Coincidence with Supernova SN 1987a in the Large Magellanic Cloud". In: *Phys. Rev. Lett.* 58 (1987), p. 1494. DOI: 10.1103/PhysRevLett.58.1494.

[15] M. G. Aartsen et al. "Neutrino emission from the direction of the blazar TXS 0506+056 prior to the IceCube-170922A alert". In: *Science* 361.6398 (2018), pp. 147–151. DOI: 10.1126/science.aat2890. arXiv: 1807.08794 [astro-ph.HE].

[16] R. Abbasi et al. "Evidence for neutrino emission from the nearby active galaxy NGC 1068". In: *Science* 378.6619 (2022), pp. 538–543. DOI: 10.1126/science.abg3395. arXiv: 2211.09972 [astro-ph.HE].

[17] Victor F. Hess. "Über Beobachtungen der durchdringenden Strahlung bei sieben Freiballonfahrten". In: *Phys. Z.* 13 (1912), pp. 1084–1091.

[18] A. M. Hillas. "The Origin of Ultrahigh-Energy Cosmic Rays". In: *Ann. Rev. Astron. Astrophys.* 22 (1984), pp. 425–444. DOI: 10.1146/annurev.aa.22.090184.002233.

[19] John Linsley. "Evidence for a primary cosmic-ray particle with energy 10^{20} eV". In: *Phys. Rev. Lett.* 10 (1963), p. 146. DOI: 10.1103/PhysRevLett.10.146.

[20] D. J. Bird et al. "The Cosmic ray energy spectrum observed by the Fly's Eye". In: *Astrophys. J.* 424 (1994), pp. 491–502. DOI: 10.1086/173906.

[21] Tadeusz Wibig and Arnold W. Wolfendale. "At what particle energy do extragalactic cosmic rays start to predominate?" In: *J. Phys. G* 31 (2005), pp. 255–264. DOI: 10.1088/0954-3899/31/3/005. arXiv: astro-ph/0410624.

[22] J. R. Jokipii and G. Morfill. "Ultrahigh-energy cosmic rays in a galactic wind: Acceleration at the termination shock". In: *ICCR International Symposium on the Astrophysical Aspects of the Most Energetic Cosmic Rays*. 1990.

[23] A. M. Hillas. "Can diffusive shock acceleration in supernova remnants account for high-energy galactic cosmic rays?" In: *J. Phys. G* 31 (2005), R95–R131. DOI: 10.1088/0954-3899/31/5/R02.

[24] Alexander Aab et al. "The Pierre Auger Cosmic Ray Observatory". In: *Nucl. Instrum. Meth. A* 798 (2015), pp. 172–213. DOI: 10.1016/j.nima.2015.06.058. arXiv: 1502.01323 [astro-ph.IM].

[25] A. Abdul Halim et al. "Constraining the sources of ultra-high-energy cosmic rays across and above the ankle with the spectrum and composition data measured at the Pierre Auger Observatory". In: *JCAP* 05 (2023), p. 024. DOI: 10.1088/1475-7516/2023/05/024. arXiv: 2211.02857 [astro-ph.HE].

[26] Alexander Aab et al. "Measurement of the cosmic-ray energy spectrum above 2.5×10^{18} eV using the Pierre Auger Observatory". In: *Phys. Rev. D* 102.6 (2020), p. 062005. DOI: 10.1103/PhysRevD.102.062005. arXiv: 2008.06486 [astro-ph.HE].

[27] Kenneth Greisen. "End to the cosmic ray spectrum?" In: *Phys. Rev. Lett.* 16 (1966), pp. 748–750. DOI: 10.1103/PhysRevLett.16.748.

[28] G. T. Zatsepin and V. A. Kuzmin. "Upper limit of the spectrum of cosmic rays". In: *JETP Lett.* 4 (1966), pp. 78–80.

[29] Luis A. Anchordoqui. "Ultra-High-Energy Cosmic Rays". In: *Phys. Rept.* 801 (2019), pp. 1–93. DOI: 10.1016/j.physrep.2019.01.002. arXiv: 1807.09645 [astro-ph.HE].

[30] B. P. Abbott et al. "Observation of Gravitational Waves from a Binary Black Hole Merger". In: *Phys. Rev. Lett.* 116.6 (2016), p. 061102. DOI: 10.1103/PhysRevLett.116.061102. arXiv: 1602.03837 [gr-qc].

[31] Kumiko Kotera and Joseph Silk. "Ultrahigh Energy Cosmic Rays and Black Hole Mergers". In: *Astrophys. J. Lett.* 823.2 (2016), p. L29. DOI: 10.3847/2041-8205/823/2/L29. arXiv: 1602.06961 [astro-ph.HE].

[32] Péter Mészáros et al. "Multi-Messenger Astrophysics". In: *Nature Rev. Phys.* 1 (2019), pp. 585–599. DOI: 10.1038/s42254-019-0101-z. arXiv: 1906.10212 [astro-ph.HE].

[33] Jonas P. Pereira et al. "Binary coalescences as sources of Ultra-High Energy Cosmic Rays". In: (July 2023). arXiv: 2307.06200 [astro-ph.HE].

[34] M. G. Aartsen et al. "First observation of PeV-energy neutrinos with IceCube". In: *Phys. Rev. Lett.* 111 (2013), p. 021103. DOI: 10.1103/PhysRevLett.111.021103. arXiv: 1304.5356 [astro-ph.HE].

[35] M. G. Aartsen et al. "Evidence for High-Energy Extraterrestrial Neutrinos at the IceCube Detector". In: *Science* 342 (2013), p. 1242856. DOI: 10.1126/science.1242856. arXiv: 1311.5238 [astro-ph.HE].

[36] Mark G. Aartsen et al. "Multimessenger observations of a flaring blazar coincident with high-energy neutrino IceCube-170922A". In: *Science* 361.6398 (2018), eaat1378. DOI: 10.1126/science.aat1378. arXiv: 1807.08816 [astro-ph.HE].

[37] R. Abbasi et al. "Improved Characterization of the Astrophysical Muon–neutrino Flux with 9.5 Years of IceCube Data". In: *Astrophys. J.* 928.1 (2022), p. 50. DOI: 10.3847/1538-4357/ac4d29. arXiv: 2111.10299 [astro-ph.HE].

[38] M. Ackermann et al. "Observation of high-energy neutrinos from the Galactic plane". In: *Science* 380.6652 (2023), p. 1338. DOI: 10.1126/science.adc9818.

[39] M. G. Aartsen et al. "IceCube-Gen2: the window to the extreme Universe". In: *J. Phys. G* 48.6 (2021), p. 060501. DOI: 10.1088/1361-6471/abbd48. arXiv: 2008.04323 [astro-ph.HE].

[40] S. Adrian-Martinez et al. "Letter of intent for KM3NeT 2.0". In: *J. Phys. G* 43.8 (2016), p. 084001. DOI: 10.1088/0954-3899/43/8/084001. arXiv: 1601.07459 [astro-ph.IM].

[41] Matteo Agostini et al. "The Pacific Ocean Neutrino Experiment". In: *Nature Astron.* 4.10 (2020), pp. 913–915. DOI: 10.1038/s41550-020-1182-4. arXiv: 2005.09493 [astro-ph.HE].

[42] A. I. Mukhin et al. "Energy Dependence of Total Cross-sections for Neutrino and Anti-neutrino Interactions at Energies Below 35-GeV". In: *Sov. J. Nucl. Phys.* 30 (1979), p. 528.

[43] D. S. Baranov et al. "Measurement of the $\nu_\mu N$ Total Cross-section at 2–30 GeV in a Skat Neutrino Experiment". In: *Phys. Lett. B* 81 (1979), pp. 255–257. DOI: 10.1016/0370-2693(79)90536-7.

[44] S. J. Barish et al. "Study of neutrino interactions in hydrogen and deuterium. II. Inelastic charged-current reactions". In: *Phys. Rev. D* 19 (1979), p. 2521. DOI: 10.1103/PhysRevD.19.2521.

[45] S. Ciampolillo et al. "Total Cross Section for Neutrino Charged Current Interactions at 3 GeV and 9 GeV". In: *Phys. Lett. B* 84 (1979), pp. 281–284. DOI: 10.1016/0370-2693(79)90303-4.

[46] J. G. H. de Groot et al. "Inclusive Interactions of High-Energy Neutrinos and anti-neutrinos in Iron". In: *Z. Phys. C* 1 (1979), p. 143. DOI: 10.1007/BF01445406.

[47] D. C. Colley et al. "Cross-sections for Charged Current ν and $\bar{\nu}$ Interactions in the Energy Range 10 to 50 GeV". In: *Z. Phys. C* 2 (1979), p. 187. DOI: 10.1007/BF01474659.

[48] J. G. Morfin et al. "Total Cross-sections and Nucleon Structure Functions in the Gargamelle SPS Neutrino / Antineutrino Experiment". In: *Phys. Lett. B* 104 (1981), pp. 235–238. DOI: 10.1016/0370-2693(81)90598-0.

[49] N. J. Baker et al. "Total Cross-sections for $\nu_\mu n$ and $\nu_\mu p$ Charged-Current Interactions in the 7-foot Bubble Chamber". In: *Phys. Rev. D* 25 (1982), pp. 617–623. DOI: 10.1103/PhysRevD.25.617.

[50] J. P. Berge et al. "Total Neutrino and Antineutrino Charged Current Cross section Measurements in 100, 160, and 200 GeV Narrow Band Beams". In: *Z. Phys. C* 35 (1987), p. 443. DOI: 10.1007/BF01596895.

[51] V. B. Anikeev et al. "Total cross-section measurements for ν_μ, $\bar{\nu}_\mu$ interactions in 3–30 GeV energy range with IHEP-JINR neutrino detector". In: *Z. Phys. C* 70 (1996), pp. 39–46. DOI: 10.1007/s002880050078.

[52] W. G. Seligman. "A Next-to-Leading Order QCD Analysis of Neutrino-Iron Structure Functions at the Tevatron". PhD thesis. Columbia University, 1997.

[53] M. Tzanov et al. "Precise measurement of neutrino and anti-neutrino differential cross sections". In: *Phys. Rev. D* 74 (2006), p. 012008. DOI: 10.1103/PhysRevD.74.012008. arXiv: hep-ex/0509010.

[54] Q. Wu et al. "A Precise measurement of the muon neutrino-nucleon inclusive charged current cross-section off an isoscalar target in the energy range $2.5 < E_\nu < 40$ GeV by NOMAD". In: *Phys. Lett. B* 660 (2008), pp. 19–25. DOI: 10.1016/j.physletb.2007.12.027. arXiv: 0711.1183 [hep-ex].

[55] P. Adamson et al. "Neutrino and Antineutrino Inclusive Charged-current Cross Section Measurements with the MINOS Near Detector". In: *Phys. Rev. D* 81 (2010), p. 072002. DOI: 10.1103/PhysRevD.81.072002. arXiv: 0910.2201 [hep-ex].

[56] Y. Nakajima et al. "Measurement of Inclusive Charged Current Interactions on Carbon in a Few-GeV Neutrino Beam". In: *Phys. Rev. D* 83 (2011), p. 012005. DOI: 10.1103/PhysRevD.83.012005. arXiv: 1011.2131 [hep-ex].

[57] K. Abe et al. "Measurement of the inclusive ν_μ charged current cross section on carbon in the near detector of the T2K experiment". In: *Phys. Rev. D* 87.9 (2013), p. 092003. DOI: 10.1103/PhysRevD.87.092003. arXiv: 1302.4908 [hep-ex].

[58] R. Acciarri et al. "Measurements of Inclusive Muon Neutrino and Antineutrino Charged Current Differential Cross Sections on Argon in the NuMI Antineutrino Beam". In: *Phys. Rev. D* 89.11 (2014), p. 112003. DOI: 10.1103/PhysRevD.89.112003. arXiv: 1404.4809 [hep-ex].

[59] K. Abe et al. "Measurement of the inclusive ν_μ charged current cross section on iron and hydrocarbon in the T2K on-axis neutrino beam". In: *Phys. Rev. D* 90.5 (2014), p. 052010. DOI: 10.1103/PhysRevD.90.052010. arXiv: 1407.4256 [hep-ex].

[60] M. G. Aartsen et al. "Measurement of the multi-TeV neutrino cross section with IceCube using Earth absorption". In: *Nature* 551 (2017), pp. 596–600. DOI: 10.1038/nature24459. arXiv: 1711.08119 [hep-ex].

[61] Mauricio Bustamante and Amy Connolly. "Extracting the Energy-Dependent Neutrino-Nucleon Cross Section above 10 TeV Using IceCube Showers". In: *Phys. Rev. Lett.* 122.4 (2019), p. 041101. DOI: 10.1103/PhysRevLett.122.041101. arXiv: 1711.11043 [astro-ph.HE].

[62] M. G. Aartsen et al. "Measurements using the inelasticity distribution of multi-TeV neutrino interactions in IceCube". In: *Phys. Rev. D* 99.3 (2019), p. 032004. DOI: 10.1103/PhysRevD.99.032004. arXiv: 1808.07629 [hep-ex].

[63] R. Abbasi et al. "Measurement of the high-energy all-flavor neutrino-nucleon cross section with IceCube". In: *Phys. Rev. D* 104.4 (Nov. 2020), p. 022001. DOI: 10.1103/PhysRevD.104.022001. arXiv: 2011.03560 [hep-ex].

[64] Rasha Abbasi et al. "Measuring the Neutrino Cross Section Using 8 years of Upgoing Muon Neutrinos Observed with IceCube". In: *PoS* ICRC2021 (2021), p. 1158. DOI: 10.22323/1.395.1158. arXiv: 2108.04965 [astro-ph.HE].

[65] V. S. Berezinsky and G. T. Zatsepin. "Cosmic rays at ultrahigh-energies (neutrino?)" In: *Phys. Lett. B* 28 (1969), pp. 423–424. DOI: 10.1016/0370-2693(69)90341-4.

[66] M. G. Aartsen et al. "Differential limit on the extremely-high-energy cosmic neutrino flux in the presence of astrophysical background from nine years of IceCube data". In: *Phys. Rev. D* 98.6 (2018), p. 062003. DOI: 10.1103/PhysRevD.98.062003. arXiv: 1807.01820 [astro-ph.HE].

[67] Alexander Aab et al. "Probing the origin of ultra-high-energy cosmic rays with neutrinos in the EeV energy range using the Pierre Auger Observatory". In: *JCAP* 10 (2019), p. 022. DOI: 10.1088/1475-7516/2019/10/022. arXiv: 1906.07422 [astro-ph.HE].

[68] P. Allison et al. "Constraints on the diffuse flux of ultrahigh energy neutrinos from four years of Askaryan Radio Array data in two stations". In: *Phys. Rev. D* 102.4 (2020), p. 043021. DOI: 10.1103/PhysRevD.102.043021. arXiv: 1912.00987 [astro-ph.HE].

[69] A. Anker et al. "Targeting ultra-high energy neutrinos with the ARIANNA experiment". In: *Adv. Space Res.* 64 (2019), pp. 2595–2609. DOI: 10.1016/j.asr.2019.06.016. arXiv: 1903.01609 [astro-ph.IM].

[70] Ulrich F. Katz. "The ORCA Option for KM3NeT". In: (2013). arXiv: 1402.1022 [astro-ph.IM].

[71] J. A. Aguilar et al. "The Next-Generation Radio Neutrino Observatory – Multi-Messenger Neutrino Astrophysics at Extreme Energies". In: (July 2019). arXiv: 1907.12526 [astro-ph.HE].

[72] Jaime Álvarez-Muñiz et al. "The Giant Radio Array for Neutrino Detection (GRAND): Science and Design". In: *Sci. China Phys. Mech. Astron.* 63.1 (2020), p. 219501. DOI: 10.1007/s11433-018-9385-7. arXiv: 1810.09994 [astro-ph.HE].

[73] Andres Romero-Wolf et al. "An Andean Deep-Valley Detector for High-Energy Tau Neutrinos". In: *Latin American Strategy Forum for Research Infrastructure*. Feb. 2020. arXiv: 2002.06475 [astro-ph.IM].

[74] A. V. Olinto et al. "The POEMMA (Probe of Extreme Multi-Messenger Astrophysics) observatory". In: *JCAP* 06 (2021), p. 007. DOI: 10.1088/1475-7516/2021/06/007. arXiv: 2012.07945 [astro-ph.IM].

[75] Q. Abarr et al. "The Payload for Ultrahigh Energy Observations (PUEO): a white paper". In: *JINST* 16.08 (2021), P08035. DOI: 10.1088/1748-0221/16/08/P08035. arXiv: 2010.02892 [astro-ph.IM].

[76] A. D. Avrorin et al. "High-Energy Neutrino Astronomy and the Baikal-GVD Neutrino Telescope". In: *Phys. At. Nucl.* 84.4 (2021), pp. 513–518. DOI: 10.1134/S1063778821040062. arXiv: 2011.09209 [astro-ph.HE].

[77] Steffen Hallmann et al. "Sensitivity studies for the IceCube-Gen2 radio array". In: *PoS* ICRC2021 (2021), p. 1183. DOI: 10.22323/1.395.1183. arXiv: 2107.08910 [astro-ph.HE].

[78] Lisa Johanna Schumacher et al. "PLEνM: A global and distributed monitoring system of high-energy astrophysical neutrinos". In: *PoS* ICRC2021 (2021), p. 1185. DOI: 10.22323/1.395.1185. arXiv: 2107.13534 [astro-ph.IM].

[79] Abby Bishop et al. "Concept Study of a Radio Array Embedded in a Deep Gen2-like Optical Array". In: *37th International Cosmic Ray Conference*. July 2021. arXiv: 2108.00283 [astro-ph.HE].

[80] Godwin Komla Krampah et al. "The NuMoon Experiment: Lunar Detection of Cosmic Rays and Neutrinos with LOFAR". In: *PoS* ICRC2021 (2021), p. 1148. DOI: 10.22323/1.395.1148.

[81] Anthony M. Brown et al. "Trinity: an imaging air Cherenkov telescope to search for Ultra-High-Energy neutrinos". In: *PoS* ICRC2021 (Sept. 2021), p. 1179. DOI: 10.22323/1.395.1179. arXiv: 2109.03125 [astro-ph.IM].

[82] Roshan Mammen Abraham et al. "Tau Neutrinos in the Next Decade: from GeV to EeV". In: *2022 Snowmass Summer Study*. Mar. 2022. arXiv: 2203.05591 [hep-ph].

[83] Markus Ackermann et al. "High-Energy and Ultra-High-Energy Neutrinos". In: *2022 Snowmass Summer Study*. Vol. 36. Mar. 2022, pp. 55–110. DOI: 10.1016/j.jheap.2022.08.001. arXiv: 2203.08096 [hep-ph].

[84] J. A. Aguilar et al. "Design and Sensitivity of the Radio Neutrino Observatory in Greenland (RNO-G)". In: *JINST* 16.03 (2021). [Erratum: JINST 18, E03001 (2023)], P03025. DOI: 10.1088/1748-0221/16/03/P03025. arXiv: 2010.12279 [astro-ph.IM].

[85] B. P. Abbott et al. "Multi-messenger Observations of a Binary Neutron Star Merger". In: *Astrophys. J. Lett.* 848.2 (2017), p. L12. DOI: 10.3847/2041-8213/aa91c9. arXiv: 1710.05833 [astro-ph.HE].

[86] K.G. Jansky. "Directional Studies of Atmospherics at High Frequencies". In: *Proceedings of the Institute of Radio Engineers* 20.12 (1932), pp. 1920–1932. DOI: 10.1109/JRPROC.1932.227477.

[87] Riccardo Giacconi et al. "Evidence for x Rays From Sources Outside the Solar System". In: *Phys. Rev. Lett.* 9 (1962), pp. 439–443. DOI: 10.1103/PhysRevLett.9.439.

[88] W. L. Kraushaar and G. W. Clark. "Search for Primary Cosmic Gamma Rays with the Satellite Explorer XI". In: *Phys. Rev. Lett.* 8 (3 Feb. 1962), pp. 106–109. DOI: 10.1103/PhysRevLett.8.106. URL: https://link.aps.org/doi/10.1103/PhysRevLett.8.106.

[89] Albert Einstein. "Über Gravitationswellen". In: *Sitzungsber. Preuss. Akad. Wiss. Berlin (Math. Phys.)* 1918 (1918), pp. 154–167.

[90] Thomas K. Gaisser, Ralph Engel, and Elisa Resconi. *Cosmic Rays and Particle Physics: 2nd Edition*. Cambridge University Press, June 2016. ISBN: 978-0-521-01646-9.

[91] Alessandro De Angelis, Giorgio Galanti, and Marco Roncadelli. "Transparency of the Universe to gamma rays". In: *Mon. Not. Roy. Astron. Soc.* 432 (2013), p. 3245. DOI: 10.1093/mnras/stt684. arXiv: 1302.6460 [astro-ph.HE].

[92] A. Goldstein et al. "An Ordinary Short Gamma-Ray Burst with Extraordinary Implications: Fermi-GBM Detection of GRB 170817A". In: *Astrophys. J. Lett.* 848.2 (2017), p. L14. DOI: 10.3847/2041-8213/aa8f41. arXiv: 1710.05446 [astro-ph.HE].

[93] Daniel Kasen et al. "Origin of the heavy elements in binary neutron-star mergers from a gravitational wave event". In: *Nature* 551 (2017), p. 80. DOI: 10.1038/nature24453. arXiv: 1710.05463 [astro-ph.HE].

[94] Matthew F. Carney, Leslie E. Wade, and Burke S. Irwin. "Comparing two models for measuring the neutron star equation of state from gravitational-wave signals". In: *Phys. Rev. D* 98.6 (2018), p. 063004. DOI: 10.1103/PhysRevD.98.063004. arXiv: 1805.11217 [gr-qc].

[95] B. P. Abbott et al. "GW170817: Measurements of neutron star radii and equation of state". In: *Phys. Rev. Lett.* 121.16 (2018), p. 161101. DOI: 10.1103/PhysRevLett.121.161101. arXiv: 1805.11581 [gr-qc].

[96] B. P. Abbott et al. "A gravitational-wave standard siren measurement of the Hubble constant". In: *Nature* 551.7678 (2017), pp. 85–88. DOI: 10.1038/nature24471. arXiv: 1710.05835 [astro-ph.CO].

[97] A. Albert et al. "Search for High-energy Neutrinos from Binary Neutron Star Merger GW170817 with ANTARES, IceCube, and the Pierre Auger Observatory". In: *Astrophys. J. Lett.* 850.2 (2017), p. L35. DOI: 10.3847/2041-8213/aa9aed. arXiv: 1710.05839 [astro-ph.HE].

[98] S. Di Pace. "Status of Advanced Virgo and upgrades before next observing runs". In: *Phys. Scripta* 96.12 (2021), p. 124054. DOI: 10.1088/1402-4896/ac2efc.

[99] Ralph Engel, David Seckel, and Todor Stanev. "Neutrinos from propagation of ultrahigh-energy protons". In: *Phys. Rev. D* 64 (2001), p. 093010. DOI: 10.1103/PhysRevD.64.093010. arXiv: astro-ph/0101216.

[100] Kseniya V. Ptitsyna and Sergei V. Troitsky. "Physical conditions in potential sources of ultra-high-energy cosmic rays. I. Updated Hillas plot and radiation-loss constraints". In: *Phys. Usp.* 53 (2010), pp. 691–701. DOI: 10.3367/UFNe.0180.201007c.0723. arXiv: 0808.0367 [astro-ph].

[101] F. W. Stecker et al. "High-energy neutrinos from active galactic nuclei". In: *Phys. Rev. Lett.* 66 (1991). [Erratum: Phys.Rev.Lett. 69, 2738 (1992)], pp. 2697–2700. DOI: 10.1103/PhysRevLett.66.2697.

[102] R. J. Protheroe. "High-energy neutrinos from blazars". In: *ASP Conf. Ser.* 121 (1997), p. 585. arXiv: astro-ph/9607165.

[103] Karl Mannheim. "High-energy neutrinos from extragalactic jets". In: *Astropart. Phys.* 3 (1995), p. 295. DOI: 10.1016/0927-6505(94)00044-4.

[104] Eli Waxman and John N. Bahcall. "High-energy neutrinos from cosmological gamma-ray burst fireballs". In: *Phys. Rev. Lett.* 78 (1997), pp. 2292–2295. DOI: 10.1103/PhysRevLett.78.2292. arXiv: astro-ph/9701231.

[105] Kohta Murase and Kunihito Ioka. "TeV–PeV Neutrinos from Low-Power Gamma-Ray Burst Jets inside Stars". In: *Phys. Rev. Lett.* 111.12 (2013), p. 121102. DOI: 10.1103/PhysRevLett.111.121102. arXiv: 1306.2274 [astro-ph.HE].

[106] Ersilia Guarini et al. "Multi-messenger detection prospects of gamma-ray burst afterglows with optical jumps". In: *JCAP* 06.06 (2022), p. 034. DOI: 10.1088/1475-7516/2022/06/034. arXiv: 2112.07690 [astro-ph.HE].

[107] Mou Roy. "Ultrahigh-energy neutrinos from supernova remnants". In: *J. Phys. G* 25 (1999), pp. 129–134. DOI: 10.1088/0954-3899/25/1/011. arXiv: astro-ph/9901215.

[108] Brandon Wolfe et al. "Neutrinos and Gamma Rays from Galaxy Clusters". In: *Astrophys. J.* 687 (2008), pp. 193–201. DOI: 10.1086/591723. arXiv: 0807.0794 [astro-ph].

[109] Ke Fang and Angela V. Olinto. "High-energy neutrinos from sources in clusters of galaxies". In: *Astrophys. J.* 828.1 (2016), p. 37. DOI: 10.3847/0004-637X/828/1/37. arXiv: 1607.00380 [astro-ph.HE].

[110] Rasha Abbasi et al. "A time-independent search for neutrinos from galaxy clusters with IceCube". In: *PoS* ICRC2021 (2021), p. 1133. DOI: 10.22323/1.395.1133. arXiv: 2107.10080 [astro-ph.HE].

[111] Tsvi Piran. "Magnetic fields in gamma-ray bursts: A Short overview". In: *AIP Conf. Proc.* 784.1 (2005). Ed. by Elisabete M. de Gouveia Dal Pino, German Lugones, and Alexander Lazarian, pp. 164–174. DOI: 10.1063/1.2077181. arXiv: astro-ph/0503060.

[112] Kohta Murase et al. "High-energy cosmic-ray nuclei from high- and low-luminosity gamma-ray bursts and implications for multi-messenger astronomy". In: *Phys. Rev. D* 78 (2008), p. 023005. DOI: 10.1103/PhysRevD.78.023005. arXiv: 0801.2861 [astro-ph].

[113] D. N. Burrows et al. "Discovery of the Onset of Rapid Accretion by a Dormant Massive Black Hole". In: *Nature* 476 (2011), p. 421. DOI: 10.1038/nature10374. arXiv: 1104.4787 [astro-ph.HE].

[114] P. Kumar et al. "A model for the multiwavelength radiation from tidal disruption event Swift J1644+57". In: *Mon. Not. Roy. Astron. Soc.* 434 (2013), pp. 3078–3088. DOI: 10.1093/mnras/stt1221. arXiv: 1304.1545 [astro-ph.HE].

[115] Nicholas Senno, Kohta Murase, and Peter Mészáros. "High-energy Neutrino Flares from X-Ray Bright and Dark Tidal Disruption Events". In: *Astrophys. J.* 838.1 (2017), p. 3. DOI: 10.3847/1538-4357/aa6344. arXiv: 1612.00918 [astro-ph.HE].

[116] Todd A. Thompson et al. "Magnetic fields in starburst galaxies and the origin of the fir-radio correlation". In: *Astrophys. J.* 645 (2006), pp. 186–198. DOI: 10.1086/504035. arXiv: astro-ph/0601626.

[117] Jun Kataoka and Lukasz Stawarz. "X-ray emission properties of large scale jets, hotspots and lobes in active galactic nuclei". In: *Astrophys. J.* 622 (2005), p. 797. DOI: 10.1086/428083. arXiv: astro-ph/0411042.

[118] S. P. Reynolds, B. M. Gaensler, and F. Bocchino. "Magnetic fields in supernova remnants and pulsar-wind nebulae". In: *Space Sci. Rev.* 166 (2012), pp. 231–261. DOI: 10.1007/s11214-011-9775-y. arXiv: 1104.4047 [astro-ph.GA].

[119] Abdul I. Asvarov. "Size distribution of supernova remnants and the interstellar medium: the case of M 33". In: *Astron. Astrophys.* 561 (2014), A70. DOI: 10.1051/0004-6361/201322774. arXiv: 1311.5166 [astro-ph.GA].

[120] Todd A. Thompson, Eliot Quataert, and Norman Murray. "Radio Emission from Supernova Remnants: Implications for Post-Shock Magnetic Field Amplification and the Magnetic Fields of Galaxies". In: *Mon. Not. Roy. Astron. Soc.* 397 (2009), p. 1410. DOI: 10.1111/j.1365-2966.2009.14889.x. arXiv: 0902.1755 [astro-ph.HE].

[121] A. de la Chevrotière et al. "SEARCHING FOR MAGNETIC FIELDS IN 11 WOLF–RAYET STARS: ANALYSIS OF CIRCULAR POLARIZATION MEASUREMENTS FROM ESPaDOnS*". In: *The Astrophysical Journal* 781.2 (Jan. 2014), p. 73. DOI: 10.1088/0004-637X/781/2/73. URL: https://dx.doi.org/10.1088/0004-637X/781/2/73.

[122] Jonathan Arons. "Magnetars in the metagalaxy: an origin for ultrahigh-energy cosmic rays in the nearby universe". In: *Astrophys. J.* 589 (2003), pp. 871–892. DOI: 10.1086/374776. arXiv: astro-ph/0208444.

[123] Kohta Murase, Peter Meszaros, and Bing Zhang. "Probing the birth of fast rotating magnetars through high-energy neutrinos". In: *Phys. Rev. D* 79 (2009), p. 103001. DOI: 10.1103/PhysRevD.79.103001. arXiv: 0904.2509 [astro-ph.HE].

[124] Ke Fang, Kumiko Kotera, and Angela V. Olinto. "Newly-born pulsars as sources of ultrahigh energy cosmic rays". In: *Astrophys. J.* 750 (2012), p. 118. DOI: 10.1088/0004-637X/750/2/118. arXiv: 1201.5197 [astro-ph.HE].

[125] Rafael Alves Batista et al. "Open Questions in Cosmic-Ray Research at Ultrahigh Energies". In: *Front. Astron. Space Sci.* 6 (2019), p. 23. DOI: 10.3389/fspas.2019.00023. arXiv: 1903.06714 [astro-ph.HE].

[126] M. L. Lister et al. "MOJAVE. XVII. Jet Kinematics and Parent Population Properties of Relativistically Beamed Radio-Loud Blazars". In: *Astrophys. J.* 874.1 (2019), p. 43. DOI: 10.3847/1538-4357/ab08ee. arXiv: 1902.09591 [astro-ph.GA].

[127] Enrico Fermi. "On the Origin of the Cosmic Radiation". In: *Phys. Rev.* 75 (1949), pp. 1169–1174. DOI: 10.1103/PhysRev.75.1169.

[128] Dimitrios Giannios, Dmitri A. Uzdensky, and Mitchell C. Begelman. "Fast TeV variability in blazars: jet in a jet". In: *Mon. Not. Roy. Astron. Soc.* 395 (2009), p. 29. DOI: 10.1111/j.1745-3933.2009.00635.x. arXiv: 0901.1877 [astro-ph.HE].

[129] Elisabete M. de Gouveia Dal Pino et al. "Magnetic Reconnection, Cosmic Ray Acceleration, and Gamma-Ray emission around Black Holes and Relativistic Jets". In: *PoS* BHCB2018 (2018). Ed. by Rita Cassia Anjos and Carlos Henrique Coimbra Araujo, p. 008. arXiv: 1903.08982 [astro-ph.HE].

[130] S. R. Kelner, Felex A. Aharonian, and V. V. Bugayov. "Energy spectra of gamma-rays, electrons and neutrinos produced at proton-proton interactions in the very high energy regime". In: *Phys. Rev. D* 74 (2006). [Erratum: Phys.Rev.D 79, 039901 (2009)], p. 034018. DOI: 10.1103/PhysRevD.74.034018. arXiv: astro-ph/0606058.

[131] S. R. Kelner and F. A. Aharonian. "Energy spectra of gamma-rays, electrons and neutrinos produced at interactions of relativistic protons with low energy radiation". In: *Phys. Rev. D* 78 (2008). [Erratum: Phys.Rev.D 82, 099901 (2010)], p. 034013. DOI: 10.1103/PhysRevD.82.099901. arXiv: 0803.0688 [astro-ph].

[132] R. U. Abbasi et al. "The energy spectrum of cosmic rays above $10^{17.2}$ eV measured by the fluorescence detectors of the Telescope Array experiment in seven years". In: *Astropart. Phys.* 80 (2016), pp. 131–140. DOI: 10.1016/j.astropartphys.2016.04.002. arXiv: 1511.07510 [astro-ph.HE].

[133] Eli Waxman and John N. Bahcall. "High-energy neutrinos from astrophysical sources: An Upper bound". In: *Phys. Rev. D* 59 (1999), p. 023002. DOI: 10.1103/PhysRevD.59.023002. arXiv: hep-ph/9807282.

[134] Raj Gandhi et al. "Neutrino interactions at ultrahigh-energies". In: *Phys. Rev. D* 58 (1998), p. 093009. DOI: 10.1103/PhysRevD.58.093009. arXiv: hep-ph/9807264.

[135] Francis Halzen et al. "The AMANDA neutrino telescope". In: *Nucl. Phys. B Proc. Suppl.* 77 (1999). Ed. by N. J. C. Spooner and V. Kudryavtsev, pp. 474–485. DOI: 10.1016/S0920-5632(99)00469-7. arXiv: hep-ex/9809025.

[136] P. A. Cherenkov. "Visible luminescence of pure liquids under the influence of γ-radiation". In: *Dokl. Akad. Nauk SSSR* 2.8 (1934), pp. 451–454. DOI: 10.3367/UFNr.0093.196710n.0385.

[137] M. G. Aartsen et al. "Improvement in Fast Particle Track Reconstruction with Robust Statistics". In: *Nucl. Instrum. Meth. A* 736 (2014), pp. 143–149. DOI: 10.1016/j.nima.2013.10.074. arXiv: 1308.5501 [astro-ph.IM].

[138] Shiqi Yu et al. "Direction Reconstruction using a CNN for GeV-Scale Neutrinos in IceCube". In: *PoS* ICRC2021 (2021), p. 1054. DOI: 10.22323/1.395.1054. arXiv: 2107.02122 [astro-ph.HE].

[139] John G. Learned and Sandip Pakvasa. "Detecting tau-neutrino oscillations at PeV energies". In: *Astropart. Phys.* 3 (1995), pp. 267–274. DOI: 10.1016/0927-6505(94)00043-3. arXiv: hep-ph/9405296.

[140] M. G. Aartsen et al. "Flavor Ratio of Astrophysical Neutrinos above 35 TeV in IceCube". In: *Phys. Rev. Lett.* 114.17 (2015), p. 171102. DOI: 10.1103/PhysRevLett.114.171102. arXiv: 1502.03376 [astro-ph.HE].

[141] Rasha Abbasi et al. "Summary of IceCube tau neutrino searches and flavor composition measurements of the diffuse astrophysical neutrino flux". In: *PoS* ICRC2023 (2023), p. 1122. DOI: 10.22323/1.444.1122. arXiv: 2308.15213 [astro-ph.HE].

[142] Teppei Katori et al. "Test of Lorentz Violation with Astrophysical Neutrino Flavor at IceCube". In: *8th Meeting on CPT and Lorentz Symmetry*. 2020, pp. 166–169. DOI: 10.1142/9789811213984_0042. arXiv: 1906.09240 [hep-ph].

[143] R. Abbasi et al. "All-flavor constraints on nonstandard neutrino interactions and generalized matter potential with three years of IceCube DeepCore data". In: *Phys. Rev. D* 104.7 (2021), p. 072006. DOI: 10.1103/PhysRevD.104.072006. arXiv: 2106.07755 [hep-ex].

[144] Giovanni Renzi and Juan A. Aguilar. "Search for dark matter annihilations in the center of the Earth with IceCube". In: *38th International Cosmic Ray Conference*. Aug. 2023. arXiv: 2308.02920 [astro-ph.HE].

[145] Juan Antonio Aguilar Sanchez et al. "Search for Dark Matter annihilation in the center of the Earth with IceCube". In: *PoS* ICRC2023 (2023), p. 1393. DOI: 10.22323/1.444.1393.

[146] R. Abbasi et al. "Search for neutrino lines from dark matter annihilation and decay with IceCube". In: (Mar. 2023). arXiv: 2303.13663 [astro-ph.HE].

[147] Avrirubm A. D. et al. "Baikal-GVD: status and first results". In: *PoS* ICHEP2020 (2021), p. 606. DOI: 10.22323/1.390.0606. arXiv: 2012.03373 [astro-ph.HE].

[148] Z. P. Ye et al. *Proposal for a neutrino telescope in South China Sea*. July 2022. arXiv: 2207.04519 [astro-ph.HE].

[149] Tian-Qi Huang et al. "Proposal for the High Energy Neutrino Telescope". In: *PoS* ICRC2023 (2023), p. 1080. DOI: 10.22323/1.444.1080.

[150] P. W. Gorham et al. "Constraints on the ultrahigh-energy cosmic neutrino flux from the fourth flight of ANITA". In: *Phys. Rev. D* 99.12 (2019), p. 122001. DOI: 10.1103/PhysRevD.99.122001. arXiv: 1902.04005 [astro-ph.HE].

[151] A. Nepomuk Otte et al. "Trinity: An Air-Shower Imaging Instrument to detect Ultrahigh Energy Neutrinos". In: (July 2019). arXiv: 1907.08727 [astro-ph.IM].

[152] S. Prohira et al. "Observation of Radar Echoes From High-Energy Particle Cascades". In: *Phys. Rev. Lett.* 124.9 (2020), p. 091101. DOI: 10.1103/PhysRevLett.124.091101. arXiv: 1910.12830 [astro-ph.HE].

[153] Stephanie Wissel et al. "Prospects for high-elevation radio detection of >100 PeV tau neutrinos". In: *JCAP* 11 (2020), p. 065. DOI: 10.1088/1475-7516/2020/11/065. arXiv: 2004.12718 [astro-ph.IM].

[154] M. G. Aartsen et al. "The IceCube Neutrino Observatory: Instrumentation and Online Systems". In: *JINST* 12.03 (2017), P03012. DOI: 10.1088/1748-0221/12/03/P03012. arXiv: 1612.05093 [astro-ph.IM].

[155] Paolo Fermani. "Status and results from the ANTARES and KM3NeT-ARCA neutrino telescopes". In: *PoS* NuFact2019 (2020), p. 032. DOI: 10.22323/1.369.0032.

[156] Steven W. Barwick. "ARIANNA: A New Concept for UHE Neutrino Detection". In: *J. Phys. Conf. Ser.* 60 (2007). Ed. by Francis Halzen, Albrecht Karle, and T. Montaruli, pp. 276–283. DOI: 10.1088/1742-6596/60/1/060. arXiv: astro-ph/0610631.

[157] P. Allison et al. "Design and Initial Performance of the Askaryan Radio Array Prototype EeV Neutrino Detector at the South Pole". In: *Astropart. Phys.* 35 (2012), pp. 457–477. DOI: 10.1016/j.astropartphys.2011.11.010. arXiv: 1105.2854 [astro-ph.IM].

[158] P. W. Gorham et al. "The Antarctic Impulsive Transient Antenna Ultra-high Energy Neutrino Detector Design, Performance, and Sensitivity for 2006-2007 Balloon Flight". In: *Astropart. Phys.* 32 (2009), pp. 10–41. DOI: 10.1016/j.astropartphys.2009.05.003. arXiv: 0812.1920 [astro-ph].

[159] Jiwoo Nam et al. "High-elevation synoptic radio array for detection of upward moving air-showers, deployed in the Antarctic mountains". In: *PoS* ICRC2019 (2020), p. 967. DOI: 10.22323/1.358.0967.

[160] Justin D. Bray et al. "Limit on the ultrahigh-energy neutrino flux from lunar observations with the Parkes radio telescope". In: *Phys. Rev. D* 91.6 (2015), p. 063002. DOI: 10.1103/PhysRevD.91.063002. arXiv: 1502.03313 [astro-ph.HE].

[161] Simon Bacholle. "The EUSO-SPB instrument". In: *PoS* ICRC2017 (2018), p. 384. DOI: 10.22323/1.301.0384.

[162] Alexander Aab et al. "The Pierre Auger Observatory Upgrade - Preliminary Design Report". In: (Apr. 2016). arXiv: 1604.03637 [astro-ph.IM].

[163] H. Tokuno et al. "The status of the Telescope Array experiment". In: *J. Phys. Conf. Ser.* 293 (2011). Ed. by Yifang Wang, p. 012035. DOI: 10.1088/1742-6596/293/1/012035.

[164] Roshan Mammen Abraham et al. "Tau neutrinos in the next decade: from GeV to EeV". In: *J. Phys. G* 49.11 (2022), p. 110501. DOI: 10.1088/1361-6471/ac89d2. arXiv: 2203.05591 [hep-ph].

[165] G. A. Askar'yan. "Excess negative charge of an electron-photon shower and its coherent radio emission". In: *Zh. Eksp. Teor. Fiz.* 41 (1961), pp. 616–618.

[166] E. Zas, F. Halzen, and T. Stanev. "Electromagnetic pulses from high-energy showers: Implications for neutrino detection". In: *Phys. Rev. D* 45 (1992), pp. 362–376. DOI: 10.1103/PhysRevD.45.362.

[167] Alice Bean. "RICE Limits on the Diffuse Ultra-High Energy Neutrino Flux". In: *AIP Conf. Proc.* 870.1 (2006). Ed. by T. M. Liss, pp. 212–214. DOI: 10.1063/1.2402620.

[168] Steven W. Barwick et al. "A First Search for Cosmogenic Neutrinos with the ARIANNA Hexagonal Radio Array". In: *Astropart. Phys.* 70 (2015), p. 12. DOI: 10.1016/j.astropartphys.2015.04.002. arXiv: 1410.7352 [astro-ph.HE].

[169] P. W. Gorham et al. "Observations of the Askaryan effect in ice". In: *Phys. Rev. Lett.* 99 (2007), p. 171101. DOI: 10.1103/PhysRevLett.99.171101. arXiv: hep-ex/0611008.

[170] M. Ahlers et al. "GZK Neutrinos after the Fermi-LAT Diffuse Photon Flux Measurement". In: *Astropart. Phys.* 34 (2010), pp. 106–115. DOI: 10.1016/j.astropartphys.2010.06.003. arXiv: 1005.2620 [astro-ph.HE].

[171] Jonas Heinze et al. "Cosmogenic Neutrinos Challenge the Cosmic Ray Proton Dip Model". In: *Astrophys. J.* 825.2 (2016), p. 122. DOI: 10.3847/0004-637X/825/2/122. arXiv: 1512.05988 [astro-ph.HE].

[172] Andrés Romero-Wolf and Máximo Ave. "Bayesian Inference Constraints on Astrophysical Production of Ultra-high Energy Cosmic Rays and Cosmogenic Neutrino Flux Predictions". In: *JCAP* 07 (2018), p. 025. DOI: 10.1088/1475-7516/2018/07/025. arXiv: 1712.07290 [astro-ph.HE].

[173] Rafael Alves Batista et al. "Cosmogenic photon and neutrino fluxes in the Auger era". In: *JCAP* 01 (2019), p. 002. DOI: 10.1088/1475-7516/2019/01/002. arXiv: 1806.10879 [astro-ph.HE].

[174] Jonas Heinze et al. "A new view on Auger data and cosmogenic neutrinos in light of different nuclear disintegration and air-shower models". In: *Astrophys. J.* 873.1 (2019), p. 88. DOI: 10.3847/1538-4357/ab05ce. arXiv: 1901.03338 [astro-ph.HE].

[175] Ke Fang et al. "Testing the Newborn Pulsar Origin of Ultrahigh Energy Cosmic Rays with EeV Neutrinos". In: *Phys. Rev. D* 90.10 (2014). [Erratum: Phys.Rev.D 92, 129901 (2015)], p. 103005. DOI: 10.1103/PhysRevD.90.103005. arXiv: 1311.2044 [astro-ph.HE].

[176] P. Padovani et al. "A simplified view of blazars: the neutrino background". In: *Mon. Not. Roy. Astron. Soc.* 452.2 (2015), pp. 1877–1887. DOI: 10.1093/mnras/stv1467. arXiv: 1506.09135 [astro-ph.HE].

[177] Ke Fang and Kohta Murase. "Linking High-Energy Cosmic Particles by Black Hole Jets Embedded in Large-Scale Structures". In: *Nature Phys.* 14.4 (2018), pp. 396–398. DOI: 10.1038/s41567-017-0025-4. arXiv: 1704.00015 [astro-ph.HE].

[178] Marco Stein Muzio, Michael Unger, and Glennys R. Farrar. "Progress towards characterizing ultrahigh energy cosmic ray sources". In: *Phys. Rev. D* 100.10 (2019), p. 103008. DOI: 10.1103/PhysRevD.100.103008. arXiv: 1906.06233 [astro-ph.HE].

[179] Xavier Rodrigues et al. "Active Galactic Nuclei Jets as the Origin of Ultrahigh-Energy Cosmic Rays and Perspectives for the Detection of Astrophysical Source Neutrinos at EeV Energies". In: *Phys. Rev. Lett.* 126.19 (2021), p. 191101. DOI: 10.1103/PhysRevLett.126.191101. arXiv: 2003.08392 [astro-ph.HE].

[180] Marco Stein Muzio, Glennys R. Farrar, and Michael Unger. "Probing the environments surrounding ultrahigh energy cosmic ray accelerators and their implications for astrophysical neutrinos". In: *Phys. Rev. D* 105.2 (2022), p. 023022. DOI: 10.1103/PhysRevD.105.023022. arXiv: 2108.05512 [astro-ph.HE].

[181] Arjen van Vliet, Rafael Alves Batista, and Jörg R. Hörandel. "Determining the fraction of cosmic-ray protons at ultrahigh energies with cosmogenic neutrinos". In: *Phys. Rev. D* 100.2 (2019), p. 021302. DOI: 10.1103/PhysRevD.100.021302. arXiv: 1901.01899 [astro-ph.HE].

[182] Daniel Biehl et al. "Tidally disrupted stars as a possible origin of both cosmic rays and neutrinos at the highest energies". In: *Sci. Rep.* 8.1 (2018), p. 10828. DOI: 10.1038/s41598-018-29022-4. arXiv: 1711.03555 [astro-ph.HE].

[183] Henso Abreu et al. "Detecting and Studying High-Energy Collider Neutrinos with FASER at the LHC". In: *Eur. Phys. J. C* 80.1 (2020), p. 61. DOI: 10.1140/epjc/s10052-020-7631-5. arXiv: 1908.02310 [hep-ex].

[184] M. G. Aartsen et al. "Observation of High-Energy Astrophysical Neutrinos in Three Years of IceCube Data". In: *Phys. Rev. Lett.* 113 (2014), p. 101101. DOI: 10.1103/PhysRevLett.113.101101. arXiv: 1405.5303 [astro-ph.HE].

[185] M. G. Aartsen et al. "Evidence for Astrophysical Muon Neutrinos from the Northern Sky with IceCube". In: *Phys. Rev. Lett.* 115.8 (2015), p. 081102. DOI: 10.1103/PhysRevLett.115.081102. arXiv: 1507.04005 [astro-ph.HE].

[186] M. G. Aartsen et al. "Observation and Characterization of a Cosmic Muon Neutrino Flux from the Northern Hemisphere using six years of IceCube data". In: *Astrophys. J.* 833.1 (2016), p. 3. DOI: 10.3847/0004-637X/833/1/3. arXiv: 1607.08006 [astro-ph.HE].

[187] Markus Ahlers and Francis Halzen. "Opening a New Window onto the Universe with IceCube". In: *Prog. Part. Nucl. Phys.* 102 (2018), pp. 73–88. DOI: 10.1016/j.ppnp.2018.05.001. arXiv: 1805.11112 [astro-ph.HE].

[188] R. Abbasi et al. "The IceCube high-energy starting event sample: Description and flux characterization with 7.5 years of data". In: *Phys. Rev. D* 104 (2021), p. 022002. DOI: 10.1103/PhysRevD.104.022002. arXiv: 2011.03545 [astro-ph.HE].

[189] Markus Ackermann et al. "Astrophysics Uniquely Enabled by Observations of High-Energy Cosmic Neutrinos". In: *Bull. Am. Astron. Soc.* 51 (2019), p. 185. arXiv: 1903.04334 [astro-ph.HE].

[190] Markus Ackermann et al. "Fundamental Physics with High-Energy Cosmic Neutrinos". In: *Bull. Am. Astron. Soc.* 51 (2019), p. 215. arXiv: 1903.04333 [astro-ph.HE].

[191] Carlos A. Argüelles et al. "Fundamental physics with high-energy cosmic neutrinos today and in the future". In: *PoS* ICRC2019 (2020), p. 849. DOI: 10.22323/1.358.0849. arXiv: 1907.08690 [astro-ph.HE].

[192] Guo-yuan Huang et al. "Probing new physics at future tau neutrino telescopes". In: *JCAP* 02.02 (2022), p. 038. DOI: 10.1088/1475-7516/2022/02/038. arXiv: 2112.09476 [hep-ph].

[193] A. Anker et al. "White Paper: ARIANNA-200 high energy neutrino telescope". In: (Apr. 2020). arXiv: 2004.09841 [astro-ph.IM].

[194] Valerio Bertone, Rhorry Gauld, and Juan Rojo. "Neutrino Telescopes as QCD Microscopes". In: *JHEP* 01 (2019), p. 217. DOI: 10.1007/JHEP01(2019)217. arXiv: 1808.02034 [hep-ph].

[195] L. N. Lipatov. "Reggeization of the Vector Meson and the Vacuum Singularity in Nonabelian Gauge Theories". In: *Sov. J. Nucl. Phys.* 23 (1976), pp. 338–345.

[196] E. A. Kuraev, L. N. Lipatov, and Victor S. Fadin. "Multi-Reggeon Processes in the Yang-Mills Theory". In: *Sov. Phys. JETP* 44 (1976), pp. 443–450.

[197] E. A. Kuraev, L. N. Lipatov, and Victor S. Fadin. "The Pomeranchuk Singularity in Nonabelian Gauge Theories". In: *Sov. Phys. JETP* 45 (1977), pp. 199–204.

[198] I. I. Balitsky and L. N. Lipatov. "The Pomeranchuk Singularity in Quantum Chromodynamics". In: *Sov. J. Nucl. Phys.* 28 (1978), pp. 822–829.

[199] Francois Gelis et al. "The Color Glass Condensate". In: *Ann. Rev. Nucl. Part. Sci.* 60 (2010), pp. 463–489. DOI: 10.1146/annurev.nucl.010909.083629. arXiv: 1002.0333 [hep-ph].

[200] John Ellis, Kazuki Sakurai, and Michael Spannowsky. "Search for Sphalerons: IceCube vs. LHC". In: *JHEP* 05 (2016), p. 085. DOI: 10.1007/JHEP05(2016)085. arXiv: 1603.06573 [hep-ph].

[201] Ernest M. Henley and Jamal Jalilian-Marian. "Ultra-high energy neutrino-nucleon scattering and parton distributions at small x". In: *Phys. Rev. D* 73 (2006), p. 094004. DOI: 10.1103/PhysRevD.73.094004. arXiv: hep-ph/0512220.

[202] Luis A. Anchordoqui et al. "Probing low-x QCD with cosmic neutrinos at the Pierre Auger Observatory". In: *Phys. Rev. D* 74 (2006), p. 043008. DOI: 10.1103/PhysRevD.74.043008. arXiv: hep-ph/0605086.

[203] Javier L. Albacete, José I. Illana, and Alba Soto-Ontoso. "Neutrino-nucleon cross section at ultrahigh energy and its astrophysical implications". In: *Phys. Rev. D* 92.1 (2015), p. 014027. DOI: 10.1103/PhysRevD.92.014027. arXiv: 1505.06583 [hep-ph].

[204] J. Alvarez-Muniz et al. "Phenomenology of high-energy neutrinos in low-scale quantum-gravity models". In: *Phys. Rev. Lett.* 88 (2002), p. 021301. DOI: 10.1103/PhysRevLett.88.021301. arXiv: hep-ph/0107057.

[205] Amy Connolly, Robert S. Thorne, and David Waters. "Calculation of High Energy Neutrino-Nucleon Cross Sections and Uncertainties Using the MSTW Parton Distribution Functions and Implications for Future Experiments". In: *Phys. Rev. D* 83 (2011), p. 113009. DOI: 10.1103/PhysRevD.83.113009. arXiv: 1102.0691 [hep-ph].

[206] Chien-Yi Chen, P. S. Bhupal Dev, and Amarjit Soni. "Standard model explanation of the ultrahigh energy neutrino events at IceCube". In: *Phys. Rev. D* 89.3 (2014), p. 033012. DOI: 10.1103/PhysRevD.89.033012. arXiv: 1309.1764 [hep-ph].

[207] D. Marfatia, D. W. McKay, and T. J. Weiler. "New physics with ultra-high-energy neutrinos". In: *Phys. Lett. B* 748 (2015), pp. 113–116. DOI: 10.1016/j.physletb.2015.07.002. arXiv: 1502.06337 [hep-ph].

[208] Katherine J. Mack, Ningqiang Song, and Aaron C. Vincent. "Signatures of microscopic black holes and extra dimensions at future neutrino telescopes". In: *JHEP* 04 (2020), p. 187. DOI: 10.1007/JHEP04(2020)187. arXiv: 1912.06656 [hep-ph].

[209] Alfonso Garcia et al. "Complete predictions for high-energy neutrino propagation in matter". In: *JCAP* 09 (2020), p. 025. DOI: 10.1088/1475-7516/2020/09/025. arXiv: 2004.04756 [hep-ph].

[210] Alfonso García et al. https://github.com/pochoarus/NuPropEarth. NuPropEarth. 2021.

[211] Christian Glaser et al. "NuRadioMC: Simulating the radio emission of neutrinos from interaction to detector". In: *Eur. Phys. J. C* 80.2 (2020), p. 77. DOI: 10.1140/epjc/s10052-020-7612-8. arXiv: 1906.01670 [astro-ph.IM].

[212] Christian Glaser et al. "NuRadioReco: A reconstruction framework for radio neutrino detectors". In: *Eur. Phys. J. C* 79.6 (2019), p. 464. DOI: 10.1140/epjc/s10052-019-6971-5. arXiv: 1903.07023 [astro-ph.IM].

[213] Daniel García-Fernández, Anna Nelles, and Christian Glaser. "Signatures of secondary leptons in radio-neutrino detectors in ice". In: *Phys. Rev. D* 102.8 (2020), p. 083011. DOI: 10.1103/PhysRevD.102.083011. arXiv: 2003.13442 [astro-ph.HE].

[214] Christian Glaser, Daniel García-Fernández, and Anna Nelles. "Prospects for neutrino-flavor physics with in-ice radio detectors". In: *PoS* ICRC2021 (2021), p. 1231. DOI: 10.22323/1.395.1231.

[215] Peter B. Denton and Yves Kini. "Ultra-High-Energy Tau Neutrino Cross Sections with GRAND and POEMMA". In: *Phys. Rev. D* 102 (2020), p. 123019. DOI: 10.1103/PhysRevD.102.123019. arXiv: 2007.10334 [astro-ph.HE].

[216] R. Alves Batista et al. "EuCAPT White Paper: Opportunities and Challenges for Theoretical Astroparticle Physics in the Next Decade". In: (Oct. 2021). arXiv: 2110.10074 [astro-ph.HE].

[217] Raymond Brock et al. "Handbook of perturbative QCD: Version 1.0". In: *Rev. Mod. Phys.* 67 (1995), pp. 157–248. DOI: 10.1103/RevModPhys.67.157.

[218] Janet M. Conrad, Michael H. Shaevitz, and Tim Bolton. "Precision measurements with high-energy neutrino beams". In: *Rev. Mod. Phys.* 70 (1998), pp. 1341–1392. DOI: 10.1103/RevModPhys.70.1341. arXiv: hep-ex/9707015.

[219] Carlo Giunti and Chung W. Kim. *Fundamentals of Neutrino Physics and Astrophysics*. Oxford: Oxford Univ., 2007. ISBN: 978-0-19-850871-7. DOI: 10.1093/acprof:oso/9780198508717.001.0001. URL: https://cds.cern.ch/record/1053706.

[220] J. A. Formaggio and G. P. Zeller. "From eV to EeV: Neutrino Cross Sections Across Energy Scales". In: *Rev. Mod. Phys.* 84 (2012), pp. 1307–1341. DOI: 10.1103/RevModPhys.84.1307. arXiv: 1305.7513 [hep-ex].

[221] Raj Gandhi et al. "Ultrahigh-energy neutrino interactions". In: *Astropart. Phys.* 5 (1996), pp. 81–110. DOI: 10.1016/0927-6505(96)00008-4. arXiv: hep-ph/9512364.

[222] C. Andreopoulos et al. "The GENIE Neutrino Monte Carlo Generator". In: *Nucl. Instrum. Meth. A* 614 (2010), pp. 87–104. DOI: 10.1016/j.nima.2009.12.009. arXiv: 0905.2517 [hep-ph].

[223] F. D. Aaron et al. "Combined Measurement and QCD Analysis of the Inclusive $e^{\pm}p$ Scattering Cross Sections at HERA". In: *JHEP* 01 (2010), p. 109. DOI: 10.1007/JHEP01(2010)109. arXiv: 0911.0884 [hep-ex].

[224] H. Abramowicz et al. "Combination of measurements of inclusive deep inelastic $e^{\pm}p$ scattering cross sections and QCD analysis of HERA data". In: *Eur. Phys. J. C* 75.12 (2015), p. 580. DOI: 10.1140/epjc/s10052-015-3710-4. arXiv: 1506.06042 [hep-ex].

[225] Amanda Cooper-Sarkar and Subir Sarkar. "Predictions for high energy neutrino cross-sections from the ZEUS global PDF fits". In: *JHEP* 01 (2008), p. 075. DOI: 10.1088/1126-6708/2008/01/075. arXiv: 0710.5303 [hep-ph].

[226] M. Glück, P. Jimenez-Delgado, and E. Reya. "Charged current neutrino-nucleon total cross section at high energies". In: *Phys. Rev. D* 81 (2010), p. 097501. DOI: 10.1103/PhysRevD.81.097501. arXiv: 1003.3168 [hep-ph].

[227] Martin M. Block, Loyal Durand, and Phuoc Ha. "Connection of the virtual $\gamma^* p$ cross section of ep deep inelastic scattering to real γp scattering, and the implications for νN and ep total cross sections". In: *Phys. Rev. D* 89.9 (2014), p. 094027. DOI: 10.1103/PhysRevD.89.094027. arXiv: 1404.4530 [hep-ph].

[228] V. P. Goncalves and D. R. Gratieri. "Estimating nonlinear QCD effects in ultrahigh energy neutrino events at IceCube". In: *Phys. Rev. D* 90.5 (2014), p. 057502. DOI: 10.1103/PhysRevD.90.057502. arXiv: 1406.5890 [hep-ph].

[229] Carlos A. Argüelles et al. "High-energy behavior of photon, neutrino, and proton cross sections". In: *Phys. Rev. D* 92.7 (2015), p. 074040. DOI: 10.1103/PhysRevD.92.074040. arXiv: 1504.06639 [hep-ph].

[230] Richard D. Ball et al. "Parton distributions with small-x resummation: evidence for BFKL dynamics in HERA data". In: *Eur. Phys. J. C* 78.4 (2018), p. 321. DOI: 10.1140/epjc/s10052-018-5774-4. arXiv: 1710.05935 [hep-ph].

[231] R Aaij et al. "Prompt charm production in pp collisions at $\sqrt{s} = 7$ TeV". In: *Nucl. Phys. B* 871 (2013), pp. 1–20. DOI: 10.1016/j.nuclphysb.2013.02.010. arXiv: 1302.2864 [hep-ex].

[232] Roel Aaij et al. "Measurements of prompt charm production cross-sections in pp collisions at $\sqrt{s} = 13$ TeV". In: *JHEP* 03 (2016). [Erratum: JHEP 09, 013 (2016), Erratum: JHEP 05, 074 (2017)], p. 159. DOI: 10.1007/JHEP03(2016)159. arXiv: 1510.01707 [hep-ex].

[233] Roel Aaij et al. "Measurements of prompt charm production cross-sections in pp collisions at $\sqrt{s} = 5$ TeV". In: *JHEP* 06 (2017), p. 147. DOI: 10.1007/JHEP06(2017)147. arXiv: 1610.02230 [hep-ex].

[234] D. Seckel. "Neutrino-photon reactions in astrophysics and cosmology". In: *Phys. Rev. Lett.* 80 (1998), pp. 900–903. DOI: 10.1103/PhysRevLett.80.900. arXiv: hep-ph/9709290.

[235] I. Alikhanov. "Hidden Glashow resonance in neutrino–nucleus collisions". In: *Phys. Lett. B* 756 (2016), pp. 247–253. DOI: 10.1016/j.physletb.2016.03.009. arXiv: 1503.08817 [hep-ph].

[236] Rhorry Gauld. "Precise predictions for multi-TeV and PeV energy neutrino scattering rates". In: *Phys. Rev. D* 100.9 (2019), p. 091301. DOI: 10.1103/PhysRevD.100.091301. arXiv: 1905.03792 [hep-ph].

[237] Bei Zhou and John F. Beacom. "Neutrino-nucleus cross sections for W-boson and trident production". In: *Phys. Rev. D* 101.3 (2020), p. 036011. DOI: 10.1103/PhysRevD.101.036011. arXiv: 1910.08090 [hep-ph].

[238] Bei Zhou and John F. Beacom. "W-boson and trident production in TeV–PeV neutrino observatories". In: *Phys. Rev. D* 101.3 (2020), p. 036010. DOI: 10.1103/PhysRevD.101.036010. arXiv: 1910.10720 [hep-ph].

[239] W. Czyz, G. C. Sheppey, and J. D. Walecka. "Neutrino production of lepton pairs through the point four-fermion interaction". In: *Nuovo Cim.* 34 (1964), pp. 404–435. DOI: 10.1007/BF02734586.

[240] J. Lovseth and M. Radomiski. "Kinematical distributions of neutrino-produced lepton triplets". In: *Phys. Rev. D* 3 (1971), pp. 2686–2706. DOI: 10.1103/PhysRevD.3.2686.

[241] Peter Ballett et al. "Neutrino Trident Scattering at Near Detectors". In: *JHEP* 01 (2019), p. 119. DOI: 10.1007/JHEP01(2019)119. arXiv: 1807.10973 [hep-ph].

[242] Sheldon L. Glashow. "Resonant Scattering of Antineutrinos". In: *Phys. Rev.* 118 (1960), pp. 316–317. DOI: 10.1103/PhysRev.118.316.

[243] M. G. Aartsen et al. "Detection of a particle shower at the Glashow resonance with IceCube". In: *Nature* 591.7849 (2021). [Erratum: Nature 592, E11 (2021)], pp. 220–224. DOI: 10.1038/s41586-021-03256-1. arXiv: 2110.15051 [hep-ex].

[244] Dan Hooper. "Measuring high energy neutrino-nucleon cross sections with future neutrino telescopes". In: *Phys. Rev. D* 65 (2002), p. 097303. DOI: 10.1103/PhysRevD.65.097303. arXiv: hep-ph/0203239.

[245] S. Hussain et al. "Cross section dependence of event rates at neutrino telescopes". In: *Phys. Rev. Lett.* 97 (2006), p. 161101. DOI: 10.1103/PhysRevLett.97.161101. arXiv: hep-ph/0606246.

[246] E. Borriello et al. "Disentangling neutrino-nucleon cross section and high energy neutrino flux with a km^3 neutrino telescope". In: *Phys. Rev. D* 77 (2008), p. 045019. DOI: 10.1103/PhysRevD.77.045019. arXiv: 0711.0152 [astro-ph].

[247] S. Hussain, D. Marfatia, and D. W. McKay. "Upward shower rates at neutrino telescopes directly determine the neutrino flux". In: *Phys. Rev. D* 77 (2008), p. 107304. DOI: 10.1103/PhysRevD.77.107304. arXiv: 0711.4374 [hep-ph].

[248] Daniele Fargion. "Discovering Ultra-High-Energy Neutrinos Through Horizontal and Upward τ Air Showers: Evidences in Terrestrial Gamma Flashes?" In: *Astrophys. J.* 570 (2002), pp. 909–925. DOI: 10.1086/339772. arXiv: astro-ph/0002453.

[249] Rasha Abbasi et al. "Measuring total neutrino cross section with IceCube at intermediate energies ($\sim$100 GeV to a few TeV)". In: *PoS* ICRC2021 (2021), p. 1132. DOI: 10.22323/1.395.1132. arXiv: 2107.09764 [astro-ph.HE].

[250] Amanda Cooper-Sarkar, Philipp Mertsch, and Subir Sarkar. "The high energy neutrino cross-section in the Standard Model and its uncertainty". In: *JHEP* 08 (2011), p. 042. DOI: 10.1007/JHEP08(2011)042. arXiv: 1106.3723 [hep-ph].

[251] A. R. Bell. "Cosmic ray acceleration". In: *Astropart. Phys.* 43 (2013), pp. 56–70. DOI: 10.1016/j.astropartphys.2012.05.022.

[252] Alexander Aab et al. "Inferences on mass composition and tests of hadronic interactions from 0.3 to 100 EeV using the water-Cherenkov detectors of the Pierre Auger Observatory". In: *Phys. Rev. D* 96.12 (2017), p. 122003. DOI: 10.1103/PhysRevD.96.122003. arXiv: 1710.07249 [astro-ph.HE].

[253] Alexander Aab et al. "Features of the Energy Spectrum of Cosmic Rays above 2.5×10^{18} eV Using the Pierre Auger Observatory". In: *Phys. Rev. Lett.* 125.12 (2020), p. 121106. DOI: 10.1103/PhysRevLett.125.121106. arXiv: 2008.06488 [astro-ph.HE].

[254] R. U. Abbasi et al. "Mass composition of ultrahigh-energy cosmic rays with the Telescope Array Surface Detector data". In: *Phys. Rev. D* 99.2 (2019), p. 022002. DOI: 10.1103/PhysRevD.99.022002. arXiv: 1808.03680 [astro-ph.HE].

[255] K. Kotera, D. Allard, and A. V. Olinto. "Cosmogenic Neutrinos: parameter space and detectabilty from PeV to ZeV". In: *JCAP* 10 (2010), p. 013. DOI: 10.1088/1475-7516/2010/10/013. arXiv: 1009.1382 [astro-ph.HE].

[256] A. Mucke et al. "SOPHIA: Monte Carlo simulations of photohadronic processes in astrophysics". In: *Comput. Phys. Commun.* 124 (2000), pp. 290–314. DOI: 10.1016/S0010-4655(99)00446-4. arXiv: astro-ph/9903478.

[257] S. Hummer et al. "Simplified models for photohadronic interactions in cosmic accelerators". In: *Astrophys. J.* 721 (2010), pp. 630–652. DOI: 10.1088/0004-637X/721/1/630. arXiv: 1002.1310 [astro-ph.HE].

[258] Leonel Morejon et al. "Improved photomeson model for interactions of cosmic ray nuclei". In: *JCAP* 11 (2019), p. 007. DOI: 10.1088/1475-7516/2019/11/007. arXiv: 1904.07999 [astro-ph.HE].

[259] Walter Winter. "Photohadronic Origin of the TeV-PeV Neutrinos Observed in IceCube". In: *Phys. Rev. D* 88 (2013), p. 083007. DOI: 10.1103/PhysRevD.88.083007. arXiv: 1307.2793 [astro-ph.HE].

[260] Mauricio Bustamante and Irene Tamborra. "Using high-energy neutrinos as cosmic magnetometers". In: *Phys. Rev. D* 102.12 (2020), p. 123008. DOI: 10.1103/PhysRevD.102.123008. arXiv: 2009.01306 [astro-ph.HE].

[261] Walter Winter, Julia Becker Tjus, and Spencer R. Klein. "Impact of secondary acceleration on the neutrino spectra in gamma-ray bursts". In: *Astron. Astrophys.* 569 (2014), A58. DOI: 10.1051/0004-6361/201423745. arXiv: 1403.0574 [astro-ph.HE].

[262] Denise Boncioli, Anatoli Fedynitch, and Walter Winter. "Nuclear Physics Meets the Sources of the Ultra-High Energy Cosmic Rays". In: *Sci. Rep.* 7.1 (2017), p. 4882. DOI: 10.1038/s41598-017-05120-7. arXiv: 1607.07989 [astro-ph.HE].

[263] Daniel Biehl et al. "Cosmic-Ray and Neutrino Emission from Gamma-Ray Bursts with a Nuclear Cascade". In: *Astron. Astrophys.* 611 (2018), A101. DOI: 10.1051/0004-6361/201731337. arXiv: 1705.08909 [astro-ph.HE].

[264] P. A. Zyla et al. "Review of Particle Physics". In: *PTEP* 2020.8 (2020), p. 083C01. DOI: 10.1093/ptep/ptaa104.

[265] M. G. Aartsen et al. "Energy Reconstruction Methods in the IceCube Neutrino Telescope". In: *JINST* 9 (2014), P03009. DOI: 10.1088/1748-0221/9/03/P03009. arXiv: 1311.4767 [physics.ins-det].

[266] Sandip Pakvasa. "Neutrino Flavor Goniometry by High Energy Astrophysical Beams". In: *Mod. Phys. Lett. A* 23 (2008). Ed. by Pauchy W. Y. Hwang, Xiao-Gang He, and Kin-Wang Ng, pp. 1313–1324. DOI: 10.1142/S0217732308027680. arXiv: 0803.1701 [hep-ph].

[267] Ningqiang Song et al. "The Future of High-Energy Astrophysical Neutrino Flavor Measurements". In: *JCAP* 04 (2021), p. 054. DOI: 10.1088/1475-7516/2021/04/054. arXiv: 2012.12893 [hep-ph].

[268] Iván Esteban et al. "The fate of hints: updated global analysis of three-flavor neutrino oscillations". In: *JHEP* 09 (2020), p. 178. DOI: 10.1007/JHEP09(2020)178. arXiv: 2007.14792 [hep-ph].

[269] Iván Esteban et al. http://www.nu-fit.org/. NuFit 5.0. 2020.

[270] Marco Stein Muzio. *Private communication*. 2021.

[271] Babak Abi et al. "Deep Underground Neutrino Experiment (DUNE), Far Detector Technical Design Report, Volume I Introduction to DUNE". In: *JINST* 15.08 (2020), T08008. DOI: 10.1088/1748-0221/15/08/T08008. arXiv: 2002.02967 [physics.ins-det].

[272] K. Abe et al. "Hyper-Kamiokande Design Report". In: (May 2018). arXiv: 1805.04163 [physics.ins-det].

[273] Fengpeng An et al. "Neutrino Physics with JUNO". In: *J. Phys. G* 43.3 (2016), p. 030401. DOI: 10.1088/0954-3899/43/3/030401. arXiv: 1507.05613 [physics.ins-det].

[274] Mauricio Bustamante, Victor Valera, and Christian Glaser. "Detailed prospects for the discovery of ultra-high-energy neutrinos in IceCube-Gen2". In: *In preparation* (2022).

[275] Francesco Fenu. "The cosmic ray energy spectrum measured using the Pierre Auger Observatory". In: *PoS* ICRC2017 (2017). Ed. by Darko Veberic, p. 486. DOI: 10.22323/1.301.0486.

[276] Jose Bellido. "Depth of maximum of air-shower profiles at the Pierre Auger Observatory: Measurements above $10^{17.2}$ eV and Composition Implications". In: *PoS* ICRC2017 (2018). Ed. by Darko Veberic, p. 506. DOI: 10.22323/1.301.0506.

[277] Jonas Heinze and Anatoli Fedynitch. https://github.com/joheinze/PriNCe. PriNCe. 2020.

[278] Yoshiki Tsunesada et al. "Energy Spectrum of Ultra-High-Energy Cosmic Rays Measured by The Telescope Array". In: *PoS* ICRC2017 (2018), p. 535. DOI: 10.22323/1.301.0535.

[279] Douglas Bergman and Thomas Stroman. "Telescope Array measurement of UHECR composition from stereoscopic fluorescence detection". In: *PoS* ICRC2017 (2018), p. 538. DOI: 10.22323/1.301.0538.

[280] Douglas Bergman. "Telescope Array Combined Fit to Cosmic Ray Spectrum and Composition". In: *PoS* ICRC2021 (2021), p. 338. DOI: 10.22323/1.395.0338.

[281] Rafael Alves Batista et al. "CRPropa 3—a Public Astrophysical Simulation Framework for Propagating Extraterrestrial Ultra-High Energy Particles". In: *JCAP* 05 (2016), p. 038. DOI: 10.1088/1475-7516/2016/05/038. arXiv: 1603.07142 [astro-ph.IM].

[282] Arjen van Vliet. *Private communication*. 2021.

[283] M. Ajello et al. "The Luminosity Function of Fermi-detected Flat-Spectrum Radio Quasars". In: *Astrophys. J.* 751 (2012), p. 108. DOI: 10.1088/0004-637X/751/2/108. arXiv: 1110.3787 [astro-ph.CO].

[284] M. Ajello et al. "The Cosmic Evolution of Fermi BL Lacertae Objects". In: *Astrophys. J.* 780 (2014), p. 73. DOI: 10.1088/0004-637X/780/1/73. arXiv: 1310.0006 [astro-ph.CO].

[285] Xavier Rodrigues et al. "Neutrinos and Ultra-High-Energy Cosmic-Ray Nuclei from Blazars". In: *Astrophys. J.* 854.1 (2018), p. 54. DOI: 10.3847/1538-4357/aaa7ee. arXiv: 1711.02091 [astro-ph.HE].

[286] Philipp Baerwald, Svenja Hummer, and Walter Winter. "Magnetic Field and Flavor Effects on the Gamma-Ray Burst Neutrino Flux". In: *Phys. Rev. D* 83 (2011), p. 067303. DOI: 10.1103/PhysRevD.83.067303. arXiv: 1009.4010 [astro-ph.HE].

[287] Xavier Rodrigues. *Private communication*. 2021.

[288] *The Pierre Auger Observatory: Contributions to the 34th International Cosmic Ray Conference (ICRC 2015)*. Sept. 2015. arXiv: 1509.03732 [astro-ph.HE].

[289] M. G. Aartsen et al. "The IceCube Neutrino Observatory - Contributions to ICRC 2017 Part II: Properties of the Atmospheric and Astrophysical Neutrino Flux". In: (Oct. 2017). arXiv: 1710.01191 [astro-ph.HE].

[290] P. Giommi et al. "A simplified view of blazars: clearing the fog around long-standing selection effects". In: *Mon. Not. Roy. Astron. Soc.* 420 (2012), p. 2899. DOI: 10.1111/j.1365-2966.2011.20044.x. arXiv: 1110.4706 [astro-ph.CO].

[291] M. G. Aartsen et al. "Constraints on Ultrahigh-Energy Cosmic-Ray Sources from a Search for Neutrinos above 10 PeV with IceCube". In: *Phys. Rev. Lett.* 117.24 (2016). [Erratum: Phys.Rev.Lett. 119, 259902 (2017)], p. 241101. DOI: 10.1103/PhysRevLett.117.241101. arXiv: 1607.05886 [astro-ph.HE].

[292] Michael Unger, Glennys R. Farrar, and Luis A. Anchordoqui. "Origin of the ankle in the ultrahigh energy cosmic ray spectrum, and of the extragalactic protons below it". In: *Phys. Rev. D* 92.12 (2015), p. 123001. DOI: 10.1103/PhysRevD.92.123001. arXiv: 1505.02153 [astro-ph.HE].

[293] Anatoli Fedynitch et al. "Hadronic interaction model Sibyll 2.3c and inclusive lepton fluxes". In: *Phys. Rev. D* 100.10 (2019), p. 103018. DOI: 10.1103/PhysRevD.100.103018. arXiv: 1806.04140 [hep-ph].

[294] M. G. Aartsen et al. "Characteristics of the diffuse astrophysical electron and tau neutrino flux with six years of IceCube high energy cascade data". In: *Phys. Rev. Lett.* 125.12 (2020), p. 121104. DOI: 10.1103/PhysRevLett.125.121104. arXiv: 2001.09520 [astro-ph.HE].

[295] A. M. Dziewonski and D. L. Anderson. "Preliminary reference earth model". In: *Phys. Earth Planet. Interiors* 25 (1981), pp. 297–356. DOI: 10.1016/0031-9201(81)90046-7.

[296] V. A. Kudryavtsev. "Muon simulation codes MUSIC and MUSUN for underground physics". In: *Comput. Phys. Commun.* 180 (2009), pp. 339–346. DOI: 10.1016/j.cpc.2008.10.013. arXiv: 0810.4635 [physics.comp-ph].

[297] N. Davidson et al. "Universal Interface of TAUOLA Technical and Physics Documentation". In: *Comput. Phys. Commun.* 183 (2012), pp. 821–843. DOI: 10.1016/j.cpc.2011.12.009. arXiv: 1002.0543 [hep-ph].

[298] Torbjorn Sjostrand, Stephen Mrenna, and Peter Z. Skands. "PYTHIA 6.4 Physics and Manual". In: *JHEP* 05 (2006), p. 026. DOI: 10.1088/1126-6708/2006/05/026. arXiv: hep-ph/0603175.

[299] Alfonso Garcia and Aart Heijboer. "High-energy neutrino event simulation at NLO in Genie for KM3NeT and other observatories". In: *PoS* ICRC2019 (2020), p. 895. DOI: 10.22323/1.358.0895. arXiv: 1908.10077 [hep-ex].

[300] Sigfrid Stjärnholm, Oscar Ericsson, and Christian Glaser. "Neutrino direction and flavor reconstruction from radio detector data using deep convolutional neural networks". In: *PoS* ICRC2021 (2021), p. 1055. DOI: 10.22323/1.395.1055.

[301] Shirley Weishi Li, Mauricio Bustamante, and John F. Beacom. "Echo Technique to Distinguish Flavors of Astrophysical Neutrinos". In: *Phys. Rev. Lett.* 122.15 (2019), p. 151101. DOI: 10.1103/PhysRevLett.122.151101. arXiv: 1606.06290 [astro-ph.HE].

[302] L. D. Landau and I. Pomeranchuk. "Limits of applicability of the theory of bremsstrahlung electrons and pair production at high-energies". In: *Dokl. Akad. Nauk Ser. Fiz.* 92 (1953), pp. 535–536.

[303] A. B. Migdal. "Bremsstrahlung and pair production in condensed media at high-energies". In: *Phys. Rev.* 103 (1956), pp. 1811–1820. DOI: 10.1103/PhysRev.103.1811.

[304] Frank G. Schröder. "Radio detection of Cosmic-Ray Air Showers and High-Energy Neutrinos". In: *Prog. Part. Nucl. Phys.* 93 (2017), pp. 1–68. DOI: 10.1016/j.ppnp.2016.12.002. arXiv: 1607.08781 [astro-ph.IM].

[305] David Saltzberg et al. "Observation of the Askaryan effect: Coherent microwave Cherenkov emission from charge asymmetry in high-energy particle cascades". In: *Phys. Rev. Lett.* 86 (2001), pp. 2802–2805. DOI: 10.1103/PhysRevLett.86.2802. arXiv: hep-ex/0011001.

[306] P. Miocinovic et al. "Time-domain measurement of broadband coherent Cherenkov radiation". In: *Phys. Rev. D* 74 (2006), p. 043002. DOI: 10.1103/PhysRevD.74.043002. arXiv: hep-ex/0602043.

[307] Alexander Aab et al. "Probing the radio emission from air showers with polarization measurements". In: *Phys. Rev. D* 89.5 (2014), p. 052002. DOI: 10.1103/PhysRevD.89.052002. arXiv: 1402.3677 [astro-ph.HE].

[308] P. Schellart et al. "Polarized radio emission from extensive air showers measured with LOFAR". In: *JCAP* 10 (2014), p. 014. DOI: 10.1088/1475-7516/2014/10/014. arXiv: 1406.1355 [astro-ph.HE].

[309] T. Huege. "Radio detection of cosmic ray air showers in the digital era". In: *Phys. Rept.* 620 (2016), pp. 1–52. DOI: 10.1016/j.physrep.2016.02.001. arXiv: 1601.07426 [astro-ph.IM].

[310] S. Barwick et al. "South Polar in situ radio-frequency ice attenuation". In: *J. Glaciol.* 51 (2005), pp. 231–238. DOI: 10.3189/172756505781829467.

[311] Christian Glaser. "Neutrino direction and energy resolution of Askaryan detectors". In: *PoS* ICRC2019 (2020), p. 899. DOI: 10.22323/1.358.0899. arXiv: 1911.02093 [astro-ph.IM].

[312] Ilse Plaisier et al. "Direction Reconstruction for the Radio Neutrino Observatory Greenland (RNO-G)". In: *PoS* ICRC2021 (2021), p. 1026. DOI: 10.22323/1.395.1026.

[313] Christian Glaser et al. "Deep learning reconstruction of the neutrino energy with a shallow Askaryan detector". In: *PoS* ICRC2021 (2021), p. 1051. DOI: 10.22323/1.395.1051.

[314] Steve Barwick et al. "Capabilities of ARIANNA: Neutrino Pointing Resolution and Implications for Future Ultra-high Energy Neutrino Astronomy". In: *PoS* ICRC2021 (2021), p. 1151. DOI: 10.22323/1.395.1151.

[315] J. A. Aguilar et al. "Reconstructing the neutrino energy for in-ice radio detectors: A study for the Radio Neutrino Observatory Greenland (RNO-G)". In: *Eur. Phys. J. C* 82.2 (2022), p. 147. DOI: 10.1140/epjc/s10052-022-10034-4. arXiv: 2107.02604 [astro-ph.HE].

[316] P. Allison et al. "Performance of two Askaryan Radio Array stations and first results in the search for ultrahigh energy neutrinos". In: *Phys. Rev. D* 93.8 (2016), p. 082003. DOI: 10.1103/PhysRevD.93.082003. arXiv: 1507.08991 [astro-ph.HE].

[317] A. Anker et al. "Neutrino vertex reconstruction with in-ice radio detectors using surface reflections and implications for the neutrino energy resolution". In: *JCAP* 11 (2019), p. 030. DOI: 10.1088/1475-7516/2019/11/030. arXiv: 1909.02677 [astro-ph.IM].

[318] Jaime Alvarez-Muñiz et al. "Askaryan radiation from neutrino-induced showers in ice". In: *Phys. Rev. D* 101.8 (2020), p. 083005. DOI: 10.1103/PhysRevD.101.083005. arXiv: 2003.09705 [astro-ph.HE].

[319] P. Allison et al. "Design and performance of an interferometric trigger array for radio detection of high-energy neutrinos". In: *Nucl. Instrum. Meth. A* 930 (2019), pp. 112–125. DOI: 10.1016/j.nima.2019.01.067. arXiv: 1809.04573 [astro-ph.IM].

[320] Christian Glaser and Steven W. Barwick. "An improved trigger for Askaryan radio detectors". In: *JINST* 16.05 (2021), T05001. DOI: 10.1088/1748-0221/16/05/T05001. arXiv: 2011.12997 [astro-ph.IM].

[321] Jakob van Santen et al. "toise: a framework to describe the performance of high-energy neutrino detectors". In: *JINST* 17.08 (Feb. 2022), T08009. DOI: 10.1088/1748-0221/17/08/T08009. arXiv: 2202.11120 [astro-ph.IM].

[322] A. Anker et al. "Probing the angular and polarization reconstruction of the ARIANNA detector at the South Pole". In: *JINST* 15.09 (2020), P09039. DOI: 10.1088/1748-0221/15/09/P09039. arXiv: 2006.03027 [astro-ph.IM].

[323] Myoungchul Kim et al. "Arrival direction reconstruction of ultra-high-energy neutrinos with ARA". In: *PoS* ICRC2019 (2020), p. 933. DOI: 10.22323/1.358.0933.

[324] Geoffrey George Gaswint. "Quantifying the Neutrino Energy and Pointing Resolution of the ARIANNA Detector". PhD thesis. University of California, Irvine, 2021.

[325] A. Anker et al. "Measuring the Polarization Reconstruction Resolution of the ARIANNA Neutrino Detector with Cosmic Rays". In: *JCAP (in press)* (2022). arXiv: 2112.01501 [astro-ph.HE].

[326] Yue Pan et al. "A neural network based UHE neutrino reconstruction method for the Askaryan Radio Array (ARA)". In: *PoS* ICRC2021 (2021), p. 1157. DOI: 10.22323/1.395.1157.

[327] Simon De Kockere et al. "Simulation of in-ice cosmic ray air shower induced particle cascades". In: *Phys. Rev. D* 106.4 (Feb. 2022), p. 043023. DOI: 10.1103/PhysRevD.106.043023. arXiv: 2202.09211 [astro-ph.HE].

[328] Carlos A. Argüelles, Teppei Katori, and Jordi Salvadó. "New Physics in Astrophysical Neutrino Flavor". In: *Phys. Rev. Lett.* 115 (2015), p. 161303. DOI: 10.1103/PhysRevLett.115.161303. arXiv: 1506.02043 [hep-ph].

[329] Mauricio Bustamante, John F. Beacom, and Walter Winter. "Theoretically palatable flavor combinations of astrophysical neutrinos". In: *Phys. Rev. Lett.* 115.16 (2015), p. 161302. DOI: 10.1103/PhysRevLett.115.161302. arXiv: 1506.02645 [astro-ph.HE].

[330] C. A. Argüelles et al. "Snowmass White Paper: Beyond the Standard Model effects on Neutrino Flavor". In: *2022 Snowmass Summer Study*. Mar. 2022. arXiv: 2203.10811 [hep-ph].

[331] Clancy W. James et al. "Overview of lunar detection of ultra-high energy particles and new plans for the SKA". In: *EPJ Web Conf.* 135 (2017). Ed. by S. Buitnik et al., p. 04001. DOI: 10.1051/epjconf/201713504001. arXiv: 1704.05336 [astro-ph.IM].

[332] Eiji Kido. "Status and prospects of the TAx4 experiment". In: *PoS* ICRC2019 (2020). Ed. by I. Lhenry-Yvon et al., p. 312. DOI: 10.22323/1.358.0312.

[333] Adam Nepomuk Otte. "Studies of an air-shower imaging system for the detection of ultrahigh-energy neutrinos". In: *Phys. Rev. D* 99.8 (2019), p. 083012. DOI: 10.1103/PhysRevD.99.083012. arXiv: 1811.09287 [astro-ph.IM].

[334] Sigfrid Stjärnholm et al. "Deep-learning based event reconstruction for shallow in-ice UHE neutrino detectors". In: *PoS* ARENA2022 (2023), p. 019. DOI: 10.22323/1.424.0019.

[335] Abby Bishop et al. "Benefits of Looking for Coincident Events, Taus, and Muons with the Askaryan Radio Array". In: *PoS* ICRC2023 (2023), p. 1169. DOI: 10.22323/1.444.1169. arXiv: 2308.07401 [astro-ph.HE].

[336] Victor B. Valera, Mauricio Bustamante, and Olga Mena. "Joint measurement of the ultra-high-energy neutrino spectrum and cross section". In: (Aug. 2023). arXiv: 2308.07709 [astro-ph.HE].

[337] Uzair Abdul Latif et al. "Simulation of radio signals from cosmic-ray cascades in air and ice as observed by in-ice Askaryan radio detectors". In: *PoS* ICRC2023 (2023), p. 346. DOI: 10.22323/1.444.0346.

[338] Rasha Abbasi et al. "The next generation neutrino telescope: IceCube-Gen2". In: *PoS* ICRC2023 (2023), p. 994. DOI: 10.22323/1.444.0994. arXiv: 2308.09427 [astro-ph.HE].

[339] Veniamin Berezinsky, Eray Sabancilar, and Alexander Vilenkin. "Extremely High Energy Neutrinos from Cosmic Strings". In: *Phys. Rev. D* 84 (2011), p. 085006. DOI: 10.1103/PhysRevD.84.085006. arXiv: 1108.2509 [astro-ph.CO].

[340] V. A. Ryabov et al. "Prospects for ultrahigh-energy particle observation based on the lunar orbital LORD space experiment". In: *Adv. Space Res.* 58 (2016), pp. 464–474. DOI: 10.1016/j.asr.2016.04.030.

[341] Cyril Creque-Sarbinowski, Jeffrey Hyde, and Marc Kamionkowski. *High-Energy Astrophysical Neutrinos from Cosmic Strings*. June 2022. arXiv: 2206.06377 [hep-ph].

[342] Markus Ahlers, Klaus Helbing, and Carlos Pérez de los Heros. "Probing Particle Physics with IceCube". In: *Eur. Phys. J. C* 78.11 (2018), p. 924. DOI: 10.1140/epjc/s10052-018-6369-9. arXiv: 1806.05696 [astro-ph.HE].

[343] Rana X. Adhikari et al. *Report of the Topical Group on Cosmic Probes of Fundamental Physics for for Snowmass 2021*. Sept. 2022. arXiv: 2209.11726 [hep-ph].

[344] R. Aloisio, V. Berezinsky, and A. Gazizov. "Ultra High Energy Cosmic Rays: The disappointing model". In: *Astropart. Phys.* 34 (2011), pp. 620–626. DOI: 10.1016/j.astropartphys.2010.12.008. arXiv: 0907.5194 [astro-ph.HE].

[345] Markus Ahlers and Francis Halzen. "Minimal Cosmogenic Neutrinos". In: *Phys. Rev. D* 86 (2012), p. 083010. DOI: 10.1103/PhysRevD.86.083010. arXiv: 1208.4181 [astro-ph.HE].

[346] Victor Branco Valera, Mauricio Bustamante, and Christian Glaser. "The ultra-high-energy neutrino-nucleon cross section: measurement forecasts for an era of cosmic EeV-neutrino discovery". In: *JHEP* 06 (2022), p. 105. DOI: 10.1007/JHEP06(2022)105. arXiv: 2204.04237 [hep-ph].

[347] Jason Arakawa et al. "Neutrino Detection without Neutrino Detectors: Discovering Collider Neutrinos at FASER with Electronic Signals Only". In: *Phys. Rev. D* 106 (2022), p. 052011. DOI: 10.1103/PhysRevD.106.052011. arXiv: 2206.09932 [hep-ph].

[348] Ivan Esteban, Steven Prohira, and John F. Beacom. "Detector requirements for model-independent measurements of ultrahigh energy neutrino cross sections". In: *Phys. Rev. D* 106.2 (2022), p. 023021. DOI: 10.1103/PhysRevD.106.023021. arXiv: 2205.09763 [hep-ph].

[349] E. Aslanides et al. *A deep sea telescope for high-energy neutrinos*. May 1999. arXiv: astro-ph/9907432.

[350] I. A. Belolaptikov et al. "The Baikal underwater neutrino telescope: Design, performance and first results". In: *Astropart. Phys.* 7 (1997), pp. 263–282. DOI: 10.1016/S0927-6505(97)00022-4.

[351] M. G. Aartsen et al. "Measurement of South Pole ice transparency with the IceCube LED calibration system". In: *Nucl. Instrum. Meth. A* 711 (2013), pp. 73–89. DOI: 10.1016/j.nima.2013.01.054. arXiv: 1301.5361 [astro-ph.IM].

[352] Daniele Fargion, Andrea Aiello, and Roberto Conversano. "Horizontal tau air showers from mountains in deep valley: Traces of UHECR neutrino tau". In: *26th International Cosmic Ray Conference*. June 1999. arXiv: astro-ph/9906450.

[353] R. U. Abbasi et al. "Search for Ultra-High-Energy Neutrinos with the Telescope Array Surface Detector". In: *J. Exp. Theor. Phys.* 131.2 (2020), pp. 255–264. DOI: 10.31857/S0044451020080052. arXiv: 1905.03738 [astro-ph.HE].

[354] Damiano F. G. Fiorillo, Gennaro Miele, and Ofelia Pisanti. "Tau Neutrinos with Cherenkov Telescope Array". In: (July 2020). arXiv: 2007.13423 [hep-ph].

[355] A. Nepomuk Otte et al. "Trinity: An Air-Shower Imaging System for the Detection of Ultrahigh Energy Neutrinos". In: *PoS* ICRC2019 (2020), p. 976. DOI: 10.22323/1.358.0976. arXiv: 1907.08732 [astro-ph.IM].

[356] Makoto Sasaki and George Wei-Shu Hou. *Neutrino Telescope Array Letter of Intent: A Large Array of High Resolution Imaging Atmospheric Cherenkov and Fluorescence Detectors for Survey of Air-showers from Cosmic Tau Neutrinos in the PeV-EeV Energy Range*. Aug. 2014. arXiv: 1408.6244 [astro-ph.IM].

[357] Antonio Marinelli, Pasquale Migliozzi, and Andreino Simonelli. "Acoustic neutrino detection in a Adriatic multidisciplinary observatory (ANDIAMO)". In: *Astropart. Phys.* 143 (2022), p. 102760. DOI: 10.1016/j.astropartphys.2022.102760. arXiv: 2109.15199 [astro-ph.IM].

[358] Steven Barwick and Christian Glaser. "Radio Detection of High Energy Neutrinos in Ice". In: (Aug. 2022). arXiv: 2208.04971 [astro-ph.IM].

[359] I. Kravchenko et al. "RICE limits on the diffuse ultrahigh energy neutrino flux". In: *Phys. Rev. D* 73 (2006), p. 082002. DOI: 10.1103/PhysRevD.73.082002. arXiv: astro-ph/0601148.

[360] Ewa M. Holt. "The Auger Engineering Radio Array and multi-hybrid cosmic ray detection". In: *J. Phys. Conf. Ser.* 718.5 (2016), p. 052019. DOI: 10.1088/1742-6596/718/5/052019. arXiv: 1704.07240 [astro-ph.HE].

[361] D. Ardouin et al. "Radioelectric Field Features of Extensive Air Showers Observed with CODALEMA". In: *Astropart. Phys.* 26 (2006), pp. 341–350. DOI: 10.1016/j.astropartphys.2006.07.002. arXiv: astro-ph/0608550.

[362] H. Falcke et al. "Detection and imaging of atmospheric radio flashes from cosmic ray air showers". In: *Nature* 435 (2005), pp. 313–316. DOI: 10.1038/nature03614. arXiv: astro-ph/0505383.

[363] M. P. van Haarlem et al. "LOFAR: The LOw-Frequency ARray". In: *Astron. Astrophys.* 556 (2013), A2. DOI: 10.1051/0004-6361/201220873. arXiv: 1305.3550 [astro-ph.IM].

[364] P. A. Bezyazeekov et al. "Measurement of cosmic-ray air showers with the Tunka Radio Extension (Tunka-Rex)". In: *Nucl. Instrum. Meth. A* 802 (2015), pp. 89–96. DOI: 10.1016/j.nima.2015.08.061. arXiv: 1509.08624 [astro-ph.IM].

[365] S. Prohira et al. "The Radar Echo Telescope for Cosmic Rays: Pathfinder experiment for a next-generation neutrino observatory". In: *Phys. Rev. D* 104.10 (2021), p. 102006. DOI: 10.1103/PhysRevD.104.102006. arXiv: 2104.00459 [astro-ph.IM].

[366] Yaocheng Chen. "TAROGE experiment and reconstruction technique for near-horizon impulsive radio signals induced by ultra-high energy cosmic rays". In: *PoS* ICRC2021 (2021), p. 263. DOI: 10.22323/1.395.0263.

[367] Taylor Barrella, Steven Barwick, and David Saltzberg. "Ross Ice Shelf in situ radio-frequency ice attenuation". In: *J. Glaciol.* 57 (2011), pp. 61–66. DOI: 10.3189/002214311795306691. arXiv: 1011.0477 [astro-ph.IM].

[368] J. Avva et al. "An in situ measurement of the radio-frequency attenuation in ice at Summit Station, Greenland". In: *J. Glaciol.* 61 (2015), pp. 1005–1011. DOI: 10.3189/2015JoG15J057. arXiv: 1409.5413 [astro-ph.IM].

[369] J. A. Aguilar et al. "In situ, broadband measurement of the radio frequency attenuation length at Summit Station, Greenland". In: *Journal of Glaciology* (2022), p. 1. DOI: 10.1017/jog.2022.40. arXiv: 2201.07846 [astro-ph.IM].

[370] C. Glaser et al. "Deep-learning-based reconstruction of the neutrino direction and energy for in-ice radio detectors". In: (May 2022). arXiv: 2205.15872 [astro-ph.IM].

[371] Ke Fang et al. "Identifying Ultrahigh-Energy Cosmic-Ray Accelerators with Future Ultrahigh-Energy Neutrino Detectors". In: *JCAP* 12 (2016), p. 017. DOI: 10.1088/1475-7516/2016/12/017. arXiv: 1609.08027 [astro-ph.HE].

[372] Damiano F. G. Fiorillo, Mauricio Bustamante, and Victor B. Valera. "Near-future discovery of point sources of ultra-high-energy neutrinos". In: 03 (May 2022), p. 026. DOI: 10.1088/1475-7516/2023/03/026. arXiv: 2205.15985 [astro-ph.HE].

[373] Aya Ishihara. "The IceCube Upgrade - Design and Science Goals". In: *PoS* ICRC2019 (2021), p. 1031. DOI: 10.22323/1.358.1031. arXiv: 1908.09441 [astro-ph.HE].

[374] Mauricio Bustamante and Markus Ahlers. "Inferring the flavor of high-energy astrophysical neutrinos at their sources". In: *Phys. Rev. Lett.* 122.24 (2019), p. 241101. DOI: 10.1103/PhysRevLett.122.241101. arXiv: 1901.10087 [astro-ph.HE].

[375] Dave Z. Besson, Ilya Kravchenko, and Krishna Nivedita. "Polarization angle dependence of vertically propagating radio-frequency signals in South Polar ice". In: *Astropart. Phys.* 144 (2023), p. 102766. DOI: 10.1016/j.astropartphys.2022.102766. arXiv: 2110.13353 [astro-ph.IM].

[376] Ryan Rice-Smith. "Assessing the Background Rate due to Cosmic Ray Core Scattering from Internal Reflection Layers in the South Pole Ice Cap". In: *Neutrino 2022*. Zenodo, 2022. DOI: 10.5281/zenodo.6785120.

[377] H. Jeffreys. *The Theory of Probability*. Oxford Classic Texts in the Physical Sciences. OUP Oxford, 1998. ISBN: 9780191589676. URL: https://books.google.dk/books?id=vh9Act9rtzQC.

[378] Johannes Buchner. "UltraNest — a robust, general purpose Bayesian inference engine". In: *The Journal of Open Source Software* 6 (2021), p. 3001. DOI: 10.21105/joss.03001. arXiv: 2101.09604 [stat.CO].

[379] Johannes Buchner. "A statistical test for Nested Sampling algorithms". In: *Statistics and Computing* 26 (2016), p. 383. DOI: 10.1007/s11222-014-9512-y. arXiv: 1407.5459 [stat.CO].

[380] Johannes Buchner. "Collaborative Nested Sampling: Big Data vs. complex physical models". In: *Publications of the Astronomical Society of the Pacific* 131 (2019), p. 108005. DOI: 10.1088/1538-3873/aae7fc. arXiv: 1707.04476 [stat.CO].

[381] T. Pierog et al. "EPOS LHC: Test of collective hadronization with data measured at the CERN Large Hadron Collider". In: *Phys. Rev. C* 92.3 (2015), p. 034906. DOI: 10.1103/PhysRevC.92.034906. arXiv: 1306.0121 [hep-ph].

[382] Sergey Ostapchenko. "Monte Carlo treatment of hadronic interactions in enhanced Pomeron scheme: I. QGSJET-II model". In: *Phys. Rev. D* 83 (2011), p. 014018. DOI: 10.1103/PhysRevD.83.014018. arXiv: 1010.1869 [hep-ph].

[383] James H. Adams et al. "White paper on EUSO-SPB2". In: (Mar. 2017). arXiv: 1703.04513 [astro-ph.HE].

[384] Jörg R. Hörandel. "GCOS - The Global Cosmic Ray Observatory". In: *PoS* ICRC2021 (2021), p. 027. DOI: 10.22323/1.395.0027. arXiv: 2203.01127 [astro-ph.HE].

[385] R. U. Abbasi et al. "Surface detectors of the TAx4 experiment". In: *Nucl. Instrum. Meth. A* 1019 (2021), p. 165726. DOI: 10.1016/j.nima.2021.165726. arXiv: 2103.01086 [astro-ph.IM].

[386] Jakob van Santen et al. https://github.com/icecube/toise. toise. 2022.

[387] F. W. Stecker. "Diffuse Fluxes of Cosmic High-Energy Neutrinos". In: *Astrophys. J.* 228 (1979), pp. 919–927. DOI: 10.1086/156919.

[388] Will Thompson et al. "TAMBO: Searching for Tau Neutrinos in the Peruvian Andes". In: *PoS* ICRC2023 (2023), p. 1109. DOI: 10.22323/1.444.1109.

[389] A. Anker et al. "A search for cosmogenic neutrinos with the ARIANNA test bed using 4.5 years of data". In: *JCAP* 03 (2020), p. 053. DOI: 10.1088/1475-7516/2020/03/053. arXiv: 1909.00840 [astro-ph.IM].

[390] Victor Branco Valera, Mauricio Bustamante, and Christian Glaser. "Near-future discovery of the diffuse flux of ultrahigh-energy cosmic neutrinos". In: *Phys. Rev. D* 107.4 (Oct. 2023), p. 043019. DOI: 10.1103/PhysRevD.107.043019. arXiv: 2210.03756 [astro-ph.HE].

[391] V. A. Allakhverdyan et al. "Deep-Water Neutrino Telescope in Lake Baikal". In: *Phys. At. Nucl.* 84.9 (2021), pp. 1600–1609. DOI: 10.1134/S1063778821090064.

[392] V. A. Balkanov et al. "The Lake Baikal Neutrino Telescope NT-200: Status, results, future". In: *Nucl. Phys. B Proc. Suppl.* 75 (1999). Ed. by O. Saavedra and A. Castellina, pp. 409–411. DOI: 10.1016/S0920-5632(99)00308-4.

[393] M. Ageron et al. "ANTARES: the first undersea neutrino telescope". In: *Nucl. Instrum. Meth. A* 656 (2011), pp. 11–38. DOI: 10.1016/j.nima.2011.06.103. arXiv: 1104.1607 [astro-ph.IM].

[394] Shih-Hao Wang et al. "TAROGE-M: radio antenna array on antarctic high mountain for detecting near-horizontal ultra-high energy air showers". In: *JCAP* 11 (2022), p. 022. DOI: 10.1088/1475-7516/2022/11/022. arXiv: 2207.10616 [astro-ph.HE].

[395] Eiji Kido. "Status and prospects of the TAx4 experiment". In: *EPJ Web Conf.* 210 (2019). Ed. by I. Lhenry-Yvon et al., p. 06001. DOI: 10.1051/epjconf/201921006001.

[396] Rasha Abbasi et al. "Sensitivity studies for the IceCube-Gen2 radio array". In: *PoS* ICRC2021 (2021), p. 1183. DOI: 10.22323/1.395.1183. arXiv: 2107.08910 [astro-ph.HE].

[397] Rhorry Gauld and Juan Rojo. "Precision determination of the small-x gluon from charm production at LHCb". In: *Phys. Rev. Lett.* 118.7 (2017), p. 072001. DOI: 10.1103/PhysRevLett.118.072001. arXiv: 1610.09373 [hep-ph].

[398] M. G. Aartsen et al. "Search for a diffuse flux of astrophysical muon neutrinos with the IceCube 59-string configuration". In: *Phys. Rev. D* 89.6 (2014), p. 062007. DOI: 10.1103/PhysRevD.89.062007. arXiv: 1311.7048 [astro-ph.HE].

[399] M. G. Aartsen et al. "Atmospheric and astrophysical neutrinos above 1 TeV interacting in IceCube". In: *Phys. Rev. D* 91.2 (2015), p. 022001. DOI: 10.1103/PhysRevD.91.022001. arXiv: 1410.1749 [astro-ph.HE].

[400] M. G. Aartsen et al. "Measurement of the Atmospheric ν_e Spectrum with IceCube". In: *Phys. Rev. D* 91 (2015), p. 122004. DOI: 10.1103/PhysRevD.91.122004. arXiv: 1504.03753 [astro-ph.HE].

[401] M. G. Aartsen et al. "A combined maximum-likelihood analysis of the high-energy astrophysical neutrino flux measured with IceCube". In: *Astrophys. J.* 809.1 (2015), p. 98. DOI: 10.1088/0004-637X/809/1/98. arXiv: 1507.03991 [astro-ph.HE].

[402] Damiano F. G. Fiorillo and Mauricio Bustamante. "Bump hunting in the diffuse flux of high-energy cosmic neutrinos". In: *Phys. Rev. D* 107.8 (2023), p. 083008. DOI: 10.1103/PhysRevD.107.083008. arXiv: 2301.00024 [astro-ph.HE].

[403] Claudio Kopper, William Giang, and Naoko Kurahashi. "Observation of Astrophysical Neutrinos in Four Years of IceCube Data". In: *PoS* ICRC2015 (2016), p. 1081. DOI: 10.22323/1.236.1081.

[404] IceCube Collaboration. *Observation of Astrophysical Neutrinos in Four Years of IceCube Data*. https://icecube.wisc.edu/science/data/HE-nu-2010-2014. 2015 (accessed October 21, 2015). URL: https://icecube.wisc.edu/science/data/HE-nu-2010-2014.

[405] Claudio Kopper. *Observation of Astrophysical Neutrinos in Six Years of IceCube Data*. Talk given at the International Cosmic Ray Conference 2017, July 15, 2017, Busan, https://indico.snu.ac.kr/indico/event/.

[406] Carlos A. Argüelles, Jordi Salvadó, and Christopher N. Weaver. "nuSQuIDS: A toolbox for neutrino propagation". In: *Comput. Phys. Commun.* 277 (2022), p. 108346. DOI: 10.1016/j.cpc.2022.108346. arXiv: 2112.13804 [hep-ph].

[407] P. Jain et al. "Extra dimensions and strong neutrino nucleon interactions above 10^{19} eV: Breaking the GZK barrier". In: *Phys. Lett. B* 484 (2000), pp. 267–274. DOI: 10.1016/S0370-2693(00)00647-X. arXiv: hep-ph/0001031.

[408] Damir Bečirević et al. "Seeking leptoquarks in IceCube". In: *JHEP* 06 (2018), p. 032. DOI: 10.1007/JHEP06(2018)032. arXiv: 1803.10112 [hep-ph].

[409] Damiano F. G. Fiorillo et al. "Searches for dark matter decay with ultra-high-energy neutrinos endure backgrounds". In: (July 2023). arXiv: 2307.02538 [astro-ph.HE].

[410] Rasmus W. Rasmussen et al. "Astrophysical neutrinos flavored with Beyond the Standard Model physics". In: *Phys. Rev. D* 96.8 (2017), p. 083018. DOI: 10.1103/PhysRevD.96.083018. arXiv: 1707.07684 [hep-ph].

[411] C. A. Argüelles et al. "Snowmass white paper: beyond the standard model effects on neutrino flavor: Submitted to the proceedings of the US community study on the future of particle physics (Snowmass 2021)". In: *Eur. Phys. J. C* 83.1 (2023), p. 15. DOI: 10.1140/epjc/s10052-022-11049-7. arXiv: 2203.10811 [hep-ph].

[412] R. U. Abbasi et al. "The Cosmic-Ray Energy Spectrum between 2 PeV and 2 EeV Observed with the TALE detector in monocular mode". In: *Astrophys. J.* 865.1 (2018), p. 74. DOI: 10.3847/1538-4357/aada05. arXiv: 1803.01288 [astro-ph.HE].

[413] R. U. Abbasi et al. "The Cosmic-Ray Composition between 2 PeV and 2 EeV Observed with the TALE Detector in Monocular Mode". In: *Astrophys. J.* 909.2 (2021), p. 178. DOI: 10.3847/1538-4357/abdd30. arXiv: 2012.10372 [astro-ph.HE].

[414] Philipp Baerwald, Mauricio Bustamante, and Walter Winter. "Are gamma-ray bursts the sources of ultra-high energy cosmic rays?" In: *Astropart. Phys.* 62 (2015), pp. 66–91. DOI: 10.1016/j.astropartphys.2014.07.007. arXiv: 1401.1820 [astro-ph.HE].

[415] F.N. Fritsch and J. Glaser Butland. "A Method for Constructing Local Monotone Piecewise Cubic Interpolants". In: *SIAM J. Sci. Stat. Comp.* 5 (1984), p. 300. DOI: 10.1137/0905021.

[416] Anthony M. Brown et al. "Trinity: An Imaging Air Cherenkov Telescope to Search for Ultra-High-Energy Neutrinos". In: *37th International Cosmic Ray Conference*. Sept. 2021. arXiv: 2109.03125 [astro-ph.IM].

[417] Alan Coleman et al. *In preparation*. 2023.

[418] Jeffrey Lazar et al. "Prometheus: An Open-Source Neutrino Telescope Simulation". In: (Apr. 2023). arXiv: 2304.14526 [hep-ex].

[419] Alan Coleman et al. "Ultra-High-Energy Cosmic Rays: The Intersection of the Cosmic and Energy Frontiers". In: (May 2022). arXiv: 2205.05845 [astro-ph.HE].

[420] Rasha U. Abbasi et al. "IceCube Data for Neutrino Point-Source Searches Years 2008-2018". In: (Jan. 2021). DOI: 10.21234/CPKQ-K003. arXiv: 2101.09836 [astro-ph.HE].

[421] Alexander Aab et al. "Observation of a Large-scale Anisotropy in the Arrival Directions of Cosmic Rays above 8×10^{18} eV". In: *Science* 357.6537 (2017), p. 1266. DOI: 10.1126/science.aan4338. arXiv: 1709.07321 [astro-ph.HE].

[422] Rogerio de Almeida et al. "Large-scale and multipolar anisotropies of cosmic rays detected at the Pierre Auger Observatory with energies above 4 EeV". In: *PoS* ICRC2021 (2021), p. 335. DOI: 10.22323/1.395.0335.

[423] Alexander Aab et al. "Cosmic-ray anisotropies in right ascension measured by the Pierre Auger Observatory". In: *Astrophys. J.* 891 (2020), p. 142. DOI: 10.3847/1538-4357/ab7236. arXiv: 2002.06172 [astro-ph.HE].

[424] Rasha U. Abbasi et al. "Indications of Intermediate-Scale Anisotropy of Cosmic Rays with Energy Greater Than 57 EeV in the Northern Sky Measured with the Surface Detector of the Telescope Array Experiment". In: *Astrophys. J. Lett.* 790 (2014), p. L21. DOI: 10.1088/2041-8205/790/2/L21. arXiv: 1404.5890 [astro-ph.HE].

[425] Alexander Aab et al. "An Indication of anisotropy in arrival directions of ultra-high-energy cosmic rays through comparison to the flux pattern of extragalactic gamma-ray sources". In: *Astrophys. J. Lett.* 853.2 (2018), p. L29. DOI: 10.3847/2041-8213/aaa66d. arXiv: 1801.06160 [astro-ph.HE].

[426] Alexander Aab et al. "Large-scale cosmic-ray anisotropies above 4 EeV measured by the Pierre Auger Observatory". In: *Astrophys. J.* 868.1 (2018), p. 4. DOI: 10.3847/1538-4357/aae689. arXiv: 1808.03579 [astro-ph.HE].

[427] Rasha U. Abbasi et al. "Search for Large-scale Anisotropy on Arrival Directions of Ultra-high-energy Cosmic Rays Observed with the Telescope Array Experiment". In: *Astrophys. J. Lett.* 898.2 (2020), p. L28. DOI: 10.3847/2041-8213/aba0bc. arXiv: 2007.00023 [astro-ph.HE].

[428] Peter Tinyakov et al. "The UHECR dipole and quadrupole in the latest data from the original Auger and TA surface detectors". In: *PoS* ICRC2021 (2021), p. 375. DOI: 10.22323/1.395.0375. arXiv: 2111.14593 [astro-ph.HE].

[429] Alexander Aab et al. "Searches for Anisotropies in the Arrival Directions of the Highest Energy Cosmic Rays Detected by the Pierre Auger Observatory". In: *Astrophys. J.* 804.1 (2015), p. 15. DOI: 10.1088/0004-637X/804/1/15. arXiv: 1411.6111 [astro-ph.HE].

[430] Jihyun Kim et al. "Hotspot Update, and a new Excess of Events on the Sky Seen by the Telescope Array Experiment". In: *PoS* ICRC2021 (2021), p. 328. DOI: 10.22323/1.395.0328.

[431] Rasha U. Abbasi et al. "Indications of a Cosmic Ray Source in the Perseus-Pisces Supercluster". In: (Oct. 2021). arXiv: 2110.14827 [astro-ph.HE].

[432] Günter Sigl, Francesco Miniati, and Torsten A. Ensslin. "Ultrahigh-energy cosmic rays in a structured and magnetized universe". In: *Phys. Rev. D* 68 (2003), p. 043002. DOI: 10.1103/PhysRevD.68.043002. arXiv: astro-ph/0302388.

[433] Klaus Dolag et al. "Mapping deflections of ultrahigh energy cosmic rays in constrained simulations of extragalactic magnetic fields". In: *JETP Lett.* 79 (2004), p. 583. DOI: 10.1134/1.1790011. arXiv: astro-ph/0310902.

[434] Günter Sigl, Francesco Miniati, and Torsten A. Ensslin. "Ultrahigh energy cosmic ray probes of large scale structure and magnetic fields". In: *Phys. Rev. D* 70 (2004), p. 043007. DOI: 10.1103/PhysRevD.70.043007. arXiv: astro-ph/0401084.

[435] Klaus Dolag et al. "Constrained simulations of the magnetic field in the local Universe and the propagation of UHECRs". In: *JCAP* 01 (2005), p. 009. DOI: 10.1088/1475-7516/2005/01/009. arXiv: astro-ph/0410419.

[436] Azadeh Keivani, Glennys R. Farrar, and Michael Sutherland. "Magnetic Deflections of Ultra-High Energy Cosmic Rays from Centaurus A". In: *Astropart. Phys.* 61 (2014), p. 47. DOI: 10.1016/j.astropartphys.2014.07.001. arXiv: 1406.5249 [astro-ph.HE].

[437] Stefan Hackstein et al. "Propagation of ultrahigh energy cosmic rays in extragalactic magnetic fields: a view from cosmological simulations". In: *Mon. Not. Roy. Astron. Soc.* 462.4 (2016), p. 3660. DOI: 10.1093/mnras/stw1903. arXiv: 1607.08872 [astro-ph.CO].

[438] Rafael Alves Batista et al. "Implications of strong intergalactic magnetic fields for ultrahigh-energy cosmic-ray astronomy". In: *Phys. Rev. D* 96.2 (2017), p. 023010. DOI: 10.1103/PhysRevD.96.023010. arXiv: 1704.05869 [astro-ph.HE].

[439] Glennys R. Farrar and Michael S. Sutherland. "Deflections of UHECRs in the Galactic magnetic field". In: *JCAP* 05 (2019), p. 004. DOI: 10.1088/1475-7516/2019/05/004. arXiv: 1711.02730 [astro-ph.HE].

[440] Floyd William Stecker. *Cosmic gamma rays*. 1971.

[441] Raymond J. Protheroe and Peter L. Biermann. "A New estimate of the extragalactic radio background and implications for ultrahigh-energy gamma-ray propagation". In: *Astropart. Phys.* 6 (1996). [Erratum: Astropart. Phys. 7, 181 (1997)], p. 45. DOI: 10.1016/S0927-6505(96)00041-2. arXiv: astro-ph/9605119.

[442] Paolo S. Coppi and Felix A. Aharonian. "Constraints on the VHE emissivity of the universe from the diffuse GeV gamma-ray background". In: *Astrophys. J. Lett.* 487 (1997), p. L9. DOI: 10.1086/310883. arXiv: astro-ph/9610176.

[443] Alexander Aab et al. "A search for point sources of EeV photons". In: *Astrophys. J.* 789.2 (2014), p. 160. DOI: 10.1088/0004-637X/789/2/160. arXiv: 1406.2912 [astro-ph.HE].

[444] Alexander Aab et al. "Search for photons with energies above 10^{18} eV using the hybrid detector of the Pierre Auger Observatory". In: *JCAP* 04 (2017). [Erratum: JCAP 09, E02 (2020)], p. 009. DOI: 10.1088/1475-7516/2017/04/009. arXiv: 1612.01517 [astro-ph.HE].

[445] Yu. A. Fomin et al. "Constraints on the flux of $\sim (10^{16} - 10^{17.5})$ eV cosmic photons from the EAS-MSU muon data". In: *Phys. Rev. D* 95.12 (2017), p. 123011. DOI: 10.1103/PhysRevD.95.123011. arXiv: 1702.08024 [astro-ph.HE].

[446] Wolf D. Apel et al. "KASCADE-Grande Limits on the Isotropic Diffuse Gamma-Ray Flux between 100 TeV and 1 EeV". In: *Astrophys. J.* 848.1 (2017), p. 1. DOI: 10.3847/1538-4357/aa8bb7. arXiv: 1710.02889 [astro-ph.HE].

[447] Rasha U. Abbasi et al. "Constraints on the diffuse photon flux with energies above 10^{18} eV using the surface detector of the Telescope Array experiment". In: *Astropart. Phys.* 110 (2019), p. 8. DOI: 10.1016/j.astropartphys.2019.03.003. arXiv: 1811.03920 [astro-ph.HE].

[448] Steven H. Margolis, David N. Schramm, and Rein Silberberg. "Ultrahigh-Energy Neutrino Astronomy". In: *Astrophys. J.* 221 (1978), p. 990. DOI: 10.1086/156104.

[449] Hugo A. Ayala Solares et al. "Multimessenger Gamma-Ray and Neutrino Coincidence Alerts Using HAWC and IceCube Subthreshold Data". In: (Aug. 2020). DOI: 10.3847/1538-4357/abcaa4. arXiv: 2008.10616 [astro-ph.HE].

[450] Robert Stein et al. "A tidal disruption event coincident with a high-energy neutrino". In: *Nature Astron.* 5.5 (2021), p. 510. DOI: 10.1038/s41550-020-01295-8. arXiv: 2005.05340 [astro-ph.HE].

[451] Rose M. Baltrusaitis et al. "Limits on astrophysical ν_e flux at $E_\nu > 10^{19}$ eV". In: *Astrophys. J. Lett.* 281 (1984), p. L9. DOI: 10.1086/184273.

[452] Rose M. Baltrusaitis et al. "Limits on Deeply Penetrating Particles in the $> 10^{17}$ eV Cosmic Ray Flux". In: *Phys. Rev. D* 31 (1985), p. 2192. DOI: 10.1103/PhysRevD.31.2192.

[453] Nikolai G. Lehtinen et al. "FORTE satellite constraints on ultra-high energy cosmic particle fluxes". In: *Phys. Rev. D* 69 (2004), p. 013008. DOI: 10.1103/PhysRevD.69.013008. arXiv: astro-ph/0309656.

[454] Peter W. Gorham et al. "Experimental limit on the cosmic diffuse ultrahigh-energy neutrino flux". In: *Phys. Rev. Lett.* 93 (2004), p. 041101. DOI: 10.1103/PhysRevLett.93.041101. arXiv: astro-ph/0310232.

[455] Rasha U. Abbasi et al. "An upper limit on the electron-neutrino flux from the HiRes detector". In: *Astrophys. J.* 684 (2008), p. 790. DOI: 10.1086/590335. arXiv: 0803.0554 [astro-ph].

[456] Olaf Scholten et al. "Improved flux limits for neutrinos with energies above 10^{22} eV from observations with the Westerbork Synthesis Radio Telescope". In: *Phys. Rev. Lett.* 103 (2009), p. 191301. DOI: 10.1103/PhysRevLett.103.191301. arXiv: 0910.4745 [astro-ph.HE].

[457] Clancy W. James et al. "LUNASKA experiments using the Australia Telescope Compact Array to search for ultra-high energy neutrinos and develop technology for the lunar Cherenkov technique". In: *Phys. Rev. D* 81 (2010), p. 042003. DOI: 10.1103/PhysRevD.81.042003. arXiv: 0911.3009 [astro-ph.HE].

[458] Naoko Kurahashi, Justin Vandenbroucke, and Giorgio Gratta. "Search for Acoustic Signals from Ultra-High Energy Neutrinos in 1500 km^3 of Sea Water". In: *Phys. Rev. D* 82 (2010), p. 073006. DOI: 10.1103/PhysRevD.82.073006. arXiv: 1007.5517 [hep-ex].

[459] Sander ter Veen et al. "A new limit on the Ultra-High-Energy Cosmic-Ray flux with the Westerbork Synthesis Radio Telescope". In: *Phys. Rev. D* 82 (2010), p. 103014. DOI: 10.1103/PhysRevD.82.103014. arXiv: 1010.6061 [astro-ph.HE].

[460] Ilya Kravchenko et al. "Updated Results from the RICE Experiment and Future Prospects for Ultra-High Energy Neutrino Detection at the South Pole". In: *Phys. Rev. D* 85 (2012), p. 062004. DOI: 10.1103/PhysRevD.85.062004. arXiv: 1106.1164 [astro-ph.HE].

[461] Pedro Abreu et al. "Search for point-like sources of ultra-high energy neutrinos at the Pierre Auger Observatory and improved limit on the diffuse flux of tau neutrinos". In: *Astrophys. J. Lett.* 755 (2012), p. L4. DOI: 10.1088/2041-8205/755/1/L4. arXiv: 1210.3143 [astro-ph.HE].

[462] Patrick Allison et al. "Constraints on the Ultra-High Energy Neutrino Flux from Gamma-Ray Bursts from a Prototype Station of the Askaryan Radio Array". In: *Astropart. Phys.* 88 (2017), p. 7. DOI: 10.1016/j.astropartphys.2016.12.003. arXiv: 1507.00100 [astro-ph.HE].

[463] Max L. Ahnen et al. "Limits on the flux of tau neutrinos from 1 PeV to 3 EeV with the MAGIC telescopes". In: *Astropart. Phys.* 102 (2018), p. 77. DOI: 10.1016/j.astropartphys.2018.05.002. arXiv: 1805.02750 [astro-ph.IM].

[464] Alexander Aab et al. "Limits on point-like sources of ultra-high-energy neutrinos with the Pierre Auger Observatory". In: *JCAP* 11 (2019), p. 004. DOI: 10.1088/1475-7516/2019/11/004. arXiv: 1906.07419 [astro-ph.HE].

[465] Alexander Aab et al. "A Search for Ultra-high-energy Neutrinos from TXS 0506+056 Using the Pierre Auger Observatory". In: *Astrophys. J.* 902.2 (2020), p. 105. DOI: 10.3847/1538-4357/abb476. arXiv: 2010.10953 [astro-ph.HE].

[466] Satoru Ogawa et al. "Observation of Optical Transients and Search for PeV-EeV Tau Neutrinos with Ashra-1". In: *PoS* ICRC2019 (2021), p. 970. DOI: 10.22323/1.358.0970.

[467] Paolo Lipari. "Proton and Neutrino Extragalactic Astronomy". In: *Phys. Rev. D* 78 (2008), p. 083011. DOI: 10.1103/PhysRevD.78.083011. arXiv: 0808.0344 [astro-ph].

[468] Andrea Silvestri and Steven W. Barwick. "Constraints on Extragalactic Point Source Flux from Diffuse Neutrino Limits". In: *Phys. Rev. D* 81 (2010), p. 023001. DOI: 10.1103/PhysRevD.81.023001. arXiv: 0908.4266 [astro-ph.HE].

[469] Kohta Murase, John F. Beacom, and Hajime Takami. "Gamma-Ray and Neutrino Backgrounds as Probes of the High-Energy Universe: Hints of Cascades, General Constraints, and Implications for TeV Searches". In: *JCAP* 08 (2012), p. 030. DOI: 10.1088/1475-7516/2012/08/030. arXiv: 1205.5755 [astro-ph.HE].

[470] Markus Ahlers and Francis Halzen. "Pinpointing Extragalactic Neutrino Sources in Light of Recent IceCube Observations". In: *Phys. Rev. D* 90.4 (2014), p. 043005. DOI: 10.1103/PhysRevD.90.043005. arXiv: 1406.2160 [astro-ph.HE].

[471] Kohta Murase and Eli Waxman. "Constraining High-Energy Cosmic Neutrino Sources: Implications and Prospects". In: *Phys. Rev. D* 94.10 (2016), p. 103006. DOI: 10.1103/PhysRevD.94.103006. arXiv: 1607.01601 [astro-ph.HE].

[472] Ke Fang and M. Coleman Miller. "A New Method for Finding Point Sources in High-energy Neutrino Data". In: *Astrophys. J.* 826.2 (2016), p. 102. DOI: 10.3847/0004-637X/826/2/102. arXiv: 1603.09306 [astro-ph.IM].

[473] Imre Bartos et al. "The IceCube Pie Chart: Relative Source Contributions to the Cosmic Neutrino Flux". In: *Astrophys. J.* 921.1 (2021), p. 45. DOI: 10.3847/1538-4357/ac1c7b. arXiv: 2105.03792 [astro-ph.HE].

[474] Andrea Palladino et al. "Can astrophysical neutrinos trace the origin of the detected ultra-high energy cosmic rays?" In: *Mon. Not. Roy. Astron. Soc.* 494.3 (2020), p. 4255. DOI: 10.1093/mnras/staa1003. arXiv: 1911.05756 [astro-ph.HE].

[475] Charles D. Dermer, Kohta Murase, and Hajime Takami. "Variable Gamma-ray Emission Induced by Ultra-High Energy Neutral Beams: Application to 4C +21.35". In: *Astrophys. J.* 755 (2012), p. 147. DOI: 10.1088/0004-637X/755/2/147. arXiv: 1203.6544 [astro-ph.HE].

[476] Walter Winter. "Neutrinos from Cosmic Accelerators Including Magnetic Field and Flavor Effects". In: *Adv. High Energy Phys.* 2012 (2012), p. 586413. DOI: 10.1155/2012/586413. arXiv: 1201.5462 [astro-ph.HE].

[477] Kohta Murase, Yoshiyuki Inoue, and Charles D. Dermer. "Diffuse Neutrino Intensity from the Inner Jets of Active Galactic Nuclei: Impacts of External Photon Fields and the Blazar Sequence". In: *Phys. Rev. D* 90.2 (2014), p. 023007. DOI: 10.1103/PhysRevD.90.023007. arXiv: 1403.4089 [astro-ph.HE].

[478] Damiano F. G. Fiorillo et al. "Unified thermal model for photohadronic neutrino production in astrophysical sources". In: *JCAP* 07 (2021), p. 028. DOI: 10.1088/1475-7516/2021/07/028. arXiv: 2103.16577 [astro-ph.HE].

[479] Andrew M. Hopkins and John F. Beacom. "On the normalisation of the cosmic star formation history". In: *Astrophys. J.* 651 (2006), p. 142. DOI: 10.1086/506610. arXiv: astro-ph/0601463.

[480] Shigeo S. Kimura, Kohta Murase, and Kenji Toma. "Neutrino and Cosmic-Ray Emission and Cumulative Background from Radiatively Inefficient Accretion Flows in Low-Luminosity Active Galactic Nuclei". In: *Astrophys. J.* 806 (2015), p. 159. DOI: 10.1088/0004-637X/806/2/159. arXiv: 1411.3588 [astro-ph.HE].

[481] Shigeo S. Kimura, Kohta Murase, and Peter Mészáros. "Soft gamma rays from low accreting supermassive black holes and connection to energetic neutrinos". In: *Nature Commun.* 12.1 (2021), p. 5615. DOI: 10.1038/s41467-021-25111-7. arXiv: 2005.01934 [astro-ph.HE].

[482] Abraham Loeb and Eli Waxman. "The Cumulative background of high energy neutrinos from starburst galaxies". In: *JCAP* 05 (2006), p. 003. DOI: 10.1088/1475-7516/2006/05/003. arXiv: astro-ph/0601695.

[483] Irene Tamborra, Shin'ichiro Ando, and Kohta Murase. "Star-forming galaxies as the origin of diffuse high-energy backgrounds: Gamma-ray and neutrino connections, and implications for starburst history". In: *JCAP* 09 (2014), p. 043. DOI: 10.1088/1475-7516/2014/09/043. arXiv: 1404.1189 [astro-ph.HE].

[484] Andrea Palladino et al. "IceCube Neutrinos from Hadronically Powered Gamma-Ray Galaxies". In: *JCAP* 09 (2019), p. 004. DOI: 10.1088/1475-7516/2019/09/004. arXiv: 1812.04685 [astro-ph.HE].

[485] Enrico Peretti et al. "Cosmic ray transport and radiative processes in nuclei of starburst galaxies". In: *Mon. Not. Roy. Astron. Soc.* 487.1 (2019), p. 168. DOI: 10.1093/mnras/stz1161. arXiv: 1812.01996 [astro-ph.HE].

[486] Enrico Peretti et al. "Contribution of starburst nuclei to the diffuse gamma-ray and neutrino flux". In: *Mon. Not. Roy. Astron. Soc.* 493.4 (2020), p. 5880. DOI: 10.1093/mnras/staa698. arXiv: 1911.06163 [astro-ph.HE].

[487] Antonio Ambrosone et al. "Starburst galaxies strike back: a multi-messenger analysis with Fermi-LAT and IceCube data". In: *Mon. Not. Roy. Astron. Soc.* 503.3 (2021), p. 4032. DOI: 10.1093/mnras/stab659. arXiv: 2011.02483 [astro-ph.HE].

[488] Kohta Murase, Susumu Inoue, and Shigehiro Nagataki. "Cosmic Rays Above the Second Knee from Clusters of Galaxies and Associated High-Energy Neutrino Emission". In: *Astrophys. J. Lett.* 689 (2008), p. L105. DOI: 10.1086/595882. arXiv: 0805.0104 [astro-ph].

[489] Kumiko Kotera et al. "Propagation of ultrahigh energy nuclei in clusters of galaxies: resulting composition and secondary emissions". In: *Astrophys. J.* 707 (2009), p. 370. DOI: 10.1088/0004-637X/707/1/370. arXiv: 0907.2433 [astro-ph.HE].

[490] Veniamin S. Berezinsky, Pasquale Blasi, and Vladimir S. Ptuskin. "Clusters of Galaxies as a Storage Room for Cosmic Rays". In: *Astrophys. J.* 487 (1997), p. 529. DOI: 10.1086/304622. arXiv: astro-ph/9609048.

[491] Jaime Álvarez-Muñiz and Peter Mészáross. "High energy neutrinos from radio-quiet AGNs". In: *Phys. Rev. D* 70 (2004), p. 123001. DOI: 10.1103/PhysRevD.70.123001. arXiv: astro-ph/0409034.

[492] Uri Keshet et al. "Gamma-rays from intergalactic shocks". In: *Astrophys. J.* 585 (2003), p. 128. DOI: 10.1086/345946. arXiv: astro-ph/0202318.

[493] Doron Kushnir and Eli Waxman. "Nonthermal emission from clusters of galaxies". In: *JCAP* 08 (2009), p. 002. DOI: 10.1088/1475-7516/2009/08/002. arXiv: 0903.2271 [astro-ph.HE].

[494] Andrii Neronov and Dmitri Semikoz. "Radio-to-Gamma-Ray Synchrotron and Neutrino Emission from Proton–Proton Interactions in Active Galactic Nuclei". In: *JETP Lett.* 113.2 (2021), p. 69. DOI: 10.1134/S0021364021020028. arXiv: 2012.04425 [astro-ph.HE].

[495] Andrea Palladino et al. "Interpretation of the diffuse astrophysical neutrino flux in terms of the blazar sequence". In: *Astrophys. J.* 871.1 (2019), p. 41. DOI: 10.3847/1538-4357/aaf507. arXiv: 1806.04769 [astro-ph.HE].

[496] Armen M. Atoyan and Charles D. Dermer. "High-energy neutrinos from photomeson processes in blazars". In: *Phys. Rev. Lett.* 87 (2001), p. 221102. DOI: 10.1103/PhysRevLett.87.221102. arXiv: astro-ph/0108053.

[497] Armen M. Atoyan and Charles D. Dermer. "Neutral beams from blazar jets". In: *Astrophys. J.* 586 (2003), p. 79. DOI: 10.1086/346261. arXiv: astro-ph/0209231.

[498] Chiara Righi et al. "EeV astrophysical neutrinos from flat spectrum radio quasars". In: *Astron. Astrophys.* 642 (2020), A92. DOI: 10.1051/0004-6361/202038301. arXiv: 2003.08701 [astro-ph.HE].

[499] Luke O'C. Drury, Felix A. Aharonian, and Heinrich J. Völk. "The Gamma-ray visibility of supernova remnants: A Test of cosmic ray origin". In: *Astron. Astrophys.* 287 (1994), p. 959. arXiv: astro-ph/9305037.

[500] Jaime Álvarez-Muñiz and Francis Halzen. "Possible high-energy neutrinos from the cosmic accelerator RX J1713.7-3946". In: *Astrophys. J. Lett.* 576 (2002), p. L33. DOI: 10.1086/342978. arXiv: astro-ph/0205408.

[501] Francesco L. Villante and Francesco Vissani. "How precisely neutrino emission from supernova remnants can be constrained by gamma ray observations?" In: *Phys. Rev. D* 78 (2008), p. 103007. DOI: 10.1103/PhysRevD.78.103007. arXiv: 0807.4151 [astro-ph].

[502] Di Xiao et al. "Revisiting the Contributions of Supernova and Hypernova Remnants to the Diffuse High-energy Backgrounds: Constraints on Very High Redshift Injection". In: *Astrophys. J.* 826.2 (2016), p. 133. DOI: 10.3847/0004-637X/826/2/133. arXiv: 1604.08131 [astro-ph.HE].

[503] Kohta Murase. "New Prospects for Detecting High-Energy Neutrinos from Nearby Supernovae". In: *Phys. Rev. D* 97.8 (2018), p. 081301. DOI: 10.1103/PhysRevD.97.081301. arXiv: 1705.04750 [astro-ph.HE].

[504] Irene Tamborra and Kohta Murase. "Neutrinos from Supernovae". In: *Space Sci. Rev.* 214.1 (2018), p. 31. DOI: 10.1007/s11214-018-0468-7.

[505] Ke Fang. "High-Energy Neutrino Signatures of Newborn Pulsars In the Local Universe". In: *JCAP* 06 (2015), p. 004. DOI: 10.1088/1475-7516/2015/06/004. arXiv: 1411.2174 [astro-ph.HE].

[506] Xiang-Yu Wang et al. "High-energy Cosmic Rays and Neutrinos from Semi-relativistic Hypernovae". In: *Phys. Rev. D* 76 (2007), p. 083009. DOI: 10.1103/PhysRevD.76.083009. arXiv: 0705.0027 [astro-ph].

[507] Kohta Murase et al. "High Energy Neutrinos and Cosmic-Rays from Low-Luminosity Gamma-Ray Bursts?" In: *Astrophys. J. Lett.* 651 (2006), p. L5. DOI: 10.1086/509323. arXiv: astro-ph/0607104.

[508] Nicholas Senno, Kohta Murase, and Peter Mészáros. "Choked Jets and Low-Luminosity Gamma-Ray Bursts as Hidden Neutrino Sources". In: *Phys. Rev. D* 93.8 (2016), p. 083003. DOI: 10.1103/PhysRevD.93.083003. arXiv: 1512.08513 [astro-ph.HE].

[509] Bohdan Paczynski and Guang-Hua Xu. "Neutrino bursts from gamma-ray bursts". In: *Astrophys. J.* 427 (1994), p. 708. DOI: 10.1086/174178.

[510] Mauricio Bustamante et al. "Neutrino and cosmic-ray emission from multiple internal shocks in gamma-ray bursts". In: *Nature Commun.* 6 (2015), p. 6783. DOI: 10.1038/ncomms7783. arXiv: 1409.2874 [astro-ph.HE].

[511] Tetyana Pitik, Irene Tamborra, and Maria Petropoulou. "Neutrino signal dependence on gamma-ray burst emission mechanism". In: *JCAP* 05 (2021), p. 034. DOI: 10.1088/1475-7516/2021/05/034. arXiv: 2102.02223 [astro-ph.HE].

[512] Glennys R. Farrar and Andrei Gruzinov. "Giant AGN Flares and Cosmic Ray Bursts". In: *Astrophys. J.* 693 (2009), p. 329. DOI: 10.1088/0004-637X/693/1/329. arXiv: 0802.1074 [astro-ph].

[513] Xiang-Yu Wang et al. "Probing the tidal disruption flares of massive black holes with high-energy neutrinos". In: *Phys. Rev. D* 84 (2011), p. 081301. DOI: 10.1103/PhysRevD.84.081301. arXiv: 1106.2426 [astro-ph.HE].

[514] Lixin Dai and Ke Fang. "Can tidal disruption events produce the IceCube neutrinos?" In: *Mon. Not. Roy. Astron. Soc.* 469.2 (2017), p. 1354. DOI: 10.1093/mnras/stx863. arXiv: 1612.00011 [astro-ph.HE].

[515] Cecilia Lunardini and Walter Winter. "High Energy Neutrinos from the Tidal Disruption of Stars". In: *Phys. Rev. D* 95.12 (2017), p. 123001. DOI: 10.1103/PhysRevD.95.123001. arXiv: 1612.03160 [astro-ph.HE].

[516] B. Theodore Zhang et al. "High-energy cosmic ray nuclei from tidal disruption events: Origin, survival, and implications". In: *Phys. Rev. D* 96.6 (2017). [Addendum: Phys. Rev. D 96, 069902 (2017)], p. 063007. DOI: 10.1103/PhysRevD.96.063007. arXiv: 1706.00391 [astro-ph.HE].

[517] Claire Guépin et al. "Ultra-High Energy Cosmic Rays and Neutrinos from Tidal Disruptions by Massive Black Holes". In: *Astron. Astrophys.* 616 (2018). [Erratum: Astron. Astrophys. 636, C3 (2020)], A179. DOI: 10.1051/0004-6361/201732392. arXiv: 1711.11274 [astro-ph.HE].

[518] Walter Winter and Cecilia Lunardini. "A concordance scenario for the observed neutrino from a tidal disruption event". In: *Nature Astron.* 5.5 (2021), p. 472. DOI: 10.1038/s41550-021-01343-x. arXiv: 2005.06097 [astro-ph.HE].

[519] Kohta Murase and Masataka Fukugita. "Energetics of High-Energy Cosmic Radiations". In: *Phys. Rev. D* 99.6 (2019), p. 063012. DOI: 10.1103/PhysRevD.99.063012. arXiv: 1806.04194 [astro-ph.HE].

[520] Luis A. Anchordoqui et al. "Performance and science reach of the Probe of Extreme Multimessenger Astrophysics for ultrahigh-energy particles". In: *Phys. Rev. D* 101.2 (2020), p. 023012. DOI: 10.1103/PhysRevD.101.023012. arXiv: 1907.03694 [astro-ph.HE].

[521] Cosmin Deaconu. "Searches for Ultra-High Energy Neutrinos with ANITA". In: *PoS* ICRC2019 (2020), p. 867. DOI: 10.22323/1.358.0867. arXiv: 1908.00923 [astro-ph.HE].

[522] Rasha Abbasi et al. "Indirect search for dark matter in the Galactic Centre with IceCube". In: *PoS* ICRC2021 (July 2021), p. 524. DOI: 10.22323/1.395.0524. arXiv: 2107.11224 [astro-ph.HE].

[523] Darko Veberic, ed. *The Pierre Auger Observatory: Contributions to the 35th International Cosmic Ray Conference (ICRC 2017)*. Aug. 2017. arXiv: 1708.06592 [astro-ph.HE].

[524] Carlos A. Argüelles et al. "Dark Matter decay to neutrinos". In: (Oct. 2022). arXiv: 2210.01303 [hep-ph].

[525] J. H. Oort. "The force exerted by the stellar system in the direction perpendicular to the galactic plane and some related problems". In: *Bull. Astron. Inst. Netherlands* 6 (Aug. 1932), p. 249. URL: https://ui.adsabs.harvard.edu/abs/1932BAN.....6..249O.

[526] F. Zwicky. "Die Rotverschiebung von extragalaktischen Nebeln". In: *Helv. Phys. Acta* 6 (1933). [Republished in: Gen. Rel. Grav. 41, 207 (2009)], pp. 110–127. DOI: 10.1007/s10714-008-0707-4.

[527] F. Zwicky. "On the Masses of Nebulae and of Clusters of Nebulae". In: *Astrophys. J.* 86 (1937), pp. 217–246. DOI: 10.1086/143864.

[528] V. C. Rubin et al. "Rotation velocities of 16 SA galaxies and a comparison of Sa, Sb, and SC rotation properties". In: *Astrophys. J.* 289 (1985), p. 81. DOI: 10.1086/162866.

[529] K. G. Begeman, A. H. Broeils, and R. H. Sanders. "Extended rotation curves of spiral galaxies: Dark haloes and modified dynamics". In: *Mon. Not. Roy. Astron. Soc.* 249 (1991), p. 523. DOI: 10.1093/mnras/249.3.523.

[530] Anton G. Bergmann, Vahe Petrosian, and Roger Lynds. "Gravitational Lens Models of Arcs in Clusters". In: *Astrophys. J.* 350 (Feb. 1990), p. 23. DOI: 10.1086/168359.

[531] Douglas Clowe et al. "A direct empirical proof of the existence of dark matter". In: *Astrophys. J. Lett.* 648 (2006), pp. L109–L113. DOI: 10.1086/508162. arXiv: astro-ph/0608407.

[532] George F. Smoot et al. "Structure in the COBE differential microwave radiometer first year maps". In: *Astrophys. J. Lett.* 396 (Sept. 1992), pp. L1–L5. DOI: 10.1086/186504.

[533] N. Jarosik et al. "Seven-Year Wilkinson Microwave Anisotropy Probe (WMAP) Observations: Sky Maps, Systematic Errors, and Basic Results". In: *Astrophys. J. Suppl.* 192 (2011), p. 14. DOI: 10.1088/0067-0049/192/2/14. arXiv: 1001.4744 [astro-ph.CO].

[534] Will J. Percival et al. "Baryon Acoustic Oscillations in the Sloan Digital Sky Survey Data Release 7 Galaxy Sample". In: *Mon. Not. Roy. Astron. Soc.* 401 (2010), pp. 2148–2168. DOI: 10.1111/j.1365-2966.2009.15812.x. arXiv: 0907.1660 [astro-ph.CO].

[535] Tiziana Di Matteo et al. "Direct cosmological simulations of the growth of black holes and galaxies". In: *Astrophys. J.* 676 (2008), p. 33. DOI: 10.1086/524921. arXiv: 0705.2269 [astro-ph].

[536] Michael Boylan-Kolchin et al. "Resolving Cosmic Structure Formation with the Millennium-II Simulation". In: *Mon. Not. Roy. Astron. Soc.* 398 (2009), p. 1150. DOI: 10.1111/j.1365-2966.2009.15191.x. arXiv: 0903.3041 [astro-ph.CO].

[537] Gianfranco Bertone and Dan Hooper. "History of dark matter". In: *Rev. Mod. Phys.* 90.4 (2018), p. 045002. DOI: 10.1103/RevModPhys.90.045002. arXiv: 1605.04909 [astro-ph.CO].

[538] Edward W. Kolb and Michael S. Turner. *The Early Universe*. Vol. 69. 1990. ISBN: 978-0-201-62674-2. DOI: 10.1201/9780429492860.

[539] K. Griest and M. Kamionkowski. "Supersymmetric dark matter". In: *Phys. Rept.* 333 (2000), pp. 167–182. DOI: 10.1016/S0370-1573(00)00021-1.

[540] C. B. Adams et al. "Axion Dark Matter". In: *Snowmass 2021*. Mar. 2022. arXiv: 2203.14923 [hep-ex].

[541] I. Z. Rothstein, K. S. Babu, and D. Seckel. "Planck scale symmetry breaking and majoron physics". In: *Nucl. Phys. B* 403 (1993), pp. 725–748. DOI: 10.1016/0550-3213(93)90368-Y. arXiv: hep-ph/9301213.

[542] V. Berezinsky and J. W. F. Valle. "The KeV Majoron as a dark matter particle". In: *Phys. Lett. B* 318 (1993), pp. 360–366. DOI: 10.1016/0370-2693(93)90140-D. arXiv: hep-ph/9309214.

[543] Tim Brune and Heinrich Päs. "Massive Majorons and constraints on the Majoron-neutrino coupling". In: *Phys. Rev. D* 99.9 (2019), p. 096005. DOI: 10.1103/PhysRevD.99.096005. arXiv: 1808.08158 [hep-ph].

[544] A. Boyarsky et al. "Sterile Neutrino Dark Matter". In: *Prog. Part. Nucl. Phys.* 104 (2019), pp. 1–45. DOI: 10.1016/j.ppnp.2018.07.004. arXiv: 1807.07938 [hep-ph].

[545] Bernard Carr and Florian Kuhnel. "Primordial black holes as dark matter candidates". In: *SciPost Phys. Lect. Notes* 48 (2022), p. 1. DOI: 10.21468/SciPostPhysLectNotes.48. arXiv: 2110.02821 [astro-ph.CO].

[546] Kim Griest and Marc Kamionkowski. "Unitarity Limits on the Mass and Radius of Dark Matter Particles". In: *Phys. Rev. Lett.* 64 (1990), p. 615. DOI: 10.1103/PhysRevLett.64.615.

[547] Juri Smirnov and John F. Beacom. "TeV-Scale Thermal WIMPs: Unitarity and its Consequences". In: *Phys. Rev. D* 100.4 (2019), p. 043029. DOI: 10.1103/PhysRevD.100.043029. arXiv: 1904.11503 [hep-ph].

[548] Marco Chianese et al. "Heavy decaying dark matter at future neutrino radio telescopes". In: *JCAP* 05 (2021), p. 074. DOI: 10.1088/1475-7516/2021/05/074. arXiv: 2103.03254 [hep-ph].

[549] Arman Esmaili and Pasquale Dario Serpico. "Are IceCube neutrinos unveiling PeV-scale decaying dark matter?" In: *JCAP* 11 (2013), p. 054. DOI: 10.1088/1475-7516/2013/11/054. arXiv: 1308.1105 [hep-ph].

[550] Brian Feldstein et al. "Neutrinos at IceCube from Heavy Decaying Dark Matter". In: *Phys. Rev. D* 88.1 (2013), p. 015004. DOI: 10.1103/PhysRevD.88.015004. arXiv: 1303.7320 [hep-ph].

[551] Yang Bai, Ran Lu, and Jordi Salvadó. "Geometric Compatibility of IceCube TeV-PeV Neutrino Excess and its Galactic Dark Matter Origin". In: *JHEP* 01 (2016), p. 161. DOI: 10.1007/JHEP01(2016)161. arXiv: 1311.5864 [hep-ph].

[552] Yohei Ema, Ryusuke Jinno, and Takeo Moroi. "Cosmic-Ray Neutrinos from the Decay of Long-Lived Particle and the Recent IceCube Result". In: *Phys. Lett. B* 733 (2014), pp. 120–125. DOI: 10.1016/j.physletb.2014.04.021. arXiv: 1312.3501 [hep-ph].

[553] Arman Esmaili, Sin Kyu Kang, and Pasquale Dario Serpico. "IceCube events and decaying dark matter: hints and constraints". In: *JCAP* 12 (2014), p. 054. DOI: 10.1088/1475-7516/2014/12/054. arXiv: 1410.5979 [hep-ph].

[554] Atri Bhattacharya, Mary Hall Reno, and Ina Sarcevic. "Reconciling neutrino flux from heavy dark matter decay and recent events at IceCube". In: *JHEP* 06 (2014), p. 110. DOI: 10.1007/JHEP06(2014)110. arXiv: 1403.1862 [hep-ph].

[555] Marco Chianese et al. "Low energy IceCube data and a possible Dark Matter related excess". In: *Phys. Lett. B* 757 (2016), pp. 251–256. DOI: 10.1016/j.physletb.2016.03.084. arXiv: 1601.02934 [hep-ph].

[556] M. Chianese, G. Miele, and S. Morisi. "Dark Matter interpretation of low energy IceCube MESE excess". In: *JCAP* 01 (2017), p. 007. DOI: 10.1088/1475-7516/2017/01/007. arXiv: 1610.04612 [hep-ph].

[557] Marco Chianese, Gennaro Miele, and Stefano Morisi. "Interpreting IceCube 6-year HESE data as an evidence for hundred TeV decaying Dark Matter". In: *Phys. Lett. B* 773 (2017), pp. 591–595. DOI: 10.1016/j.physletb.2017.09.016. arXiv: 1707.05241 [hep-ph].

[558] Atri Bhattacharya et al. "Update on decaying and annihilating heavy dark matter with the 6-year IceCube HESE data". In: *JCAP* 05 (2019), p. 051. DOI: 10.1088/1475-7516/2019/05/051. arXiv: 1903.12623 [hep-ph].

[559] Marco Chianese et al. "Decaying dark matter at IceCube and its signature on High Energy gamma experiments". In: *JCAP* 11 (2019), p. 046. DOI: 10.1088/1475-7516/2019/11/046. arXiv: 1907.11222 [hep-ph].

[560] Kohta Murase, Dafne Guetta, and Markus Ahlers. "Hidden Cosmic-Ray Accelerators as an Origin of TeV-PeV Cosmic Neutrinos". In: *Phys. Rev. Lett.* 116.7 (2016), p. 071101. DOI: 10.1103/PhysRevLett.116.071101. arXiv: 1509.00805 [astro-ph.HE].

[561] Antonio Capanema, Arman Esmaili, and Kohta Murase. "New constraints on the origin of medium-energy neutrinos observed by IceCube". In: *Phys. Rev. D* 101.10 (2020), p. 103012. DOI: 10.1103/PhysRevD.101.103012. arXiv: 2002.07192 [hep-ph].

[562] Antonio Capanema, Arman Esmaili, and Pasquale Dario Serpico. "Where do IceCube neutrinos come from? Hints from the diffuse gamma-ray flux". In: *JCAP* 02 (2021), p. 037. DOI: 10.1088/1475-7516/2021/02/037. arXiv: 2007.07911 [hep-ph].

[563] R. Abbasi et al. "Searches for Connections between Dark Matter and High-Energy Neutrinos with IceCube". In: (May 2022). arXiv: 2205.12950 [hep-ex].

[564] Zhen Cao et al. "Constraints on Heavy Decaying Dark Matter from 570 Days of LHAASO Observations". In: *Phys. Rev. Lett.* 129.26 (2022), p. 261103. DOI: 10.1103/PhysRevLett.129.261103. arXiv: 2210.15989 [astro-ph.HE].

[565] R. Alves Batista et al. "EuCAPT White Paper: Opportunities and Challenges for Theoretical Astroparticle Physics in the Next Decade". In: (Oct. 2021). arXiv: 2110.10074 [astro-ph.HE].

[566] Jeffrey M. Berryman et al. "Neutrino self-interactions: A white paper". In: *Phys. Dark Univ.* 42 (2023), p. 101267. DOI: 10.1016/j.dark.2023.101267. arXiv: 2203.01955 [hep-ph].

[567] Claire Guépin et al. "Indirect dark matter searches at ultrahigh energy neutrino detectors". In: *Phys. Rev. D* 104.8 (2021), p. 083002. DOI: 10.1103/PhysRevD.104.083002. arXiv: 2106.04446 [hep-ph].

[568] Markus Ahlers and Kohta Murase. "Probing the Galactic Origin of the IceCube Excess with Gamma-Rays". In: *Phys. Rev. D* 90.2 (2014), p. 023010. DOI: 10.1103/PhysRevD.90.023010. arXiv: 1309.4077 [astro-ph.HE].

[569] Markus Ahlers et al. "Galactic neutrinos in the TeV to PeV range". In: *Phys. Rev. D* 93.1 (2016), p. 013009. DOI: 10.1103/PhysRevD.93.013009. arXiv: 1505.03156 [hep-ph].

[570] Andrii Neronov and Dmitry V. Semikoz. "Evidence for the Galactic contribution to the IceCube astrophysical neutrino flux". In: *Astropart. Phys.* 75 (2016), pp. 60–63. DOI: 10.1016/j.astropartphys.2015.11.002. arXiv: 1509.03522 [astro-ph.HE].

[571] J. M. Carceller and M. Masip. "Diffuse flux of galactic neutrinos and gamma rays". In: *JCAP* 03 (2017), p. 013. DOI: 10.1088/1475-7516/2017/03/013. arXiv: 1610.02552 [astro-ph.HE].

[572] Andrii Neronov and Dmitry Semikoz. "Galactic and extragalactic contributions to the astrophysical muon neutrino signal". In: *Phys. Rev. D* 93.12 (2016), p. 123002. DOI: 10.1103/PhysRevD.93.123002. arXiv: 1603.06733 [astro-ph.HE].

[573] Peter B. Denton, Danny Marfatia, and Thomas J. Weiler. "The Galactic Contribution to IceCube's Astrophysical Neutrino Flux". In: *JCAP* 08 (2017), p. 033. DOI: 10.1088/1475-7516/2017/08/033. arXiv: 1703.09721 [astro-ph.HE].

[574] M. G. Aartsen et al. "Search for PeV Gamma-Ray Emission from the Southern Hemisphere with 5 Years of Data from the IceCube Observatory". In: *Astrophys. J.* 891 (Aug. 2019), p. 9. DOI: 10.3847/1538-4357/ab6d67. arXiv: 1908.09918 [astro-ph.HE].

[575] Ali Kheirandish. "Identifying Galactic sources of high-energy neutrinos". In: *Astrophys. Space Sci.* 365.6 (2020), p. 108. DOI: 10.1007/s10509-020-03816-3. arXiv: 2006.16087 [astro-ph.HE].

[576] Gregory S. Vance et al. "Searching for a Galactic component in the IceCube track-like neutrino events". In: (Aug. 2021). arXiv: 2108.01805 [astro-ph.HE].

[577] Y. Y. Kovalev, A. V. Plavin, and S. V. Troitsky. "Galactic Contribution to the High-energy Neutrino Flux Found in Track-like IceCube Events". In: *Astrophys. J. Lett.* 940.2 (2022), p. L41. DOI: 10.3847/2041-8213/aca1ae. arXiv: 2208.08423 [astro-ph.HE].

[578] Takahiro Sudoh and John F. Beacom. "Where are Milky Way's hadronic PeVatrons?" In: *Phys. Rev. D* 107.4 (2023), p. 043002. DOI: 10.1103/PhysRevD.107.043002. arXiv: 2209.03970 [astro-ph.HE].

[579] Pedro De la Torre Luque et al. "Prospects for detection of a galactic diffuse neutrino flux". In: *Front. Astron. Space Sci.* 9 (2022), p. 1041838. DOI: 10.3389/fspas.2022.1041838. arXiv: 2209.10011 [astro-ph.HE].

[580] Takahiro Sudoh and John F. Beacom. "Identifying Extended PeVatron Sources via Neutrino Shower Detection". In: (May 2023). arXiv: 2305.07043 [astro-ph.HE].

[581] Annika Rudolph et al. "Multi-messenger Model for the Prompt Emission from GRB 221009A". In: *Astrophys. J. Lett.* 944.2 (2023), p. L34. DOI: 10.3847/2041-8213/acb6d7. arXiv: 2212.00766 [astro-ph.HE].

[582] Annika Rudolph et al. "Multicollision Internal Shock Lepto-hadronic Models for Energetic Gamma-Ray Bursts (GRBs)". In: *Astrophys. J.* 950.1 (2023), p. 28. DOI: 10.3847/1538-4357/acc861. arXiv: 2212.00765 [astro-ph.HE].

[583] Walter Winter and Cecilia Lunardini. "Time-dependent interpretation of the neutrino emission from Tidal Disruption Events". In: *Astrophys. J.* 948.1 (May 2022), p. 42. DOI: 10.3847/1538-4357/acbe9e. arXiv: 2205.11538 [astro-ph.HE].

[584] Marco Chianese et al. "Constraints on heavy decaying dark matter with current gamma-ray measurements". In: *JCAP* 11 (2021), p. 035. DOI: 10.1088/1475-7516/2021/11/035. arXiv: 2108.01678 [hep-ph].

[585] Julio F. Navarro, Carlos S. Frenk, and Simon D. M. White. "The Structure of cold dark matter halos". In: *Astrophys. J.* 462 (1996), pp. 563–575. DOI: 10.1086/177173. arXiv: astro-ph/9508025.

[586] J. Einasto. "Kinematics and dynamics of stellar systems". In: *Trudy Astrofizicheskogo Instituta Alma-Ata* 5 (1965), pp. 87–100.

[587] A. Burkert. "The Structure of dark matter halos in dwarf galaxies". In: *Astrophys. J. Lett.* 447 (1995), p. L25. DOI: 10.1086/309560. arXiv: astro-ph/9504041.

[588] Marco Cirelli et al. "PPPC 4 DM ID: A Poor Particle Physicist Cookbook for Dark Matter Indirect Detection". In: *JCAP* 03 (2011). [Erratum: JCAP 10, E01 (2012)], p. 051. DOI: 10.1088/1475-7516/2012/10/E01. arXiv: 1012.4515 [hep-ph].

[589] Craig J. Hogan and Julianne J. Dalcanton. "New dark matter physics: clues from halo structure". In: *Phys. Rev. D* 62 (2000), p. 063511. DOI: 10.1103/PhysRevD.62.063511. arXiv: astro-ph/0002330.

[590] Paul Bode, Jeremiah P. Ostriker, and Neil Turok. "Halo formation in warm dark matter models". In: *Astrophys. J.* 556 (2001), pp. 93–107. DOI: 10.1086/321541. arXiv: astro-ph/0010389.

[591] Saikat Das, Kohta Murase, and Toshihiro Fujii. "Revisiting ultrahigh-energy constraints on decaying superheavy dark matter". In: *Phys. Rev. D* 107.10 (2023), p. 103013. DOI: 10.1103/PhysRevD.107.103013. arXiv: 2302.02993 [astro-ph.HE].

[592] Christian W. Bauer, Nicholas L. Rodd, and Bryan R. Webber. "Dark matter spectra from the electroweak to the Planck scale". In: *JHEP* 06 (2021), p. 121. DOI: 10.1007/JHEP06(2021)121. arXiv: 2007.15001 [hep-ph].

[593] Paolo Ciafaloni et al. "Weak Corrections are Relevant for Dark Matter Indirect Detection". In: *JCAP* 03 (2011), p. 019. DOI: 10.1088/1475-7516/2011/03/019. arXiv: 1009.0224 [hep-ph].

[594] Claire Guépin, Kumiko Kotera, and Foteini Oikonomou. "High-energy neutrino transients and the future of multi-messenger astronomy". In: *Nature Rev. Phys.* 4.11 (2022), pp. 697–712. DOI: 10.1038/s42254-022-00504-9. arXiv: 2207.12205 [astro-ph.HE].

[595] Glen Cowan et al. "Asymptotic formulae for likelihood-based tests of new physics". In: *Eur. Phys. J. C* 71 (2011). [Erratum: Eur. Phys. J. C 73, 2501 (2013)], p. 1554. DOI: 10.1140/epjc/s10052-011-1554-0. arXiv: 1007.1727 [physics.data-an].

[596] S. S. Wilks. "The Large-Sample Distribution of the Likelihood Ratio for Testing Composite Hypotheses". In: *Annals Math. Statist.* 9.1 (1938), pp. 60–62. DOI: 10.1214/aoms/1177732360.

[597] Iván Esteban et al. http://www.nu-fit.org/. NuFit 5.0. 2020.

[598] Francis Halzen and David Paul Saltzberg. "Tau-neutrino appearance with a 1000 megaparsec baseline". In: *Phys. Rev. Lett.* 81 (1998), p. 4305. DOI: 10.1103/PhysRevLett.81.4305. arXiv: hep-ph/9804354.

[599] Francesco Becattini and Sergio Bottai. "Extreme energy neutrino(tau) propagation through the Earth". In: *Astropart. Phys.* 15 (2001), p. 323. DOI: 10.1016/S0927-6505(00)00155-9. arXiv: astro-ph/0003179.

[600] John F. Beacom, Patrick Crotty, and Edward W. Kolb. "Enhanced Signal of Astrophysical Tau Neutrinos Propagating through Earth". In: *Phys. Rev. D* 66 (2002), p. 021302. DOI: 10.1103/PhysRevD.66.021302. arXiv: astro-ph/0111482.

[601] Sharada Iyer Dutta, Mary Hall Reno, and Ina Sarcevic. "Secondary neutrinos from tau neutrino interactions in earth". In: *Phys. Rev. D* 66 (2002), p. 077302. DOI: 10.1103/PhysRevD.66.077302. arXiv: hep-ph/0207344.

[602] Shigeru Yoshida, Rie Ishibashi, and Hiroko Miyamoto. "Propagation of extremely - high energy leptons in the earth: Implications to their detection by the IceCube Neutrino Telescope". In: *Phys. Rev. D* 69 (2004), p. 103004. DOI: 10.1103/PhysRevD.69.103004. arXiv: astro-ph/0312078.

[603] Edgar Bugaev et al. "Propagation of tau neutrinos and tau leptons through the earth and their detection in underwater / ice neutrino telescopes". In: *Astropart. Phys.* 21 (2004), p. 491. DOI: 10.1016/j.astropartphys.2004.03.002. arXiv: hep-ph/0312295.

[604] Oscar Blanch Bigas et al. "UHE tau neutrino flux regeneration while skimming the Earth". In: *Phys. Rev. D* 78 (2008), p. 063002. DOI: 10.1103/PhysRevD.78.063002. arXiv: 0806.2126 [astro-ph].

[605] Jaime Álvarez-Muñiz et al. "Comprehensive approach to tau-lepton production by high-energy tau neutrinos propagating through the Earth". In: *Phys. Rev. D* 97.2 (2018). [Erratum: Phys. Rev. D 99, 069902 (2019)], p. 023021. DOI: 10.1103/PhysRevD.97.023021. arXiv: 1707.00334 [astro-ph.HE].

[606] M. Ajello et al. “The Origin of the Extragalactic Gamma-Ray Background and Implications for Dark-Matter Annihilation”. In: *Astrophys. J. Lett.* 800.2 (2015), p. L27. DOI: 10.1088/2041-8205/800/2/L27. arXiv: 1501.05301 [astro-ph.HE].

[607] C. S. Kochanek. “Tidal disruption event demographics”. In: *Mon. Not. Roy. Astron. Soc.* 461.1 (2016), p. 371. DOI: 10.1093/mnras/stw1290. arXiv: 1601.06787 [astro-ph.HE].

[608] Simeon Reusch et al. “Candidate Tidal Disruption Event AT2019fdr Coincident with a High-Energy Neutrino”. In: *Phys. Rev. Lett.* 128.22 (2022), p. 221101. DOI: 10.1103/PhysRevLett.128.221101. arXiv: 2111.09390 [astro-ph.HE].